Tile Calorimeter

Technical Design Report

Issue:	1
Revision:	0
Reference:	CERN/LHCC 96-42
Last modified:	15 December 1996
Prepared By:	ATLAS / Tile Calorimeter Collaboration

ATLAS Collaboration

Armenia
Yerevan Physics Institute, Yerevan

Australia
Research Centre for High Energy Physics, Melbourne University, Melbourne
Australian Nuclear Science and Technology Organisation, Sydney
University of Sydney, Sydney

Austria
Institut für Experimentalphysik der Leopold-Franzens-Universität Innsbruck, Innsbruck

Azerbaijan Republic
Institute of Physics, Azerbaijan Academy of Science, Baku

Republic of Belarus
Institute of Physics of the Academy of Science of Belarus, Minsk

Brazil
Universidade Federal do Rio de Janeiro, COPPE/EE/IF, Rio de Janeiro
Instituto de Fisica, Universidade de Sao Paulo, Sao Paulo

Canada
University of Alberta, Edmonton
Department of Physics, University of British Columbia, Vancouver
University of Carleton/C.R.P.P., Carleton
Group of Particle Physics, University of Montreal, Montreal
Department of Physics, University of Toronto, Toronto
TRIUMF, Vancouver
University of Victoria, Victoria

CERN
European Laboratory for Particle Physics (CERN), Geneva

Czech Republic
Academy of Sciences of the Czech Republic, Institute of Physics, Prague
Charles University, Faculty of Mathematics and Physics, Prague
Czech Technical University in Prague, Faculty of Nuclear Sciences and
Physical Engineering, Faculty of Mechanical Engineering, Prague

Denmark
Niels Bohr Institute, University of Copenhagen, Copenhagen

Finland
Helsinki Institute of Physics, Helsinki

France
Laboratoire d'Annecy-le-Vieux de Physique des Particules (LAPP), IN2P3-CNRS, Annecy-le-Vieux
Université Blaise Pascal, IN2P3-CNRS, Clermont-Ferrand
Institut des Sciences Nucléaires de Grenoble, IN2P3-CNRS-Université Joseph Fourier, Grenoble
Centre de Physique des Particules de Marseille, IN2P3-CNRS, Marseille
Laboratoire de l'Accélérateur Linéaire, IN2P3-CNRS, Orsay
LPNHE, Universités de Paris VI et VII, IN2P3-CNRS, Paris
CEA, DSM/DAPNIA, Centre d'Etudes de Saclay, Gif-sur-Yvette

Republic of Georgia
Institute of Physics of the Georgian Academy of Sciences, Tbilisi
Tbilisi State University, Tbilisi

Germany
Physikalisches Institut, Universität Bonn, Bonn
Institut für Physik, Universität Dortmund, Dortmund
Fakultät für Physik, Albert-Ludwigs-Universität, Freiburg
Institut für Hochenergiephysik der Universität Heidelberg, Heidelberg
Institut für Informatik, Friedrich-Schiller-Universität Jena, Jena
Institut für Physik, Johannes-Gutenberg Universität Mainz, Mainz
Lehrstuhl für Informatik V, Universität Mannheim, Mannheim
Sektion Physik, Ludwig-Maximilian-Universität München, München
Max-Planck-Institut für Physik, München
Fachbereich Physik, Universität Siegen, Siegen
Fachbereich Physik, Bergische Universität, Wuppertal

Greece
Athens National Technical University, Athens
Athens University, Athens
Aristotle University of Thessaloniki, Thessaloniki

Israel
Department of Physics, Technion, Haifa
Raymond and Beverly Sackler Faculty of Exact Sciences, School of Physics and Astronomy, Tel-Aviv University, Tel-Aviv
Department of Particle Physics, The Weizmann Institute of Science, Rehovot

Italy
Dipartimento di Fisica dell' Universitá della Calabria e I.N.F.N., Cosenza
Laboratori Nazionali di Frascati dell' I.N.F.N., Frascati
Dipartimento di Fisica dell' Universitá di Genova e I.N.F.N., Genova
Dipartimento di Fisica dell' Universitá di Lecce e I.N.F.N., Lecce
Dipartimento di Fisica dell' Universitá di Milano e I.N.F.N., Milano
Dipartimento di Scienze Fisiche, Universitá di Napoli 'Federico II' e I.N.F.N., Napoli
Dipartimento di Fisica Nucleare e Teorica dell' Universitá di Pavia e I.N.F.N., Pavia
Dipartimento di Fisica dell' Universitá di Pisa e I.N.F.N., Pisa
Dipartimento di Fisica dell' Universitá di Roma 'La Sapienza' e I.N.F.N., Roma
Dipartimento di Fisica dell' Universitá di Roma 'Tor Vergata' e I.N.F.N., Roma
Dipartimento di Fisica dell' Universitá di Roma 'Roma Tre' e I.N.F.N., Roma
Dipartimento di Fisica dell' Universitá di Udine, Gruppo collegato di Udine I.N.F.N. Trieste, Udine

Japan
Department of Information Science, Fukui University, Fukui
Hiroshima Institute of Technology, Hiroshima
Department of Physics, Hiroshima University, Higashi-Hiroshima
KEK, National Laboratory for High Energy Physics, Tsukuba
Department of Physics, Faculty of Science, Kobe University, Kobe
Kyoto University of Education, Kyoto-shi
Naruto University of Education, Naruto-shi
Department of Physics, Faculty of Science, Shinshu University, Matsumoto
International Center for Elementary Particle Physics, University of Tokyo, Tokyo
Physics Department, Tokyo Metropolitan University, Tokyo
Tokyo University of Agriculture and Technology, Department of Applied Physics, Tokyo

Kazakhstan
High-Energy Physics Institute of the Kazakh Academy of Sciences, Almaty

Netherlands
FOM - Institute SAF NIKHEF and University of Amsterdam/NIKHEF, Amsterdam
University of Nijmegen/NIKHEF, Nijmegen

Morocco
Faculté des Sciences Aïn Chock, Université Hassan II, Casablanca, and Université Mohamed V, Rabat

Norway
University of Bergen, Bergen
University of Oslo, Oslo

Poland
Henryk Niewodniczanski Institute of Nuclear Physics, Cracow
Faculty of Physics and Nuclear Techniques of the Academy of Mining and Metallurgy, Cracow

Portugal
Laboratorio de Instrumentação e Física Experimental de Partículas (University of Lisboa, University of Coimbra, University Católica-Figueira da Foz and University Nova de Lisboa), Lisbon

Romania
Institute of Atomic Physics, Bucharest

Russia
Institute for Theoretical and Experimental Physics (ITEP), Moscow
P.N. Lebedev Institute of Physics, Moscow
Moscow Engineering and Physics Institute (MEPhI), Moscow
Moscow State University, Institute of Nuclear Physics, Moscow
Budker Institute of Nuclear Physics (BINP), Novosibirsk
Institute for High Energy Physics (IHEP), Protvino
Petersburg Nuclear Physics Institute (PNPI), Gatchina, St. Petersburg

JINR
Joint Institute for Nuclear Research, Dubna

Slovak Republic
Bratislava University, Bratislava, and Institute of Experimental Physics of the Slovak Academy of Sciences, Kosice

Slovenia
Jozef Stefan Institute and Department of Physics, University of Ljubljana, Ljubljana

Spain
Institut de Física d'Altes Energies (IFAE), Universidad Autónoma de Barcelona, Bellaterra, Barcelona
Physics Department, Universidad Autónoma de Madrid, Madrid
Instituto de Física Corpuscular (IFIC), Centro Mixto Universidad de Valencia - CSIC, Burjassot, and Departamento de Informatica y Electronica, Universidad de Valencia, Burjassot, Valencia

Sweden
Fysika institutionen, Lunds universitet, Lund
Royal Institute of Technology (KTH), Stockholm
University of Stockholm, Stockholm
Uppsala University, Department of Radiation Sciences, Uppsala

Switzerland
Laboratory for High Energy Physics, University of Bern, Bern
Section de Physique, Université de Genève, Geneva

Turkey
Department of Physics, Bogaziçi University, Istanbul

United Kingdom
School of Physics and Space Research, The University of Birmingham, Birmingham
Cavendish Laboratory, Cambridge University, Cambridge
Department of Physics and Astronomy, University of Edinburgh, Edinburgh
Department of Physics and Astronomy, University of Glasgow, Glasgow

School of Physics and Chemistry, Lancaster University, Lancaster
Department of Physics, Oliver Lodge Laboratory, University of Liverpool, Liverpool
Department of Physics, Queen Mary and Westfield College, University of London, London
Department of Physics, Royal Holloway and Bedford New College, University of London, Egham
Department of Physics and Astronomy, University College London, London
Department of Physics and Astronomy, University of Manchester, Manchester
Department of Physics, Oxford University, Oxford
Rutherford Appleton Laboratory, Chilton, Didcot
Department of Physics, University of Sheffield, Sheffield

United States of America
State University of New York at Albany, New York
Argonne National Laboratory, Argonne, Illinois
University of Arizona, Tucson, Arizona
Department of Physics, The University of Texas at Arlington, Arlington, Texas
Lawrence Berkeley Laboratory and University of California, Berkeley, California
Department of Physics, Boston University, Boston, Massachusetts
Brandeis University, Department of Physics, Waltham, Massachusetts
Brookhaven National Laboratory (BNL), Upton, New York
University of Chicago, Enrico Fermi Institute, Chicago, Illinois
Nevis Laboratory, Columbia University, Irvington, New York
Department of Physics, Duke University, Durham, North Carolina
Department of Physics, Hampton University, Virginia
Department of Physics, Harvard University, Cambridge, Massachusetts
Indiana University, Bloomington, Indiana
University of California, Irvine, California
Massachusetts Institute of Technology, Department of Physics, Cambridge, Massachusetts
Michigan State University, Department of Physics and Astronomy, East Lansing, Michigan
University of New Mexico, New Mexico Center for Particle Physics, Albuquerque
Physics Department, Norfolk State University, Virginia
Physics Department, Northern Illinois University, DeKalb, Illinois
Department of Physics and Astronomy, University of Oklahoma
Department of Physics, University of Pennsylvania, Philadelphia, Pennsylvania
University of Pittsburgh, Pittsburgh, Pennsylvania
Department of Physics and Astronomy, University of Rochester, Rochester, New York
Institute for Particle Physics, University of California, Santa Cruz, California
Department of Physics, Southern Methodist University, Dallas, Texas
Tufts University, Medford, Massachusetts
High Energy Physics, University of Illinois, Urbana, Illinois
Department of Physics, Department of Mechanical Engineering, University of Washington, Seattle, Washington
Department of Physics, University of Wisconsin, Madison, Wisconsin

Table Of Contents

Figure 1-i Photograph of the Tile Calorimeter collaboration taken at the end of the September 96 barrel Module 0 beam test in H8 zone.

1 Introduction

The **Tile Calorimeter** is one of the sub-detectors of the **ATLAS** general purpose pp detector designed for the Large Hadron Collider (**LHC**) to be built at **CERN**. It is a large hadronic sampling calorimeter which makes use of steel as the absorber material and scintillating plates read out by wavelength shifting (WLS) fibres as the active medium. The new feature of its design is the orientation of the scintillating tiles which are placed in planes perpendicular to the colliding beams and are staggered in depth. A good sampling homogeneity is obtained when the calorimeter is placed behind an electromagnetic compartment and a coil equivalent to a total of about two interaction lengths (λ) of material. This has been verified with Monte Carlo simulation and has been proven by the test beam results[D-3].

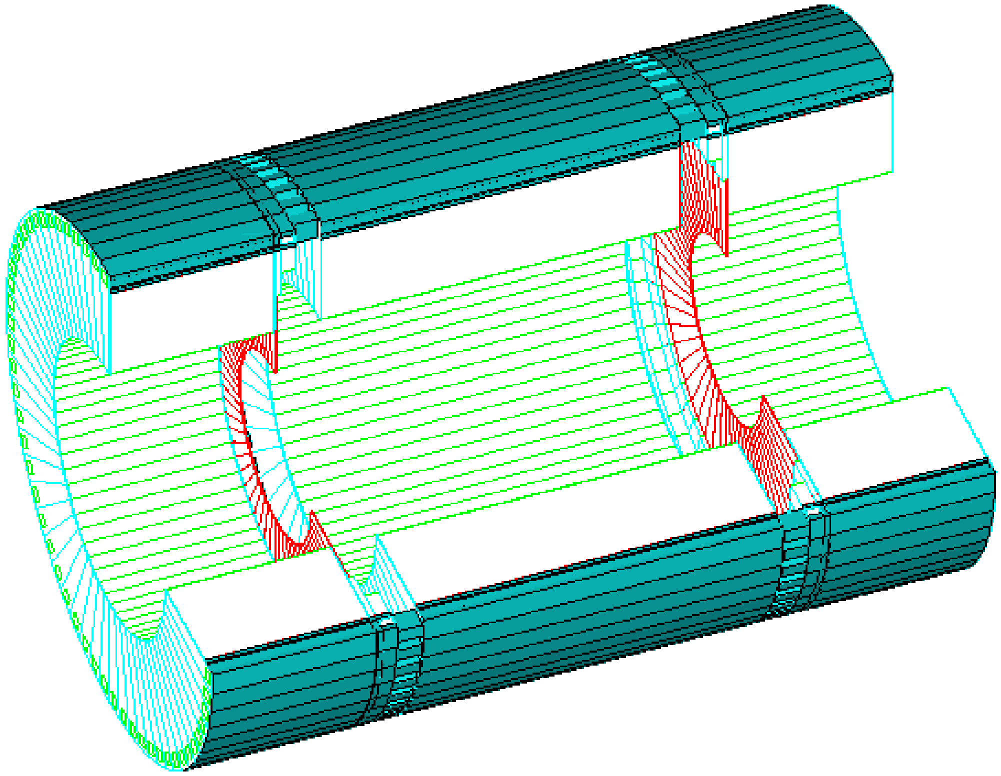

Figure 1-1 Layout view of the Tile Calorimeter barrel and extended barrels

The Tile Calorimeter consists of a cylindrical structure with an inner radius of 2280 mm and an outer radius of 4230 mm. It is subdivided into a 5640 mm long central barrel and two 2910 mm extended barrels as shown in Figure 1-1. The scintillating tiles lie in the r-ϕ plane and span the width of the module in the ϕ direction. WLS fibres running radially collect the light from the tiles along their two open edges. Readout cells are then defined by grouping together a set of fibres into a photomultiplier (PMT), to obtain a three dimensional segmentation. Radially, the calorimeter is segmented into three layers, approximately 1.4, 3.9 and 1.8 interaction lengths thick at η=0; the $\Delta\eta \times \Delta\phi$ segmentation is 0.1×0.1 (0.2×0.1 in the last radial layer, tail catcher). This calorimeter layout has been successfully proven in beam tests of large-sized prototypes as part of the RD34 project[D-5]. During 1996 a full size prototype with final ATLAS specifications (Module 0) was built and tested at the CERN SPS.

1.1 Purpose and scope of the TDR

The purpose of this document is to describe how the Tile Calorimeter detector will be constructed, assembled and installed in ATLAS. The results from the research and development work done within the collaboration since 1993 allowed the construction of the barrel Module 0 in 1996. The Module 0 was made following the scheme and techniques planned for ATLAS, and will be further improved and completed during 1997 with the construction of two extended barrel modules.

During the next years changes in the detector design and assembly scenario are possible, following changes in the overall ATLAS design, particularly in the area of the front-end electronics and the LVL1 trigger architecture. Therefore, the TDR document will have to be periodically updated.

In order to keep the TDR document at a reasonable size it is clear that the various subjects discussed will not be presented here in all the possible details. Accompanying documents for the TDR are the numerous internal notes written by the members of the collaboration. A complete list of all the internal notes can be found in Appendix A.3.1, "Internal Notes" and Appendix A.3.2, "ATLAS/Tile Calorimeter documents".

1.2 Organization of the TDR

The Tile Calorimeter TDR document is organized in 10 chapters, plus an Introduction and three Appendices. In each chapter a particular topic related to the detector is discussed.

General Description
A general description of the detector within the ATLAS environment is given. The basic design requirements as driven by the physics goals are summarized. A short review of the principle of operation is given. A summary of the expected radiation environment and magnetic fields in ATLAS, as well as their effect on the Tile Calorimeter performance, is presented. Finally the amount of material in front of the Tile Calorimeter is shown.

Performance
In this chapter, a summary of the measured detector performance obtained from beam tests of the prototypes and barrel Module 0 is discussed. Data are shown on energy resolution, linearity, and uniformity of the response for single particles. The resolution is found to be within the design goals, with a linearity of about 1%. The response uniformity to pions and muons is shown to be at the few percent level.

In addition, results from a combined test with a Liquid Argon electromagnetic calorimeter prototype are presented. The performance of the detector within the ATLAS environment and its impact on the physics of the experiment are presented in another TDR document (“Combined Calorimetry Performance”).

Muons are clearly separated from the noise, both for the prototype calorimeters and Module 0, whether all radial depths or a single one is considered. This will enable to separate muons from jets. The photoelectron yield is sufficient to ensure a good energy resolution for muon identification.

Finally the results on the cross-calibration of the ^{137}Cs source scan with both muons and pions is presented. It is shown that the Cs calibration is good enough to set the intercalibration between modules.

Mechanics

In this chapter the design parameters, construction details, assembly and installation in ATLAS are presented. The production plan and schedule are discussed in detail.

The specification of the steel for the absorber is given, including a description of the tolerance requirements. Techniques for cutting and stamping plates are discussed. The detailed assembly of sub-modules is given, including plate cleaning, gluing, welding and handling. Design and specifications of the girder, end-plates and front-plates are given.

Details on the module assembly technique (tooling, tolerance envelopes measurements and transportation fixtures) are part of the description.

The calorimeter preassembly and assembly in ATLAS are presented, together with the issues concerning the design of the support structures and of the Liquid Argon cryostat support.

Finally a detailed account of the stresses of the modules is given, including results from finite element modelling. The forces on the structures due to magnetic fields are addressed as well.

Optics

A description of the optics system, including the scintillating tiles and WLS fibres, and of its installation and infrastructure is presented.

Details are given on the tests used to certify the scintillator material used to produce the tiles by injection molding technique. The whole tile package, consisting of the injection moulded tiles, the reflective wrapping and the appropriate masking, is shown to be uniform to within 5%.

Results of tests of the fibres which are being considered are presented. Studies of light transmission, cladding, UV light absorption, stress, and fibre-to-fibre uniformity are summarized. The parameters of the test benches needed for quality control of more than 1100 km of fibres are discussed.

A detailed discussion on the fibre routing geometry is given. The process of fibre installation including their preassembly by means of plastic profiles and their grouping into bundles is described. The gluing operation and the automatised procedure of cutting and polishing the bundles is presented.

Electronics

This chapter is dedicated to the front end electronics, the calibration electronics, the calorimeter trigger system, and the mechanical and environmental aspects of the electronics installation. Recent results from Module 0, which incorporates electronics covering a 16 bit dynamic range with a digital pipeline, are presented.

A detailed description of the phototube selection process is presented. Data are shown for the current baseline photodetector, concerning the gain, the linearity, the insensitivity to magnetic fields and the uniformity. The compact structure of the PMT block is presented, along with a description of the mechanical issues concerning the drawer system.

The front-end electronics is located in the “3-in-1” card, which contains pulse (shaper+compressor) and monitor electronics. Details of the shaper and compressor are given.

The digitizing scheme and pipelines are shown for both the presently tested solution and for several other options under discussion. More R&D is needed before a final technology will be chosen. A description of the ROD (Read Out Driver) is given together with the parameters measured on a first prototype.

The monitoring electronics, designed to read out the calibration source current and the minimum bias current signals, is described. Results from a prototype are shown.

Finally, a description of the power, high and low voltage, is given.

Calibration

In this chapter the calibration systems foreseen for the detector are presented. The calibration systems discussed are based on: a laser, the ^{137}Cs source currents and minimum bias currents.

A description of the laser system is presented, including the system requirements, its components and connections to the module and the operating scenario in ATLAS. The laser control circuitry is also discussed.

A description of the ^{137}Cs source components is given for the two systems being considered - pneumatically and hydraulically driven. Details of the actual ^{137}Cs source capsule design and assembly are shown, as well as the installation and operating scenario in ATLAS.

Simulation estimates of the minimum bias currents are presented. The current expected in the various depth samplings ranges from 6 to 580 nA.

Finally, data from test beam runs with the 1m prototype calorimeters, as well as with Module 0, show the PMT stability and the calibration reproducibility.

Installation, Maintenance and Repair

The installation procedure will start in the year 2003. Issues related to the various operations are discussed. A detailed schedule is given.

Services and cabling logistics are presented. The commissioning of the detector is discussed. The different types of access to the detector are described, specifying the duration of each of them.

Finally, the modules storage and handling requirements prior to and during installation are given.

Safety

The safety issues regarding the detector and its operation are reported in this chapter.

Mechanical safety items which are discussed concern the stresses on the detector and on the detector supports both during assembly and once the structure is completed.

Electrical safety is addressed specifying the voltages and currents associated with each module. The use of halogen-free materials is mentioned.

Finally, the chapter points out the safety issues related to a 5 mCi source, and a 2 W laser.

Tile Calorimeter Test Beam Program

The Tile Calorimeter collaboration plans an extensive program of module calibration, monitoring, and component upgrades, all to be performed at the CERN SPS. The use of a low energy beam at the PS is proposed in conjunction with the Liquid Argon program.

The necessity to calibrate a fraction of the total modules production is discussed, as well as the requirement to understand long term stability. Issues regarding the calorimeter response at very low energies are raised. The importance of testing a complete ATLAS wedge in a projective geometry is stressed.

A detailed schedule until the year 2002 is given. The request includes standalone running in the SPS, an ATLAS wedge run in the SPS, and a PS run together with the Liquid Argon detector.

Project Organization and Management

The structure of the Tile Calorimeter Detector Unit is presented here. A list of the Institutes and persons involved is shown. A detailed list of the responsibilities of each institution is given. The organization within the Tile Calorimeter group itself is discussed.

The time schedules and milestones for the detector construction are shown.

Finally the cost of the detector in terms of investments and manpower is summarized.

Appendices

In the three appendix chapters, a list of all the references and abbreviations used throughout the TDR document can be found, as well as a summary of all the important numbers about the detector. A complete set of Tile Calorimeter notes and publications is listed.

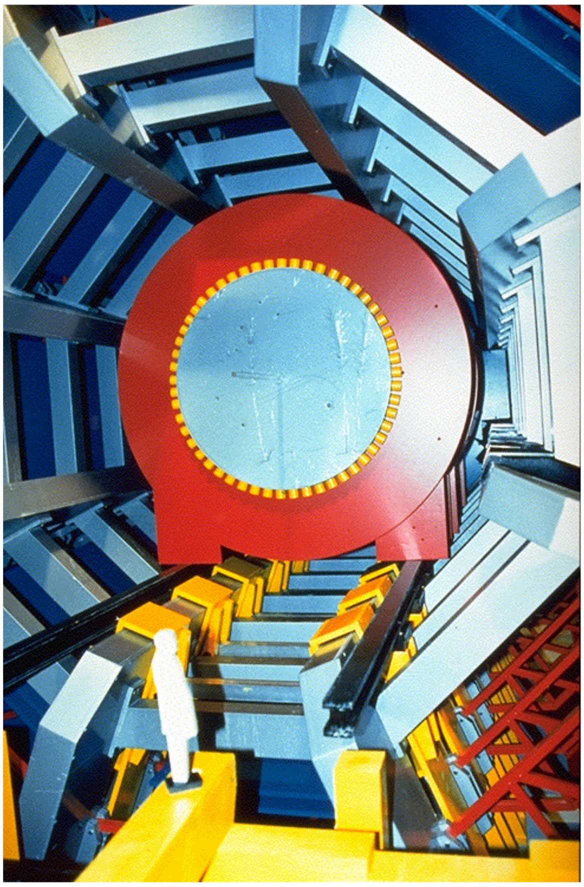

Figure 2-i The ATLAS maquette showing the Tile Calorimeter barrel (shown in red) within the muon toroid coils.

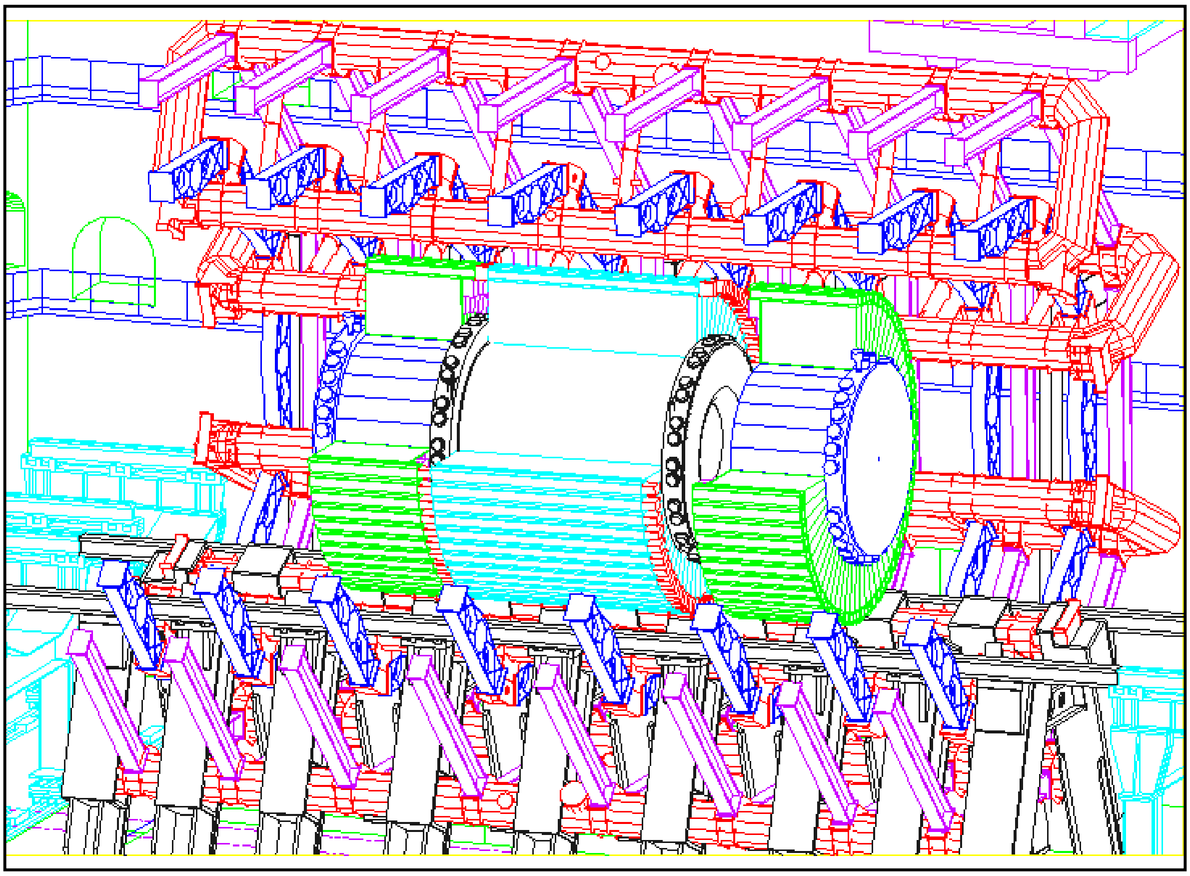

Figure 2-ii Schematic view of the Tile Cal orimeter barrel (blue) and extended barrel (green) in ATLAS.

2 General description

2.1 The principle of the detector

The Tile Calorimeter is a sampling device made out of steel and scintillating tiles, as absorber and active material respectively. It realizes a simple and very well proven idea of calorimetry, particularly suited for the LHC environment. The absorber structure is a laminate of steel plates of various dimensions, connected to a massive structural element referred to as a girder. The highly periodic structure of the system allows the construction of a large detector by assembling smaller sub-modules together. Since the mechanical assembly is completely independent from the optical instrumentation, the design becomes simple and cost effective. Simplicity has been the guideline for the light collection scheme used as well: fibres are coupled radially to the tiles along the outside faces of each module. The laminated structure of the absorber allows for channels in which the fibres run. The use of fibre read-out allows to define a tridimensional cell read-out, creating a projective geometry for triggering and energy reconstruction. A compact electronics read-out is housed in the girder of each module. Finally, the read-out of the two sides of each of the scintillating tiles into two separate photon detectors (in our case photomultipliers, PMTs) guarantees a sufficient light yield and provides a redundancy which might be needed during the long expected period of operation of the ATLAS experiment.

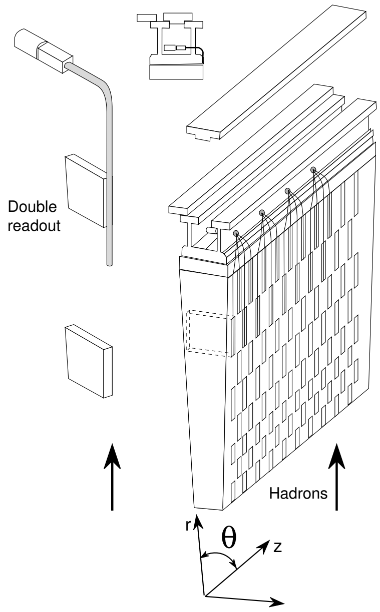

Figure 2-1 The principle of the Tile Calorimeter design.

2.2 The Tile Calorimeter as part of ATLAS

The Tile Calorimeter is designed as one **barrel** and two **extended barrel** hadron parts. The calorimeter consists of a cylindrical structure with inner and outer radius of 2280 and 4230 mm respectively. The barrel part is 5640 mm in length along the beam axis, while each of the extended barrel cylinders is 2910 mm long. Each detector cylinder is built of 64 independent wedges along the azimuthal direction. Between the barrel and the extended barrels there is a gap of about 600 mm, which is needed for the Inner Detector and the Liquid Argon cables, electronics and services. The barrel covers the region $-1.0<\eta<1.0$, and the extended barrels cover the region $0.8<|\eta|<1.7$.

Part of the gap contains an extension of the extended barrel: the Intermediate Tile Calorimeter (**ITC**), which is a structure stepped in order to maximize the volume of active material in this region, while still leaving room for the services and cables. The ITC consists of a calorimeter plug between the region $0.8<|\eta|<1.0$, and, due to severe space constraints, only scintillator between $1.0<|\eta|<1.6$. The scintillators in the region $1.0<|\eta|<1.2$ are called **gap scintillators**, and the

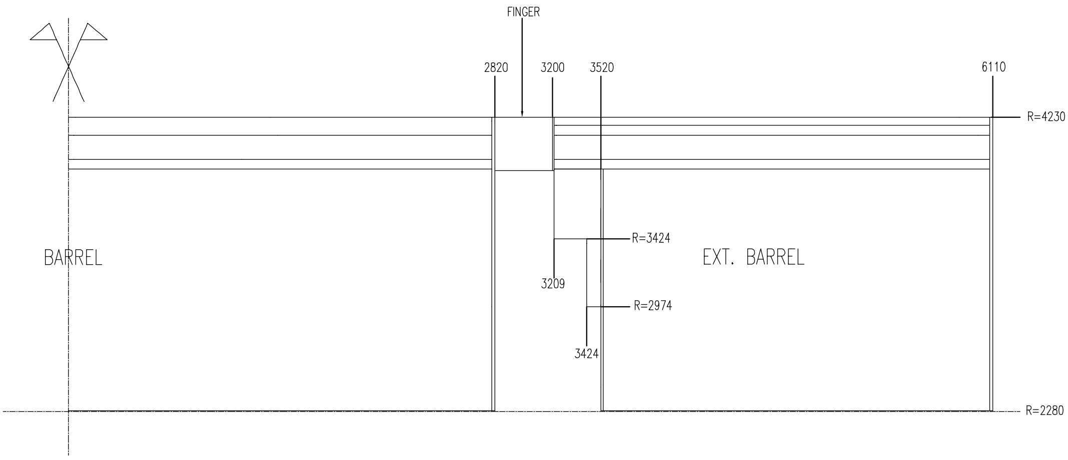

Figure 2-2 Overall schematic view of the Tile Calorimeter detector dimensions.

scintillators between $1.2<|\eta|<1.6$ are called **crack scintillators**. These last ones extend down to the region in between the barrel and the end-cap cryostats. While the plug and the gap scintillators primarily provide hadronic shower sampling, the crack scintillator plays a critical role in sampling electromagnetic showers, where the normal sampling is compromised by the dead material of the cryostat walls and the inner detector cables.

The Tile Calorimeter forms the shell of the inner part of the ATLAS detector. Within its volume, once the barrel and the extended barrels are assembled, all the sub-detectors, except the muon system, will be placed. The massive iron structure is rigid enough to support their weight, with the most important components being the full Liquid Argon cryostat and the solenoid. The structure of the Tile Calorimeter and of all the other sub-detectors inside it is self-supporting and has no mechanical connection with the outside muon system.

The main function of the Tile Calorimeter is to contribute to the energy reconstruction of the jets produced in the pp interactions and, with the addition of the end-cap and forward calorimeters, to provide a good p_T^{miss} measurement. Achieving this at the LHC is not so straightforward. The large center of mass energy (14 TeV) requires good performance over an extremely large dynamic range extending from a few GeV up to several TeV. To resolve events over a background of ~21 minimum bias events per bunch crossing a fast detector response with fine granularity is required. High radiation resistance is needed to cope with the high particle fluxes expected at the design luminosity (10^{34} $cm^{-2}s^{-1}$) over a period of 10 years of operation.

The guidelines for the design of this device are derived from the required overall physics performance which call for an intrinsic resolution for jets of:

$$\frac{\Delta E}{E} = \frac{50\%}{\sqrt{E}} \oplus 3\%, \text{ for} |\eta| < 3$$

with a segmentation of $\Delta\eta \times \Delta\phi = 0.1 \times 0.1$.

The granularity of the Tile Calorimeter is important since the electromagnetic section in front (Liquid Argon accordion calorimeter) has a fine $\Delta\eta \times \Delta\phi$ resolution. The proposed hadronic segmentation for the cells behind the electromagnetic section, will allow an efficient hadron leakage cut, needed for electron and photon identification. A reasonable longitudinal segmentation, especially around the shower max depth, enables one with an appropriate weighting technique to restore, at the level of 1-2%, the linearity of the energy response to hadron showers, intrinsically non-linear because of the non-compensating nature of the calorimeter. At the highest energies expected at the LHC, the resolution of the calorimetry is dominated by the constant term, for which the largest contribution comes from the detector non-linearity and from the calibration. It is estimated that a 5% uncorrected non-linearity can give rise to an increase in the jet cross-section at large p_T, simulating a compositeness scale of 20 TeV at 4 TeV p_T. An attempt is made to keep the constant term below the 2% level.

For the P_T^{miss} measurement a large contribution comes from the overall acceptance of the detector. To improve the detector performance in the region between the barrel and the extended barrels, the ITC plug solution will help. The crack and gap scintillators will further improve the detector performance in the gap region at large η, degraded by the presence of dead material. To avoid the presence of low energy tails in the reconstructed jets energy, the thickness of the active calorimetry is designed to be at least nine interaction lenghts (λ) of material.

To summarise, the basic considerations in the detector design are:

- good energy resolution over the whole η range covered,
- good linearity in response from the few GeV to the TeV range,
- excellent uniformity in both η and ϕ directions
- good hermeticity, with the presence of cracks and dead material reduced as much as possible.

In the following chapters the detector design and characteristics are explained in detail, and it will be shown that the achieved performance meets these guidelines. The results look rather promising up to now and there is confidence that in the difficult environment of the LHC the Tile Calorimeter will perform as required.

2.3 Detector environment

As mentioned above, the Tile Calorimeter encloses the Inner Detector and the Liquid Argon Calorimeter. Due to its position, the detector has to face three basic problems which have implications for its final performance: the level of radiation, the presence of the two magnetic fields from the inner solenoid and the outer toroids, and finally the amount and the $|\eta|$ distribution of the dead material in front of the calorimeter itself.

2.3.1 Radiation environment

The dominant source of radiation in the ATLAS detector comes from the pp interaction rate, which is of the order of 10^9 interaction per second per collision point. Most of the particles centrally produced will be absorbed in the calorimeters, and in particular in the hadron Tile Calorimeter. Other sources of radiation such as beam losses or beam gas interactions are expected to be at least two orders of magnitude smaller.

The background radiation has been evaluated with simulation programs based on the DTUJET[A.33] code for generating pp minimum bias interactions, and with the FLUKA[A.28] code which transports and showers the secondary particles created by DTUJET. When the high energy particles produced at the interaction point enter in the detector material, they begin to shower. If the material is thick (as is the case of calorimeters) the shower will develop until most of the charged particles are absorbed and only neutrons and associated photons remain and most likely escape from the calorimeter volume. These neutrons, photons and electrons (naturally produced from the photons) are produced during the lengthy shower process and form a background with essentially no time structure on the scale of the LHC bunch crossing. The neutrons, and to some smaller extent the photons and electrons, are scattered many times before they are captured, thus giving rise to a relatively uniform and isotropic 'gas' of low-energy background particles. In Figures 2-3 the isodose map of the inner detector and the calorimeters is shown. For

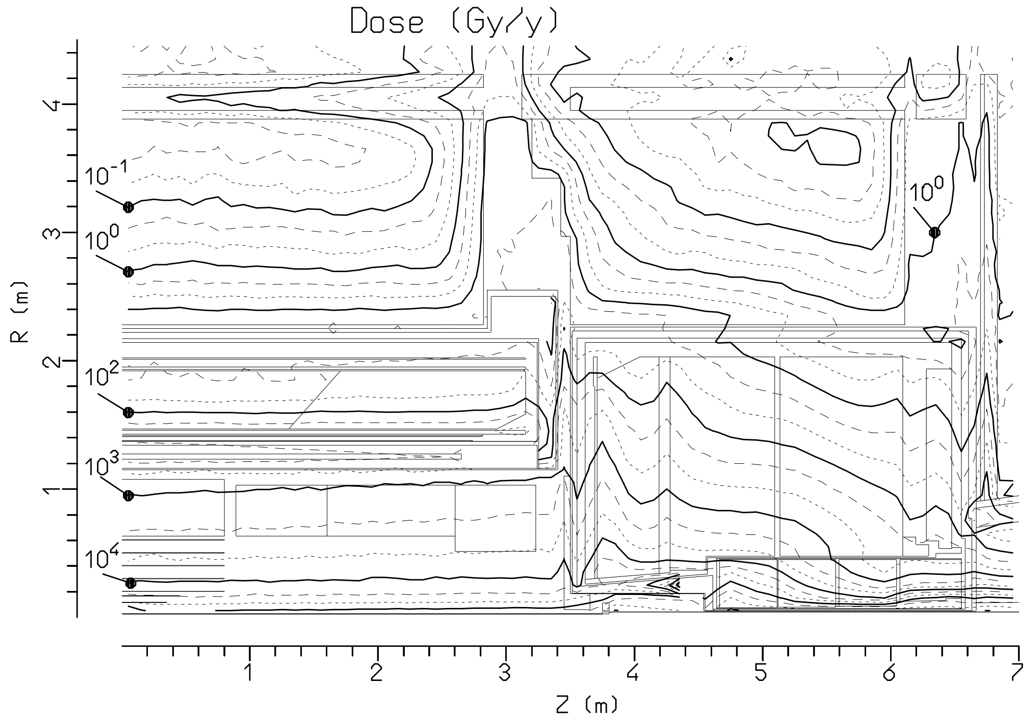

Figure 2-3 Yearly integrated dose (Gy yr^{-1}) in the inner detector and the calorimeters.

most of the volume of the Tile Calorimeter the annual dose rates are below the 20 Gy yr^{-1} line, with a maximum expected peak annual dose of ~38 Gy, at η=1.2. These radiation levels can affect the performance of the calorimeter over the long period of running due to the degradation in the light production and/or transmission in the scintillators and fibres. In addition, although the radiation levels are not high in the girder region, the front-end electronics need to be radiation tolerant in order to avoid malfunctioning and failures during operation.

A large program of irradiation tests has been performed for the active components of the detector. Different tile/fibre setups have been irradiated with doses from 650 Gy to 10kGy, at rates from 15 kGy/h down to 5.5 Gy/h. All the data have been carefully analysed and incorporated in simulation programs for the light collection. For 10 years of high luminosity running at LHC, i.e. an integrated luminosity of 3×10^5 pb^{-1}, a light loss of no more than 5% is expected in the tiles of the first longitudinal sampling, and even less for the others. Using those results and assuming no radiation damage for the Liquid Argon Calorimeter, the energy resolution and jet signal degradation is negligible. Further details on the radiation damage relative to the optics elements can be found in Chapter 5.

2.3.2 Magnetic field

The Tile Calorimeter is the return path for the flux of the solenoid, 70% of which passes through the girder structure, 25% through the active parts of the calorimeter return, and about 2%

through the front-plates. A contribution coming from the stray field of the toroidal system has to be added as well. However, this contribution tends naturally to be absorbed inside the large magnetic mass of the Tile Calorimeter girder structure. A 3D simulation program has been used to calculate the magnetic field at each point of the detector N-7,N-54. The highest field regions are at the outer edges of the barrel and extended barrels, with the maximum value, due to the toroid stray field of ~1.5 T, located at the outer girder radius. The maximum value in the scintillator does not exceed 6 ± 2 mT. Inside the girder region, the maximum varies from 80 mT at R=3.8 m to 200 mT at R=4.2 m. In order to shunt the stray toroidal field of ~120 mT at the drawer ends, a 10 cm thick iron plate is used to close the drawer. This results in a field in the PMT region near the extended barrel edge, not exceeding 20 Gauss. The total field level in the PMTs increases by ~50% for the girder magnetization from both the toroid and the solenoid.

The influence of the magnetic field on the scintillator light yield has been studied: the light output will increase by about ~1% as a consequence of the expected magnetic fieldN-42. This value is well within the accuracy of the cell-to-cell intercalibration. For the PMTs an effective shielding for up to 500 Gauss in any direction has been foreseen. The shielding will be realized by using one soft iron and one μ-metal cylinder. This will limit the signal degradation at the 1% level.

An estimation of the total forces acting on the extended barrel (without girder) gives an axial force of ~ 1 ton/rad towards the interaction point and an outwards radial force of ~ 6 ton/rad N-38. This radial magnetic force represents few% of the weight of the corresponding extended barrel sector. The axial component in the barrel vanishes because of the symmetrical configuration. Any misalignment will cause a net additional axial force.

2.3.3 Detector thickness and materials in front

The calorimeter thickness can affects significantly the overall performance. Simulation studies showed that a thickness of about 11 λ of absorber in the barrel is required to reduce the punch-through and hadron cascades at a level below that of the irreducible flux of prompt or decay muons in the muon spectrometer. On the other hand, fluctuations in the energy lost by muons traversing the calorimeter absorber dominate the muon momentum resolution at low-energy. However, due to the ability of the calorimeter to identify muons, a correction can be applied on an event-by-event basis. Apart from the muon spectrometer performance, the choice of the calorimeter thickness has to guarantee a sufficient containment of the hadronic showers. For many of the physics channels, and in particular for the SUSY particle searches, the E_T^{miss} measurement is rather important. The measurement of E_T^{miss} depends on the acceptance of the calorimeter and its thickness. It has been shown that a total of nine interaction lengths of calorimeter provides sufficient containment of the hadronic showers. Figure 2-4 shows the material budget for the calorimeter system up to the rapidity value of 1.6 The contribution of the various systems and of the dead material in between the calorimeters is visible. In Figure 2-5 the material distribution is shown just for the Tile Calorimeter alone.

Finally, an important contribution to the intrinsic calorimeter performance in terms of jet energy measurement, is the ability to recover the energy losses in the dead material located in front of the calorimeter. The biggest contribution comes from the Liquid Argon cryostat, although its thickness is kept below 2-3 radiation lenghts (X_0). From the test beam runs performed with a combined setup of electromagnetic and hadronic calorimeter prototypes, it turned out that a correction to this energy loss is possible. The correction fully restores the resolution and the linearity of the response.

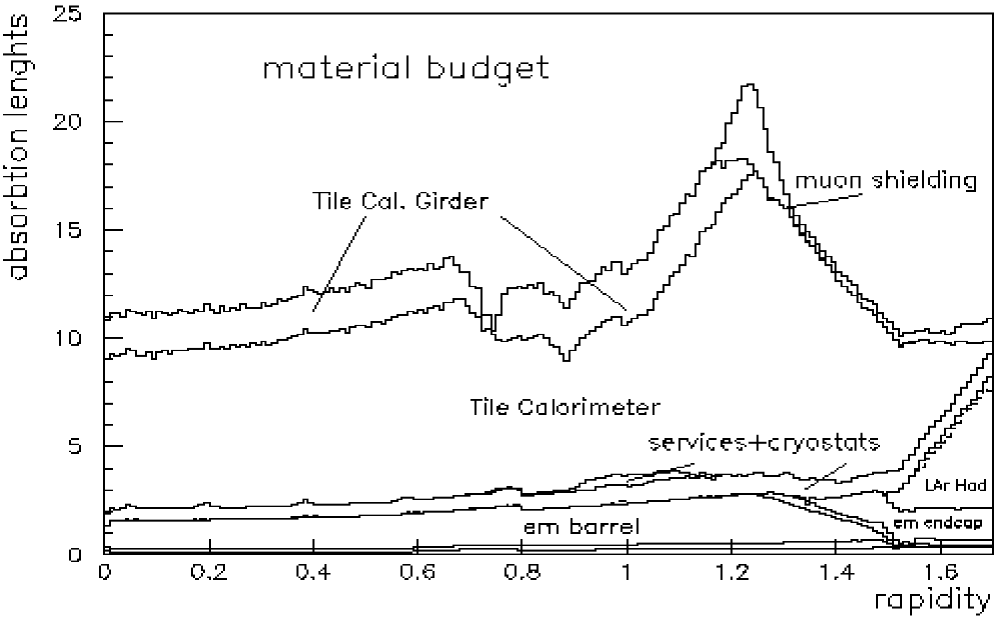

Figure 2-4 Material budget for the ATLAS detector for rapidity lower than 1.6. The contribution of each single detector is visible.

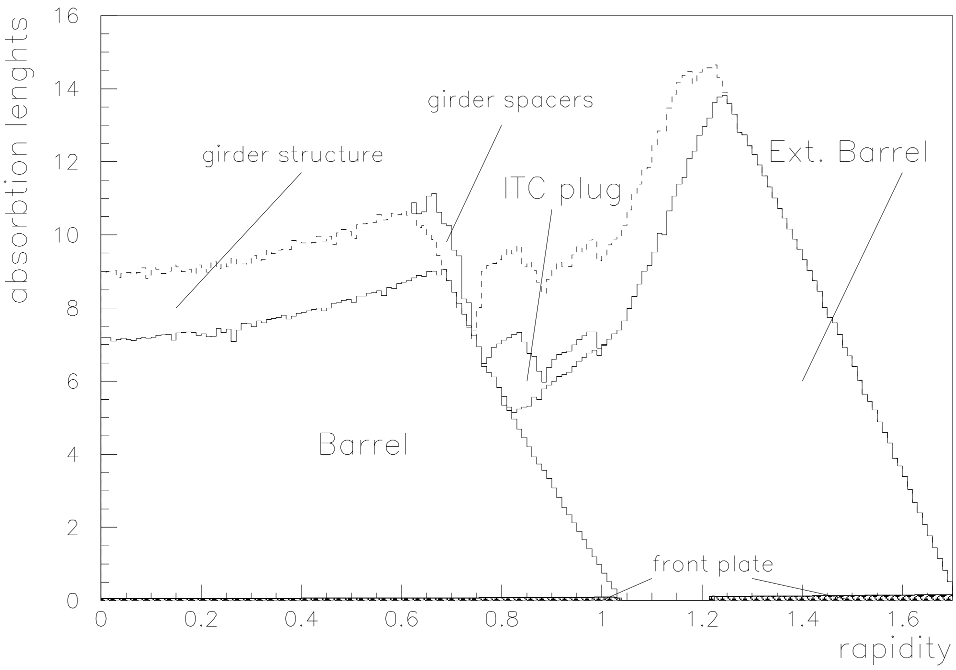

Figure 2-5 Material distribution for the Tile Calorimeter alone, for the barrel, the ext. barrel and the ITC. The labels refer to the various calorimeter active parts.

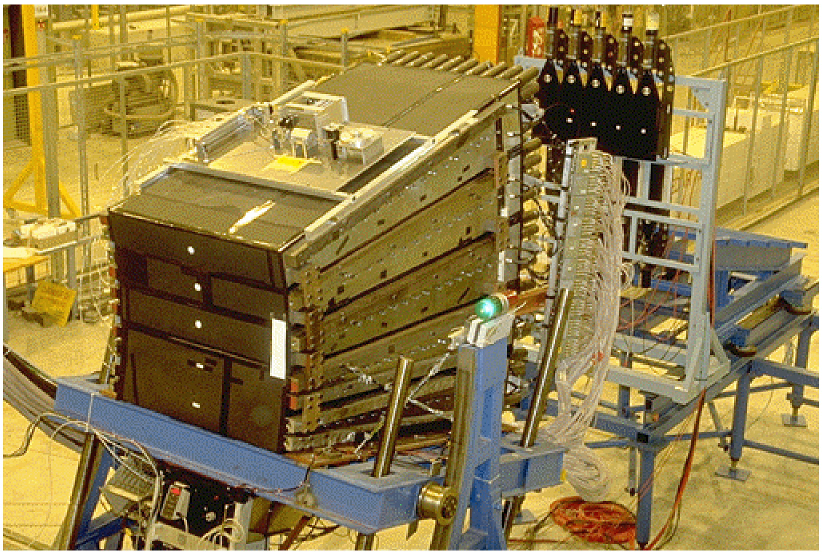

Figure 3-i The five Tile Calorimeter 1m prototype modules installed in the H8 test beam area.

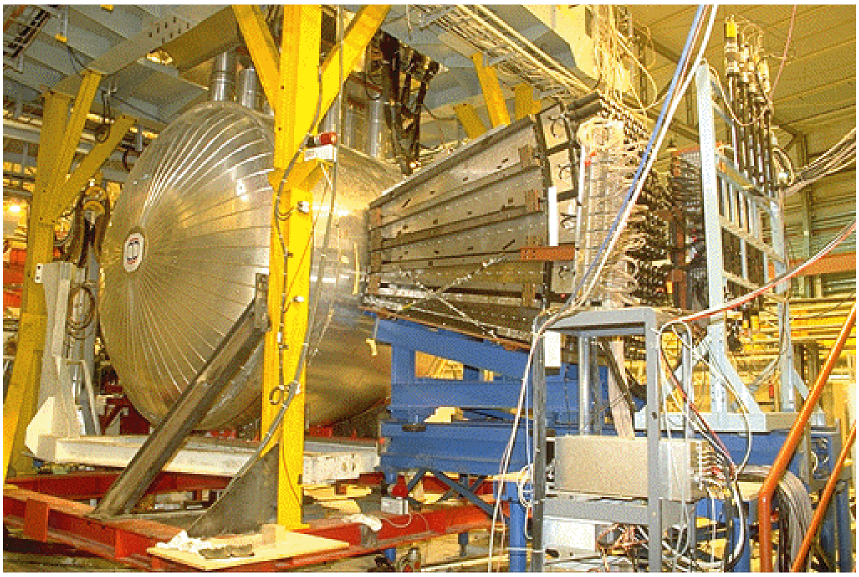

Figure 3-ii The combined Liquid Argon and Tile Calorimeter test beam setup in the H8 test beam.

Figure 3-iii A general view of the Tile Calorimeter Module 0 test beam setup.

3 Test beam performance

3.1 Introduction

The Tile Calorimeter test beam program was started in 1993, supported by the CERN RD program as RD34 [N-6]. Since then it has evolved into a major collaborative ATLAS effort with not only the Tile Calorimeter group, but also in collaboration with the Liquid Argon (LAr) community. To this date, we can categorize the test beam setups as follows:

- Tile Calorimeter standalone measurements with a reduced scale prototype stack of five modules,
- Combined measurements with the LAr electromagnetic prototype and Tile Calorimeter prototype modules,
- Full scale barrel sector (Module 0) in standalone measurements.

Early measurements were performed in the H2 beam line at the SPS at CERN, while for later measurements the H8 beam line was used. The beam lines were instrumented in a standard fashion with one threshold Cherenkov counter used for π/e separation for $E \leq 20$ GeV, a pair of delay-line wire chambers for both x and y coordinates, and scintillators to define a trigger. The scintillators defined a beam spot of around 2-3 cm, while the chambers allowed the reconstruction of the impact point on the calorimeter face to better than ± 1 mm. Data were taken with muons, pions and electrons between 10 and 400 GeV. The momentum bite of the H8 beam, $\Delta p/p$, was always less than 0.5%. Recorded event rates were about 150 per burst.

For the needs of the Tile Calorimeter a full simulation package has been developed based on the GEANT program[A.26] which describes in full detail the detector prototypes that have been used for the test beam runs. A comparison between the test beam data of the Tile Calorimeter prototype modules and different hadronic shower simulation codes (FLUKA, GHEISHA, CALOR) in the framework of the GEANT program has been madeN-92,N-69. A standalone FLUKA version[A.28] for the combined test beam simulation, and a Module 0 simulation N-102 have been used as well.

An extensive program of beam tests has been carried out demonstrating the good performance of the calorimeter that fulfils the requirements for the ATLAS hadronic barrel calorimetry. Extensive tests with pions, electrons and muons have been undertaken with the prototype modules, from which we learned most of the features of the Tile Calorimeter described in the following sections. The performances of the first full-scale pre-series module for the barrel hadron calorimeter (Module 0) have also been investigated. This data is still under study, but it bridges an important step between our 1 m prototype modules and the actual geometry to be used in ATLAS. Finally, we have shown that it is indeed possible to understand the response of an ATLAS wedge, taking data with the Liquid Argon test calorimeter upstream of the Tile Calorimeter in an almost projective geometry.

3.2 Summary of test beam results

We will show in the next sections the measured performance of the Tile Calorimeter and how it relates to the desired performance described in Chapter 2. Conclusions based on the results from test beam data on the 1 m prototype calorimeters, the full-scale pre-series Module 0, and the combined run with Liquid Argon and the Tile Calorimeter can be summarized as follows:

- The single particle hadronic energy resolution for the Tile Calorimeter alone is compatible with the design goal of $\sigma/E = 50/\sqrt{E} \oplus 3\,\%$ (for jets) up to the highest energies available[D.1].
- Linearity between 20 and 300 GeV of the order of a few percent can be achieved with the Tile Calorimeter alone. The e/π ratio for the Tile Calorimeter is found to be between 1.2 and 1.1, a relatively small deviation from the ideal compensation.
- The full-scale pre-series Module 0 was successfully read-out with the 25 ns sampling electronics, charge then reconstructed, and successfully yielded a pion resolution of 6.7% at 100 GeV.
- An ATLAS calorimeter wedge was found to successfully reconstruct pion energies between 20 and 300 GeV, with linearity of the order of 1%, and a resolution which is well inside the design goal of ATLAS.
- Uniformity of response to pions across the surfaces of a stack of Tile Calorimeter modules is found to be within 1-2% everywhere. Any fine structure seen in the distributions are routinely explainable by simulations.
- The percentage of energy leaking out the back of the ATLAS calorimeters was determined from an analysis of the shower shapes: at 300 GeV and at 9.6 λ, this amount is about 2%.
- The combined calorimeters can yield an angular measurement of hadronic showers with a resolution of about 1.5^{o} at 300 GeV.
- The Tile Calorimeter is shown to be able to achieve more than sufficient photostatistics to distinguish the muon signal from the noise. A photoelectron yield of 64 pe/GeV was obtained.
- The uniformity response to muons is not as good as to pions, as expected. Uniformity across a stack of Tile Calorimeters is found to be within 2-3%.
- The source calibration can be compared to both the pion response and muon response. It has been found that the cross-calibration of individually-paired phototubes is good to 1.1% using pions and the muon-to-source ratio for all PMTs within a module is not higher than 6% and improvements are foreseen.

3.3 Test beam setup

In the following, a short description of the three experimental setups is given.

3.3.1 Standalone setup with five prototype test modules

The data presented here with the standalone modules were taken with a prototype stack of five modules, each spanning $2\pi/64$ in the azimuthal angle ϕ, with a front face of ± 50 cm in z (horizontal direction perpendicular to the beam line) and ± 10 cm in the ϕ directionN–55. The geometry of the setup and the coordinate axis used are shown in Figure 3-1. The stack was positioned on a scanning table which allowed precision movements in θ (η direction), ϕ or z. The radial depth of the stack at η=0 is equivalent to 80.5 radiation lengths (X_o) and to 8.9 nuclear interaction lengths (λ). Towers within a module were defined as parallel to η=0 with four radial (depth) segmentations: 1.5, 2, 2.5 and 3 λ. The tower segmentation, $\Delta\eta \times \Delta\phi$, was 0.1×0.1. Scintillators were read-out with two phototubes, referred to as left or right. A rear (80×80 cm^2) and side (40×115 cm^2) scintillator wall (each 2 cm thick) were placed behind and at the beam-right side of the calorimeter modulesN-64. These muon walls allow us the possibility to tag events as either "no leakage", "longitudinal leakage", "lateral leakage", "longitudinal and lateral leakages" and assist in the identification of beam muons. Measurements were taken between 1993 and 1995 following the improvements to the optics of the Tile Calorimeter (use of double clad fibres, better tile masking, tile/fibre coupling geometry, calibration, etc.).

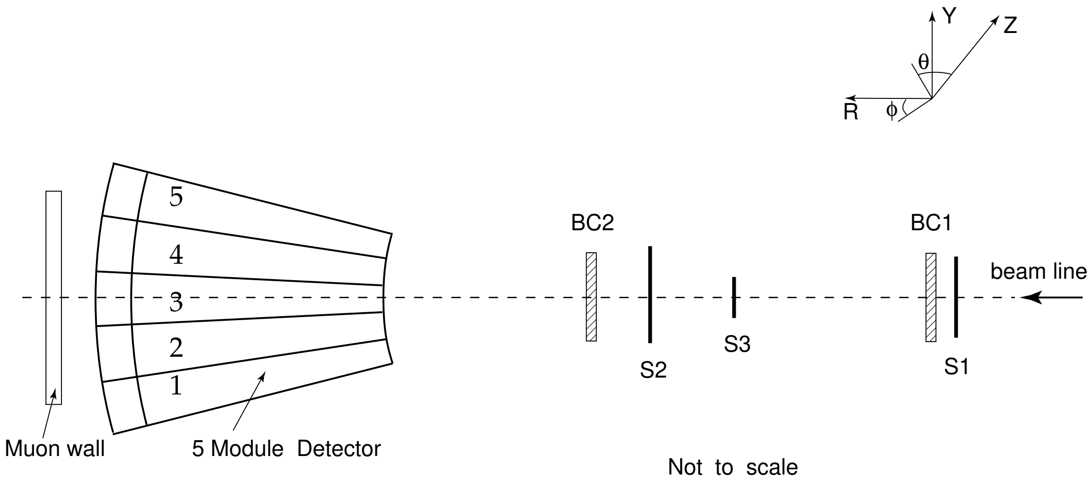

Figure 3-1 Test beam layout for the five prototype modules. The five modules are numbered for reference in the text.

3.3.2 Barrel Module 0 description

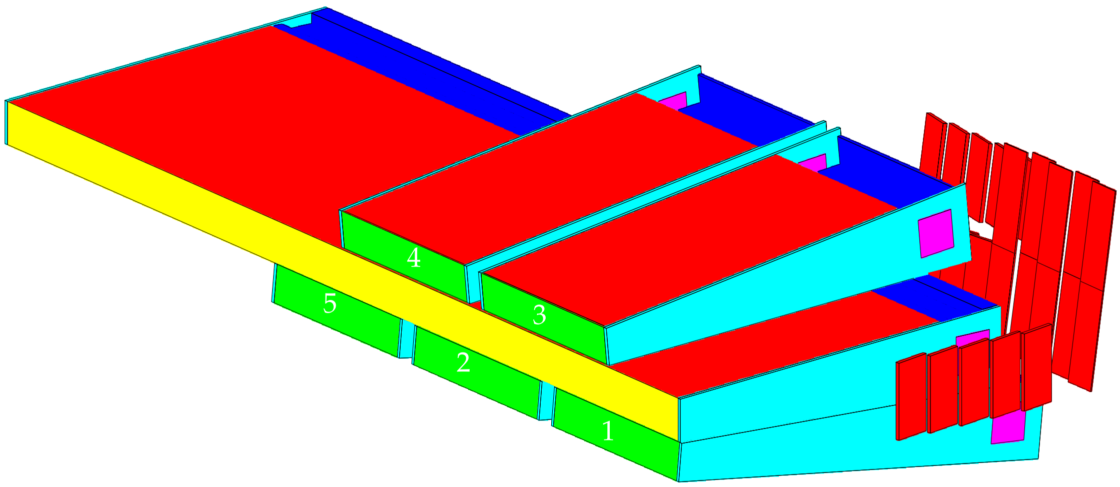

Figure 3-2 Sketch of the Module 0 test beam setup. The 1 m prototype modules are placed on top and at the bottom of Module 0, with a 10 cm gap between them. Shown are the side and back muon counters to tag leakage and assist in identifying beam muons.

The barrel Module 0 was tested in the beam in 1996 using a similar scanning table as used for the prototype modules. The five original one meter prototype modules were placed on either sides (in ϕ) of Module 0, three on one side and two on the other as shown in Figure 3-2. Scintillator walls at the side and rear of the calorimeter stack assisted in the identification of muons and shower leakage. Unlike the 1 m prototype modules which had non-projective tower read-out, Module 0 had fibre routing such that scintillating tiles were grouped in a projective fashion with towers forming a minimum of 0.1 in η. This is shown in Figure 3-3. This projective tower structure defined by the fibre routings in Module 0 will most likely be the projective geometry used in ATLAS. Scintillators were read-out with two phototubes as with the 1 m prototype modules. For the test beam run, only half of the module was equipped with read-out electronics (η=0 on the figure was actually the physical center of the structure).

The Module 0 has three depth segmentations, and the numbers in Figure 3-3 correspond to the phototube pair that each cell is read-out by. The granularity in $\Delta\eta \times \Delta\phi$ is equal to 0.1×0.1 for the first two samplings and 0.2×0.1 for the last sampling. The thickness of the module at η=0 is 1.5 λ in the first depth sampling, 4.2 λ in the second and 1.9 λ in the third. By comparison, the 1 m prototype modules had four segmentations with a total depth of 8.9 λ. The change in length also required a change in the radial sizes of the scintillator tiles. The 1 m prototype modules sampled the showers with 18 tiles, each of 100 mm in depth, while Module 0 sampled the showers with 11 tiles varying in depth from 97 to 187 mm. The front face area is of $560 \times 22\ \text{cm}^2$. More details on the module mechanics, are presented in Chapter 4.

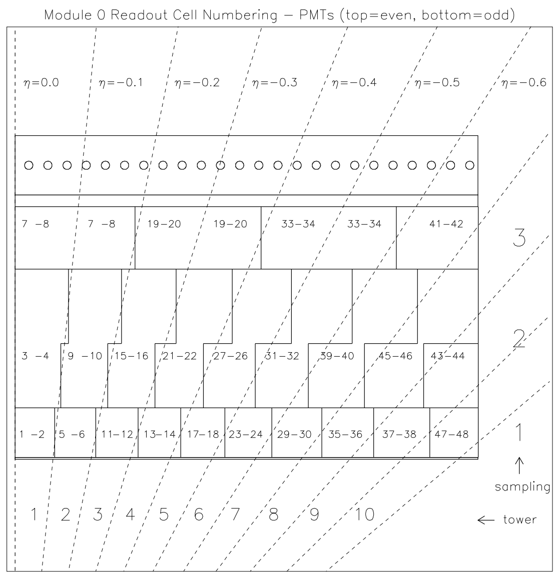

Figure 3-3 The layout of the tower geometry for Module 0. Fibre routing was such that the three depth samplings approximated η boundaries from 0<|η|<1. The numbers in the blocks correspond to the PMTs which each cell was connected to. There are two PMTs per cell read-out.

Test beam data were taken along η for values up to η=0.75 in a projective manner, and also with muons impinging at 90^{o} with respect to the η=0 plane. A ϕ scan was performed as well. The electronics read-out of Module 0 was distinctly different than that of the 1 m prototype modules. The latter had the phototube pulses digitized with standard CAMAC ADCs, while the former had the phototube signals sampled at 40MHz with the FERMI system, and the charge reconstructed accordingly (for details refer to Chapter 6).

3.3.3 Liquid Argon/Tile Calorimeter combined setup

The barrel calorimeter system of ATLAS is composed of a Liquid Argon electromagnetic (em) calorimeter with hermetic accordion geometry and the Tile Calorimeter. A first test of the electromagnetic and hadronic calorimeter prototypes in a combined setup was performed in 1994. In these tests an azimuthal sector of the ATLAS barrel calorimeter was reproduced by placing the Tile Calorimeter prototype downstream of the Liquid Argon cryostat as shown in Figure 3-4. To optimize the containment of hadronic showers the electromagnetic calorimeter was located as close as possible to the back of the cryostat. Nevertheless the distance between the active parts of the two calorimeters was about 55 cm. This is a factor of two larger than in the ATLAS design configuration, although the material in between the calorimeters is equivalent to about 1.5 X_0, which is close to the ATLAS design value. The requirements of shower containment and space constraints meant that the two calorimeters be placed with their central axes at an angle to the beam of 11.3^{o}. At this angle, owing to space constraints, the em calorimeter no longer pointed exactly to the nominal interaction point; however, cell projectivity along the azimuthal direction was maintained. At 11.3^o the two calorimeters have an active thickness of 10.3 λ (10.1 λ at η=0, to be compared with 9.6 λ at η=0 for the ATLAS detector).

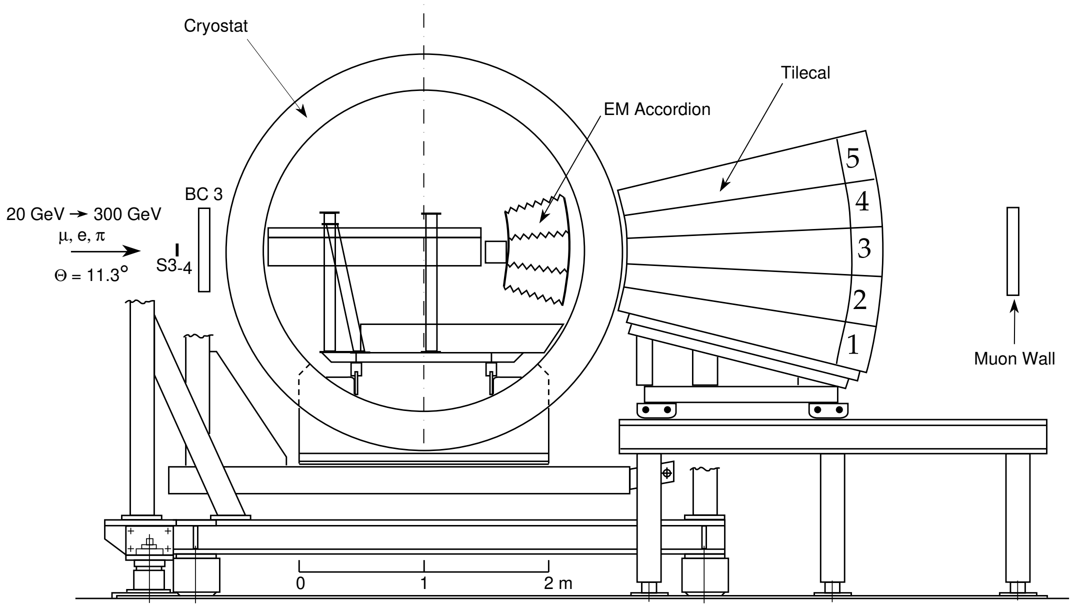

Figure 3-4 Setup of the combined Liquid Argon-Tile Calorimeter test beam configuration.

Another run was performed in 1996 using slightly different preamplifiers in the Liquid Argon, and a wider read-out region. For both running periods, preamplifiers consisting of a mixture of Si, 0T and GaAs were used.

Punchthroughs and leakage were tagged with the rear muon wall located behind the calorimeters at a distance of about 1 meter. The scintillating counters formed an array covering approximately 73 cm in the vertical and 96 cm in the horizontal direction. The muon wall counters were separated from the last Tile Calorimeter segment by 0.7 λ of structural materials. In the 1996 run, a plane of scintillators was placed on the front face of the Tile Calorimeter to sample the shower just downstream of the Liquid Argon cryostat.

3.4 Test beam performance for hadrons

In this Section the main results related to the hadron response for both the combined and the standalone setups are presented. The energy resolution, linearity, e/π ratio, and uniformity are shown. Information on the shower shape and development are also given.

3.4.1 Energy resolution and linearity

1 m prototype modules

The energy resolution for pions has been studied in the energy range from 20 to 300 GeV and at angles of incidence in θ from 0^o to 30^o using the five 1 m prototype modules. Figure 3-5 (black circles) shows the resulting σ/E as a function of $1/\sqrt{E}$ for data at θ= 20^o. In this case, the energy distributions are directly obtained from the raw data by just adding the charge measured in each cell. The energy distributions are symmetric at low energies and develop small high energy tails at high beam energy values (due to e/h>1) as well as small low energy tails due to longitudinal and transverse leakage (see Section 3.4.4.1). The E and σ values are obtained from the raw total energy sum by gaussian fits over a $\pm 2\sigma$ region from the mean. The data points are fitted with the standard expression $\sigma/E = a/\sqrt{E} + b$, where a, the stochastic term, reflects statistical fluctuations in the shower development, and where b, the constant term, reflects uncertainties in the energy measurements due to miscalibration, cracks, etc.

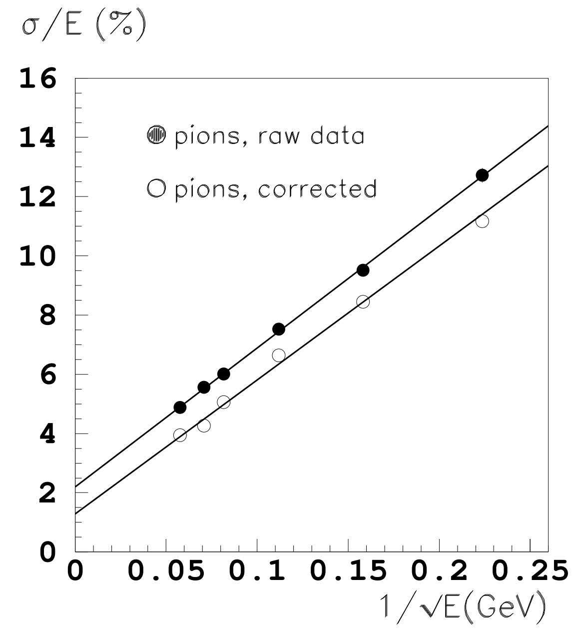

Figure 3-5 Energy resolution with and without longitudinal depth corrections for the five 1 m prototype modules.

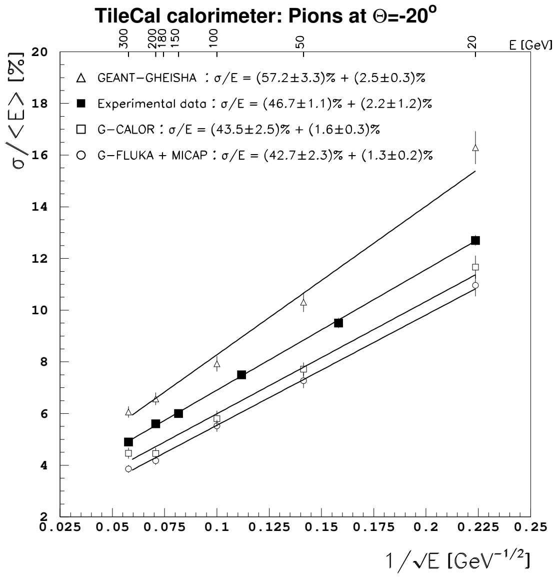

Figure 3-6 Comparison of experimental pion energy resolution, using the uncorrected result, with simulation models.

The energy resolutions can be improved (Figure 3-5 white circles) by applying weighting techniques. An algorithm that corrects downwards cells with large energy deposits (due to the local electromagnetic component in the shower from π^0 decay) has been developed. The two resulting parameters used for the correction are energy independent. On the other hand, this correction downwards leads to a systematic underestimate of the incident energy. The final energy is then obtained by adding an offset (1.7 GeV) and multiplying by a scaling factor. The stochastic term of the resolution, dominated by sampling fluctuations, is unaffected, but the constant term is reduced by about 1%. In Figure 3-6 the energy resolution for pions obtained for the experimental and the simulated data is shown. The FLUKA and CALOR packages predict almost the same values, with those of CALOR being closer to the data. Both predict better than measured resolutions, however. On the contrary, GEISHA predicts a worst resolution.

Table 3-1 summarises the results of the fit for raw and weighted data as well as for the various Monte Carlo predictions. The obtained hadron energy resolutions are competitive with those obtained with conventional sampling iron calorimeter, even when the calorimeter is exposed to hadrons without an upstream em compartment. The results confirm the ATLAS requirements in terms of energy resolution for the hadronic calorimetry: $\sigma/E = 50/\sqrt{E} \oplus 3\,\%$.

A non-linearity as a function of energy in the pion response arises due to the Tile Calorimeter non-compensation (e/h > 1). Since the fraction of electromagnetic energy in the shower increases logarithmically with energy, the relative response to pions is expected to increase slowly with energy: the non-linearity is proportional to $(e/\pi)^{-1}$. Figure 3-7 (black circles) shows the calorim-

Table 3-1 Values of the a and b parameters to fit the pion energy resolution from Ref.[A.20] and [N-92]. Shown are the incident beam angle, the stochastic and constant terms and the method of extracting these terms.

	θ^o	a(%)	b(%)	Data set
Data:				
	10	48.6 ± 1.3	2.46 ± 0.13	Raw
		46.9 ± 1.2	1.78 ± 0.12	Weighted
	20	46.9 ± 1.2	2.20 ± 0.12	Raw
		45.2 ± 1.1	1.29 ± 0.11	Weighted
	30	46.2 ± 1.4	2.13 ± 0.14	Raw data
Simulation:				
	20	57.2 ± 3.3	2.5 ± 0.3	GHEISHA
		43.5 ± 2.5	1.6 ± 0.3	G-CALOR
		42.7 ± 2.3	1.3 ± 0.2	G-FLUKA

eter response normalized to the point at 20 GeV, ($\langle Q\rangle/E_{nom}$), where $\langle Q\rangle$ is the mean energy measured in the calorimeter and E_{nom} is the nominal beam energy. For these data pions were incident at 20^o and the fit with the expression:

$$c \cdot \left(1 + \left(\frac{e}{h} - 1\right) \cdot 0.11 \cdot \log E\right) \qquad \text{3-1}$$

gives for the e/h ratio the value 1.36±0.11 [A.10]. In Figure 3-8 the measured pion energy response is compared with the various simulations. It is clear from this plot that none of the simulation packages is able to follow the data to a high accuracy.

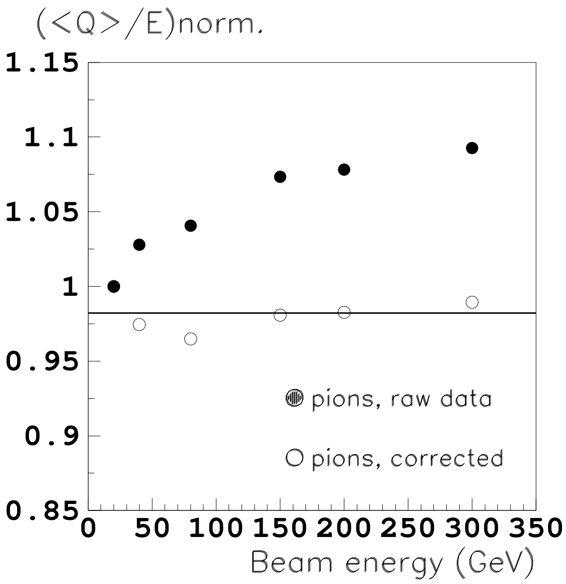

Figure 3-7 Energy response vs nominal incident energy. Both raw data and weighted data are shown. Normalization is at the 20 GeV point.

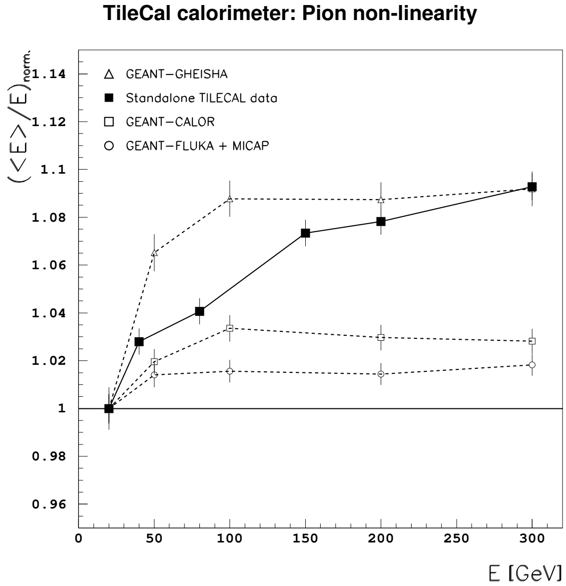

Figure 3-8 The normalized (to the 20 GeV point) relative average pion energy response (raw data) compared to the Monte Carlo predictions.

Module 0

In Figure 3-9 the reconstructed energy response for pions of 100 GeV (as well as the signal from muons which accompany the pions in the beam) is shown. The read-out of Module 0 in the test beam incorporated the FERMI system with a compressor circuit allowing us to achieve about 15 bits dynamic range. After charge calibration throughout the dynamic range, a look-up-table was constructed for each channel incorporating the calibration constants. The energy reconstruction is done by using samples of the pulse shape, correcting for the absolute offset, or pedestal, which is measured at a few points before each waveform. The details of the read-out electronics, and their performance in the test beam can be found in Chapter 6.

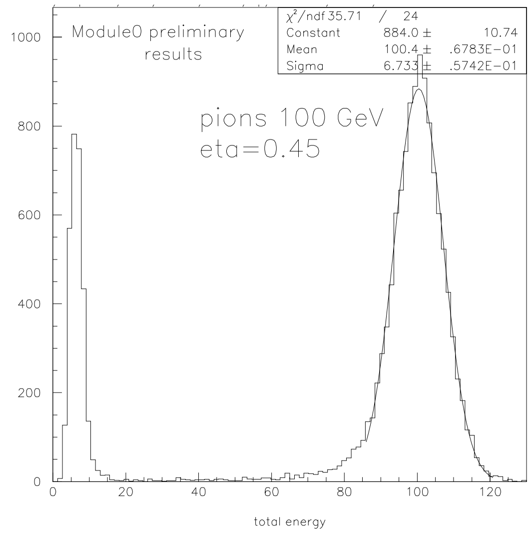

Figure 3-9 Reconstructed Module 0 energy response for pions (and muons) at 100 GeV.

Several methods of energy reconstruction have been attempted. The best estimate of the charge in the pulse is the value of the peak amplitude position. The peak can be found by a parabolic fit to the pulse near the maximum amplitude. As few as five samples can be used for an analytical calculation. Other methods are being investigated, and the best algorithm will be soon clarified. Furthermore, at the time of this writing, the calibration constants have not been thoroughly understood. Therefore the results which we present on Module 0 are still preliminary, but still show the level to which the detector will perform in ATLAS.

Combined

The main purpose of the combined test was to demonstrate that the choice of a hybrid calorimeter (Liquid Argon em Calorimeter + Tile hadronic Calorimeter) will allow one to reconstruct the energy of incident hadrons with resolution and linearity within the goals of ATLAS.

To reconstruct the hadron energy various algorithms were employed. The first method referred to in the following as the “benchmark approach”, is designed to be simple[N-67]. With this method the incident energy is reconstructed with a minimal number of energy-independent parameters. The second method, is inspired by the H1 weighting method[N-75][A.12].

The benchmark method introduces a set of three energy-independent corrections: the intercalibration between the em and the hadronic calorimeters, a correction for the energy lost in the cryostat wall separating the two calorimeters, a quadratic correction for the em calorimeter to crudely correct its non-compensating behaviour and to provide a response independent from the energy released in this compartment. Figure 3-10 shows the value of the reconstructed energy E_0 for different values of the energy deposited in the electromagnetic calorimeter. Also shown are the results of adding only the first two or the first three terms of E_0. The parameters which weight these corrections are determined by minimizing the fractional energy resolution of 300 GeV pions. The validity of the cryostat correction, expressed as the geometric energy mean of the last Liquid Argon sampling energy and the first Tile Calorimeter sampling energy, has been tested with planes of 9 mm thick scintillator (MidSampler) inserted between the cryostat and the Tile Calorimeter to sample the shower in this region.

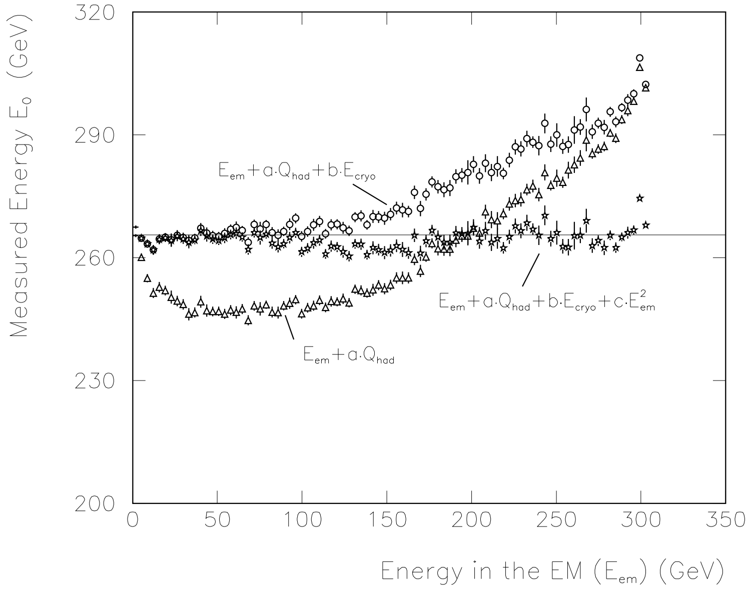

Figure 3-10 Components of the reconstructed energy (E_0) vs. the energy in the electromagnetic calorimeter using the benchmark energy reconstruction method for 300 GeV pions (combined setup).

Figure 3-11(top) shows the benchmark results compared with the predictions from the GEANT-CALOR and with the standalone FLUKA. Above 100 GeV the energy resolution of the combined calorimeter is similar to the one expected from both Monte Carlo simulations, as well as to the resolution obtained in a separate beam test of the Tile Calorimeter (Figure 3-11, bottom). At lower energies, the combined measurement resolutions are significantly larger than those obtained in the Tile Calorimeter standalone.

The weighting techniques applied in the past to the Tile Calorimeter data reduced the effect of the non-compensation correcting downwards the response of the cells with relatively large signals which are mostly due to local electromagnetic showers from π^0 decays. The H1-based weighting concept is based instead on correcting upwards the response of cells with relatively small signals, to equalise their response to that of cells with large (typically electromagnetic) deposited energies. The total energy is reconstructed correcting the energy in each cell of either calorimeter by a factor (typically > 1) which is a function of the energy in each cell and of the beam energy.

Cells' energy spectra (E_{cell}) are divided in equally populated intervals. Weights (w_i) for each intervals are fitted optimizing simultaneously resolution and linearity. The weights are fitted by the function w_i=a+b/E_{cell}. In turn, the energy dependence of the parameters a and b is fitted to a linear function. The total number of parameters is eight. No a priori knowledge of the beam energy is needed to calculate the energy dependent correction: instead, the particle energy is estimated from the raw data with a simple iterative procedure.

The resolutions obtained with the benchmark and H1-based methods are shown in Figure 3-11 (bottom). A fit to the H1-based points results in:

$$\left(\frac{(38.3 \pm 4.6)}{\sqrt{E}}\% + (1.62 \pm 0.29)\%\right) \oplus \frac{(3.06 \pm 0.18)}{E} \qquad 3\text{-}2$$

Again, at low beam energies, the resolution deteriorates appreciably, as observed with the simpler benchmark reconstruction method. This deterioration partially comes from the beam contamination at 20 GeV. As mentioned earlier, a clarification of this point will come with the analysis of the data from the last combined calorimeter test run, performed in April 1996.

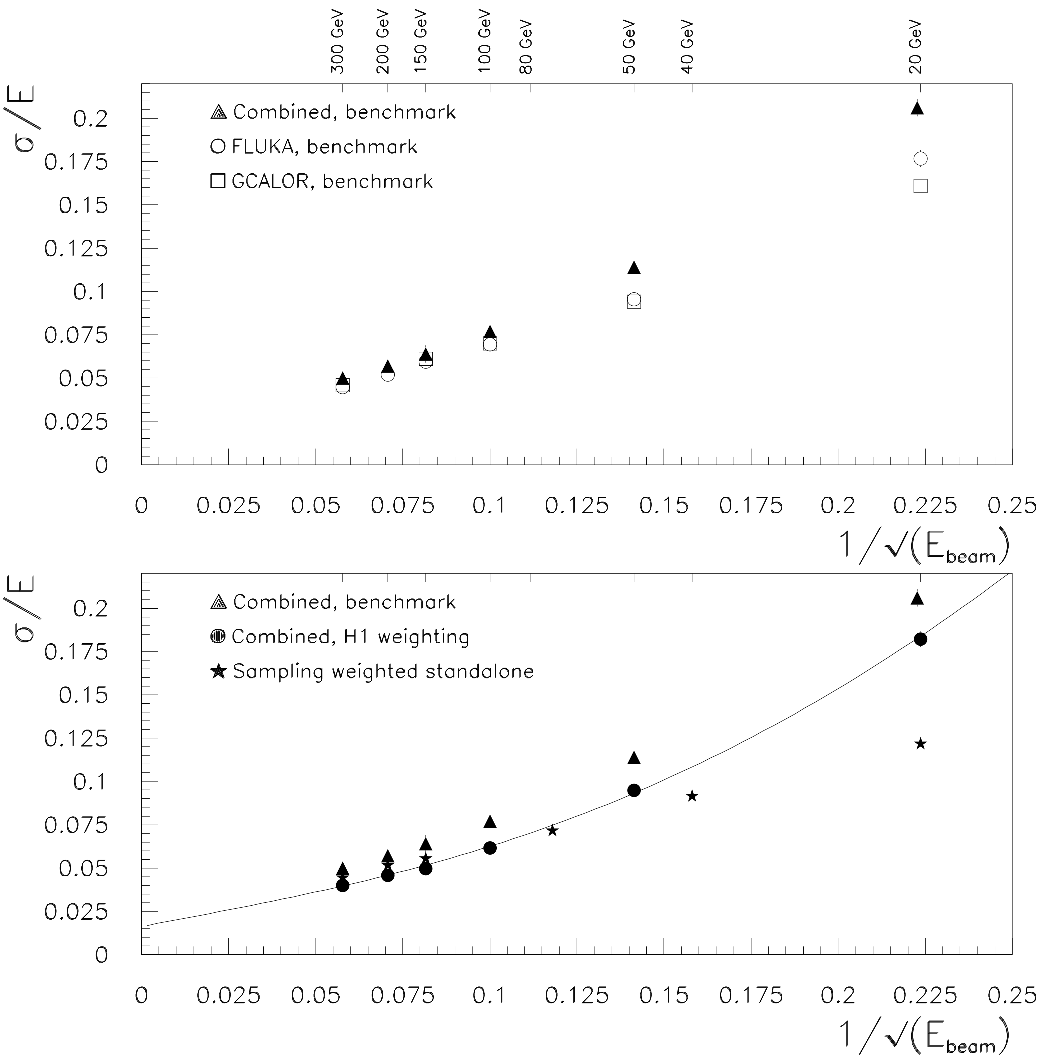

Figure 3-11 Top: The benchmark results are compared with the FLUKA and GEANT Monte Carlo predictions. Bottom: Resolution plot for the benchmark and the H1-based algorithms, compared to the standalone results.

In evaluating the non-linearity of the Tile Calorimeter, it should be noted that the procedure used to find the benchmark parameters minimizes the fractional resolution. However, the reconstructed energy is systematically underestimated, due to the fact that both calorimeters are non-compensating. For this reason, an additional step of rescaling is necessary. In this second step, the correction factor is energy-dependent (it goes from 1.12 at 300 GeV to 1.25 at 20 GeV) and allows us to obtain a pion response which is linear within ±1 % over the full energy range of the data[A.24].

For the H1-like weighting, as said before, the linearity is simultaneously optimized together with the resolution. The results are shown in Figure 3-12 as well. Both methods yield a linearity over the range to within 1%.

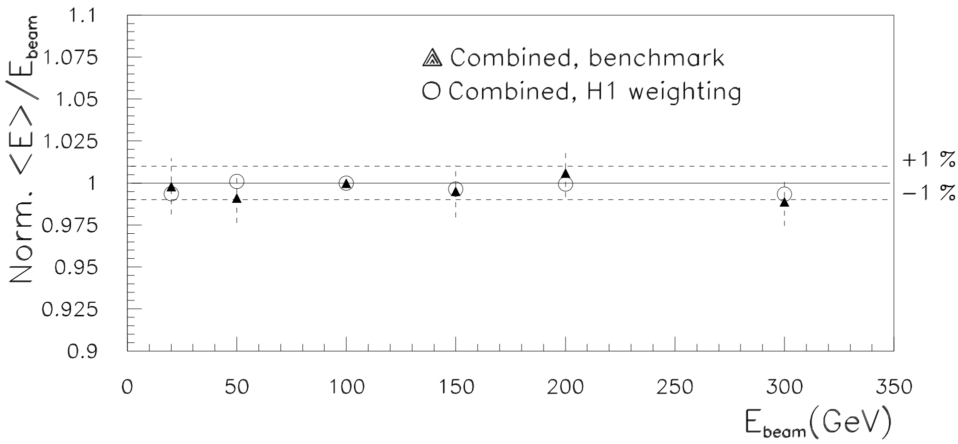

Figure 3-12 Linearity plot comparing the benchmark and the H1-like weighting technique.

3.4.2 e/π response

The Tile Calorimeter has not been designed to have a good electron performance, since it will have in front of it an electromagnetic compartment. However, it is important to understand the electron response, namely to study the e/π ratio. When studying the Tile Calorimeter response to electrons, the hadronic calorimeter can be considered as a set of different calorimeters, with variable absorber and scintillator thicknesses: from t_{Fe} = 81 to 28 mm, and from t_{Scin}= 17 to 6 mm for a θ angle between 10^{o} and 30^{o}, where t_{Fe} and t_{Scin} are the thicknesses of the absorber and the scintillator respectively[N-72]. Therefore, the electron response is a rather complicated function of E_{beam}, θ and z.

The response obtained for electrons and pions gives the possibility to extract the e/h value, that is the ratio of the calorimeter responses to the electromagnetic and non-electromagnetic (purely hadronic) components of hadron showers. An e/h value different from 1 causes deviation from linearity in the hadronic response versus energy, besides broadening the energy resolution and introducing tails in the energy distribution[A.11]. The value of the e/h ratio depends on a number of factors such as the thickness of the passive layers, the thickness of the active layers, and the sampling fraction. The e/h ratio of a sampling calorimeter with an iron - scintillator ratio less than 20 (in the case of the Tile Calorimeter this ratio is 4.7) is expected to be > 1 for the conventional orientation of tiles perpendicular to incident hadrons[A.10]. The Tile Calorimeter structure does not favour a simple relation, but rather a function such as e/π = f(E, θ, z). As an example, Figure 3-13 shows the ratio of the measured electron response to the measured pion response, e/π, as a function of z coordinate for E = 20 GeV at θ = 10^{o}. The e/π ratios averaged over two 18 mm periods are shown in Figure 3-14 as a function of the beam energy. The e/h ratios were extracted from these data by fitting them with the expression:

$$\frac{e}{\pi} = \frac{\frac{e}{h}}{1 + \left(\frac{e}{h} - 1\right) \cdot 0.11 \cdot \ln E} \qquad 3\text{-}3$$

At 20° the value of e/h= 1.34 ± 0.03 is obtained, in good agreement with the value obtained using the pion linearity response curve information (Section 3.4.1).

To determine the e/π ratio for the combined setup (with the electromagnetic and the hadronic calorimeter used for the energy reconstruction), the pion energy was defined using the bench-

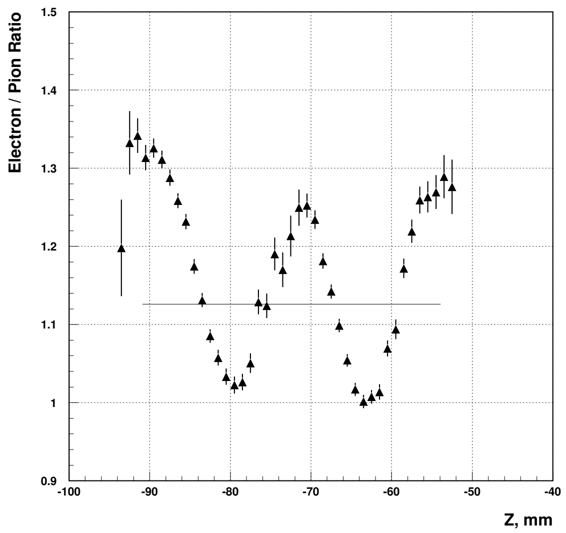

Figure 3-13 The e /π ratio for 20 GeV at 10° as a function of z measured with the 1m prototypes in standalone mode.

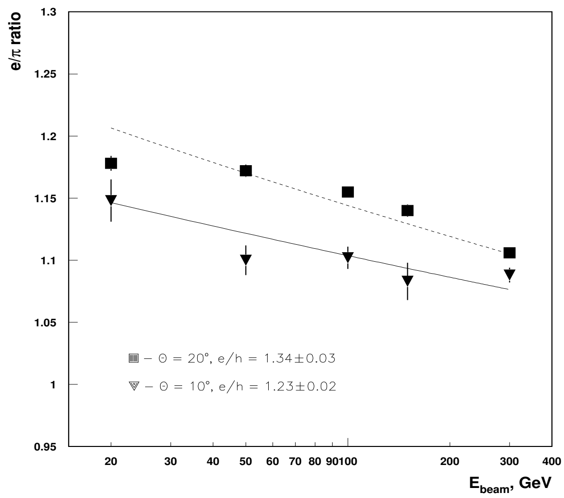

Figure 3-14 The e/π ratio as a function of energy at 10° and 20°.

mark expression but without summing up the quadratic term in the electromagnetic energy, since this term acts as a correction for the e/π ratio itself. The cryostat was added in order to avoid a systematic underestimate of the response to pions. The electron signal was reconstructed within 3% of the nominal value, so that in the ratio we used the electron beam energy with an error of 3%.

The resulting e/π ratios as a function of the pion beam energy are given in Figure 3-15; they lie between 1.24 and 1.12. The response to pions relative to electrons is seen to increase with energy as expected, because the fraction of electromagnetic energy in a pion shower increases logarithmically with energy.

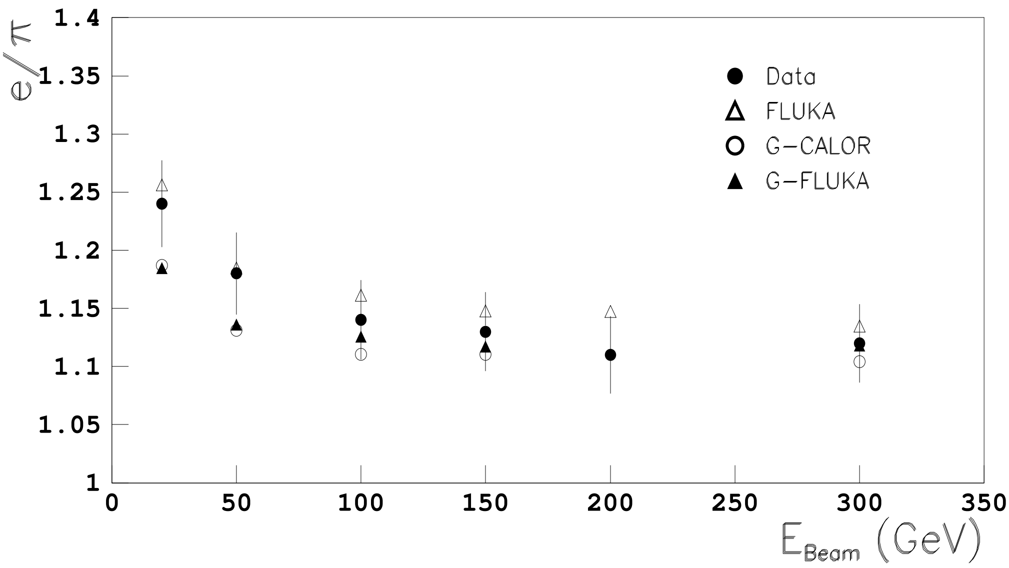

Figure 3-15 Values of the e/π ratio vs. the beam energy for the combined setup.

3.4.3 Pion response uniformity

The response uniformity to pions along the z direction has been investigated as well [N-76]. Figure 3-16 shows the response to 100 GeV pions, incident at 10^o, as a function of the impact point z on the face of the test calorimeter stack from -36 cm to 20 cm for events with a fully contained shower. The points are obtained fitting the energy spectrum at each impact point to a Gaussian (in the region $\pm 2\sigma$) and then are normalized to the mean value over the scan. The uniformity here is good at the level of 0.7% (rms). A θ angle scan from 0^o to 30^o was performed as well with 50 GeV pions incident on the test calorimeter stack. Figure 3-17 (top) shows the variation of the measured energy normalized to the 20^o point. The response is uniform except in the range from 0^o to 6°, where the response of the calorimeter is about 2% lower. The dispersion in the range from 0° to 30° is 0.8%. Figure 3-17 (bottom) shows the corresponding resolution. Above 15^o the resolution is almost constant (9%), while below it slightly deteriorates (10%).

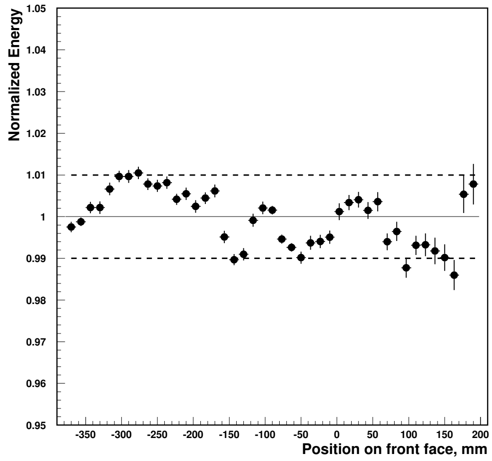

Figure 3-16 Energy uniformity scan with 100 GeV pions at 10^o for events without lateral leakage. The ratios are calculated with respect to the mean signal.

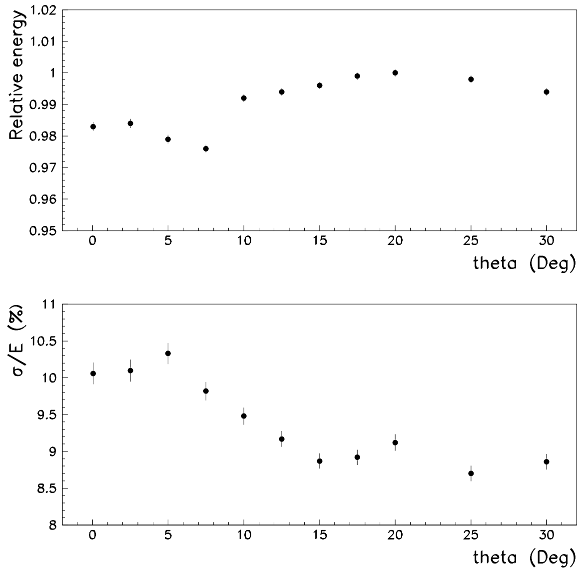

Figure 3-17 Top: Mean energy of 50 GeV pions for different incident θ angles. The values are normalized to the value at $\theta = 20^o$. Bottom: The corresponding relative resolution σ/E in percentage.

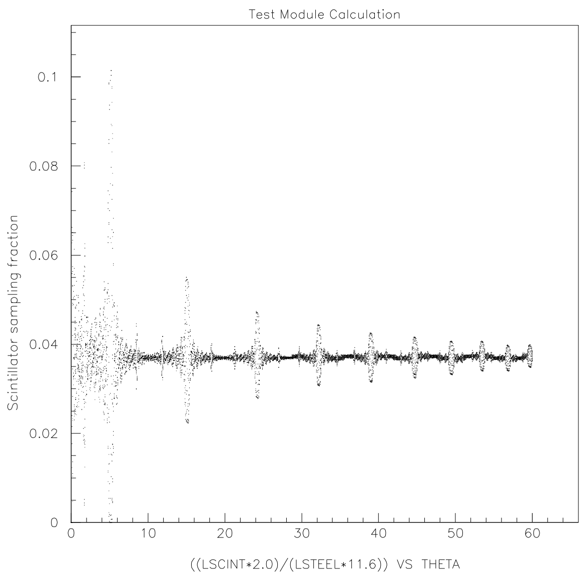

Figure 3-18 A simulation of the sampling fraction vs incident θ angle.

The inhomogeneity can be explained by looking at the sampling fraction across the Tile Calorimeter surface (see the Mechanics Chapter for details on the alignment of the scintillators in the staggered tile/iron geometry). Figure 3-21 shows the calculated variation of sampling fraction as a function of the impact angle[N-73]. Channelling angles at about 5° and 16° are clearly visible, and this structure is repeated (although the channelling is progressively attenuated) at intervals of about 11°. The effects of these variation, which show up in the standalone Tile Calorimeter geometry, will be substantially attenuated with the Liquid Argon em compartment in front (ATLAS configuration).

In a similar fashion, Figure 3-19 shows Module 0's response to muons (top) and pions (bottom)

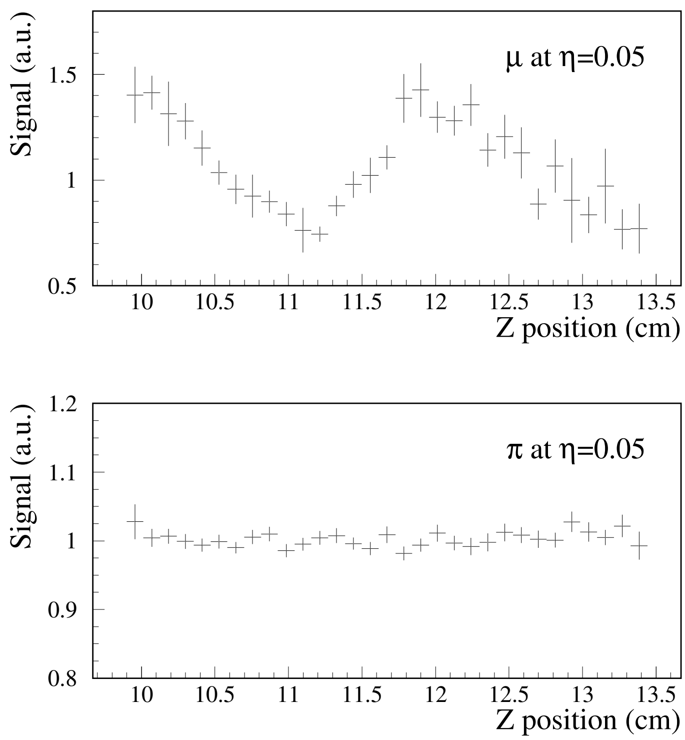

Figure 3-19 Top: A scan in z at η = 0.05 (θ=2.8°) with muons into Module 0. Bottom: The same plot for pions.

at a small angle (θ=2.86°, or equivalently η =0.05) as a function of the impact point on the front of the calorimeter. The periodic structure seen with muons at this angle is expected due to the way this calorimeter is fabricated. As one looks parallel to η= 0, the layers of active material and absorber material alternate. On the other hand, in the case of pions the showering blurrs the boundaries between active and passive material, which makes the response equivalent to a conventional parallel plate calorimeter.

The pions' response across Module 0 was studied as a function of η. An η scan changes both the z impact point, as well as the angle of incidence due to the projective nature of Module 0. Figure 3-20 shows the response to 100 GeV pions as a function of η. The dropoff in signal at the high and low η ends is due to shower leakage: at low η, the shower enters the uninstrumented section and at high η, the shower is not longitudinally contained.

For Higgs and SUSY particle searches the measurement of E_T^{miss} is important and places demands on the tolerable energy loss in cracks. In the prototype calorimeter, cracks between modules are present. These cracks are mainly due to the space needed to extract the fibres which go to the PMTs. In order to determine the effect of these cracks the five prototype modules were exposed to pion beams with energies from 20 to 300 GeV at θ=10^o[N-80]. The response uniformity was studied as a function of the vertical displacement y (ϕ scan) between two modules from the

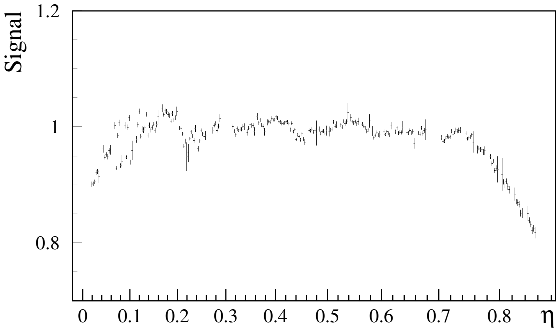

Figure 3-20 Module 0 response to 100 GeV pions over the entire η range of the calorimeter.

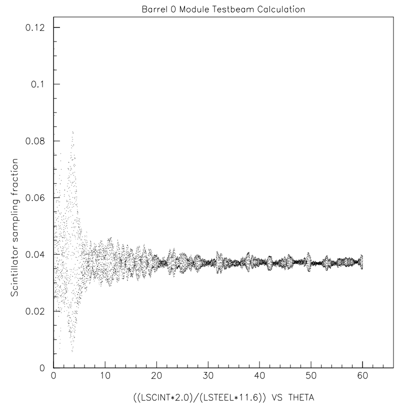

Figure 3-21 Calculation of the sampling fraction variation for Module 0.

center of module 3 to the center of module 4. This corresponds to a scan along 20 cm in the vertical direction at the entrance face of the calorimeter (ϕ = 0.56^{o} corresponds to a vertical displacement of 1 cm in y).

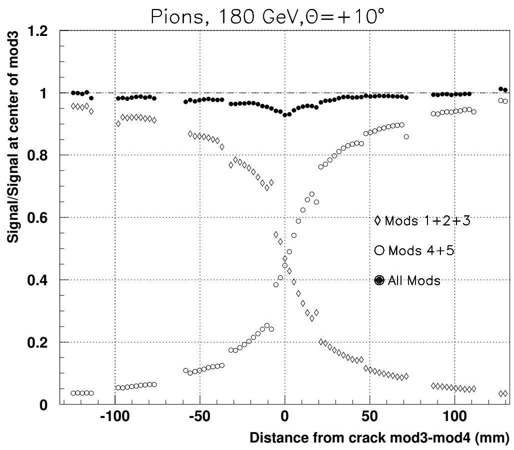

Figure 3-22 Response of the 1 m test calorimeters to 180 GeV pions as a function of the vertical coordinate y. The scan covers the region from the center of the central module (module 3) to the center of the upper module (module 4).

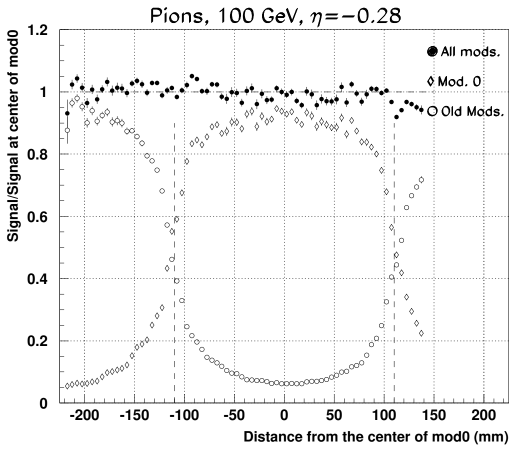

Figure 3-23 Response of Module 0 to 100 GeV pions as a function of the vertical coordinate y. The relative sum of all the modules' energy is shown as well as that of Module 0 alone.

Figure 3-22 shows, as a function of y, the sum of the signals in the modules on one side of the crack (modules 1, 2 and 3) and on the other side (modules 4 and 5), as well as the total sum normalized to the signal at the center of the module 3. The y coordinate is measured from the crack, on a line perpendicular to the crack plane and extrapolated to the depth of maximum energy deposition (65 cm). The signal response has a good uniformity with an rms of 2%. The signal response decreases by about 7% for pions in the crack region.

The ϕ dependence of Module 0 was checked with pions at 100 GeV also. In Figure 3-23 we show a vertical scan with pions across the face of Module 0, crossing the boundary into the top or bottom 1 m prototype modules. As one expects, the individual signal falls rapidly as the impact point approaches the boundary, but the energy sum of all modules remains constant to a few percent.

3.4.4 Hadron shower development

Longitudinal and transverse shower shapes were investigated by studying the energies deposited in the various depth samples of the test calorimeter stack. Figure 3-24 shows the energy deposited by 300 GeV pions in each longitudinal compartment, for data and Monte Carlo simulated events. The Monte Carlo reproduces quite well the energy deposition[N-92].

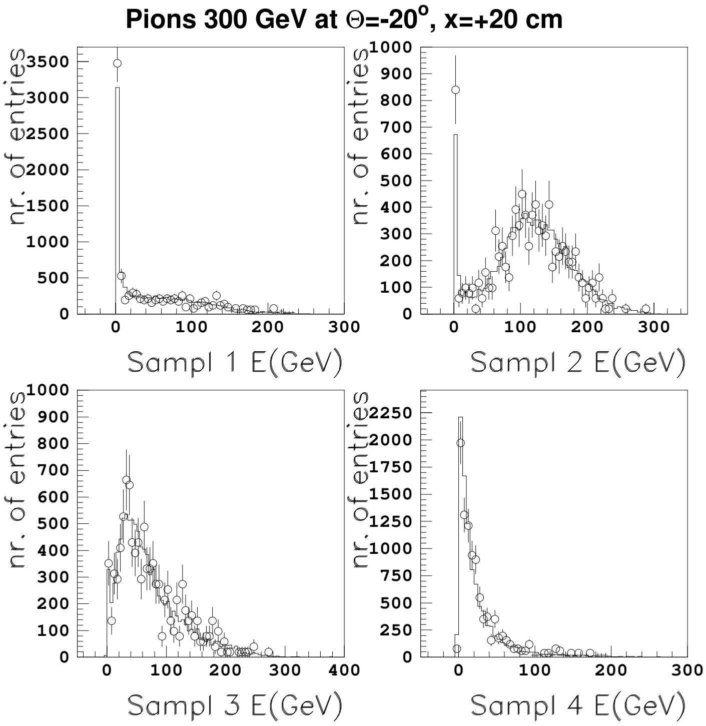

Figure 3-24 Energy deposited in each longitudinal compartment by 300 GeV pions. Experimental data (solid line) and Monte Carlo simulated events (dots) are compared.

In the combined run, particles traverse in total about 11 λ of material, including the Liquid Argon em calorimeter, the Tile Calorimeter and passive materials at the back of the Tile Calorimeter. For this study pion showers of 50, 100, 200 and 300 GeV were examined. The mean raw energy deposited in each sampling can be plotted against the calorimeter depth to give a useful representation of the longitudinal development of showers.

Figure 3-25 shows the longitudinal profiles for pions of 50 and 300 GeV compared with the Monte Carlo predictions. The GEANT simulation reproduces reasonably well the shape of the data in the hadronic compartment. However, in the electromagnetic part the simulated shower develops later than in the data. Conversely, the FLUKA results are in agreement with the data at both energies and in both calorimeters. For all the energies more than 50% of the energy is released in the hadronic compartment.

We see from the figure that about 3-4% of the energy is seen in the end of the Tile Calorimeter. Figure 3-26 shows the energy deposition in the standalone 1 m prototype calorimeters (left) and the lateral shower profile distribution (right) for 100 GeV pions incident at 10°. The data are obtained from runs which scanned the beam over large regions of z along the calorimeter front face. The deposition of energy was then plotted as a function of the energy measured in a cell which had a cell center distance z away from the beam axis. The plateau at small z is due to measurement of radially small-sized showers with a relatively large cell.

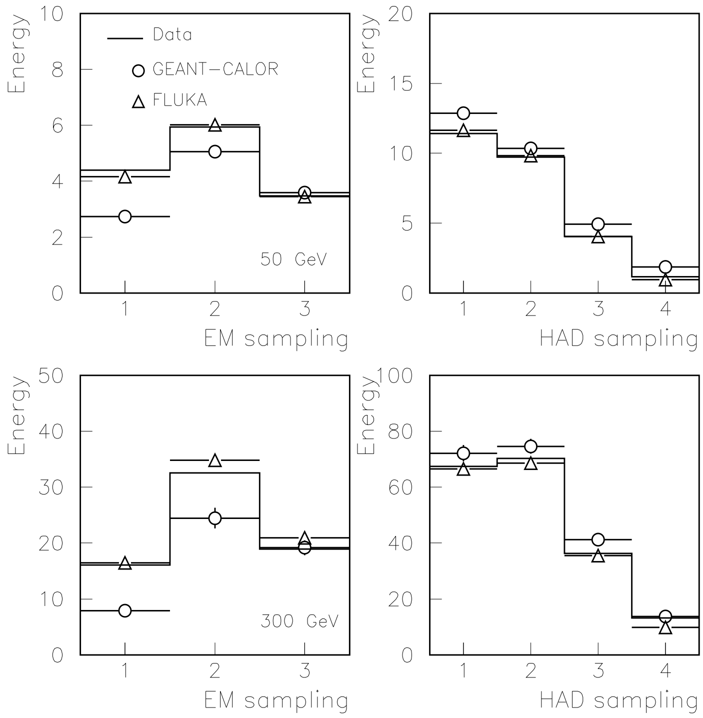

Figure 3-25 Longitudinal profiles for the electromagnetic and hadronic calorimeter for 50 and 300 GeV pions (combined setup).

The shower distribution profile represents the energy density as a function of the distance from the shower axis. By summing tower energies from the beam position out to a given tower, for all depths and all modules, one can obtain an integrated energy distribution from the beam center to the z position of any tower. The derivative of this energy distribution is the z-projection of the transverse energy density distribution in the shower. The extracted transverse energy distributions are considerably narrower than those obtained by simply looking at the lateral profiles of the energy deposit. These extracted distributions present also a prominent central core, and a surrounding halo as one would expect [A.19]. The transverse shower profile of Figure 3-26 is fit by a linear sum of a gaussian and an exponential function. The sigma of the gaussian turns out to be consistent with the two-fold Moliere radius.

3.4.4.1 Longitudinal leakage

Due to the limited dimension of the apparatus, an important concern in calorimetry is the energy leakage which causes a degradation of the energy resolution, as well as tails in the energy distributions. In addition, one important topic related with muon detection and the first level muon trigger in ATLAS, is the reliable understanding of backgrounds from hadronic shower punchthrough.

The study of hadron shower leakage in the Tile Calorimeter was performed in [N-71], [N-63], [N-76], using the back and side muon walls, which are able to tag mips as well as see some neutrons from the hadron shower, events with and without leakage are tagged.

The energy spectrum, for events with and without leakage, is shown in Figure 3-28 in a logarithmic scale for 100 GeV pions. For events with leakage the peak position is shifted to lower values and the distribution has a tail at low energies (equal to 1.5%). The fraction of energy in

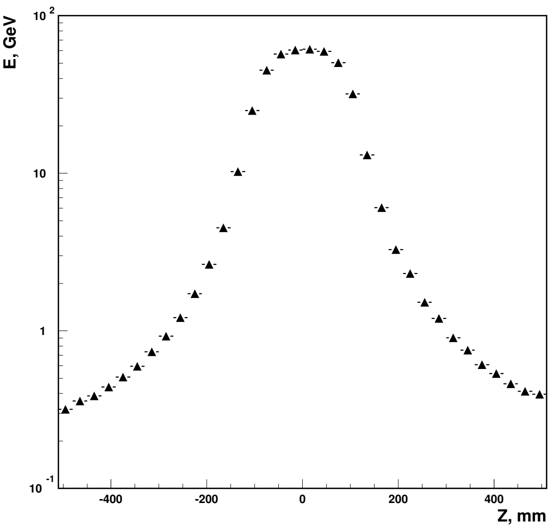

Figure 3-26 Sum of the energy deposition over the cells of all the longitudinal depths, as a function of the z-coordinate.

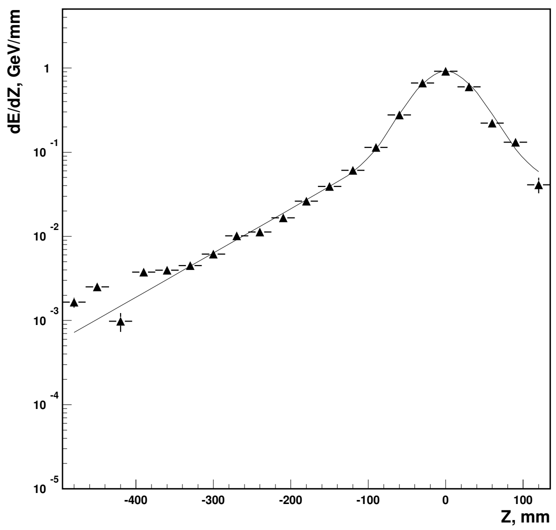

Figure 3-27 The transverse shower profile for 100 GeV pions at θ=10°.

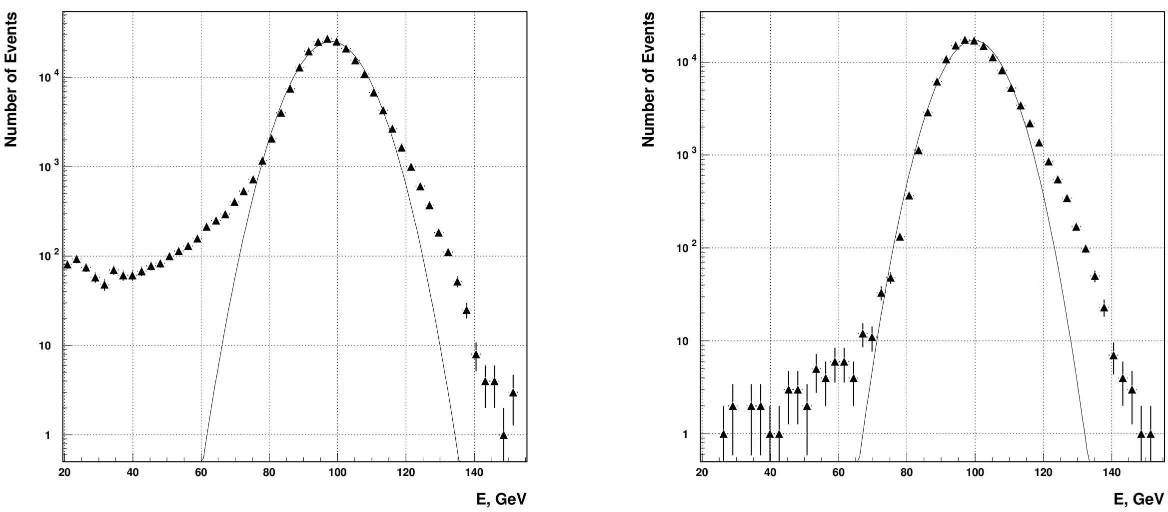

Figure 3-28 The 100 GeV incident pion energy spectra for different data samples. Left: All the events. Right: Events without longitudinal and lateral leakage.

the tail is equal to 1.77%, in agreement with the value of 1.73% for an iron thickness of 158 cm from previous measurements[A.14] and with Monte Carlo predictions (1.65±0.15)%[N-69]. Figure 3-28 (right) shows that the percentage of fully contained events which are in the low energy tail is less than 0.1%.

The probability of pion induced shower leakage is defined ([A.14] and [A.8]) as the ratio of the number of events with at least one hit in the back scintillator wall over the total number of events. The muon contamination in the pion beam has been suppressed using the calorimeter energy deposition information (see Section 3.5.1). The remaining muon background is then estimated to be around 0.5-2.0% and subtracted. The acceptance of the scintillator wall (between 55% and 65%, depending on the beam energy) is calculated from a comparison of the number of events hitting individual counters with symmetrical and asymmetrical positions of the scintillator wall with respect to the beam. The lateral distribution of leakage has been described by the sum of two exponential functions.

Figure 3-29 shows a comparison of the punchthrough probability of showers induced by pions of various energies, between Tile Calorimeter data and the RD5[A.27] results. A corresponding iron equivalent thickness (1.58 m) is assumed. The agreement between the two measurements proves that the punchthrough probability for the Tile Calorimeter prototype with longitudinal segmentation of absorber and scintillators is the same as for a classical sampling hadron calorimeter. The punchthrough probability depends approximately linearly on the pion energy: the value is 0.15% per 1 GeV. Figure 3-30 shows the energy loss for events with leakageD-5. If one

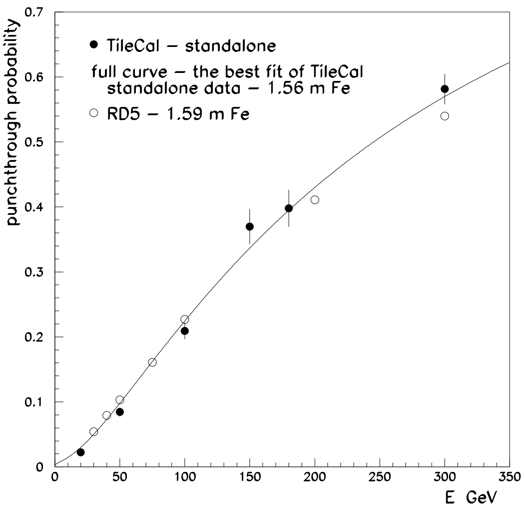

Figure 3-29 The energy dependence of punchthrough probability for fixed thickness of the absorber. Empty circles are RD5 data for 1.59 m of iron. Full circles show Tile Calorimeter data measured at θ = 10° and the full curve is the best fit of these data which corresponds to 1.56 m of iron absorber.

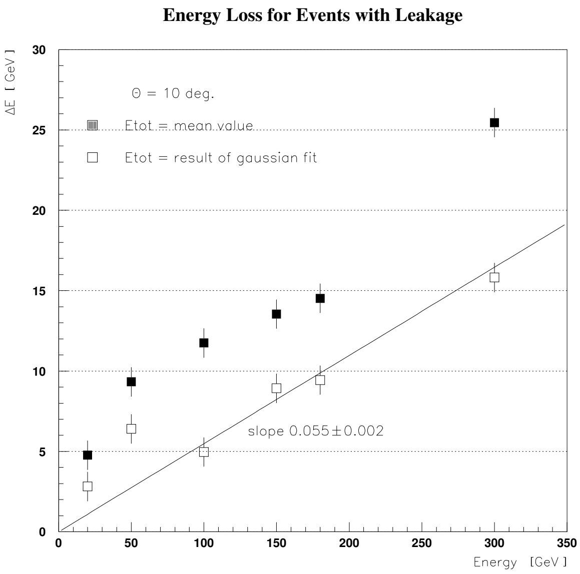

Figure 3-30 The energy loss for events with leakage as a function of the beam energy.

select events where the shower develops at the beginning of the calorimeter, the difference in the measured mean energy value is of 5.5% (from Gaussian fit). In events where the shower develops later, low energy tails appear. Therefore, the difference of mean values of deposited energy is larger than the difference of the peak values.

In the combined calorimeter test beam setup, particles incident at an angle of 11.3° traverse about 11 λ, including passive material at the back of the Tile Calorimeter. The leakage for pions of 50, 100, 200 and 300 GeV has been studied using the muon wall located behind the calorimeter (see Section 3.3.3).

The probability of longitudinal shower leakage is defined as the fraction of events with a signal in at least one of the muon wall counters. Figure 3-31 shows this probability as a function of the incident energy. The probability is corrected for the acceptance which is around 50%. The result is compared with the ones obtained by the RD5[A.27] and CCFR Collaborations for an iron equivalent thickness of 1.85 m as in the combined calorimeter setup. The dashed line shows the expectation for the ATLAS configuration (10.6 λ at η = 0). Figure 3-32 shows the average energy loss from leakage, defined as the difference between the mean energy values of events with and without a signal in the muon wall, for several beam energies. The energy loss for events with longitudinal leakage is about 3% at 100 GeV.

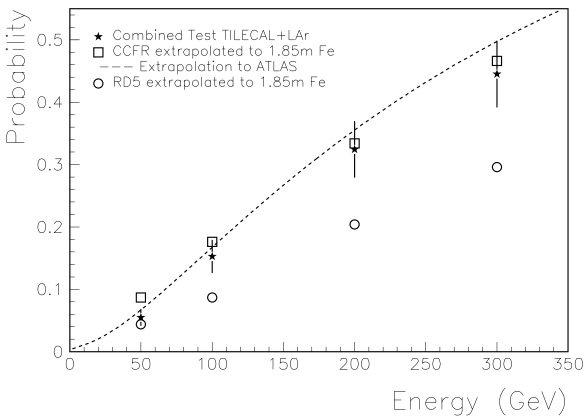

Figure 3-31 Punchthrough probability for pions. Results from RD5 and CCFR Collaboration (recalculated for 1.85 m of iron) are also plotted. The dashed line shows the expectation for the ATLAS configuration.

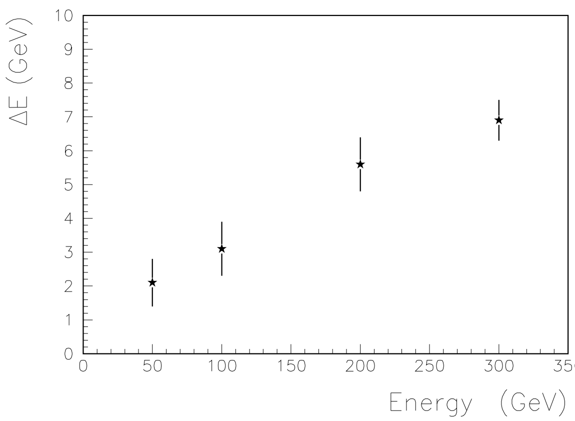

Figure 3-32 Average energy loss vs. beam energy for events with longitudinal leakage.

As shown already in the case of the standalone setup, an incomplete longitudinal shower containment causes the presence of tails in the low energy side of the reconstructed energy spectrum. Figure 3-33 shows how these low energy tails can be reduced by removing the events with a signal in the muon wall behind the calorimeter, i.e. for 300 GeV pions. This implies that there is some longitudinal leakage even after a calorimeter which is about 10 λ thick.

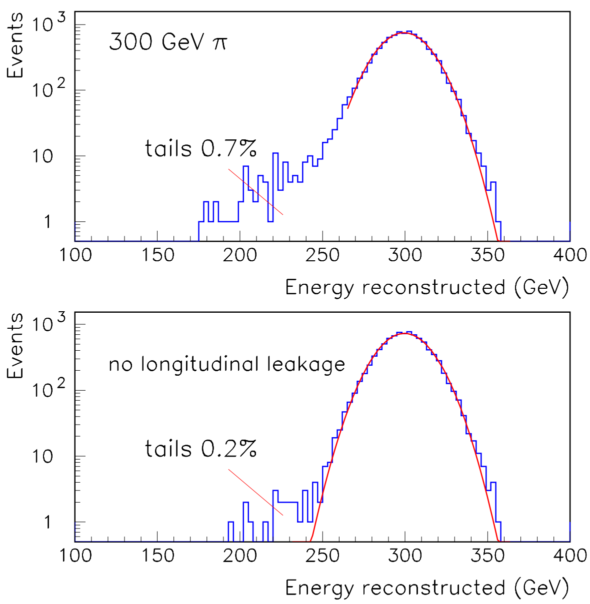

Figure 3-33 Low energy tails in the 300 GeV pion spectrum before (upper plot) and after (lower plot) rejecting the events with a signal in the muon wall.

Figure 3-34 summarises the results. The decrease of the percentage of events in the tail of the energy distribution, for different effective calorimeter depths and for 300 and 50 GeV pions incident at an angle θ of about 11° is shown. The Tile Calorimeter standalone setup corresponds to the point at 9.3 λ. The situation with 7.8 λ has been produced with the standalone setup, by keeping all the events leaving only one mip in the first sampling. The combined setup is the point at 10.3 λ. An effective depth of 7.3 λ has been realized with the combined setup by ignoring the energy fraction measured in the fourth hadronic compartment. Finally, the configuration designed in the ATLAS Technical ProposalD-1 corresponds to 9.6 λ.

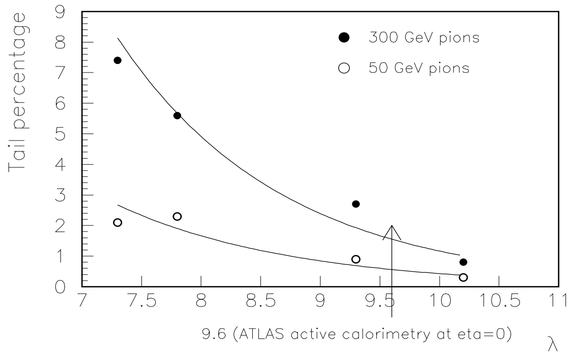

Figure 3-34 Percentage of events in the low energy tail (below 2σ) for different calorimeter depth configurations. Results are shown for 50 and 300 GeV pions.

3.4.5 Single particle angular resolution

The data collected with the combined test beam setup, were also used to determine the angular resolution of hadronic showers[N-70]. The knowledge of the direction of the decay-jets can be useful to improve the mass reconstruction of particles decaying into a pair of jets. To determine the angular resolution of the polar angle for a hadronic shower, the mean position was measured independently in each radial compartment of the electromagnetic and hadronic calorimeter on an event to event basis. The polar angle θ was determined for each event by a linear fit to the equation $\bar{z}_j = \tan(\theta) \cdot r_j + b$, where $\bar{z}_j$ is the centre of gravity of the energy deposition in a sampling *j* averaged over all contributing cells in azimuth, r_j is the known radial position of the compartment taken in the centre and b is an arbitrary intercept. For each energy the angular resolution is obtained from a Gaussian fit to the reconstructed beam angle θ. The angular resolution is shown in Figure 3-35, as a function of beam energy; it is a linear function of $1/\sqrt{E}$. The fit gives $\sigma(\theta) = (243.1 \pm 8.9)/\sqrt{E} + (12.1 \pm 0.7)$ mrad, resulting in an angular resolution of $\sigma(\theta)=1.5^{o}$ for hadron showers from 300 GeV pions. This is about a factor of four better than the Tile Calorimeter cell size. Averaging over all energies a mean polar angle $\theta=(11.23 \pm 0.01)^{o}$ was obtained, which agrees well with the nominal beam angle of 11.3°.

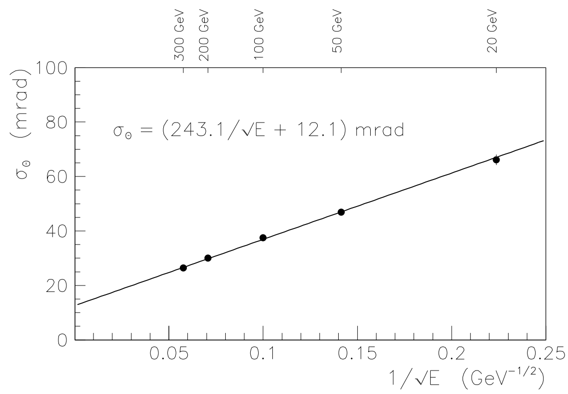

Figure 3-35 Angular resolution for pions as a function of the beam energy.

3.5 Test beam performance for muons

One of the important tasks of the hadronic calorimeter is to identify muons and to measure their energy losses in order to improve the muon energy measurement. The experimental studies of the calorimeter response to muons were limited to momenta above 10 GeV/c [N-68]. However, the good agreement between our measurements and the Monte Carlo simulations, made it possible to predict the calorimeter performances for low energy muons too. Muons with transverse momentum p_T below 2 GeV/c will stop in the absorber structure of the hadronic calorimeter. For these muons, the calorimeter is the only device in ATLAS which can identify them.

Muons with p_T above 2 GeV/c will be measured in the muon detectors after passing more than 100 X_0 of electromagnetic and hadronic calorimetry. For muons with p_T between 2 and 5 GeV/c, the calorimetric measurements are important to correct the muon energy measured in the spectrometer since a significant fraction of the energy will be absorbed in the calorimeter. Simulation studies show that calorimeter information is very useful to identify B-meson decay and b-jets with soft muon[N-23]. The probability to produce energetic knock-on electron, electron-positron pairs and gammas in the steel absorber increases with the muon energy. Electromagnetic showers developed by these particles can be measured by the calorimeter on an event-by-event base, and this information could improve low energy tails of muon energy measurements done by the muon system. The light output produced by muons in a scintillator are usually very small compared to signals from hadron showers. The requirement to also identify muons with the calorimeter puts additional demands on the dynamic range of the read-out system. Low noise and high photoelectron statistics are additional important ingredients for good performance.

All these aspects have been studied and investigated using muon beams at various energies between 10 and 300 GeV and incident polar angles θ between 0^o and 40^o. Muons impinging the calorimeter at θ = 90^o have been used for the calibration, the light yield measurements and the measurements of the spectrum of muon energy losses.

3.5.1 Muon response

The energy lost in the 1 m test Tile Calorimeter by 150 GeV muons incident at a polar angle of θ=10° is shown in Figure 3-36 for the full calorimeter (8.9 λ). The energy loss spectrum approximately follows a Landau distribution, but with large tails at high energies caused by radioactive processes as well as energetic δ-rays. The simulated energy losses are compared to the data in the figure. The width of the pedestal distribution is also shown and is about 40 MeV/cell. The spectra normalization is made to obtain the same most probable value of energy loss at 50 GeV as in the data. The simulations, which do include instrumental effects, agree well with the data.

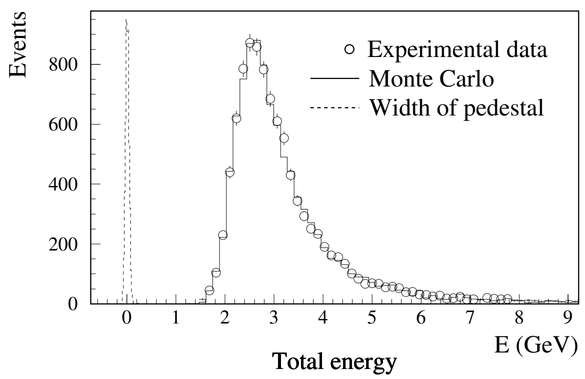

Figure 3-36 Energy loss of 150 GeV muons traversing the full test Tile Calorimeter depth. The open circles are experimental data while the full lines are simulation results with instrumental fluctuations. The pedestal width is also shown.

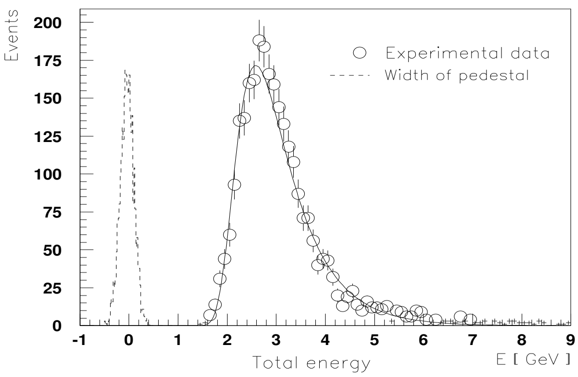

Figure 3-37 Reconstructed muon energy in Module 0 for 100 GeV muons incident at η=0.55. Shown is the muon signal from the sum of all Module 0 energy. The fit is to a Moyal function. For comparison, the width of the pedestal is shown.

Muons were also used to verify the reconstruction and identification of the muon signal in Module 0. The mechanical construction of this module is practically identical to the 1 m prototype modules with similar sampling fraction and thickness of scintillator tiles. However the module is shorter by 1 λ resulting in the scintillator tiles being shorter by 313 mm. We should thus expect the energy deposited by the muons to be 17% smaller at a fixed θ. The precision in reconstructing the signal is a strong function of the read-out system and in the case of pulse reconstruction, the algorithm used to calculate charge and subtract pedestal. Shown in Figure 3-37 is the reconstructed muon energy for 100 GeV muons incident at η=0.55. The most probable charge is about the same as that seen in the 1 m prototype modules, but slightly higher than that expected from the scintillator sizes, fibre lengths and the difference in impact angle. The width of the pedestal is wider than with 1 m prototype module electronics. We understand the pedestal width as caused by an undetermined source of coherent noise in the test beam, and we expect the width to decrease significantly after noise analysis and reduction. As mentioned before, until the calibration becomes better understood, the real value of reconstructed charge is still preliminary. Suffice to say that the muon signal is easily distinguishable from the background noise.

3.5.2 Light yield

The number of photoelectrons per GeV (Npe/GeV) of deposited energy for the 1 m prototypes constructed between 1993 and 1995 has been determined by using three different methods: neutral filtersD-4, muon data and laser information. In the following we summarize the study done with 150 GeV muons impinging on the calorimeter at θ = 90^{o}. The standard formula to determine Npe/GeV of deposited energy per calorimeter cell summed over the left and right PMTs, can be found in ref.[A.9]. Figure 3-38 shows the muon signal for these modules. Looking at the prototypes of 1993, 1994 and 1995, there is a clear improvement from 24 pe/GeV to 64 p.e./GeV. This improvement in the light yield is due to optics improvements. The effect of the photostatistics on the width of 150 GeV muon signal is shown in the figure. This figure indicates that an increase of light yield above about 48pe/GeV would not improve on the quality of the muon measurements. Nevertheless ageing effects and radiation damage will reduce the light yield and in long term we will profit of the highest light output. The fact that muons are readily seen in Sample 1 as shown in the figure is important to ATLAS physics. One technique to identify b-jets with a low PT muon, performs jet classification by applying a cut to the summed energy deposition in the last depth of the Tile Calorimeter. Since the thickness of Sample 1 in the 1 m prototype (about 30 cm) is comparable to the thickness of the last sample of the Tile Calorimeter, we can thus expect this method will become a viable tool.

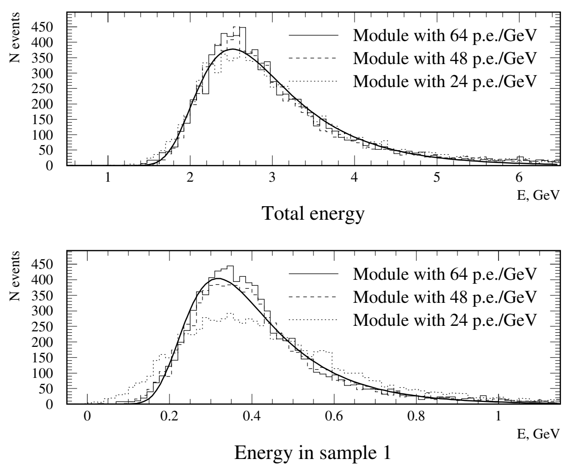

Figure 3-38 Energy measured in the test calorimeter for 150 GeV muons traversing (top) the whole Tile Calorimeter length (9 λ) and (bottom) the first sampling (1.5 λ) of three prototypes with different light yields (24, 48 and 64 pe/GeV per cell). A Moyal fit applied on the module with the highest light yield is shown as a full curve.

3.5.3 Muon response uniformity

The uniformity of the response to muons produced in ATLAS at different values of η, ϕ and z has been studied. Data from the standalone runs are presented below.

Muons with momentum of 180 GeV/c, incident at θ = 10°, were scanned across 60 cm of the 1 m prototype module stack in z. The results of the z scan are shown in Figure 3-39. The signal response is quite uniform with an rms of less than 2%.

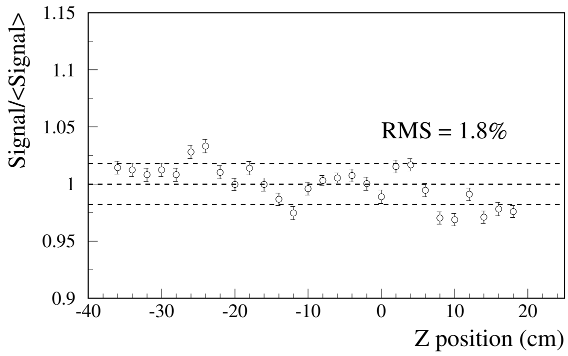

Figure 3-39 Uniformity scan along the z-direction using 180 GeV muons incident the five prototypes stack at an angle θ=10°.

The muon response dependence on the θ angle has been studied with 200 GeV muons. The signal, normalized to the same path length, is shown in Figure 3-40 as a function of the incident angle θ for data and Monte Carlo simulations. A dependence of the signal on θ within 5% is observed. This effect is also well reproduced by the Monte Carlo simulations. A similar behaviour was observed for pions and it can be understood due to the sampling fraction variation with θ (see Section 3.4.3).

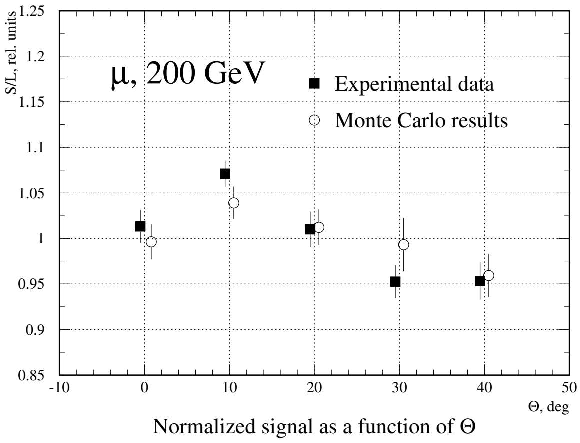

Figure 3-40 Average muon signal normalized to the same path, as a function of θ.

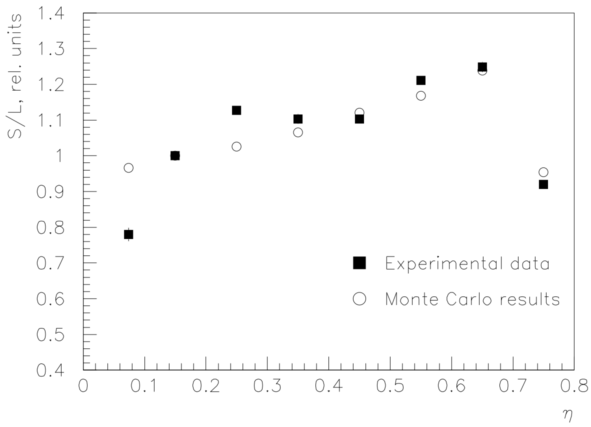

Figure 3-41 Module 0 scan in η for muons at 100 GeV.

In Figure 3-41 the response of Module 0 to muons is shown as a function of η, and compared with the Monte Carlo prediction.

The uniformity scan in ϕ has been studied using 150 GeV muons incident the 1m prototype stack at θ = 10°. Figure 3-42 shows the signal in the module below and above the interface (crack) between the two modules as a function of y (0.56° in ϕ correspond to 1 cm in y). The crack is visible by a drop in the signal of about 60% at y = 0 cm. This decrease in the crack is due to an air gap between the two modules. In this region muons have a high probability to pass through the 1.8 m of the calorimeter leaving minimal signal.

Outside the crack region a rather uniform response with σ = 2.5% of the Gaussian fit over the full module surface is observed.

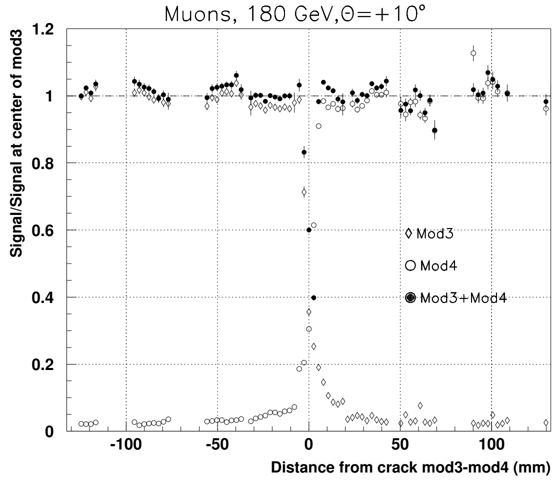

Figure 3-42 Uniformity scan along the ϕ direction using 180 GeV muons at $\theta=10^o$ for the 5 prototype stack. The distribution is of the most probable value of the energy deposited by muons

3.5.4 Muon identification

Figure 3-36 shows that it is indeed possible to well separate muons from the pedestal noise. Furthermore, reconstruction of the energy of the muon on an event-by-event basis allows us to correct the muon measurement made by the muon system to recover some of the low energy tail of the muon momentum distribution due to muon energy losses in the calorimeters[N-68].

The muon energy distributions for the experimental data and the Monte Carlo have been studied for energies between 10 and 300 GeV traversing the Tile Calorimeter at $\theta = 10^o$. The Monte Carlo data also includes muons of 2 and 5 GeV. Both the most probable value and the truncated mean of energy losses increase with muon energy (see Figure 3-43) due to the increasing probability of radioactive losses. The most probable values vary from 2.26 to 2.85 GeV for incident energies between 10 and 300 GeV. The truncated mean increases more rapidly. The same figure, on the right, shows (normalized) Module 0 results, compared with the Monte Carlo prediction.

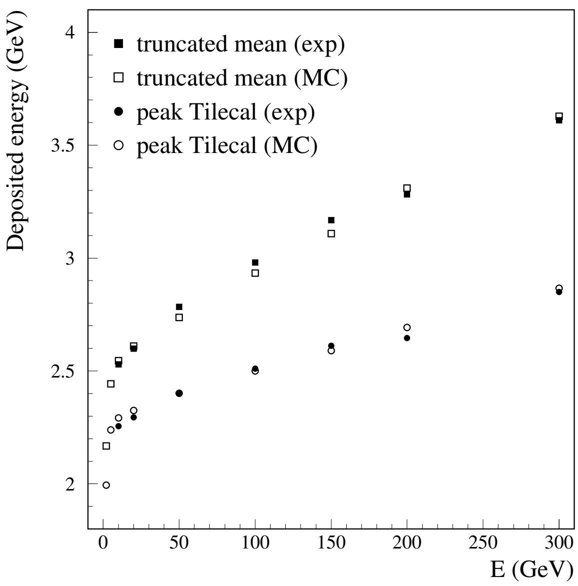

Figure 3-43 The truncated mean and the most probable values (peak) for the energy measured in the 5 prototype modules calorimeter as a function of the muon beam energy. Both experimental data and Monte Carlo results are shown.

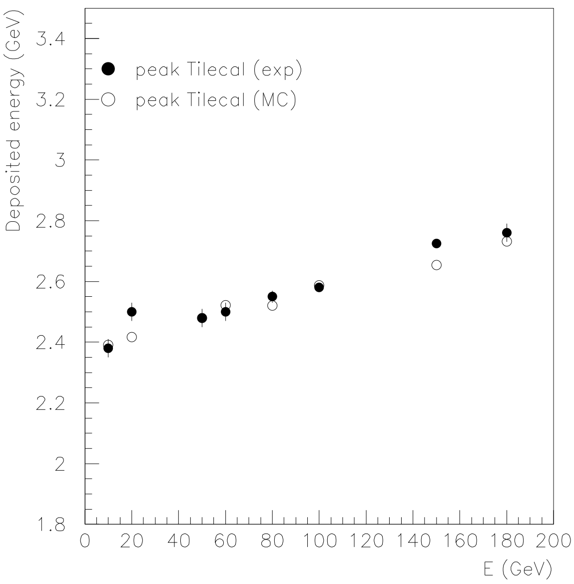

Figure 3-44 The most probable value (peak) for the energy measured in Module 0 as a function of the muon beam energy. The black points are the data, the white circles are the Module 0 simulation.

The most probable muon energy deposition in the calorimeter of about 2.5 GeV can be compared to the expected energy deposition of minimum bias events per bunch crossing for the nominal luminosity at the LHC. This amounts to about 0.1 GeV in a $\Delta\eta$ x $\Delta\phi$ = 0.1 x 0.1 calorimeter cell. Therefore, there is a comfortable margin for detecting isolated muons even at the highest luminosity, where the S/B ratio will be of the order of 10.

Different mechanisms of the muon energy losses have been tested using experimental data at $\theta=90^{o}$ (see Figure 3-45). The Tile Calorimeter data are in very good agreement with Kellner and Kotov calculations for pair production, Bhabha formula for energetic knock-on electrons and Petrukhin and Shestakov calculations for bremsstrahlung processes[D.6]. One of the important topics related with muon detection and the first level muon trigger in ATLAS, described in Section 3.4.4.1, is the reliable understanding of backgrounds from hadronic shower punchthrough. Using the Tile Calorimeter data, the punchthrough probability for jets of different energies can be predicted. The punchthrough probability for a 1 TeV jet turns out to be about 50%.

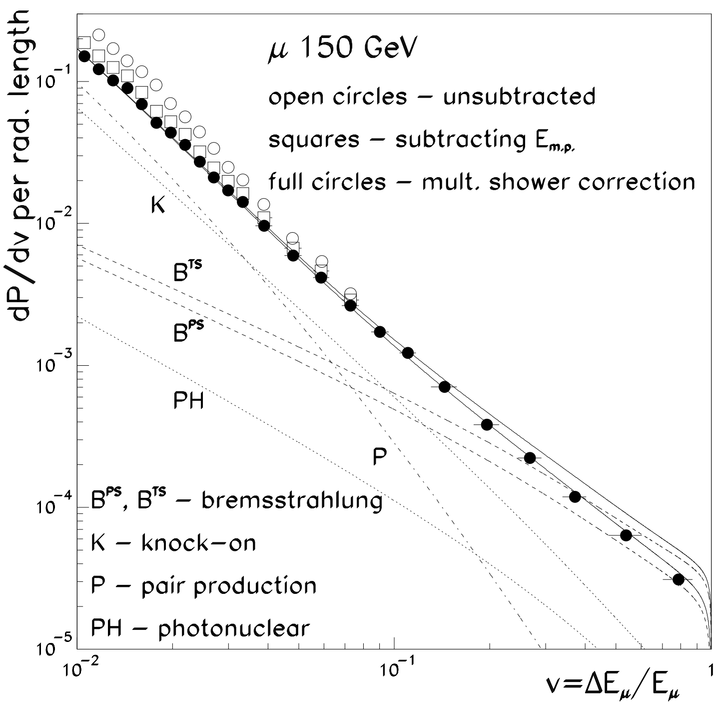

Figure 3-45 The distribution of differential loss dP/dv for 150 GeV muons in iron. The curves P, K and B for pair production, knock-on electrons production and bremsstrahlung are shown.

3.6 Calibration with particles

The Tile Calorimeter design includes the capability of running a ^{137}Cs radioactive source along axial holes, through each scintillator tile, inside the rods compressing the calorimeter modules. This feature permits us to check the response of each scintillator tile. Furthermore, it is important to know how well the calorimeter tracks the source calibration. This is important in order to have confidence that the sample of production modules not exposed to beam will have performance characteristics as well known as those modules which were calibrated in a beam.

As the source is run through the holes, the average current produced by tile activation is integrated and recorded for the tile's respective PMT. The high voltage is then set such that the integrated current is the same for each group of scintillators coupled to a phototube. Data shown below have been analysed for the 1 m prototype modules, primarily from the standalone runs.

3.6.1 Check of the calorimeter calibration with pions

In order to cross-check that the calorimeter has been correctly calibrated with the ^{137}Cs source, data of 180 GeV pions, impinging at $\theta = 0.2^o$ and covering about 70 cm of the front face of the detector in the standalone configuration, have been analysed. A substantial amount of energy is deposited in all the cells of the module and it is possible to calculate the ratio *r = (L-R)/(L+R)* for the two PMTs connected to each cell, where *L* and *R* designate the signal in either of the two PMTs. Figure 3-46 shows the *r* distribution for the 20 cells (5 towers and 4 depth segments). The distribution has an rms of 1.6% and shows no tails. Hence, the calibration of an individual PMT is good to $1.6/\sqrt{2} = 1.1\%$, giving an independent cross-check on the performance of the ^{137}Cs calibration.

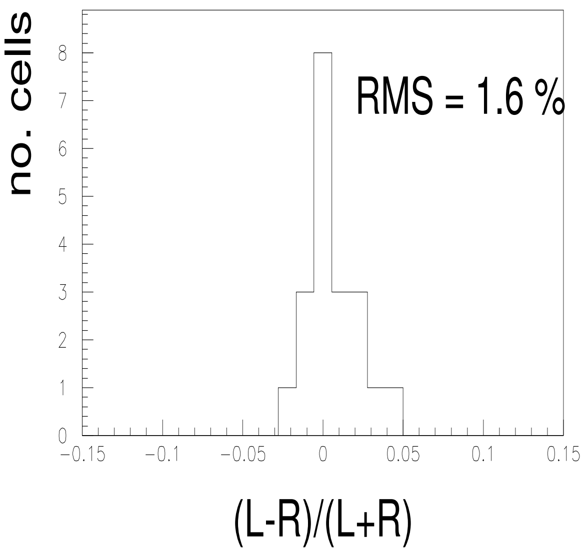

Figure 3-46 The *r* ratio distribution for the 20 cells of the central module.

As an additional cross-check, data from pions impinging at $\theta = 90^o$ in the center of tiles 2, 5, 10 and 15 (there are eighteen tiles numbered from the inner radius) of the central module have also been analysed and the result is consistent with the above.

3.6.2 Calibration with muons

In order to provide an alternative technique for the cells' intercalibration, the 1 m prototype calorimeter has been exposed (in standalone configuration) to high energy muons impinging at 90^o in the geometrical center of each of the 18 radially stacked tiles. Each depth segmentation contains several radial stacks of scintillator tiles. These stacks are read-out through 5 pair of phototubes for each depth segment, each phototube constituting a tower. In the z direction, the number of scintillator tiles per radial stack is 10. The resultant energy spectra are then fitted with a Moyal function[N-44].

3.6.2.1 Comparison of ^{137}Cs and muon signals for the tiles

For each radial tile size (1-18), the currents given by the corresponding 10 PMTs are averaged. The observed pattern across the 18 tiles obtained with source and with muons are shown in Figure 3-47.

A decrease in the muon response in the last two depth samplings as the tile number increases is observed. This effect is due to the decrease of the light yield at the center of the outside edge of a tile since the tile gets wider and the distance between the light production point and the fibre gets larger. It is possible to see that the tiles having even numbers tend to give slightly more

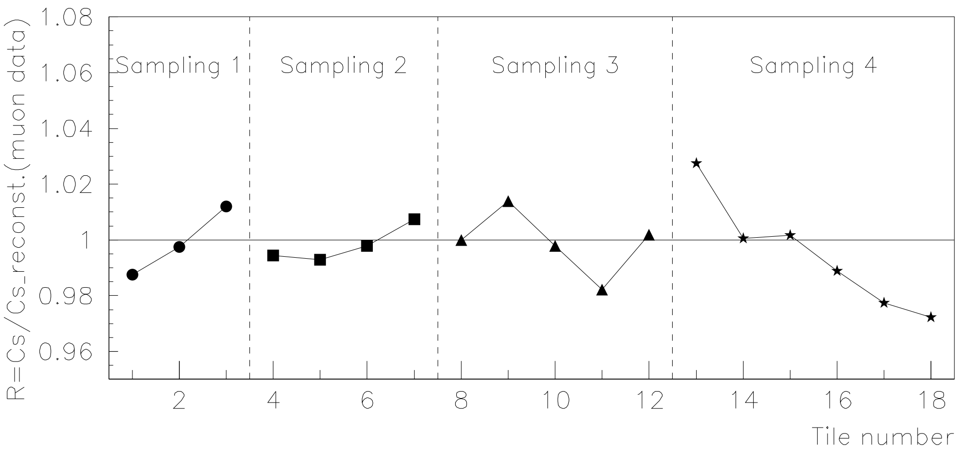

Figure 3-47 Comparison between the ^{137}Cs and the muon data for the center 1 m prototype module in the standalone run. Each point is the average of the signals from the 10 PMTs corresponding to the specific tile size. The muon data are normalized to their mean value, while the Cs data are normalized to their mean value but which excludes the last point of each sampling. Muons were incident at 90°.

light than tiles having odd numbers. This is a consequence of the fact that alternating radial stacks are connected to different sets of fibres of slightly different length. The ^{137}Cs data follow a similar pattern except for the last tile in each sampling where, due to the range in iron of the ^{137}Cs 662 keV photons, only 78% of the energy is deposited in the cell read-out. When trying to correlate ^{137}Cs with muons, the fact that the ^{137}Cs source deposits energy across two tiles has to be taken into account. In such a way it is possible to calculate the ratio of the ^{137}Cs signal over the ^{137}Cs signal reconstructed from the muon signal. The latter is calculated with the formula:

$$Cs_i = 0.78 \cdot \mu_i + 0.22 \cdot \mu_{i+1} \qquad 3\text{-}4$$

where i is the tile number within a given sampling and μ_i is the mean of the muon distribution for 10 PMTs in the i^{th} sampling. The results are shown in Figure 3-48.

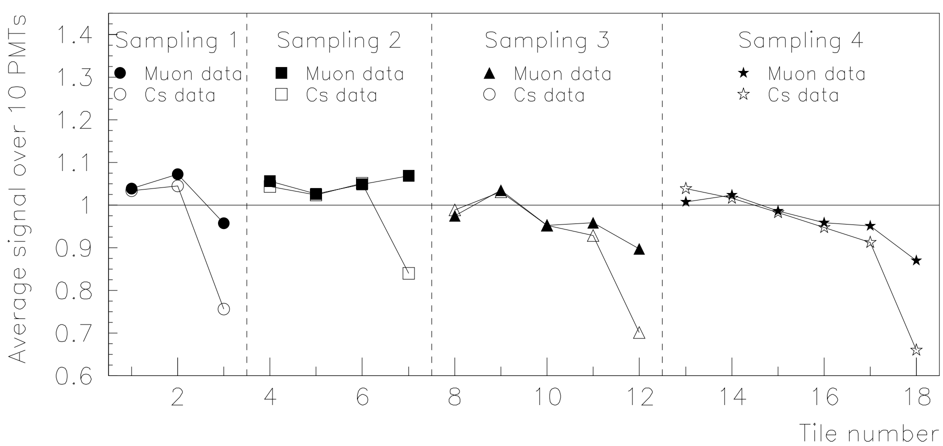

Figure 3-48 Ratio of ^{137}Cs signal over ^{137}Cs signal reconstructed using muon data.The signal is averaged over the 10 PMTs corresponding to a given tile size.

In this ratio, the effects responsible for the pattern observed in Figure 3-47 cancels to the first order.The dispersion in the resultant ^{137}Cs to muon ratio is 1.6%.

3.6.2.2 Comparison of ^{137}Cs and muon signals for the PMTs

For a given tile size, the sharing-corrected ^{137}Cs over muon signal ratio is studied as a function of the PMT number. Figure 3-49 presents results for the four samplings of the central module in the calorimeter stack. Shown are the data for each of the tile sizes in the depth vs the respective phototube they are read-out by. PMT numbering is such that the sequence 1+2, 3+4,..., corresponds to the same set of scintillator tiles.

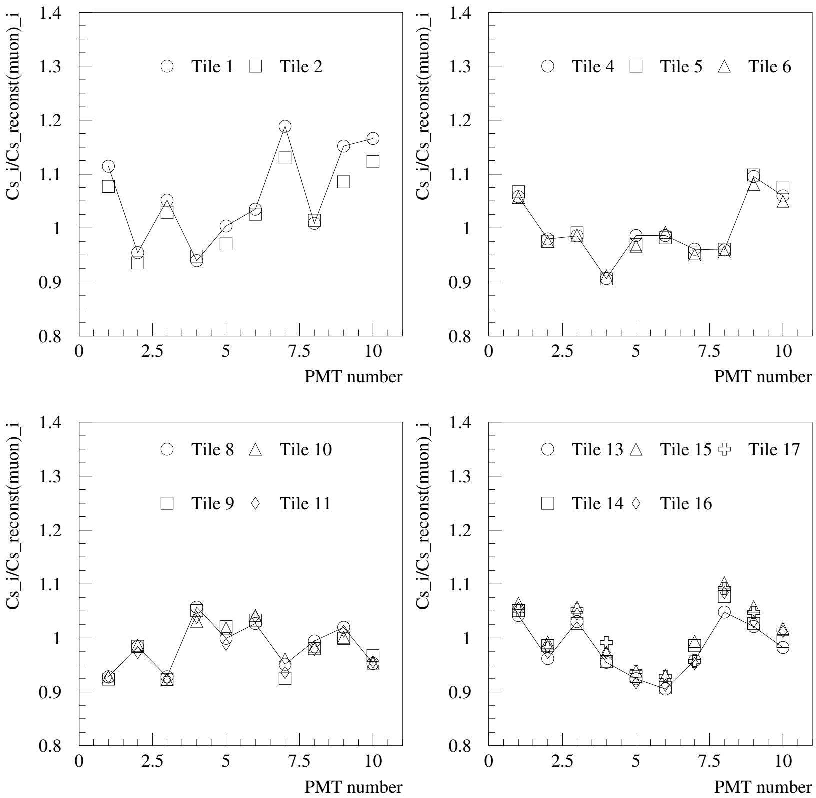

Figure 3-49 Ratio of ^{137}Cs over reconstructed ^{137}Cs using muon data for individual PMT.

Each individual distribution shows a large dispersion. Any pattern clearly is reproducible from one tile to another within a sampling. The three central modules show the same behaviour. The resulting dispersion on the ^{137}Cs/muon correlation for an individual PMT is 6% which is compatible with the dispersion of the average. Similar data taken at a later time show a similar result of 5.3%. Systematic checks have been performed. ADCs, ^{137}Cs electronic modules and cables have been interchanged. The pattern is insensitive to any of these modifications. A possible explanation is the non-linearity of the PMT responses over the large range of anode currents. Muons give a small average current due to the low rate, while the ^{137}Cs current is relatively large. A study done with pions showed that the ^{137}Cs calibration checked on cells with relatively large energy deposit is correct to 1.3%. The same study showed that for very low energy deposit, differences between the individual PMT pairs in a cell are of the level of a few percent, pointing to the PMTs non-linearity.

Figure 4-i A submodule under assembly.

Figure 4-ii View of the barrel Module 0 after assembly.

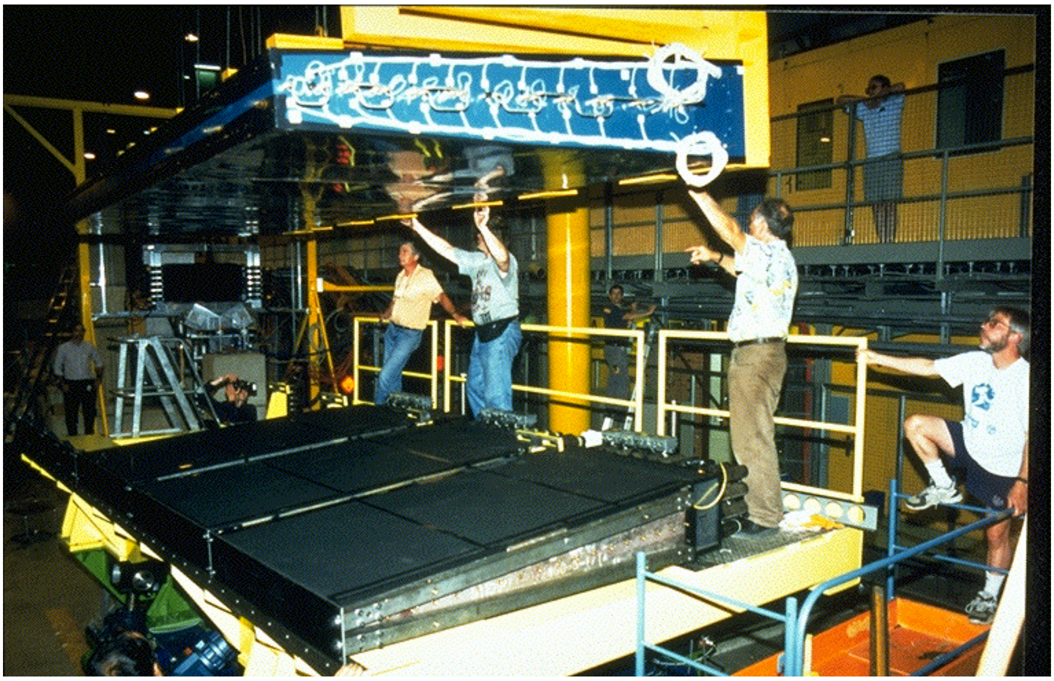

Figure 4-iii Barrel Module 0 being lowered into position on the scanning table in the H8 test beam area.

4 Mechanics

The Tile Calorimeter passive absorber is a laminated steel structure with pockets at periodic intervals to contain the scintillating tiles. The structure is built in a modular fashion to facilitate the construction. It is a self contained unit with the read-out electronics being fully contained within the calorimeter itself. In addition to its function as passive absorber, the Tile Calorimeter also provides the magnetic flux return for the ATLAS solenoid. Extensive calculations have been carried out to evaluate the effect of stray fields as well as magnetic forces on the assembly. The details of the design and engineering analysis of the structure and supports are presented below.

4.1 Detector design

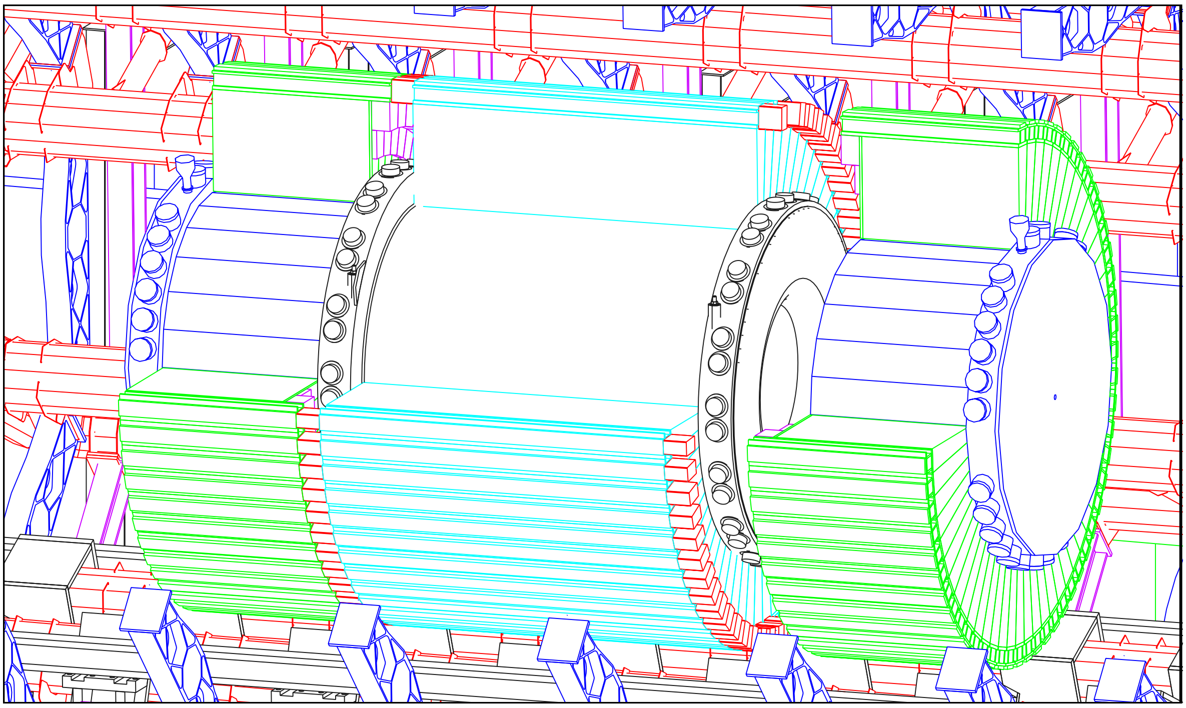

Figure 4-1 View of the calorimeter system in ATLAS. Visible are the three Tile Calorimeter assemblies -the central barrel and 2 extended barrels. Each assembly is built from 64 wedges (modules).

Figure 4-1 shows a pictorial view of the Tile Calorimeter as it sits within the muon system of the ATLAS detector. The Tile Calorimeter is built in three sections: a central barrel covering approximately from -1 to +1 in rapidity and two extended barrels extending the rapidity coverage to approximately |1.6|. Each of the three calorimeter sections is constructed from 64 modules, each covering 5.6° in azimuth.

The basic construction of a barrel module is shown in Figure 4-2. It is built out of 19 sub-modules, each separated by a design gap of 0.8 mm, mounted on a strong-back support girder which houses the read-out electronics. Its cross section is sufficient to form the primary magnetic flux return. Except for one “special” sub-module used to assure the final length of the module, all sub-modules are identical steel laminations approximately 300 mm long. The azimuthal design gap of 1.0 mm between modules corresponds to a loss of fiducial coverage of less than

0.5%. This is substantially smaller than the fraction of uninstrumented calorimetry in comparable scintillator-based hadron calorimeters built for operation at hadron colliders in recent years (e.g. UA1, UA2, CDF and ZEUS).

The assembled calorimeter structure is self-supporting through a bearing connection between modules at the inner radius and a bolted plate connection at the outer radius of the girder. By replacing this plate by elements of the support saddle, the latter is also designed to be an integral part of the calorimeter structure. This saddle connects the calorimeter to rails which provide movement for installation and alignment. It also supports the Liquid Argon calorimeter and presents a great engineering challenge.

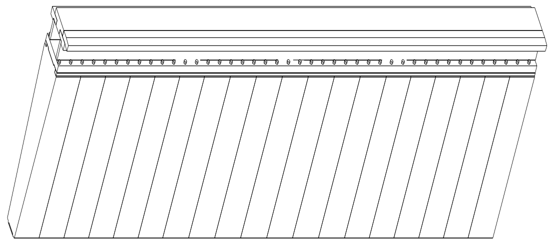

Figure 4-2 Barrel Module 0 construction (schematic).

Except for some details associated with integration with other ATLAS sub-systems, the design of an extended barrel module is identical to that of a barrel module although it involves nine rather than 19 sub-modules.

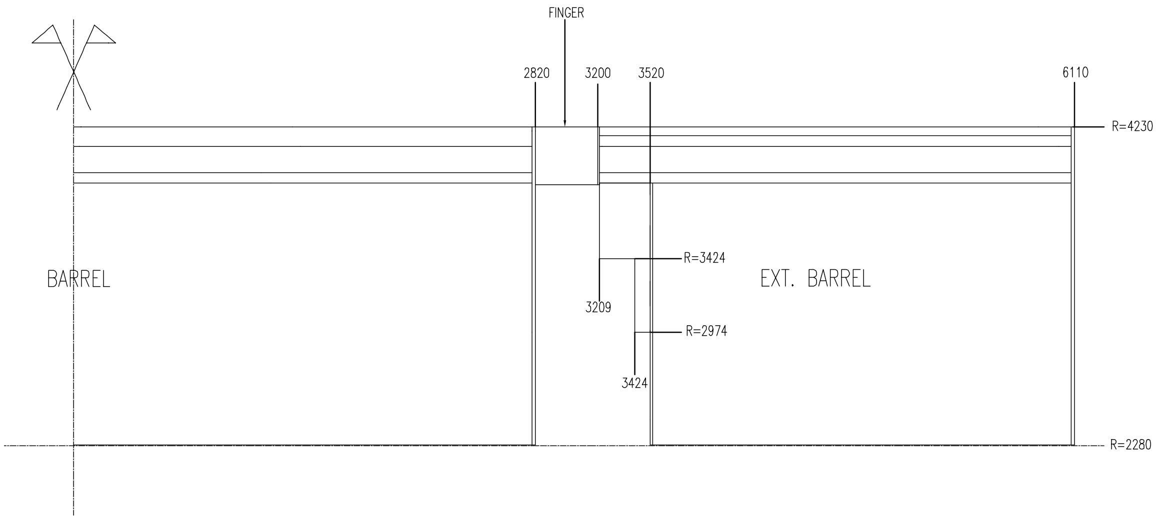

Figure 4-3 Cross section of the Tile Calorimeter cut on line of symmetry at z=0.

A 2-dimensional projection of the Tile Calorimeter is shown in Figure 4-3, in which details of the region between the barrel and extended barrel calorimeters may be seen more clearly. This region from 2820 mm to 3520 mm is called “the gap”, and is necessary for services and read-out cables to the inner detector and the Liquid Argon calorimeters. This volume is a concern for loss of energy and the Tile Calorimeter design includes a shorter sub-module (termed “the plug”) which fits within the free space around the services. This way the amount of instrumented calorimetry is maximised. This sub-module is a laminated structure which is quite similar to a standard sub-module and can be constructed on identical tooling with only minor modifications. From the point of view of ATLAS as a whole, this detector is also an important contribution to the shielding of the muon system from the intense neutron fluence in the inner detector region.

As was mentioned above, the read-out electronics is fully contained within the support girder. To allow access for maintenance and repair, the electronics is mounted in a drawer system which may be extracted from the module once the extended barrel calorimeter has been moved back by about 1.5 m (once installed, the barrel calorimeter remains stationary). Tooling will then be mounted in the gap region to allow the removal of the drawers (each weights about 50 kg) from the center to outwards in the case of the barrel and from the outside to inside in the case of the extended barrels. In the regions where interference with the supports for the Liquid Argon cryostats exists, the possibility to remove all read-outs on a single side of the detector has been foreseen. A corresponding provision has been made for the radioactive source calibration system.

The design we propose here has evolved from the RD34 program which was carried out over several years. During this period five prototype sub-modules, 1 m long, were constructed and tested in high energy beams. As a final step, in 1996, we constructed a full scale barrel prototype module (Module 0) to establish the ATLAS design and plan to construct and test two prototype extended barrel modules in 1997. These activities have provided an invaluable information and form the basis of the design presented below.

4.2 Sub-module production

Sub-modules are the basic modular elements of the mechanical assembly and represent the bulk of the calorimeter absorber structure. The design is such as to allow them to be constructed identically in the various participating laboratories, using minimal manpower and tooling. Each sub-module is a stack of steel plates of different shapes (masters and spacers) bonded together with a structural adhesive and welded with straps at the four corners.

The radial and azimuthal envelope of the laminate is determined by the precision used to cut the steel plates and by the procedure of the relative alignment of the various plates during the stacking procedure. The vertical precision and reproducibility is given by the lamination precision of the individual plates and by the use of the adhesive, which can accommodate some level of variation in the plates surface thickness and quality.

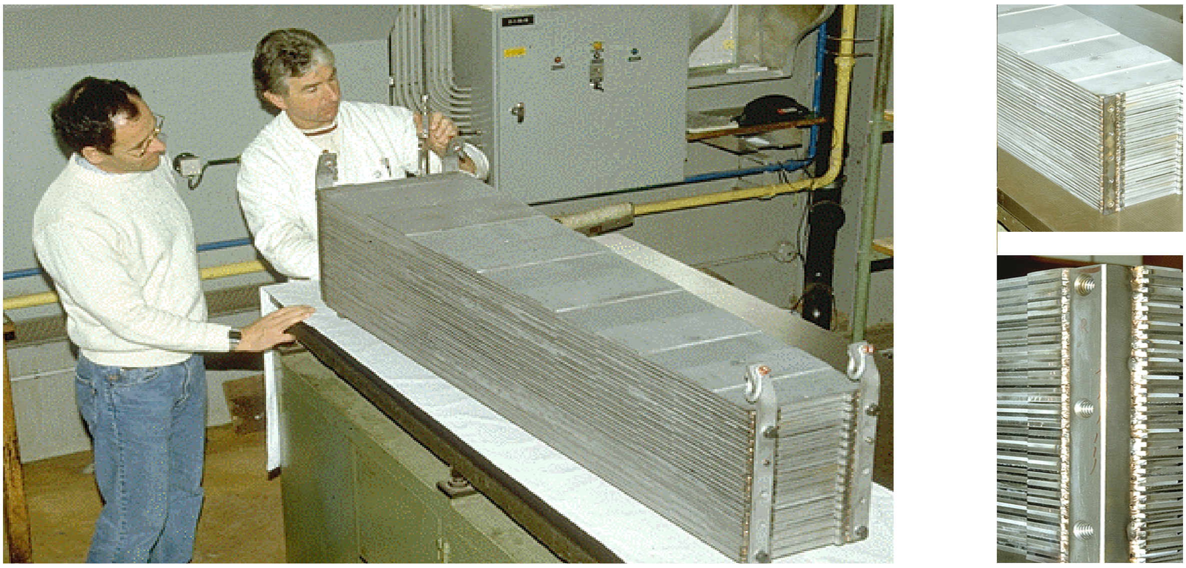

Figure 4-4 A standard sub-module.

We propose to construct 65 full wedges for the ATLAS detector. This requires the construction of 2535 sub-modules, each weighting about 900 Kg. This operation should not take more than three years of work. At the present time 28 sub-modules have been constructed for the Module 0 prototypes, which has provided valuable experience in the various fabrication and assembly steps.

4.2.1 Design and specifications

Figure 4-5 shows the assembly drawing of a sub-module, with the location of the master plates (large trapezoids, label 1) and the spacer plates (small trapezoids, labels 2 to 13).

The basic geometrical element, called a period, consists of a set of two master plates and one set of spacer plates. In a stack this structure repeats itself 16 times in the case of a standard sub-module. During construction, half period elements will be pre-assembled starting from an individual master plate and the corresponding six spacer plates (half-period a and b). The relative position of the spacers plates in the two half periods is staggered in the radial direction, to provide pockets in the structure for the subsequent insertion of the scintillator tiles. The geometry and the specifications for masters and spacers are described in Section 4.2.2. A series of holes are located on the symmetry axis of all plates. These holes allow for the insertion of calibration tubes, which pass through the whole module absorber structure, and are also used to precisely locate spacers on masters during the half-period pre-assembly by means of elastic dowels. The radial and lateral envelope of the sub-module stack is determined by the dimensions and the relative alignment of the master plates. Spacers are dimensioned to fit inside this envelope.

In the overall tolerance budget it is important to precisely locate the holes on masters and spacers, with tolerances of the order of 0.1 mm. In the ϕ dimension, spacers are shorter than masters by few mm, creating a channel which will be used to pass the read-out fibres which run out radially. The size of these fibre channels grows with the size of the spacers, from a minimum of 1.6 mm for spacer number 2, to 2.6 mm for spacer number 12. The exact dimensions and geometry are given in Figure 4-6

Once the stack is completed and the adhesive cured, four connecting strips are welded on the four radial corners. These steel bars have several functions. In the first place they will be used to manipulate sub-modules in the various assembly and storage operations. There are three threaded holes located on each strip plate for this. In addition, two of these bars (number 16 in Figure 4-5) are designed to provide for bolting a sub-module directly onto its girder. Dimensions and diameter of the bolts are designed to accommodate the foreseen level of mechanical stress.

The welding of the connecting strips is a delicate process which might introduce dimensional changes, and compromise the tolerance envelopes of the sub-module. In particular, given the small dimension of inner-radius connecting bars (number 15, in Figure 4-5) and the geometry of the spacers at the smallest radius, a small key element has been designed to ensure no gaps in the absorber structure near the welding points. The design of this small element is described in Section 4.2.2.5.

All dimensions and tolerances of the various elements in the sub-module design have been finalized as a function of the overall sub-module envelope tolerances to be:

$$\Delta R = \pm 0.1 \text{ mm}, \Delta\phi = \pm 0.275 \text{ mm}, \Delta h = +0, -0.25 \text{ mm}$$

The height dimension, h, of the sub-modules has been chosen to accommodate, in both the barrel and in the extended barrel modules, as many as possible identical sub-modules (standard

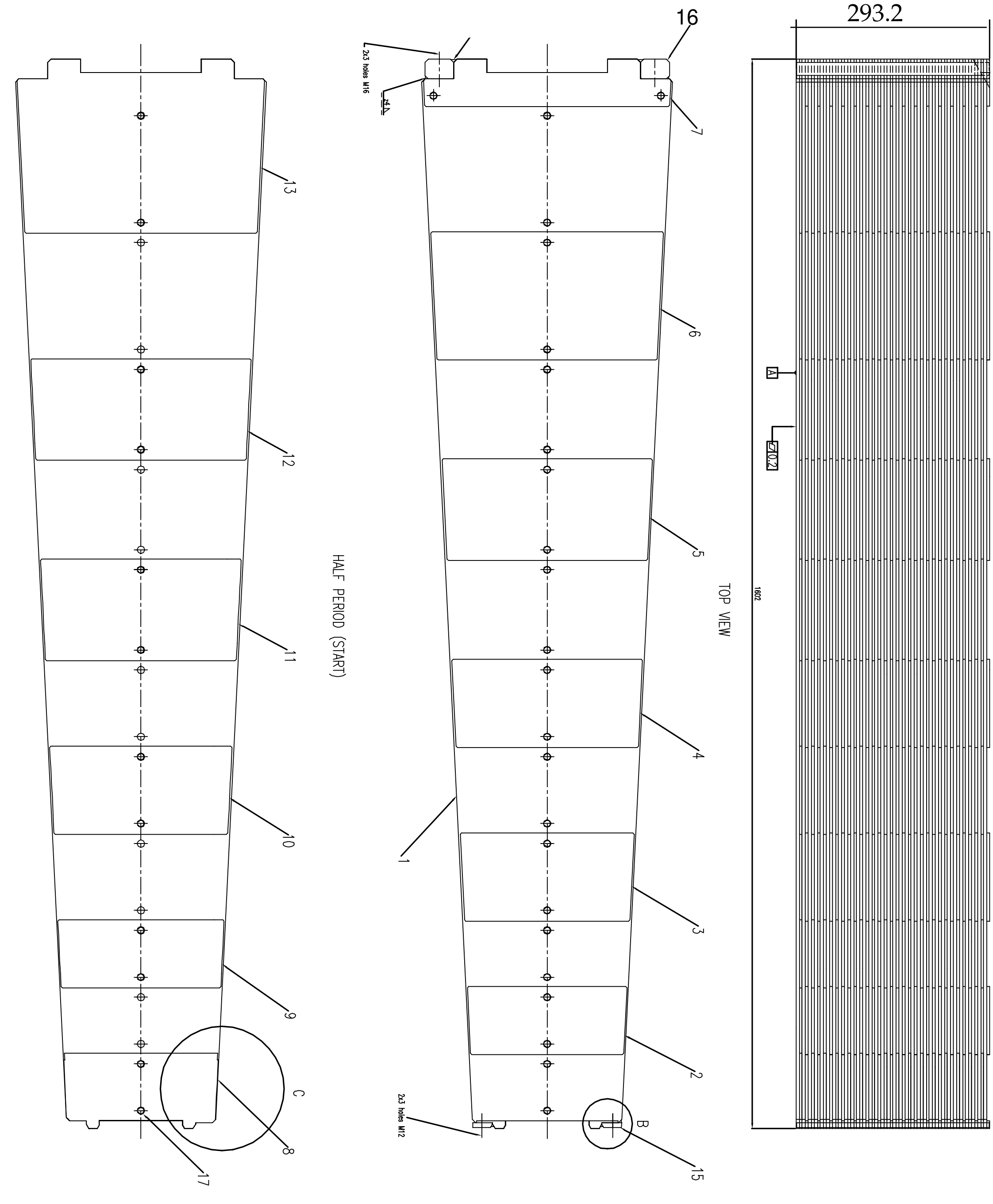

Figure 4-5 Standard sub-module assembly drawing.

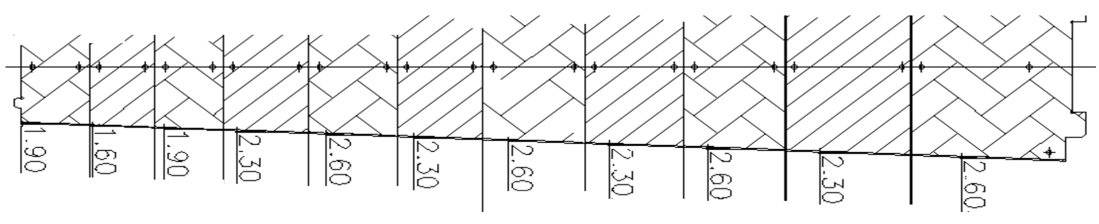

Figure 4-6 Relative location of spacers on masters in the fibre channel region.

sub-modules). This has resulted in a standard sub-module height of 293.2 mm. Special sub-modules, identical to the standard sub-modules in all the details, but for the number of half-periods, are necessary both in the barrel and in the extended barrel, to realise the needed longitudinal module length. Design and specification for these special cases, as well as for the case of the plug sub-modules are described in the following sections.

4.2.1.1 Standard sub-modules

Each barrel module consists of 18, and each extended barrel module of 8 identical standard sub-modules as shown in Figure 4-5. This accounts for a total of 2210 sub-modules of this type to be constructed.

For standard sub-modules, the number of periods to be stacked is 16, for a total height of the laminate of 293.2 mm. The weight of a sub-module is 920 Kg. The inventory of all the parts needed for the assembly and of the labels of the associated reference drawings are itemised below:

- 32 master plates: ref. drawing ATLLBSM_001
- 192 spacer plates of 12 different sizes: ref. drawing ATLLBSS_001
- 32 spacers type 13: ref. drawing ATLLBSS_001
- 384 elastic dowels type DIN7346
- 2 small connecting strips: ref. drawing ATLLBSK_001
- 2 big connecting strips: ref. drawings:ATLLBSK_001

At the present time, 28 standard sub-modules have been constructed in 6 different laboratories with no particular problems being encountered.

4.2.1.2 Special barrel sub-module

One special sub-module must be constructed for each barrel module. In this case the number of periods is 16.5, to which one has to add one layer of spacers in order to have scintillator in contact with the end-plate. In the barrel module, this special sub-module is placed at the extreme right, as the last one in the assembly. The height dimension of the stack is set to 306.4 mm for this sub-module. The catalogue of the parts and of the labels of the associated reference drawings is presented in the following table:

- 33 master plates: ref. drawing ATLLBSM_001
- 204 spacer plates of 12 different sizes: ref. drawing ATLLBSS_001
- 32 spacers type 13: ref. drawing ATLLBSS_001
- 442 elastic dowels type DIN7346
- 2 small connecting strips: ref. drawing ATLLBSK_002
- 2 big connecting strips: ref. drawings:ATLLBSK_002

Up to now one standard sub-module of this type has been constructed, fully meeting the specifications.

4.2.1.3 Special extended barrel sub-module

One special sub-module will have to be constructed for each extended barrel module. In this case the number of periods is 11 and the height of the stack is set to 201.5 mm. In an extended barrel module this special sub-module is placed as number 8 in the assembly procedure. The catalogue of the parts and of the label of the associated reference drawings is presented in the following table:

- 22 master plates: ref. drawing ATLLESM_001
- 132 spacer plates of 12 different sizes: ref. drawing ATLLESS_001
- 22 spacers type 13: ref. drawing ATLLESS_001
- 264 elastic dowels type DIN7346
- 2 small connecting strips: ref. drawing ATLLESK_002
- 2 big connecting strips: ref. drawings:ATLLESK_002

4.2.1.4 ITC special sub-module for extended barrel

The Intermediate Tile Calorimeter (ITC) is the name used to identify the special sub-module used in the 680 mm wide region between the barrel and extended barrel calorimeters. A side view of the ITC sub-module is shown in Figure 4-7.

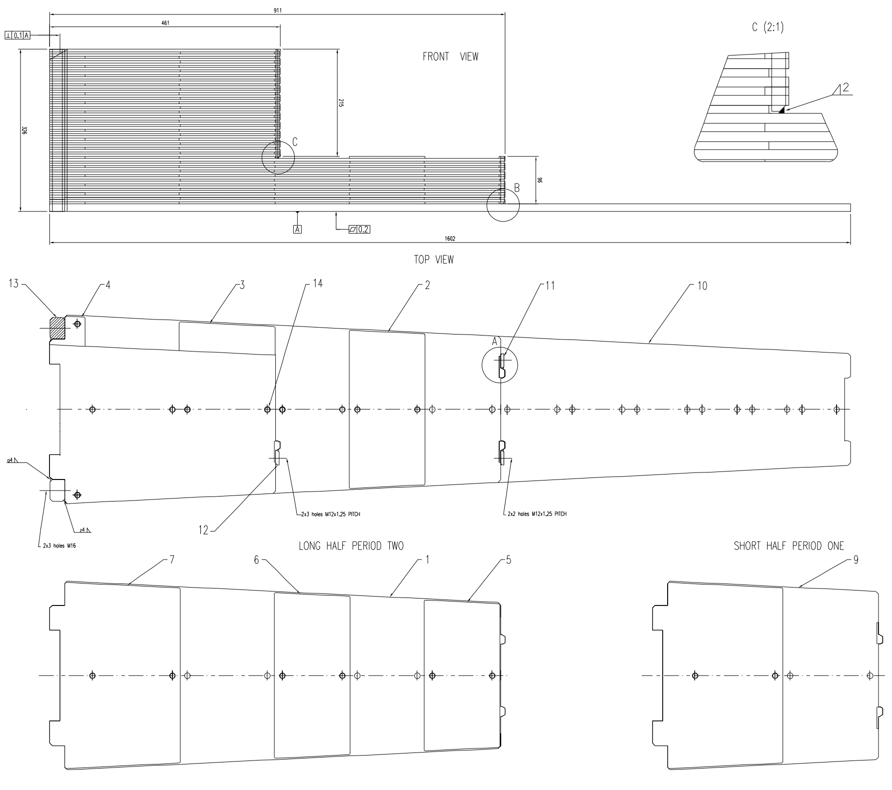

Figure 4-7 Intermediate Tile Calorimeter sub-module design.

For particles which originate at the nominal interaction point, the proposed ITC extends over approximately 0.8<|η|<1.6. The region 0.8-0.9 consists of a 311 mm thick steel-scintillator stack, similar in the design to the standard Tile Calorimeter modules. Between 0.9-1.0, the stack is

96 mm wide. The combined 0.8-1.0 region of the ITC is called the plug. At higher η, 1.0-1.6, the ITC consists of scintillator only due to severe space constraints. The scintillators between 1.0-1.2 are called gap scintillators, while those between 1.2-1.6 are called crack scintillators.The geometry is chosen to provide maximum calorimetry (and shielding) in the vicinity of the electronics boxes and services in this region of the ATLAS detector.

One special sub-module of this type will have to be constructed for each extended barrel module. It will be mounted externally, once the rest of the extended barrel structure is assembled and will rest on the internal end-plates. The shape and dimensions of this object have been the subject of a long negotiation between several ATLAS sub-detectors because of the particular location in the gap region where services and electronics from the inner detector and Liquid Argon Calorimeter have to be placed.

There are two calorimetry sections 311 and 96 mm thick, which correspond to stacks of 17 and 5 periods respectively plus a layer of spacers. The first section spans radially over scintillators 10 and 11. Section 2 starts from scintillator number 8 and spans radially to scintillator 11. To minimize costs, the design is such that all parts are kept the same as for standard sub-modules, except for the master plates which are of two different sizes. The plan for the manufacturing of these masters is simply to machine to dimension standard master plates. However, laser cutting of new masters will be employed should this prove to be more cost effective.

The catalogue of all parts and of the label of the associated reference drawings is given in the following table:

- 10 master plates: ref. drawing ATLLEPM_001
- 24 master plates: ref. drawing ATLLEPM_002
- 17 spacer plates of sizes 5,6,12: ref. drawing ATLLEPS_001
- 6 spacer plates of sizes 4,10,11: ref. drawing ATLLEPS_001
- 134 elastic dowels type DIN 7346
- 2 small connecting strips: ref. drawing ATLLEPK_001
- 2 large connecting strips: ref. drawings:ATLLEPK_002
- 2 small connecting strips: ref. drawing ATLLEPK_003

4.2.2 Components

The basic components from which a sub-module is constructed are: the absorber plates (masters and spacers); elastic steel dowels; inner radius spacer plates; structural adhesive and weld straps. The design for these components has evolved from the early days of the RD34 program to the construction of the barrel prototype module. The description and specification of all the items and the fabrication issues associated with their production is described below.

4.2.2.1 Steel specification

The 2574 sub-modules will account for an absorber mass of about 2300 tons of soft low-carbon steel of the type Fe360 (Euro-Norm 10025). The choice of this particular steel is driven mostly by its magnetic properties and by its low cost. No particular or extreme structural requirements are attached to the masters and spacers, and therefore the most common steel is sufficient.

The steel is to be procured in the form of laminated sheets of thickness 5 mm for the masters and 4.05 mm for the spacers production. The exact dimensions of these sheets (1600 mm long and 400 mm wide) have been optimized to minimize waste as a function of the cutting procedures which will be used (see Section 4.2.2.2 and Section 4.2.2.3).

The exact quantity (for 65 modules per section, including materials for the ITC and allowing 3% waste) and the requirements on quality are the following:

- 82800 sheets with dimensions 1600x400x5.0 mm^3. Thickness tolerance ±0.040 mm on a single sheet. The total weight is 2086 tons.
- 41600 sheets with dimensions 1600x400x4.05 mm^3. Thickness tolerance ±0.040 mm on a single sheet. The total weight is 849 tons.
- average sheet thickness tolerance ±0.020 mm over the whole production.

In addition, a set of requirements is given for the surface quality, roughness and for the chemical and mechanical characteristics. A first specification has been used for the procurement of the steel for the prototype construction. This will be used as the basis for the steel specification for the production procurement[N-51].

The thickness tolerance requirements are quite demanding and are the result of several years of experimental work done to optimize the stacking procedure and to use effectively the capability of the thickness compensation provided by the foreseen layer of structural adhesive. The constraints are mostly driven by the tight requirements on the final sub-module envelope dimensions. Over the last two years much experience has been gained on the status of the lamination technology, after visits and discussions with the major steel producers in the United States, Europe and Russia. The results of these investigations and of a market survey done by CERN indicate a preference for sheet production using cold rolling technology, which better satisfies our requirements. Cold rolling is normally a two phase process:

- First an hot rolled coil is produced. The steps are: melting of the ingots in an open-hearth furnace; purification and reduction of the amount of carbon and of the other elements to obtain the prescribed chemical composition; de-oxidation and subsequent casting of ingots. In the final phase, coils are hot-rolled by different procedures to a thickness of 5.3 mm.
- In a second step, possibly in a different plant, the cold rolling takes place. This uses first acid cleaning of the coil followed by cold rolling down to the nominal thickness plus 0.050 mm. At this stage, the coils are annealed in an inert atmosphere in a continuous furnace in order to remove deformed structures by recrystallisation and to eliminate internal stresses. A last pass of cold rolling is then made to achieve the final dimensions. The coil is then slit to the required width, unrolled, flattened and cut to form sheets.

The reactions and the comments of the various producers have been taken into consideration in the final steel specifications as used for the procurement of the absorber material of Module 0[N-98]. For this procurement, a single producer was selected, who had offered a product very close to our specifications at reasonable costs from early in the R&D phase of the project. Due to problems of schedule and delivery date, a specification variance was requested by the company who asked for a thickness change from 5.00 to 4.95 mm for the master plates. To compensate for this and in order to keep the overall period dimension, the 4.05 mm design thickness for the spacers was increased to 4.10 mm. Currently a second producer is being evaluated. We will base the next description of the product characteristics on these direct experiences.

Figure 4-8 shows how effectively the sheets are used in the cutting procedure. For spacers the choice has been to cut out all 12 sizes from a single sheet, thus minimizing the amount of un-used material. The total waste of material after the cutting is 15% of the sheet surface and will be accounted for in the procurement plan.

The most evident systematic effect on the thickness is the presence of a wedged profile across the width of the raw sheet. This is normally present in the hot rolled sheet and the effect cannot be completely compensated during the cold rolling process. The steel cut for Module 0 was produced in two lots. In the first lot, the perpendicular large wedge profile measured was of about 0.030 mm. In a second production in 1996, when the first production step (hot rolling) was better controlled, this wedge profile almost disappeared. The coil-to-coil reproducibility from this run was well inside the specification for all 4 mm steel and for 80% of the 5 mm coils. For the remaining coils the reproducibility was at the level of ±0.030 mm instead of ±0.020 mm. This effect has been understood and can be solved in large scale procurement by specifying a more careful selection of raw material.

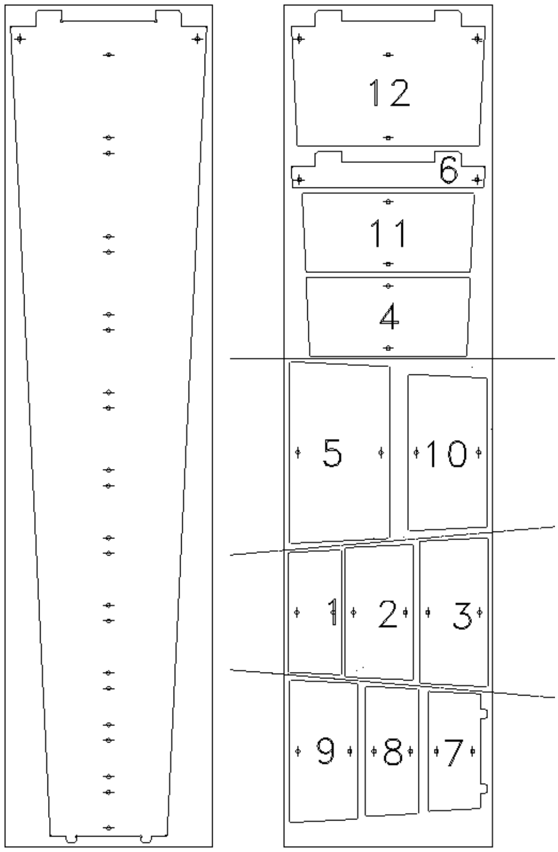

Figure 4-8 Geometry of masters and spacers cutting on single steel sheets.

The mechanical and magnetic characteristics of the steel have been measured in two of the participating labs as a cross check of the on-line information delivered by the producer. An analysis at the microscopic level of the ferritic structure has shown a typical granular structure of about 0.020 - 0.040 mm diameter. In addition, the internal stresses, the microhardness and the magnetic coercitive forces have been evaluated. In particular, the steel showed no sign of internal stresses. The anisotropy of the magnetic characteristics was measured to be negligible for the 5 mm steel and small (a few percent) in the 4 mm steel. The content of carbon is below 0.1%, the percentage of additional elements (such as Mn, Si, P, S) is less than prescribed by the norms. The influence of these additives on the mechanical properties has been measured to be less than 10%.

4.2.2.2 Master plate production

Approximately 83,000 master plates (including 3% excess to allow for rejects) are required in the assembly of all sub-modules. These plates form the basis for the mechanical structure for the absorber and are quite large (5 mm thick and approximately 1600 mm long by 400 mm wide). In addition, to minimise the fraction of uninstrumented detector, there are quite stringent tolerances placed on some critical dimensions as shown in Figure 4-9. These include the plate width which is good to 0.1 mm, the location and width of the keys which have a 0.2 mm tolerance and the position of the holes for the source calibration tubes which are required to be within 0.1 mm. Each plate weights approximately 18.6 kg.

For the early prototype sub-modules, laser cutting has been successfully used to manufacture the master plates. Although some care in setting up the laser parameters was required, it was

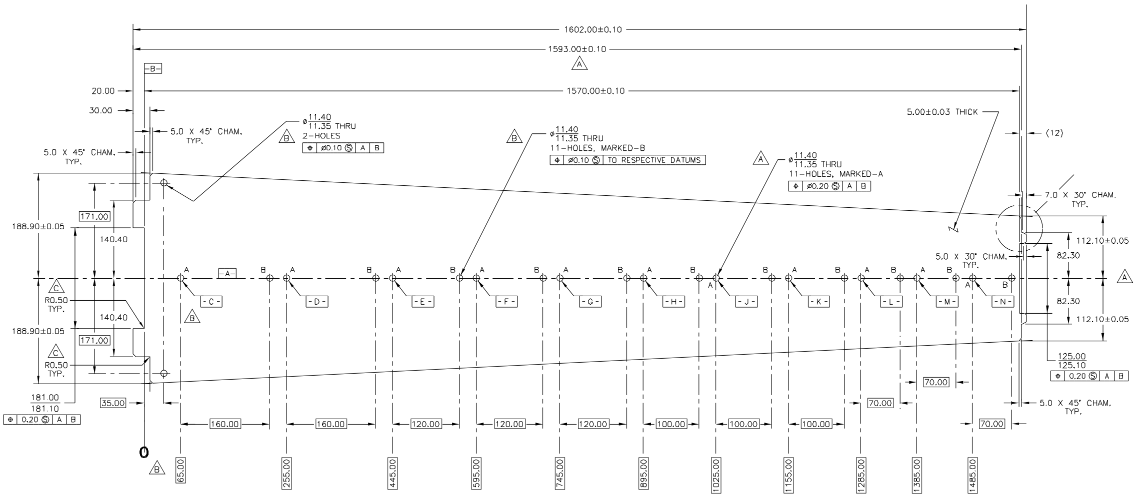

Figure 4-9 Master plate design as used for die manufacturing.

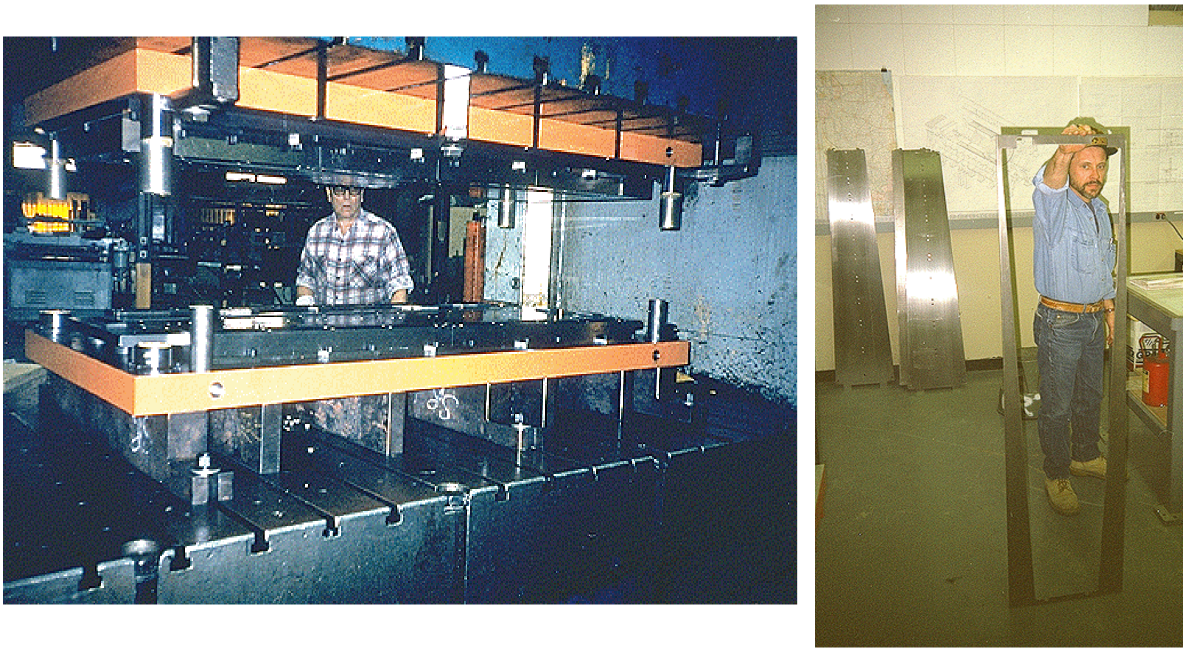

Figure 4-10 Die stamping operation on masters.

possible to meet the design specifications, albeit at the low production rate of about four plates per hour and relatively high cost. In addition, due to the single piece production, this approach requires significant inspection (for which a high precision gauge plate has been designed and fabricated). As part of the barrel prototype production, manufacturing of the master plates using die stamping has been evaluated as a means to reduce the eventual production cost. One significant design change was required by the die vendor: due to the plate thickness and the aspect ratio of the inner and outer radius keys in the plate, the vendor could not guarantee the original tolerance on the location of the key-way of 0.1 mm and requested that this tolerance be loosened to 0.2 mm as is shown in the drawing. This has only a minor impact on the ϕ gap between modules.

The stamping die installed in the press during the first production run is shown in Figure 4-10 (left) and an example of a sheet cutout following stamping is shown in Figure 4-10(right). Approximately 1000 plates were stamped for the barrel prototype module at a production rate of about 60 plates per hour. 14 plates were selected at random for a certified inspection at an independent vendor. 24 dimensions and 24 positions on the plate were selected for inspection. Figure 4-11 shows the difference between the actual and the nominal dimension for the ensemble of points defining the plate envelope. All points are within specification, which in general is ± 0.1 mm (the one point lying below -0.1 mm has in fact a specification of ± 0.25 mm). A more detailed analysis of this data shows that the plate-to-plate uniformity may be expected to be somewhat better than the general specification. A second run of 600 plates for the extended barrel prototype modules has also been completed in a single shift, demonstrating the ease with which this fabrication approach may be used to manufacture high precision master plates. This approach has the additional advantage of requiring significantly less inspection of master plates to assure that they meet specification. Due to the success of these tests, die stamping is presently the baseline for master plate production

For either laser cutting or die-stamping of master plates, it is necessary to deburr the plates following cutting (the laser leaves a low ridge due to local melting and the die a ridge where the edge breaks). We have evaluated several approaches to accomplish this and to simultaneously prepare a good (roughened) plate surface for bonding. The process selected carries the trade name "Time-Saver", and consists of a simple abrasive belt sander and a feed table. We have studied the effect of the abrasive grit sizes well as the type of roller used with the belt on the reduction in plate thickness and on the glue adhesion. These tests have shown that an abrasive grit size of 80 gives optimal surface for glue adhesion (surface roughness ISO-N6/N7, ANSI-32/63) with a well controlled reduction in plate thickness of about 4 μm. In addition, a hard-backed roller is preferred to a soft-backed roller to minimise roundover at the plate edge. This machine is relatively inexpensive. Therefore for production this operation is envisaged to be done centrally (for example at the cutting vendor) or just prior to stacking to minimise the number of times the plate must be cleaned. The choice in any given region will be selected to match the resources and facilities available.

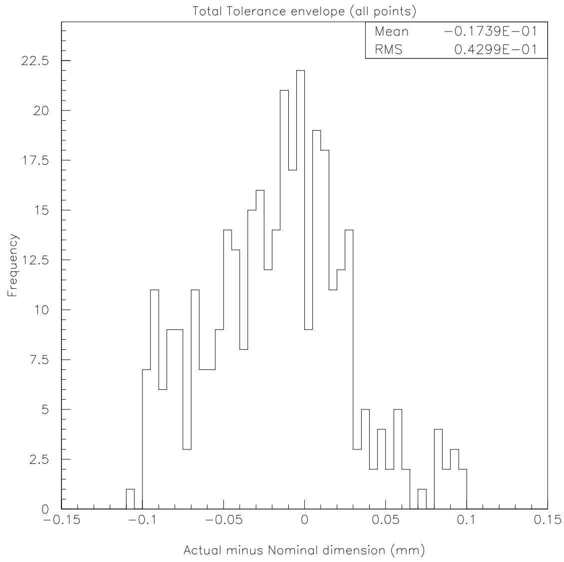

Figure 4-11 Die tolerance envelope as obtained from certified plate inspection.

For storage and shipping, the plates will be oiled, separated by oiled paper and crated. Therefore, immediately prior to gluing, the plates must be degreased. Several approaches have been successfully used during the prototype production (vapour degreasing, detergent bath, commercial plate washer) and the approach at each stacking location will be chosen again depending on resources. A final hand wipe using a clean cloth or glove is sufficient to remove any remaining residue.

4.2.2.3 Spacer plate production

About 42000 spacer periods have to be built. Each period accounts for 12 plates of different shape, to be cut out of the same sheet, and weighs approximately 15.5 kg. The detailed drawing and dimensions of all spacer plates are presented in Figure 4-12 (reference drawing ATL LESS_001). All dimensions are set such that master and not spacer plates determine the outer envelope of the sub-modules. Spacers of the staggered layers A and B overlap by 2 mm along the radial dimension, to ensure 11 continuous columns of steel close to the radial edges of the scintillators. This plays an important role in the distribution of the magnetic field lines in the absorber structure, giving an effective shielding to the scintillator. In addition, the continuous line of steel reduces plate deformation at the scintillator location during stack compression. All spacers are chamfered at the four corners to avoid sharp edges which might damage the readout fibres. As is the case for master plates, the cut surfaces must be deburred and the surface prepared for bonding. For this operation, we propose to use a similar process as for master plates.

The tolerances on the dimensions of spacer plates are less demanding, unlike the case for master plates. The only real requirement is put on the location of the holes used to position spacers on masters. The symmetric location of the holes and the distance between holes is particularly critical. There, ±0.1 mm is specified.

Three different cutting technologies have been evaluated: die stamping, laser cutting and machining. All have been determined to be capable of realising the design tolerances. The baseline scenario is to cut spacers at up to three different (regional) locations, which will simplify the transportation associated with distribution to the assembly plants. Machining does not seem to be cost effective at this moment. Die stamping is financially attractive if concentrated in one single location. In this case the inspection of each single plate is not needed, however it requires a significant investment in the procurement and operation of several different dies. Laser cutting is widely available and quite cost effective in a distributed production scenario, but requires significant inspection to ensure that the plates meet specification.The final choice will be driven by financial and logistical constraints.

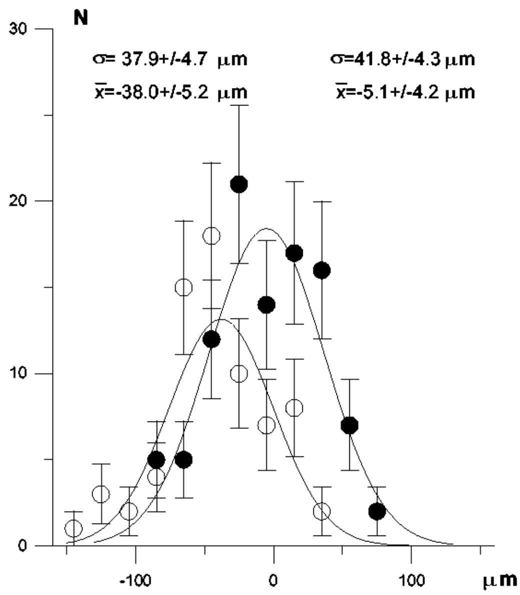

Figure 4-13 Laser cutting precision, measured for a sample of spacers cut during Module 0 production.

All spacers for the Module 0 construction have been laser cut at two different locations. The technology is based on a CO_2-laser running in single mode with a power setting between 0.5 and 5 kW. The cutting speed is typically of the order of 0.5 m per minute. The results obtained[N-74] are quite promising both concerning costs as well as for the precision of the cutting itself. An inspection of each single spacer is required. Ways to automate this are under study and have already being subject of R&D. In particular, an online monitor of the cutting procedure is very important to allow prompt intervention and correction during cutting. This operation can also be used to qualify each single spacer and to reduce waste. As shown in Figure 4-13 the achieved precision is of the order of 0.040 mm, which is better than required. We therefore

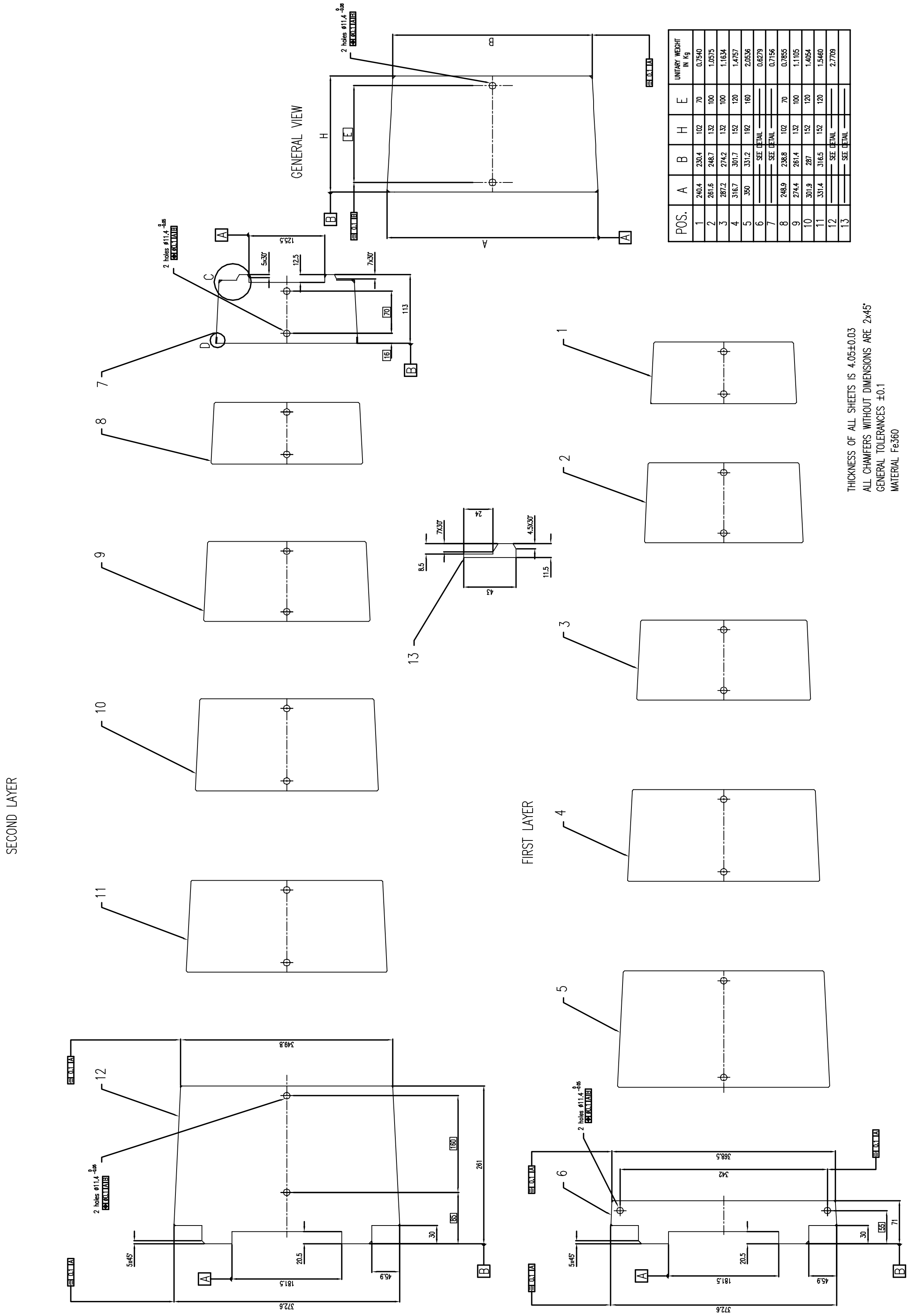

Figure 4-12 Spacer plate geometry and dimensions.

envisage that the laser cutting speed may be increased by up to a factor of two while still meeting specification. This will bring a corresponding reduction in the production cost.

4.2.2.4 Spring pins specification and manufacturing

Spring pins made out of steel with an outer diameter of 11 mm and thickness 1 mm are used to precisely position spacers on masters. This operation is done during the assembly and gluing of half periods. The height of the pins is 8 mm, 1 mm less than the half period thickness. It should be noted that, therefore, no mechanical connection exists between adjacent half periods. Elastic pins of this size and dimensions are not standard and must be manufactured to order. We require a total of about 1,000,000 pieces, including spares. Given the fact that for the manufacturing a custom die must be constructed, the production will be centralised in one place and then distributed to the module assembly plants.

4.2.2.5 Inner radius filler keys specification and manufacturing

Small key elements (Figure 4-14) are part of the sub-module assembly. These small elements are described in the reference drawings (ATL LESS_001) as spacer number 13. Each one consists of a small steel plate of about 40mm length and few mm width, with chamfers at all corners. The thickness is identical to that of normal spacers, 4.05 mm. These spacers have to be mounted on the half periods of type A, just on the key stubs of the master plate. Their function is to provide a continuous layer of steel at small radii where the side straps are welded in. The presence of this material prevents the deformation of the stack during the welding operation and in practice it prevents the space reserved for the first scintillator to be squeezed to a thickness that would prevent later insertion.

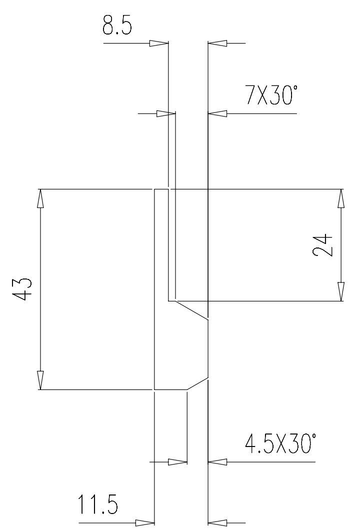

Figure 4-14 Detail of the small spacer number 13.

For the prototype construction these spacers have been produced by machining. For the final production the final technology is stamping, with a dedicated die. About 83,000 pieces have to be produced. The production will be centralized and then distributed to the assembly plants.

4.2.2.6 Weld strap specification and manufacturing

For each sub-module two pairs of connecting straps are required. The dimensions and details are shown in Figure 4-15 (reference drawing ATL LESK_001). The outer radius bar (position 2) has a thickness of 29.7 mm, the inner bar (position 1) 7 mm. Each strap contains three holes spaced by 110 mm and centred along the height. These holes allow connections using bolts of the type M16 and respectively M12. These straps are tack welded to the sub-module structure. During assembly they are precisely positioned on the stacking fixture with a set of pins located between the connecting holes.

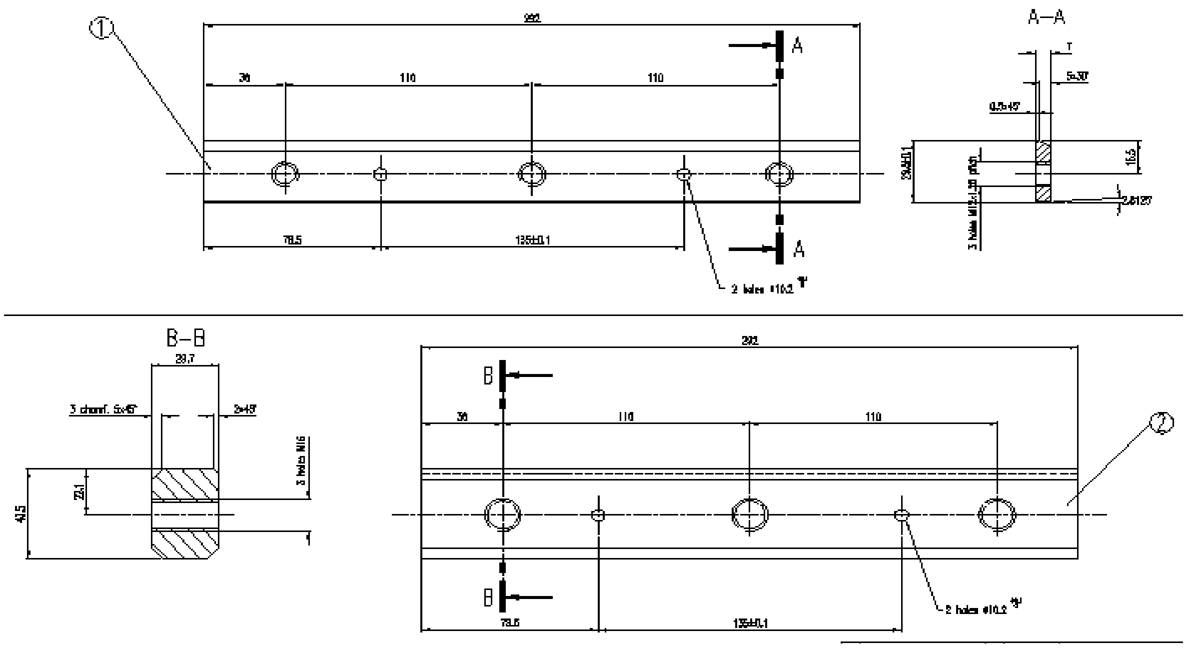

Figure 4-15 Details of the connecting straps which are welded on the 4 corners of the sub-module.

These straps have several functions. In the first place they contribute additional structural integrity to the sub-modules. During sub-module manipulation, they provide a means by which the sub-module may be connected to the manipulation fixture. The outer radius straps are used to mount sub-modules directly on the girder, while the inner radius straps form the bearing surface when the calorimeter is assembled. These straps at the inner radius introduce dead material in front of the calorimeter and are designed to be a minimum thickness consistent with their mechanical functions.

For each type of special sub-module, the dimension in height is adjusted, but all other design aspects are the same (see reference drawing ATL LESK_002 and ATL LBSK_002). A total of 5300 connecting bars of the both types are required. The manufacturing will again be centralized within a region associated to the sub-module assembly plants.

4.2.2.7 Adhesive specification

A structural adhesive, “ARALDITE” AW 106 plus hardener HV 953 U (U.S. product CIBA Y106 and HV95953U respectively) is used to bond master and spacer plates into a solid laminate. The manufacturer’s recommended glue line for this epoxy to provide maximum resistance to shear stress is 0.05 - 0.20 mm. Tests were conducted (following ISO 4578) which confirmed the manufacturer’s data sheet, which gives a maximum shear strength of 12-15 N/mm^2 for this range of glue line thickness. The steel thickness specification and design stack height have been chosen such that on average the glue line thickness will be 0.055 mm. Finite element calculations give an average shear stress in the glue of 0.1 N/mm^2 and a maximum stress concentration near the plate corners of 2.4 N/mm^2 with the assumption that all of the stress is carried by the glue and none by the four corner bars which are welded to the structure. This indicates that we have a more than adequate safety margin in both fraction of plate area bonded as well as glue line thickness.

4.2.3 Sub-module assembly

The sub-module fabrication procedure developed by the Tile Calorimeter group is described below. It is designed to be straightforward and flexible to allow minor changes at the many institutions intending to participate in sub-module fabrication, and low cost in effort and tooling, while still meeting the tight calorimeter mechanical specifications. The underlying philosophy is that the intrinsic precision in the master plates and stacking fixture are used to realise the radial and azimuthal envelope and that a structural epoxy is used to bond the plates into a laminate and to accommodate some level of variation in plate surface quality and thickness. The procedures and tooling were tested in a production mode during the fabrication of the barrel prototype module, when a total of 28 sub-modules were fabricated at seven institutions[N-88].

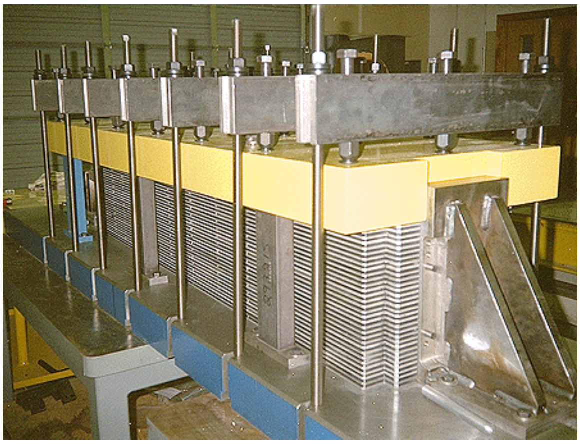

Figure 4-16 Sub-module assembly at one of the participating institutions.

An example of such an assembly is shown in Figure 4-16. With the exception of the design of the stacking fixture, which was replicated at each site and was mandatory, some flexibility was allowed for all other procedures to allow for differing institutional resources and capabilities. All variants proved successful and although probably less extensive, a similar flexibility can be anticipated for the full production. During this prototype assembly phase a regular sequence of operations was established. From this we plan the following sequence of operations during production.

Day 1 morning:

- clean masters and spacers using detergent and water baths

Day 1 afternoon:

- stack and glue sub-module
- close press for duration of polymerisation process (20 hours)

Day 2 morning:

- tack weld corner straps while sub-module is on stacking table
- remove sub-module from table to location for final welding of straps
- perform any maintenance of stacking and gluing fixtures

Day 2 afternoon:

- perform visual inspection of plates for next sub-module
- prepare materials in readiness for stacking next sub-module

Day 3 to Day 8:

- construct three additional sub-modules

Day 9:

- perform final welding of straps on four sub-modules

Day 10:

- apply surface protection agent
- measure sub-module envelope at defined inspection locations
- place sub-modules in plastic bag including a desiccant, crate and move to storage

Assuming this work plan, two sub-modules can be constructed each working week for a total of up to 96 sub-modules per year with three technicians and one complete set of assembly tools.

4.2.3.1 Stacking fixture design

The single mandatory piece of tooling is the sub-module stacking fixture. The prototype fixture is shown in operation in Figure 4-16. The two critical features of this fixture are the key brackets at either end, which are accurately aligned and sized (only the inner radius key can be seen in the figure). They fit into the inner and outer radius key slots in the master plate to define the sub-module azimuthal envelope. The inner radius key bracket is movable and faced with a pair of hard rubber gaskets such that it can press against all master plates and force them to register against the outer radius key bracket to provide a flat surface for the eventual mounting of the sub-module to the support girder. The top and bottom plates are 5 cm thick for stiffness and ground flat to define the sub-module z envelope. The final precision elements of this device are the compression columns. These are accurately machined to define the sub-module height.

Although the required precision of some of these components is quite demanding, this fixture was successfully (and inexpensively) replicated at all institutions participating in sub-module fabrication for the prototype assembly. With minor modifications, the fixture may be altered to allow assembly of shortened sub-modules (as required in the extended barrel for integration of the cryostat supports) and for fabrication of sub-modules for the Intermediate Tile Calorimeter (as described below).

4.2.3.2 Gluing procedure

The baseline design concept is to use an automated gluing machine to apply a fixed volume of glue for each shot on a grid of points, an example of which is shown in Figure 4-17. This grid has been chosen to provide glue adhesion over 80% of the plate surface and requires a shot size of 0.15-0.20 g, dependent on plate surface quality, and which will be determined for each batch of plates used. One such machine has been designed and built and was successfully used for sub-module production for the barrel prototype module. The machine is shown in operation during production of sub-modules for the barrel prototype in Figure 4-18. For this design a half period, comprising one master plate and its associated 6 spacer plates is first glued before being placed on the stacking fixture. The pot life of the epoxy is four hours and this system allowed a stack to be completed in less than three hours. Other methods have been successfully applied at several institutions. These include glue application manually using a glue gun and template, a roller system, and a fine array of glue spots. All techniques resulted in successful sub-modules and can be considered acceptable approaches should the use of an automated system be precluded for some reason. In addition, a design in which the glue application is integrated with the stacking fixture is being developed, which may reduce the level of technical effort required to assemble sub-modules.

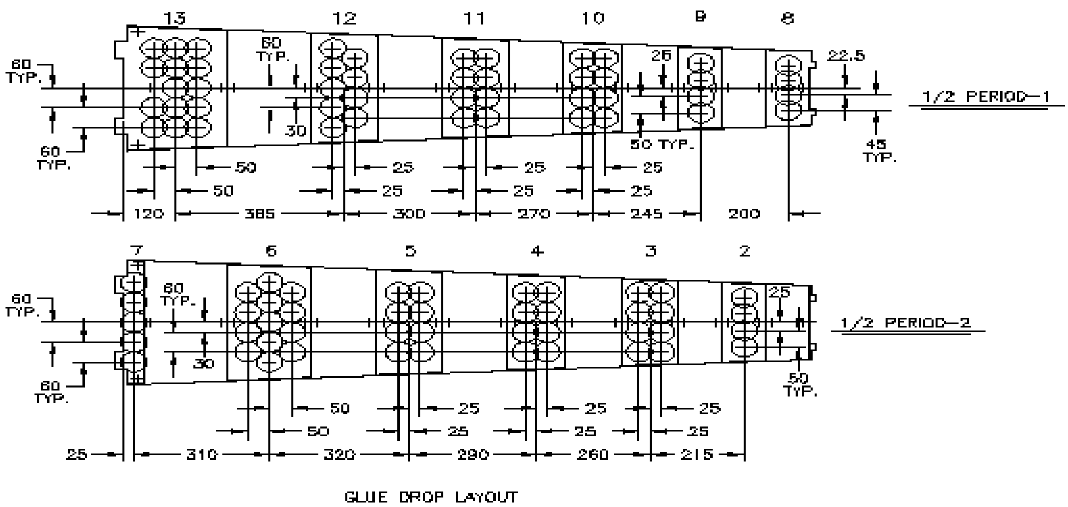

Figure 4-17 Grid used for deposition of glue drops to ensure a minimum surface coverage of 80% following stack compression.

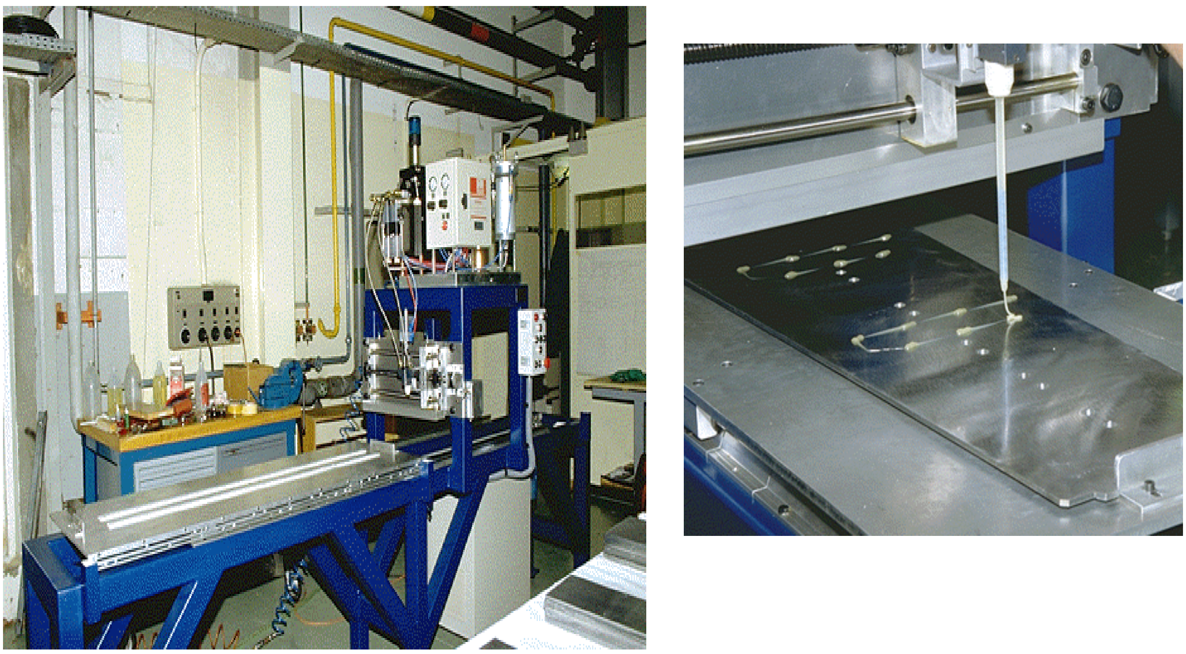

Figure 4-18 Automated glue application machine used in production of the barrel prototype module.

4.2.3.3 Stacking procedure

Whether the gluing of master plates to spacer plates is carried out on a dedicated machine or on the stacking fixture itself, the basic sub-module stacking procedure is the same. The first master plate is put on the gluing machine and the glue is applied following the grid associated with the first set of spacers. The spacers are then fastened to the master plate with steel spring pins and a second application of glue is made using the same pattern (i.e. on the spacers themselves). This half period is then placed on the stacking fixture and the gluing process repeated for the second half period, in which the spacers are offset by one radial position from the first. The full period (two master plates and two sets of alternating spacer plates) is shown in Figure 4-17. Small keys at the inner radius of the first half-period are glued in place using a cyano-acrylic adhesive and held in location on the stacking fixture using long bar magnets. The second half period is then placed on top of the first on the stacking fixture and the process repeated 16 times to complete the sub-module. The compression columns are then fitted to the stacking fixture and the load plate lowered onto the stack and torqued to 75 Nm onto the compression columns. The adhesive is then allowed to cure for 12-24 hours depending on ambient temperature prior to commencing the subsequent operation of welding on the side straps. Occasionally, some glue seeps into the scintillator slots, fibre channels and the holes through which the source calibration tubes are passed. This is easily removed with simple tools. Modification of this procedure to assemble sub-modules of different heights is straightforward.

4.2.3.4 Welding fixtures & procedures

The final operation carried out on the stacking fixture prior to removal of the sub-module is the tack-welding of the side straps to the sub-module. Several approaches were evaluated during the Module 0 program and a general welding procedure was developed which was of particular use in institutions with less experience in this type of operation. Due to their many functions, the position of these straps is important and fixtures have been developed to maintain it during welding. Minimal weld distortion of the sub-module is required and TIG welding at the strap extremities is to be used. Following removal of the sub-module from the stacking fixture, the welding of these straps is completed. Both MIG and TIG welding have been evaluated and at present the proposed procedure is to use TIG welding, following a skip pattern to minimise heat buildup and sub-module distortion. Following the completion of the Module 0 program, the weld type and welding procedures will be refined as part of the sub-module assembly procedure for production.

4.2.3.5 Surface protection

The Tile Calorimeter will be constructed over a period of several years in locations with greatly varying humidity and temperature. This is anticipated to be particularly important during the transportation from the sub-module assembly location to the module assembly location. We have therefore begun a long term study of “environment friendly” surface protection agents for mild steel. Initial studies have indicated that the coating CORTEC^{TM} may provide sufficient protection and has been used for the protection of the sub-modules constructed for the barrel prototype module. This is a water-based product and is applied by dipping the completed sub-module in a tank containing CORTEC and water in the ratio 1:5. This provides protection up to the maximum guaranteed by the manufacturer of two years (in the harshest environment). We are somewhat concerned by the maximum period of protection guaranteed by the manufacturers and therefore other products (including water-based latex paints) are presently being evaluated. The chosen protection for production will be made following the completion of long term tests in conjunction with the Module 0 program.

4.2.3.6 Sub-module envelope specification

The sub-module radial envelope is determined by the precision keys in the master plate, the key brackets in the stacking fixture and the width of the master plate itself. The tolerances on these elements have been established to meet the design module ϕ envelope of 1mm and were successfully realised for the plates and tooling used for the production of the barrel prototype module. For sub-module production, inspection of master and spacer plates will occur during their production and only a final visual inspection will be given to detect major flaws immediately prior to stacking. Alignment of the keys on the stacking fixture will be verified periodically using a gauge plate and the width of the keys (which will be subject to wear) using a gauge bar on a weekly basis and following any disassembly of the fixture. Should the keys fall out of tolerance due to wear, new keys will be fabricated. The height of the sub-module, prior to welding on of the straps is predetermined by the height of the compression columns. Since these are subject to minimal wear, this height is by definition realised. However, small plate thickness and planarity variations may be observed in different batches of steel. Therefore for each batch a dry stack will be made (one in which the sub-module is assembled without glue and compressed fully) and the thickness of the individual plates used measured to confirm the volume of glue required to realise 80% surface adhesion for the design stack height.

4.2.3.7 Intermediate Tile Calorimeter sub-module construction

ITC sub-modules will be constructed using a stacking fixture which is modified to allow the position of the inner radius key to be moveable to accommodate the different radial positions of the absorber sections. In all other respects this fixture will be identical and may therefore be used to assemble standard sub-modules in addition to the ITC sub-modules. ITC assembly will also require some additional tooling to maintain the profile during the compression but in all other aspects will be accomplished using the identical guidelines as for standard sub-modules.

4.2.3.8 Sub-module storage

In order to maximise transportation efficiency, each sub-module assembly location will require sufficient storage space to store approximately 40 completed sub-modules (this allows sufficient modules for a full truck load of about 20 tons). To provide protection from the elements each sub-module will be placed in a bag made of vapour resistant material along with a desiccant. Sub-modules will be skidded and crated in pairs, to provide both protection from mechanical damage and to facilitate subsequent handling and storage. Storage may be at the site used for sub-module assembly or module assembly depending on facilities available.

4.2.4 Sub-module handling

Sub-module handling fixtures[N-87] are required at each site at which submodules are assembled: to remove the sub-module from the table; to position sub-modules for final welding of the corner straps; for support of sub-modules while applying surface protection agents and for handling for storage and shipping to the module assembly location. In addition, at the locations where modules are assembled, sub-modules must be rotated from the inner radius into the vertical position and lifted onto the girder for mounting. Some attention has been given to the tooling required to perform these operations and specific solutions developed to ensure that they may be carried out in a safe and straightforward fashion using simple and cheap fixtures.

4.2.4.1 Sub-module handling fixtures

Eyebolts may be used for a simple straight lift (as from off the stacking table). In addition, a fixture has been developed to allow easy and safe manipulation and rotation of sub-modules. Attachment of these fixtures to the sub-module is via the tapped holes in each of the four corner straps. This special purpose lifting/rotation fixture, shown in Figure 4-19 has been developed to allow manual rotation of a sub-module into any one of eight fixed positions. This fixture attaches via plates to the ends of the sub-module and contains a lockable trunnion to allow rotation. Other similar approaches were developed at several of the institutions participating in sub-module production since the tooling is simple and in many cases could be adapted from existing fixtures.

The fixture used to rotate the sub-module to the vertical position for mounting onto the girder also attaches to tapped holes in the straps at the inner and outer radius of the sub-module, as shown in Figure 4-20. Once rotated to the vertical position a lock pin is inserted to fix the moveable bracket to the fixed support and thereby ensure that the sub-module is truly vertical before removal of the bolts fixing the rotation bracket to the sub-module. The sub-module may then be lifted onto the girder using the lifting bracket attached to the inner radius straps.

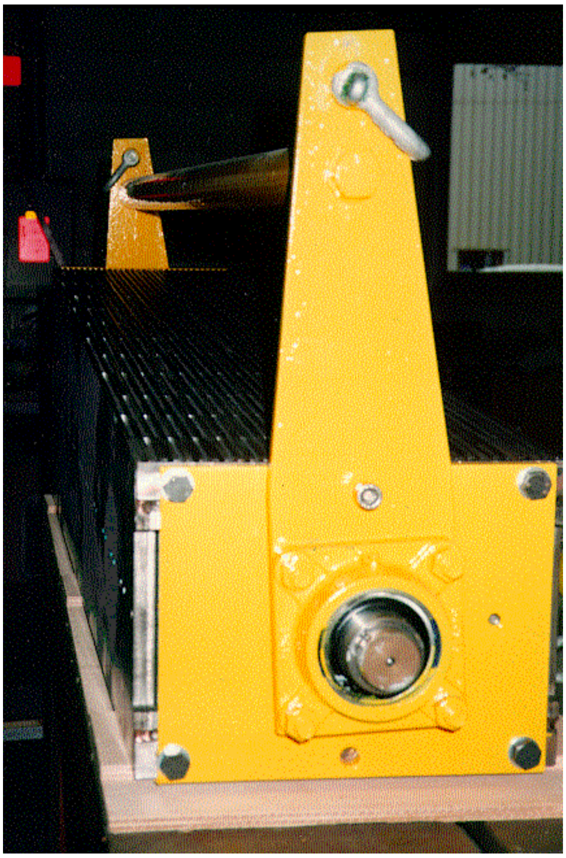

Figure 4-19 Sub-module manipulation tool.

4.2.4.2 Sub-module handling stress analysis

Sub-modules are generally to be lifted using a spreader bar. The connection to the sub-module can take two forms: using four eye-bolts which attach directly to the M12 holes in each of the corner straps; via a connecting plate and trunnion bolted (using two M12 bolts per strap) to the inner and outer radius straps. The stresses in these connections are wholly determined by the cross section of the connection being considered, their number and the weight of the sub-module[N-31].

The worst case stress is clearly obtained when using four eyebolts to lift a sub-module. The stress in this case in each of the bolts is 19.5 N/mm^2. While lifting from the table, the corner straps are only tack welded in five locations on each strap. Each tack weld is 16mm long by 5mm wide and the resulting shear stress in these welds is 2.8 N/mm^2. In both cases the calculated stresses are substantially below the yield stress of 248 N/mm^2 and well below the maximum allowed stress. Clearly, this is the worst case for the weld stress. Once the straps are fully welded to the sub-module structure, the maximum handling stress is wholly determined by the lifting bolts as given above.

Finite element modelling has been used to estimate the maximum shear stress in the glue used to bond master and spacer plates. In this calculation, as a worst case scenario, no support from the corner straps was assumed. For a simple beam support of the sub-module, the average maximum shear stress in the glue is calculated to be 0.1 N/mm^2 and the maximum average shear stress to be 2.4 aN/mm^2 and which occurs near the module corners. The glue used has been chosen such as to accept this level of shear stress (with an acceptable safety margin) and measurements have been made to confirm the manufacturer's specification.

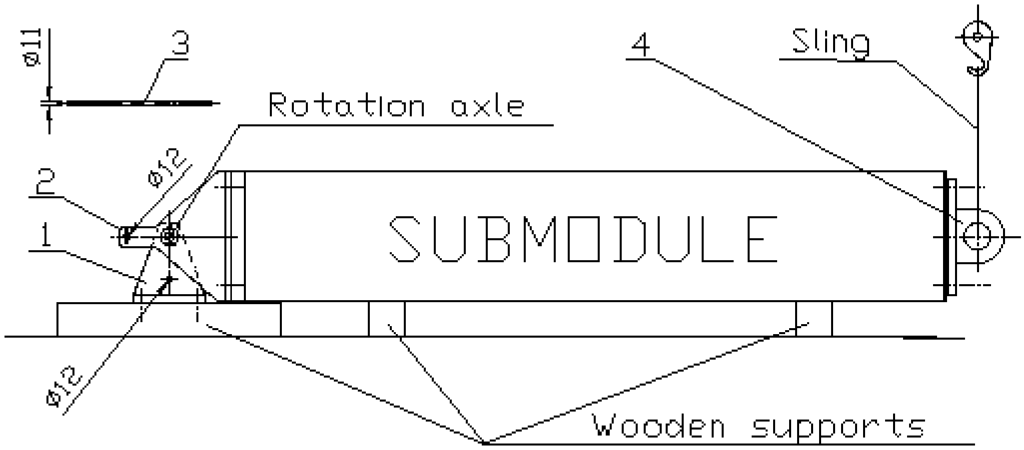

Figure 4-20 Principle of the tool used to rotate a sub-module into the vertical position.

4.2.4.3 Sub-module envelope

In addition to a standard set of height measurements made on all sub-modules fabricated, a detailed set of height and feature measurements were made on a single sub-module (chosen arbitrarily). For this sub-module, the set of measurements for the deviation from the nominal dimension along the ϕ direction is shown in Figure 4-21. The spread of the measured values is well inside the specification. The ϕ envelope measurements revealed a single plate which was out of specification by approximately 50 μm. The plate was found to be curved and further work is in progress to understand the cause (a number of factors such as internal stresses, and bowing of the raw sheet plate are candidates under investigation). The gauge plate used to verify the stamped plate envelope will also be modified to better identify such plates prior to their being used for stacking at which point the outwardly bowed edge may be planed if necessary to minimise waste.

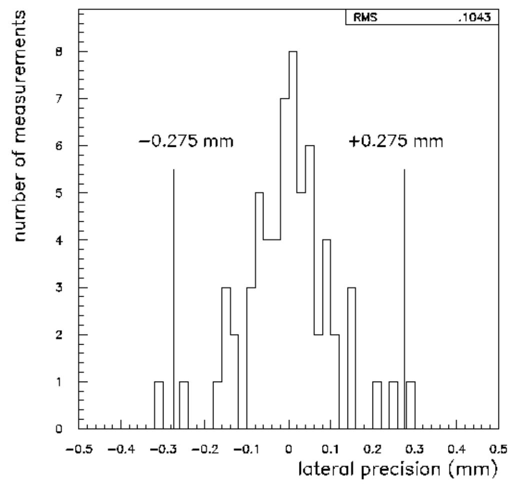

Figure 4-21 Distribution in ϕ dimension (measured minus nominal) for one of the first set of sub-modules assembled.

4.2.4.4 Sub-module mechanical testing

As is discussed in Section 4.6 below we have some issues concerning the inner radius bearing loads on the sub-modules in the assembled calorimeter. A preliminary structural analysis indicates that they may be significant and we have initiated a series of mechanical tests on spare sub-modules to quantify their structural integrity. The static and finite element results have been used as a guide for the minimum applied loads. We will also load key elements to failure. The tests include:

- Shear failure test of the welded front-plate: A setup which simulate three sub-modules at the inner radius, connected with one front-plate, has been realised. The plate and welds failed at a press load of 85 tons, which corresponds to a sharing stress of 340 N/mm^2 in the plate itself.

- A torsional load test, in which the sub-module is supported at one corner and the load applied diametrically to the support. This type of load caused torsional rotation of the sub-modules, allowing a measurement of the sub-module torsional stiffness.
- Front-plate bearing load test, in which the sub-module is supported uniformly on the front- plate bearing surface (via a soft shim) and the load is applied only to the bearing surface from above. Here we have tested two cases. The first one where the load is applied on the small 7 mm strap. The maximum value applied load was about 78 tons which gives a compressed stress on the bearing surface equal to 340 N/mm^2. In a second test we have load directly the master plates, increasing that way the effective bearing surface by at least a factor four. The maximum value we have applied was 270 N/mm^2.
- Non uniform loading of the master plates. Only nine master plates in the central part of the sub-module closed to the front-plate were loaded from the top surface. The rest of the master plates on each side of the sub-module were supported on their bottom surface. This load caused shearing of the front-plate and the glue layer between masters and spacers. The maximal applied value of the force was about 80 tons.

The design constraint we are following in terms of normal engineering practices calls for the maximum stress to be below 130 N/mm^2. We have therefore demonstrated a more than adequate safety margin if we follow this specification. These tests are continuing and will be one of the tasks for the work in 1997.

4.3 Modules Production

Modules production will be carried out in three locations, one for all barrel modules and two for all the extended barrels. Except for minor modifications in the end-plates in the region of the barrel Liquid Argon supports, all barrel modules are identical. In the case of the endcap modules, substantial modifications to the design are required for the modules located near the supports for the endcap Liquid Argon Calorimeters. The design of standard modules and the design changes needed in the extended barrel are discussed below.

4.3.1 Module design

The main features of the module design are shown schematically in Figure 4-22. The sub-modules are attached to a girder on a high precision key. Access holes are cut in the outer surface of the girder for use in installation of the read-out fibres and are covered by a thick plate to provide magnetic shielding. The girder tube is used to support the read-out fibres and provides the space for read-out electronics. Finally, end-plates are fastened on each end of the completed modules to provide additional strength as well as to light tight the girder assembly. We now discuss the details associated with each of these issues below.

4.3.1.1 Design of a barrel module

The barrel calorimeter is constructed from 64 identical barrel modules. A picture of a barrel module is shown in Figure 4-23. It comprises 18 standard sub-modules each 293.2 mm long and one special sub-module 332.6 mm long bolted onto the support girder and connected together at the inner radius by a 10 mm plate welded into the key slot. In the baseline, two end-plates are

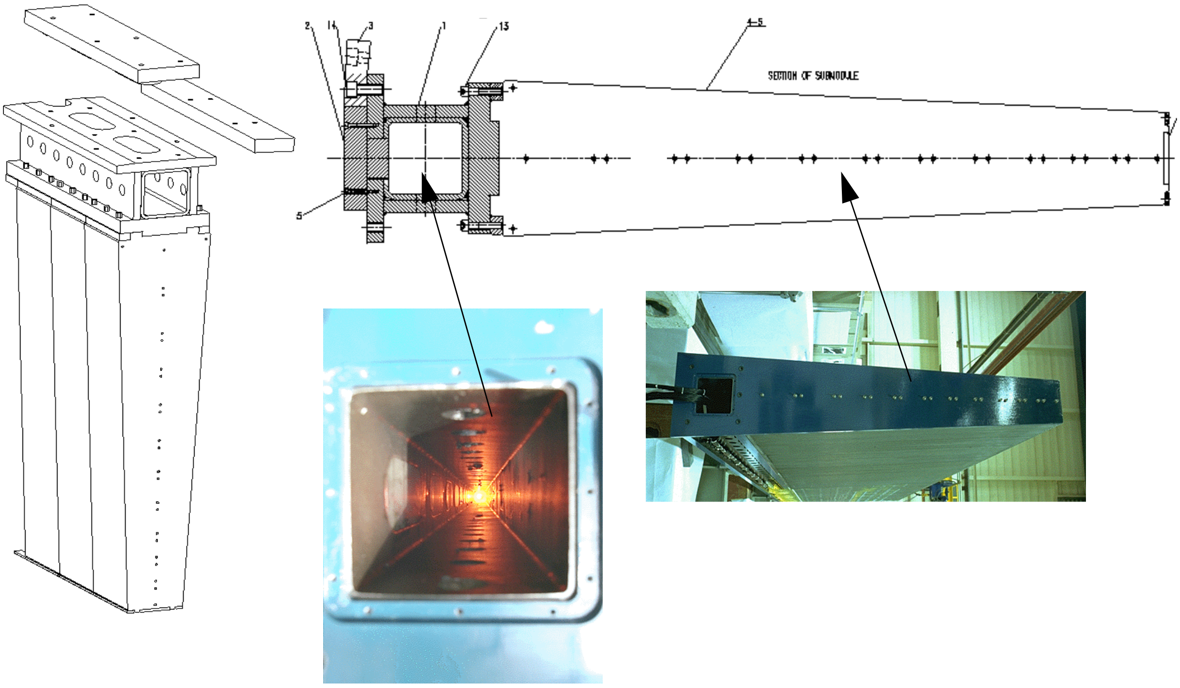

Figure 4-22 Principle of a module assembly and module cross-section.

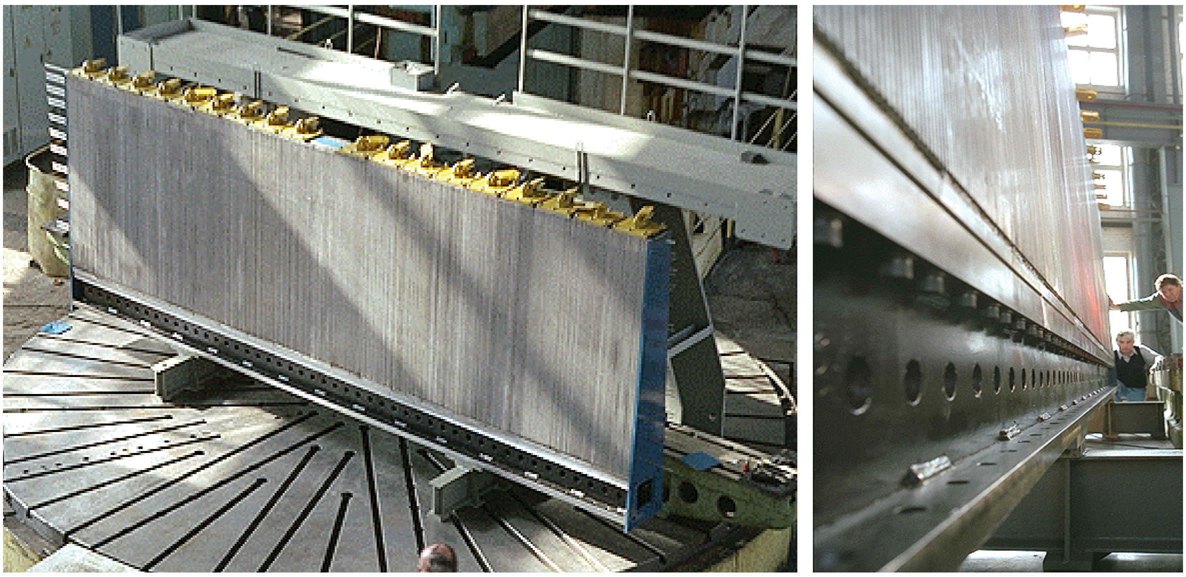

Figure 4-23 Barrel module, built from 19 individual sub-modules bolted onto the girder structure.

bolted to the girder and welded to the inner radius plate. A design gap of 0.8 mm between sub-modules and between sub-modules and the end-plates is included to accommodate manufacturing tolerances. The azimuthal positioning of sub-modules is maintained by the mating between the key in the girder and the key slot in sub-modules. The bolt connection between sub-modules and the girder is shimmed during the assembly process to define precisely the azimuthal orientation and surface planarity of all sub-modules as they are mounted to the girder. A special connecting block (not shown on drawing) is used in the calorimeter assembly to carry the magnetic flux between the barrel and extended barrel modules, where services and space are at a premium.

4.3.1.2 Design of an extended barrel module.

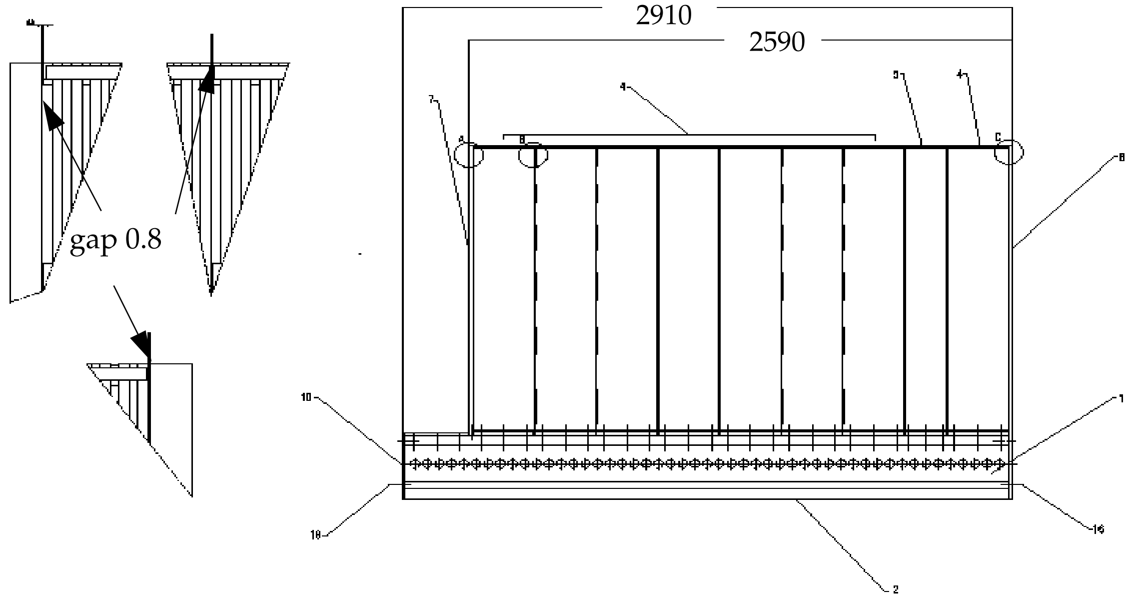

Figure 4-24 Extended barrel, standard module design.

As shown in Figure 4-24, an extended barrel module is comprised of eight standard sub-modules of length 293.2 mm and one special sub-module 201.5 mm in length. The mounting concept is identical to that for a barrel module. The girder for the extended barrel is also longer than the instrumented region since it is designed to span the gap between the two sections and to provide the support for the Intermediate Tile Calorimeter sub-module, which is mounted behind the interior end-plate.

4.3.1.3 Special case modules

The principal area of mechanical interference with the standard module geometry comes from the supports for the Liquid Argon cryostats. In the barrel region these supports are wholly external to the Tile Calorimeter volume and therefore there are no special modifications required of the barrel absorber structure. However, services from other detector systems must be mounted on the Tile Calorimeter in the gap. These impose constraints on the calibration system and on access to the electronics and are discussed in detail below. The extended barrel, on the other hand, must provide an internal support for the endcap calorimeter and cryostat. This necessitates shortening three sub-modules by approximately 100 mm radially to provide space for a mounting bracket as shown in Figure 4-44. In addition to this modification to these sub-modules (which corresponds to removing the first scintillator layer) there is also the difference that the inner radius plate will not be welded across this region to allow for the expected large differential shear loads. Work on the design details associated with these issues is coupled with the evolving design for the calorimeter support, the support saddle and the results from finite element modelling of the structure and is a task to be continued in 1997 and 1998.

4.3.2 Additional module components

In addition to the sub-module, which forms the absorber for the Tile Calorimeter, there are several key module components whose function and specification require some discussion. These comprise the mounting girder and front and end-plates which complete the module structure and the stainless steel tubes used to provide access for the calibration sources. In the discussion given below, the general description of these components is given.

For all components, there are special case modifications in specific regions of the calorimeter: in the vicinity of the calorimeter support saddle where module-to-module connections are modified; in the regions where the Liquid Argon cryostats are located, which require special structural modifications in addition to having access interferences between these supports and tile services; in the region between barrel and extended barrel calorimeters, where radial interferences exist between Tile Calorimeter access and components and services in this region.

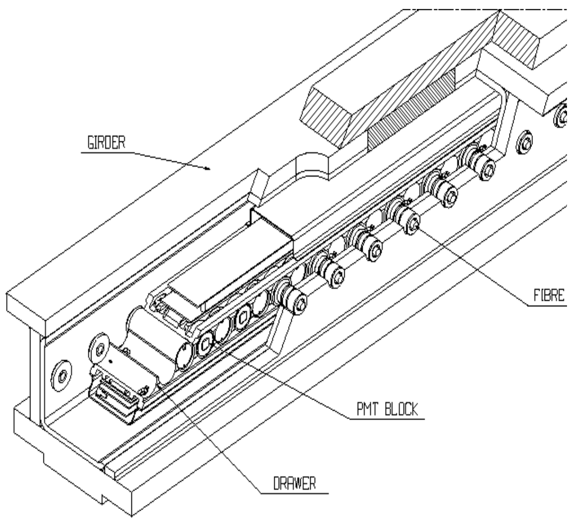

Figure 4-25 Girder and contained services for read-out (schematic).

4.3.2.1 Girder design and specifications

The girder used as the mounting structure for sub-modules is the principal structural element of the calorimeter as a whole. It contributes about a quarter of the calorimeter weight and represents a significant fraction of the total cost of the mechanical structure[N-35]. As shown schematically in Figure 4-25, it also provides the physical space for the photomultiplier tubes and electronics used to read-out the wavelength shifting fibres and must shield them from stray magnetic field as discussed below. The cross-section in this structure must also be sufficient to return the magnetic flux from the solenoid. One of its surfaces provides the bearing and shimming surface used to set the azimuthal gap between modules to a nominal value of 1 mm. Each girder is connected to its neighbours by a series of connection plates and the assembled structure must be capable of accommodating the static load of the assembled calorimeter.

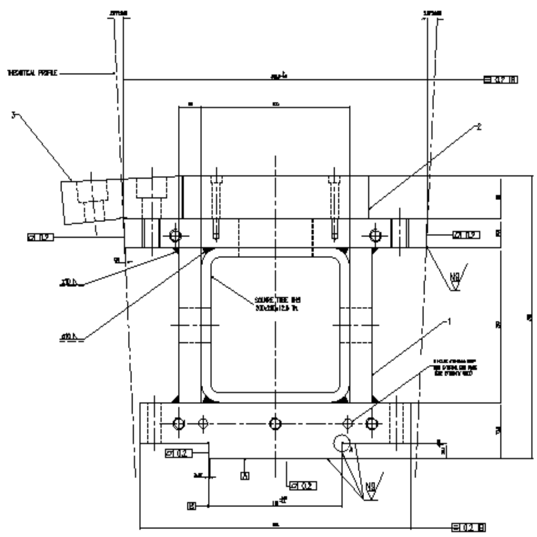

Figure 4-26 Module support girder cross section.

Finally, the Tile Calorimeter must provide the support for the Liquid Argon Calorimeters with minimum loss of hadronic energy measurement and must itself be supported from rails in a fashion which must minimise the loss of fiducial acceptance to the ATLAS muon system. These latter constraints place particularly significant demands on the girder and its connections.

The girder cross-section is shown in Figure 4-26. The weight of the girder is 3.6 tons for the barrel and 1.6 tons for the extended barrel. The design is based on the use of a standard size structural tube to form the volume in which the read-out electronics reside and which requires a minimum amount of precision machining to reduce costs. Additional steel plates are welded to this tube to complete the structure, with the majority of the material being required as magnetic shield rather than for its structural strength.

The sole precision surfaces are the key which mates to the key slot in the sub-modules and the bearing surface between modules, both of which are central to realising the 1 mm design ϕ gap between modules. The design calls for the key to be flat to 0.2 mm along its full length of nearly 6 m (in the case of the barrel) with a width which is constant within 0.1 mm. The bearing surfaces are flat to within 0.2 mm. Low precision holes are cut in the sides of the girder for mounting the read-out fibres. The holes in the outer radius part of the structure are used for servicing the fibre bundle and polishing tool during installation. They introduce some complication for magnetic shielding and may be reduced in number following completion of the prototype program, when the fibre installation requirements are better understood.

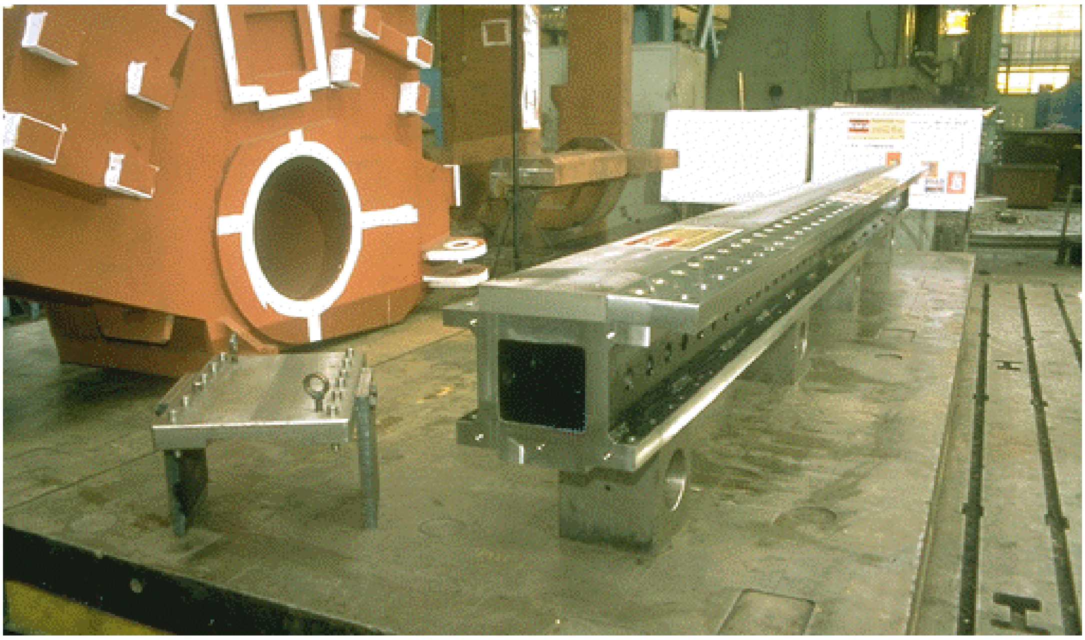

Figure 4-27 Module 0 girder constructed in winter 1996 at the FORTPRES C.U.G. S.A Cluj-Napoca company in Romania.

One barrel girder was fabricated for the construction of Module 0. It fully met specifications and in particular was fabricated with a key width with 0.015 mm of the nominal dimension along its entire length.

Although not solely a module component, it is appropriate to address the module-to-module connecting plate in the context of the girder. The standard plate is shown in Figure 4-28 (shaded region). Six such plates, approximately 90 cm long each, are used along the length of a barrel module to form this (bolted) connection between modules. Three are used for the connections between extended barrel modules.

The connection plates establish the radial positioning and the angle between modules. In the region where the structural analysis indicates that significant tension loads between modules are present at the outer radius (such as below the support saddle) this plate design is modified to provide pin connections in addition to the bolts to resist these loads. Finite element analysis of the calorimeter structure indicate that the design of this connecting plate may not be optimal for the minimisation of stress in the welds connecting the steel plates to the inner tube.

These stresses approach (and in the case of two modules in the detector exceed) the maximum allowed stress. We are therefore evaluating alternatives to this design (such as combining the cover plate with one of the connecting plates) in order to stiffen the overall structure and thereby reduce the stresses on these welds. Finally, as is the case for other module components, this connection is modified in the region of the support saddle and of the supports for the Liquid Argon cryostats and is discussed further below in Section 4.5.

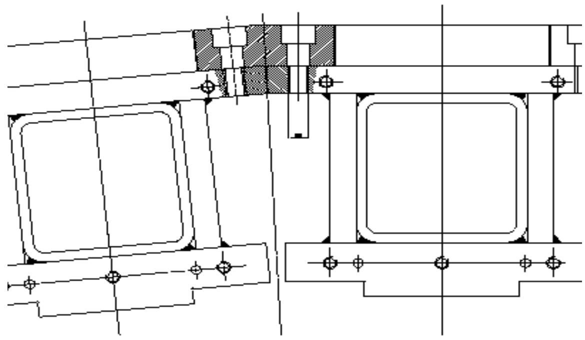

Figure 4-28 Module connection plate (cross section).

4.3.2.2 End-plates

The baseline design includes a 20 mm thick end-plate at either end of a barrel module, which is bolted to the girder and welded to the inner radius plate. In the case of the extended barrel module, the end-plate closest to the interaction point is 15 mm thick to minimise uninstrumented material, and sits between the ITC sub-module and the first standard sub-module of the extended barrel. The end-plates extend to the outer radius of the girder where they are bolted to the module structure. Except for the thickness and for minor differences associated with the different connections to the girder, the profile below the girder and layout of these plates is identical to a standard master plate.

Although functionally simple, these plates pose a significant manufacturing issue due to the need to cut holes in such thick plates for access to the calibration tubes and an access port for the electronics drawer. The original motivation for them was to carry bearing loads in the assembled calorimeter such that the inner radius connection would see no load at all. In the present design this plate is bearing. Finite element analysis done up to the present time has not included the end-plates in the structure and indicates no particular need for additional support from them. However, these plates are also located in the regions of the supports for the cryostats. In these regions we anticipate large differential bearing loads and have further increased the thickness of this plate to 50 mm in the lower half of the extended barrel to carry them. Finite element calculations done indicate that here the cryostat support greatly increases the bearing loads at the inner radius (by up to a factor of three over that coming from the calorimeter alone). Although this may be accommodated by a (somewhat undesirable) increase in the bearing surface by use of a fraction of the master plate area, we are evaluating the possibility of transferring much of this load to the end-plates and have a conceptual design of how this might be accomplished. Initial finite element calculations indicate that our baseline solution is acceptable. However a more detailed analysis is required to develop and optimize the design and is in progress. This work will be part of the 1997 program.

Finally, the end-plates play a significant role in magnetic flux return. This is discussed in detail in Section 4.9.

4.3.2.3 Front -plate

The analogue of the girder support ring at the outer radius, which aligns and connects sub-modules, is a plate which is inserted in the key slot at the inner radius: the front-plate. The functions of this plate are to connect sub-modules, thereby stiffening the assembled structure, and to provide a connecting element to transfer bearing loads at the inner radius in the assembled calorimeter. This plate contributes uninstrumented material in front of the first sensitive layers and is therefore one of the few structural elements in the Tile Calorimeter where physics performance places a (modest) constraint on the mechanical design. A plate thickness of 10 mm has been chosen as a workable compromise between physics and mechanical requirements. Finite element modelling is being used to evaluate the stresses in this plate and confirm this solution. These are discussed below in Section 4.6.

4.3.2.4 Calibration tubes

The module has been designed to allow calibration of each scintillator layer by a radioactive source which travels down an 8 mm OD stainless steel tube. These tubes are inserted into the holes in the spring pins which couple master and spacer plates together at the half-period level. The tolerances are specified to ensure that the tubes are adequately aligned when sub-modules are mounted on the girder. Since the tubes are inserted following instrumentation of the module with scintillator tiles, they have the additional feature to hold all the tiles in place and thereby to obviate the need to design a fastener. Although there are two such holes in each scintillator tile, the calibration tubes are inserted into alternate holes, as shown schematically in Figure 4-29, to facilitate routing and the use of a small number of calibration sources. A rod is inserted in the second hole and in the regions of the supports this rod is used as an additional structural element. This system is also one which requires some modifications the regions of the supports and in the region between the barrel and extended barrel calorimeters. The details are discussed below in Section 8.

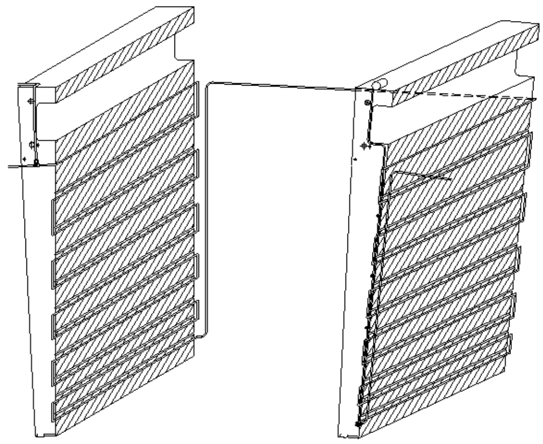

Figure 4-29 Calibration source tube insertion in barrel module (schematic).

4.3.3 Module assembly

Also in this case, the concept behind the procedure we have developed is to keep all operations as simple as possible, with minimal tooling and manpower. A first experience with this operation has been gained during the assembly of the barrel Module 0 in the spring 1996 at the JINR in Dubna[N-94]. In two other locations (Argonne ANL and Barcelona IFAE) we will assemble the extended barrel modules, starting with a first full prototypes in spring 1997. The development of this procedure has been part of a collective engineering effort over many months and once finalised will be mandatory in the three production plants we envisage to be participating in module assembly. The details of the implementation of this scheme will take in account the particular logistics and infrastructure of each location.

Module assembly will take place in the six o’clock position. It begins with the installation of the girder on the support base (Section 4.3.3.2). In the longitudinal direction the girder is installed firmly to the bracket left face, while in the transverse direction the girder is firmly attached with clamps to the main support table. Shims are adjusted in between table and girder to bring the

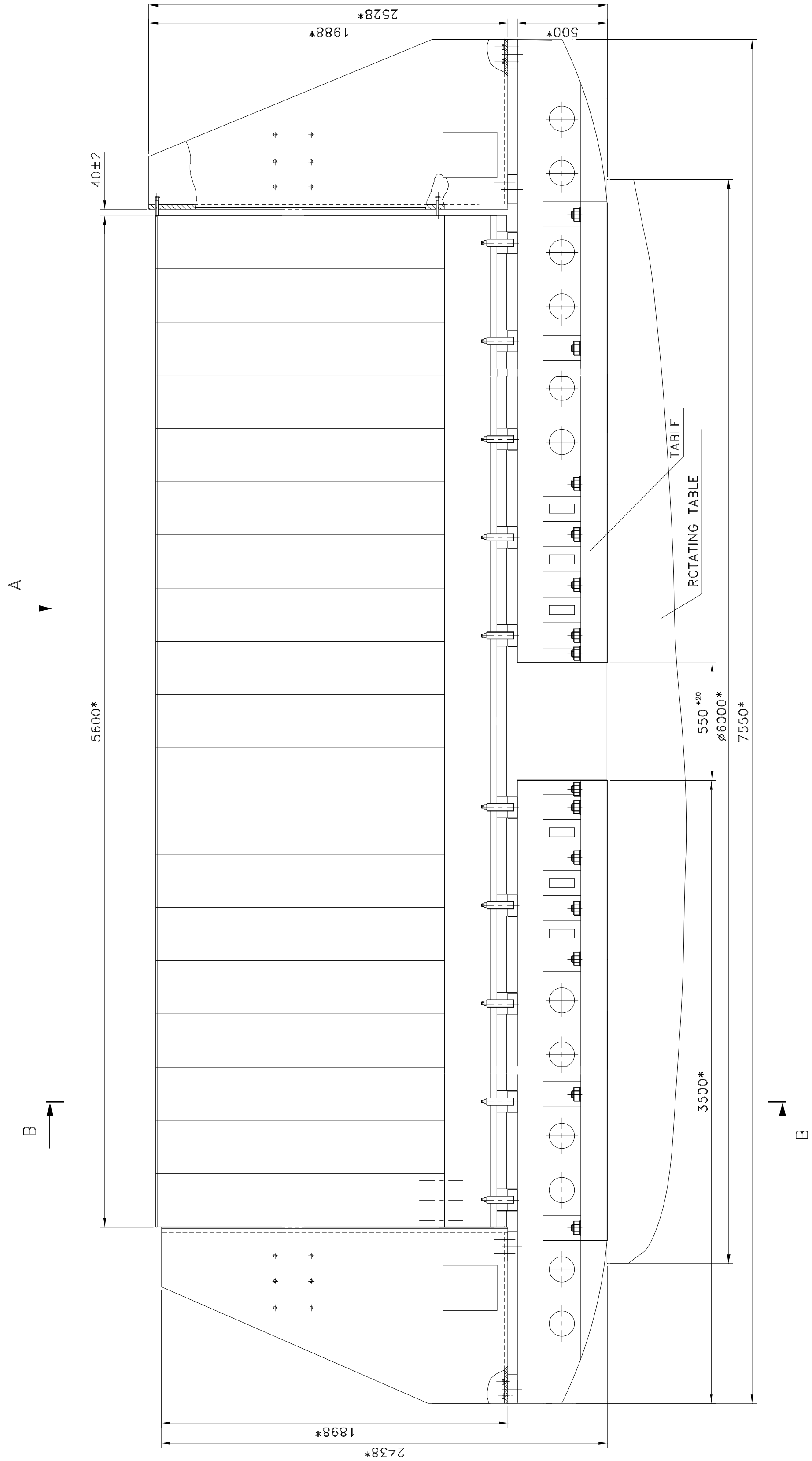

Figure 4-30 Schematic of the module assembly tooling.

surface of the inner key of the girder to a perfectly horizontal position. This is a delicate operation and requires a few hours and the use of a high precision electronic level to determine the best horizontal plane. We expect two to three iterations of measuring and shimming will be necessary.

All 19 (nine for the extended barrel) sub-modules are then prepared for the installation. One by one they are moved into the vertical position using a dedicated tool and a bracket fixed with six M12 bolts to the inner radius straps. This bracket, which is used to move the sub-module with the crane to the final position on the girder, is then kept in place until all operations on the sub-module are completed. Prior to mounting each sub-module, it is visually inspected and any small defects are removed. A flow of compressed air will be used to remove dust and any residual small pieces of material from the surfaces to be mounted.

One by one all sub-modules are moved and fixed to the girder, with the following set of operations:

- transport of the sub-module into the installation position on top of the girder
- insertion of two guide studs (M16x100) inside two opposite and diagonally located holes in the connecting straps. These studs are used to guide the sub-module while it is lowered down to the final position on the girder key
- once the module is resting on the girder, the studs are removed
- by means of two small and simple screw jacks the sub-module is moved with high precision to the final position (longitudinal movement)
- the sub-module is fixed with six M16 bolts on the girder and the bolts tightened uniformly

At this point the sub-module non-perpendicularity is determined accurately in two directions using a 2 m long precision straight-edge ruler, a plate inserted in the inner radius key and a precision electronic mini-level. The results of this operation is the preparation of a set of calibrated shims (precision 0.010 mm) that are inserted into the four corners of the sub-module. This operation of measuring and insertion of shims is done iteratively (typically two times) until the sub-module is in a perfect position. To insert the shims a simple screw jack, inserted in the holes of the girder (see Figure 4-32) is used. Once the position is final, the six M16 screws are tightened with a dynamometric key. As a cross-check the end position of the last installed sub-module is measured with respect to the front face of the girder.

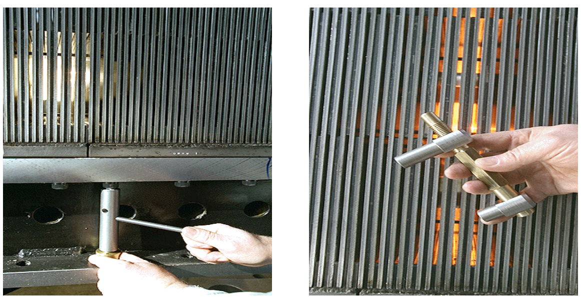

Figure 4-31 Simple tools used to adjust precisely the position of the sub-modules.

By design a longitudinal gap of 0.8 mm is kept between adjacent sub-modules. This makes the installation procedure simpler and less dependent on the quality of sub-module manufacturing. During the first operations for Module 0, we determined that sub-modules could be mounted without any constraint on pre-selection. As an additional exercise 1 sub-module already mounted between adjacent sub-modules was removed and substituted with an other sub-module without any particular difficulty. Thus during mass production there will be some flexibility and the possibility for later corrective intervention and module substitution. To have additional contact between sub-modules at the two extremes, a set of two gaskets are glued in place (on spacer number 7). The dimension is calculated on a module by module basis to match to the theoretical position of the next sub-module.

This entire procedure is repeated 19 times until all sub-modules are in place. During the assembly for Module 0, this whole operation required only three working days (24 hours), including a preliminary learning phase.

Once the module has been measured using an external reference and it has been verified that it fits inside its allocated envelope, the front-plate is welded into the inner radius key. The welding is done starting from the middle of the module. To prevent movement and deformation of the front-plate during the welding, the plate is clamped to the sub-module key using the lifting brackets. A temporary spacer, forced between adjacent sub-modules, restrains longitudinal shrinkage during welding. The weld seam is alternatively imposed on each side with a length up to 50 mm for one step. The entire operation (see Figure 4-32) is quite demanding and requires for a skilled welder about one day to be complete (eight hours). During our first experience with Module 0, the overall shrinkage of the front-plate was kept below 1 mm over the 5600 mm of length. No evident deformation on the sub-module to sub-module alignment or location was measured subsequently.

Figure 4-32 Welding of the front-plate during the module assembly.

As a final operation the face brackets are removed and the end-plates are clamped in position to the module face. At the bottom, the plates are fixed by bolts, on the top they are welded to the front-plate. Then all calibration tubes are inserted and the module is measured again and qualified for the next steps (storage, transport and instrumentation).

With our experience from the assembly of Module 0 we estimate that during production the whole assembly procedure may be completed in one working week by two technicians, a crane operator and a welding specialist (the latter required for one day only). Most of the time is spent in the manipulation of the individual sub-modules and in the module geometry control.

4.3.3.1 Differences between barrel and extended barrel assembly

To a large extent, there will be no difference in the assembly of barrel and extended barrel modules other than the number of sub-modules and the location of the special sub-module. The Intermediate Tile Calorimeter (ITC) sub-module is mounted in the same way as all others but placed externally to the interior end-plate. The final approach for ITC sub-module installation is not yet proven and this will be part of the 1997 exercise. From the design point of view the baseline approach will be to first connect the ITC module to the front-plate, to mount both elements together with the usual technique, and then to weld them together.

Unlike the case of the barrel, where all modules are identical, in the extended barrel there will be six special modules (three on either side of the calorimeter for each detector side). This accommodate the modifications needed for the Liquid Argon cryostat supports and for the cryostat installation. For these modules, the difference is in the two outer sub-modules, which will be shorter in radius by the space taken by the first spacer. In addition, the front-plate will be shorter and will interconnect only the seven internal sub-modules. A special plate is required to fasten the end-plates to the shorter modules. Furthermore, for another 12 modules the external end- plate will not be mounted in place during this assembly operation. It is replaced by a large plate (5 cm thick), which spans across all modules which are sitting directly on the calorimeter support saddle. This plate will support the cryostat directly and relieves the stress on the saddle itself (see Section 4.5.2).

4.3.3.2 Assembly tooling

The assembly of modules requires a set of special tools[N-90], which have been developed up to now in a very pragmatic way, trying to minimize investments and using existing infrastructure and laboratory equipment as much as possible. Three locations will have to be equipped with this particular tooling, one laboratory for the barrel modules and two laboratories for the extended barrels. Each of these laboratories must be equipped with a 30 tons crane (15 tons for the case of the extended barrels) for handling the assembled module. In addition, all three laboratories must be equipped with the handling fixtures described in Section 4.2.4.1, and in particular the fixture used to rotate sub-modules into the vertical position for mounting onto the girder.

The bulk of the tooling is given by the girder support table and the related infrastructure. It consists of two marble tables ($400 \times 500 \times 3500\ \text{mm}^3$) placed end to end and furnished with a set of tunable supports and clamps placed every 70 cm. The girder is placed on these supports and fixed in position using the holes already present in the outer girder plate. At the two extremes of the girder two face brackets are mounted to form the external reference system. Each of these brackets presents a precisely machined vertical surface which is placed perpendicular to the girder key surface. The precision of this basis is of 0.10 mm/m. Its function is to guide the correct vertical positioning of sub-modules. Some aspects of this design are being re-evaluated for the assembly of the two extended barrel prototype modules. In particular, we are considering the use of a laser alignment system. This will also require two precision end pieces to establish an external reference, however the detailed design will be somewhat different from that described here. Finally, an essential element of the tooling is an access scaffold mounted on one side of the support beam. This allows access to the inner key of the module for inspection during the various assembly steps.

4.3.3.3 Module envelope specification and measurement

The module envelope is determined by the cumulative fabrication and assembly tolerances from master plate stamping through final mounting of the sub-modules on the girder. The features of the components which contribute are: the key slot width and position on a master plate; the width of a master plate; the alignment and widths of the keys on the stacking fixture; and the key width and position on the girder. An analysis of the cumulative tolerances on these components as presently designed, yields a maximum tolerance zone of ±0.625 mm for what we consider to be the limits of cost effective manufacturing. We are therefore considering a modification of the calorimeter design to accommodate a 1.5 mm ϕ gap rather than the 1 mm which was our original goal (the impact on the physics performance of the calorimeter is likely to be negligible). The initial set of measurements done on Module 0 indicates an envelope precision of the order of 0.400 mm. If needed the gap increase can be accomplished by a simple radial translation of 2.5 mm, which can be recovered in the global calorimeter envelope by a minor adjustment of the outer plate thickness in the girder. A final decision on this change will be made in 1997, following the construction of the two extended barrel prototype modules.

It is essential that each module fit within its tolerance envelope for the successful assembly of the calorimeter. In the sub-module assembly phase, this is maintained by component quality control during production and assembly (master plate fabrication and stacking). Following module assembly the full tolerance envelope for each module will be verified using the external reference system established as part of the assembly tooling. At present we have only conceptual designs for the system required to establish the geometrical envelope of each module as it is assembled: a mechanical solution based on a precision straight edge and two precision end-plates which themselves define the envelope; a laser based alignment and surveying system. It is our judgement that either approach could realise the necessary precision and the choice will be made in 1997 once experience has been gained through the fabrication of three full size prototype modules. Similarly, we have not yet considered what course of action to take should a module fail to fit within the tolerance envelope. This will depend on the failure mode, but may be a simple as the use of a hand grinder to remove minor surface defects not detected during the earlier phases of construction.

4.3.4 Module handling and handling fixtures

Figure 4-33 Module handling during Module 0 installation at the SPS: rotation from a six o'clock position to a three o'clock position and then horizontal transport.

Two types of module manipulations are foreseen. In each of the assembly plants (three), modules will be always resting on the girder in the six o'clock position, placed on two independent supports. Each module must be handled in this position for transfer away from the initial assembly tooling and to a storage location, and before being either instrumented or transported to CERN. Therefore a simple and economical tool, to be copied four times, has been designed (see Figure 4-34). The module rests on two plates bolted to the bottom of the girder, and is connected to a high beam to pairs of four rods distributed along the length of the module. Before lifting, the rods are tightened and the module is trapped on two guiding plates connected to the main beam, which will prevent any transverse motion. This fixture weighs approximately 2 tons. This tool will also be used at CERN to manipulate modules in the storage place and to lower down individual modules into the ATLAS pit for the final assembly. In the latter case, a simple modification can allow up to three modules to be carried simultaneously.

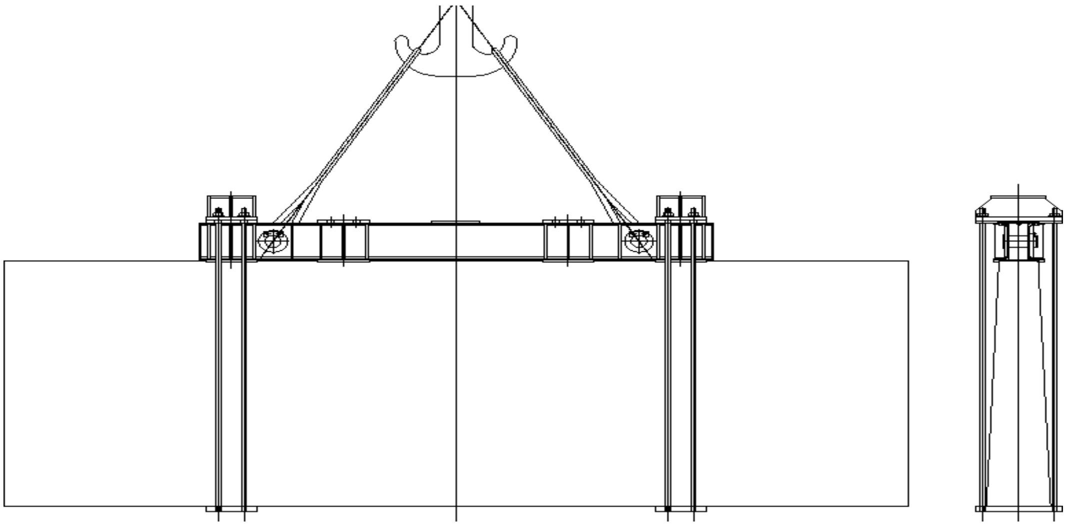

Figure 4-34 Module lifting device. This device will be present in all assembly plants.

At CERN, each module needs to be rotated and positioned around its longitudinal axis. This is necessary to place modules on the testbeam table, but especially to build up the final cylindrical structure. For this purpose a second type of fixture has been designed. The main idea is to support the module from a set of angle brackets fixed to the outer radius surface of the girder. The prototype of this fixture is shown in Figure 4-33, while being used for manipulation of the barrel prototype module. The number of angle brackets needed is a compromise between the structural needs, the efficiency in the operation of connecting and the interference during assembly with the calorimeter support structures. This tool is unique and should be used for both the barrel and extended barrel modules. Six brackets are needed for the barrel module and three for an extended barrel module. The angle brackets, interconnected at the two extremes with structural beams are then connected with two solid chains to a main beam, supported on the crane hook. Two coupled step motors will allow to drive the chain such to rotate the angle brackets around the longitudinal axis.

4.3.4.1 Module transportation fixtures

We anticipate that two module assembly locations will be on continental Europe and one in the United States. Road or rail transportation will be used to convey within continental Europe to CERN. Road transportation has been used for moving Module 0 from JINR, Dubna to CERN. In this case, due to a limitation on the type of truck available, the barrel module was transported on its side in the three o'clock position on a three point support as shown in Figure 4-35 with the center support beneath the girder. This approach has been chosen to isolate the module from deformation in the truck bed whilst the truck is moving. To distribute the load at the narrow end of the module, a structural channel is bolted to the inner radius plate. In this position, the girder deflection is 1.3 mm and the stress is 300 kg/cm^2, which is substantially lower than the proportional limit of 1600 kg/cm^2. To damp vibration whilst the truck is in motion, the girders ends were reclined on dampers constructed to have a plastic deformation at about 400 kg force. Finally, administrative speed limits were placed on the truck; 50 km/hr. in Russia, CIS and Poland and 60 km/hr. in Germany and France.

Figure 4-35 Module 0 transportation on a truck in the 3 o'clock position.

We anticipate using a special purpose container for shipping modules from the United States to CERN. This has been successfully done in the past with modules for the ZEUS calorimeter at DESY and a similar approach will be adopted for the ATLAS modules. The system is designed to fit within a standard 20 ft ocean-freight shipping container and is shown in Figure 4-36. The module will be transported in the six o'clock position resting on the girder and is supported by a framework of structural steel. Pneumatic pads, designed to carry loads with a minimum of low frequency vibration will be used to isolate the module from shock loads up to 3-5 g. Accelerometers will be mounted to the module during shipping and used to monitor the maximum acceleration, which may be a maximum of 1- 1.5 g. Road transportation will be used to and from the port of entry and departure. In this case a "low-loader" vehicle will be used to minimise instability during cornering and to allow highway speeds to be permitted. The sea container used for transportation of the ZEUS modules is available to be modified for our use. A second and possibly a third ones will be fabricated, if needed, to meet the assembly schedule.

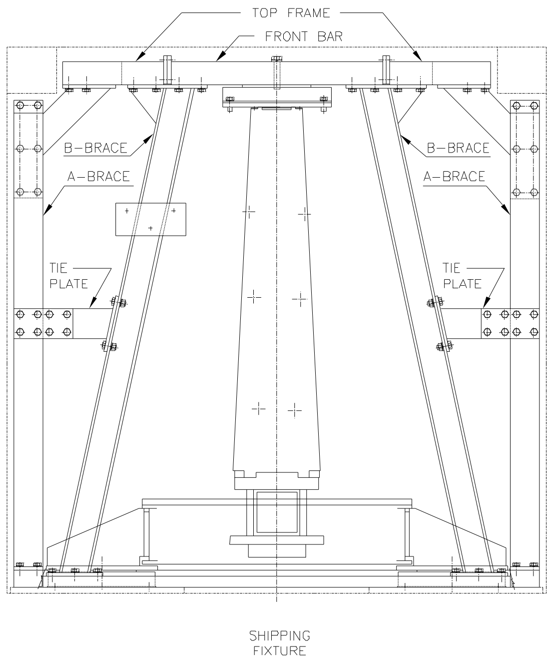

Figure 4-36 Special purpose container for transatlantic shipping (schematic).

4.3.4.2 Module storage

Module storage does not pose a significant problem since in general modules will be instrumented and tested as immediately following mechanical assembly and then shipped to CERN. Should interim storage be required the modules may be placed simply on the floor, on the girder. Stabilisers may be bolted to the girder to provide additional security and covers used to exclude dirt and dust.

4.4 Drawer production

An important constraint in ATLAS, is (reasonably) fast access to the Tile Calorimeter read-out without incurring major disruption of the other detector sub-systems. The Tile Calorimeter has therefore been designed with a moveable drawer system[N-43] containing the PMTs and the read-out electronics. The drawer slides inside the support girder of each module. In the case of a faulty read-out, these drawers can be removed once the endcaps have been withdrawn approximately 1.5 m. The faulty elements may then be repaired in place (if minor) or a replacement drawer installed while the drawer containing faulty read-out elements is removed to a refurbishment area.

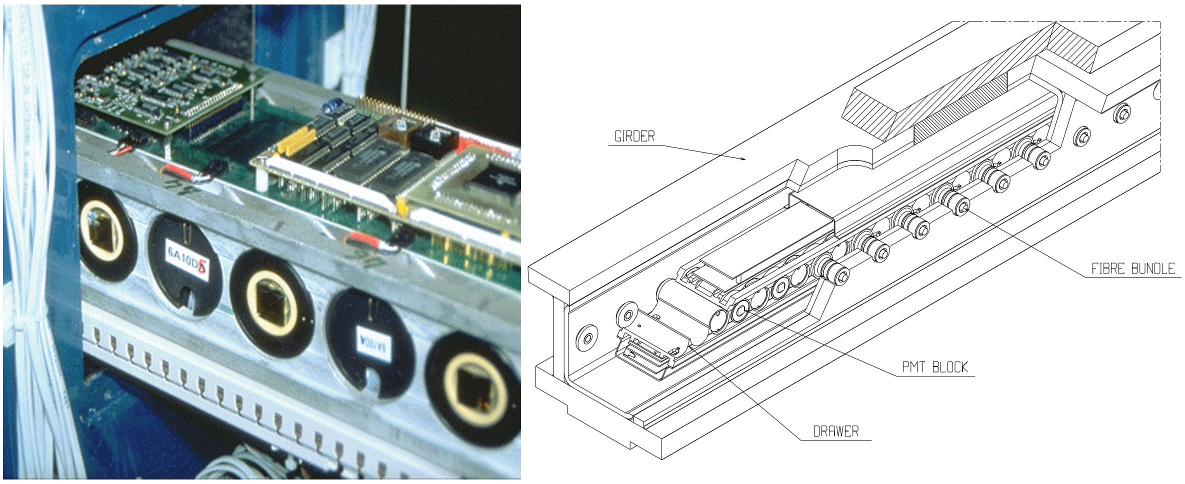

Figure 4-37 Drawer design and functional elements. On the left a photograph of the Module 0 drawer instrumented during insertion.

The drawer design and functionality as they sits within the support girder are shown schematically in Figure 4-37. Many issues contribute to the set of mechanical constraints on the system. Internal to the Tile Calorimeter the key constraints come from:

- the girder dimensions and tolerances
- the PMTs location versus the main components of the residual magnetic fields
- the size and number of PMTs and PMT blocks
- the tolerances for positioning the PMTs with respect to the fibre bundle
- the location of the electronics cabling and links to the Trigger, DAQ system and power supplies cooling

In addition, there are more global constraints arising from integration with other ATLAS detector sub-systems:

- compatibility with return yoke sections which form the magnetic contact between barrel and endcap girders
- ease of access to drawers for servicing
- integration with services in the gap between barrel and endcap calorimeters (such as for the Liquid Argon cryogenics and electronics)

In our baseline design, all drawers are assumed to have the same basic components (to minimise tooling costs) with four kinds of PMT block filling depending on the associated calorimeter cells. A group of two drawers (termed a "super-drawer") serves a half barrel or single extended barrel module and forms a single electronics unit. This can be extracted outward from the barrel or outward from the extended barrel for servicing as shown in Figure 4-37.

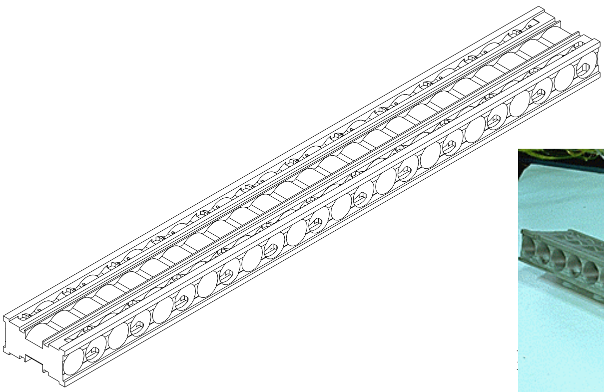

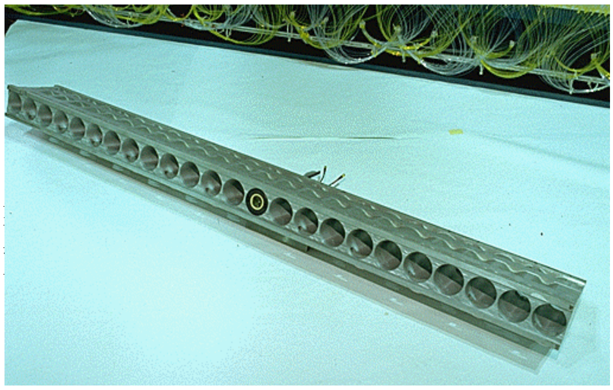

Figure 4-38 Drawer shell indicating structure formed by sand casting, schematic and Module 0.

As it is shown schematically in Figure 4-37, PMTs are mounted within the drawer normally to its face, to facilitate optical coupling and to minimise the effects of the residual magnetic fields. They are located on a pitch of 116 mm along the length of the drawer and staggered by a half-cell on either side to maximise packing. The precision with which the PMTs must be aligned with respect to the read-out fibres is determined by the area of the fibre bundle, which in turn depends on the number of fibres in a particular read-out cell (as discussed in Section 6). This results in a position tolerance of 2.6 mm in the barrel and 1.0 mm in the extended barrel. A tolerance of 1.0 mm is specified for all drawers to realise full interchangeability. The drawer shell itself is a complex geometrical structure with precision elements as shown in Figure 4-38. The critical elements are the holes which receive the PMT block, where a misalignment would adversely affect uniformity and interchangeability. These holes have the tolerances of (+0.15 mm, +0.05 mm) to match the corresponding tolerances of (0 mm,-0.2 mm) on the PMT blocks. The drawer shell itself is manufactured using an aluminium alloy via sand-casting, with subsequent machining to form the holes receiving the PMT blocks. This has been determined to be the most cost effective approach for fabricating this precision structure.

4.4.1 Girder ring installation

The girder ring (shown in Figure 4-39) is used to glue and align the fibre bundle relative to the location of the PMT. In addition, these rings are used as an alignment and support element and function as the slides on which the drawer containing the phototubes and electronics is mounted in the girder. We have adopted a design in which the exterior edge of this ring is used as the "rail" on which the drawer slides to be inserted into the girder. The precise installation of the set of rings is accomplished using a custom fixture (a "dummy drawer", see Figure 4-39), which provides a simple method by which the PMT which is precisely positioned in the drawer shell may be aligned to its associated fibre bundle. A precision stop is also fixed within the girder when the fibre rings are glued in place to maintain subsequent alignment following removal and re-insertion. This is located at the position corresponding to the large fibre bundle. This approach has been chosen to largely decouple the precision required for fibre mounting from the planarity and linearity tolerance of the girder face.

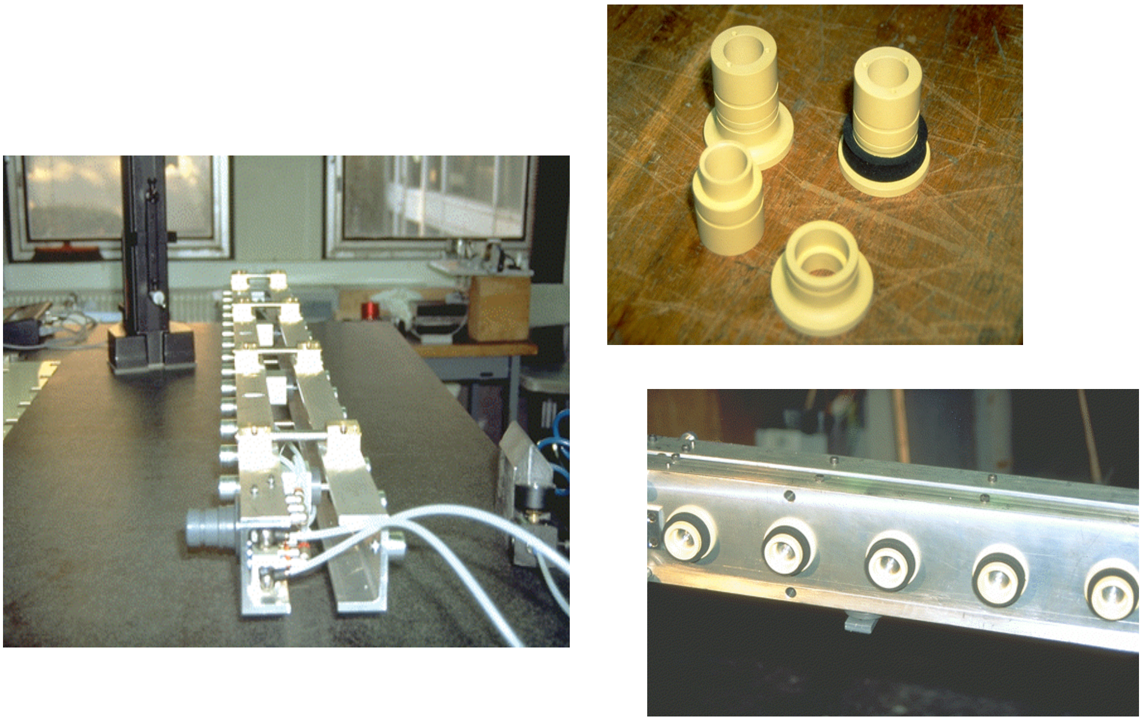

Figure 4-39 Girder rings and their installation tool.

4.4.2 Patch panels and connections

Patch panels located at the ends of the girder are used to convey signals and services into the electronics in the drawers. An initial design has been developed for use with the barrel prototype module and meets the basic design criteria and is shown schematically in Figure 4-40. Some development of this design is however expected as the constraints and mechanical limitations in the gap region become better understood.

The drawer electronics must be cooled during operation. Our baseline design proposes the use of a water based cooling system capable of removing the expected heat load in a stable state mode (however forced air cooling has also been considered). The cooling pipes run inside the drawer and are coupled to an external water supply at the patch panel via flexible hoses.

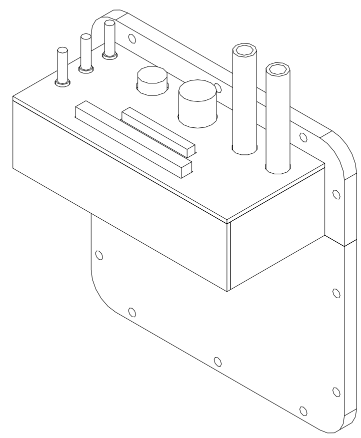

Figure 4-40 Patch panel and connections to be installed at the ends of the girder to provide services for the drawer electronics.

4.4.3 Installation and maintenance

Drawer installation will require special purpose fixtures to maintain the alignment of the drawer to the drawer guides inside the girder during insertion. Since the weight of a single drawer is significant, this fixture must also be capable of fully supporting the drawer during this operation in any of the 64 azimuthal orientations around the calorimeter. No firm design for this fixture has been completed at the present time. However, a concept which appears attractive is to mount a motorised cart on rails which attach to the girder and end-plate of the extended barrel calorimeter. This should be capable of carrying about 0.5 tons and supporting the drawer (and people) in any orientation.

4.5 Calorimeter assembly

The basic concept underlying the calorimeter assembly procedure is that the 64 modules, once assembled into the calorimeter form a cylinder which is a self-supporting structure. Each module rests on the module below and is supported on two well defined bearing surfaces at the innermost and at the outermost radii. The main structural elements in the assembly are the girders, which are coupled by connection plates fastened at the outer radius. In the case of the barrel, six such plates are used to form a bolted (bolts M24) connection between adjacent modules with only three being required for the extended barrels. These connecting plates will also be used for radial alignment of modules during the assembly process. For longitudinal alignment we propose to use an external fixture at one end of the structure. During the assembly of the upper half of each calorimeter section, which is done with the Liquid Argon cryostat in place, additional fixtures will be used if deemed necessary for mechanical protection of the cryostat.

A second important concept is the assembly sequence. The cylinder will be built up, using an assembly fixture, starting from the lower modules and built up until the final few modules are inserted as a unit. The assembly must be stable in all intermediate configurations and fixtures will be used as necessary. Shims, placed at the two bearing surfaces, ensure that the contact between modules is well controlled and occurs only at these two surfaces and allow individual adjustment of the position of each module within the design azimuthal gap of 1 mm. The shim sizes will also take account of overall structure deformation as measured during the assembly such that sufficient space is available for the installation of the final modules. They will also be chosen such that stresses between modules during the assembly are always generally in compression (the barrel modules in the region below the saddle would ordinarily see tension at both inner and outer radii, this is compensated by use of a compression belt). This scheme is based on an extensive analysis of deflections, discussed in more detail in Section 4.6.

The entire structure sits on dedicated supports (saddles) placed symmetrically on the left and on the right side, resting on the main rail system and coupled together using heavy beams. The barrel and the two extended barrel calorimeters are mechanically independent and may move individually on the rail system to provide access to the inner part of the ATLAS detector.

As an additional complexity, the Tile Calorimeter must provide the support of the detectors placed inside, and in particular of the Liquid Argon cryostat. The weight of this is of the order of 300 tons for the barrel and 250 tons for each of the end-caps. Concerning the barrel, the baseline solution is to have the cryostat directly supported on four feet placed at the four extremes and resting directly on the saddle and the overall calorimeter support system. The four feet are placed at an angle of 45^o and are housed inside the gap region. For the extended barrels the situation is more complex because of the differences in the internal support of the mass of the Liquid Argon Calorimeter inside the cryostats and the need to minimize the amount of dead material in front of the calorimeter. In this case, the support is different for the front (the location closest to the interaction point) and back of the cryostat. In front, the cryostat will rest directly, through two dedicated feet, on the inner surface of the Tile Calorimeter. On the back, the two feet sit on heavy end-plates which transmit the weight directly to the support saddle. The particular position of the cryostat feet will require an important modification of few modules in that region. Further details are presented in Section 4.5.3.

Compounding the problems from the support of the Liquid Argon loads is the fact that the location of the main rail system is constrained by the position of the toroid coils, which forces the separation of the main rails to be narrower than is optimal for the distribution of weight of the Tile Calorimeter.

This introduces additional stresses on the lower part of the Tile Calorimeter. A belt which connects the left and right saddle at least at the two extreme z-positions, will release part of these stresses from the calorimeter itself. The design and functioning of this element are described in the next sections.

The Liquid Argon cryostat also has two chimneys to house the feedthroughs carrying the Liquid Argon signal cables. These trap the cryostat inside the Tile Calorimeter cylinder once this is assembled. In addition, they impose severe constraints on the assembly of the upper part of the tile structure, once the cryostat is in place. All these procedures are described in Section 4.5.4.

4.5.1 Support saddle

The overall support of all calorimeters and inner detector will be based on support structures (saddles) which will be sitting on the main ATLAS rail system (described in the integration TDR). Between the saddle and the rails there is the movement system which allows barrels and extended barrel to be moved in place after being assembled on the two sides of the ATLAS cavern. The extended barrels will also have to move to provide access to the inner part of ATLAS during shutdown periods. For the barrel, the support consists of four pairs of saddles, interconnected with a heavy structural beam. Each pair of saddles is interconnected near to the calorimeter bearing surface using steel plates. The supports will be fabricated using non-magnetic steel, the external saddles having to be placed at the two extremes of the barrel and the internal one near to the center. This space between saddles is required to allow for module manipulation during installation. The extended barrels are about half as long as the barrel and therefore require just two pairs of saddles placed at the extreme z-positions. The design of the individual saddle, the connection and the way the saddles are interconnected is identical to that for the barrel.

Each saddle weighs about 2 tons. Figure 4-41 shows the way contact and the transfer of forces is done between the calorimeter girders and the saddle. The saddle will be in direct contact with six modules (number 22 to 27) and will have two functions. First of all a transfer of the shearing stresses between calorimeter and saddle, is made via a key element mounted on the lowest part of the saddle. This key will be inserted into a slot in the girder of the module above and must provide about 13500 mm^2 of bearing surface. It should stand 105 tons of shearing force. This approach requires high precision in the key, the key housing slot and needs a special design effort. Secondly, the normal forces will be distributed by a set of bolts (M36) running through the saddle perpendicular to the girder surface. This will ensure the distribution of the normal forces along the saddle, with no shear stress transfer. This, however, does not imply any special requirement to be placed on the quality of surface of the saddle plate in that region. The module number 22 (counting from the top) will also be bolted at the girder location to the saddle itself. The final detailed engineering design of this support system is not complete and will be part of the 1997 engineering effort.

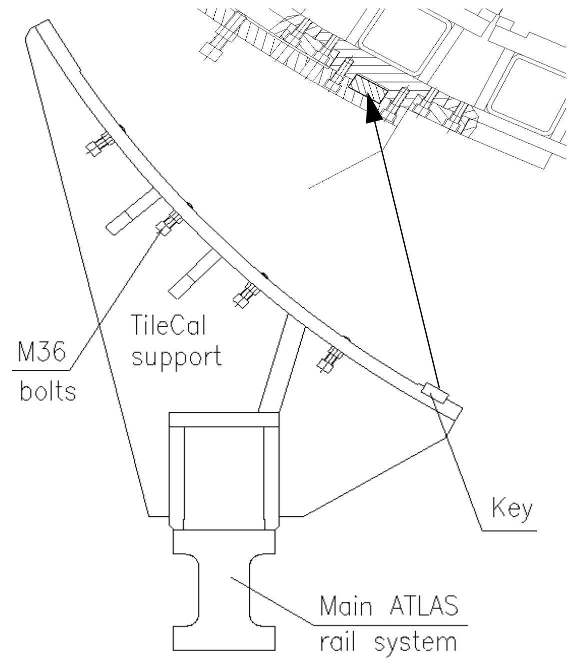

Figure 4-41 Cross-section of the saddle system, with details of the contact between saddle and girders.

4.5.2 Barrel cryostat support

The barrel cryostat weight is about 300 tons during operation. The distribution of the weight between the cold and the warm part has been designed in a way that allows the Liquid Argon detector to be supported on four feet. The general arrangement of these feet is shown schematically in Figure 4-42. The contact surface between the cryostat and the feet is placed on the warm flange of the cryostat, near to the location of the feedthrough channels. The angular distance between 2 supports in ϕ is 90^o. This allows a support using dedicated feet placed externally to the barrel cylinder in the radial direction and resting directly on the saddle support structure. Finite element calculations done recently indicate that contrary to expectations, the barrel cryostat contributes significantly to the tension loads in the calorimeter connections below the saddle at the outer radius and large compression loads at the inner radius. The former are resisted in our design using a pre-tensioned belt. In 1997 we propose to evaluate whether a redesign of the end-plates and their interconnection may be used to alleviate the bearing load at the inner radius.

Figure 4-43 shows a cross section of one of the four feet used to support the barrel cryostat and the way by which the support is transferred to the Tile Calorimeter support structure. The bearing surface between cryostat and the support is about 35100 mm^2. A first set of calculations have been performed to design and to dimension these mechanical supports. Particular care has

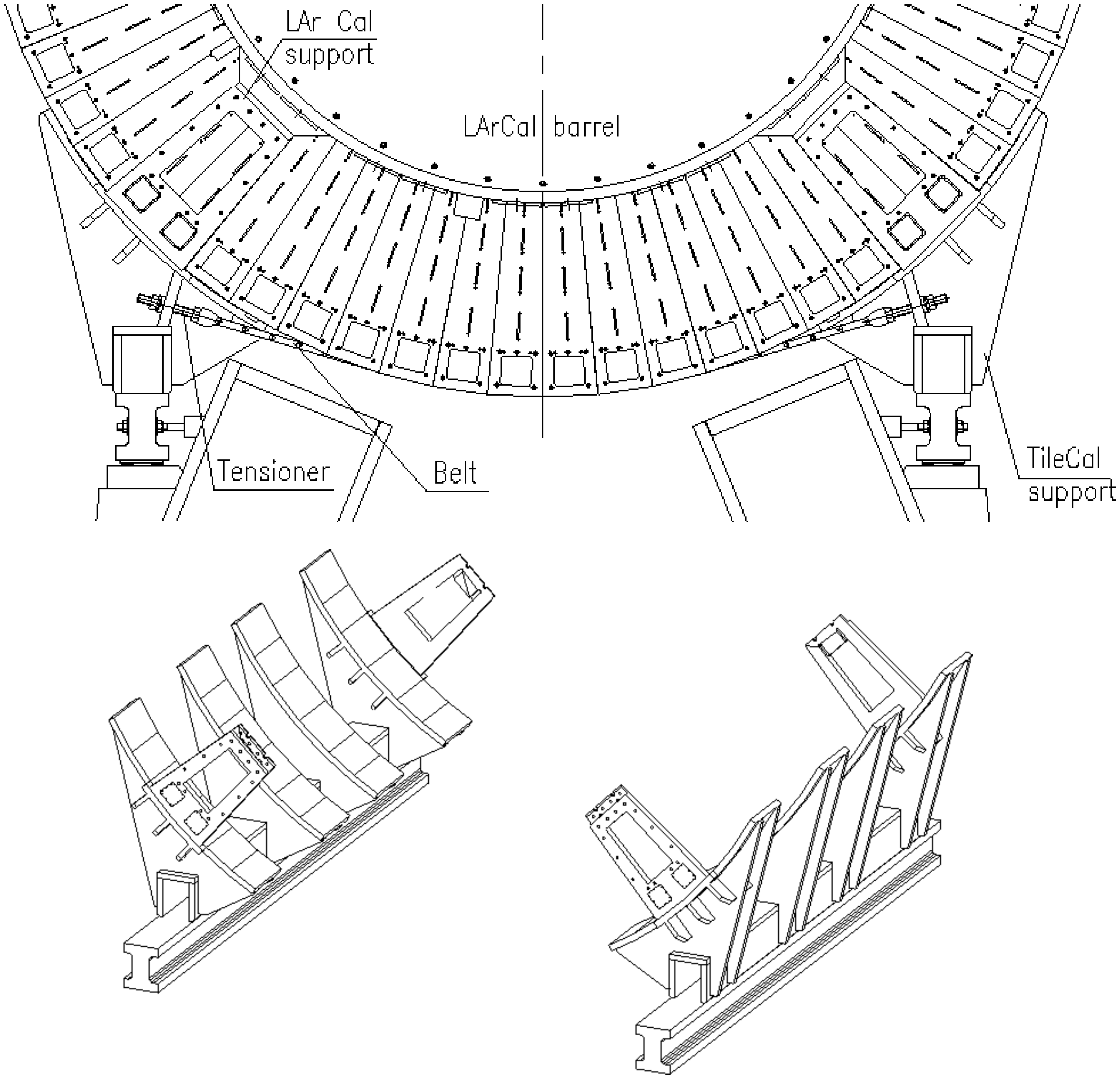

Figure 4-42 Support of the barrel Liquid Argon cryostat on 4 dedicated feet external to the tile structure. The lower figure presents a 3-D view of the saddle and support alone.

been taken to minimize the amount of material, to avoid compromising the physics performance in that region. The total thickness of this stainless steel support is 85 mm.

The internal part of the plate has been cut out to allow access to the calorimeter calibration tubes. These feet will be bolted in place to the Tile Calorimeter end-plates. To prevent buckling and because the end-plate is relatively weakly connected to the calorimeter body at the inner radius, an additional connection to the sub-module structure is provided by use of compression rods.

These run inside the module in the second hole (only one of the two available holes is used for the source tubes). Eleven such rods will be inserted in each of the two modules connected to the support feet. The design of all the support elements allows at least 15% of the normal stresses to be transferred tangentially, as required by CERN safety regulations. The connection to the Liquid Argon structure is done in such a way that on one side (positive z) the connection is fixed and the cryostat can not move. On the other side, a low friction material will be used in the interconnection, to allow small dimensional changes of the cryostat position during the various thermal phases.

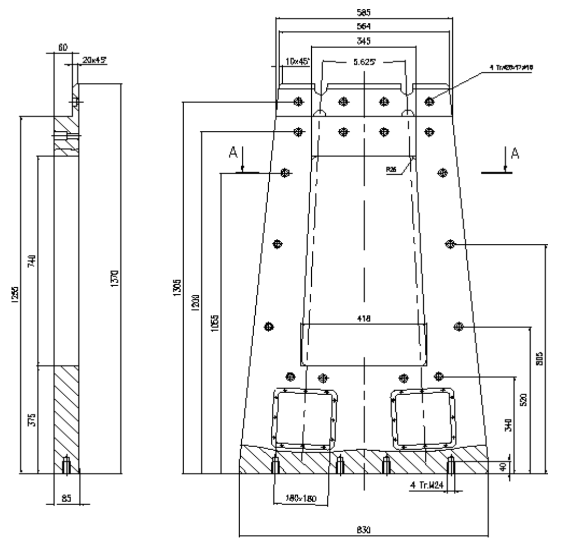

Figure 4-43 Detail of the Liquid Argon support.

4.5.3 Extended barrel cryostat support

The situation is very different for the extended barrel, where the design of the cold and warm vessel cryostat support does not allow the same type and geometry for the feet as is to be used for the barrel. In this case, the four supports of the Liquid Argon are located at the inner radius of the outer vessel, approximately 300 mm inside the Tile Calorimeter envelope in z. At this location the feet enter the space reserved for the Tile Calorimeter and therefore require some mechanical modification of several sub-modules. Furthermore, the angular position is almost ±85°, which complicates the weight transfer to the rail system. Details and motivation for such a choice can be found in the Liquid Argon TDR. Finally, the distribution of weight is not symmetrical between front and back feet (83 tons for each of the two front feet, 37 tons for the two locations on the back).

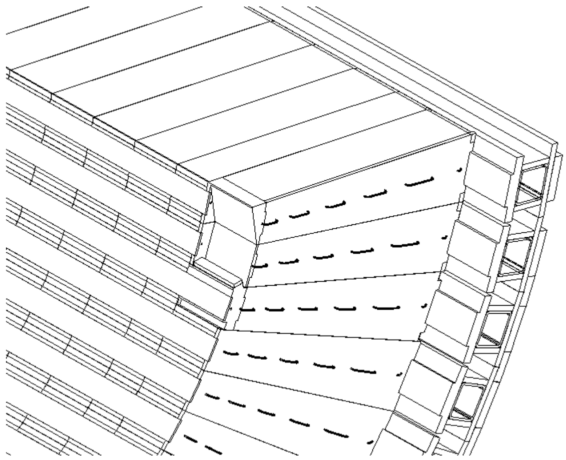

Figure 4-44 Cryostat support on the Tile Calorimeter extended barrel (front end support).

The compromise reached after an in-depth engineering investigation is to support the two feet of the cryostat, placed on the front face near to the center of the detector, directly on the inner part of the Tile Calorimeter body. This will add substantially to the bearing surface needed at small radius between adjacent modules, which will have to be increased by about 200%. In addition, space must also be provided inside the tile envelope to accommodate the two feet. This requires a modification of the module geometry for at least three modules under each support foot on each extended barrel. This is accomplished by using special submodules which are radially shorter by the length of one spacer (roughly 100 mm).

This solution provides a bearing surface of about 12500 mm^2 (50 x 250 mm^2) for the cryostat feet. Figure 4-45 shows, conceptually, the special modifications to be done to these sub-modules and the way bearing loads are transferred from the upper module through to the lower one in this particular region.

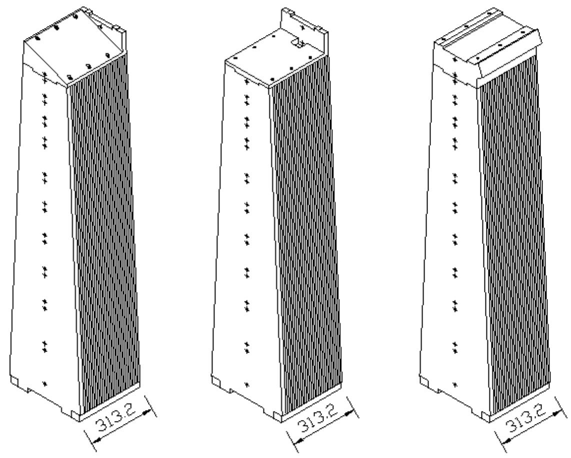

Figure 4-45 Detail of the modifications and additional parts needed for the three sub-modules.

For the outermost support feet, the weight on the feet is large (2x83 tons) and demands even greater stress carrying capability on the Tile Calorimeter. In this case the impact of the supports on physics performance is not significant and we have adopted a solution in which the total weight is taken by a solid end-plate (5 cm thick) which will rest directly on the support saddle (Figure 4-46). This plate spans over six sub-modules where it replaces the standard end-plate. The connection to the girder remains the same for these modules. A modification which makes use of bolts will be used for the front-plate connection at the inner radius. The 50 mm thickness of this plate will occupy the clearance space between Tile and the Liquid Argon feedthrough chimney, the latter now being in contact with the support plate. Again as for the barrel support, some cut-outs must be made in the support plate to allow access and installation of the calibration tubes.

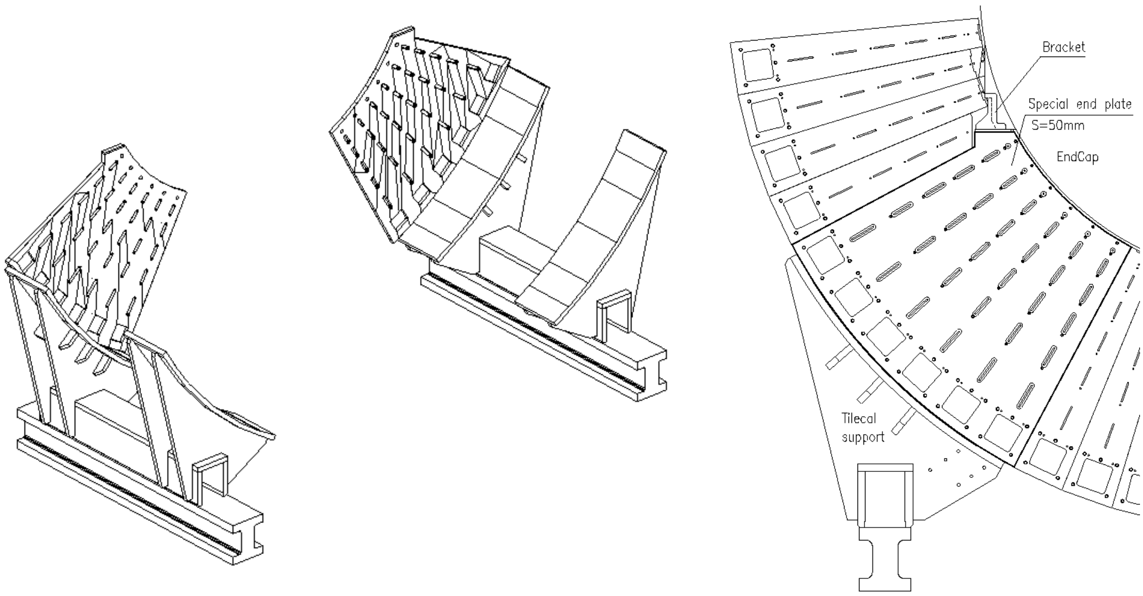

Figure 4-46 Detail of the way the back of the extended barrel cryostat in mounted on the Tile Calorimeter support. This is done with a 50 mm plate which sit directly on the support saddle.

As is the case for the barrel cryostat support, we are uneasy with the large (bearing) loads transmitted to the inner radius of the Tile Calorimeter by the support of the Liquid Argon calorimeter. Although an increase in bearing surface at the inner radius is in principal possible, this solution is not desirable from the point of view of physics or cost. In 1997, we therefore propose to evaluate the possibility of carrying some or most of these loads by a redesigned end-plate. One concept to be studied is to form a solid connection between the 50 mm end-plates supporting the load for the outer feet and to perhaps redesign this plate solely as an element of the cryostat support. If this proves to be useful in reducing the loads seen by the Tile Calorimeter structure then we will continue by evaluating the applicability of this solution to the other cryostat supports.

4.5.3.1 Belt support

The support of the cryostats and the non-optimal distance between the two rails of the support structure add additional requirements on the strength of the connections between modules in the lower region of the detector. In particular, the modules numbered from 28 to 37 are affected by shear stresses above acceptable values. In addition, the cryostat load increases the tension forces at the outer radius connecting plates in the modules below the saddle above that arising from their own weight. These tension loads are resisted by pinned connections between the plates. The obvious approach to accommodating a greater tension load by increasing the number of pins is not possible, due to lack of space on these plates. One way to solve this problem is to connect the left and right saddles directly, thereby balancing the left and right moments of the entire system. The problem is especially important at the two extremes of the cylinder, where the weight of the cryostats is applied.

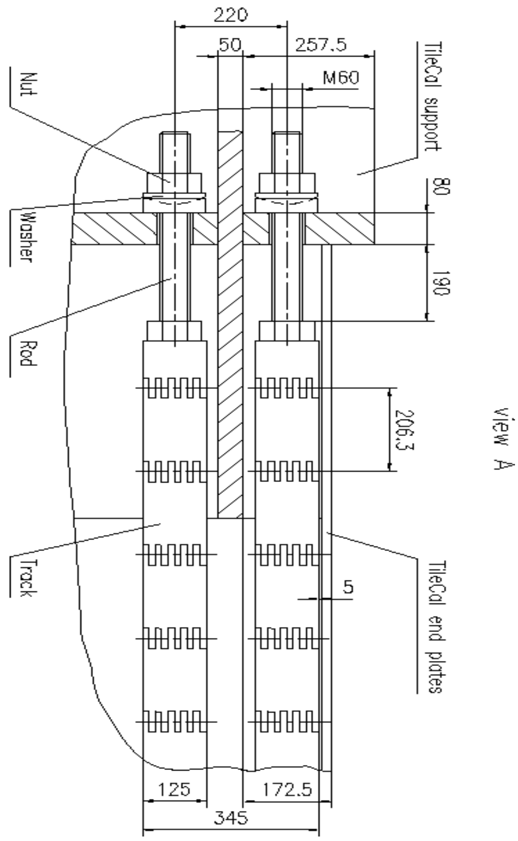

Figure 4-47 A detail of the structural belt connecting the left and right saddle.

The proposal is to cut the cover and the connections of the girders for those modules by 150 mm at both ends of the cylinders, freeing some radial space. This provides 50 mm of space in which to accommodate a support connecting one saddle to the other (see Figure 4-42). This space being limited, we have chosen a solution which makes use of a tension belt rather than a beam as would be customary. As is shown in Figure 4-47, this belt is composed by elements of the size of one module (about 400 mm). The belt will be prestressed to about 75 tons, which is about the same as the horizontal component of the cryostat load, and connected to the saddle, near to the structural beam.The precise pre-tension load will be determined following completion of a detailed 3-dimensional finite element analysis of the entire calorimeter system and support structure.

4.5.4 Assembly sequence

The assembly of one entire cylinder will be a very complex operation. An assembly scenario has been worked out, taking particular into account the limited resources and the severe constraints imposed by the concurrent assembly of other major ATLAS sub-systems. The model must also balance the need to speed up the operations by use of pre-assembled supermodule as much as possible, with the need to minimise the complexity of the various operations:

1. The left and right saddle structures are mounted in place on the ground floor, on the top of the ATLAS pit. The two parts are connected with a temporary sets of beams, as illustrated in Figure 4-48.
2. In a second step the lower part of the cylinder in assembled. One by one ten modules are moved in place, interconnected at inner and outer radii and fixed to the temporary cross beams. While the construction takes place, the exact location of each wedge is measured with respect to an external reference. This data is used in conjunction with a finite element model of the calorimeter to compute the thickness of the shims to be installed between the module bearing surfaces.
3. The entire structure, the saddles and the supermodule with ten modules, is then lifted down with the main crane into the ATLAS pit and mounted on the main rail system. The crane is attached to two strong cross beams as shown in Figure 4-48. The weight of this assembly will just fit in the maximum capability of the main crane system (about 240 tons). One week of operations is foreseen (Figures 4-49 and 4-50).
4. One by one then, alternating left and right, all modules in direct contact with the saddle are moved in place and interconnected. The first module which includes the key is particular delicate and requires difficult and precise rigging. Three weeks of operations are foreseen.
5. The assembly is then completed up to the half cylinder and the cryostat support feet mounted in place. The source calibration system will be installed and used to check out the assembled modules in place. All joints between modules will also be made light tight at this time, since this will be the last moment when unrestricted access to the inner cylinder surface is possible. Two weeks of operations are foreseen. A large fraction of this time will be taken to measure the exact position of the assembly and if necessary to apply some corrections.
6. The Liquid Argon cryostat, fully instrumented with the detector inside is lifted down and installed on the support feet. The lower temporary cross bars are removed and the interconnection between modules completed for the lower ten modules. The prestressed belt is installed in place and once more the whole system is surveyed. Four weeks of operations are foreseen.
7. The second half of the cylinder assembly is completed. One module at the time, alternating left and right, are installed in place. Most of the work goes again into the exact measurement and in the calculation of the shims. Here the rigging operations are more difficult because of the presence of the cryostat since the installation clearance between the Tile Calorimeter and cryostat on the side of the feedthroughs is only of the order of 1 cm. At each step the connections at the inner radius for light tightness are made while this surface is still reachable. Six weeks of operations are planned. At the end of this step, the cylinder is almost finished, except for the last few upper modules. At this critical moment, the space remaining must be sufficient for their installation.
8. In the final operation, the remaining modules (one, or a supermodule of few modules) are inserted and the cylinder is completed. One week of operations is foreseen there.

The entire operation in the ATLAS pit takes 15-17 weeks for each of the cylinders. More time will probably be taken for the assembly of the first cylinder, and less with the last one. A more detailed discussion on the overall assembly plan will be described in Chapter 8.

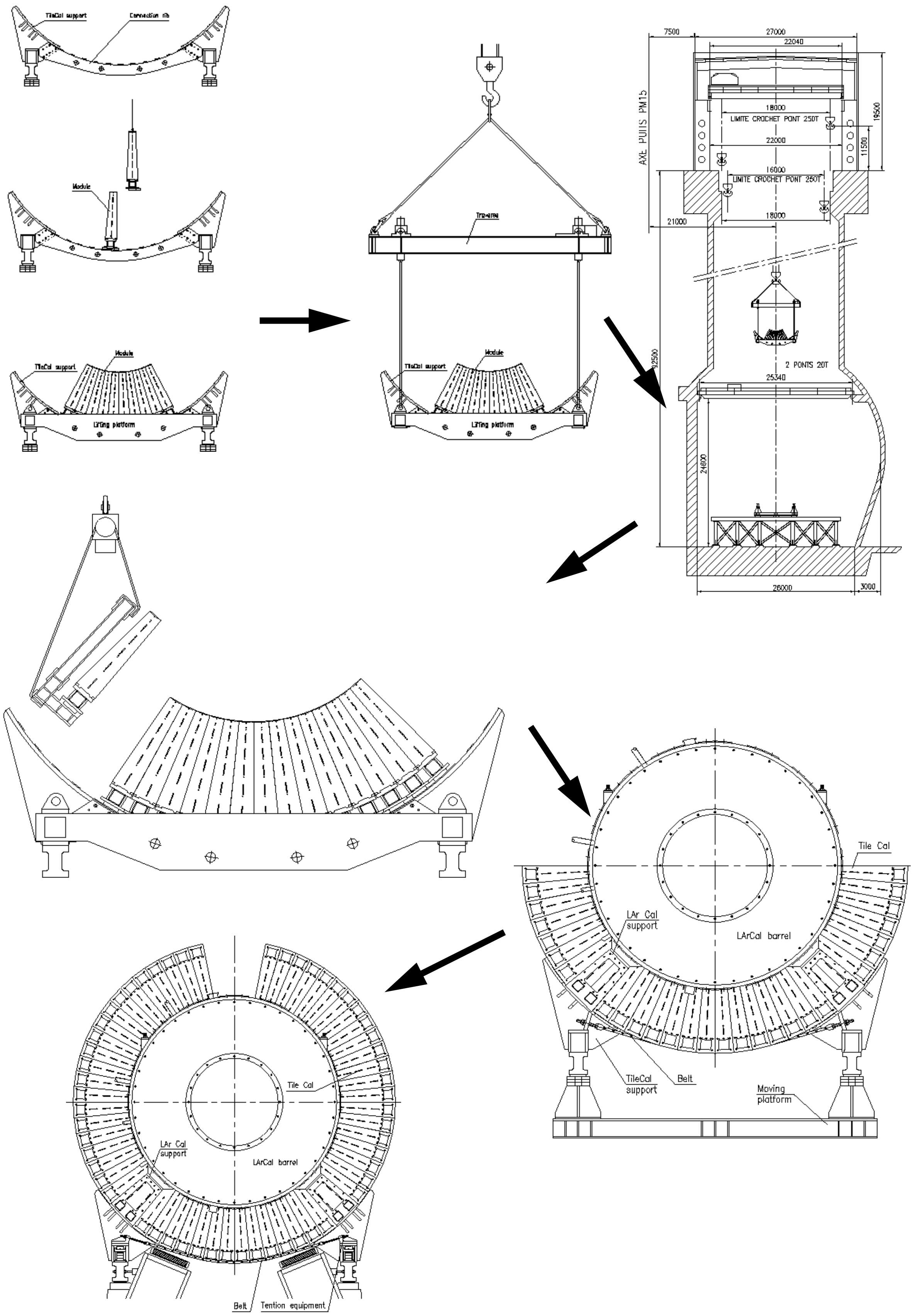

Figure 4-48 Schematic description of the various installation phases as described in the text below.

4.5.5 Pre-assembly plan

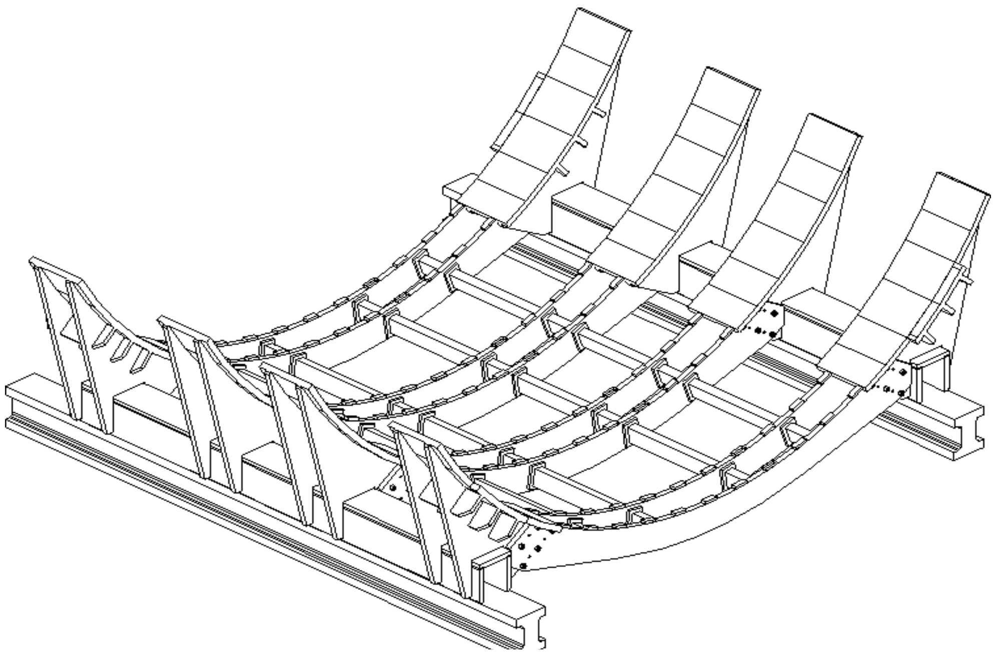

Figure 4-49 Platform used to do the pre-assembly and then used to install in the ATLAS pit the lower part of the cylinder. The weight of this structure is about 30 tons.

We plan to pre-assemble the barrel and at least one of the extended barrels the year prior to the beginning of the assembly operations in the ATLAS pit. We expect to gain a substantial amount of experience in the various steps from this. A crane with a 60 tons lifting capacity will be sufficient for the barrel pre-assembly and proportionally smaller for the extended barrel pre-assembly. All shims used, and deformations of the structure during assembly will be measured and cross-checked with FEA calculations. These data will serve as a basis for any possible corrections to the final operation plan. At present, our proposal for the ten or so modules mounted in the cradle for installation as a unit, is that, once connected, for the pre-assembly they remain unchanged in the cradle until mounted in the ATLAS detector.

4.6 Structural analysis

We have embarked on an extensive analysis of deflections and stresses in the assembled calorimeter structure. Basic results have been obtained from a classical 2-dimensional analytical calculation and these are now being used to establish the credibility of results obtained using finite modelling techniques. This work is going on and, in particular, details associated with the support of the Liquid Argon cryostats are evolving as their effect on the calorimeter and its support saddle are better understood. This study has several aspects. They range from the stresses in bolted and welded connections to the stresses and deflections in the structure as a whole during installation. As a first requirement we have compared results from a static calculation, a 2-dimensional finite element model, and a 3-dimensional finite element model to establish the reliability of our analysis. We have now initiated a study of the support saddles and the effect of the loads from the support of the Liquid Argon calorimeters on forces and deflections in the calorimeter structure, the support saddles and the ATLAS main rail system. Initial results and the details and assumptions used in the models are discussed below.

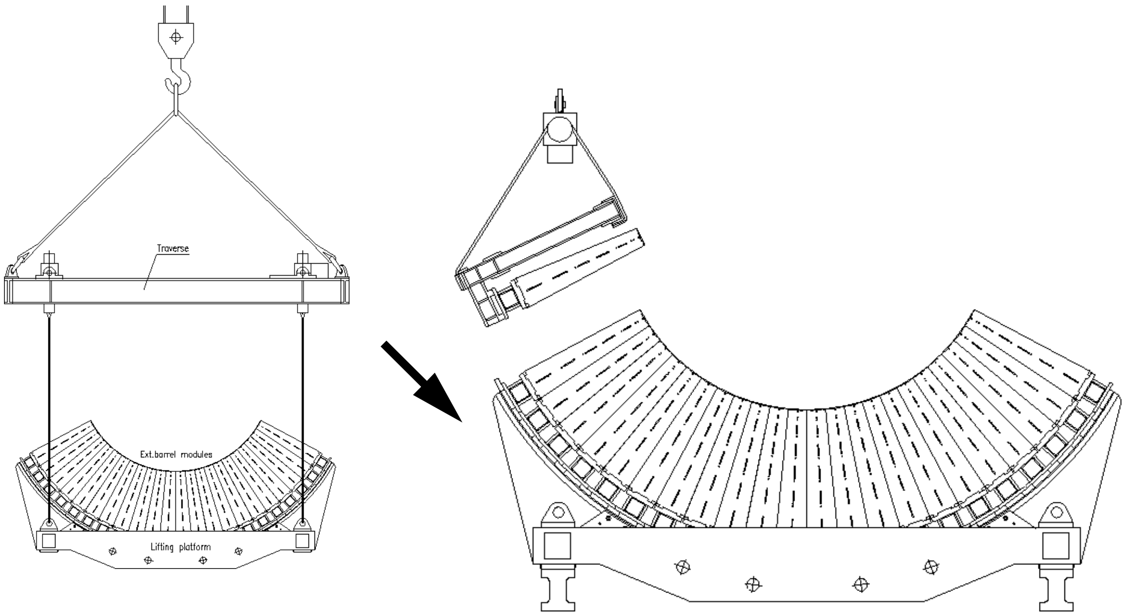

Figure 4-50 For the extended barrel more modules pre-assembled on the surface will be lowered down in the ATLAS pit, using the main surface crane of 270 tons capacity.

4.6.1 Sub-module stress & deflection calculations

The Tile Calorimeter sub-modules should be approximately rigid. This means that when transported or moved (rotated, lifted or placed on a table) no permanent deformation may occur. Early in the Tile Calorimeter R&D program, an analysis of stresses inside a sub-module under various conditions was carried out to ensure that this was the case. The weight of a sub-module is approximately 900 kg and for these calculations we have assumed that the maximum acceleration during any handling operation are smaller than 1/3 g. Three cases of sub-module position, in addition to three different methods for supporting the sub-module, were considered:

- master plates positioned vertically and supported at opposite sides (either suspended or supported from below)
- master plates lying flat horizontally and supported at the inner and outer radius
- master plates lying on edge horizontally and supported on a beam at the outer radius

Finite element and analytical approaches were used to compute the maximum shear stress in the structure and in the glue. The holes in the plates were not considered significant and were not accounted for in these calculations. From these calculations we concluded that in order to limit stress concentration, the sub-module should always be supported through an appropriately thick plate. The maximum shear stress in the glue is a function of glue thickness and is calculated to be 5.3 N/mm^2 for a glue line thickness of 0.01 mm and 2.4 N/mm^2 for a glue line thickness of 0.05 mm. Therefore, for our design glue line thickness of 0.05 mm, we have an adequate safety factor and conclude that our sub-module design fulfils our requirement that it not permanently deform during expected handling conditions.

4.6.2 Module stress and deflection calculations from finite element modelling

In order to calculate stress states in the module when it is in vertical or horizontal position and differently supported, a 3D model using the ANSYS program was built, in which we made use of the symmetry at the half of the length of the module. The girder was modelled by plate elements with appropriate thicknesses. Each sub-module was assumed to be infinitely stiff. All sub-modules are connected to the girder by beam elements which model the bolt connections. At the inner radius the connection between sub-modules is through the front-plate and it is modelled using link elements. The cross-sections of these link elements was determined such that they reflected the bending and shearing stiffness of the front-plate.

The model predicted the maximum value of displacement of 0.43 mm for a module lifted vertically. For the horizontal position two methods of supporting the module have been considered. In the first one only the girder is used to support the module. In the second method, the module is supported at ten points, two of them at the outer radius and eight at the inner radius. In either position of the module, the maximum value of the equivalent stress in the girder is nowhere larger than 89 N/mm^2. The stresses in the bolts are also not high, the maximum being 53 N/mm^2. In the front-plate stresses are even smaller, being nowhere larger than 15 N/mm^2. The maximum displacement (0.75 mm) is reached for the case when the module is in the horizontal position and is supported only by the girder.

4.6.3 Calorimeter static analysis

Assuming that the Tile Calorimeter is composed of infinitely stiff elements (the modules and the support saddles) connected only at some points, a 2D static analysis can be carried out. The result of such an analysis can give a good estimate of the interconnecting forces between modules. They also provide a basis for cross-checking analysis of more detailed numerical calculations in which deformations of the Tile Calorimeter structure are taken into account. In this section we present first the assumptions, then the method leading to static equilibrium equations for the Tile Calorimeter structure and finally the results of calculations based on these equations.

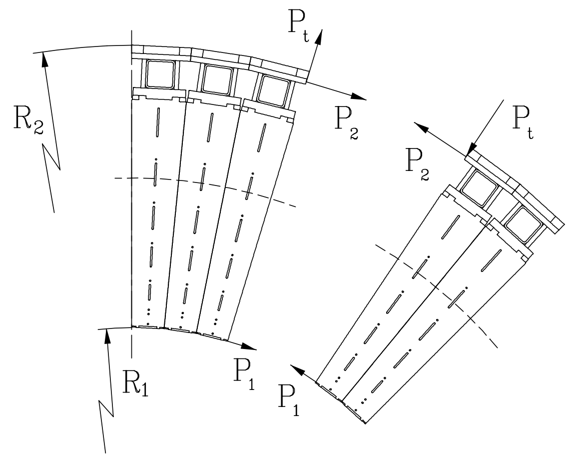

Figure 4-51 Module forces, force diagram.

At the outer radius (R_2 = 4175 mm) each module is connected to its neighbouring modules by pin connections. At the inner radius (R_1 = 2285 mm) the connection between modules is only through bearing surfaces with the coefficient of friction equal to zero. As a result of these assumptions, between two modules we have three forces to define, that is P_1, P_2, P_t as shown in Figure 4-51. The connection between the saddle and the Tile Calorimeter is by a pin and by a bearing surface without friction as indicated in Figure 4-52. In addition, only vertical forces can be transmitted from the rails to the support saddles. Because of the vertical symmetry we need consider only half of the Tile Calorimeter. For the barrel section, there are two pairs of feet at each of the ends of the calorimeter. These feet transfer the forces coming from the weight of the Liquid Argon calorimeter (AB) directly to the four saddles. For the extended barrel we have two different situations for the support of the endcap Liquid Argon (AE) calorimeter. In the first one the additional forces (AE_1) are acting at

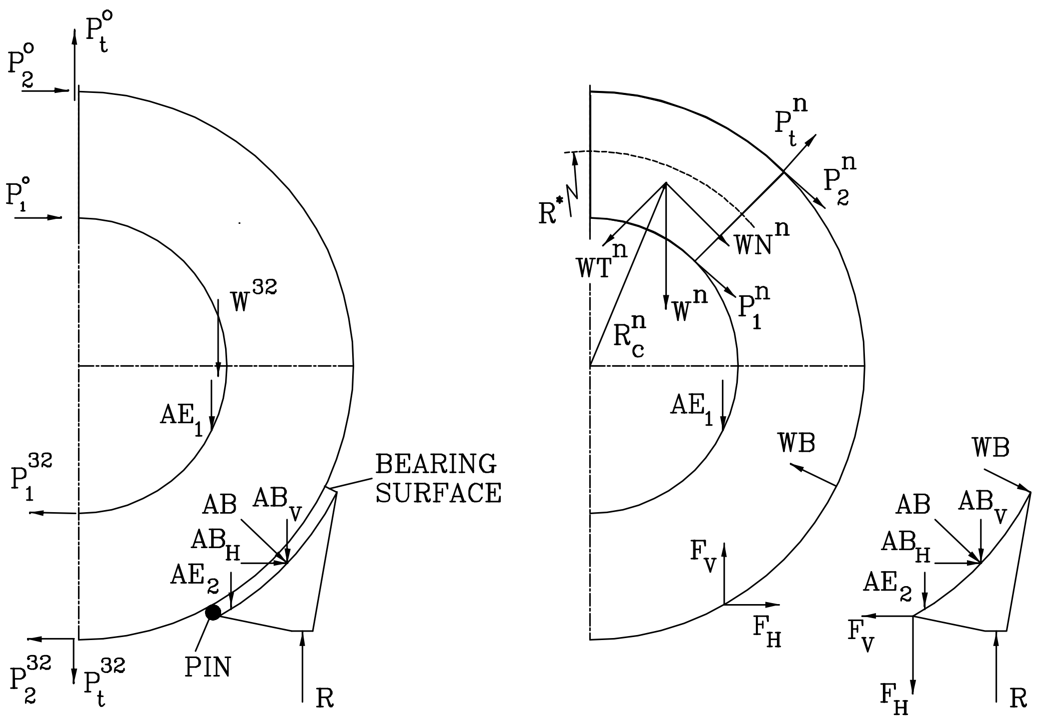

Figure 4-52 Calorimeter bearing forces, force diagram.

the inner radius and are distributed over the width of one sub-module. In the second case the force (AE_2) is transmitted directly to the saddle by a special end-plate.

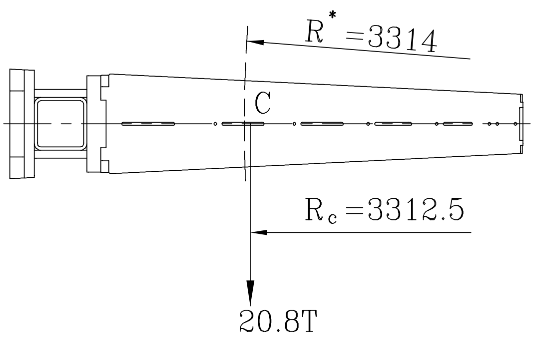

Figure 4-53 Module center of gravity definition.

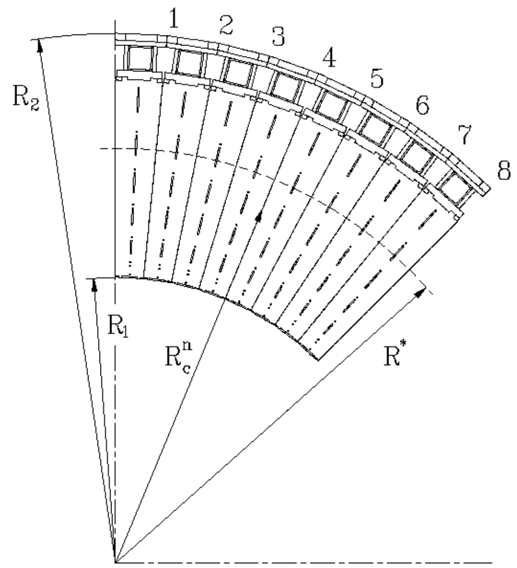

Figure 4-54 Module radial numbering scheme.

The gravity center of the module cross-section is placed on the symmetry line at the radius R_c = 3312.5 mm (Figure 4-53). Using the following formula, where $\alpha = \pi/32$:

$$R^* = R_c \cdot \frac{\alpha}{2 \cdot \sin(\alpha/2)} \qquad 4\text{-}1$$

The total weight of the module (20.8 tons) can be redistributed on a cylindrical surface shown in Figure 4-53 as a dotted line. The radius of the cylindrical surface R* is equal to 3314 mm. Assuming now that:

$$\alpha^n = n \cdot \frac{\pi}{32} \qquad 4\text{-}2$$

where n takes the values from 1 to 32, Equation 4-1 can be used to calculate the radius of the gravity center for a supermodule composed of "n" modules as indicated in Figure 4-54, that is:

$$R_c^n = R^* \cdot \frac{2 \cdot \sin\left(\frac{\alpha^n}{2}\right)}{\alpha^n} \qquad 4\text{-}3$$

The forces between modules are defined in the following way. First, from the global equilibrium equations we calculate the reaction force R and P_1^{32}, P_2^{32} (Figure 4-52). The additional forces:

$$W^{32} = 32 \times 20.8 \times 9810/5600 = 1166 \text{ N/mm} \qquad 4\text{-}4$$

$$AB_H = AB_V = (AB)/(\sqrt{2}) \text{ and, } AB = \sqrt{2} \cdot 150 \times 9810/(2 \times l_x) \text{ N/mm} \qquad 4\text{-}5$$

$$AE_1 = 37 \times 9810/293 \text{ N/mm and, } AE_2 = 83 \times 9810/l_x \text{ N/mm} \qquad 4\text{-}6$$

with l_x= 675 mm, are defined by the weights of the Tile Calorimeter module, the Liquid Argon barrel Calorimeter (AB) and the Liquid Argon endcap Calorimeter (AE), respectively. Moreover, since the final operation of the Tile Calorimeter assembly procedure is to connect two modules at the top of the Tile Calorimeter we can assume that $P_1^0 = P_2^0 = P_t^0 = 0$ (see Figure 4-52).

Finally, from the condition of vertical symmetry we have $P_t^{32} = 0$.

From the equilibrium equations for the saddle we can now calculate the forces between the saddle and the modules (F_H, F_V and WB, see Figure 4-52). Finally, the forces between modules, P_1^n,P_2^n,P_t^n, are calculated from the equilibrium equations of a supermodule composed of "n" modules.

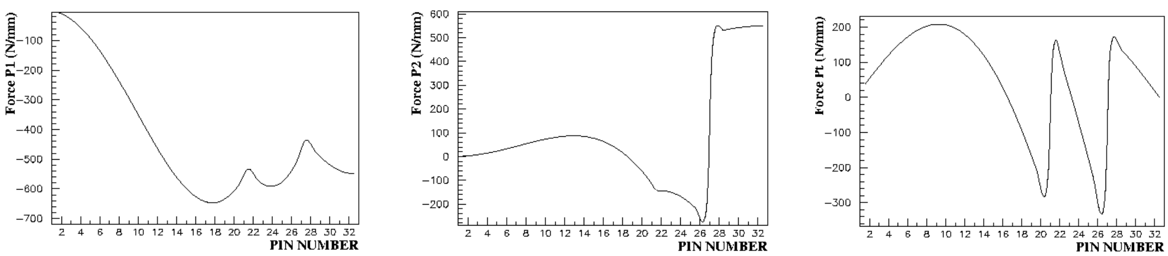

Figure 4-55 Inner radius, outer radius and normal forces for barrel Tile Calorimeter load alone

The first set of results, assuming that the forces AB, AE_1 and AE_2 are equal to zero, are shown in Figure 4-55. The "pin number" is defined in Figure 4-54. The results presented are valid for a situation in which no external loads (such as from the barrel and endcap Liquid Argon Calorimeters) are applied to the Tile Calorimeter structure and as such are applicable to the central part of the barrel and extended barrel. This is valid because, in the barrel our design calls for the cryostat support brackets to be directly coupled to the support saddle, and in the extended barrel because we have chosen to somewhat isolate the ring of sub-modules supporting the cryostats from the other sub-modules in the calorimeter. In this situation, our design bearing surface at the inner radius is sufficient to support the load. At the outer radius, below the saddle, the connections are in tension and the Tile Calorimeter design includes pin connections to accommodate this load.

The Tile Calorimeter supports are required to also support the Liquid Argon Calorimeters and cryostats. Our design goal has been to couple these additional loads directly to the support saddle as much as possible and to isolate the Tile Calorimeter structure from them. The barrel Liquid Argon Calorimeter load (AB) is taken by a support which is connected directly to the support saddle. In the case of the endcap calorimeters (AE), we have adopted a different solution at each end: nearest to the interaction point the support is placed directly on the inner radius of the calorimeter; the support furthest from the interaction point is coupled through a 50 mm plate to the support saddle. In both cases, the front-plate connecting the ring of sub-modules at the support is not welded into the key in order to preclude Liquid Argon Calorimetere shear stresses in this regions. Because of these additional forces AB, AE_1, AE_2, to which the Tile Calorimeter is subjected, values of the interconnecting forces P_1^n, P_2^n and P_t^n will be different in the region close to the ends. The specific design of these supports results in there being three regions to consider:

- for the barrel close to the both end (AE_1 =0, AE_2 =0)
- for the extended barrel close to the front end (AB=0, AE_2 =0)
- for the extended barrel close to the back end (AB=0, AE_1 =0).

The results for the barrel support region are shown in Figure 4-56. The inner radius plate is now in tension in the region below the saddle and the tension force at the outer radius has approximately doubled and will be resisted using the support belt added to the structure.

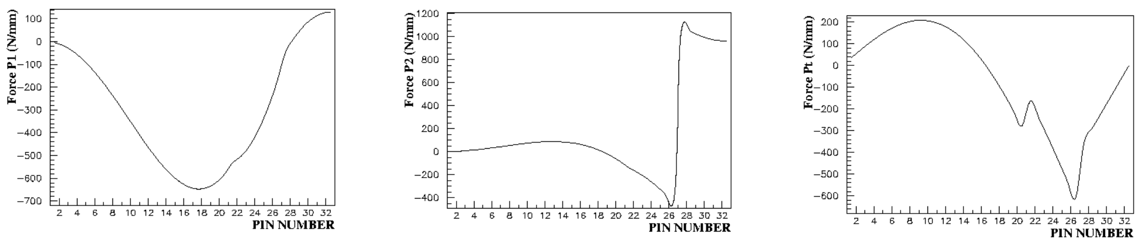

Figure 4-56 Inner radius, outer radius and normal forces for the Tile Calorimeter plus barrel cryostat calorimeter loads.

The analysis for the front and back support of the extended barrel are shown in Figure 4-57 and Figure 4-58. For these cases, the bearing loads at the inner radius have increased by a factor between two and three over the load from the Tile Calorimeter alone. A simple solution is to increase the bearing surface by allowing some of this load to be carried by the master plates (see Section 4.2.4.4). We are also considering ways in which the end-plate design and coupling may be modified to support part or all of this additional load.

In order to cross-check these results, we compared values of the forces P_1^{32}, P_2^{32}, and P_t^{32} calculated from the global equilibrium equations with values of the same forces obtained from the equilibrium of a supermodule composed of 32 modules. The results are identical.

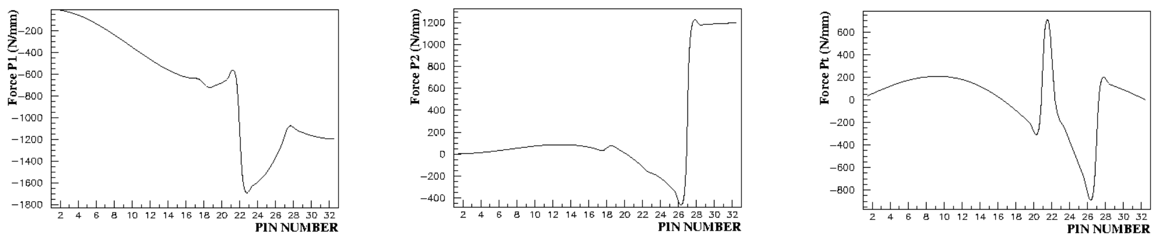

Figure 4-57 Inner radius, outer radius and normal forces for the Tile Calorimeters plus endcap cryostat calorimeter loads for front support.

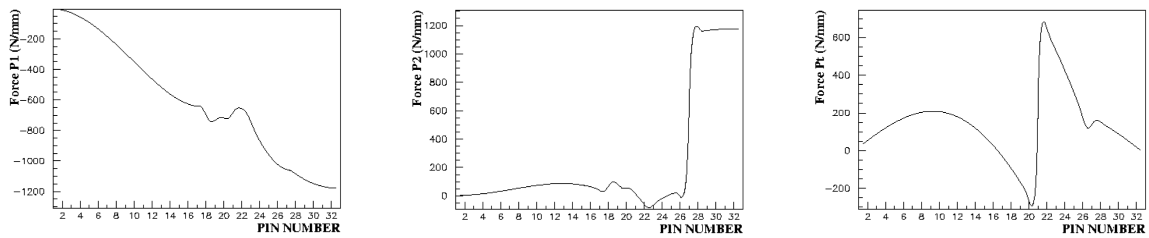

Figure 4-58 Inner radius, outer radius and normal forces for the Tile Calorimeter plus endcap cryostat calorimeter loads for back support.

We have cross-checked this analytical result using finite element modelling of the structure using the ANSYS program. A 2-dimensional finite element model of Tile Calorimeter was constructed in which the connections between neighbouring modules and between the support and the Tile Calorimeter were assumed in the same way as in the static analysis. There results are in excellent agreement.

The following conclusions can be drawn from the static analysis. In the central part of the barrel and in the whole extended barrel the forces at the inner radius cause compression of the modules. For the central parts the minimal value of P_1 is equal to -647 N/mm. In the front part of the extended barrel the minimal value of this force is 2.6 times larger in magnitude (Figure 4-57) and 1.8 time in the back part (Figure 4-58). In the end parts of the barrel the minimal value of compression is the same as for the central part, but at the bottom there is tension between modules caused by the AB calorimeter load (Figure 4-56). At the outer radius, the highest value of P_2 is at the bottom part of the Tile Calorimeter. For the central parts of the barrel and extended barrel the maximal values are the same and equal to 549 N/mm (Figure 4-55). In the end parts of the barrel a value of this force is 2.0 times bigger (Figure 4-56) and in the end regions of the extended barrel it is 2.2 times bigger (Figures 4-57 and 4-58). The minimal value of the shearing force between modules is equal to -330 N/mm in the central part of the barrel and the extended barrel (Figure 4-55). In the end parts of the barrel this force is 1.9 times smaller (Figure 4-56). In the front part of the extended barrel it is 2.7 times smaller (Figure 4-57). In the back part the extreme value is equal to 670 N/mm (Figure 4-58).

4.6.4 3-Dimensional finite element analysis of the extended barrel

A preliminary study using a 3-dimensional finite element modelling to compute the deformations and stresses in the calorimeter structure has also been carried out for the extended barrel calorimeter section. The additional loads from the endcap Liquid Argon Calorimeter have not been included for this initial study. In this analysis although a complete extended barrel was examined, only half of the extended barrel was actually modelled by applying symmetric boundary conditions at the six o'clock position. In addition, it was assumed that there was no contact across the top of the extended barrel at the 12 o'clock position. As was the case for the static analysis described earlier it was assumed that the modules were connected by a bearing force at the front-plate and a bearing and radial force at the outer radius. A further assumption was that the extended barrel was supported only at z=0 and z=2.6 m (modules 22 through 27 in the "pin" numbering scheme used above.) To mimic the support saddle, the extended barrel was restrained from movement at these locations (in the vertical, horizontal directions as well as from rotation in the x, y, and z directions).

The model assumptions and conditions used for the finite element model are:

- 3-dimensional model of both extended barrel and support
- full extended barrel modelled - open at 12 o'clock position
- sub-modules modelled using solid elements
- front-plate modelled using plate elements
- girder modelled using plate elements
- girder to sub-module connection using 1 mm bolts
- bearing force at the front-plate was modelled using gap elements
- the connection along the back-plate was modelled using plate elements which spanned the 0.5 mm gap between modules and was connected to the girder with beam elements which modelled the connecting bolts

It should be noted that the sub-modules were modelled using solid elements since the problem became too large when individual master and spacer plates were modelled.

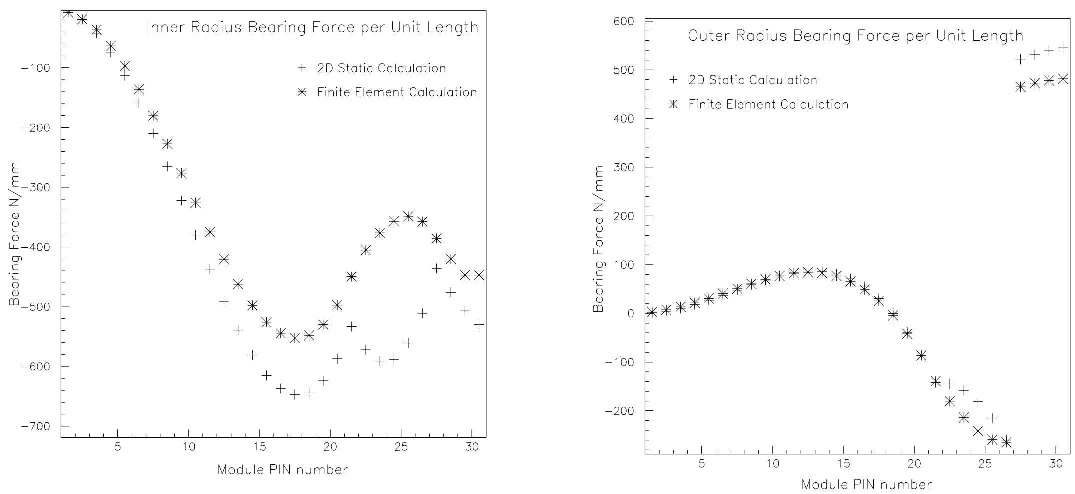

Figure 4-59 Inner and outer radius forces obtained from finite element analysis, compared with those of a 2-dimensional statics calculation.

The distribution of the bearing forces at the inner and outer radius are shown in Figure 4-59, where they are compared with the results from the static calculation of Section 4.6.3 above. The bearing load at the inner radius is in compression throughout the extended barrel. The maximum compressive force at the inner radius is 141 metric tons. The connection at the outer radius is initially in tension but become compression at the area in which the extended barrel is supported. The maximum tensile force at the outer radius occur below the area of support and is 96 metric tons. The results of the two analyses compare very well for both the bearing and radial forces at the outer radius. The radial shearing loads are also in good agreement. Differences arise between the analyses in the region of the saddle. This is due simply to the different methods used for modelling the saddle. The comparison of the bearing force at the inner radius shows that the analysis are also very similar, the small differences can be attributed to the fact that the 3-dimensional analysis takes into account the stiffness of the modules and deflections whereas the static analysis is based upon infinitely rigid modules.

4.6.5 Optimization of the support saddle

A preliminary finite element analysis of the support saddle has been carried so to establish its general features. The model conditions and assumptions were:

- support saddle modelled using plate elements as shown in Figure 4-60,
- support modelled using thick plate elements,
- radial connection between support and extended barrel at each module using six 25 mm bolts (the size of these bolts has subsequently been increased to 36 mm),
- shear connection between support and extended barrel at the 27th module,
- each support is restrained only in the vertical direction at the rail.

In addition, the 3-D finite element model of the calorimeter itself was used to model the applied load.

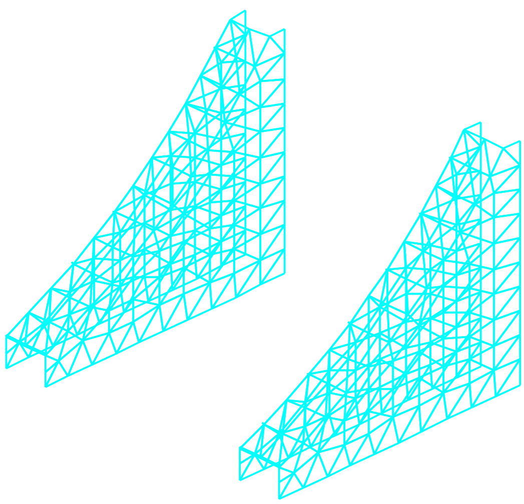

Figure 4-60 Finite element mesh used to model support saddle.

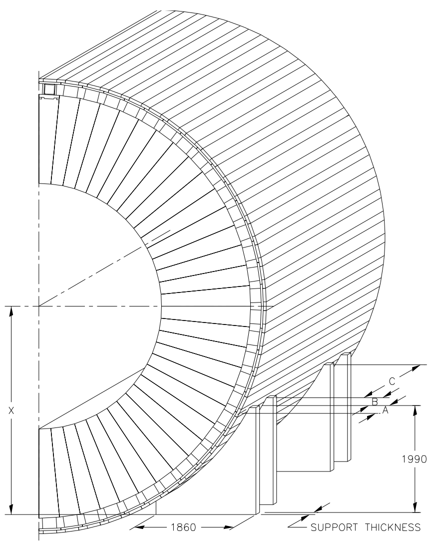

Figure 4-61 Saddle parameters varied in finite element analysis of supports.

The connection between the extended barrel and the support saddle consists of the shear connection at the bottom of the saddle and six bolts which could only carry radial force along the length of each saddle for a total of 24 bolts. Nine different cases were examined in which the thickness of the saddle, its width, location along the length of the extended barrel, and the height of the rail support were all varied as indicated schematically in Figure 4-61. The thickness of the saddle support was varied from 25 mm to 75 mm, the separation between support on the same saddle from 147 to 294 mm, the location of the first support on the saddle from the inner edge to the outer edge of the first saddle, the distance between supports from approximately 150 cm to 235 cm and the vertical location of the support relative to the rail by approximately 40 cm. In addition, to verify that the lateral load on the rail was small, one case was run in which the supports were restrained from lateral movement. For this coarse approximation of the support saddle geometry, the maximum stresses in the saddle itself range from 70 to 120 N/mm^2 for the nine cases considered.

Figure 4-62 shows the variation of the bearing force at the inner radius for the nine cases. The pattern of forces does not change significantly as the parameters of the support saddle are varied. A similar conclusion is obtained for the load distribution at the outer radius as well as for the radial loads. However, it should be noted that the forces shown are total forces which are summed along the length of the modules. When the variation of these forces along the length of the module are examined significant difference arise.

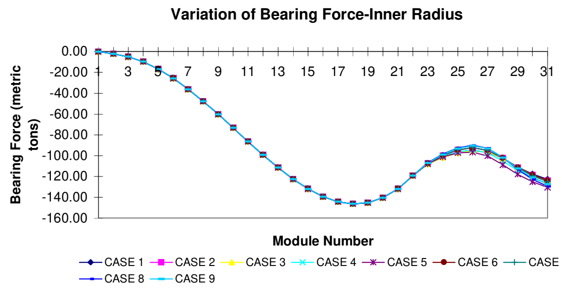

Figure 4-62 Inner radius bearing loads from 3-dimensional finite element analysis of the calorimeter structure alone for nine support cases as described in the text.

Figure 4-63 shows the variation of the bearing forces at the inner and outer radius along z at the interface between modules 27 and 28 for two cases. In case 1 the saddle is located 293 mm from the end of the extended barrel while in case 2 the saddle is located at the very end of the extended barrel. In both cases, the support is the width of one sub-module. The x-axis indicates the nodes in the analysis. These are at every module boundary and at the ends in the analysis of the inner radius force and include nodes at the center of every sub-module in the case of the outer radius analysis. The very high concentrated forces which occur at the location of the support indicate that examining the total or average force at each interface alone will not result in an accurate understanding of the forces which must be carried. This work is continuing, with further analysis being conducted in which the load of the cryostat will be applied. Since the cryostat load in the extended barrel is concentrated at the ends with the back end of the extended barrel carrying nearly twice the load of the front end, a concentration of the forces described above is expected. The location of the saddle and its width will be optimized to reduce the high peak forces along the interfaces between modules.

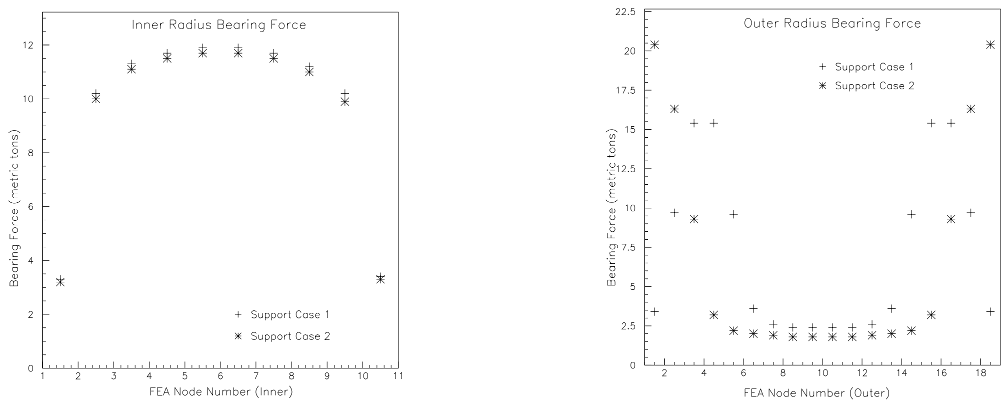

Figure 4-63 Variation in bearing forces at inner and outer radius as a function of support saddle: case 1, saddle on first and last sub-module; case 2, saddle on second and eight sub-module. In both cases the saddle covers the full width of one sub-module. The x-axis is the FEA node as described in the text.

Our preliminary conclusions, using this rather coarse model of the saddle, is that the support should be as wide as possible and the saddle plates should have a thickness of 50 mm. There is no indication of any significant transverse load being applied to the ATLAS main rail system. The placement of the saddle, however, can strongly affect the localised forces in the calorimeter structure and requires further study using a more accurate model of the Tile and Liquid Argon support. With the demonstrated agreement between the static and finite element calculations, we are now equipped with the tools to optimize the design of these supports, a task to be done in 1997.

4.6.6 Calorimeter deflection envelope

We have used the 3-dimensional finite element model to make a preliminary study of the effect of the support saddle on the deformation of the calorimeter structure. Figure 4-64 shows the deflection of the center of the inner radius of the extended barrel alone. The maximum horizontal displacement occurs at the top of the extended barrel and it corresponds to about 1.2 mm. This deflection decreases to zero at module 10 and then reverses direction to a maximum of 1.1 mm just above the area of support. The change in direction of the horizontal deflection is due to the "egg-shelling" of the extended barrel. Similarly, the maximum vertical deflection is -2.9 mm at the top of the barrel. No significant dependence on the design of the support saddle is observed within the range of the investigated parameters.

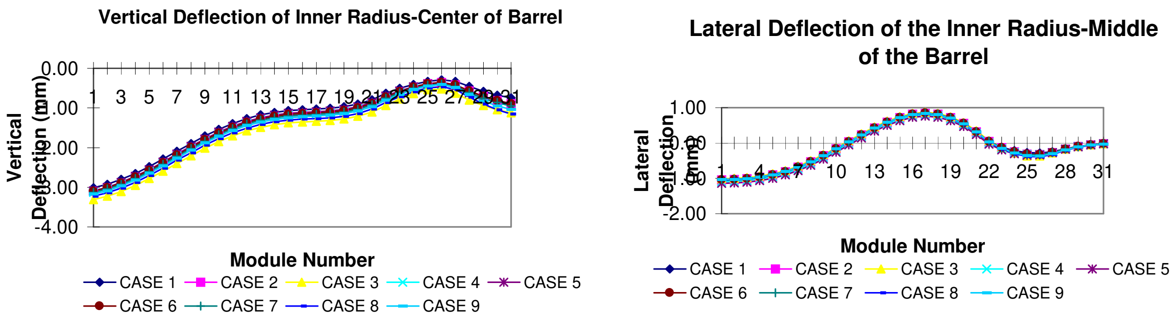

Figure 4-64 3-D FEA calculations of lateral and vertical displacement at the center of the extended barrel.

A 2-dimensional finite element model has been used to obtain a preliminary evaluation of the additional deflections of the calorimeter structure when the load from the Liquid Argon cryostats is applied to the barrel and to the extended barrel calorimeters. We describe first the situation in which there is only the load from the Tile Calorimeter itself. In this case, the final shape of the structure is similar to an "egg-shell" with the vertical diameter reduced by 4.0 mm and the horizontal diameter increased by 4.2 mm. The geometric center of this shape is displaced downwards by 3.5 mm relative to the undeformed center. The additional loads from the barrel and endcap Liquid Argon Calorimeters can be expected to increase this deformation. We have established an upper limit on the deformation caused by them using a 2-D finite element model of the structure in the immediate vicinity of these loads (Table 4-1). There are three cases: the end of the barrel calorimeter (both sides being identical); the outer region of the extended barrel; the inner region of the extended barrel. At the end of the barrel, the vertical diameter is reduced by 8.8 mm, the horizontal diameter increased by 10.6 mm and the geometric center displaced downwards by 2.0 mm. At the inner region of the extended barrel, the vertical diameter is reduced by 5.7 mm, the horizontal diameter increased by 5.4 mm and the geometric center displaced downwards by 1.0 mm. Finally, at the outer end of the extended barrel, the vertical diameter is reduced by 0.5 mm, the horizontal diameter increased by -3.2mm and the geometric center displaced downwards by 5.3 mm. It is clear from this preliminary analysis that the support of the Liquid Argon Calorimeters has a significant effect on the Tile Calorimeter envelope. A detailed analysis of the design using 3-dimensional finite element modelling is to be carried out in 1997 with the goal to optimize the design of the supports and of the calorimeter connections where necessary. Within this analysis, we shall also study the option of modifying shim sizes during calorimeter assembly to minimise the deformation in the structure. Finally, the design of the calorimeter support system does not at present include any jacking system to establish the final height of the calorimeter relative to the beam line. This will also be considered in the work being done in 1997 using the results from finite element modelling to specify the stroke required for such a system.

Table 4-1 Results of finite element calculation of the expected deformation after assembly.

	End Region of Barrel (Inc. Liquid Argon load)	Front region of extended barrel (Inc. Liquid Argon load)	Back region of extended barrel (Inc. Liquid Argon load)	Tile Calorimeter load only- at the center of barrel
Reduction in vertical diameter (mm)	8.8	5.7	0.5	4.0
Increase in horizontal diameter (mm)	10.6	5.4	-3.2	4.2
Downwards displacement of geometric center (mm)	2.0	1.0	5.3	3.5

4.6.7 Calorimeter load analysis during assembly

This aspect of the Tile Calorimeter design is at present under consideration, a prerequisite being a reliable finite element model of the structure and a detailed understand of the supports for the Liquid Argon cryostats. An initial study has been used to assess the stress and deflections in three specific configurations: half barrel; half barrel plus Liquid Argon calorimeter load; fully assembled calorimeter (Tile Calorimeter plus Liquid Argon). No serious problems were identified. A detailed analysis of this using finite element techniques is included in the lists of tasks for 1997.

4.7 Barrel-extended barrel region

Since the region between the barrel and the extended barrel is filled with services for other ATLAS sub-systems it is necessary to instrument it as much as possible with active calorimeter. We discuss the design and integration of this additional calorimeter (“the plug”) below.

4.7.1 Intermediate Tile Calorimeter design and integration

As can be seen in Figure 4-65 the region between the barrel and extended barrel calorimeters is an extremely difficult region to engineer, as it requires the integration of services, supports and mechanical components associated with several ATLAS detector sub-systems. The main interferences, as seen by the Tile Calorimeter, comes from the electronics boxes and feeds through chimneys of the Liquid Argon Calorimeter. These determine the geometrical shape and size of

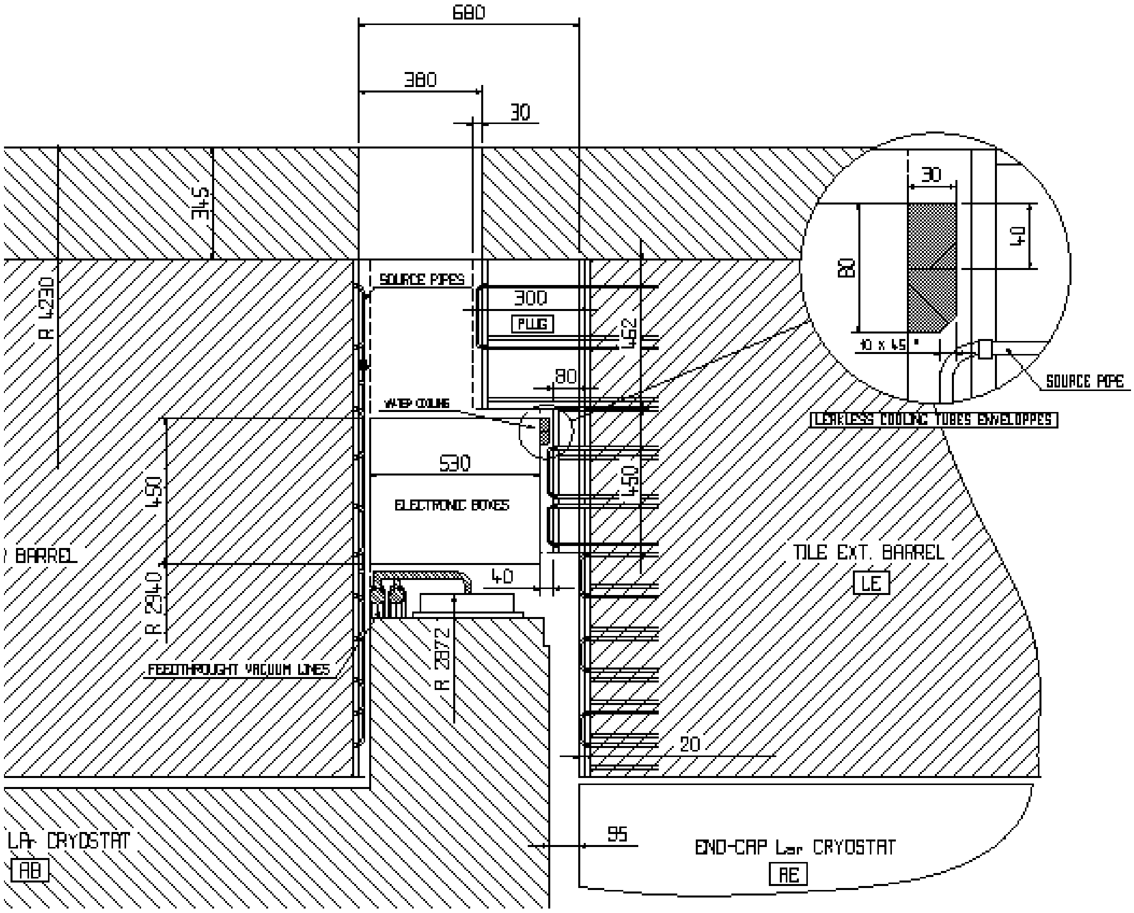

Figure 4-65 Details of the gap region, where the plug and the scintillator layers are installed.

the gap-filler sub-module (ITC). The design therefore includes a 780 mm gap between the barrel and the extended barrel modules to provide room for these services and components.

For particles which originate at the nominal interaction point, the proposed ITC extends over approximately $0.8<|\eta|<1.6$. The region 0.8-0.9 consists of a 311 mm thick steel-scintillator stack, similar in design to the standard Tile Calorimeter sub-modules. Between 0.9-1.0, the stack is 96 mm wide. The combined 0.8-1.0 region of the ITC is also called the plug. At higher η's, 1.0-1.6, the ITC consists of scintillator only due to severe space constraints. The scintillators between 1.0-1.2 are called gap scintillators, while those between 1.2-1.6 are called crack scintillators. A side view of the ITC is shown in Figure 4-7.

The 15 mm end-plate provides the backbone for the ITC. The plug is welded to the end-plate at the inner and outer radii through bars. The end-plate is welded to the sub-modules through the strap at the inner radius. The entire plug end-plate assembly is attached to the girder through 6 bolts. The gap scintillators are attached to the end-plate directly with small posts. They will be made light tight with an aluminium cover, also attached to the end-plate.

A significant mechanical issue is the allocation of space to route the fibres from the scintillator sections to their phototubes and electronics. Intrinsic to this is the use of an optical connector. One option is to simply increase the ϕ gap in a region of the sub-module. A second option being studied is the use of a 20 mm special fibre channel along the edges of a master plate in the plug. The master plate will be cut back in phi to accommodate this channel and the channel fastened to the plate end prior to stacking. The weld bar at the outer radius must also be notched to allow for fibre routing. This scheme is capable of providing a large number of fibres for the ITC scintillators if needed to increase the light yield. It requires modification to the standard plan for plug sub-module assembly and fibre routing but offers considerable flexibility in the number and routing of the read-out fibres. Two ITC sub-modules have to be fabricated for use with the extended barrel prototypes being built for testing in the 1997 testbeam.

4.7.2 Installation scheme

The plug end-plate is attached to the girder using a procedure similar to that for standard sub-modules. Therefore, the plug will be in place when the modules are installed in the collision hall. No ϕ shims will be used for the plug in order to avoid large stresses - they will independently be supported by the girders.

The scintillator sections will be installed last. They will be removable for service and replacement in the event of radiation damage. They will be supported by the end-plate. Fibre ribbon connectors will be used to transport the optical signal.

4.8 Calorimeter alignment

At the present time, only a conceptual analysis of the calorimeter alignment based on past collider experience has been developed. Distance scales and shower characteristics in a hadron calorimeter are such that the alignment specification is primarily defined by mechanical constraints. From the point of view of reconstruction of the four-momentum of a hadron jet, knowledge at the few mm level is sufficient at all levels of data processing until the final constrained fit reconstruction of a higgs decay into two or four jets. This sets the scale for the placement of the hadron calorimeter radially and longitudinally to of order 2 mm. This matches well with the mechanical tolerances on module length and on the expected structural deformation. The placement should be known by surveying each module to an accuracy of approximately 0.5 mm in the detector reference system, which is the likely realisable precision of the system envisaged (photographic surveying). Targets will be fastened to modules during fabrication for this purpose and will be used additionally during module assembly for calculation of the shim thickness to be used as modules are stacked.

The general specification of global alignment holds for each calorimeter section independently. Therefore, there is no additional constraint on the relative alignment of barrel and extended barrel calorimeters.

The Tile Calorimeter forms the basic support structure for all components mounted inward toward the interaction point (including the Liquid Argon Calorimeters and the inner tracker, both of which have as yet to fully specify the range of their mounting and alignments schemes). In addition, analysis of the deformation envelope of the Tile Calorimeter is coupled to the actual support of these detectors (in particular of the Liquid Argon Calorimeter) and finite element modelling of this is in a preliminary stage. It may be necessary to assess the Tile Calorimeter alignment specification and implementation with respect to these external forces, and therefore detailed discussion of this important issue with justification for the specification and a realisable implementation for the survey scheme will be presented in the ATLAS Integration TDR.

4.9 Magnetic field analysis

The Tile Calorimeter provides the magnetic flux return for the ATLAS solenoid and in addition is subjected to residual fields from the muon toroids. These fields may have a significant effect on the design of the detector. Firstly, the read-out electronics must be enclosed within the calorimeter structure in a region well shielded from these fields. In addition, the scintillator response itself is sensitive to magnetic fields and we must also consider the effect of these fields within the body of the calorimeter and the implications for the calibration. Finally, the magnetic forces between the barrel and the two extended barrel calorimeters may be significant and must be evaluated to establish a safe engineering design. Extensive calculations have been carried out to compute the magnetic field distribution([N-38],[N-50],[N-54],[N-58]). These are discussed below with some of the implications for the design.

4.9.1 Field strength distribution

The field source consists of a central solenoid and three sets of eight superconducting air-core

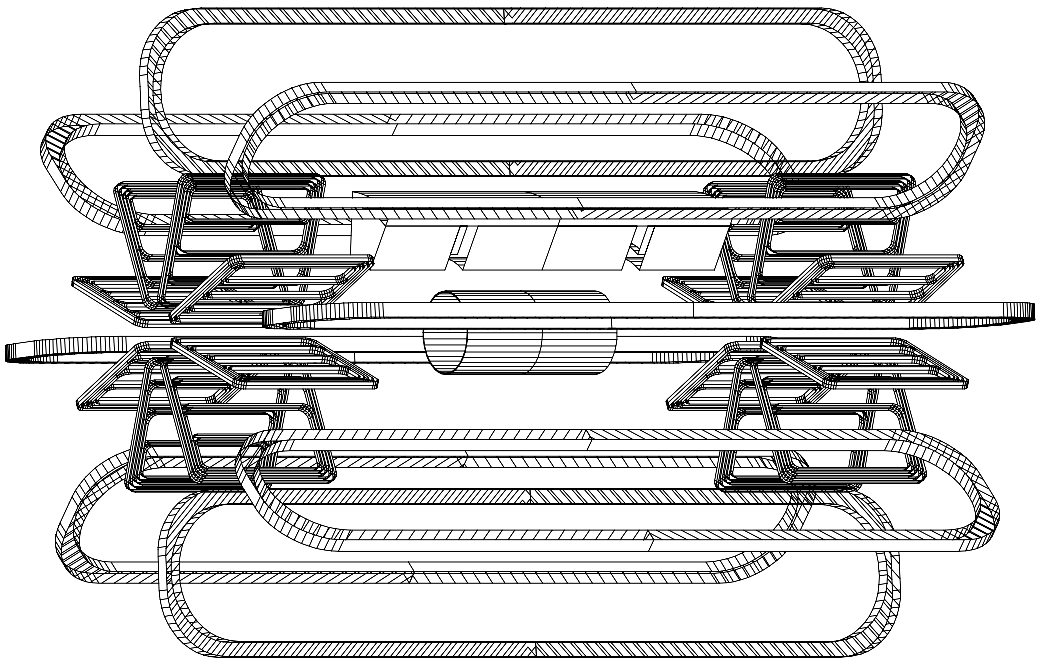

Figure 4-66 ATLAS magnetic system structure.

toroid coils as shown in Figure 4-66. There, one can also see the separate sections comprising the Tile Calorimeter iron, subdivided into the central barrel and two extended barrels. Each section consists of a set of sub-modules with the structure described in Section 4.2. The key elements of the sub-module structure, which are relevant for the magnetic field analysis are the front-plate, the laminated absorber structure (master and spacer plates) and the girder.

VF electromagnetic software OPERA-TOSCA and CERN POISCR codes were used for the field analysis of the magnetic field distribution in the Tile Calorimeter. Along with realistic 3-dimensional presentation of the magnetic system, simplified models have been employed to give an idea of the distribution of magnetic flux lines distribution. As an example of this approach the magnetic flux lines, passing through the Tile Calorimeter iron, are shown in Figure 4-67. This map was obtained using the 2D computer model of the system. Due to the configuration symmetry, only a minimal part of the system is shown there. One can see the extended barrel, plug and part of the barrel in the upper region of the Figure. Below, a quarter of solenoid is also shown. The center of coordinates coincides with the Interaction Point (IP).

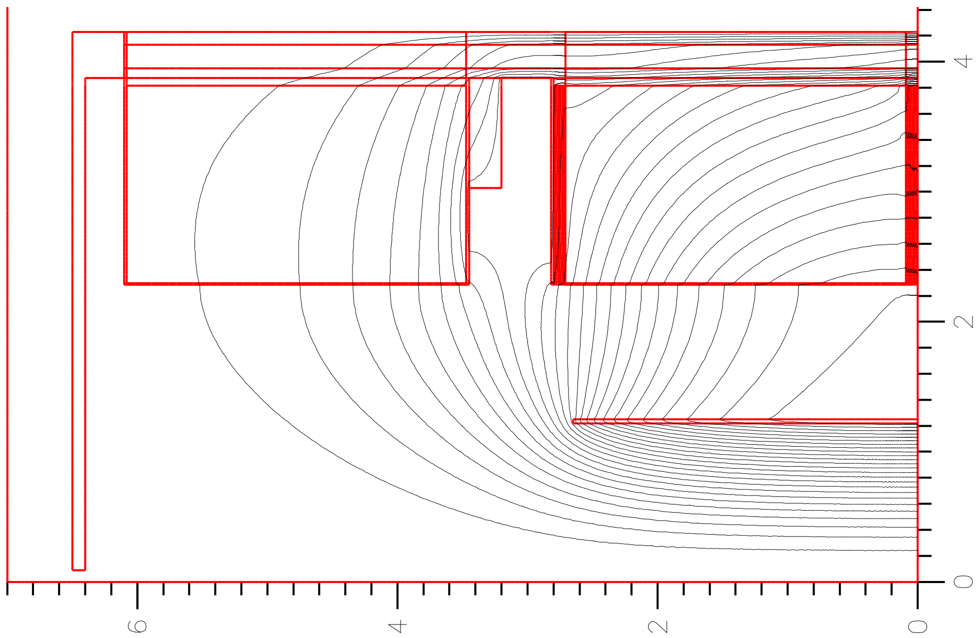

Figure 4-67 Magnetic field: flux lines map.

According to the computer simulation, the return flux of the solenoid mainly passes through the Tile Calorimeter support structure (>50% at the center). It was also found that the highest field regions are located at the edges of the barrel and of the extended barrel, with a maximum at the girder radius. However, the maximum induction in the scintillator does not exceed 10 mT. The field in the region of the photomultiplier tubes does not exceed 20 Gauss.

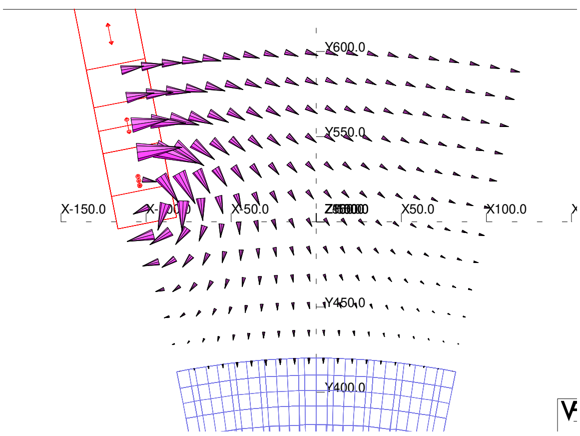

Figure 4-68 Field map in the region between the Tile Calorimeter and the barrel toroid.

The field pattern in the interface region between the Tile Calorimeter and the Barrel Toroid is shown in Figure 4-68. The Barrel Toroid coil is seen at the left upper part of the Figure. The Tile Calorimeter is depicted in the bottom part. Due to the symmetry of the structure only a minimal part of the geometry is given. The length of the arrows represents the induction value at the observation points. A detailed stray field calculation, based on the 3D model, gives a maximum field value of approximately 0.4 T near to the girder surface.

The field component distributions in the plane normal to the barrel axis are shown in Figure 4-69. A 3D computer model was used to produce these maps, in which the finite element method

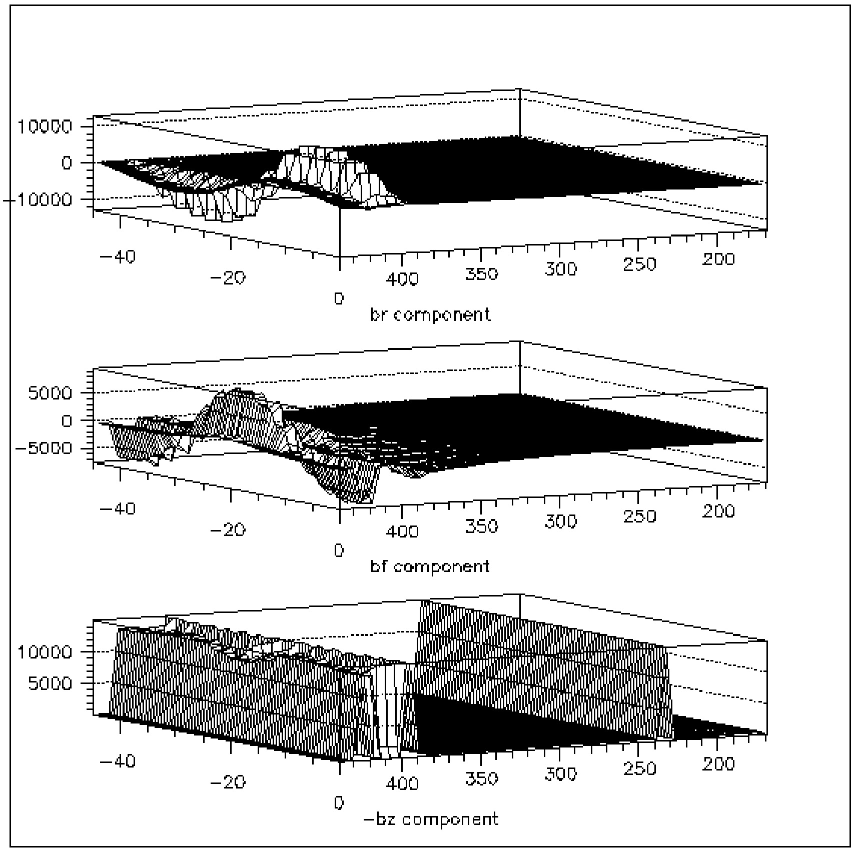

Figure 4-69 Field components (Gauss) in the plane normal to the barrel axis (Z=32cm) in the radial range 200-400 cm and the azimuthal range -45^{o} < ϕ < 0^{o}.

was employed for the interpolation procedure. This simulation confirmed previous estimations of the magnetic field values in PMTs and scintillators.

Some additional results from the simplified Tile Calorimeter magnetic field calculations were also obtained. This way the effects of glue gaps, end-plates, front-plates, laminated layer near girder, 2 mm iron layers between tiles have been estimated.

4.9.2 Coupling forces between barrel and extended barrel

In contrast to the local magnetic field estimation in the scintillators and at PMTs positions, the ponderomotive force is a global quantity of the solution. For its calculation an overall Tile Calorimeter field map is needed. To this purpose a computer model with a continuous anisotropic iron with an appropriate stacking factor inside an active zone of the Tile Calorimeter was employed (“easy axis” direction along the radial coordinate). The anisotropy property of the model is connected with the lamination direction of the tile structure, normal to the Tile Calorimeter axis.The Tile Calorimeter lamination structure with staggered pockets within the laminations is not a pure classical lamination which is a set of parallel thin iron plates with small air gaps between them. Nevertheless, introduction of this anisotropy property into the model provides some approximation of the real tile structure. The calculation of the forces acting on the extended barrel (excluding the girder) gives a radial force of 1.1 ton/radian, directed to the Tile Calorimeter axis, and an axial force of 1.3 ton/radian, directed towards the central plane normal to the detector axis. The radial magnetic force represents only 2% of the weight of the corresponding extended barrel sector and therefore adds only a minimal additional load to the design criteria.

Although the axial force component in the barrel vanishes because of the symmetrical configuration, any misalignment will cause a net axial force. To obtain an order of magnitude for this force, one can make an estimate for half of the barrel only. Calculations show that a radial force of 5.9 ton/radian is directed towards the Tile Calorimeter axis, and an axial force of 4.9 ton/radian is directed towards the central plane, normal to the detector axis. Again these forces are small compared to the gravitational load of the absorber structure itself.

4.10 Production plan & schedule

The mechanical design and the construction method for the barrel and for the extended barrel calorimeters have been worked out using a combined engineering effort from all the institutions involved. The focus of this effort has been the development of a production plan which would allow the distribution of the assembly of sub-modules and modules amongst the participating institutions to obtain the lowest effective production cost. This also took into account the existing infrastructures and the differences between the various geographical situations. An important advantage in this effort is that in our design we may unfold completely the mechanical work from the subsequent optical and electronic instrumentation.

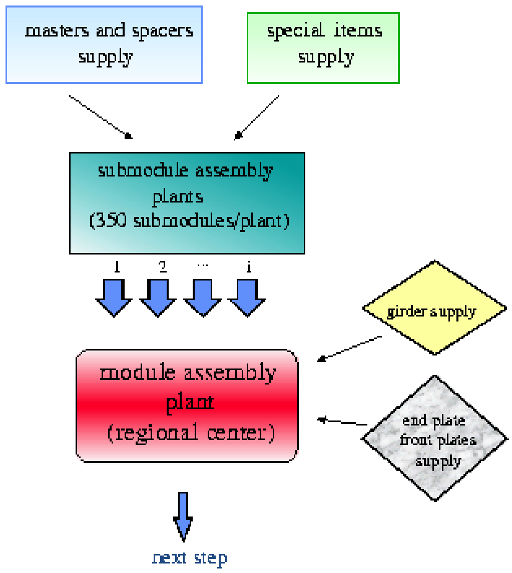

Figure 4-70 Concept of regional centres and sub-module assembly plants.

Three major pieces of equipment have to be constructed; a barrel and two extended barrels. From the outset, one constraint on the design has been the ability to construct all modular parts outside CERN and to bring to CERN finished and well-tested modules. Therefore the concept of three regional centres came about naturally, each one with the task of constructing the modules of one entire cylinder. These three centres must be capable of handling the weight of the assembled modules as well as the space to provide storage for a large part of the production. For the barrel section, the choice has been JINR in Dubna, where key equipment and facilities already exist to handle and store 20 tons objects. This laboratory also has all the necessary support in technical and engineering manpower to accomplish this task. From there, the assembled modules may be transported to CERN either by road or by rail. For the extended barrels, one center will be in the USA, at Argonne National Laboratory, which allows the effort of several universities to be focused effectively. As is the case for JINR Dubna, all necessary resources required for module handling and storage exist there and they have extensive experience in the construction of large detector systems (e.g. CDF and ZEUS calorimeters). In particular, they have experience with overseas transportation of ZEUS calorimeter module and do not therefore anticipate any problems with the transportation of extended barrel modules (weighing 10 tons) to CERN. The second extended barrel regional center is in Spain (IFAE Barcelona), where a dedicated laboratory with all necessary infrastructure is now being built. From there the transportation to CERN is not a particular issue (road or rail are both feasible).

Around these three regional centres we will have several sub-module assembly plants, equipped with the necessary sub-module assembly tooling and ready to construct and provide about 350 sub-modules to the regional centres over a period of three years. This job is suited to university laboratories, equipped with a crane up to 1.5 tons and able to provide space for the necessary equipment and for intermediate storage of about 40 sub-modules. In these laboratories, three technicians will be involved in the manufacturing. Nine such centres have been already identified, and eight of them have already participated in the Module 0 construction phase. Further details about this are discussed in the resource and planning chapter.

The procurement and the preparation of the base material (for example the spacer and master plates) are to be done in a similar way. The steel will be procured centrally and distributed for the cutting and surface preparation to the regional centres. These will then supply the sub-module assembly plants. Three laboratories will be responsible for the procurement of the girders, and a few other laboratories will provide small items, to be centrally distributed, where for economical reason one single production is most cost effective.

The final assembly and installation in the ATLAS cavern will be a common effort between all participating institutions.

4.10.1 Module 0 prototypes

Starting at the end of 1995 we have initiated a pre-production prototype program. A full size prototype of a barrel module has been constructed and two full size modules of the extended barrel will be built in the spring of 1997. Procurement and assembly have been performed in the spirit of testing the construction techniques proposed for mass production, while at the same time allowing some experience with the distributed construction environment. Eight of the nine foreseen sub-module plants have been involved, and six complete sets of assembly tools have been constructed. Each module is assembled in one of the regional centres. The barrel Module 0 was constructed at JINR in Dubna; much experience has already been gained and a first iteration of optimization has been carried out for the extended barrel prototype production. For some of the procured items a market survey was executed, and a few candidate producers were tested.

The mechanics chapter of the TDR is heavily based on this work. The final specifications for all items will be based on it.

4.10.2 Production schedule

The overall schedule is driven by the requirement that the detector be ready for installation in the ATLAS pit by the beginning of 2003. By that date, one out of eight modules will have to be calibrated at the SPS. The year 2002 will be dedicated to the preassembly on the surface, in a special hall at CERN. This will be an essential part of the assembly procedure and the entire year 2002 will be dedicated to this task. This step requires, therefore, that the modules be ready and fully instrumented by the beginning of 2002.

For the purely mechanical part of the construction this leaves a time span between 1997 and 2000 for the mass production of 65 modules for each of the two extended barrels and of 65 modules for the barrel (including the time for the transport to CERN).

Once the Module 0 phase is completed, in the summer 1997, the initial phase of the procurement must begin. The plan is to be able to cut and start delivery to the sub-module assembly plants in the second quarter of 1998. Production of sub-modules will cover three years up to the end of year 2000. In parallel, module assembly will start in 1999 and it will end in the middle of 2001. Girder production will have to begin delivery in the early 1999, after all preparation phases are over. The same is valid for the end-plates, front-plates and calibration tube procurement. All materials for the final installation, such as support structure and calorimeter assembly fixtures will be procured in the year 2000.

The year 1997 will be dedicated to write all technical specifications for the various components and to initiate the tendering process for the major items, e.g. the 3100 tons of laminated steel. The experience made with the prototype construction showed that this phase is potentially more time consuming, and we are therefore allowing some additional time for it to be completed. Delivery of the first batches of steel to the cutting plants will take place between the end of 1997 and the beginning of 1998. The cutting of spacers, if done with the laser technique, could extend over the entire 1998 period.

Figure 4-71 summarizes the time schedule for all these construction phases.

4.10.3 Procurement plan

The procurement of items is done as much as possible in a distributed way, trying to minimize the transportation costs. Most of the final technical specifications will be written during 1997, and the tendering procedure will start right after that. Technical drawings and specifications will be as much as possible formulated in an uniform way and centrally maintained on the engineering database at CERN. The final responsibility of the execution of the orders and of the correct quality control and follow up of the procedure in the various countries will be distributed among the participating institutions involved in the procurement. For some large items, clusters of institutions will pool resources together:

- **laminated 5 mm steel for masters**: to minimize transportation cost and resources, two procurement sites are foreseen, one in continental Europe and one in the USA. The USA steel will be used for the two extended barrels and will have to be transported to Spain after cutting. The total quantity required for the barrel and both extended barrels amounts to 2086 tons, to assemble 65 modules allowing a 3% contingency. The steel for Module 0s has been already successfully procured.
- **laminated 4 mm steel for spacers**: one procurement site is foreseen in the Europe. The quarter of it needed in the USA will be shipped there after cutting. The total quantity required amounts to 849 tons for the barrel and both extended barrels, to assemble 65 modules allowing a 3% contingency. The steel for Module 0 has been already successfully procured.
- **master cutting**: the baseline technology is matrix punching. The master plates for both extended barrel calorimeters will be cut using the already existing matrix, constructed in the R&D phase, in the USA. For the barrel the cutting will take place in Russia. If possible the same matrix will be used, if not a second matrix will be constructed. Final R&D work in this direction will be finalised in 1997.
- **spacer cutting**: the baseline technology is laser cutting. This will be done in two different places, for the barrel in Russia and for the whole extended barrels in Spain. After cutting,

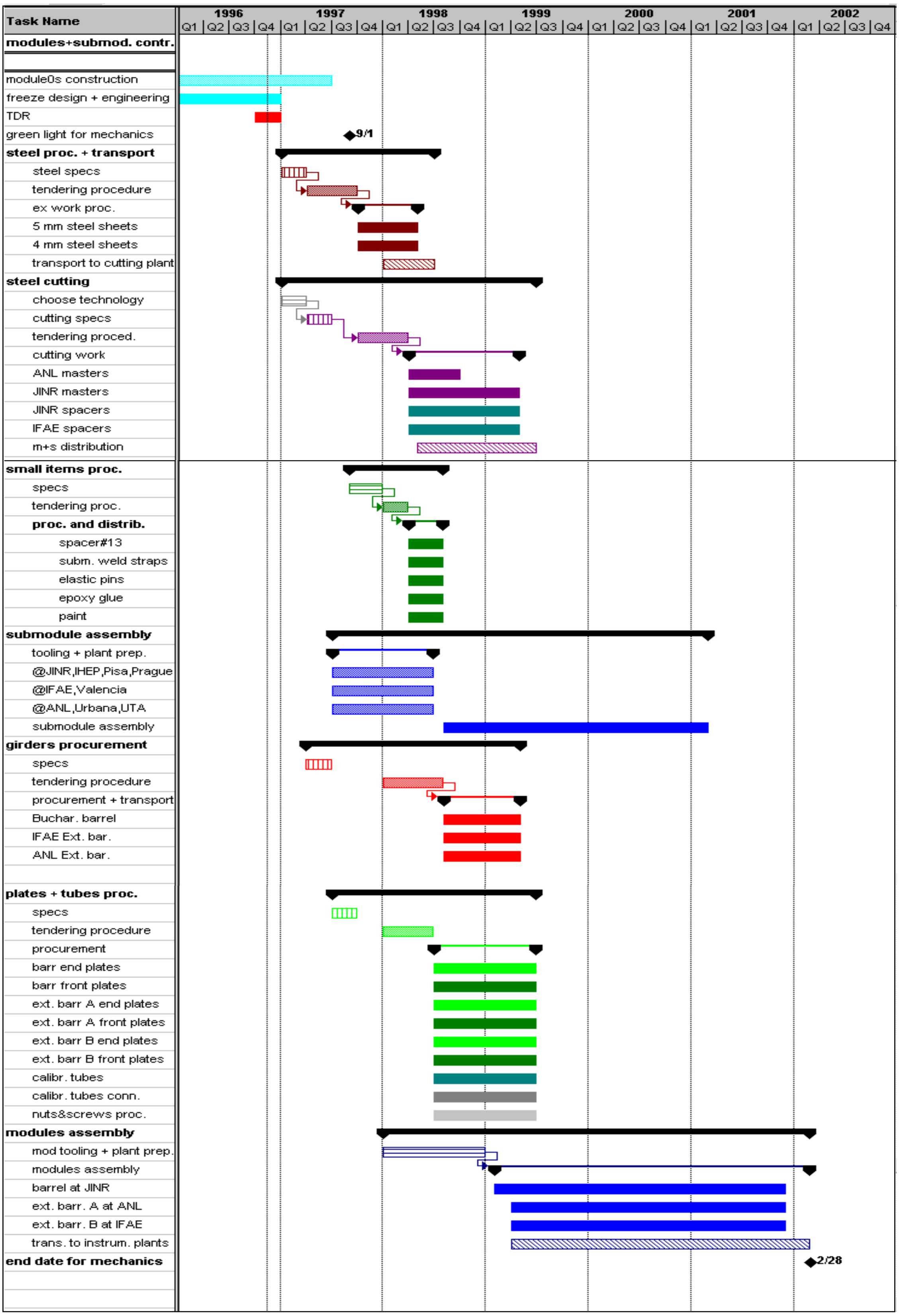

Figure 4-71 Schedule of the mechanical activities, for the construction of modules and sub-modules.

the spacer plates will be distributed to the sub-module assembly plants. In both places experience will have already been cumulated with the prototype and Module 0 work.

- **spacers #13 and elastic dowels**: fabrication of these small spacers requires custom tooling. They will be procured centrally and then distributed. The same is valid for the elastic dowels
- **connecting straps**: this item will be the responsibility of each sub-module assembly plant. These can be procured locally, the economical aspect will determine the choice.
- **structural adhesive and protection paint**: to optimize the cost two large orders will be placed, one for the USA and one for Europe. The material will then be distributed
- **girders**: these will be procured in three different locations, one for the barrel and one for each of the extended barrels. Good experience has been already obtained with the procurement for Module 0. In each location we will procure 65 girders. This will be an item where resources have to be pooled together by several institutions.
- **end and front-plates and bolts**: these will be procured in three locations, near to the regional centres. The quantity for each procurement will be for 65 modules.
- **calibration tubes and connector**: these will be procured centrally and distributed. The quantity of tubes is 16 km, cut in 4290 pieces.
- **module and sub-module assembly tooling**: this will be the responsibility of the institutions involved in the assembly. Once the Module 0 phase is over most of the tooling will already have been constructed and be operational.
- **drawers**: 540 drawers will be constructed in one location using the casting technique. The specific tooling was already developed for the Module 0.
- **girder rings**: 13000 girder ring, including the foam rings will be molded. This will be done centrally by one institution and then distributed, together with appropriate installation tool.
- **calorimeter supports and final assembly tooling**: these items will be centrally procured late in the year 2000, pooling together resources from several institutions. The final specifications will be done in the next two years. This includes the support saddles, the belt system, the rail system and the temporary support for the assembly of the lower part. The manipulation tools, including the turn-over device, needed for the final assembly, are constructed in the framework of the Module 0, because they are already needed at this stage.

The exact sharing of responsibilities between the Institutions is described in Chapter 11.

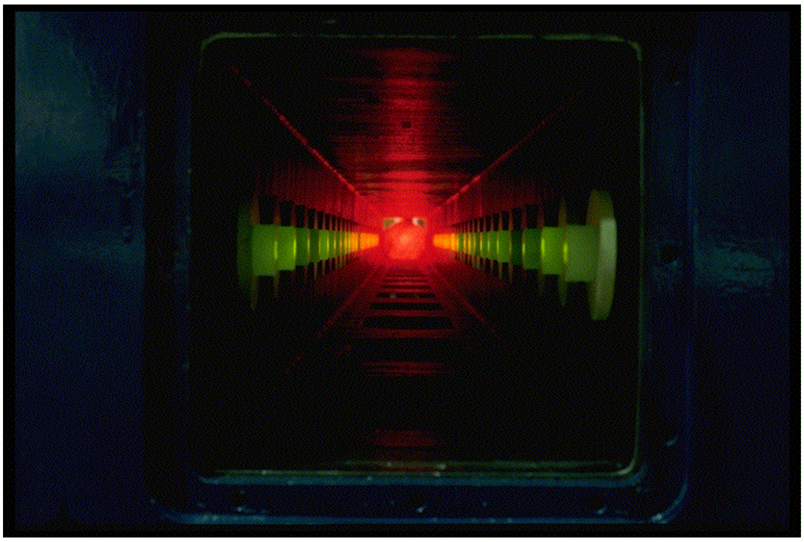

Figure 5-i A view of the fibre bundles from inside the girder.

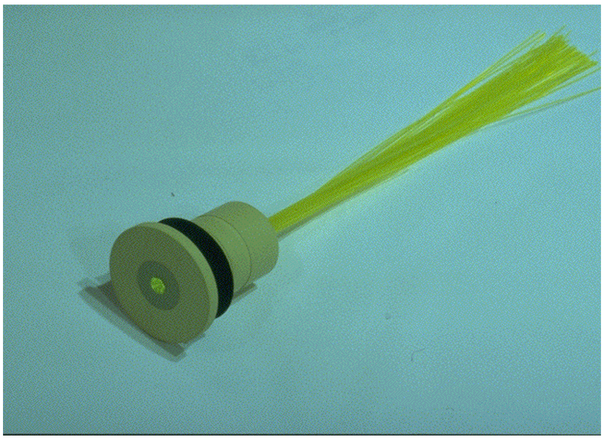

Figure 5-ii A fibre bundle with its girder ring.

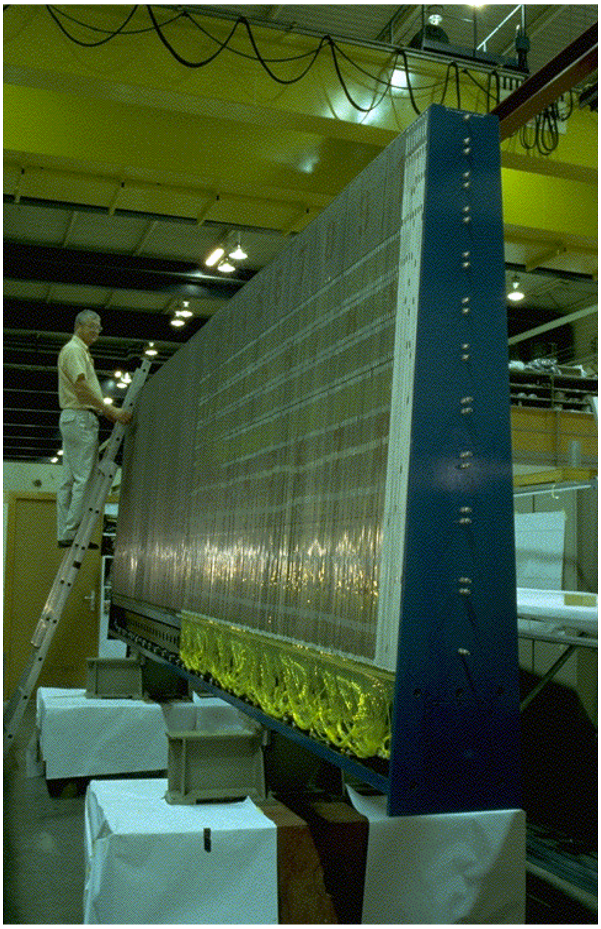

Figure 5-iii Barrel Module 0 following its instrumentation with scintillators and readout fibres.

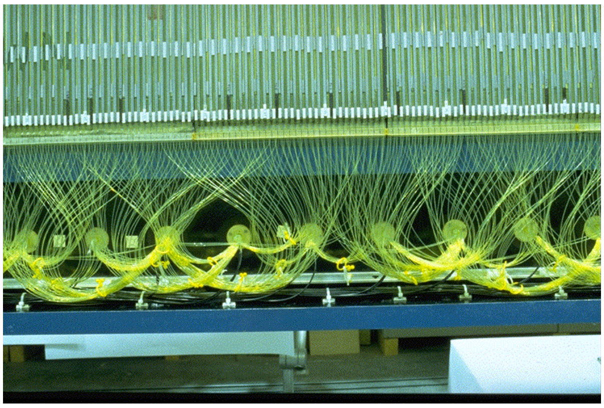

Figure 5-iv The routing of the fibres into the girder.

5 Optics

The Tile Calorimeter is a sampling calorimeter using steel as the passive absorber and scintillating tiles as the active medium. The unique feature of this hadron calorimeter is the orientation of the scintillating tiles relative to the direction of the particles from the interaction point. In this detector, as shown in Figure 5-1, the tiles point radially to the beam line. Eleven sets of tiles of radial sizes from 97 mm to 187 mm form the longitudinal segmentation of the detector. A pair of wavelength shifting (WLS) fibres running radially collect light from the tiles at both of their ϕ edges. Read-out cells are defined by grouping together a set of fibres onto a photomultiplier tube (PMT), to obtain three dimensional segmentation. At η=0 the radial depths correspond to approximately 1.4, 4.0 and 1.8 λ. The $\Delta\eta \times \Delta\phi$ segmentation formed by the module geometry and scintillator cell structure is 0.1×0.1, where η is the pseudorapidity and ϕ is the azimuthal angle in radians. In the last radial layer, which is a tail catcher, the segmentation is 0.2×0.1.

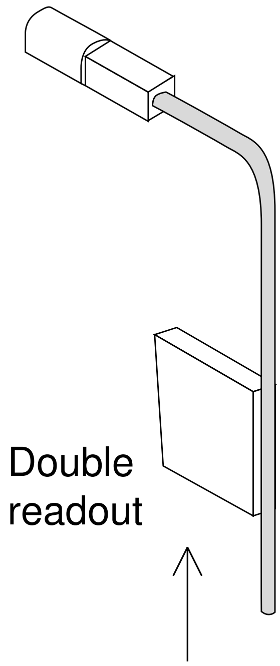

Figure 5-1 Main optical elements of the Tile Calorimeter. Tile, fibre, light mixer and PMT are shown (drawing not to scale). The arrow indicates the direction of the incoming particles (radial direction).

Ionizing particles crossing the tiles induce the production of light in the base material of the tiles, with wavelengths in the UV range which subsequently is converted to visible light by scintillator dyes. This scintillation light propagates through the tile to its edges, where it is absorbed by the WLS fibres and shifted to a longer wavelength (chosen to match the sensitive region of the PMT photocathode). A fraction of the light re-emitted in the fibre is captured and propagated via total internal reflection to the PMT where it is detected. A light mixer is placed between the fibres and the photocathode to optimize detection uniformity. The ends of the fibres away from the PMTs are aluminized.

The driving philosophy behind the optics is to achieve and maintain a uniform, minimum light yield so that the resolution of the detector is not compromised by a lack of photostatistics. A photoelectron yield of 0.5 photoelectron/mip at normal incidence/tile is enough to achieve the required energy resolution. This translates to about 20 pe/GeV, and was easily achieved in our first 1 m prototype modulesD-4. However, to ensure that the muon signal is visible within each radial depth, this number is a lower limit and a safety factor should be added. Calculations for similar calorimeters[A.36] show that with 1 pe/mip at normal incidence/tile the muon signal is visible within each cell, and that is confirmed by the results presented in Chapter 3. Non-uniformity throughout the detector should also be kept small so as not to impact the constant term of the resolution. Our baseline goal is an rms non-uniformity within a cell up to 10%, which was also achieved in the 1 m prototype modules.

No parameter can be tuned independently in the system to achieve our requirements. The light budget and uniformity are coupled to the amount of light a tile produces times the fraction of light a fibre can absorb and deliver to the phototubes. At this point, there is the additional effect of phototube quantum efficiency and photocathode uniformity. In this Chapter we will present our experience on these topics. In particular we will present the following:

scintillator characteristics and wrapping:
58.5 tons of injection molded scintillator will be produced. Expectations are that the tile response to charged particles across its area will yield a uniformity of 5%. This can be met by masking of the tiles with appropriate reflecting and absorbing materials. R&D is under way to determine the ageing characteristics of the scintillator and its light output, and the automation of masking and wrapping tiles;

studies of wavelength shifting fibres (WLS):
The choice of fibre manufacturer to provide 1120 km of WLS fibre will not be made until 1998. Studies of fibres from three manufacturers have been made on the parameters of light yield, attenuation length, UV light reduction, uniformity and short and long term stress tolerance. Test benches have been developed to generate quickly a quality control report based on some of these parameters;

fibre insersion:
Robotics are being investigated to insert fibres into the calorimeters. A mechanical plastic profile is discussed which will gather the fibres and couple them to the edges of the tiles. A fibre mass-aluminization process has been developed for production work;

fibre routing:
A design of fibre routing has been worked out and implemented in the barrel Module 0. This work will be followed up in the extended barrel Module 0's instrumentation in 1997;

treatement of fibre ends:
The fibre bundles cutting and polishing prototype tool is discussed. Further R&D will be done based on our experience with this tool to make several production devices;

results from barrel Module 0:
Experience with the implementation of these items on the barrel Module 0 will be discussed in the respective sections;

We now discuss each of these components in turn and address their specification, performance as measured using prototypes, fabrication and installation.

5.1 The scintillator system

The scintillating tiles are the active medium of the Tile Calorimeter. The cost per tile and production rate are important parameters in the choice of the tile materials and production technology. These issues have led us to the choice of injection molding technology for tile production for the Tile Calorimeter. Having selected this technology, it is important to determine the performance factors. Light yield, uniformity of response within a tile and tile-to-tile uniformity are key performance issues. A total of approximately 460,000 scintillating tiles will be required for the Tile Calorimeter, half in the barrel, one quarter in each of the extended barrel sections, and a small number in the ITC. Each of the calorimeter sections - barrel, extended barrel, and ITC - will be equipped with tiles of the same dimensions.

5.1.1 Design and specifications

5.1.1.1 Geometry and tolerances

The Tile Calorimeter contains 11 different sizes of trapezoidal shaped tiles, ranging from about 200 mm to 400 mm in ϕ length and 97 mm to 187 mm in radial width. The general tile geometry is shown in Figure 5-2. The wavelength shifting fibres are placed in contact with the non-parallel edges of the tiles. Table 5-1 lists the dimensions and weights of the 11 sizes of tiles required for the calorimeter. All tiles are 3 mm thick. Each tile has two holes, 9 mm in diameter, through the surface for the passage of the calibration source tubes.

The general tolerances in all the tile dimensions and holes are ±0.10 mm. These tolerances are required to allow an easy insertion of the tiles into the scintillator gaps, the insertion of the calibration tubes through the holes of the tiles and to insure good contact with the WLS fibres at the outer edges.

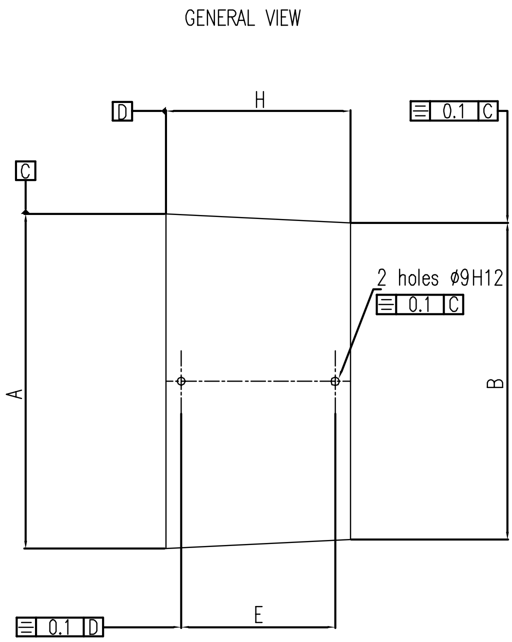

Figure 5-2 Drawing of a trapezoidal shaped tile.

Table 5-1 Tile dimensions and weights. The labelling of the dimensions is the one that is shown in the drawing of the tile in Figure 5-2.

tile #	A (mm)	B (mm)	H (mm)	E (mm)	weight (kg)
1	231	221.3	97	70	0.0698
2	240.8	231.3	97	70	0.0721
3	250.6	241	97	70	0.0751
4	262	249.5	127	100	0.1023
5	274.8	262.3	127	100	0.1074
6	287.5	275	127	100	0.1125
7	302.3	287.8	147	120	0.1366
8	317	302.6	147	120	0.1434
9	331.7	317.3	147	120	0.1503
10	350.4	332	187	160	0.2010
11	369	350.7	187	160	0.2120

A breakdown of the number of injection molded scintillating tiles needed for each of the calorimeter types is shown in Table 5-2. The total weight of the tiles to be produced is 58.5 tons.

Table 5-2 Number of injection molded tiles per size needed for the barrel, extended barrel and ITC calorimeters.

	# periods/module	# modules	# tiles
Barrel	305	65	19825
Ext. barrel	139	130	18070
ITC	17	130	2210
Total			**40105**
Total for 11 sizes + 5% spares			**463500**

5.1.1.2 Light yield

Finite photostatistics gives a contribution to the calorimeter resolution, to be added in quadrature to the intrinsic sampling resolution. A requirement that we adopt is to be able to see the muon signal within each depth sampling. Therefore, as was discussed before, the photoelectron yield must be of the order of 1 photoelectron per mip per tile. The photoelectron yield is a complex factor depending not only on the light output of the tiles, but also on the light collection efficiency, the PMT choice and the fibre choice. In general all these issues need to be addressed in the following sections in order to have a complete optical system capable of producing the required photostatistics.

Furthermore, this detector is expected to operate a minimum of 10 years. Typical ageing rates for a scintillator-WLS system amount to about 1-3% loss of light per year. As an example, the STIC calorimeter of DELPHI detector, made with the same kind of scintillator that we intend to use and Y7 WLS fibres from Kuraray, reports a signal loss of 2% per year during the first two years of operation[A.47]. In addition, we anticipate some (modest) loss of light output in the scintillator from radiation damage (approximately 0.5%/year at full luminosity.) To provide safety margin for ageing and other effects we set as requirement a minimum light yield > 1.2 pe/mip/tile at production. This yield is measured with a standard setup based on all optical techniques we plan to use in ATLAS for the calorimeters and in the test beam(N-10,N-24,N-65,N-81,N-86).

5.1.1.3 Uniformity

A non-uniformity of tile response can degrade the performance of the calorimeters. Due to the size of hadron showers and the sharing of the energy in between the electromagnetic and the hadronic calorimeter, the degradation in resolution caused by this effect is not as severe in the Tile Calorimeter as in electromagnetic calorimeters. If a random non-uniformity in the read-out of the cells exists at the level of 10% (rms), an addition to the constant term can be expected up to about 1%. Again, as seen by the read-out, any non-uniformity includes contributions from: non-uniformity inside a tile, tile-to-tile fluctuations, tile-to-fibre coupling, fibre-to-fibre fluctuations, variations of the response across the PMT photocathode, and fluctuations inside a cell due to the fact that more than one tile is read by the same fibre. This last effect introduces radial fluctuations of the order of 5% and cannot be improved without substantially increasing the number of fibres.

To realize an overall non-uniformity of 10% rms, it will be necessary to keep non-uniformity inside a tile, tile to tile fluctuations and fibre to fibre fluctuations each below 5%.

5.1.2 Scintillator production

The standard technology for the production of plastic scintillator uses styrene polymerization between high quality glass plates. The required procedure for glass surface preparation and the long polymerization time result in a high price and a slow production rate for the scintillators produced using this method. Subsequent machining and polishing operations would also be required to produce tiles in the shapes required for the Tile Calorimeter.

An injection molding technique for scintillator production has been developed by IHEP-Protvino[A.18]. This technique is well adapted for mass production of tiles of the sizes and shapes required by the Tile Calorimeter. The production rate is high, and for the quantity required by the Tile Calorimeter, the cost is a small fraction of the cost of commercial scintillator. In addition, no secondary mechanical operation is needed for the final product. Scintillator produced with the injection molding technique has been proved to have inferior light yields compared to cast scintillator. However, requiring a few photoelectrons, it is possible to use this process, but at the expense of being carefully selective in the other parts of the optics.

Early prototype work (RD34) indicated that injection molded scintillator could indeed provide sufficient light yield to meet our specification for the Tile CalorimeterD-4. With its lower cost than the alternative technologies, injection molding has been chosen for production of the scintillating tiles for the Tile Calorimeter.

5.1.2.1 The injection molding technique

Commercially available optically transparent granulated polystyrene (pellet size about 3 mm) is used as the scintillation matrix base. The polystyrene is dried in a furnace at a temperature of 60-70 ^{o}C and is then mixed with finely dispersed wavelength shifting dyes. The prepared mixture is loaded into the molding machine hopper, where it is directed continuously by a screw into a heated cylinder while simultaneously being mixed. At the exit of the cylinder, the temperature reaches about 200 ^{o}C. The melted polystyrene mixture is injected into the mold under a pressure of about 700 Atm. After the plastic is injected, the mold is cooled to 50 ^{o}C, then is opened and the tile is removed. This whole cycle lasts less than two minutes per tile.

Scintillating dyes can be easily affected by the high temperature in the injection cylinder and may be damaged or destroyed if temperatures exceed about 190^{o}C. On the other hand, increasing the injection temperature and pressure improves the transparency of polystyrene and reduces the local stresses. Consequently, the scintillator production temperature must be kept at the level of 170-190 ^{o}C, and the injection parameters must be optimized for each mold. Careful monitoring by operators is also required.

Five batches of scintillator, with a total of about 10,000 tiles have been produced in the course of the RD34 program, and production parameters and operation have steadily improved. As is discussed below the light yield, uniformity and production yield of the final two batches met our requirements. These represent a modest production level. The remaining work to be done in 1997 & 1998 is to expand the production capacity to prepare for the production of the 460,000 tiles required.

5.1.2.2 Mold design

The first issue in mold design is to achieve the tolerances in tile dimensions and therefore a precision of 100 μm on mold edges have been required. The reproducibility of the tile dimensions is determined primarily by the stability of the thermal shrinkage constant between different batches of polystyrene and will be accommodated for a regular basis during production. For each tile width, three different lengths of tiles are required. To minimize tooling costs adjustable molds have been designed. This technique was used for the production of tiles for the barrel Module 0 prototype.

A second issue for mold design concerns the surface quality of the tile. Light generated by an ionizing particle passing through a tile is internally reflected between the tile surfaces as in a light-guide. The attenuation of the light depends strongly on the surface quality. Surface roughness and non-planarity leads to light dispersion and losses. To meet this goal we have set a precision of 20 μm on all mold surfaces.

Additional mold design considerations include: the size, location and direction of the injection ports and the shape of the molding channel. Optimization of these parameters have been established empirically in the RD34 program by measuring the light output of the tiles. In addition, the mold must survive the pressure and temperature of melted polystyrene for many cycles. At the present time, the molds fabricated as part of the R&D program are not designed for mass production. Development of such molds will be done as part of the production planning in 1997 and 1998.

5.1.2.3 Raw materials

The wavelength shifting process consists of a sequence of light absorptions and emissions in the chosen dye system. As part of RD34 program we made a careful study of the dependence of dopants and dopant concentration on light output of tiles of our required geometries and determined that the conventional combination of paraterphenyl (PTP) and POPOP could be successfully used in injection molding. In a binary scintillator such as we propose, the initial radiation at the wavelengths 240-300 nm induced by the ionizing particle is transmitted through the polystyrene lattice until it is absorbed by a primary fluor molecule PTP. PTP emits light in the range 320-400 nm which is absorbed by POPOP and converted to a longer blue wavelength. Concentrations of the dyes are chosen to maximize the efficiency of light absorption by the next molecule in the chain while minimizing reabsorption by the previous type. From measurements of tile light yield and uniformity using radioactive sources we have determined that 1.5% PTP as the primary fluor, and 0.04% POPOP as the secondary fluor are close to optimal for our situationN-86.

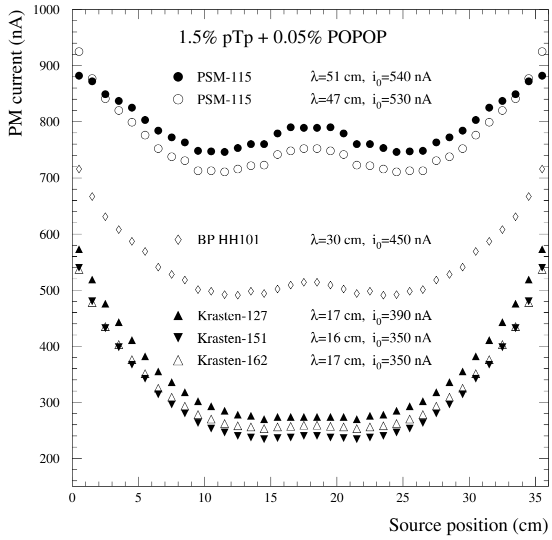

Figure 5-3 Tiles light yield for different types of polystyrene. The 2 values for PSM-115 give an indication of the production reproducibility.

PTP is produced in Europe, in the Ukraine and in the USA. These products were found to be similar in price and in performance. POPOP is also produced by the same sources. Polystyrene is a very common industrial product and has many suppliers. The most transparent grades of polystyrene from about ten of these sources have been tested and the transparencies of sample plates (without dyes) measured to select the most promising for their use as scintillator bases. Tiles of a standard geometry and dopant concentration were produced and their response to a radioactive source measured. The summed signal from fibres reading out each edge of the tile as a function of source position is shown in Figure 5-3. The product PSM-115 gives the best response. PSM-115 is produced in Kazakhstan by AKPO, has a monomer content <0.1% and water contamination <0.1%[A.46].

We have evaluated the batch to batch reproducibility for one product (PSM-115). Although all batches were certified to be practically the same, the tiles produced differed significantly (as much as 50% difference) in the light transmission. We believe that the polystyrene transparency is affected by small impurities or additives (vaseline oil for improving the melt flowing index and akrovax for improving granule stability are added to PSM-115). PSM-115 also has traces of tretbutyl, used for slowing the self-polymerization of styrene during storage. We conclude that a careful specification and testing of the polystyrene will be necessary to assure constant quality and we will develop procedures to achieve this as part of the production preparation to be done in 1997 and 1998.

5.1.2.4 Light yield uniformity

The uniformity of the light output of a tile depends on the local light yield uniformity and on the tile transparency. Local scintillation response under X-ray stimulation was measured by doing scans along the tile. This kind of measurement is sensitive to the homogeneity of the dopants distribution in the tile and to the tile thickness. A very good agreement was obtained among the different scans, showing good uniformity in terms of light yield. The results obtained in one scan made along the bottom of the tile are presented in Figure 5-4. The response uniformity has an rms of 2.1%.

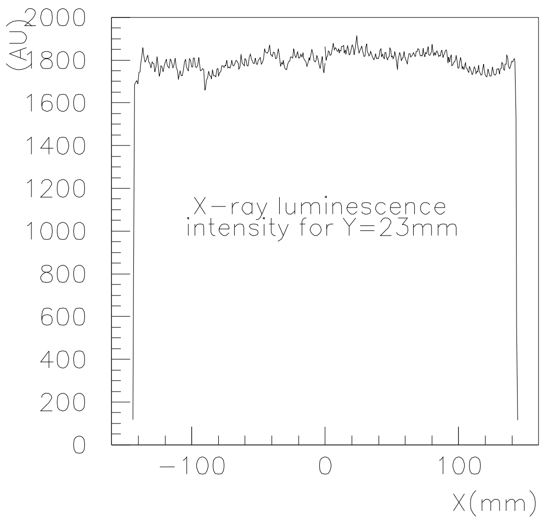

Figure 5-4 Local scintillation response under X-ray stimulation along one scintillating tile.

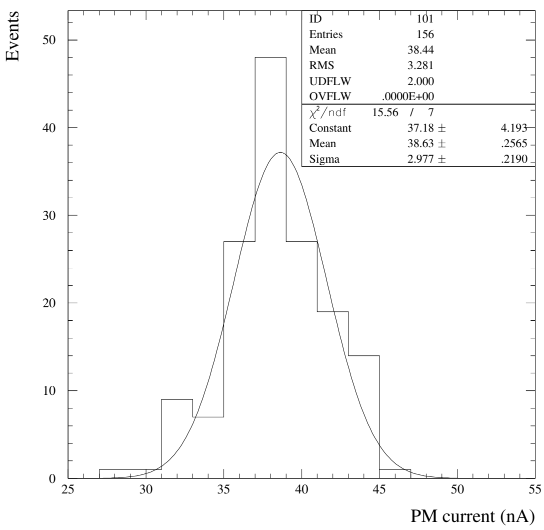

Figure 5-5 Quality control for the largest tile during 1995 production. All produced tiles were measured. The light output is proportional to the PMT current and has a spread with σ=7.7%. Tiles in the distribution tails were rejected.

The fluctuation in tile properties depends on both the raw material properties and the stability of the molding machine operation. The analysis of the machine parameters - temperatures in the heating zones and in the mold itself, injection and locking pressures, the plastic flow stream, and the injection port profile - is not straightforward. In the present production these variables are controlled by the mold operator. However, we have designed and tested a mold with an internal pressure sensor to improve the monitoring and to control the stability of the injection parameters for future production runs.

Approximately one ton of scintillating tiles have been produced in five batches at IHEP for the ATLAS Tile Calorimeter prototypes. Two tile geometries were used with the same 3 mm thickness for the tiles. In an early prototype, all the tiles had the same width of about 100 mm with 18 different lengths ranging from approximately 200 to 370 mm. The latest tiles, produced in 1996, had the final Tile Calorimeter geometry as described in Section 5.1.1.1 and were produced using adjustable molds similar to the molds envisaged for the mass production.

During production, the tile quality was monitored using the response to a ^{90}Sr radioactive source. The test setup consisted of the tile coupled to a single Kuraray Y11 fibre, which was read out using a FEU-84 photomultiplier tube. The PMT current was measured for two source locations near and far from the read-out fibreN-86.

Figure 5-5 shows the response distribution for the near position for the largest size of tile manufactured in 1995 for the last prototype module (approximately 10×36 cm^2) and for which all tiles were measured during the production process. The variation in tile quality during production is attributed to variations in the injection parameters. Only the tiles with response within about 10% of the mean value were selected for usage in the prototype calorimeter.

For the 1996 production of Module 0 tiles, a computer controlled injection molding machine was used. The operation of this machine was very stable. Sample measurements of every 10th to 20th tile did not show significant fluctuations in the light yield. However, the quality of polystyrene used for that run was worse than in the 1995 production.

We have studied the light output uniformity of a sample of 10 tiles of each size produced for Module 0N-81. Figure 5-6 shows the mean signal as a function of the width/area for each of the 11 tile sizes. The linear dependence with the ratio width/area is seen (as expected from other studiesN-66 and Monte Carlo simulation.) The rms spread in response for each set of tiles varies from 1.5 - 4.1% in good agreement with our specificationsN-81.

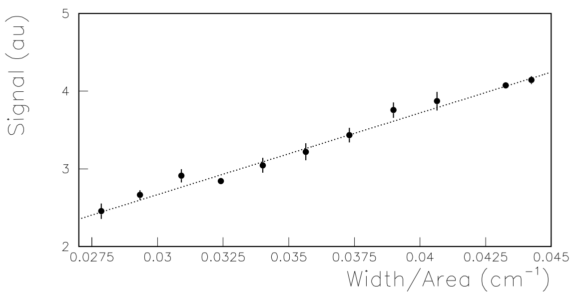

Figure 5-6 Tile light output for the 11 sizes of tile used in Module 0 production.

5.1.2.5 Attenuation length

The effective attenuation length, measured in terms of light from the fibre versus distance of the source from the end of the scintillator, depends on the material and also on the tile geometry and surface quality. The existence of internal stresses, flow lines and other plastic deformations seen in the injection molded tiles may also affect their optical quality. The effective attenuation length for the smallest and largest tiles of Module 0, as well for the reference tile of 1995 production are indicated in Figure 5-7. The smallest tile of Module 0 has an effective attenuation length of the order of 50 cm. The attenuation length of the largest tile of the prototypes (black dots in the figure) is about 47 cm, while the value obtained for the largest tile of Module 0 is only 38 cm, but the area of this tile is twice the area of the prototype tile. This worse transparency is due to the large tile area and to the worse quality of the polystyrene used for the Module 0 production.

5.1.3 Scintillator wrapping

Before the scintillating tiles are inserted into the Tile Calorimeter, they are wrapped with a covering material. The wrapper protects the optically reflective surface of the tile from contact with materials having an index of refraction which would spoil the internal reflection of the light, provides protection from scratches or other mechanical damage and, in addition, enhances the light yield by redirecting some of the light which is not captured by internal reflections back into the tile. To achieve a non-uniformity across the tiles below 5%, a non reflective mask will be printed on the wrapper near each fibre to absorb part of the light .

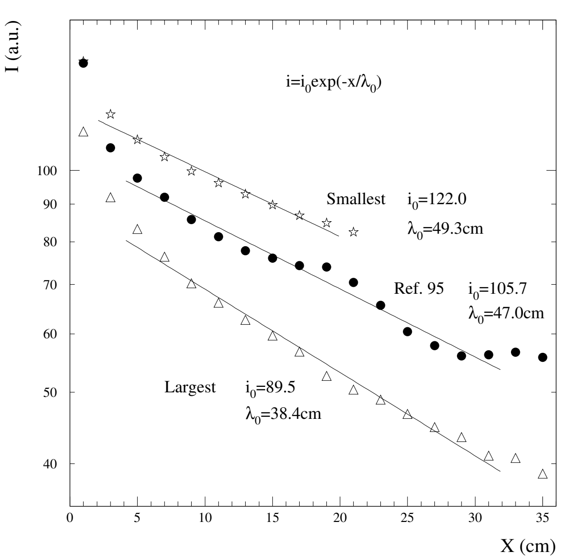

Figure 5-7 Attenuation length measurements for the 1995 and 1996 tile productions. The full dots correspond to the 1995 reference tile, size #18 (the largest of the prototypes), and the open symbols correspond to Module 0 tiles.

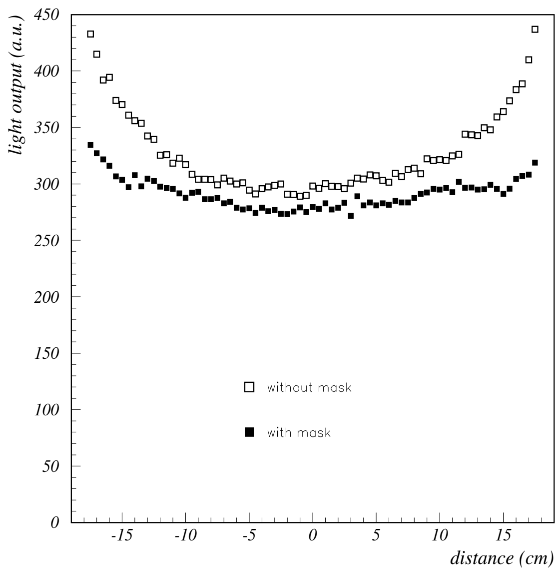

Figure 5-8 Central scan for tile #11 of Module 0, without mask and with mask. Without mask, the rms is 11%, and it is reduced to 4.5% with the mask.

5.1.3.1 Wrapping material

Measurements have been made on a variety of reflective materials to find the most suitable one. Besides reflectivity and diffusion, other important parameters are thickness, mechanical toughness and easiness for mask imprinting. Tyvek^{TM} has been chosen with respect to paper or other potential wrapping materials because of its high reflectance and toughness. Tyvek is made of high density polyethylene fibres. Of the several types of Tyvek available, Tyvek 1055B has been found to have high reflectivity and is specified for the wrapping material. Its thickness is in the range of 70-200 μm and the density is 40-44 g/m^2. The opacity is 97% and the measured reflectivity is about 95%. The gain in light output is of the order of 5-10%, when compared to an ordinary paper wrapping, and about 20% when compared with unwrapped tiles.

Masking

The response across the surface of an unmasked (but wrapped) tile is shown in Figure 5-8. The non-uniformity associated with light near the read-out fibres exceeds our design requirement of 5% over the surface of the tile. This non-uniformity across the tile surface also depends on the tile size and on the relative position of the ionizing radiation.To reduce this non-uniformity we apply a mask on the Tyvek wrapper to absorb part of the light which would otherwise be re-

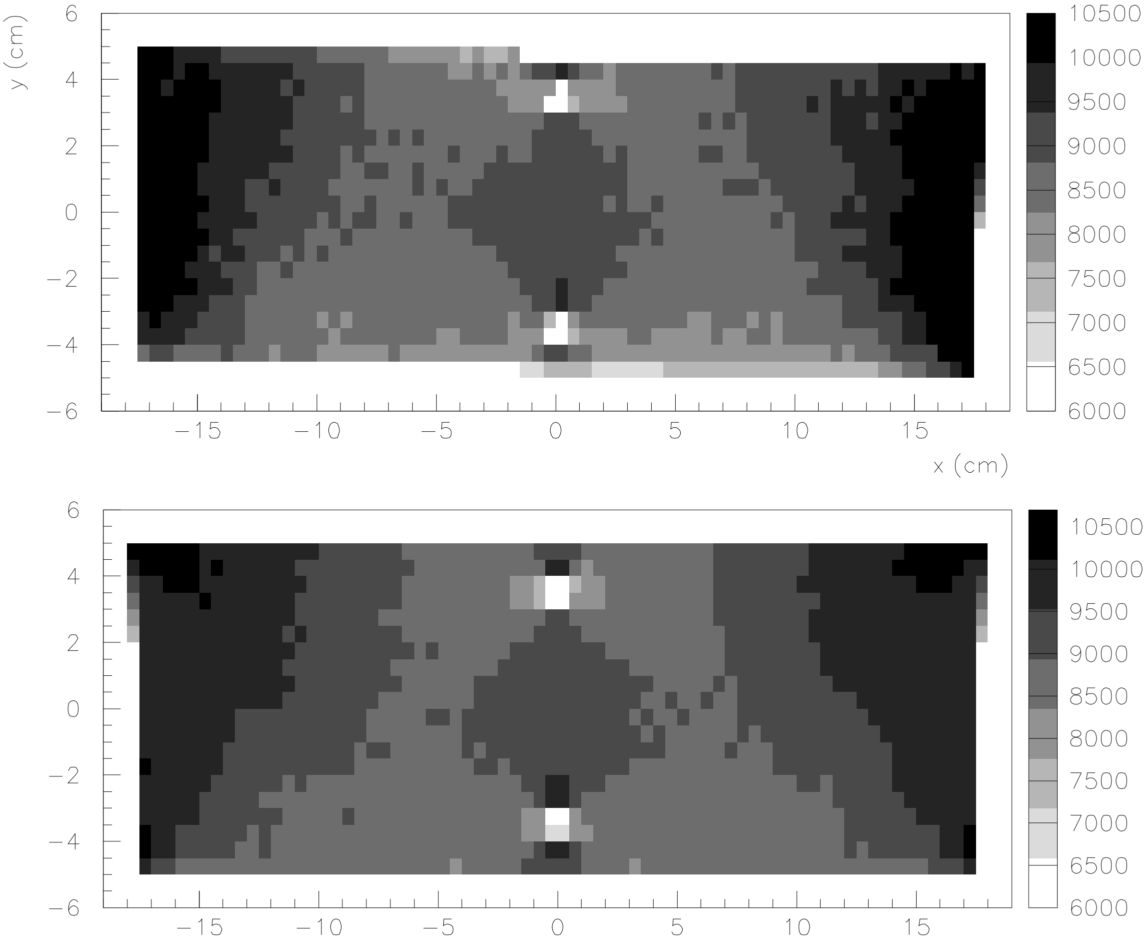

Figure 5-9 2D scan of tile #17 of the prototype modules without mask. On top is shown the measurement in the laboratory using a ^{90}Sr source, and at bottom is the simulation result. The grey scale is in arbitrary units.

flected back into the tile. A variety of approaches has been used to apply a non-reflective mask to the wrapper. These include the application of black electrical tape, tedlar strips, and ink imprinting or dipping. All give comparable results in terms of optimizing uniformity. However, for mass production and to allow flexibility in the mask pattern, only ink imprinting or stamping appears to be cost effective. Part of the work to be done in 1997 entails improving the masking technique for mass production. The result of such a mask can be seen in Figure 5-8. The non-uniformity across the surface is considerably reduced.

Mask design has progressed empirically by systematic bench studies of the tile response to a radioactive source, but also using Monte Carlo simulation[A.38]. An important observation made during this work was that the mask effect extends well beyond the physical limits of the masked region. The final optimization of the mask to be used for tiles in the barrel Module 0 was carried out using the Monte Carlo program, which had been calibrated to a set of bench measurements made by scanning a source across the surface of a tile[A.48]. The ideal mask should cover a complex surface given by the regions where the light output is more than 5% above the tile average. Figure 5-9(top) shows a 2D scan of an unmasked tile #17 of the prototype modules made with a collimated ^{90}Sr source. The grey scale indicates the light output intensity in each point. The Monte Carlo calculation for the unmasked tile response is shown in Figure 5-9(bottom). Good agreement with source data is observed. For the Module 0 only a trapezoidal black strip was used. We propose to further optimize the mask pattern using this program as part of the work to be done in 1997.

Figure 5-10 shows a comparison between the tile response to a radioactive source and the response given by the Monte Carlo calculation. The plotted values correspond to a central scan of tile #8 of Module 0 made with the source (open symbols), and to the scan made in the test beam with 180 GeV muons (full symbols, preliminary online results). Monte Carlo and bench results agree to within 5% over the scan.

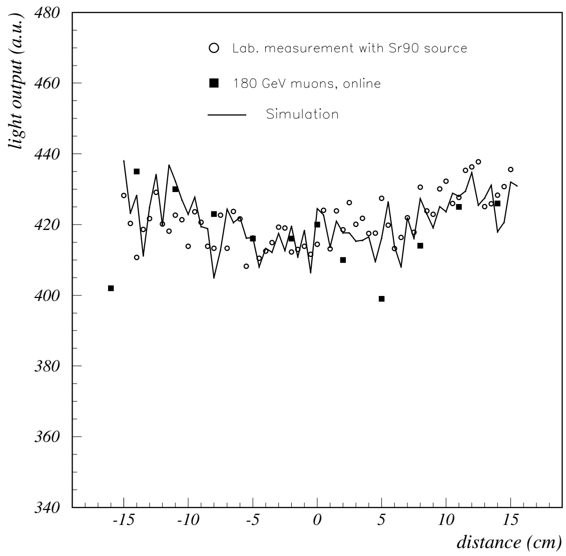

Figure 5-10 Simulation, bench results and muon beam online results for a tile #8 from the Module 0 production. Central scans along the tile were normalized. The line corresponds to the simulation results.

The design goal is to have a light yield which is uniform within ±5 % across the surface of the tile. A mask consisting of a simple black band of appropriate width was used for the 6 largest tiles of Module 0. The measured response of a set of tiles used to check the validity of the masking proposal for Module 0 is summarized in Table 5-3, where these results are compared to the results for a set of unmasked tiles. The non-uniformity is below 5% and meets our requirements. In Table 5-4 are shown the results for all the tile sizes of Module 0 with the final masking and wrapping design. Three transverse scans were made for each of the tiles. In this table are compared the light output in the center of the tiles and the average for the three scans. The results show that the evaluation of the light budget with the central value is adequate. In the same table it is shown the non-uniformity evaluated as rms for the full three scans. The results show also that the non-uniformity stands below the target value of 5% for all the tiles except for #5 and #11. For these tiles a better masking is required.

Table 5-3 Rms values of tile light output for a scan along the central line of Module 0 tiles, without and with mask. The average light loss caused by the mask is also shown.

Tile #	non-uniformity without masking (%)	non-uniformity with masking (%)	average light loss due to masking (%)
7	6.2	3.3	4.0
9	6.8	3.2	10.3
11	10.9	4.5	9.8

Central scans for some of the tile sizes of Module 0 with the masks are shown in Figure 5-11. For Module 0, it was decided that no masking was required on the 5 smallest tiles, because their uniformity was acceptable, and this decision would allow a faster production of the sleeves to wrap the tiles. From the figure and Table 5-4 we can conclude that a small mask would have been useful for the tiles that were not masked (1 to 5).

Table 5-4 Light output and non-uniformity for the tiles of Module 0. I_{center} is the light output at the center of the tile and $I_{average}$ is the average of 3 transverse scans along the tile.

Tile #	I_{center} (a.u.)	$I_{average}$ (a.u.)	rms/$I_{average}$ (%)
1	579	560	4.0
2	605	578	4.3
3	546	534	5.0
4	552	540	5.2
5	466	469	6.1
6	427	414	3.7
7	429	421	4.5
8	450	447	4.0
9	369	362	3.7
10	378	369	4.2
11	334	345	5.5

5.1.3.2 Wrapping technique

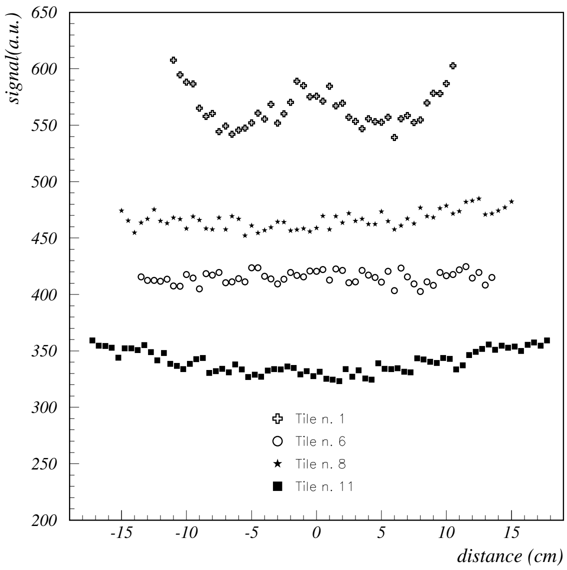

Figure 5-11 Central scans for some of the Module 0 tile sizes. Tiles #6 to #11 have been masked.

In wrapping the tiles, both for labour efficiency and to minimize potential damage to the scintillator, it is important to keep the manual handling operations to a minimum. Two options have been considered. One approach considered for the fabrication of the wrapper is the use of a machine similar to that which might be used to wrap bars of chocolate and is capable of folding and taping a precut Tyvek wrapper around a tile. With this technique it would also be possible to leave pockets at the ends for inserting the WLS fibres and would allow a similar fibre coupling scheme to that used successfully for many of the prototype modules instrumented as part of the RD34 program. A second option, used for the barrel Module 0, is to make Tyvek sleeves cut to the shape and length of the tiles. Since the sleeve is open at each end, this wrapper is well suited to mating the WLS fibres to the ends of the tiles using the ‘profiles’ described later in Section 5.4.2. It is simple and cost effective and is proposed as the baseline for this design.

The fabrication approach chosen as our baseline was evaluated by fabricating 1000 sleeves for the instrumentation of barrel Module 0. The sleeves were fabricated by a company which makes Tyvek tubing used for irrigation and filters. Their process forms the sleeves with a welded seam meeting our dimensional tolerances. They were able to adapt their tooling to cut the tapered shapes and punch the holes to match the shape of the tiles. The only tooling required by the Tile Calorimeter group for the sleeve wrapping method is an insertion tool used to align the sleeve with the tile and hold the sleeve open at the entry end. The sleeve is simply pulled over the tile by hand. We expect that eventually this operation will be done as the tiles come out of the mold, eliminating any additional wrapping that would otherwise be required for shipping.

The baseline includes the printing of a mask on the sleeve before it is formed and welded. This was not implemented for the Module 0 sleeves. The masking for those sleeves was applied after the sleeves were made by hand dipping the sleeves in ink. For the next set of sleeves, to be produced for the first extended barrel modules in 1997, we will purchase a pad printing machine which will be setup in the manufacturer's production line. This will provide more flexibility in the design of the mask pattern.

5.1.4 Scintillator production and handling

Although there are 11 different tile sizes, there are only four different radial widths. By making molds with changeable inserts, we are able to produce all sizes with four molds. For each mold width, the production will start from longer tiles. However, since all tile sizes will be needed at the beginning of module production, we will have to make several (3) production cycles including all sizes of tiles. The mold surfaces will have to be repolished to remove traces left by the inserts after each cycle.

The production is foreseen to be done in one of the participating institutions. Eventually the task, depending on manpower, may be subcontracted to one of our industrial partners. Production time may range from one to four years, depending on the number of available injection machines, on the design of the molds and on the number of shifts per day. The present module production and installation schedule suggests that a minimum of 2 machines operating for a standard shift per day will be necessary.

The tiles will also be wrapped with Tyvek sleeves during production. In addition, to reducing overall handling of tiles, the wrapping also serves as protection during storage and transportation to the module instrumentation locations.

Figure 5-12 Insertion of the tiles in Module 0.

It is reasonable to consider shipments to each module instrumentation location to occur every 3 to 6 months. Intermediate storage for approximately 80 000 tiles will be required at the production or storage facility.

5.1.5 Issues needing further R&D

Scintillator made with the injection molding technique has shown some fluctuation of light-output and light attenuation length. It also seems to be possible to further improve the average light yield and the transparency of the scintillating tiles. To provide the stability required for production over several years, and to try to improve the scintillating tiles uniformity and light output, R&D on the injection molding technique will continue. The scintillator production and testing is expected to continue into 1997 and 1998 to establish the final characteristics for mass production. Three specific areas are foreseen: scintillator raw material optimization, dye optimization, and long term stability.

5.1.5.1 Plastic optimization

The most critical item is to find a way to select polystyrene with good transparency at the time the material is ordered. As part of this effort we intend to establish a common database to store the results from different contributing institutes and to compare them. This will be used to maintain a procurement record during production.

We have recently discovered that the light yield from tiles decreases by about 10% within the first day after production. This may be a potential source for improvement of the light yield. Polystyrene transparency may also be improved with further studies of the effect of additives.

5.1.5.2 Dye optimization

Improvement of the light yield and transparency may be found by a systematic investigation of new WLS additives. For example, we have tested PPO as primary dye and found an increase of 10% in light yield compared to the PTP, as can be seen in Figure 5-13. New additives must be studied to determine their radiation hardness and aging properties. Studies are required to understand the effect of molding parameters on emission and absorption spectra of the dyes.

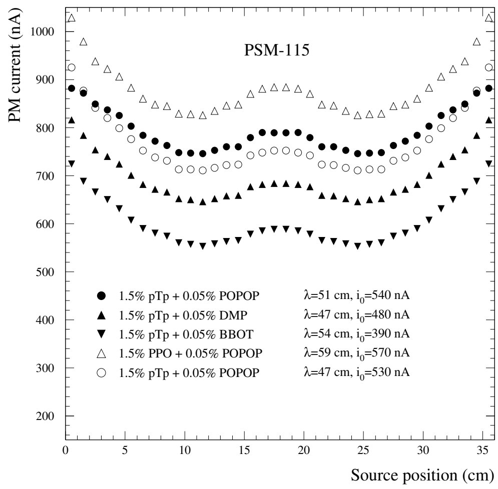

Figure 5-13 Tile light output for different scintillator dyes.

5.1.5.3 Long term stability

Natural scintillator ageing and its radiation hardness depends on the components used. An important factor is the presence of unpolymerized monomer in polystyrene. According to general experience the monomer concentration should not exceed 0.1% for optical quality polystyrene. Molded scintillator has been used for as long as 10 years in experiments at IHEP. No deterioration of calorimeters performance has been seen given a sensitivity of the order of a few percent.

The ATLAS detector is planned to be operated for about 10 years. For this reason it is necessary to evaluate the deterioration of the scintillation tiles over that period of time. In 1997 and 1998 we will carry out a series of artificial ageing studies, using elevated temperatures to accelerate the relevant chemical reactions. The relation between ageing at room temperature and at an elevated temperature is given by $dA/dt=k(T)A$, where A is the concentration of reagent, $k(T) = k_0 \cdot e^{E/(RT)}$ is the chemical reaction rate constant, and T, R and E are the temperature, gas constant and activation energy, respectively[A.4].

Two samples of molded scintillating tiles wrapped with Tyvek were kept at a temperature of 70 ^{o}C for 25 days with intermittent time breaks for measurements. Using the above formula with an activation energy for polystyrene of 91.19 kJ/mol[A.5], the quotient of the reaction rate constants at 70 ^{o}C and 20 ^{o}C is equal to 235. According to our calculations mentioned above this corresponds to the total natural ageing of up to 16 years.

.The results for light yield and attenuation length degradation are shown in Figure 5-14. The values plotted are the ratios after/before the heating process. The step rise of attenuation length just after the start of heating may be caused by some annealing processes in scintillation tiles at higher temperature. Taking the first point as a reference, a 5% degradation of attenuation length at the point corresponding to 10 years is observed. Unfortunately, the rate coefficient k(T) depends exponentially on the value of activation energy. As an example, a 10% deviation for the activation energy corresponds to the interval from -40% to +80% of the ageing time. These studies will be continued to reduce this uncertainty, e.g., by measuring at different elevated temperatures to determine the coefficient k.

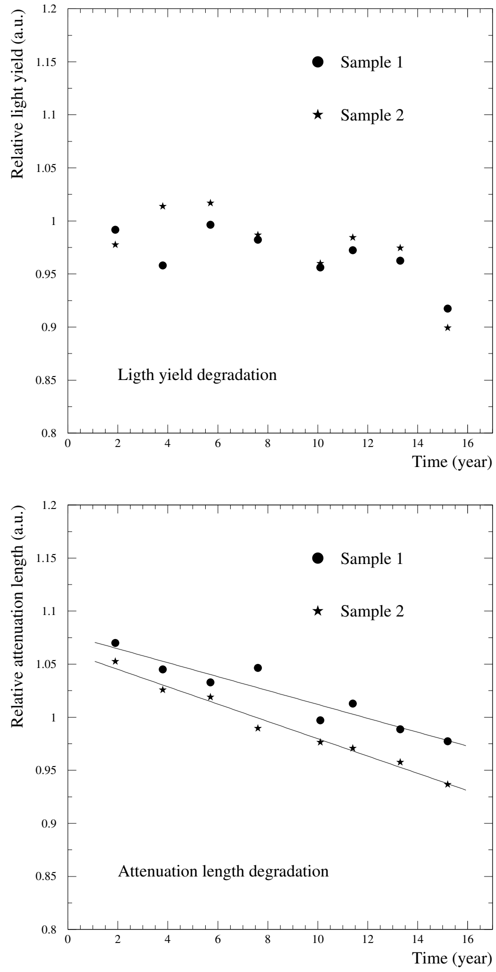

Figure 5-14 Expected degradation of scintillation tile properties as a function of time (from measurements at elevated temperature).

The value of the activation energy we used was measured for scintillator with the same fluorescent additives, but produced by means of bulk polymerization[A.5]. According to our current measurements the total deterioration of the scintillation tile properties caused by natural ageing should not exceed a 10% level after 10 years of operation.

There was a suggestion that low temperatures may cause damage to the bulk polymerized scintillation tiles surface. We exposed injection molded scintillators for a few weeks during russian winter to temperatures of about -20 ^{o}C. No changes in the tile response were observed after this exposure and we do plan to continue this study.

Another factor which affects the ageing of the tiles is the surface crazing. Heating the tiles may reduce this effect. We have injection molded tiles that were produced more than 10 years ago. A visual inspection found no surface defects. However, examples of tiles produced in the prototype program will be stored and monitored periodically.

5.2 The WLS fibres

The WLS fibres are a key part of the optical read-out system. Each fibre collects scintillation light from one or two tiles and transmits it to a PMT in the girder. This is accomplished by the fluor in the fibre which absorbs the blue light from the scintillator and re-emits it at a longer wavelength. The light subsequently propagates along the fibre by total reflection. The light collection should be efficient, fast, with low attenuation along the fibre length and the fibres should be radiation hard.

The cell structure of the calorimeter is obtained by appropriate grouping of the fibres to the same PMT. Figure 5-15 shows the cell structure of half of a wedge of the barrel calorimeter to obtain pseudo-projective towers. Figure 5-16 shows one of the cell structures proposed for the extended barrel modules. The paths of the fibres should be optimized to get the best uniformity inside the cells and the maximum light yield.

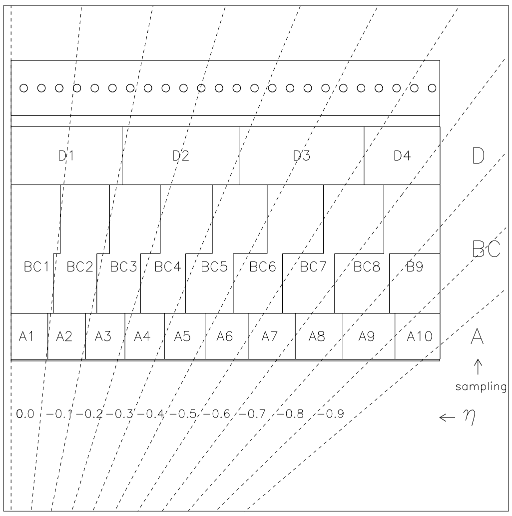

Figure 5-15 Cell geometry of half of a barrel module. The fibres of each cell are routed to one PMT. The PMTs are located in the open circles shown in the girder region.

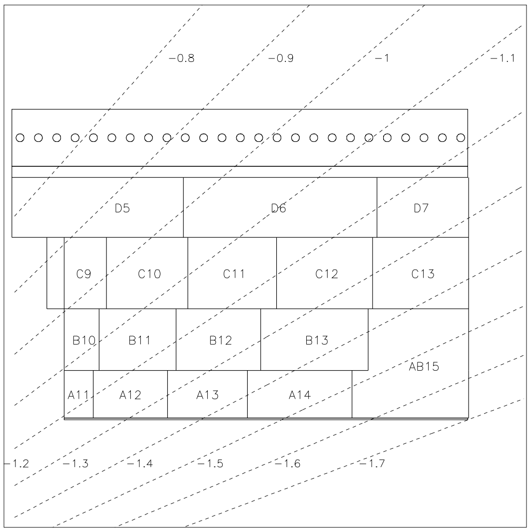

Figure 5-16 Proposed cell geometry for the extended barrel modules (version “a la barrel”).

Four fibres are required to read out one side of each half-period. The total number of fibres required to build the 65 barrel and the 130 extended barrel modules is 640,000. In the barrel the length of the fibres ranges between 85 cm and 210 cm, depending on which cell is to be read and the location of the half-period. In the extended barrel the fibre length ranges from 90 cm to 230 cm. The total length of fibre required is 550 km for the barrel modules and 275 km for each extended barrel, which includes a 5% contingency, leading to 1120 km of fibre, including the ITC. The exact fibre lengths by read-out cell are a function of the read-out geometry and are discussed in detail in Section 5.3 below.

WLS fibres, 1 mm in diameter, doped with a fast (< 10 ns decay time) shifter have been chosen as our baseline. Such fibres are commercially available and are produced by Bicron[1], Kuraray[2] and Pol.Hi.Tech[3], both as single clad and double clad fibres. The early prototype work showed that single clad fibres give adequate performance in terms of calorimeter energy resolution, but that the double clad fibres which have recently become available, give a better signal/noise ratio for muons. Improvements have been made over the last few years, and therefore the final choice of the fibres has yet to be made. The choice of the fibres will be made in 1998.

1. Bicron, USA. Fibres labelled as BCFxxx, etc.
2. Kuraray, Japan. Fibres labelled as Y11, etc.
3. Pol.Hi.Tech, Italy. Fibres labelled as Sxxx, etc.

5.2.1 Optical and mechanical properties

To get the maximum light during the useful lifetime of the calorimeter, the WLS fibres have been selected to have the following requirements:

- the absorption spectrum of the fibre should match the emission spectrum of the scintillator and the emission spectrum of the fibre should match the quantum efficiency of the photomultiplier. This is practically achieved in commercial fibres by shifting the blue scintillator light either to 480 nm or to 495 nm, depending on the manufacturer's choice of dopants. The trade off is either to better match the bialcali photocathode sensitivity region or to have a longer attenuation length related to Rayleigh scattering,
- the fibres should have maximum light yield and attenuation length. The upper limit of the light yield is given by the refractive indices of the materials. A photoelectron yield above 0.5 photoelectrons/mip at normal incidence to a 3 mm scintillating tile is sufficient for the required energy resolution of the calorimeter,
- the fibres should be flexible and suffer minimum damage by the stress due to the curvature on the paths in the calorimeter. Curvature radii as small as 5 cm are needed in the calorimeter instrumentation,
- the direct fibre response (Cerenkov and scintillation light) to ionizing particles should be small in order to avoid large signals in the crack region between modules. Therefore ultra violet absorber dopants should be added to the fibres to reduce the response to direct ionizing particles by a factor 2-3 while reducing at most 10% of the light yield from the scintillators,
- they should be radiation hard, for a total dose of 400 Gy,
- natural ageing over ten years should be negligible.

Since the light yield is an important parameter for the final choice of fibres we have concentrated our efforts on double clad fibres which were shown to improve the light yield by a factor 1.2 to 1.5 when compared to single clad fibres of the same type. As an example the double clad fibres Y11(200)MS (from Kuraray) are composed of a 0.896 mm diameter core, made of doped polystyrene with a refractive index of 1.59, an inner cladding 30 μm thick made of PMMA with refractive index 1.49 and an outer cladding 20 μm thick made of fluorinated PMMA with refractive index 1.42. Figure 5-17 shows a cross section of a Y11 double clad fibre.

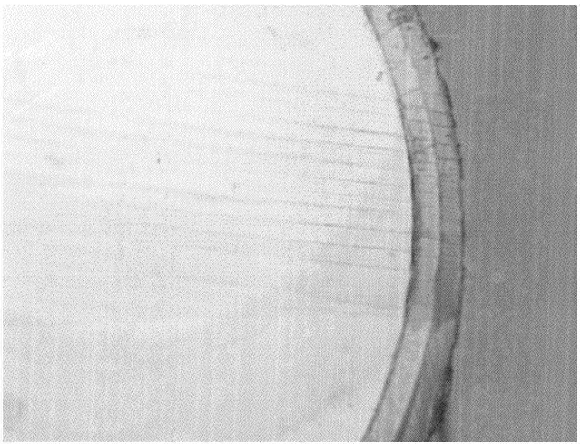

Figure 5-17 Cross section of a Kuraray double clad Y11 fibre. The core (brighter region) is on the left, and the 2 claddings are visible.

5.2.1.1 Light yield and attenuation length

Sample fibres from the three producers indicated above have been investigated in a comparative way in our laboratories by two of the participating institutions(N-34,N-48,N-57,N-95,N-96). As an example, one of the setups is shown in Figure 5-18. Fibres are stretched on an optical bench and are excited at different distances from the PMT using light from an injected molded scintillating tile. The light yield (PMT current) is measured for several positions of the tile along the length of the fibres. The results are typically fitted with a single exponential using only points with a distance to the PMT larger than 50 cm, or with a sum of two exponentials using all the measured points.

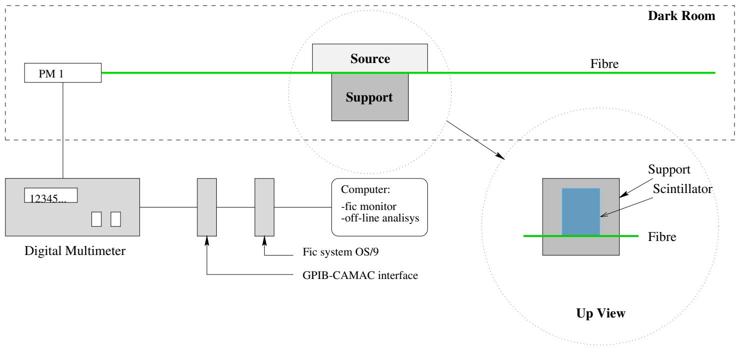

Figure 5-18 Test bench to study optical fibre properties.

Values of light yield and attenuation length (L_{att}) for typical fibres are shown in Table 5-5. The quantity N_0, the amount of unattenuated light, proportional to the light output of the fibre, is also included in the table. N_0 is measured in photoelectrons after a cross-calibration of the multimeter using the single photo-electron peak in the distribution as measured using an R1635-02 PMTN-48. For the Bicron and Pol.Hi.Tech fibres, the increase in light yield obtained from the double clad fibre relative to the single clad fibres is about 20-40% as shown in Figure 5-19 and in Table 5-5, and is in good agreement with what has been obtained for Kuraray fibre as shown in Figure 5-20. In addition, although the Bicron double clad fibre has a shorter effective attenuation length at large distances along the fibre, the net light yield as measured at 140 cm is similar to the one obtained by the Pol.Hi.Tech and quite competitive to that obtained with the Kuraray double clad fibre. Attenuation curves for some of these samples of commercially available WLS fibres are shown in Figure 5-19. The curves reflect the conclusions above and suggest that the summary characteristics given in Table 5-5 may be used as a simple discriminant between fibres.

Table 5-5 Light yield (number of photoelectrons) and attenuation length for typical single (sc) and double (dc) clad fibres. The PMT used is a Hamamatsu R1635-02, having a quantum efficiency of ~12% in the green region.

Fibre	L_{eff} (cm)	N_0 (p.e)	N (140 cm) (p.e.)
Y11(200)MS 600 ppm UVA dc	286	2.95	2.08
BCF99 sc	183	2.57	1.20
BCF99 dc	220	3.19	1.70
S048 sc	269	2.15	1.27
S248 dc	290	2.77	1.71

Globally, in the range of fibre lengths used by the Tile Calorimeters (85-220 cm), the Y11 double clad fibre still gives about 20% more light than the other fibres, as it can be seen in Figure 5-19.

The Tile Calorimeter has read-out fibres of many different lengths. It is therefore useful to present normalized fibre data as a function of length along the fibre. In Figure 5-20, we show this relative response for a variety of fibres tested as part of the RD34 program in which BCF91A was used as the standard. Although there is a large difference between single and double clad fibres, for either type of fibre this ratio is approximately constant along the length of the fibre.

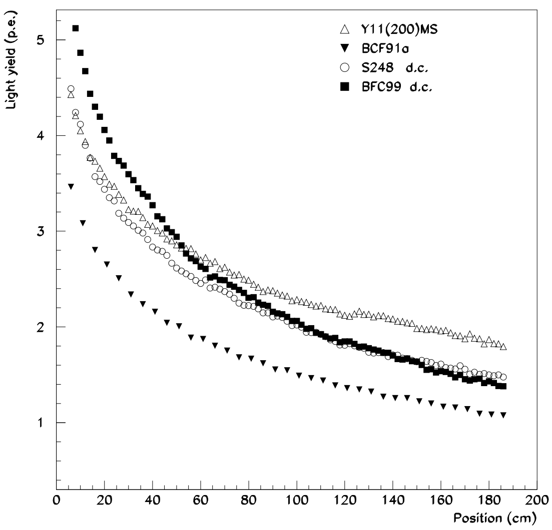

Figure 5-19 Attenuation curves for typical fibres. The new BCF99 and S248 double clad fibres are compared with the single clad BCF91A and with Y11(200)MS from Kuraray. BCF99 has twice the dopant concentration of the BCF91A (PMT is a Hamamatsu R1635-02).

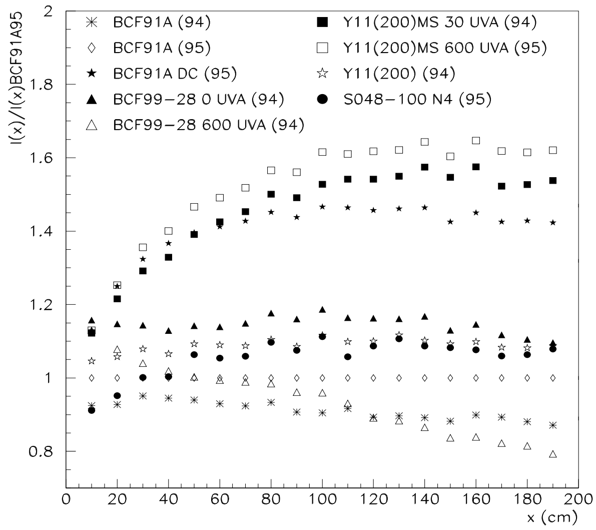

Figure 5-20 Fibre response along the length of the fibres, normalized for each distance to the response of BCF91A single clad fibres. Results for double clad (BCF91A dc, Y11(200)MS with UVA) and single clad fibres are presented (PMT is an EMI 9813KB).

5.2.1.2 Time response properties

The time characteristics requirements of the Tile Calorimeter at the LHC are not so stringent as for a central tracker. Nonetheless, it is desirable to check that the light signal from WLS fibres coupled to our chosen scintillator does not have a long decay time in order to avoid pile-up of signals from several bunch crossings. It is also important to know the response speed of the WLS fibres in order to estimate the read-out timing of the calorimeter. Since the excitation time is nearly instantaneous, the response speed is primarily determined by the de-excitation time (decay time) of the fibre dopants.

Table 5-6 Decay times of WLS fibres. The time resolution of the system has been measured to be equal to 0.7 nsec. The percentage value inside brackets indicates the relative weight of the component. No entry for τ_2 means that a single time constant is consistent with the time response.

Fibre	τ_1 (ns)	τ_2 (ns)
Bicron BCF91A	5.7 +- 0.1 (98%)	0.86 +- 0.05 (2%)
Kuraray Y11(200)MS	5.7 +- 0.1	-
Pol.Hi.Tech. S048	3.7 +- 0.2	-
Pol.Hi.Tech. S048 with UVA	8.7 +- 0.7 (90%)	3.4 +- 0.1 (10%)

Tests were made with a photomultiplier reading out the signal from a piece of scintillator coupled to a WLS fibre and providing the start signal for a qVt (operating in t mode.) The WLS fibre is read out by a second photomultiplier that provides the stop. Since the arrival of a large number of photons leads to a distorted measurement of the time spectrum, a highly absorbing filter (95%) is used to limit the signal to single photons. A typical spectrum is shown in Figure 5-21.

The time spectra were fitted using the a sum of 2 exponentials with decay times τ_1 and τ_2. Table 5-6 shows the results of these measurement made on fibres from the different producers.

In general the decay time constants are well matched to the LHC crossing time of 25 nsec. It is interesting to note, however, that in the case of the S048 fibre, the addition of UV absorber significantly increases the measured decay time.

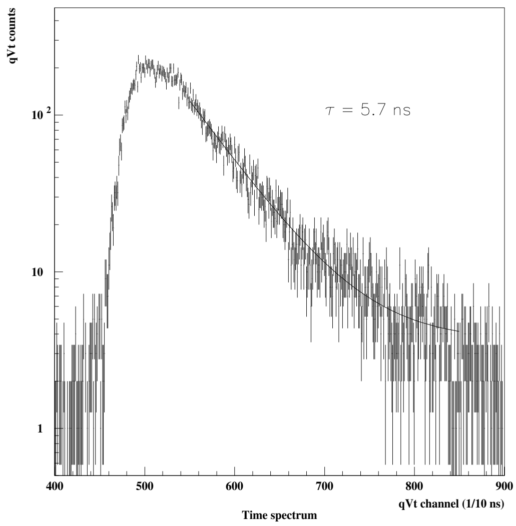

Figure 5-21 A typical time spectrum of a Kuraray Y11(200)MS fibre.

5.2.1.3 Mechanical properties

Flexibility of the WLS fibres for the Tile Calorimeter is essential. The routing of the fibres to the PMTs requires that they are bent with radii of curvature as small as 5 cm. Within the curved section of a fibre, a large fraction of the light transmitted is reflected at the outer surface of the cladding. The bending can affect the optical properties of the fibres, since it may introduce mechanical damage to the fibre surface as can be seen by comparing Figure 5-22 and Figure 5-23. The bent fibres curved to very small radii show small micro-cracks in the cladding as compared to the unbent fibres.

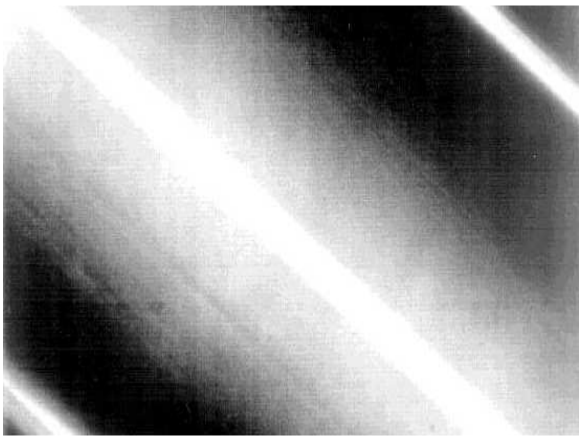

Figure 5-22 Microscopic picture of a straight fibre.

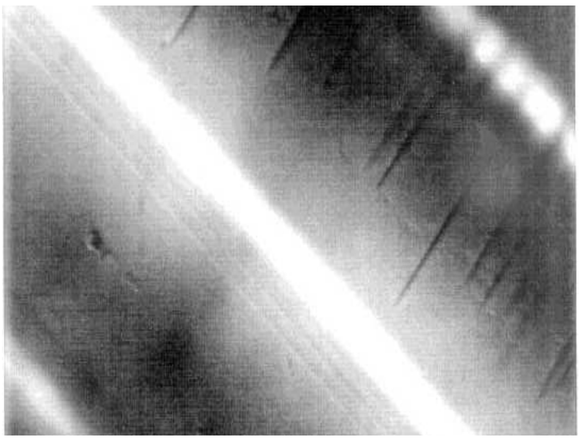

Figure 5-23 Picture of a fibre curved at a very small radius of 2.5cm. The micro-cracks in the cladding are visible.

Bending effects have been studied by measuring the reduction of light yield as a function of the bending radius. The time evolution of the light loss has been a subject of continuous study. The fibres from the 3 producers were evaluated, including a series of special fibres produced by Pol.Hi.Tech. The Pol.Hi.Tech special fibres are varieties of the S048 type having different “elasticity” that will be labelled as S048elXX, where XX is a number identifying the degree of elasticity.

Fibres were wound (one 360 degree turn) on disks of 20, 15, 10 and 5 cm diameter for about 48 hours and then their optical properties were measured (while keeping the fibres wound) and compared with the ones measured before the stress. The results are shown in Figure 5-24. It is clear that below a critical radius the fibres start losing light due to the curvature. That critical radius depends on the fibre type. S048 with elasticity from 1 to 4 and BCF91A lose about 30% of the light for a radius of about 4 cm while Y11MS and S048 with elasticity from 5 to 10 are stable to bending radii as small as 2.5 cm. We attribute the lower light yield after the fibre is bent to the damage of the cladding as seen in Figure 5-23.

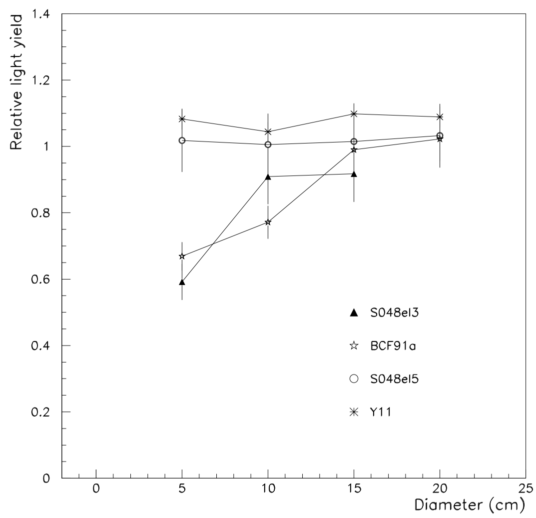

Figure 5-24 Relative light output for some fibres as a function of bending diameter.

To measure the time evolution of the light loss, a set of 16 fibres (12 Pol.Hi.Tech fibres with different "elasticity", 2 Y11MS fibres and 2 BCF91A fibres) has been regularly monitored over more than one year. For historical reasons, the fibre tests done at present have concentrated on a minimum bend radius of 2.5 cm. As part of the fibre routing study carried out for Module 0, we now have a design in which the minimum bend radius is approximately 5 cm. In these long term tests, a drop of light of 5-10% is noticed immediately after the fibre is wound on the disk. At longer times a slow decrease of light output is noticed. The decay time is larger than the time of the measurement, with time constants of many tens of years, and is thus subject to large errors. On average the special series of S048 fibres produced by Pol.Hi.Tech appear to be more stable than the Y11MS and BCF91A fibres. In the real calorimeter the bending radii will be larger that the 2.5 cm adopted in the tests by a factor of 2. However the results already obtained (decay half times of tens of years) in a pessimistic geometry, make us confident that this will be not a serious problem. An improved set of measurements will be done in 1997 and 1998.

5.2.1.4 UV absorber

Experimental tests on the first Tile Calorimeter 1m prototype modules have shown that muons or pions impinging on the crack region between scintillators produce an enhancement of the calorimeter signal, leading to appreciable non-uniformities. The anomalous signal was expected to be from scintillation or Cerenkov light in the fibres. This effect can be reduced with the addition of small concentrations of UV absorber (UVA) to the mixture used in standard commercial fibres.

A sample of fibres with proprietary UVA was obtained from each of the producers. The response of the fibres to charged particles (electrons from the ^{90}Sr β-source) incident directly on the fibre and to light from a Tile Calorimeter blue scintillator as function of the UVA concentration is comparedN-95. Results of the light output response as a function of the distance for Y11 fibres with and without UVA are shown in Figure 5-25. The UVA used in these fibres is effective in suppressing the direct response by a factor 2.9, while keeping the response to the scintillator light practically unchanged for a concentration of 1000 ppm.

Figure 5-26 shows the ratio of the light output at 140 cm for Y11, BCF99-28 and S048 fibres with and without UVA dopant as function of the UVA concentration. The concentration of UVA in the Bicron fibres needs some optimization in order to reduce the 10% loss of scintillator light

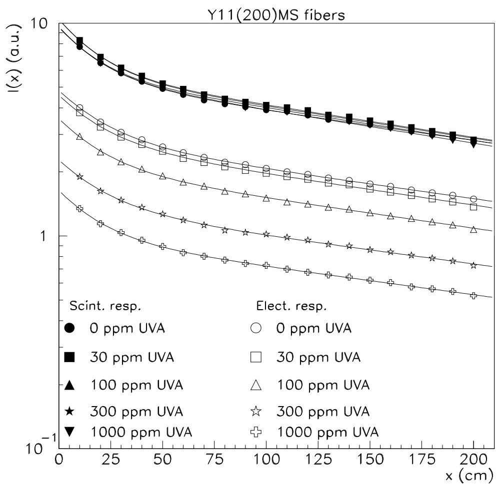

Figure 5-25 Response of Kuraray Y11(200)MS fibres to scintillator light (black symbols) and to electrons (open symbols), as a function of the distance, and for several concentrations of UVA. From the fibres without UVA (open dots) to the fibres with 1000 ppm UVA, the suppression factor is about 3.

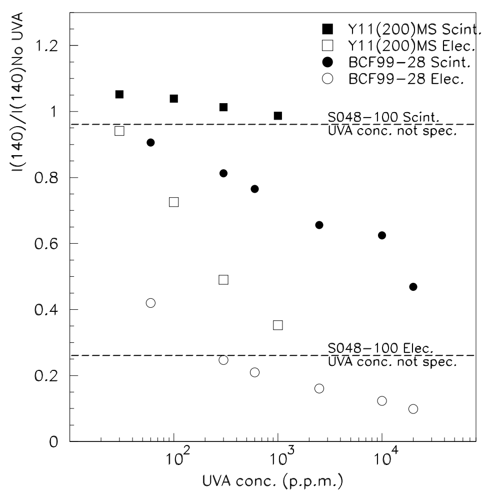

Figure 5-26 Ratio I_{UVA}/I_{noUVA} at a distance of 140 cm for the several types of fibres, as a function of the UVA concentration, for scintillator light and for direct response to electrons.

while achieving a factor 2.4 in the suppression of direct response. Pol.Hi.Tech S048-UVA fibres are also effective in the suppression of fibre direct response while keeping the scintillator response. However the fibres used in the test were not yet optimized in light yield and the concentration of UVA was not specified. Therefore further investigation is necessary.

The instrumentation of the Tile Calorimeter with Y11(200)MS fibres doped with 600 ppm UVA, considerably improved its uniformity (<2% globally)N-80.

5.2.1.5 Fibre aluminization and reflectivity

One way to improve the effective attenuation length and the light output of the fibre system is to aluminize the end of the fibre away from the PMT. The aluminization technique should ensure uniformity, stability with time and radiation hardness.

Typical reflectivities in the range 70-85% have been achieved, with the effective attenuation length in fibres with an aluminized end being above 4 m, compared to 2.5-3 m for non-aluminized fibres. For Module 0 we have collected some experience in the aluminization technique. The aluminization process consists of several operations:

- group fibres in bundles,
- cut and polish one end of the bundles,
- aluminize.

Fibre preparation

Fibre ends to be alumized are first polished to provide an optically flat surface on which to deposit the aluminium layer. The polishing is done for groups of about 1000 fibres bundled in collars and mechanically restrained. The fibre ends are then polished using a standard diamond cutter. Care is taken to avoid damage to the fibre cladding. In this respect, there are some evidences that the fibres are especially sensitive and some additional R&D will be required to improve the polishing technique for production.

Aluminization technique

Magnetron sputtering has been used to obtain metal films with good reflectivity, good uniformity, increased adhesion and decreased thermal shock when compared with thermal evaporation. Those properties depend on plasma deposition conditions and on the topography of the substrate surface. Lower discharge pressure, higher deposition rate and low roughness obtained by special polishing procedures, improve the specular reflectivity.

In the first phase of the aluminization R&D, reduced scale studies were performed in short optical fibres (40 cm length), using a small deposition system. Reflectivities of 70% for Al films 110 nm thick were obtained. These studies were used to establish the operating parameters.

To perform real scale aluminization of long fibres an apparatus allowing aluminization of fibres with lengths of the order of 2 m was designed and constructed. This device will be tested as a viable production facility during 1997. For Module 0, since this facility was not available, a commercial company was used to apply the aluminization to the fibres.

Mirror protection with a polymer

The aluminium coating sputtered onto the end of the WLS fibre is fragile and it is desirable to protect it from flaking and scratching during handling and installation. Each aluminized fibre will be coated with a proprietary UV cure polymer (UVBT115HSAL). The polymer was originally used on aluminized fibres in the CDF endplug upgrade and was developed to satisfy the following criteria:

- The uncured polymer/solvent must not damage (craze) either the polystyrene core or the PMMA cladding.
- The cured polymer thickness needs to be less than 20 microns.
- The cured polymer must have excellent adhesion to the aluminium and the fibre cladding.
- The cured polymer must resist any damage to the aluminium coating under any foreseeable handling conditions.
- The coating needs to be curable by UV light, using a wavelength/exposure time that will not damage the wavelength shifting dyes in the fibres.

No mirror damage was observed in the installation of over 30 000 fibres in the CDF hadron endplug calorimeter or in the Module 0 fibres similarly protected. This technique was also successfully used for the 2500 fibres installed in Module 0 (but with a polymer thickness greater than 20 microns).

Reflectivity results from Module 0 production

The attenuation lengths of the aluminized fibres and the coefficient of reflectivity have been measured for a sample of fibres prepared in the same way as for Module 0N-89. This is a destructive test, and therefore its scope is limited. The measurement is carried out in two steps. First, the aluminized fibre is coupled to a tile and read-out PMT and the signal is measured as a function of the position of the scintillator relative to the read-out end (the scintillator being excited by a radioactive source). In the second step, the mirror end is cut, and blackened and the series of measurements repeated. A typical pair of measurements is shown in Figure 5-27.

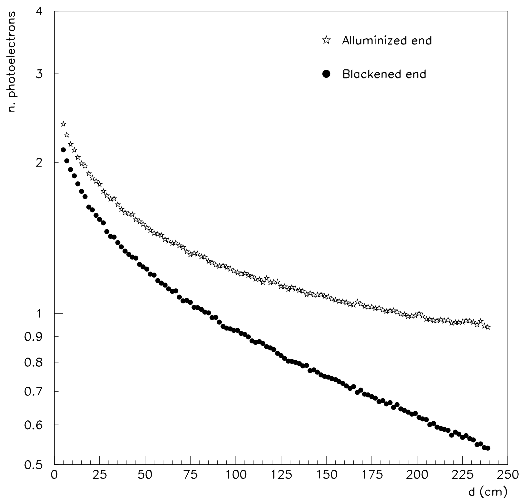

Figure 5-27 Example of curve of attenuation with the extremity aluminized or blackened.

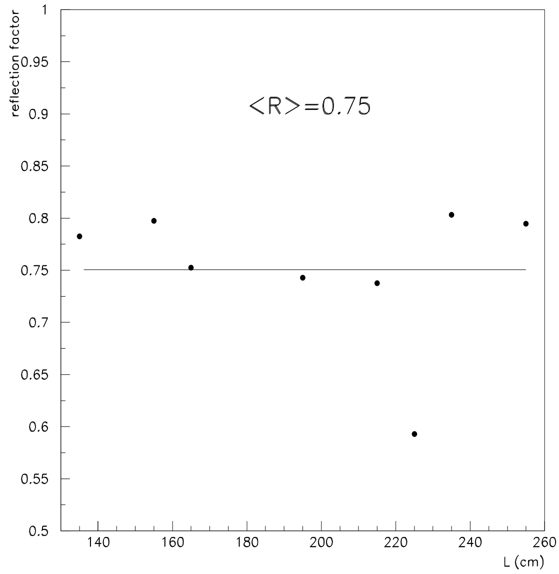

Figure 5-28 Reflection factor vs. fibre length for Module 0 fibres.

In principle, the ratio of the light output at the mirror end of the fibre gives directly the reflection factor. In fact this cannot be read out directly from the data shown in Figure 5-27, since for technical reasons, the excitation of the fibre cannot be performed at the very end of the fibre next to the mirror. For this reason, to calculate the reflectivity R, the fibre excitation curve is fitted with a double exponential function. The fit is then extrapolated to the extremity of the fibre and R is computed. The results, for a sample of fibres of various lengths from the production run for Module 0 are shown in Figure 5-28. The mean value of R is $\langle R \rangle = 0.75$ with a dispersion $\sigma = 0.069$. Excluding the anomalously low value for the 225 cm long (attributed to a measurement error) $\langle R \rangle = 0.77$ and $\sigma = 0.028$.

5.2.2 Quality control of fibres

The number of fibres required to instrument the calorimeter is about 650 000. The quality control will be done in three phases: first at the producer for each batch, and then in the laboratories of two of the participating institutes, before and after aluminization. Since our requirements on the fibre to fibre fluctuations allow a spread of ±5% in the light output at distances where the fibres collect the light produced in the tiles, the producers will normally provide fibres within this specification. Therefore, only a quality control of some fraction of the fibres will be required.

We expect that the delivery of the fibres to equip the Tile Calorimeter will be done in about 100 stacks within a period of about two years. For each stack we plan to test a subsample of 50 fibres to characterize that stack and to check that there are no failures in the quality control of the producer. Each stack of fibres will then be polished and aluminized in several smaller groups of fibres.

The aluminization of the fibres will be done in groups of about 1000 fibres. In a similar way to the control before the aluminization, a sample of 50-100 fibres from each aluminized group will be tested, to ensure that the aluminized fibres are inside the pre-defined parameters.

According to the criteria defined above, the estimated number of fibres to be tested is around 60 000. To allow the test of the fibres in a time saving and efficient way, fibre test benches were developed. As an example, the implementation and performance of a test bench optimized for large scale quality control of WLS fibres is described below.

Fibre test benches

In the past, several devices were constructed for the measurement of the light yield and of the attenuation length of fibres. In the simplest configuration a single fibre is longitudinally scanned by a scintillator coupled to a radioactive source, and the light output is read by a photomultiplier. The main disadvantage in this mode is the time spent in replacing fibres especially when a large number of fibres must be tested. An important improvement was achieved by introducing an additional degree of freedom allowing the transverse movement between the excited scintillator and the fibres. With this configuration many fibres can be installed on a supporting table that positions a selected fibre in front of the read-out system.

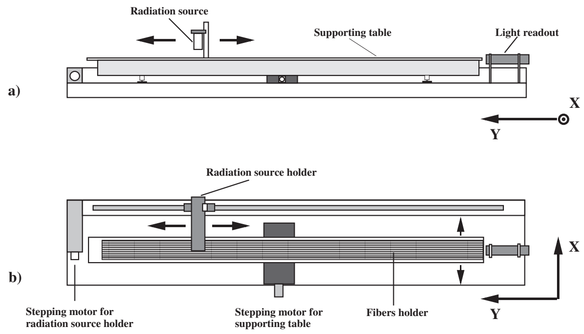

Figure 5-29 Test bench for fibre quality control: a) side view; b) top view.

The test bench described here has been operated for the quality control of the WLS fibres equipping the STIC/DELPHII calorimeter, when 10,000 fibres were scanned[A.30].

The test bench is schematically shown in Figure 5-29. It consists of a X-Y MicroControle optical table equipped with two independent movements driven by two stepping motors along orthogonal directions. This table supports a removable holder that contains the fibres to be tested and is complemented by a light read-out system based on a photomultiplier. The 2.3 m long table is moved in the X direction, perpendicular to the fibre's length. Each fibre is automatically positioned in front of the light read-out using the X motor, and the Y motor moves the scintillator along the fibre length. At each position the light output from that fibre is recorded.

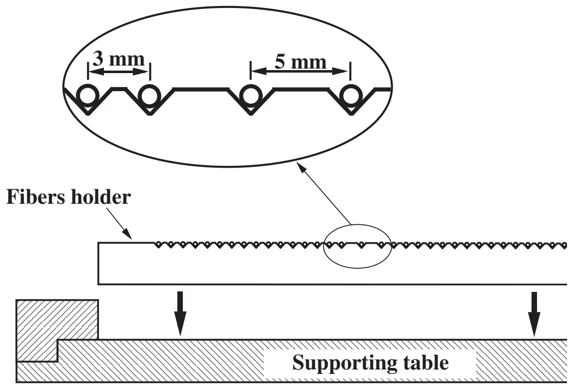

Figure 5-30 Cross view of the supporting table and fibre holder.

The X-Y table consists of three main components: the main support (which is fixed), the supporting table and the radiation source/scintillator holder. This holder moves along the Y-axis in steps of 100µm. The distance between the holder and the supporting table changes by less than a few tenths of a mm when displacing the holder between the extremes of the table. The supporting table is loaded with the fibre holder and moves along the X-axis in steps of 25µm. The movement of the table ensures a constant distance between all fibres and the light read-out within a precision of the order of 50µm.

A cross view of the supporting table and one fibre holder is shown in Figure 5-30. Each fibre holder consists of a matte black anodized aluminium plate with 33 V-shaped grooves to receive one fibre each. The use of two identical holders allows us to reduce the dead time: one set of fibres is automatically measured while the second holder is filled with new fibres. To maximize the number of fibres to be tested in each measurement while keeping the cross-talk at a small level, alternate grooves are populated and each holder is filled with 16 fibres, 6 mm apart from each other, plus one additional reference fibre in the central groove. One fixed reference fibre is inserted in a black painted groove drilled along the table length and is fixed to the supporting table. The signal from this fixed reference fibre provides a monitor of the stability of the read-out chain and scintillator. The light output of the reference fibre of one of the holders during 28 days is shown in Figure 5-31 after normalization to the fixed reference fibre. The spread of the light output during the 28 days is 2.5%.

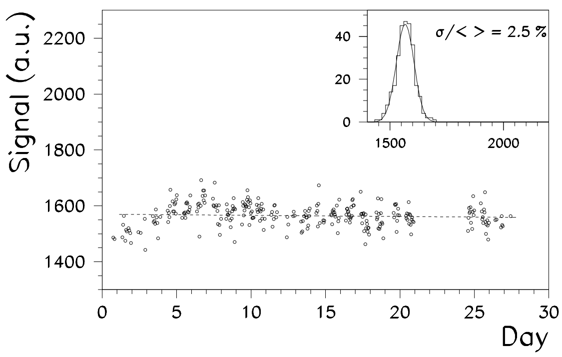

Figure 5-31 Stability of the light output of the reference fibre of one the holders along 28 days.

The movements of both motors and the read-out are computer controlled. The interface with the user is provided by a front panel, where several parameters can be checked and/or modified. The on-line data analysis, consists mainly in the evaluation of the light output and attenuation length for the measured fibres, which are depicted with relevant plots on a report page. This is very useful for a real time control of the ongoing measurements and efficient troubleshooting. The mean value and RMS of the extrapolated light yield I_0 and attenuation length L_{eff} distributions are evaluated on-line for each measurement set. An example of light yield distribution is shown in Figure 5-32.

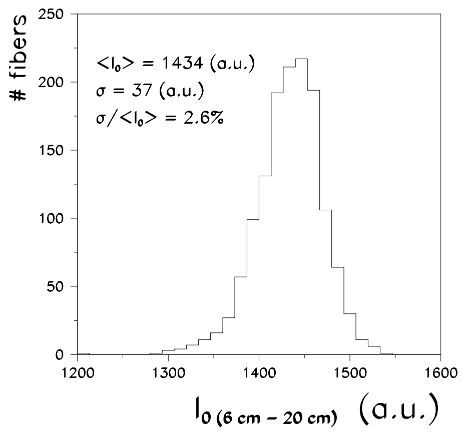

Figure 5-32 Example of a distribution of light yield for 1391 half meter long fibres.

A total of 10 000 fibres were tested, selected and packed in one month. The Tile Calorimeter fibres are longer, so their handling will be slower, and we estimate that about 7500 may be tested per month, allowing to test up to 10% of the total number of fibres for the Tile Calorimeter in the 2 laboratories in a time scale as short as 4 months. The quality control will be done over a longer time scale, coinciding with the delivery of the fibres and their aluminization rate.

Samples of aluminized fibres produced for Module 0 were tested. The number of fibres of each length was small (5 to 15) and the aluminium was not removed. The data (fibre response versus distance) is fitted with a single exponential for distances along the fibre above 70 cm, giving an effective attenuation length (L_{eff}) and light yield (I_0) for the aluminized fibres. These values, as well as values at points where the fibres read tiles in the calorimeter (10 cm from the end of the fibre as example point), are shown in Table 5-7. For this last point there are 2 values, the measured one and the one calculated using the fit. The respective fluctuations are very small, of the order of 2% or less, both for the measurement and the calculated value.

Table 5-7 Quality control of samples of Module 0 aluminized fibres. The data is fitted with a single exponential using points distant more than 70 cm of the PMT. Effective attenuation lengths are sensitive to the length of fibre that is analysed, as well as the respective fluctuations. I(L-10) are the values (experimental and obtained from the fit) of the light output at 10 cm from the aluminized end of the fibre.

Length (cm)	number of fibres	I_0 (a.u.)	rms (%)	L_{eff} (cm)	rms (%)	I(L-10) exp. (a.u.)	rms (%)	I(L-10) fit (a.u)	rms (%)
135	16	1.305	2.2	806	12.4	1.115	1.4	1.115	1.6
155	5	1.217	1.1	632	7.3	0.974	2.7	0.966	2.1
165	5	1.213	0.2	642	3.1	0.961	0.5	0.952	0.7
195	5	1.166	0.9	500	4.8	0.821	0.6	0.805	0.9
235	15	1.158	1.3	450	2.4	0.728	2.1	0.702	1.4
250	7	1.109	0.9	441	2.9	0.674	1.7	0.643	1.7

Fibre to fibre response from Module 0 production

Many factors contribute to fibre to fibre response fluctuations. These include fibre diameter, fibre light yield and attenuation length and the aluminization. To quantify the fibre-to-fibre differences due to the process of production, we have measured fibres from the production run for Module 0 using the procedures outlined in Section 5.2.1.5 using a double exponential function and reflection coefficient N-89. Eight groups consisting of 10 fibres of each length (255, 235, 225, 215, 195, 165, 155 and 135 cm) have been measured. All fibres were double clad Kuraray Y11 and were prepared using the procedures followed for the production of fibres for Module 0.

The optical characteristics of these fibres are summarized in Table 5-8 in which we have quoted also the value of the dispersion of the optical characteristics. From these data we can see two characteristic behaviours:

Table 5-8 Values of attenuation length-long component (L_{att}) and light yield (I_0) for a sample of Y11(200)MS fibres of several lengths.

length (cm)	Latt(cm)		I_0 (n.p.e)	
	Mean	**RMS (%)**	**Mean**	**RMS (%)**
255	254.0	2.1	1.67	3.6
235	243.3	5.0	1.59	10.7
225	234.7	2.2	1.56	5.8
215	219.3	3.9	1.64	4.3
195	205.3	2.5	1.70	5.9
165	187.3	4.6	1.98	8.6
155	195.3	7.9	1.93	4.7
135	176.0	4.9	2.21	3.2
Mean		**4.1**		**5.8**

- The attenuation length increases with the fibre length. This effect is reproducible with a MonteCarlo simulation of the light propagation in a fibreN-91. Since the light yield is not a pure exponential as a function of the distance from the PMT, but flattens off at large distances, the average slope decreases for long fibres.

- The number of photoelectrons is rather stable for fibres longer than 195 cm but increases for shorter fibres as a consequence of the contribution of the reflected light at the fibre end.

We can conclude that the light yield and attenuation length of the tested fibres produced for the barrel pre-series Module 0 are uniform with a dispersion of about 5% within each group. The dispersion of the light output for a fixed distance in the fibre is smaller than the values obtained for the parameters, because the fit parameters are very sensitive to the fit procedure, and the number of fibres measured for each size is small.

5.3 Fibre routing

The general layout of the Tile Calorimeter geometry is described in the beginning of Chapter 5. In the ϕ direction the read-out cell is naturally projective because of the wedge structure of the modules. Each module covers $\Delta\phi$=0.1. In η the modules are just pseudo projective. The cell geometry of half of a barrel module is shown in Figure 5-33. The girder with the holes for the PMTs is on the top of the figure, and the cells are shown below the girder, covering an area of about $2.8 \times 1.5\ \text{m}^2$ (half module). The dashed lines are η lines spaced by $\Delta\eta$=0.1. The cells are made by grouping together in the same PMT read-out bundle, fibres coming from different scintillators and related to the same radial depth. There are 3 independent radial sampling depths in total. The granularity is $\Delta\eta$=0.1 for the two inner samplings and $\Delta\eta$=0.2 for the outer one (tail catcher).

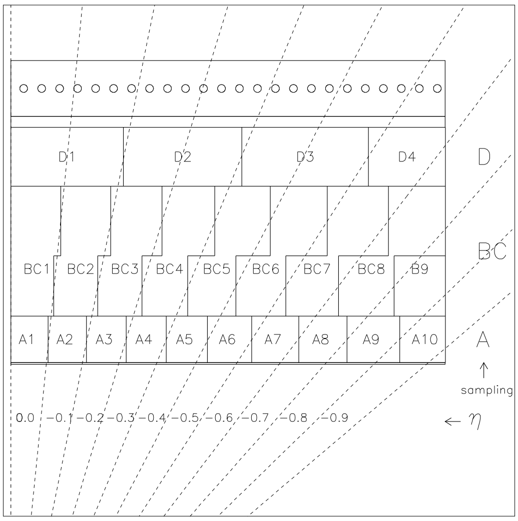

Figure 5-33 Cell geometry of half of a barrel module. The fibres of each cell are routed to one PMT. The PMTs are located in the open circles shown in the girder region.

The light output of a cell depends on many parameters. The light budget - the product of the tile response with the fibre response - is the demanding parameter. The cells within the Tile Calorimeter group several tile sizes and several fibre lengths, in general leading to non-uniformities of light output within a cell and between cells themselves. It is the purpose of the fibre routing design to minimize these fluctuationsN-107.

Light budget calculations (presented in Section 5.3.2 below) were necessary to design a fibre routing configuration satisfying the following conditions:

- non-uniformity within cells should be minimized (prototype results of about 5% are used as guiding numbers)N-66;
- light output should be maximized in order to keep photostatistics at the level of prototype values;
- fibre length should be minimal for optimum light output, to minimize the volume of fibre in the girder region and also to minimize the cost;

- non-uniformity among cells should be small to allow different PMTs to have similar gains;
- the number of different fibre lengths should be kept small to allow an efficient fibre insertion procedure.

With the 1m prototype modules it was found that the average light output of all the cells of one module was very similar. The cells grouping the smallest tiles are read out by the longest fibres, and the cells grouping the largest tiles are read out by the shortest fibres, in such a way that the higher light output of the small tiles compensates the larger light attenuation in the long fibres which read them out.

5.3.1 Geometry

The Tile Calorimeter modules have three radial samplings labelled A, BC and D, as it is shown in Figure 5-33. The configuration that allows the maximum light output (minimum fibre length) should have the PMT of each cell located in the girder in a Z position coincident with the geometrical center of the cell, for cells of samplings A and D. For cells of sampling BC there are 2 sub-samplings with different fibre lengths and different tile light output, deteriorating the uniformity within the cell, so the respective PMT positions should be eventually displaced to the B or C side, to balance tile/fibre light output for the tiles of the two sub-samplings. This ideal scenario is not possible because there is a limited number of PMT holes in the girder, and the cells have to be distributed by those holes. The PMTs of the BC cells are initially centered as well as possible, then the A and D cells are assigned to the closest of the remaining holes. After calculating the light yields for this configuration, the process is iterated until the optimum light uniformity is found for the BC cells.

5.3.1.1 Depth segmentation

The cell division of the 3 samplings of the Tile Calorimeter is shown in Figure 5-33. The BC sampling combines 2 separate sub-samplings B and C to give more pseudo-projectivity.

- The average radius of sampling A is 2445 mm. This sampling groups the scintillating tiles 1, 2 and 3 which are the three smaller ones. In each period, tiles 1 and 3 are read out by the same WLS fibre, and tile 2 is read out by another fibre. In sampling A the total number of cells per barrel module is 40.
- The average radius of sub-sampling B is 2790 mm. This sub-sampling groups tiles 4, 5 and 6. Tiles 4 and 6 are read out by one fibre and tile 5 by another one. For sub-sampling C, the average radius is 3210 mm. Sub-sampling C groups tiles 7, 8 and 9. Tiles 7 and 9 are read out by one fibre and tile 8 by another one. In sampling BC the total number of cells per barrel module is 36.
- Sampling D groups tiles 10 and 11, and each tile is read out by one fibre. The average radius of this sampling is 3625 mm.

The number of tiles of each size grouped in each cell is shown in Table 5-9.

Two options were tested to define the lengths of the fibres. The first option was to make every fibre as short as possible. The second option allowed only two fibre lengths within a cell (or subcell in the BC case), one length for the fibres that read the center tiles of the cell and another length for the fibres that read the outer tiles. The first option was not acceptable because the large spread of fibre lengths leads to large transverse non-uniformities in the light yield within a cell. The second option of constant fibre length inside a cell gives the best possible transverse

Table 5-9 Number of tiles per cell, for each tile size.

Tile #	1	2	3		4	5	6		7	8	9		10	11
Cell				**Cell**				**Cell**				**Cell**		
A1	13	13	13	**B1**	15	15	15	**C1**	17	18	17	**D1**	40	39
A2	13	14	13	**B2**	16	15	16	**C2**	18	17	18	**D2**	41	42
A3	14	14	14	**B3**	15	16	15	**C3**	18	18	18	**D3**	45	44
A4	14	14	14	**B4**	16	16	16	**C4**	18	19	18	**D4**	27	27
A5	15	14	15	**B5**	17	17	17	**C5**	20	19	20			
A6	15	16	15	**B6**	18	17	18	**C6**	20	20	20			
A7	17	16	17	**B7**	18	19	18	**C7**	21	22	21			
A8	17	17	17	**B8**	20	19	20	**C8**	20	20	20			
A9	18	19	18	**B9**	18	18	18							
A10	16	16	16											

uniformity but results in an excess of fibre that has to be accommodated inside the girder. Experience using a mock up[1] demonstrated that this option was feasible, and it is chosen as the baseline. This solution, with a relative small number of different fibre lengths, has the advantage of simplicity of fibre preparation operations.

5.3.2 Light budget

5.3.2.1 Tiles

It was previously shown in Figure 5-6 that the light output from the tiles is inversely proportional to the tile area and directly proportional to the tile-fibre coupling length. The tiles for Module 0 were the first tiles produced with areas up to twice that of the largest tiles of the 1m prototype modules. A set of 11 tiles, one of each size, was measured to get a representative parameterization of the light yield *vs* size. This parameterization was used in the light budget calculation to estimate the tile light yield.

5.3.2.2 Fibres

The light output of aluminized fibres has been parameterized as the sum of two exponential functions of the transmission distance with reflection at the far end, as discussed in Section 5.2. The parameters used were based on the measurement of 1.5 and 2 m long fibres used on the 1995 1 m prototype modules (Kuraray Y11(200)MS, with 600 ppm of UV absorber), except that the reflection coefficient was estimated from preliminary measurements of a few fibres from Module 0 production, with a value of 70%. The fibres of Module 0 are of the same type as the ones used in the 1995 1 m prototype modules. Table 5-10 shows the relative components of the short and long attenuation lengths used in the parameterization for different fibre lengths.

1. We thank Pol.Hi.Tech for the fibres given to instrument the mock up.

Table 5-10 Fibre parameters. The fibre response is parameterized with the sum of 2 exponentials (short and long).

Length (cm)	I_0^{short} (a.u.)	L_{att}^{short} (cm)	I_0^{long} (a.u.)	L_{att}^{long} (cm)
200	3.08	20.8	4.72	303
150	3.06	20.8	4.82	315
100	3.17	19.3	5.02	260
used for all fibre lengths	3.1	20	4.8	310

At any point along the length of the fibre, the deviation of the actual light output from the parameterized value may reach ±5 % (see Figure 5-34) in the fibre length range that we are most interested, which is 1.2 to 2 m corresponding to BC cells. Measurement of shorter fibres (1 m long, also in Table 5-10) showed a small deviation of the parameters, which should be taken into account in the future for more accurate light budget calculations.

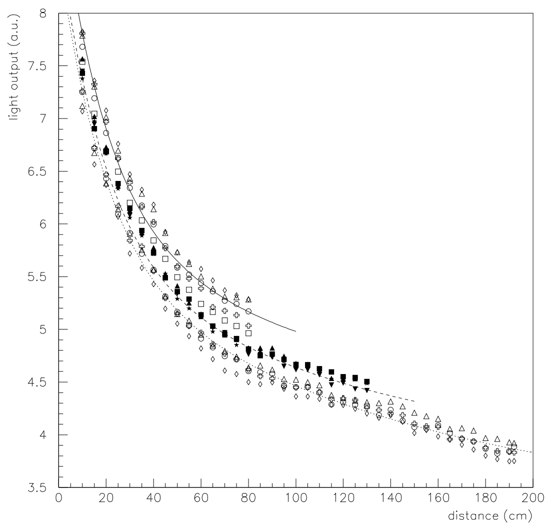

Figure 5-34 Light output for 2, 1.5 and 1 m long aluminized fibres used in the 1995 1m prototype modules. The lines correspond to the parameterization obtained for each fibre length, using the average reflection coefficient. Each symbol corresponds to one individual fibre, and the small spread obtained in sets of 5 fibres is visible.

5.3.3 Barrel configuration

After several iterations, an acceptable solution was found which provided good uniformity inside the BC cells without compromising the light output of the cells of samplings A and D. This configuration and the respective fibre lengths are shown in Figure 5-35 for Side 1 of the barrel. The fibre lengths used shown in Figure 5-35 are the minimum fibre lengths calculated for each cell, except for sub-cells C1, C2 and C6 that have an extra length of 10 cm to improve the uniformity inside the respective BC cells. A corresponding solution was obtained for Side 2 (noting that the Side 2 PMTs are displaced by 58 mm relative to Side 1). The PMT locations of the girder that are used are represented as black circles in Figure 5-35, with the respective number written above the circle. Hole 28 is not used. Under the circle, the label of the cell that is read-out by the PMT is shown. Inside the cells, apart from the respective label there are 4 numbers. The numbers at left are the fibre lengths in cm, and in front of each fibre length is the number of fibres with that length. The shorter fibre reads the intermediate tile of the cell, and the longer one reads the other 2 tiles. BC cells are described with 2 sets of numbers, one for sub-cell B and the other one for sub-cell C.

The global light output (tile+fibre) for each cell has been calculated using the tile light output and fibre light output presented in Section 5.3.2. This is shown as a function of the read-out cell for the Side 1 in Figure 5-36, where the light output has been normalized to the light output of the smaller tile of each cell. For each tile size there is a number for each cell, which is 1 for the smallest tile size of the cell and the relative light output for the other tile sizes.

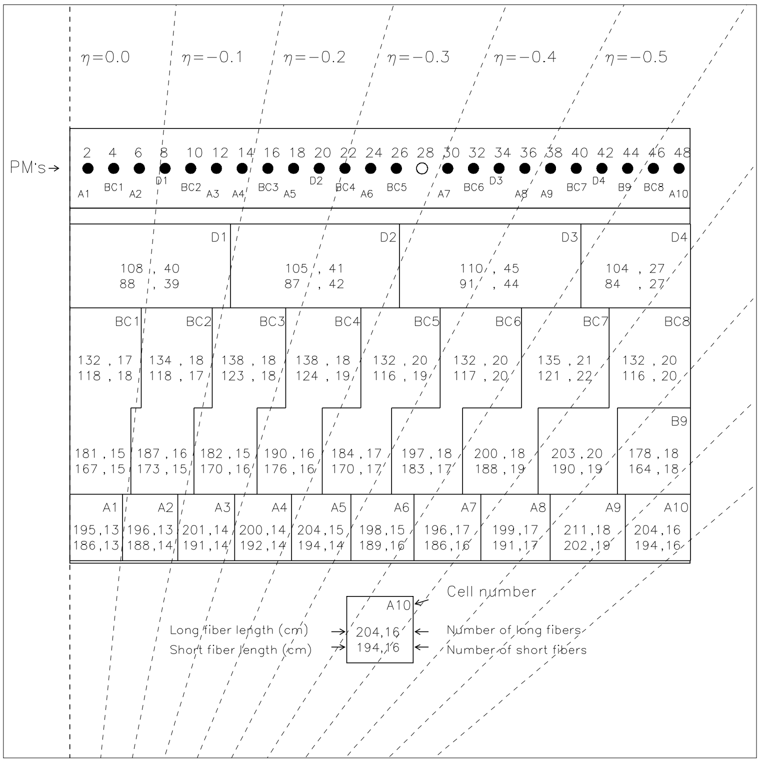

Figure 5-35 Cell configuration and fibre lengths for side 1 of barrel Module 0.

Table 5-11 Summary of lengths and quantities of fibres for barrel (B), extended barrels (EB) and ITC.

	B	EB	ITC	Total B	Total EB	Total
# half-periods	610	278	max 34	39650	18070	75790
# fibres	8	8				
Total fibres	4880	2224	102	317200	144560	619580+5%
Aver. length	155+10 cm	170+10 cm	115+10 cm			
Total length	8052 m	4005 m	130 m	523 km	260 km	1062+5%km

The resulting total fibre length for the barrel and each extended barrel is summarized in Table 5-11.

5.3.3.1 Extended barrel configuration and further developments

Two extended barrel modules will be built by July 1997, and we are preparing the optimal geometry and routing configuration for them. A baseline solution has been worked out on the basis of the experience of the barrel Module 0 and an alternative algorithm has been recently developed. This uses a routing algebra to optimize the path by which the fibre was routed to the PMT, whilst maintaining a maximum possible radius of curvature. The algebra provided a simple code by which one could easily specify this route resulting in a easy implementation. This will be evaluated during the instrumentation of the extended barrel modules and a decision on the routing design will finally be made. If necessary, one of the two extended barrel modules will be instrumented following the baseline approach and the second using this alternative ap-

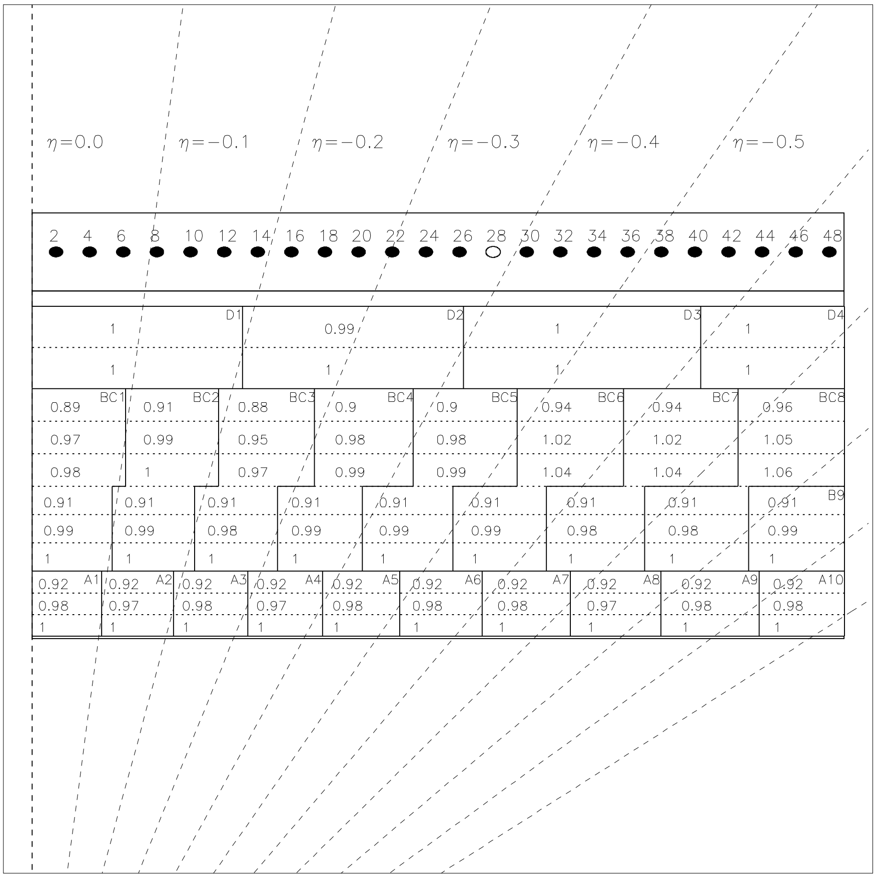

Figure 5-36 Light budget for side 1 of Module 0 (relative values).

proach to provide experimental data on which to base this decision. Mock up work has been made using both routing solutions, and this work demonstrated that both of them are feasible.

An alternative cell structure has also been proposed for the extended barrel. This has the advantage that it reduces the total (Barrel+Ext. Barrel + ITC) number of fibres by 12% and the total fibre length by about 8%. However, it has the important disadvantage that it provides a less pseudo projective cell read-out. In this case, the two options must be studied using primarily Monte Carlo data. This work is in progress and a decision will be made in 1997.

5.4 Fibre installation

The very large number of fibres needed for the detector makes the insertion task of optical fibres a repetitive and monotonous task. Manual fibre insertion was used for the 1m prototype modules and Module 0 instrumentation. Furthermore, handling of the fibres risks damage which may not be realized until after module assembly. Therefore we are investigating the use of robots to provide an automated solution which is justified in technical and manpower areas.

The technical solution proposed as baseline assumes that the optical fibres are supported by a special profile into which they are inserted by a robot handling machine. These special profiles are then assembled in the grooves between the iron master plates of the modules.

The fibre installation scheme was developed as part of the Module 0 instrumentation (with minor changes as are indicated below). The first phase consists of preparation of the module with fixtures and components more easily installed when the surface of the module is free of fibres. This consists of the following operations:

- insertion of bundle tubes and bundle rings;
- installation of rails to fix the fibre bundles;
- installation of one comb on each sub-module to organize the fibre sequence;
- installation of a fibre separator (loom) to allow an easy bundling.

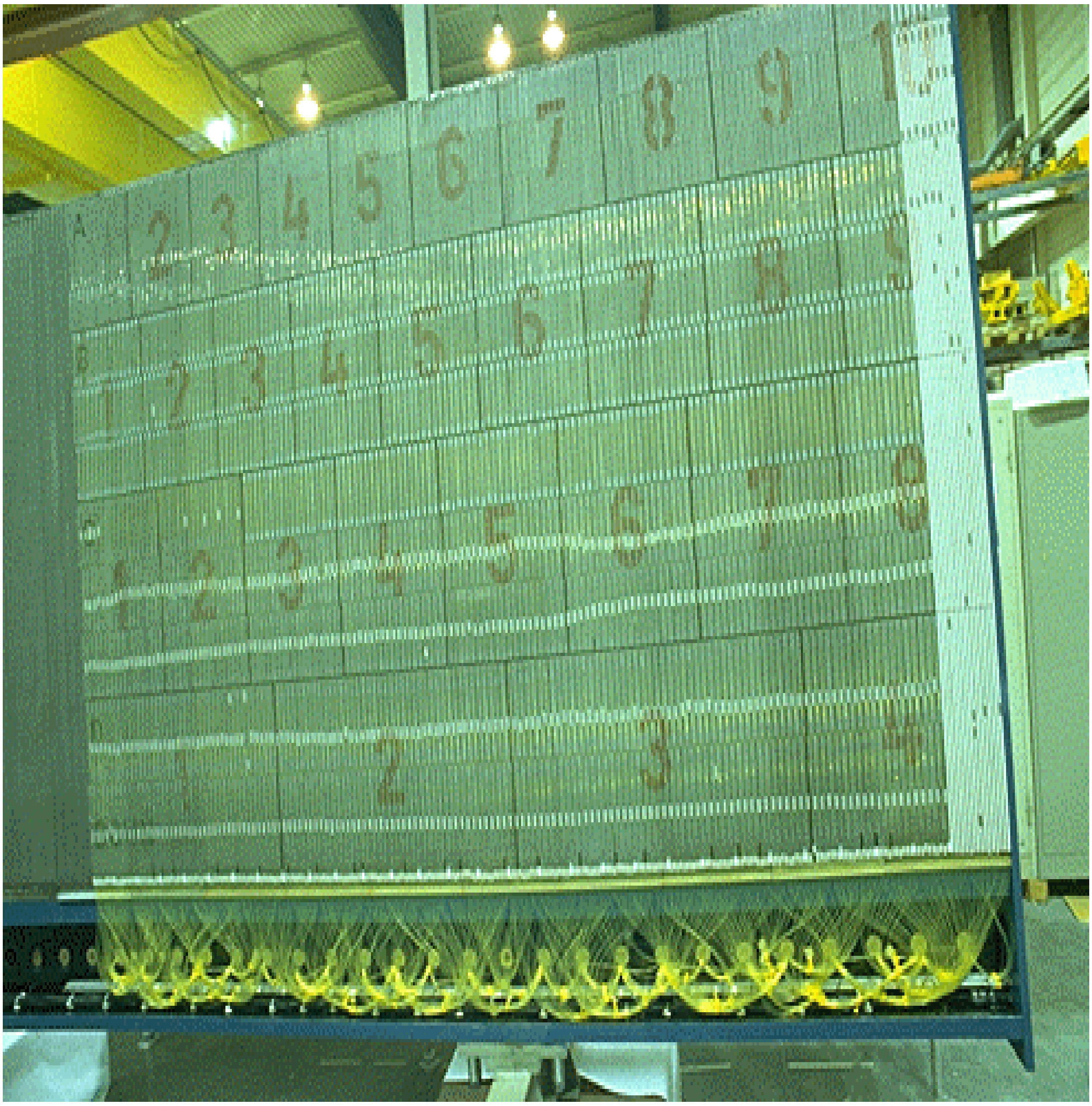

Figure 5-37 Half of the barrel Module 0 instrumented with fibres.

After the preparation of the module, the sequence of operations for the fibre insertion is the following:

- the fibres are cut and inserted into the profiles;
- the profiles are inserted into the grooves between master plates of the module;
- the fibres are organized in a well defined sequence using a comb after the exit of the profile, and sorted to identify depth and cell using a fixture akin to a loom;
- the fibres are bundled and routed to their appropriate PMT;
- the fibre bundles are glued into the bundle tubes;
- the fibre bundles are polished.

All these operations are described in detail below, as well as the Module 0 experience.

5.4.1 Module preparation

The module is installed in the vertical position, with the girder at the bottom. The boundaries of each cell are painted on the module and the PMT holes in the girder are labelled. Rails are installed along the girder. The fibre bundles will be tied to holders that are allowed to move along these rails.

Bundle tubes and bundle rings are inserted in the girder rings (see Figure 5-40). The bundle tubes are open at one of the sides and closed at the side that goes inside the girder. The fibre bundles will be inserted inside these tubes, in such a way that all the fibres touch the closed end of the tubes. These rings have different internal diameters, depending on the number of fibres of the cell. The bundle rings are inserted inside the bundle tubes, and will be used to adjust the fibre ends and during the bundle gluing procedure. Each bundle tube is screwed to the respective girder ring, and the bundle rings are left free to move inside.

Plastic combs for the fibre alignment are carefully aligned with the grooves defined by adjacent steel master plates. These plastic combs are glued to the girder using contact glue (neoprene).

A fibre separator similar to a loom is installed along the girder. The fibre separator is a structure to keep the fibres of each sample in a separated position, allowing an easy detection of insertion errors and a fast bundle making procedure. It consists of 2 supporting bars placed in the extremities of the module, located only a few centimetres higher than the bottom of the girder. The bars hold to the girder using clamps, and are perpendicular to the module. A set of wires runs from one bar to the other, spaced by about 2 cm. The wires should be soft and free of grease because the fibres will be in contact with them. The wire nearest to the girder prevents the contact of the fibres with the girder.

5.4.2 Fibre insertion

To hold the optical fibres in the fibre grooves of the modules and provide the tile-fibre optical coupling a special profile has been designed. This profile is made of a plastic material with relative elasticity in order to allow the boxing in the grooves of the modules by a simple pressure action. The profile cross section has a closed non-regular shape to allow an easy fibre insertion and routing inside the profile and to enhance the profile elasticity. Figure 5-38 shows the cross section shape of the profile, outside and inside the groove. The profile, which can be easily pressed into the groove, holds a WLS fibre against the edge of the tile. Fibres carrying light from previous layers are routed inside of the profiles, isolating them from subsequent tiles. There are profiles with 2 sizes, one adapted to the sub-periods that have a tile with size #1, and the other one adapted to the sub-periods that have a tile size #2. The latter are shorter by 10 cm, and the positions of the holes to allow the fibres to move from under the profile into it are different in the two kinds of profiles.

Systematic measurements of the module gap widths were made in one sub-module built in 1996. The measurements were taken along the gaps in steps of 5 cm. Results for the gap widths in the region of the scintillating tiles give an average of 4.20 ±0.13 mm. Similar results were obtained for the average gap widths in the spacer region but with an average of 4.34 ±0.12 mm, much higher than the nominal value 4.25 ±0.05 mm. In order to match with the realistic values, the dimensions of the profiles need still to be optimized. Additionally, preliminary results from the test beam show that when profiles are used there is a loss of about 20% of the light when compared with the situation in which the fibre is surrounded by aluminized mylar in the coupling region. Measurements in the laboratory show a light loss of 10-15% for similar conditions. It was found that this is due mainly to the shape of the profiles that are almost round in the corners in the face that is in contact with the fibres. Further development is required to make the corners sharp.

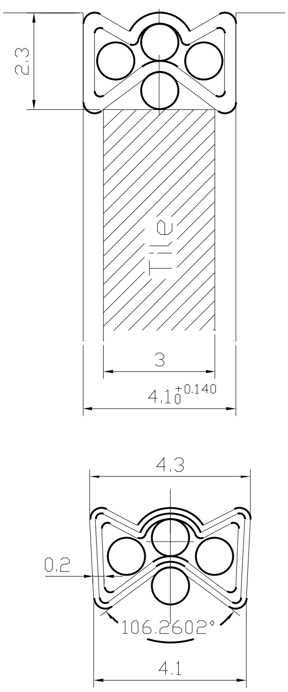

Figure 5-38 Profile cross section, with fibres. Dimensions are in mm.

In the present configuration the profiles are made of high impact white polystyrene (HIP) doped with TiO_2 to provide good diffusor reflectivity. The aluminization of the profiles in the region of the tile-fibre coupling is also being considered.

5.4.2.1 Insertion of fibres inside the profiles

The operation of insertion of optical fibres inside the special profiles has been divided in three major tasks:

- feeding and fixing the special profile into the insertion table,
- insertion of the optical fibres inside the profile,
- removing the special profile plus the fibres from the insertion table.

In order to meet the specifications, the insertion procedure has been designed to allow the simultaneous insertion of the four distinct fibres to each profile and to allow the insertion in the two types of profiles in an almost concurrent way.

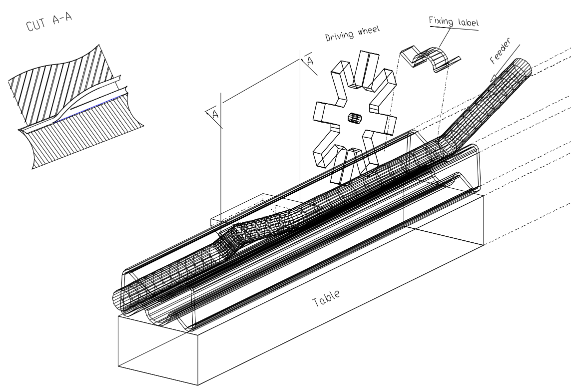

Figure 5-39 Basic principle of the fibre advance mechanism for the automatization of the fibre insertion.

The expected performance of this insertion robot will be one set of profile plus fibres every ninety seconds. This allows us to estimate an overall insertion time for the barrel and extended barrel of 18.5 months. This insertion time is critical since the overall time given in the Tile Calorimeter schedule for this operation is 18 months.

5.4.2.2 Automation tooling

The robotized system for fibre insertion in the profiles consists of two insertion tables with fixing devices to fix the profile to the table during the insertion process. These tables have horizontal motion to allow concurrent insertion of the two types of profiles using only one fibre insertion mechanism. This insertion mechanism is located in the central position, and consists of four almost identical individual fibre insertion devices. These devices operate in parallel allowing simultaneous insertion of the four fibres in each profile. It consists of the advance mechanism and the fibre storage. Figure 5-39 shows the basic principle of the fibre advance mechanism. The optical fibre storage allows up to twenty different sizes of optical fibres.

5.4.2.3 Profile installation into the grooves

The profiles will be inserted into the grooves between master plates, and the respective fibres will be sorted in a previously defined sequence in the comb and in the fibre separator. This operation is relatively easy, and requires a minimum set of tooling to put the profile in place.

5.4.3 Fibre bundles

After the insertion of the profiles with the fibres in the module, the fibres are hanging in the vertical position, in groups defined by the sampling or sub-sampling to which they belong. To form the read-out cells, the fibres have to be grouped in bundles and routed to the respective PMTs. The bundles will be gathered into a bundle tube mounted in the girder, then epoxy is injected into the tube to fix the fibres in place and allow the polishing of the bundle.

5.4.3.1 Bundle assembly and installation

The fibre bundles are made in the sequence given by the fibre separator, starting from the fibres located nearest to the girder (fibres of cells A), and finishing with the fibres of the cells D located in the outmost position of the fibre separator. In this sequence, the conflict between fibres in bundles and fibres still in vertical position is minimal.

The bundles are arranged in sub-bundles. For each bundle, typically two sub-bundles are made, one grouping the fibres located at left of the PMT, and the other with the fibres located at the right. Very wide cells require more sub-bundles, to avoid conflict between bundles. Inside each sub-bundle, the fibres are moved one by one to positions where they cross as little as possible and have minimal stress.

The fibres of each cell are grouped, and a lamp is used to check if all of them are in the correct position, illuminating the free end of the bundle and checking that the light emerges near the aluminized ends of the fibres. If it is found that there is no error, the bundle is adjusted in such a way that all the fibres have the ends together. The fibre bundle is then inserted into the bundle tube, together with the clear fibres used for laser calibration (2 per PMT). Short dummy fibres are used to complete the bundle rings, and the fibres of the bundle are held together with a cable tie protected with a sponge. This process is repeated for all the cells. Then the bundles of fibres are ready to be glued.

5.4.3.2 Bundle gluing

The steps to glue the fibre bundles are the following:

- The bundle of fibres is inserted into the 38 mm long bundle ring (see Figure 5-40). Each bundle includes 2 clear fibres from the laser monitoring system. There are two sizes of tubes, one 11.5 mm diameter that hold 103 fibres and another 8 mm diameter that holds 46 fibres. Any extra space in the ring is filled with dummy fibres.
- The fibre bundles are secured with plastic straps, leaving about 1cm outside the ring and protecting the fibre bundle with a sponge.
- The bundle ring is inserted (with the fibres) partway into the bundle tube leaving about 1.5 cm outside the tube.
- A measured amount of epoxy (Bicron 600) is injected into the bundle tube using a syringe with a long flexible tip. This tip is inserted into a groove made in the bundle ring for this purpose.

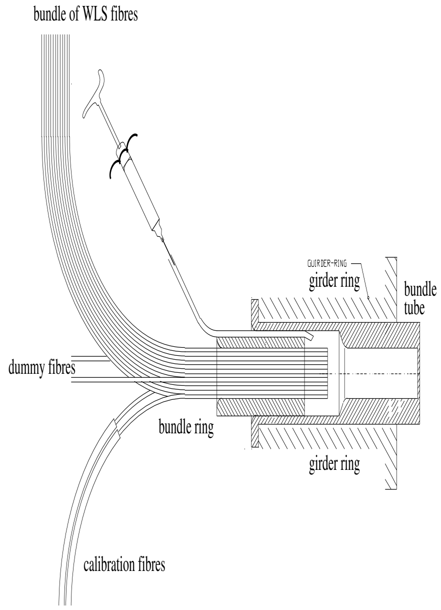

Figure 5-40 Gluing the fibre bundles. The main bundle of fibres is coming from the top. The 2 calibration fibres are coming from the bottom, and 2 short dummy fibres used to fill the bundle ring are also shown.

- The fibre bundle is pushed into the bundle tube until the ends of the fibres are in contact with the bottom of the tube.
- The bundle ring is pushed into the tube until it seat against the shoulder inside the tube.
- More dummy fibres are inserted if required to fill completely the bundle ring.

After the gluing operation, the cable ties around the bundles are removed, and each sub-bundle is tied to the still free-moving supports of the rail. Some of the bundles need some extra fixation points, and for that, self-gluing supports are positioned along the girder. When all the bundles are tied in place, the free moving points along the rail are glued using epoxy.

5.4.4 Bundle polishing

After being glued into the bundle tubes, the fibre bundle ends need to be cut to length and polished. These operations are not easy since the ends of the bundles are located inside the girder. Furthermore, the placement of the PMT block to the fibre bundle is only a few tenths of a mm, so the cutting tolerance must be quite good along the length of the entire girder.

5.4.4.1 Requirements

The bundle tubes are positioned into reference rings which are epoxied to the inside of the girder, aligned by means of a special mounting tool. This design provides good durability and rigidity, with a placement tolerance of ±0.1 mm in all directions.

With the fibre bundle protruding along the inside length of the girder, this chain of reference rings serves as a precise reference for the mating of the fibre bundles to the PMT blocks inside the drawer system. These reference surfaces are spaced by a 116 mm period and the Side 1 and Side 2 rings are shifted by half of that period. The task of the cutting and polishing tool is to provide a polished end of the bundle leaving a 0.5 ±0.3 mm excess of fibre bundle above the inside surfaces of the reference rings, along the entire length of the 5.86 m long barrel modules and the 2.86 m long extended barrel modules. The end quality of the polished bundle surface should provide more than 95% light transmission.

5.4.4.2 General design and cutting-polishing procedure

The tool consists of a robot-like device which fits inside the girder and travels from one end to the other, cutting and polishing the protruding bundles. On the main body of the tool there is a precise high speed motor-driven spindle with a combination cutting and polishing head as shown in Figure 5-41. Polished ways on the body of the tool are used to align the polishing tool on its passage through the girder in a similar manner to which the drawer is aligned to the fibre bundles. Spring loaded rollers on the sides and the top of the main body provide pressure to keep the tool aligned to the girder.

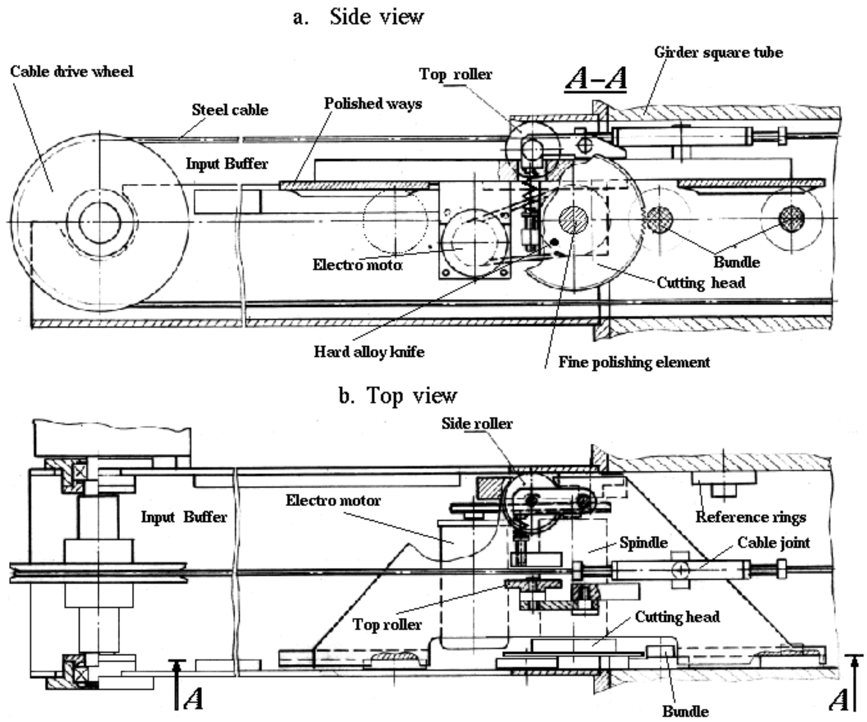

Figure 5-41 Fibre bundle cutting/polishing tool.

Cutting and polishing is realized during the continuous movement of the body of the tool which is driven by a loop of steel cable. The geared drive motor provides a speed at the level of

0.5-1.5 mm/sec. During the bundle processing, the cutting heads are positioned around 3 rings, two on the cutting side and one on the opposite side.

The cutting-polishing head consists of a saw-type cutter with an outer radius of 62.5 mm which cuts the fibre bundle to a rough height above the reference ring surface. A hard alloy milling cutter is fixed at an outer radius of 25-28 mm on the cutting head and a fine polishing element is mounted at a radius <24 mm. All these components are mounted on the massive steel holder, which is fixed on the axis of the drive spindle.

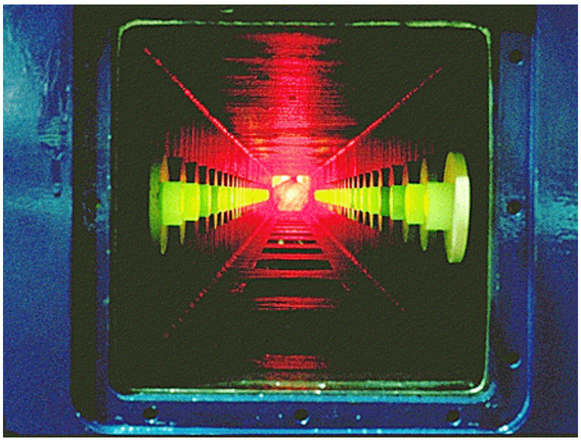

Figure 5-42 View of the Module 0 fibre bundles inside the girder before cutting and polishing.

The cutting-polishing procedure is performed in the following steps. As the cutting head moves past the fibre bundle to be cut, the saw cuts about 5 mm off the bundle end leaving an excess of approximately 0.8mm above the surface of the reference ring. As the tool moves forward, the hard alloy knife cuts approximately 0.3 mm thickness leaving the required excess of 0.5 mm above the reference ring surface. The fine polishing element in the central region of the head then takes a very fine cut to improve the quality of polishing.

Module 0 experience

Cutting and polishing tests done on a dedicated, full-scale mock up and the work done on Module 0 have given us insight into design problems and suggestions for improvement to the cutting tool. Some of the more noticeable observations during operation were the following:

- Removal of the cutting/polishing chips is very important to the smooth operation of the tool. The design of a new tool should incorporate chip evacuation;
- The positioning and placement of the reference rings is a good alignment tool, and is preferred over the use of the non-flat girder tube floor surface;

With further tests with maquettes, one needs to optimize different parameters of the tool and refine the cutting-polishing procedure. The following efforts need to be devoted to the R&D program to develop a second generation production cutting tool:

- The optimization of the spindle RPM and the choice of the cutter configuration;
- The tool placement speed to the bundle, which is coupled to the speed of the spindle;
- Obtain the minimal vertical and horizontal pressure between the girder and the tool to minimize the friction. In parallel, decide on the use of the low friction materials;
- Redesign of the tool drive system along the girder.

These efforts are underway and a prototype of the production cutting tool will be available for use in 1997 on the Module 0 extended barrels. The time for the completion of one barrel module is expected to be approximately 5-6 hours, including tooling installation on the entrance and exit of the girder.

5.4.5 Fibre installation in the Module 0

The fibre installation procedure described above was followed for the instrumentation of the Module 0, with the exception that profiles were only used for the read-out of a few tiles. In almost all the module, the fibre-tile coupling was made using the 1 m prototypes method.

From the data in Table 5-11, the fibres were cut to the correct length using a paper cutter and stored in plates grouped in bundles. Each group was labelled with their respective length, number of fibres and cell label.

Table 5-12 Time spent for insertion of the fibres in the half barrel Module 0.

Task	time for a 2 persons team
fibre cutting and insertion	4 weeks
check of cell correction and bundle making	1 day
sub-bundle making	< 1 day
adjusting fibre ends and adding dummy fibres to fill the rings	almost 2 days
gluing the fibre bundles	1 day

With the module in the vertical position, and the girder at the bottom, the fibres were inserted vertically, going down towards the girder, to avoid damage of the aluminized ends. The insertion sequence was from bottom to top, because top fibres run above bottom fibres. For each half-period, 1.5 cm long profiles were inserted at the bottom end of the steel grooves in between adjacent masters, to avoid fibre damage through contact with the sharp edges of the masters. This protection will be naturally achieved when the profiles are used.

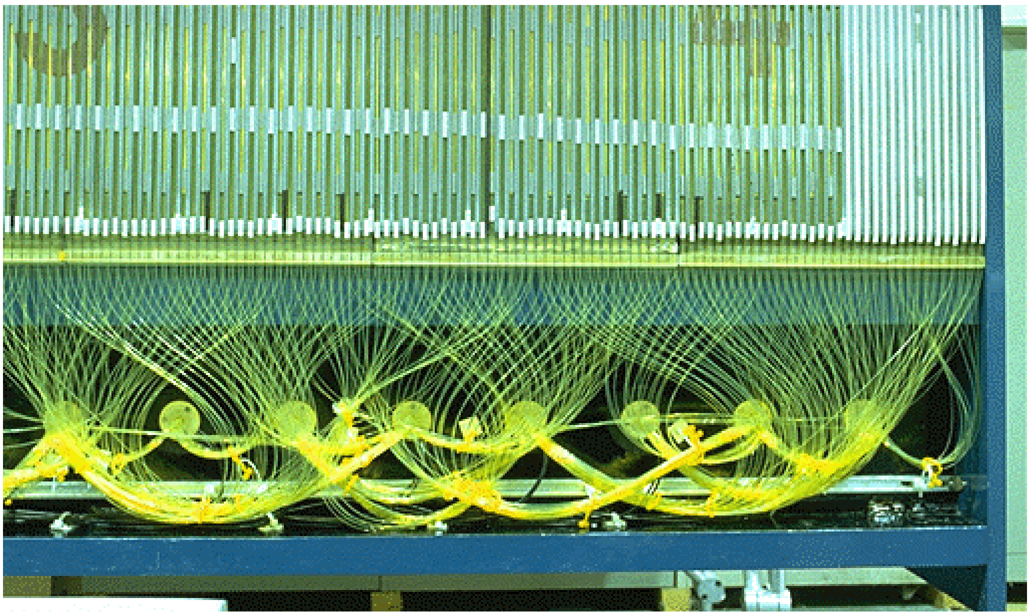

Figure 5-43 Typical fibre bundles in Module 0. The rail where the bundles are tied is visible as the bright ruler that runs along the girder. The region instrumented with profiles is seen at the top right corner of the picture.

Typical bundles obtained in the Module 0 are shown in Figure 5-43.

The approximate time to instrument half of the Module 0 with fibres is shown in Table 5-12, calculated in days for a team of 2 persons. Manual insertion of the fibres was the most consuming task, taking almost 4 weeks for the 2 person equivalent team. This amount of time will be clearly reduced once the profile scheme is implemented. We expect to fully instrument one barrel module in 2 weeks during production.

5.5 Installation of connectors and laser fibres

Each fibre bundle will be provided with two clear plastic fibres which are routed to the end of the girder to a optical connector (distribution connector). This optical connector will couple the quartz laser fibres from the laser in the control room. Each of these fibres coming from the control room is coupled to a fibre to fibre connector that can be adjusted to control the light sent to each moduleN-93. The installation of the laser fibres and the respective connectors consists of the following sequence of tasks:

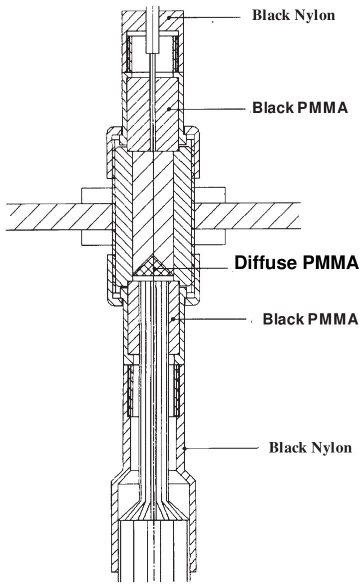

Figure 5-44 Distribution connector. One fibre coming from the laser enters at the top, and the light is distributed to a bundle of the fibres that exit at the bottom.

- Polish the clear optical fibre from the laser box,
- For each channel, glue (using fast glue) the fibre from the laser box to the input side of the adjustable connector,
- Cut, with a cleaving machine, a quartz clear optical fibre to the desired length,
- Glue (using fast glue) the quartz fibre to the output side of each adjustable connector,
- Place the adjustable connector in the patch panel,
- Put a cover, for mechanical and optical protection, over each quartz fibre,
- Glue the quartz fibre in the distribution connector (input side),
- Glue, using Bicron optical glue, the bundle of fibres (each one previously glued in a bundle for each PMT) to the distribution connector (output side),
- Polish the previous bundle,
- Place the distribution connector in the patch panel,
- Route and fix the quartz fibre.

5.6 Radiation Hardness

For the LHC operating at a luminosity of 10^{34} cm^{-2}s^{-1}, the expected maximum dose in the Tile Calorimeter coming from charged particles and neutrons is about 40 Gy/year at η=1.2[A.31].

This radiation field can affect the quality of the optical components made of plastic materials, namely the scintillating tiles and the WLS fibres. Both light yield and transmission through the tiles and fibres may decrease with increasing dose and degrade the calorimeter performance, namely its resolution. The monitoring of the calorimeter response with radioactive sources over the duration of the experiment is foreseen, will allow the recalibration of the system. Nevertheless in order to evaluate the lifetime of the detector and to select and/or optimize the tiles and fibres, radiation damage tests of these materials are mandatory.

Since the radiation field is composed of various types of particles, radiation damage tests should be performed in different types of available radiation fields (photon, electron and hadron fluxes) and at dose rates as close as possible to the realistic values (14mGy/h).

Scintillating tiles and several types of WLS fibres foreseen to be used in the Tile Calorimeter have been irradiated with different radiation fields and at several dose rates in order to assure the extrapolation to realistic conditions. The experience from other detectors was used, namely the experimental results obtained by the SDC, CDF and ZEUS collaborations for scintillating tiles and fibres made of similar materials.

5.6.1 Scintillating tiles

The molded scintillating tiles based on PSM-115 polystyrene produced at IHEP proved to be more radiation resistant than polystyrene or PVT samples produced by bulk-polymerizationN-86. Various samples of PSM-115 tiles with standard WLS dyes concentration (1.5% PTP and 0.04% POPOP), wrapped with Tyvek were exposed to radiation of different types and at several dose rates. The measurements after irradiation were compared with values before irradiation. The reproducibility was continuously monitored measuring non-irradiated reference tiles. Dosimetry was done in most of the cases with alanine dosimeters.

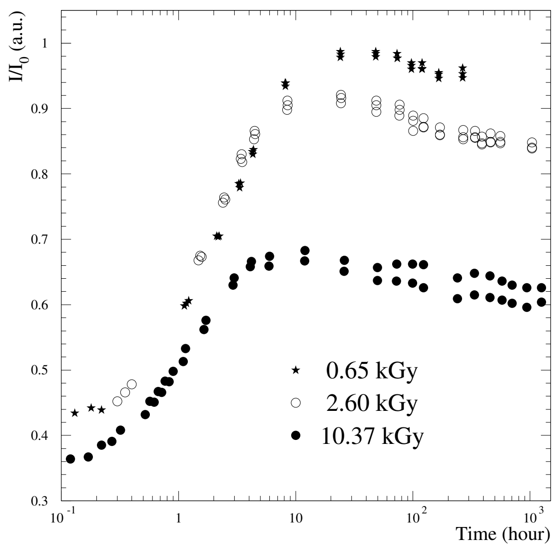

Figure 5-45 Relative light yield versus recovery time for tiles irradiated with several doses.

Irradiations with ^{137}Cs and ^{60}Co radioactive sources

Tiles of $3 \times 50 \times 170\ \text{mm}^3$ were irradiated uniformly in a flux of ^{137}Cs source at a dose rate of 216 Gy/h, at room temperature in air. The tiles were exposed at different doses, from 0.65 kGy to 10.4 kGy. The measurements were done at different distances from read-out fibres (not irradiated) at regular time intervals starting just after the end of irradiation. In Figure 5-45 the recovery of light output after irradiation, followed by some degradation and finally stabilization is illustrated. Typical values for the permanent damage are shown in Table 5-13.

Similar tests were done in a ^{60}Co source using the same type of tiles with $3 \times 100 \times 200\ \text{mm}^3$ dimensions. The tiles were irradiated uniformly at a dose rate of 16 Gy/h and dose of 3 kGyN-2. The ratio of light output some hours after irradiation and before irradiation is about 0.96, an optimistic value when compared with the results presented in Table 5-13.

Irradiations with hadrons

Table 5-13 Ratio of light output after irradiation and before irradiation for x=13.5 cm and dose rate = 216 Gy/h.

Dose(kGy)	I/I0(20min after ir.)	I/I0(10h after ir.)	I/I0(> 4d after ir.)
0.65	0.45	1.0	0.95
2.6	0.45	0.92	0.85
10.4	0.37	0.70	0.60

Tiles were exposed to a flux of secondary particles (mostly soft hadrons) originating from the internal Al-target of the 70 GeV IHEP proton accelerator. The dose rate was about 72 Gy/h - 108 Gy/h. The experimental results indicate that the hadron irradiation may cause a higher level of radiation damage in comparison with γ-irradiation for doses over 1 kGy but it is necessary to improve the accuracy of dosimetry for more precise conclusionsN-86.

5.6.2 WLS fibres

Several types of fibres are potential candidates to be used in the Tile Calorimeter, and samples of almost all the candidate fibres have been irradiated in a ^{60}Co source or in a nuclear reactor.

Irradiation with a ^{60}Co source

The irradiation facility is equipped with several lead shieldings in order to obtain large regions of uniform radiation field (about 2 m x 0.5 m) and 3 different dose rates: position A with a dose rate of 40 Gy/h, position B with 11 Gy/h and position C with 5.5 Gy/h. The smallest dose rate is still much higher that the expected one for the Tile Calorimeter at the ATLAS experiment, but a compromise between low dose rate and time for the test has to be established(N-78,N-84).

Fibres with a length of 2 m were irradiated with the following dose profiles: a negligible dose rate between 0 and 50 cm (<2 Gy/h for position A and <0.3 Gy/h for positions B and C) and a mean dose of ~1.4 kGy in the last 150 cm for all the irradiation positions. The fibre light output was measured before and after irradiation. The summary of the results for the light loss at distances of 180 cm for the irradiations with the 3 dose rates is shown in Table 5-14.

Table 5-14 Ratio of the light output - R(180) - after and before irradiation at a distance of 180 cm from the PMT. Fibres were irradiated with an uniform dose (~1.4 kGy) between 50 cm and 200 cm, and measured 4 hours and 60 to 90 days after the end of the irradiation. Rc(180) is the same as R(180) but calculated from the attenuation lengths measured before and after the irradiation using one single exponential function.

Fibre type	A, 4 h	A, 90 day	B, 4 h	B, 60 day	C, 4 h	C, 60 day	Rc(180)
BCF99-28 No UVA	0.78	0.86	0.74	0.85	0.78	0.82	0.84
BCF 600 ppm UVA	0.72	0.79	0.67	0.77	0.72	0.74	0.79
BCF91-A	0.84	0.81	0.76	0.83	0.79	0.74	0.78
Y11(200)MS	0.82	0.90	0.83	0.93	0.86	0.89	0.91
Y11 1000 ppm UVA	0.77	0.87	0.81	0.90	0.84	0.87	0.90
S048-100-4	0.39	0.57	---	---	0.54	0.62	0.66
S048-100 UVA	0.58	0.77	---	---	0.71	0.78	0.77

The last two columns of Table 5-14 show respectively the relative light output at 180 cm, R(180), measured for dose rate C after 60 days of recovery, and Rc(180) calculated using the attenuation lengths of the fibres (taken from single exponential fits) before and after irradiation. The measured and calculated values for each fibre are very similar, showing that for these long fibres (length > 1 m) the main damage comes from degradation of the attenuation length.

The results do not show clear dose rate effects. However we point out that the S048-100 fibres tend to have a higher degradation just after the end of irradiation (4 hours) for higher dose rates than for the lower dose rates. No dose rate dependence was observed in the permanent damage (60 to 90 days after the end of irradiation), up to $\pm 5\%$.

Figure 5-46 and Figure 5-47 illustrate one set of measurements done with the smaller dose rate, and the radiation damage of fibres without UVA and with UVA are compared. As it is shown, S048-100 fibres with UVA are radiation harder than the S048 without UVA, but that is not the case for the other types of fibres.

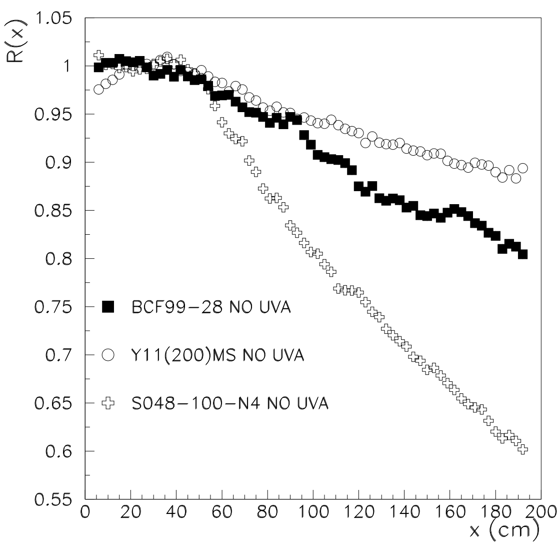

Figure 5-46 Ratio light output after/before irradiation for typical fibres without UVA, irradiated in a ^{60}Co source at a dose rate of 5.5 Gy/h and a total dose of 1.4 kGy.

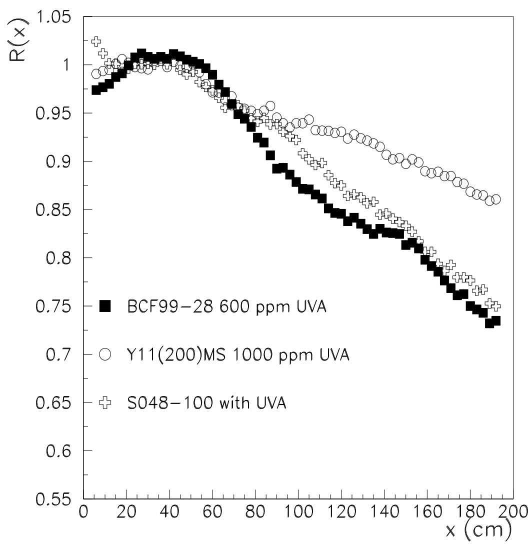

Figure 5-47 Ratio light output after/before irradiation for typical fibres with UVA, irradiated in a ^{60}Co source at a dose rate of 5.5 Gy/h and a total dose of 1.4 kGy.

Among the fibres without UVA, the Y11(200)MS fibres are the least damaged losing between 7% and 11% in light output at x=180 cm. The BCF99-28 fibres lose between 14% and 18% and the S048-100-N4 fibres lose 38% to 43%. For the fibres with UVA, the Y11(200)MS fibres with 1000 ppm of UVA are the less damaged losing between 10% and 13% in light output at x=180 cm, the BCF99-28 fibres with 600 ppm of UVA lose between 21% and 26% and the S048-100-N4 fibres lose about 22%.

Irradiation in a nuclear reactor

Single and double clad Bicron BCF91A (1995 production) and Kuraray Y11(200) fibres (1993 production), were irradiated in the mixed field (80% γ + 20% neutrons) of the Portuguese Research Nuclear Reactor (RPI). Five 150 cm long fibres of each type were tested. A non-uniform dose between 100 and 150 cm with a 'peak' total dose of 10 kGy and dose rate of about 15 kGy/h was applied. Table 5-15 summarizes the preliminary results obtained for the ratio R(x) at x = 130 cm.

Table 5-15 Relative light yield at 130 cm for fibres irradiated in a reactor with a mixed field of γ and neutrons versus the time after irradiation.

Fibre type	1 hour	3 hours	20 hours	6 days	20 days
BCF91-A	0.26	0.30	---	0.76	0.79
BCF91-A DC	0.37	0.40	---	0.76	0.76
Y11(200)	0.20	0.22	0.60	0.70	0.72
Y11(200)M	0.19	0.22	0.64	0.70	0.72

The recovery process was monitored between 1 hour and 20 days after the end of the irradiation. The initial damage is very strong (of the order of 70-80%). The fibres recover in about 6 days to the permanent damage, since no difference was observed between 6 days and 20 days after the end of irradiation. The permanent damage is 28% for the Y11(200) fibres (single and double cladding), and somewhat smaller for the BCF91A fibres (21% for double cladding and 24% for single cladding). Single and double clad fibres show similar permanent damages.

Summary on fibre irradiation tests

No dose rate effects were observed, at least in the range of dose rates and in the conditions of these experiments. For some fibres, the damage induced by γ radiation is similar to the damage induced by neutrons, as far as the dose is the same and the conversion flux-dose is realistic. Double and single clad fibres irradiated in a mixed field of γ's and neutrons showed similar damage.

Fibres with a length of 2 m irradiated with a uniform field of 1.4 kGy along 150 cm (the 50 cm near the photodetector are not irradiated) suffer mainly from degradation of the attenuation length. At the distance of 180 cm the best tested Kuraray fibres lose about 10%. The best fibres from Bicron lose about 15%, and Pol.Hi.Tech lose about 25%.

5.6.3 Radiation hardness of scintillating tiles and WLS fibres

Several tile/WLS fibres assemblies in the TILECAL configuration were also irradiated in a ^{60}Co source. PSM-115 tiles of $200 \times 100 \times 3\ \mathrm{mm}^3$ and $350 \times 100 \times 3\ \mathrm{mm}^3$ were irradiated almost uniformly with a dose of about 3 kGy, and the dose rate was 16 Gy/h.

Two fibres of the same quality coupled to the tile are used in the measurements. The light reduction after irradiation for 2 tile/fibre assembly types (PSM-115 with BCF91A and with Y11(200)M fibres) is about the same in both cases within the experimental errors. With the BCF91A fibres the light loss one day after irradiation is about 14%, and with the Y11(200)M the reduction is 11%N-6. These values increase to 22 and 19% respectively one month after the irradiation. This light loss for the assembly PSM-115/Y11(200)M is consistent with similar results obtained by the SDC collaboration for the tile assembly SCSN81/Y7. The SDC have measured the light loss for a wide range of doses and the data obtained can be parameterized approximately with the sum of two exponentials. The relative light output after/before irradiation is given approximately by $R = 0.824 \cdot e^{-D/43} + 0.157 \cdot e^{-D/1.35}$ where D is the dose in kGy([A.25],[A.31]). The data obtained irradiating the injection molding tiles and the most radiation hard fibres are in good agreement with this parameterization for doses of the order of the kGy, but for higher doses (about 10 kGy) the value of R obtained for our scintillator is smaller than the one calculated from the parameterization.

5.6.4 Future R&D

Search for polystyrene and dopants to produce the tiles are underway. Tiles with new products will be irradiated and tested. New fibres are being produced by both Bicron and Pol.Hi.Tech. The new fibres will be irradiated and tested and the final choice of fibres will be dependent also on those results. Radiation damage tests of fibres under mechanical stress are important and will begin very soon. The most typical fibres will be tested.

5.6.5 Light loss and performance degradation

To evaluate the effect of the radiation damage on the performance of the calorimeter, jets of 300 GeV were generated using GEANT and FLUKA in the ATLAS configuration (Liquid Argon em and Tile hadron Calorimeter). For 10 years of running at LHC, a light loss due to radiation damage of about 5% is expected in the tiles of the first longitudinal sampling, and less for the other tiles. Using those results, and assuming no radiation damage for the Liquid Argon em Calorimeter, the loss in the jet signal is 2% and the energy resolution changes from 2.73 to 2.97% (2.89% after recalibration), which is a negligible degradation[A.31].

5.7 Scintillators and fibres for high η end of ITC

At high η values, 1.0-1.6, the ITC consists of scintillator only due to severe space constraints. The gap scintillators between 1.0-1.2 and the crack scintillators between 1.2-1.6 will be discussed below along with their proposed read-out. While the plug sub-modules and the gap scintillators primarily provide hadronic shower sampling, the crack scintillators play a critical role in sampling electromagnetic showers. They are located in the transition region between the barrel and endcap electromagnetic calorimeters and sample showers occurring in the dead material of the cryostat walls and in the inner detector cables. The energy sampled by these tiles are added to the energy measured in the rest of the Tile Calorimeter.

There is 1 ITC per extended barrel module for a total of 128 modules. The baseline design calls for 2 gap and 2 crack tiles (for segmentation in η) per module for a total of 256 gap tiles and 256 crack tiles. The segmentation for each of the gap tiles is 0.1×0.1 in $\Delta\eta \times \Delta\phi$, while the crack tiles are 0.2×0.1 in $\Delta\eta \times \Delta\phi$. The shape of these tiles will be trapezoidal, with the gap tiles about 330 mm in η and 250 mm in ϕ while the crack tile will be about 345 mm in η and 240 mm in ϕ. The space constraints limit the maximum thickness of the gap and crack assemblies, including the light tight covers, to 20 mm for the gap and 8 mm for the crack. The gap tiles will have a thickness of 12 mm, and the crack tiles will have a thickness of 4-6 mm.These tiles may be produced either by injection molding or by conventional casting. A study is currently underway to determine which technique is preferable under constraints of low cost and high light yield.

The design of the scintillator sections of the ITC will be optimized for the highest light yield using the fewest number of fibres, all in a very compact profile. The light budget required for these tiles is around 5 photoelectrons/mip. The requirement comes from the need to calibrate these tiles with a certain precision using muons and from the need to use the same electronics for all parts of the Tile Calorimeter. This value should be attainable based on our experiences with D0, CDF, and the midsampler in the April, 1996, testbeam run. Furthermore the uniformity of response across the tile surface should be better than 5%.

An issue not yet resolved is the design of the read-out fibres which couple the scintillator sections to their read-out phototubes. Intrinsic to this design is the use of a light tight optical connector coupling the green WLS fibres in the tiles to clear fibres running along the ϕ gap into the respective PMTs. For the baseline design, three additional PMTs are needed for each ITC module: two to read out the two separate crack tiles, and one to read out the pair of gap tiles. Since the fibre bundle is small from these regions, we are considering the use of smaller, less expensive photomultipliers. The plug section of each ITC will contain, running along both ϕ edges, a bundle of 10 clear fibres of 1 mm diameter, with optical connectors fixed to the plug sub-module at its inner radius. One connector will receive the WLS fibres from the crack tiles, the other from the gap tiles. The connectors allow the crack and gap tiles to be easily installed or removed from the detector.

Several designs for the tiles-fibres coupling are being considered. One design for the crack tiles will have WLS fibres attached to their ϕ edges with the fibres formed into a ribbon. Fibre ribbon connectors will be used to mate into one of the optical connectors fixed to the plug. Another design being considered will have a sigma groove machined into the surface of each of the two tiles, and two WLS fibres placed in this groove. The fibres will be routed to the connector. For the gap scintillators, two different designs similar to the crack scintillators are being considered. In the sigma design, the two pair of fibres from the gap tiles will be routed to the other connector. The second option is the use of multi-fibre ribbons running along the middle of the gap tiles which are split into two pieces ~0.05 in η to make room for the source tubes. The use of multi-fibred connectors will allow us the option to increase the number of coupling fibres should the light level not be sufficient. The choice between the sigma grooves and the ribbon fibre will be experimentally determined in 1997.

The maximum radiation exposure in this region is approximately 10 kGy over the course of a 10 year run. Such a dose would result in a decrease of light yield by at least a factor of 2. We expect to replace the crack tiles every four to five years due to radiation damage. The construction, installation and fibre routing has been worked out in order to facilitate the easy removal and installation of these tiles.

Two ITC sub-modules are to be fabricated for use with the extended barrel modules being built for testing in the 1997 testbeam.

5.8 Production plan and schedule

The optical elements for the Tile Calorimeter have been developed or searched in the market and tested by the participating institutions. Design of the optical read-out with the best integration of the optical elements to allow the maximum performance of the calorimeter has been made. The R&D work either in the elements or in the design is not yet finished, and will continue until the production phase that will start in 1998. The schedule for the optics is shown in Figure 5-48.

The scintillator will be produced by injection molding technique in one institution, starting in 1998, and the production will be made during a period of 4 years. The scintillating tiles will be wrapped in the same place at the same rate of the production.

The decision on the fibre choice is not yet made. The R&D on this item will continue for 2 years more. Then one or more producers will be selected for the production. The fibre preparation will be done in 2 institutions.

There are 3 instrumentation plants, one for the barrel and 2 for the extended barrels. The wrapped scintillators and the fibres inserted in the profiles will be send to the instrumentation plants. The time foreseen for the instrumentation of the optical elements is 2 weeks per module.

The full instrumented modules will be tested with a cesium source.

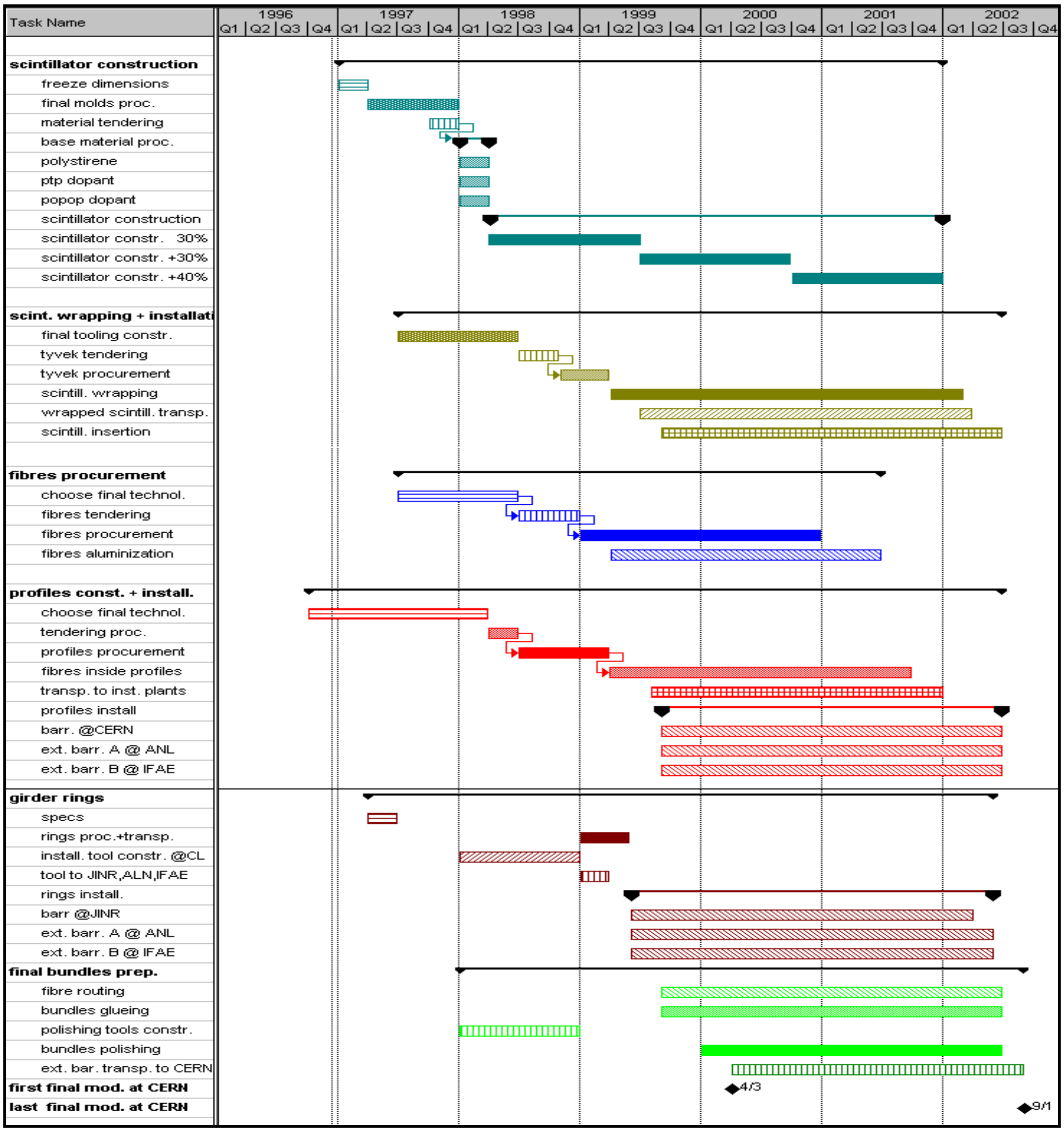

Figure 5-48 Schedule for optics operations.

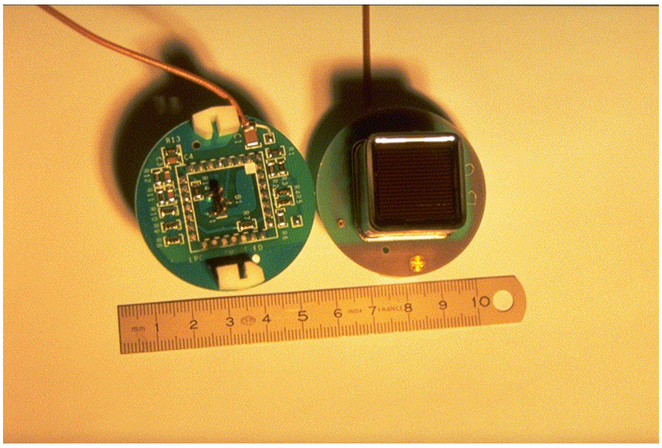

Figure 6-i A photomultipiler with its base.

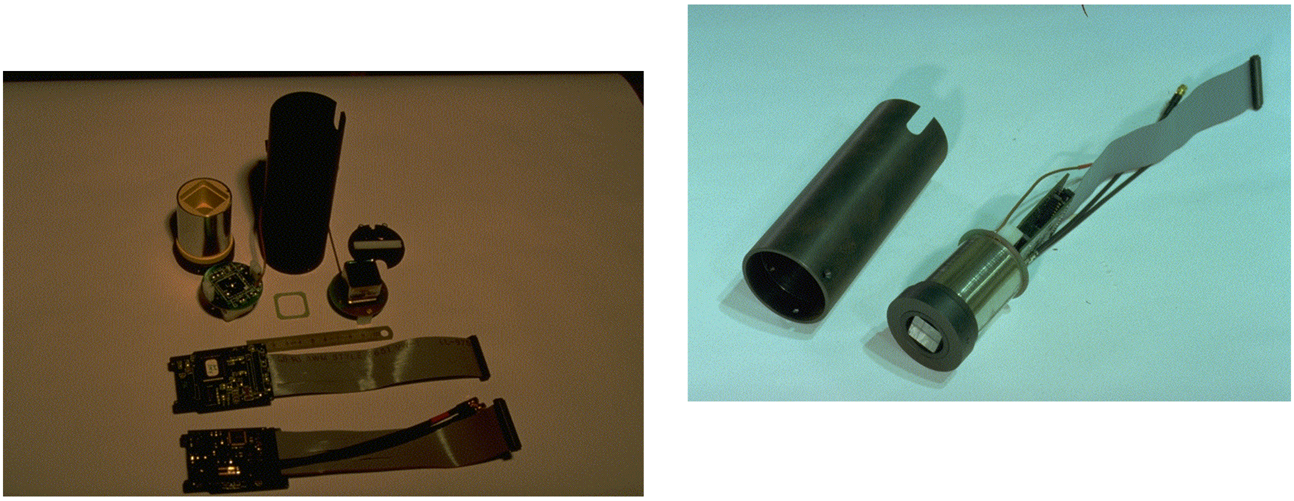

Figure 6-ii The components of a photomultiplier block before (left) and after assembly (right).

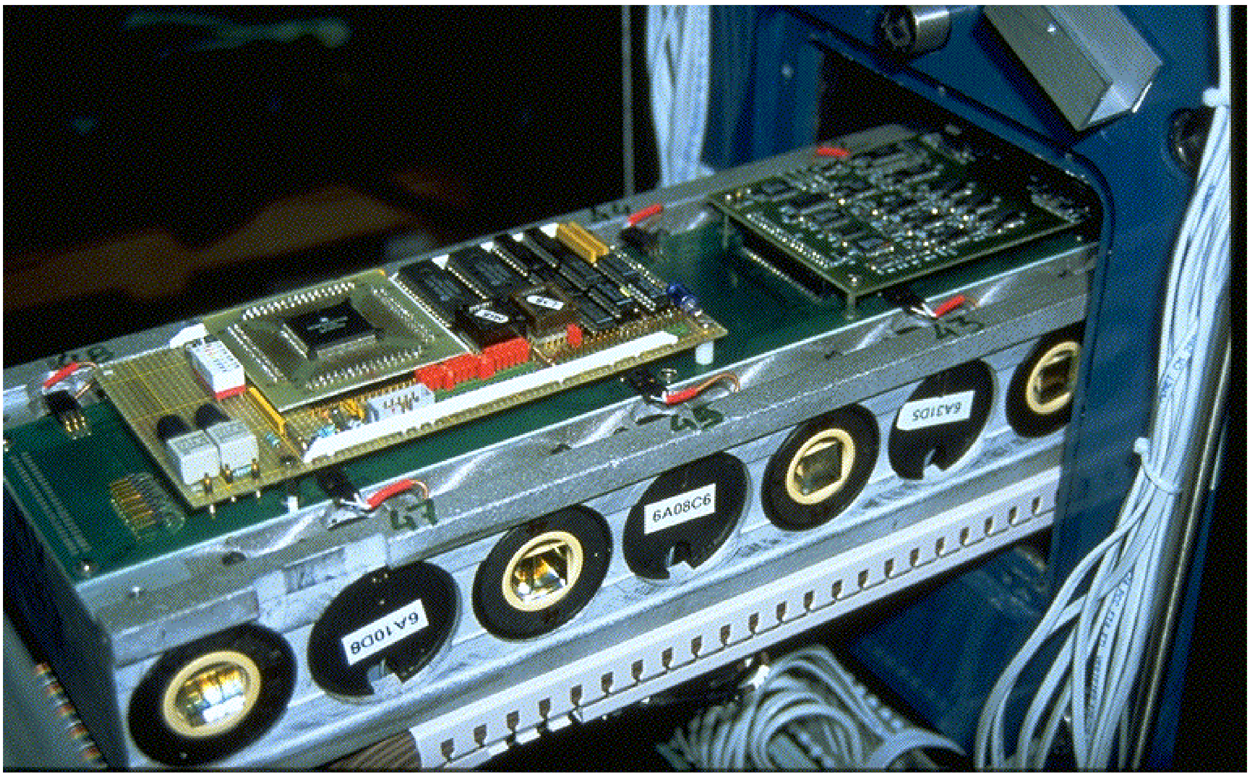

Figure 6-iii The fully equipped drawer during insertion in the girder.

6 Electronics

6.1 Introduction

6.1.1 General requirements

The electronics for the Tile Calorimeter read-out are designed to take advantage of a fast light read-out, with low noise and a limited number of channels. The overall design is simple and compact; all front-end and digitizing electronics are situated in the back-beam region of the calorimeters on a system of removable super-drawers containing up to 24 pairs of PMTs. Phototube HVs are locally regulated. Pipelines and digitizers are located locally, and the digital information is transferred to the RODs in the counting room via a few cables or optical fibres. A schematic of the read-out flow is shown in Figure 6-1.

Each cell of the Tile Calorimeter is read-out by two PMTs in order to provide redundancy in the light read-out and improve spatial uniformity. The total number of channels is approximately 10 310, which includes 3% spare parts and 1 spare module for each of the sections of the Tile Calorimeters. The breakdown is given in Table 6-1

Table 6-1 Breakdown of Tile Calorimeter read-out channels. A super-drawer physically consists of 2 drawers.

	Number of Calorimeter Cells[a]	Number of Read-out Channels	Number of Super-Drawers
Barrel Wedge	46	92	2
Total Barrel	*2990*	*5980*	*130*
Extended Barrel Wedge	14	28	1
Total Extended Barrel	*1820*	*3640*	*130*
ITC Wedge	3	3	
Total ITC	*390*	*390*	*Read-out via Extended Barrel super-drawers*

a. Including spares: 65 wedges/barrel, 65 wedges/each extended barrel, 65 wedges/each ITC.

Input signal characteristics

The light read-out is fast because the light is produced by scintillating tiles and WLS fibres, giving a signal with a typical rise time of 5.5 ns and a width of about 17 ns. This speed is mainly determined by the properties of the fibres. The measured transit time shift of the light along the three sampling depths is small (approximately 2 ns), and the electronic output signals are provided by very fast PMTs with a rise time of ~1 ns and a transit time of ~2 ns.

The light read-out before the shapers has a very low noise level due to the use of PMTs with dark currents of less than 100 pA at their nominal gains. The shaping section, which is the dedicated interface between the PMTs and the pipeline, must be made as noise-free as possible in order to allow measurements of low-energy signals, such as those from muons.

Dynamic range

From test beam results, we expect the photoelectron yield will be at least 50 pe/GeV. Detailed simulations have shown that at full luminosity, several events per year will deposit the equivalent of 1.5 TeV in a single cell, while energetic muons typically deposit 350 MeV in a single cell. This implies a 16 bit dynamic range for the Tile Calorimeter energy measurements. At the same time, the energy resolution of the Tile Calorimeter is such that an electronics precision of 10 bits is adequate to measure the largest signals.

Minimum bias noise

The pile-up noise from minimum-bias events depends strongly upon the radial sampling and the luminosity. At full luminosity, the RMS noise corresponds to about 90 MeV and 7 MeV in the inner and outer radial samplings in the barrel section of the Tile Calorimeter.

Environmental requirements

The design of the electronics read-out is constrained mainly by the available space, residual magnetic fields from the solenoid and toroids, and radiation. All of the Tile Calorimeter read-out electronics in the ATLAS cavern are located inside the calorimeter modules, within the iron girders which also serve as the first level of magnetic shielding for the PMTs.

The remnant magnetic fields inside the drawers are not equal in every direction or location, but they are always below 20 Gauss. The most sensitive components, such as the PMTs and their individual HV regulation system, must be arranged or designed for these specific conditions in order to maintain a cell calibration accuracy of 1%

Monte Carlo simulations of radiation levels show that the iron of the hadronic detector itself (and in addition the large amount of plastic tiles) considerably reduces radiation levels inside the girders. The maximum expected dose from 10 years operation at full luminosity is about 20 Gy. Radiation-tolerant electronics should be adequate for this, but explicit tests are planned.

The large iron mass of the Tile Calorimeter contributes also to the temperature stability inside the modules, but a dedicated cooling system must evacuate heat dissipated by the electronics, maintaining stable local temperatures to within 1^{o}C. The local temperatures on the integrated circuits must in any case not exceed 40^{o}C.

Calibration

The electronics calibration must have a precision much better than that of the upstream calibrations, which include the Cesium source system (1% precision) and the laser system (0.5% precision). Different calibration requirements exist for the electronics calibration systems, which include charge injector pulse analyses for physics, and current measurements for HV calibrations.

Trigger

The trigger requirements are dependent upon the choice between a digital and an analog solution. There is no intrinsic trigger limitation in the digital approach, so the minimal analog approach is considered in this Chapter. Inside a trigger tower, the electronic noise is about 35 MeV, which is near the minimum bias noise at high luminosity.

The minimum energy sensitivity in a trigger tower is supposed to be 1 GeV, so considering a calorimeter energy resolution not lower than 50% it appears that a 25% electronic resolution is adequate. The highest trigger signals before saturation correspond to about 250 GeV. Thus in a single tower the dynamic range for a bunch crossing identification is about 250:0.25 = 1000. Therefore a 10 bit dynamic range is suited to a level-1 trigger tower capability from 1 to 250 GeV.

6.1.2 Chapter overview

In this Chapter, the various components of the Tile Calorimeter electronics are presented in the following order:

- The PMT blocks
- The drawers and super-drawers
- The fast pulse electronics
- The calibration electronics
- The power supplies

Finally the production plans for the components and the assembly schedule are given.

6.1.3 Read-out organization

The general design of the electronics read-out is based upon two modular sub-systems: the PMT blocks and the super-drawers:

The PMT block is an assembly of three main parts: a light mixer, a PMT, a divider, and a so-called 3-in-1 base. The PMT block is contained within a cylindrical shell which acts as magnetic shielding. The 3-in-1 base contains:

- A fast shaper electronics interface between the PMT and the pipeline dedicated to the pulse analysis,
- A slow integrator circuit for measuring the current from Cesium calibrations and minimum bias events,
- Control logic.

The 3-in-1 base is directly connected to the PMT via the divider which works as a socket for the PMT without using any cables, minimizing noise and connection faults, and helps reduce the time and cost of assembly.

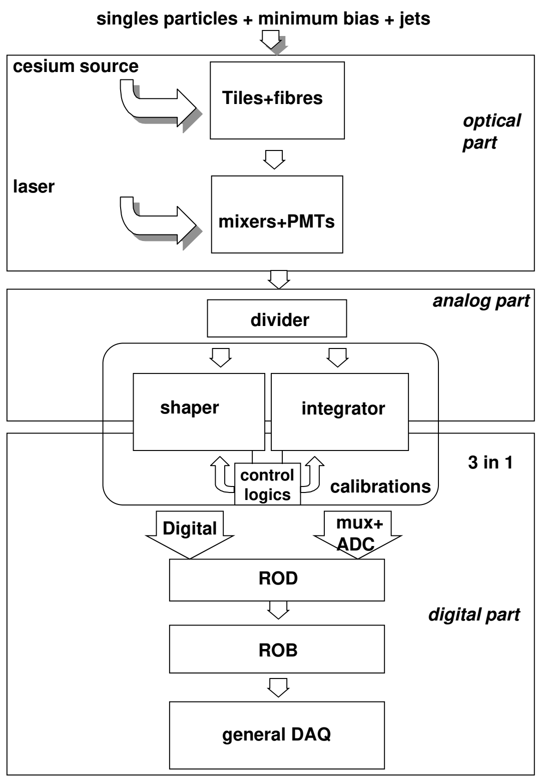

Figure 6-1 General scheme of the Tile Calorimeter Read-out

The super-drawers are located inside the back beam of the Tile Calorimeter modules and contain the PMT blocks, the pipelines, and the HV distributors. Each super-drawer consists of two physical drawers, which are coupled from the electronics point of view. There are 256 super-drawers in ATLAS, with up to 24 PMT blocks in each drawer. In Figure 6-2 it can be seen that there is a super-drawer for each half-barrel module and for each extended barrel module. The movement of the end-caps by more than 2 meters allows drawers in the barrel to be extracted for maintenance. Access to drawers in the end caps is possible from the outside, and only requires movement of the toroid. The electronics boards for the individual HV adjustments of PMTs are connected on long bus boards mounted on the side of each drawer, while the digitizing electronics cards are connected to equivalent mother boards (which are half the length of the HV controller boards) on the opposite side of the drawer.

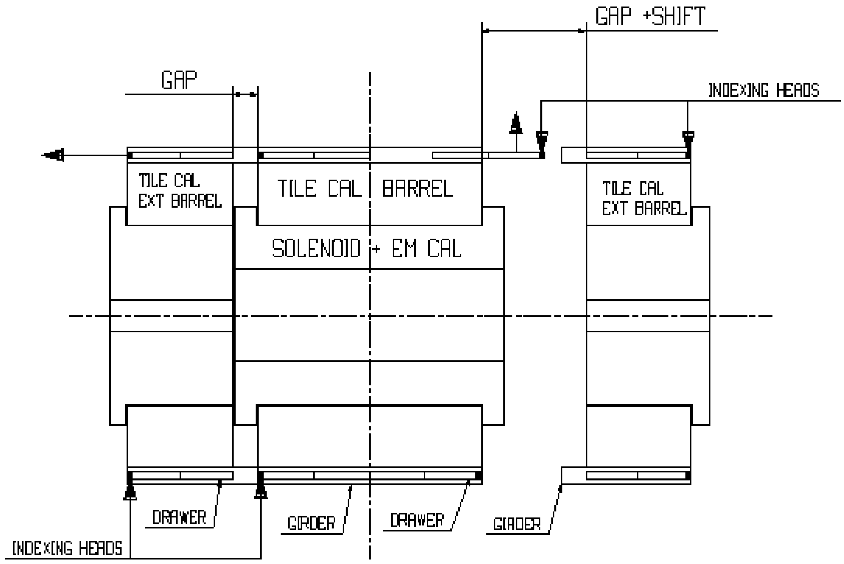

Figure 6-2 Location of the super-drawers in the Tile Calorimeter, showing access possibilities.

The only Tile Calorimeter electronics outside the super-drawers are located in the electronics room, and consist of the HV source power supply, the Level-1 trigger, the Tile Calorimeter Read-Out Drivers (RODs), and the control electronics for the three calibration systems. The location of the low voltage power supplies is yet undetermined, and largely depends upon the magnetic environment in the cavern.

The general scheme of the calorimeter read-out is given in Figure 6-1. The electronics are divided into three main sections:

- The optical part, consisting of the PMTs and the electronics for the Cesium source and laser calibration systems,
- The analog part, including the 3-in-1 base, the electronics for calibrating the shaper and integrator, and the HV power supply,
- The digital part, including the pipelines and the standard ATLAS read-out scheme (ROD and ROB).

The Level-1 calorimeter trigger segments the calorimeter into towers with size of around 0.1 x 0.1. In the Tile Calorimeter, trigger towers are incomplete for angles near the gaps between the barrel and extended barrel, but complete elsewhere. The complete towers consist of five phototubes in a 2+2+1 partition in the three layers, and cover the rapidity ranges $-0.7<\eta<0.7$ in the barrel and $1.1<|\eta|<1.3$ in the extended barrel. The incomplete towers correspond to the gap regions $0.7<|\eta|<1.1$ and $1.3<|\eta|<1.6$. In the range $0.7<|\eta|<1.1$, towers contain 4 phototubes (2 each in the first and second layer), while in the range $1.3<|\eta|< 1.6$ towers contain 3 cells (2 in the second layer and one in the third layer). Trigger thresholds are expected to be lowered for energy deposits in incomplete towers. The total number of trigger towers is about 2000. Details of the trigger scheme are presented in Section 6.4.6.

6.2 PMT Blocks

The function of a PMT block is to convert light signals from the calorimeter cells into electronic signals. Each PMT block contains a photomultiplier tube, the light mixer which serves as the interface between the PMT and the fibre bundle, a high-voltage divider, and a 3-in-1 base which is the interface with the electronics read-out (see Figure 6-3). The light mixer views the fibre bundle across an air gap less than 1 mm. There is one PMT block assigned to each of the 10 010 fibre bundles in the Tile Calorimeters. A conceptual drawing of the features of a PMT block are shown in Figure 6-3.

The specifications, designs and tests of the main components are presented in the following sections. Several considerations must be taken into account in the design of the PMT blocks:

- The PMT block is installed in a dedicated hole inside a drawer. Its length must not exceed the 145 mm width of a drawer, and its diameter may be no more than 116 mm, since a minimum thickness of 2 mm of drawer material is needed between two holes in order to insure the stiffness of the drawer.
- The size and the shape of the PMT must be optimized to provide a high light acceptance, while leaving enough space within the PMT block for the divider the and 3-in-1 base.
- The size and shape of the light mixer must be similarly optimized.
- The PMT block must provide sufficient magnetic shielding to insure the performance of the photomultiplier tubes.
- Space must be made for cabling between the PMT block and the electronics boards attached to the super-drawer.

The components of a PMT block are as follows:

- A single soft iron cylinder with a thickness of 3 mm, an external diameter of 54 mm and a length of 145 mm.
- A mu-metal cylinder 1 mm thick, and 50 mm long, with a gap of 3 mm between itself and the iron cylinder.
- A soft iron front ring, 12 mm thick. There is a gap of 6 mm between the ring and the mu-metal cylinder, in which a light mixer is inserted.
- A small PMT, 20 mm long, with a square cross section of $28 \times 28\ \mathrm{mm}^2$ and a square photocathode of $18 \times 18\ \mathrm{mm}^2$.
- A square light mixer $18 \times 18\ \mathrm{mm}^2$, 43 mm long, with a 0.5 mm thick gap washer in front of the PMT face.
- A circular divider board which also acts as a socket for the PMT.
- A 3-in-1 board.
- A soft iron end-cap, 3 mm thick, closing the PMT block.

The light mixer and the PMT are mechanically supported by a plastic element, which also isolates the PMT metallic package (connected to the HV). This support piece is made of high electrical resistant material (NORYL) and can be produced either by casting or by machining.

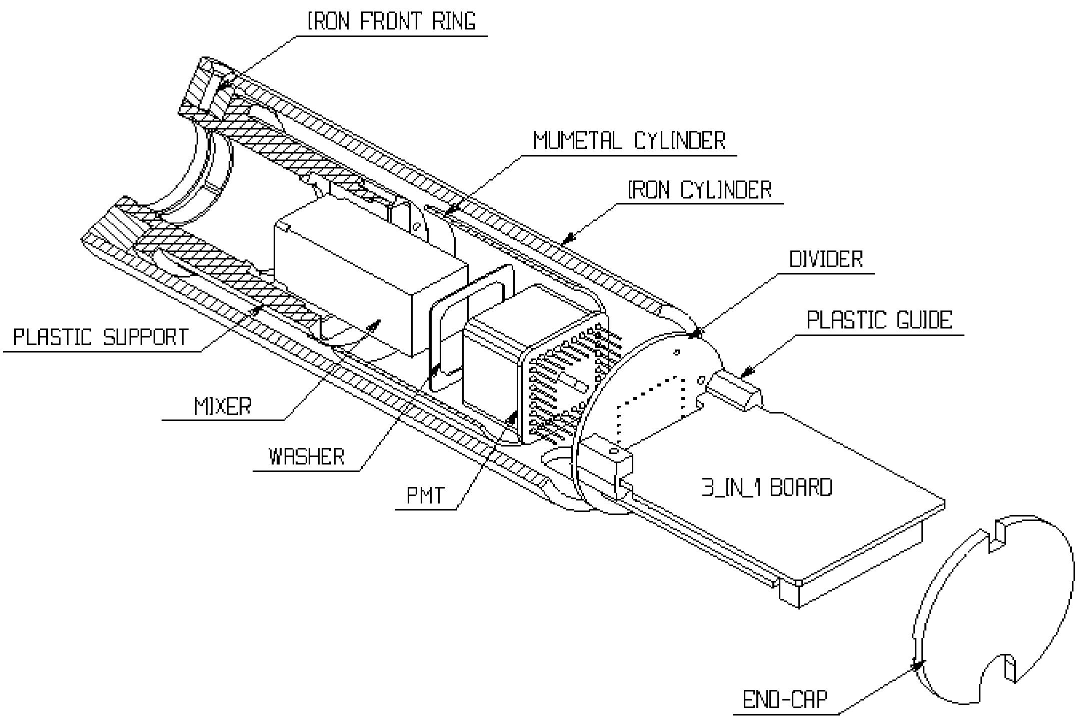

Figure 6-3 Arrangement of a PMT block.

Figure 6-4 is a photograph of the different elements of the PMT block assembly for Module 0, including the light mixer, PMT, HV divider, 3-in-1 board, and the shielding structure. Figure 6-5 is a photograph of a fully cabled PMT block produced for Module 0. The weight is about 1.2 kg. 53 such PMT blocks were assembled, of which 46 units were installed in Module 0.

6.2.1 Photomultipliers

The output of the PMT block is a shaped electronic signal which is subsequently digitized by electronics inside the super-drawer. The conversion of the light signal from the fibre bundles to electrical charge is done by the photomultipliers in the PMT blocks. The following sections outline the requirements, baseline solutions, and tests performed to investigate a suitable photomultiplier for the Tile Calorimeter.

6.2.1.1 Requirements

The main requirements for the PMTs are summarized in Table 6-2. The nominal gain must be suited both to the physics measurements and to the interfaces with the electronics read-outs. The physics constraints have two aspects:

- The PMT must operate in a well-defined manner (linear) with light produced from small signals (muons) to high signals (large energy deposits in a single cell),
- The PMT must operate in a well-defined manner for current measurements for calibrations using integrated charges from minimum bias events in the last depth sampling (small current values, depending upon luminosity) to larger Cesium source currents.

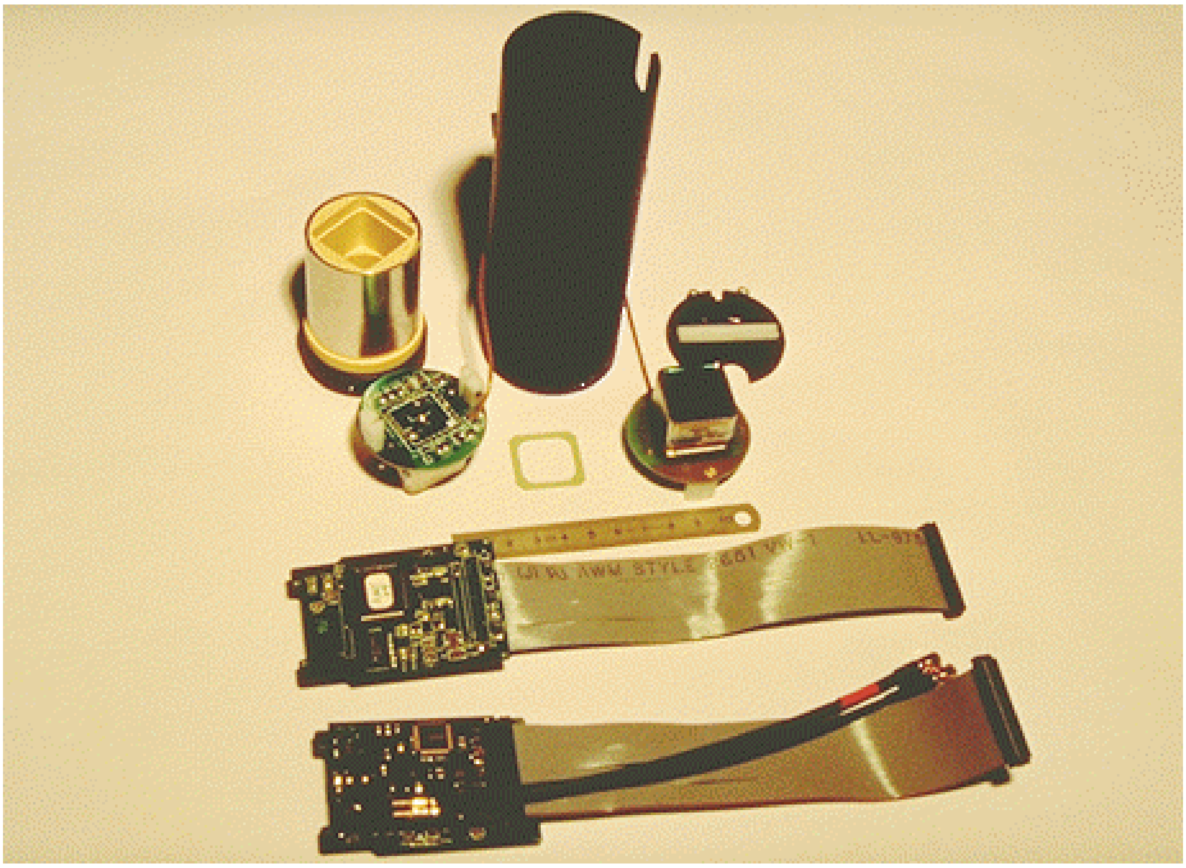

Figure 6-4 Elements of a PMT block.

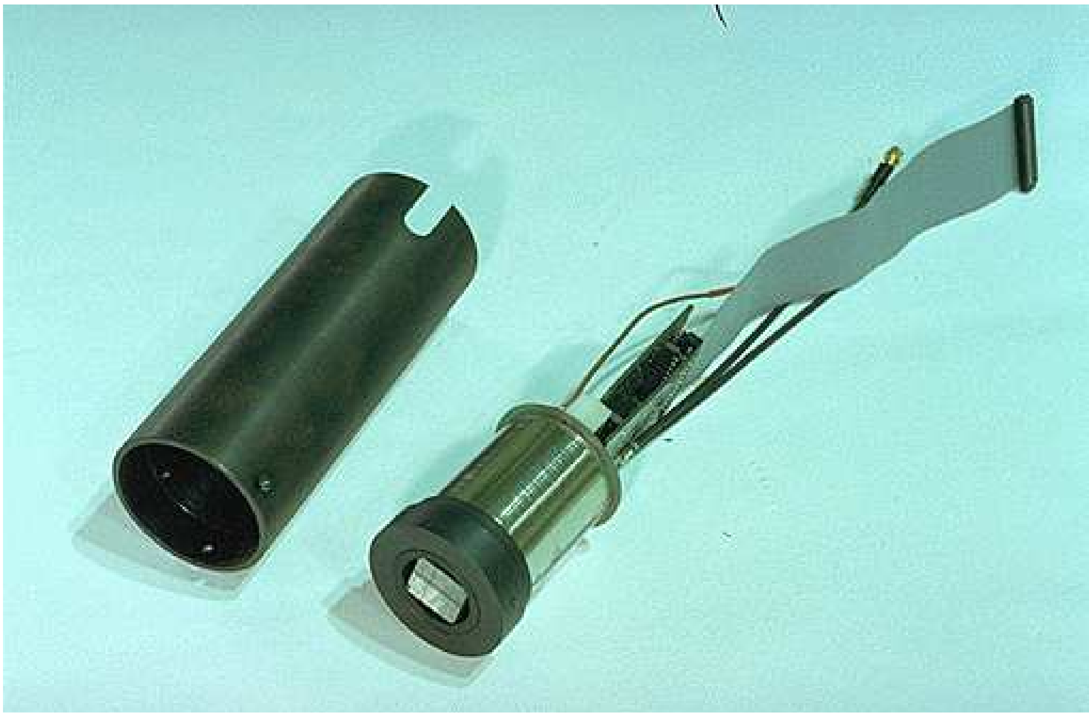

Figure 6-5 Assembled PMT block for Module 0.

Table 6-2 Phototube requirements.

Quantity	Requirement
Quantum efficiency at 480 nm	> 18%
Nominal gain with full efficiency	10^5
Dark current at nominal gain	< 1 nA
Rise time	< 2.5 ns
High voltage at nominal gain	< 1000 V
Gain variation of 1% with shielding in every direction	500 Gauss
Max. non-linearity for pulses of 15 ns and 50 mA currents	< 2%
Useful photocathode area	> 300 mm^2
Length	< 50 mm

Test beam studies (see Chapter 7) indicate that a minimum gain of 10^5 is required to allow measurements of muons, which would deposit roughly 350 MeV in a single cell. At the same time, pulses coming from the highest energy particles must be measured without a saturation of the read-out pipeline. Simulations have shown that, at full luminosity, several events per year are expected to deposit the equivalent of 1.5 TeV in a single cell. The gain of the PMT must be large enough to maintain a linear response over the entire dynamic range, yet not so large as to saturate the input of the digitizing circuit. Using the conservative hypothesis of 50 photoelectrons per GeV and the equivalent of 1 TeV per PMT, a PMT gain of 10^5 is found to provide the necessary dynamic range.

The maximum allowable dark current is mainly constrained by the requirements of the current measurements, which have a dynamic range between some tens and hundreds of nA, depending upon whether source calibrations or minimum bias events in various samplings at different luminosities are being measured (see Chapter 7). The dark current must therefore be less than 1 nA at the nominal gain.

Test beam measurements using PMTs with a very fast rise time (about 0.6 ns for the R5600 PMT) have shown that the Tile Calorimeter pulse rise time is close to 5.5 ns. In order to keep this speed, the PMT rise time must be faster than 2.5 ns.

A high voltage power supply system has been specially designed for the Tile Calorimeter PMTs. Regulation of the system is based on the use of optocouplers, so that it is entirely insensitive to residual magnetic fields in the drawers (see Section 6.2.3). Component costs are strongly dependent on the HV range, and in particular the resistor costs increase significantly for values above 1 kV. In addition the design of such a system (including the cabling aspect) is simplified when the upper voltages are restricted. Therefore, the PMT high voltage should be less than 1000 V at the nominal gain. A safety margin of about 200 V should be included to take into account varying cell responses.

Effects of stray magnetic fields from the three ATLAS magnets must not disturb the intercalibration of the cells, which is done with an accuracy of ~1%. Although the intercalibration will be performed with the magnets turned on, the assembly of the PMTs in their magnetic shieldings must maintain the gains at the same level of precision. Initial estimates show variations of less than 1% for fields of up to 500 Gauss in any direction. These limits will be reviewed later using more realistic field simulations, in order to insure a large safety factor in the shielding design.

The non-linearity of the tile calorimeter must be less than 2% in order to measure high energy jets with sufficient precision for compositeness searches [A.40].

Additional requirements on the PMTs not listed in Table 6-2 are:

- A photocathode area which matches the size and shape of the light mixer N-43,
- A low sensitivity to temperature (less than 0.5% per degree),
- A long term gain stability of about 2%, which can be corrected at a level of 0.5% using the laser monitoring system and the current calibration,
- An acceptable level of ageing of the photocathode due to cumulative illumination,
- Insensitivity to low level neutron fluxes (below 10^{11} neutrons per year).

6.2.1.2 Baseline solution and tests

Reviews and tests of commercially available PMTs have been performed, with the purpose of

Table 6-3 Characteristics of the Hamamatsu R5900 Photomultiplier tubes.

Quantity	**PMT R5900**
Quantum efficiency at 480 nm	16.9%
Nominal gain with full efficiency	10^5
Dark current at nominal gain	< 100 pA
Rise time	1.4 ns
High voltage at nominal gain	665 V
Gain variation of 1% with shielding in every direction	800 Gauss (B transverse) 200 Gauss (B longitudinal)
Max. non-linearity for pulses of 15 ns and 50 mA currents	< 1%
Useful photocathode area	324 mm^2
Length	20 mm

selecting a single type of PMT for the whole Tile Calorimeter. The goal is to have 10,310 PMTs delivered by a single manufacturer to 6 institutes, who will all share the responsibility of testing and characterizing the phototubes, and assembling the PMT blocks. One commercially available PMT has been used as a baseline solution (Hamamatsu R5900). Its characteristics are outlined in Table 6-3. Tests of this baseline PMT are described in the following sections with more comprehensive details found in N-83, N-108 and N-97. The PMT is still being evaluated, along with PMTs from other suppliers.

Existing PMTs

An initial review of commercially available PMTs with characteristics approaching the requirements in Table 6-2, has been performed. The photomultipliers fall into three typical categories which are characterized by the arrangement and shapes of the dynodes.

Classical linear focusing PMTs have the following properties:

- good linearity over a large dynamic range,

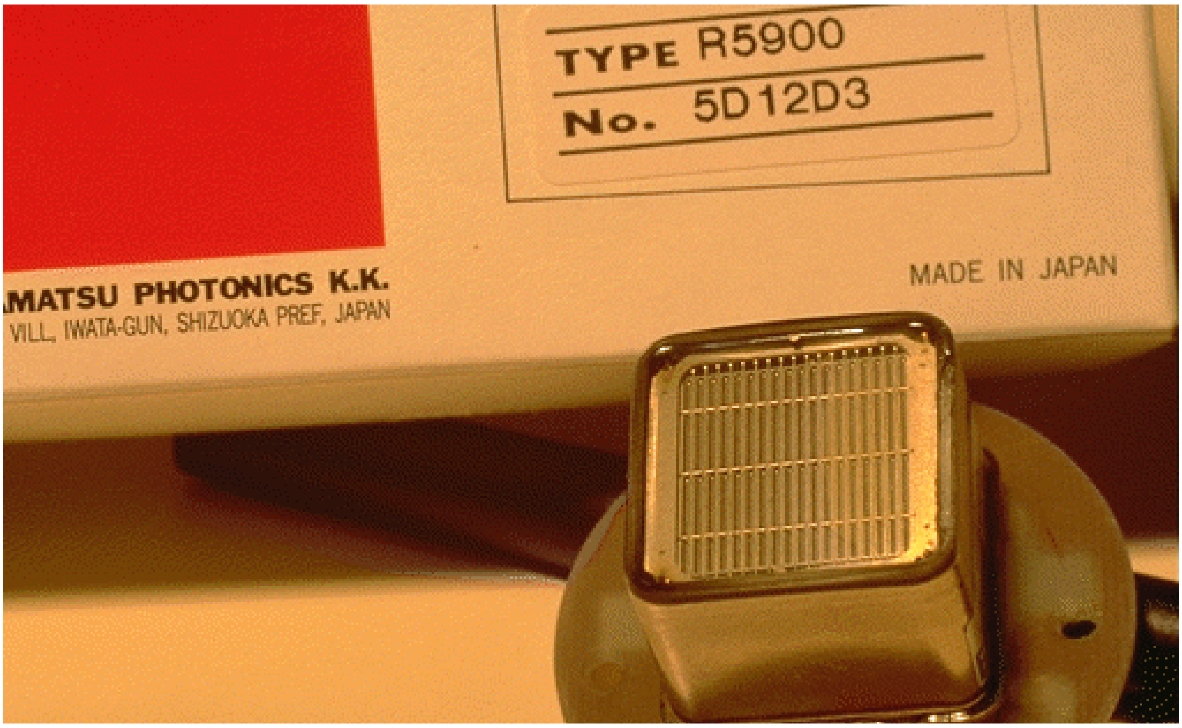

Figure 6-6 The Hamamatsu R5900 PMT.

- large sizes,
- sensitivity to magnetic fields,
- low cost.

Mesh PMTs are characterized by:

- linear structure of the dynodes,
- low sensitivity to magnetic fields,
- large size,
- high cost.

Circular focusing PMTs have the following properties:

- focusing structure just behind the photocathode and a circular shape of the dynodes,
- linear structure of the dynodes,
- compact size,
- very low sensitivity to magnetic fields,
- relatively poor linearity and slower speed,
- medium cost.

The best overall candidates were found to be circular focusing PMTs made by Hamamatsu (R1924, R3191-04, R4162) and EMI (9111B, 9112B), although some preliminary tests and examinations of the official data sheets were not fully in favour of these final choices.

Compactness of the PMT (with its light mixer partner) is a key element in the design of the PMT block (see beginning of Section 6.2). Compactness is also strongly associated with magnetic field insensitivity since it implies a structure with closely spaced dynodes.

New PMTs from Hamamatsu, characterized by a metal channel dynode structure with a metal package (R5600 and R5900) have been found to be both compact, and have good linearity. The Tile Calorimeter activities have been concentrated on these PMTs, which were developed in collaboration with the manufacturer, and are now commercially available.

Characteristics of R5900 PMT

The dimensions of the R5900 PMT are shown in Figure 6-7. The length is 20 mm, without the pins. The photocathode has a square shape ($18 \times 18\ \mathrm{mm}^2$) which perfectly fits the optimum square size of the light mixer (see Section 6.2.2). The metal housing is connected to the cathode potential, and the so-called Metal Channel Dynode structure has a 10-stage amplification. Each stage is made of a thin metallic plate, the dynode profile of which is obtained by micrograving. The multiplier structure is a stack of these dynodes, with gaps of about 1 mm between the elements. The secondary emission is achieved by the deposition of a suitable material. A plane of thin metallic strips is inserted between the photocathode and the first dynode in order to focus the photoelectrons and to maintain the detection efficiency.

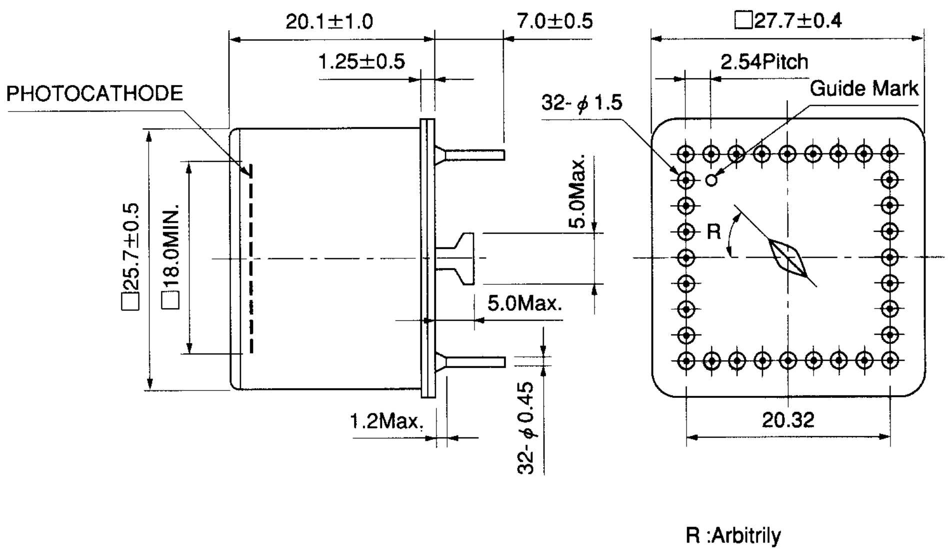

Figure 6-7 Dimensions of the Hamamatsu R5900 PM. The PMT is square-shaped.

Figure 6-8 shows typical manufacturer's curves on amplification and quantum efficiency for the R5900 PMT. The nominal gain of 10^5 corresponds to a high voltage of ~650 V, with a dark current of about 0.3 nA. These values are obtained by using a non-optimized divider (1.5:1.5:1.5:1.0 ... 1.0:0.5). The maximum voltage should not exceed 1000 V. The photocathode material is Bialkali with a borosilicate window, and the quantum efficiency is close to 18% at 480 nm.

The temporal characteristics include:

- Typical anode rise-time of 1.4 ns,
- Typical transit time spread of 0.3 ns (for a transit time of several ns).

The pulse linearity exhibits of ±2 % gain deviation for a typical current of 50 mA.

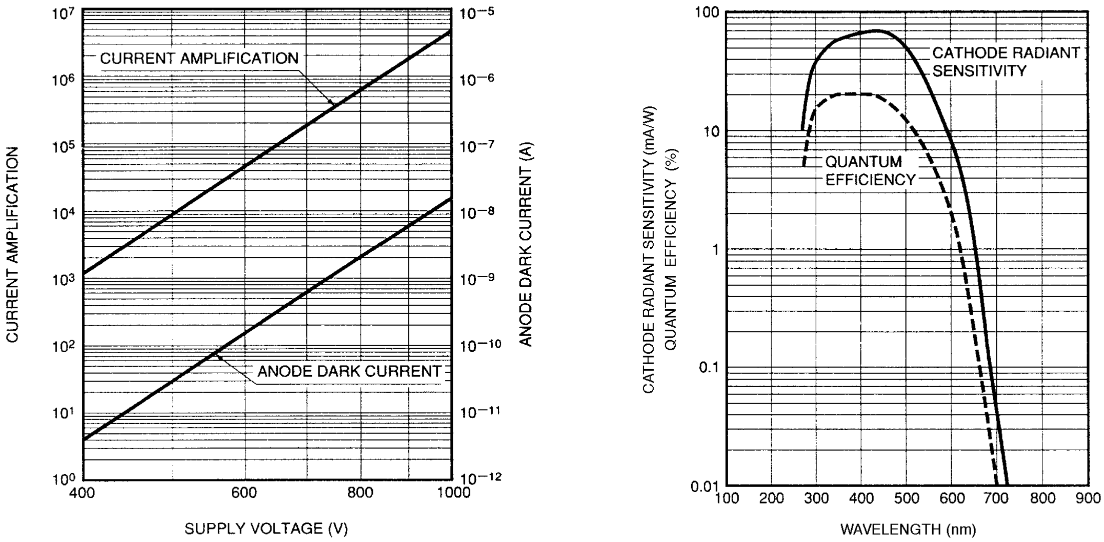

Figure 6-8 Typical current amplification and quantum efficiency curves for the R5900 PMT.

Figure 6-9 shows an example of the relative gain variation as a function of the magnetic flux density, for different field orientations. There is not a full insensitivity, but there are no sharp gain variations, and the field effects are such that a dedicated shielding would easily provide the required protection.

From these data it appears that the R5900 PMT should satisfy most of the requirements listed in Table 6-2. It has been noted previously that these PMTs were developed in direct collaboration between the Tile Calorimeter community and the manufacturer.

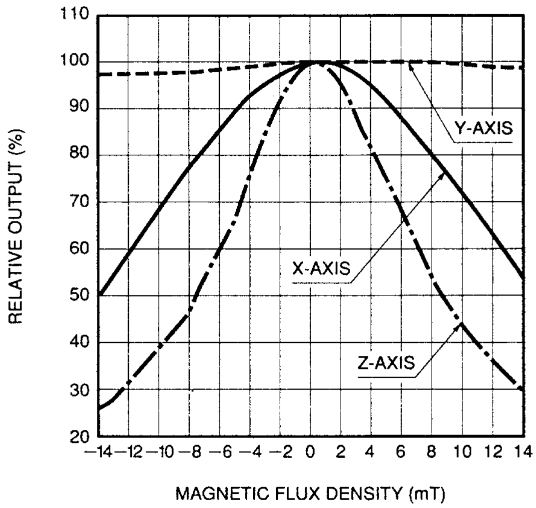

Figure 6-9 Variation in gain for the R5900 PMT as a function of the magnetic field

The development of the R5900 PMT has proceeded through the following steps:

1. Enlargement of the useful area to the equivalent of four R5600 PMTs put side-by-side,
2. Improvements to the dynode structure and consequently to the uniformity of the response,
3. Improvement of the optical structure between the photocathode and the first dynode, and reduction of the photocathode resistivity by increasing the electrical contact between the photocathode and the metal package,
4. Increasing in the quantum efficiency.

A parallel improvement (required by the Tile Calorimeter collaboration) concerns a reduction of the number of stages from 10 to 8, in order to increase the supply voltage by about 100 V for the same nominal gain. By doing so, there is an increase in the safety margin on the linearity range. This also leads to a length reduction of about 5mm, which provides extra space in the PMT block for the electronics. Part of the space savings gain is due to the fact that the present package is not fully occupied.

Test results

For the 1996 program, 65 of the most recently improved Hamamatsu R5900 PMTs were procured. These were extensively tested and characterized by four institutions within the collaboration.

The manufacturer's recommended high voltage divider chain was found not to be optimal for the Tile Calorimeter requirements and development work was performed to obtain a suitable voltage partition. Figure 6-10 shows results of the photocathode current measurements performed on two sets of R5900 PMTs, corresponding to manufacturer development generation 3 (top plot) and 2 (bottom plot) above. The currents are given as a function of the voltage between the photocathode and the first dynode (with all other dynodes grounded). The effect of the improvement in the electrical connection of the photocathode, from the second to the third step is clear; a less resistive photocathode causes the photocurrent to reach the plateau more quickly. Using the second step PMTs, the efficiencies were optimum for photocathode voltages of more than 100 V, whereas all but one of the 3rd generation PMTs are fully efficient at about 30V. This measurement is an element of the protocol for the selection of PMTs. It is also used in the optimization of the divider (see Section 6.2.4).

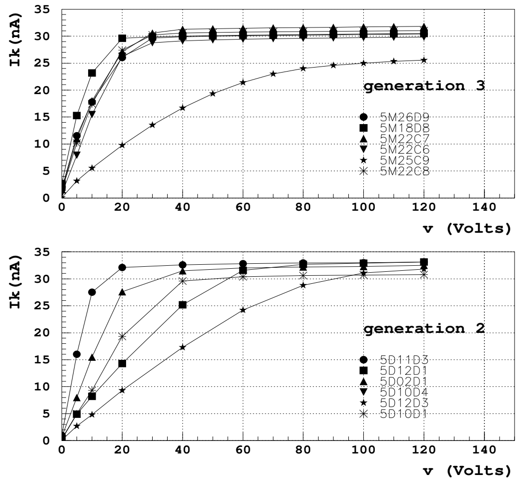

Figure 6-10 Photocathode voltage optimization.

Figure 6-11 gives the amplification curves of a set of PMTs (3rd generation) used in Module 0 with the standard divider. The data are well reproduced by fitting the gain G versus the applied High Voltage V with the usual law [A.41]:

$$G = \alpha \cdot V^{\beta}.$$

Considering all of the PMTs used in Module 0, the mean value of the parameter β is equal to 8.328 ±0.048, with an r.m.s. of 0.39; the potential is measured in volts. The values are seen to have only a small dispersion. The value of β corresponds to the typical performance of 10-stage multipliers. After adjustments using the Cs source, the gain G is found to be:

$$\langle G \rangle = 1.006 \pm 0.031 \times 10^5 \qquad \mathrm{rms}(G) = 0.18 \times 10^5,$$

which is near to the usual values obtained with classical 10-stage PMTs.

The average HV which corresponds to the nominal gain of 10^5 is:

$$\langle HV \rangle = (665 \pm 79)\mathrm{V}.$$

Therefore these PMTs need a rather low HV. From these results, it follows that an adjustment of the gain at a level of 0.5% requires a stabilization of the HV with an accuracy of 0.4 V. This represents an important requirement to the power supply system (see Section 6.6).

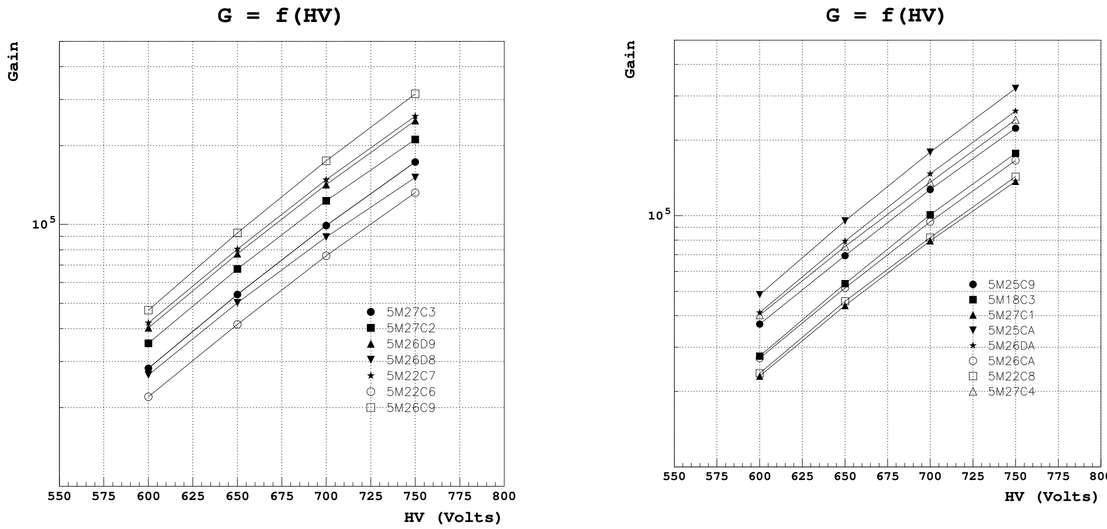

Figure 6-11 Amplification curves as a function of the HV.

Figure 6-12 shows the dark current measurements of the same PMTs as a function of the applied high voltage using the standard divider. Most of the PMTS have a current lower than 100 pA at the nominal gain (except one PMT which exhibits a sharp increase above 700 V).

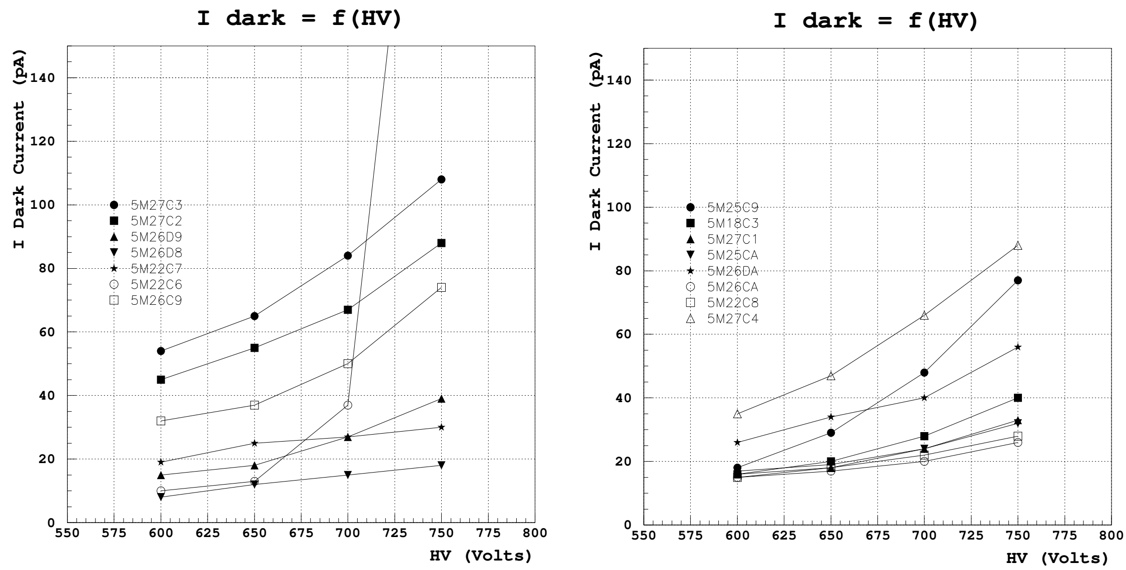

Figure 6-12 Dark current measurements of the R5900 PMT as a function of applied high voltage.

The protocol for the selection of PMTs takes into account the values of α and β, and the dark current at the nominal gain.

Figure 6-13 gives a sample linearity measurement for a PMT with the standard divider as a function of the number of photoelectrons. For higher illuminations, tests of 15 PMTs show some dispersion in the linearity performance. This is one reason that we are considering an 8-stage configuration. Figure 6-14 shows the linearity results of such a new PMT from Hamamatsu at the nominal gain, for various divider configurations. It satisfies the linearity requirements at the expected anode current limit of 50 mA. Clearly this new PMT evolution must be extensively tested before a definitive decision is reached. The development of a suitable 8-stage PMT could bring a valuable safety factor in the linearity, which would help compensate for the effects of long term ageing.

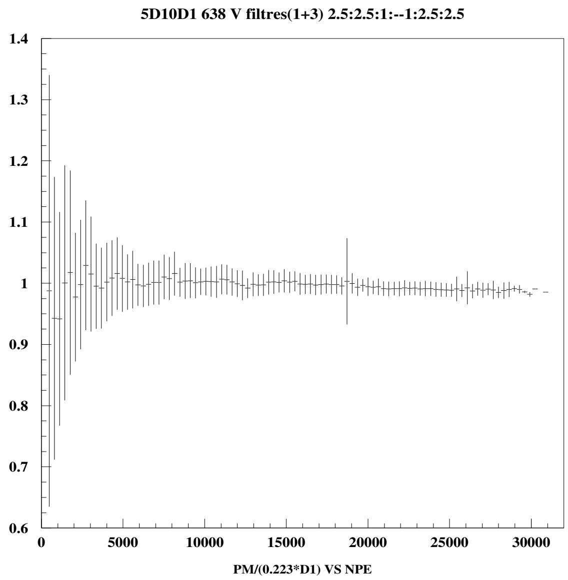

Figure 6-13 Differential non-linearity measurements for an R5900 PMT as a function of the number of photoelectrons.

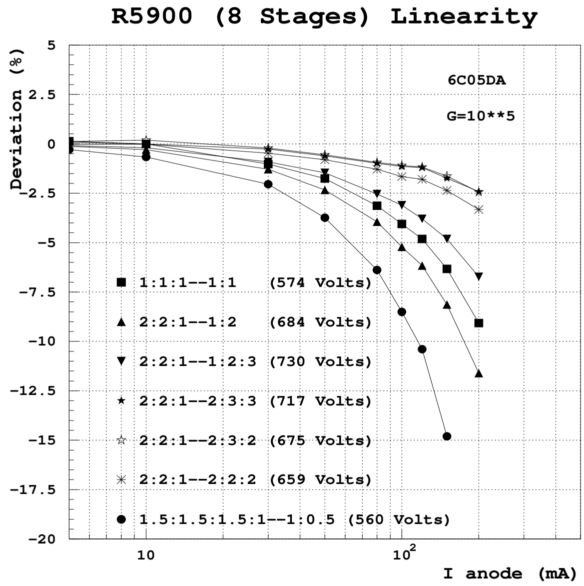

Figure 6-14 Linearity of an 8-stage R5900 PMT at nominal gain, for various voltage configurations.

Exhaustive studies of the 8-stage tube are found in references [A.41] and N-83.

Despite good initial results with the R5900 PMT, there are more improvements and studies which need to be made. The quantum efficiency is below the Tile Calorimeter requirements, and lifetime studies have yet to be performed. Improvement of the quantum efficiency is in progress, in parallel with the development of the 8-stage R5900 PMT.

Module 0 has been equipped with the 10-stage R5900 PMT. From a group of 65 tested PMTS, 46 were selected for use in the module. The analysis of the PMT performance is in progress as part of the general framework of Module 0 tests. PMTs from a second manufacturer are being evaluated, and a final selection will be made in 1998.

6.2.1.3 Characterization and test benches

The procurement, testing, and installation of 10 310 phototubes requires a non-trivial level of organization and quality control. After delivery, all PMTs must be characterized in order to do a first selection. The PMTs must be grouped in sets with similar operating parameters so that PMTs inside a given super-drawer have gains which can be corrected by trimming high voltages within the 350 V range of the distributors (see Section 6.6.2).

An initial protocol was defined for testing and selecting the 46 PMTs used in Module 0 from a set of 65 delivered PMTs. This protocol was used by the four institutes who shared the purchase. For the main production, the six institutes responsible for the PMTs procurement will test their phototubes, and they will then assemble and test the PMT blocks too.

The protocol for Module 0 is a first step towards the final protocol which will be used for ATLAS. The protocol considers:

1. The measurement of the photocathode sensitivity as a function of the applied voltage between the photocathode and the first dynode as seen in Figure 6-10.
2. The dark current as a function of HV.
3. The efficiency plateau as a function of HV.
4. The homogeneity of the parameters (α and β) in the gain law (Section 6.2.1.2).

From the previous section it was shown that the behaviour of these PMTs was homogeneous with as small dispersion around the mean value. The test protocol will evaluate the PMT by rejecting it if its operating parameters are outside some predetermined limit based on the rms of the distributions.

The linearity measurements are time consuming, and have not been used systematically.

Development of a PMT test bench prototype is in progress. This model will be reproduced by the six institutes who share this activity. By taking into account the total number of PMTs (about 10000) and the delivery rate by the manufacturer (between 500 and 1000 per month), each test bench will need to evaluate 30 PMTs per week. Due to the small size of the PMTs and their insensitivity to the earth's magnetic field, the test benches will have a small size. The design uses as many standardized components as possible, and the testing process will be automated.

Figure 6-15 gives a simplified scheme of the PMT test setup. There are three parts:

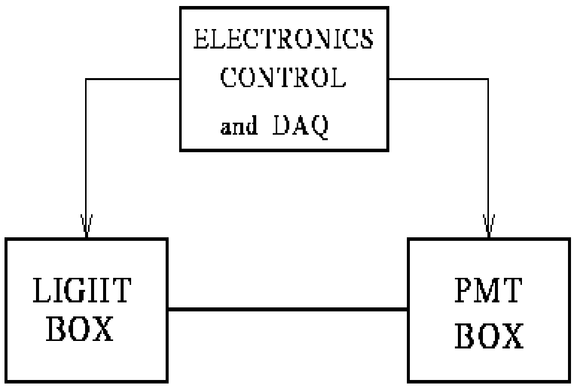

Figure 6-15 Simplified scheme of the PMT test bench

- The PMT box, which contains the 30 PMTs to be tested, as 5 PMTs kept permanently throughout the test period to study long term stability, and a photodiode for the light intensity calibration of each channel. Optical fibres bring light to each PMT, and the 36 photodetectors are positioned on a movable frame so that the photodiode may be moved in front of each optical fibre. Light from the Light box (described below) is distributed to each fibre using a square light mixer. The PMT box is temperature stabilized at an ambient temperature to within 1 degree, using electrical thermocoolers and silicon temperature probes.
- The Light box, which transmits the light to the PMT box by the use of a liquid light guide. It contains two types of light sources at 480nm:
  - a DC light (Quartz Tungsten Halogen lamp coupled to an interferential filter), for the measurements of certain characteristics and the continuous level from minimum bias events,
  - a pulsed light (a very intense fast blue LED made of Gallium Nitride) to study, for example, the photocathode and anode sensitivities as a function of the applied voltages.

  These two kinds of lights may be merged to simulate real working conditions.
- The electronics control and the DAQ.

The test procedure has two steps. The first step uses special programmable dividers to measure photocathode sensitivity and light collection efficiency, anode sensitivity, dark current, anode stability over a short period (some hours), and the absolute current amplification as a function of the HV (from the previous measurements).

The second step measures the characteristics of PMTs with their own standard dividers to calculate their relative gain curve, overall efficiency, dark current, linearity, and their medium term stability (over some days).

Long term stability is studied using the five permanent PMTs. A full operation requires about 4 days per week, including the heating times.

All results are stored in a common data base in order to apply the further selection criteria, and to group the PMTs (with their individual dividers) into sets to be installed in each super-drawer.

6.2.2 Light mixers

Most PMTs exhibit large variations in response over their photocathode surfaces, but the light extracted from the fibres inside a given bundle must be independent of the fibre location at the photocathode. The role of the light guide is to mix the light coming from the fibres so that there is no correlation between the position of a fibre and the area of the photocathode which receives its light.

The light mixers must have the following characteristics:

- Uniform light output (at a level of at least 90%),
- High light acceptance (dictated by optics),
- Low light attenuation (a few percent),
- A short length to provide space for the 3-in-1 base (no more than 50 mm),
- An air gap less then 1 mm between the PMT block and the fibre bundle to allow movement of the drawer,
- No Cerenkov light from incoming particles.

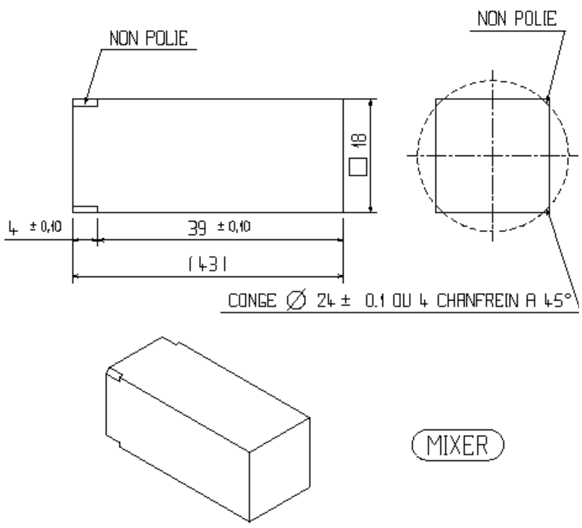

Figure 6-16 Square light mixer for the Tile Calorimeter.

Initial work done by SPACAL and RD1 at CERN, and later confirmed by work done at Fermilab[A.17], demonstrated that a square light guide with a length of 1.9 times its side exhibits the best performance. The maximum variations in uniformity are about 10% and it is recommended that the photodetector contain the entire cross section of the light guide. Light mixers of this type were used in the first 5 Tile Calorimeter prototypes and for Module 0. A sketch of the light mixer is shown in Figure 6-16.

From an optical point of view, air gaps introduce a sizeable loss of light. However, this loss is stable and independent of the size of the gap, as long as it is within a range of ~1 mm. This 1 mm space between the fibre bundles and the light mixers in the PMT blocks is sufficient to allow movement of the drawers.

6.2.2.1 Optimization and design

The cross section of the light guide is constrained by the maximum size of the fibre bundles and the accuracy in positioning the drawers (which support the light guides) in front of the bundles. The optimum cross section is $18 \times 18\mathrm{mm}^2$ N-39. Only one light guide size will be used, so that all pieces may be produced in a single production run.

Monte Carlo simulations of the mixing uniformity and the acceptance [A.41] give the following results for the optimum positioning and length of the mixers:

- The air gap between the fibre bundle and the light mixer should be no more than 1 mm,
- The air gap between the photocathode and the light mixer should be less than a few tenths of a mm,
- The length of the mixer should be greater than 30 mm.

Figure 6-17 illustrates the evolutions of the uniformity and of the acceptance as a function of the mixer length, in apex units, for two fibre positions; fibre 1 is near the external part of the largest bundle, and fibre 2 is in the center. It appears that for mixer lengths of at least 1.5 times the apex (diameter of the circumscribed circle), the results are independent of the fibre positions.

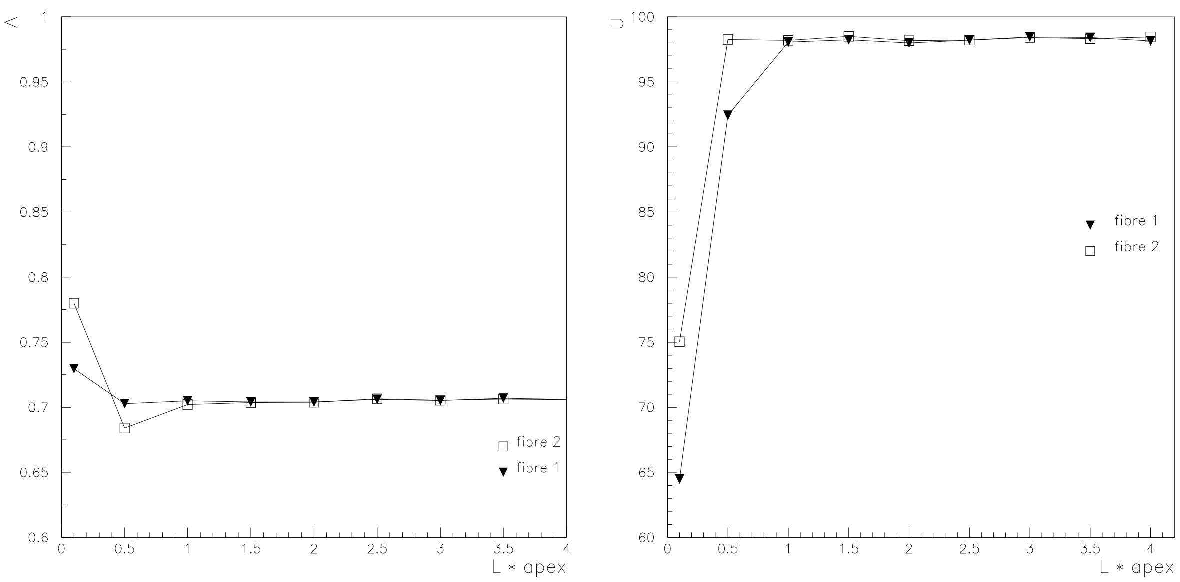

Figure 6-17 Monte Carlo results on the acceptance and uniformity of PMT response as a function of mixer length. A is the ratio of photocathode light to incident light, and U is the uniformity of illumination of the photocathode. The results are shown for fibres near and far from the center of the light mixer.

Measurements have been performed using a R5900 PMT with light mixers of various lengths from 30 to 57 mm and the same square cross section of 18×18 mm^2. The 30, 35 and 57 mm long mixers were found to be unsuitable because of inadequate light uniformity in the two first cases and excessive light attenuation in the last case. The optimum tested lengths were 43 and 50 mm. Figure 6-18 shows the response of a R5900 PMT without and with a 35 mm long light guide in front. The PMT which was used at this moment corresponds to the 2nd generation production. Using the 3rd generation clearly improves the photocathode uniformity.

The final choice of length will be made by taking into account the two other constraints, which are the magnetic shielding (see Section 6.2.3) and the space required by the 3-in-1 base. Data

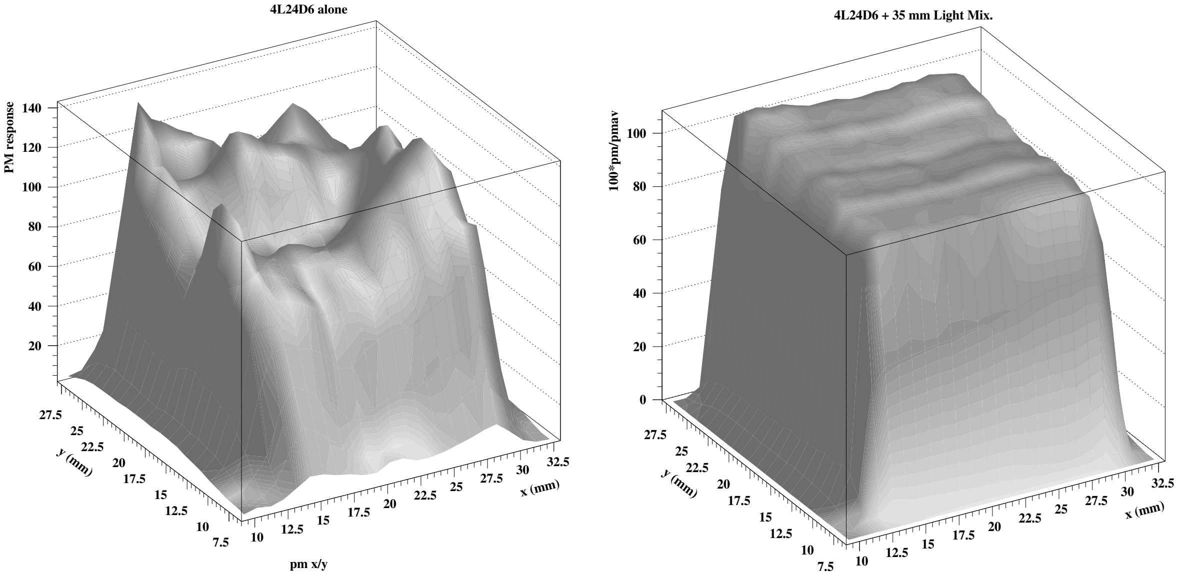

Figure 6-18 The measured response of a R5900 PMT without (left) and with (right) a light mixer as a function of the fibre position.

from the September 1996 beam tests of Module 0 must be analysed before a decision is made on the necessity of using special UV dopants to suppress any Cerenkov light.

6.2.3 Magnetic shielding

6.2.3.1 Requirements

The accuracy on the intercalibration of cells, using the Cesium source system, is at a level of 1%. Magnetic shielding must prevent residual fields from the ATLAS solenoid and toroids from producing PMT gain variations at a level higher than this. The initial specifications for the shieldings called for a protection up to 500 Gauss in every direction. Full 3-dimensional magnetic field simulations are now available (N-50,N-54,N-58), and new specifications with a safety factor of the order of some tens will be based on these results. Other constraints on the shielding design are the available space inside the drawers and the optimum length of the light mixers.

6.2.3.2 Optimization and design

The PMT blocks inside the drawers, as shown in Figure 6-19, are positioned in such a way that the main components of the residual magnetic fields are perpendicular to the PMT axis, thus making shielding easier to implement. Simulations indicate that in the worst cases, the perpendicular components would be less than 20 Gauss, while the longitudinal fields would be less than 5 Gauss.

Results of studies N-42 on the performance of phototmultipliers with different dynode geometries in magnetic fields exclude the use of PMTs with the classical linear arrangement of dynodes in the ATLAS environment. Figure 6-20 shows the response of an R5600 PMT from Hamamatsu (similar to the R5900, but with a round photocathode), and a classical linear dynode PMT, both with a double magnetic shielding made of iron and mumetal cylinders. At all orientations, an efficiency plateau exists for the R5600 PMT. In fact, within the 1% requirements, these PMTs can be used up to:

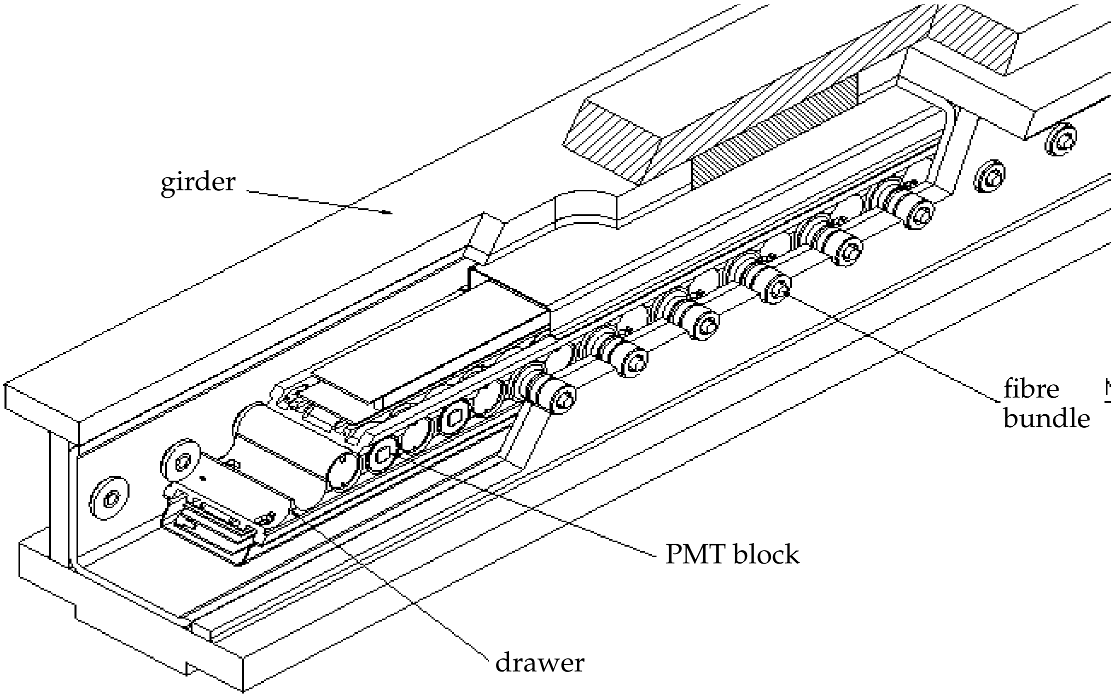

Figure 6-19 Arrangement of PMT blocks inside a super-drawer.

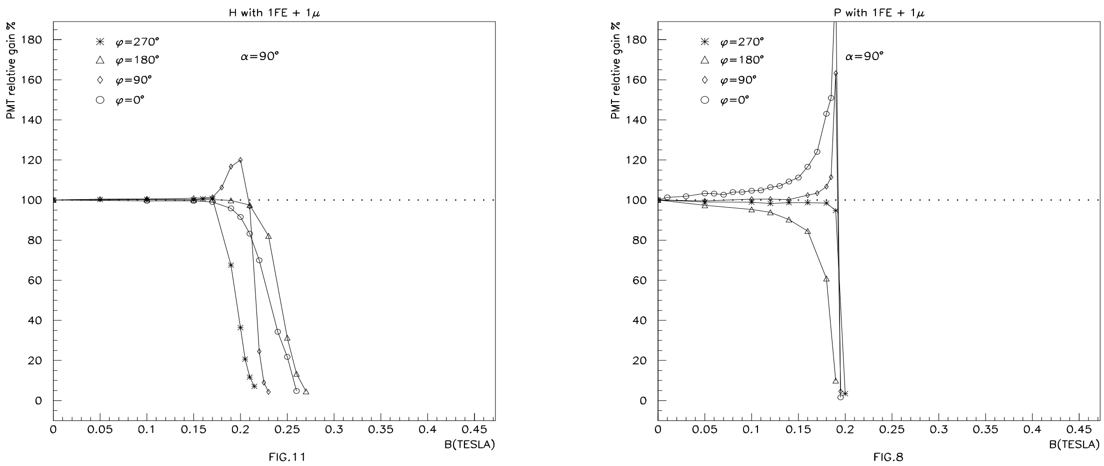

Figure 6-20 Relative performance of R5600 (left) and classical (right) PMTs in a magnetic field.

- 1700 Gauss, for a transverse field, and
- 600 Gauss, for a longitudinal field.

Additional studies have been performed with the R5900 PMTs, which have a square photocathode area which matches the optimized shape of the light mixers. Figure 6-21 shows the resulting optimized shielding design, which includes:

- an iron external cylinder (a),
- a μmetal internal cylinder (b),
- an iron front-ring (c),
- an iron end-cap(d).

The various dimensions are optimized, including the sizes of the gaps between the front ring and the light mixer, between the light mixer and the μmetal and between the μmetal and the iron cylinder. The optimum positioning of the front face of the PMT inside the shielding requires a light mixer which is at least 42 mm long.

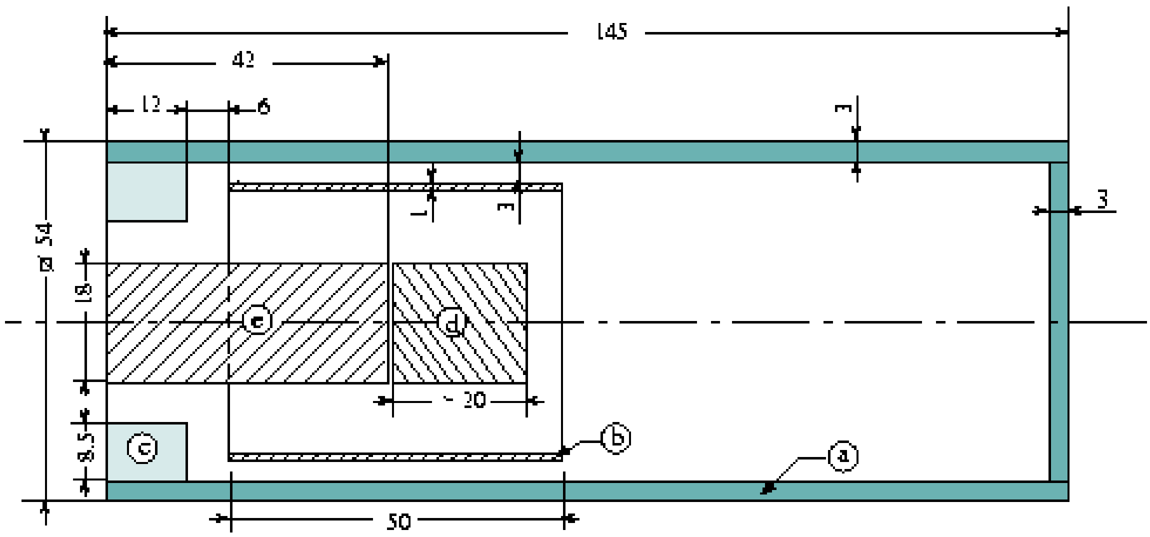

Figure 6-21 Arrangement of the magnetic shielding for the R5900 PMT.

The relative gains for phototubes in longitudinal and transverse fields using this design are shown in Figure 6-22. The PMTs can be used in fields up to 800 Gauss for a transverse field, and 200 Gauss for a longitudinal field. By comparison with the expected fields, the safety factors are at least 40 for a transverse field, and 50 for a longitudinal field.

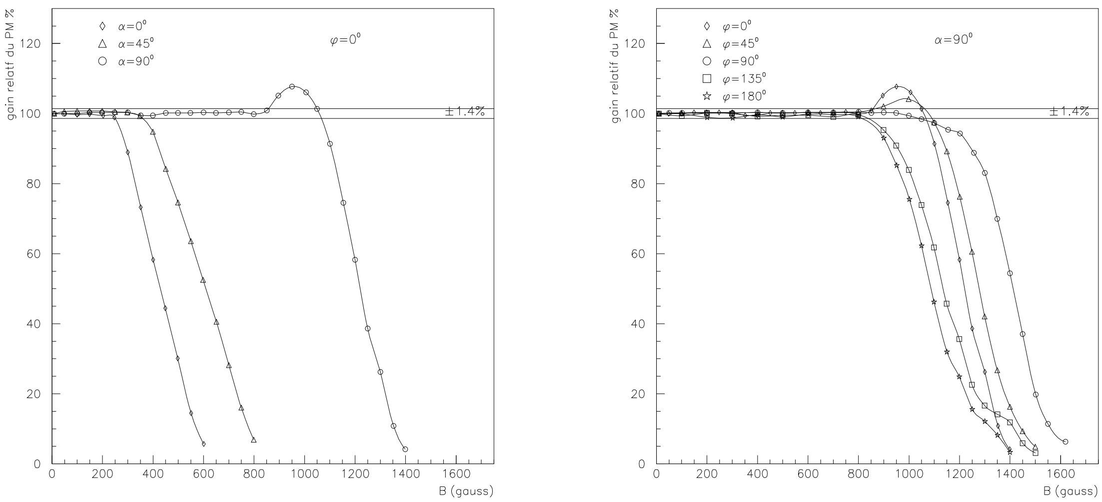

Figure 6-22 Relative gains of a R5900 PMT with optimized shielding.

Future developments which are expected to improve the performance in magnetic fields include:

- Use of the standard Tile Calorimeter divider (2.5:2.5:1.0 ... 1.0:2.5:2.5), instead of the previous uniform voltage partition (see Section 6.2.4), which will increase the electric field where sensitivity to the magnetic field is the largest,
- Use of the 8-stage R5900 PMT which is, a priori, less sensitive to the magnetic fields. The more compact arrangement will lead to a better shielding system.

The results of the optimization of the light mixers and the magnetic shieldings will be considered in the design of the PMT blocks.

6.2.4 Dividers

The primary purpose of the divider is to partition the high voltage between the dynodes of the PMT. The Tile Calorimeter divider also serves as a socket allowing connection of the PMT to the front-end electronics without any interconnecting wires. This design minimizes the capacitance between the PMT and the electronics, and is important to reduce noise and unreliable connections.

6.2.4.1 Requirements

The calorimeter detection efficiency measured on prototypes is presently at the level of 50 photoelectrons/GeV. Therefore, the dynamic range in the final ATLAS configuration before amplification extends up to 50K photoelectrons as discussed earlier. It is therefore necessary to avoid operating the PMT with too large a gain. A PMT operating with a gain of 10^5 results in an anode charge of 800 pC at the upper end of the dynamic range, corresponding to an anode current of 53 mA.

PMTs generally provide good linearity in anode output current over a wide range of incident light levels. The typical linearity of the R5900 as specified by the manufacturer is ~3% for an anode current of 50 mA and a pulse of 30 ns. However, if the incident light input is too large, the output begins to deviate from the ideal linearity.

The anode linearity is limited by two factors: the space charge effect, and the voltage divider configuration. In the former case, the average DC current flowing through the anode may also affect PMT linearity in pulsed mode. If the electrode voltages are assumed to be provided by a resistive divider across a stabilized power supply, the anode current tends to lessen the potential between the final dynode and the anode. This perturbation can be ignored if the output current is small. However when the incident light level is increased, the voltage distribution of each dynode varies considerably. Since the overall cathode-to-anode voltage is kept constant by the HV source, the loss of the interdynode voltage at the latter stages is redistributed to the previous stages, and an increase of the amplification is seen in the first stages.

6.2.4.2 Divider design

The choice of resistors of the voltage divider is mainly governed by the amount of current which flows through it. This current is estimated using a factor of 100 above the mean anode current. In the Tile Calorimeter, the mean anode current comes mainly from pile-up events which occur at each bunch-crossing. Using the worst-case scenario of an average of 40 minimum bias events at each bunch crossing, one finds an average value for the anode current of the order of 2 μA. This value induces a voltage divider current equal to 200 μA. In an isovoltage partition (1:1:1:1 ... 1:1) with a typical high voltage of 650 Volts and a PMT amplification of 10^5, the individual values of the divider resistors are 50 $K\Omega$. The corresponding interdynode voltage is equal to 60 Volts.

When an intense light pulse enters the PMT, a large current flows in the latter dynode stages, considerably affecting the voltage repartition and thus changing the PMT response. To avoid this problem, storage capacitors may be connected to the last stages. These capacitors supply the photomultiplier tube with an electric charge during the pulse duration and restrain the voltage drop between the last dynodes and the anode.

If the pulse width is sufficiently short, it is possible to derive an estimate of the capacitor. We assume that the largest pulse Q_0 corresponds to 800 pC with a pulse duration of 15 ns. The charge stored in the capacitor is $C \times V$, where V is the average interdynode voltage (60V). To achieve a good linearity, we require $C \times V \gg 100Q_0$. Therefore, C should be much greater than 1.3 nF.

6.2.4.3 Divider optimization

An intense light pulse could induce a high space charge in the final dynode stages. This space charge also affects the pulse linearity, and depends on the peak value and the width of the anode current. This space charge effect also depends on the electric field strength between each dynode. To compensate for this effect, higher voltages are applied to the final stages so that the electric field strength between each dynode is enhanced. Linearity can thus be optimized by suitable partitioning of the interdynode voltage.

Figure 6-23 represents the differential linearity curves with a (1:1:1 ... 1:1:1) partition and a (2.5:2.5:1 ... 1:2.5:2.5) repartition, both with a gain of 10^5, as a function of the photoelectron yield. These figures demonstrate at least qualitatively the improvement in linearity due to the new voltage repartition.

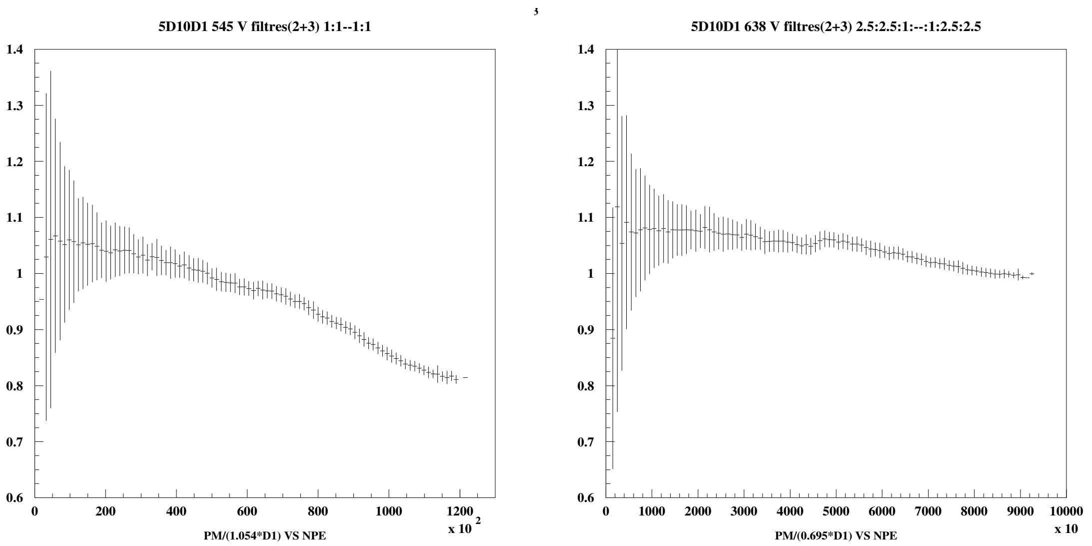

Figure 6-23 Differential linearities for (1:1 ... 1:1) (left) and (2.5:2.5:1 ... 1:2.5:2.5) (right) repartitions.

Such a voltage repartition has several advantages:

- Increasing the interdynode voltage on the first stages improves the PMT collection efficiency.

- As the 10-stage baseline PMT was first designed to operate with a typical amplification of 10^6, a lower amplification corresponds to a rather low HV (500-600 Volts). This leads to a poor PMT efficiency, since the interdynode voltage is ~44 Volts. With the 2.5:2.5:1 ... 1:2.5:2.5 configuration, the overall high voltage is increased by roughly 100 volts, so the voltage on the first stage becomes ~100 Volts.

Figure 6-24 is a circuit diagram of the voltage divider design. Capacitors of 22 nF are chosen for their large safety factor, and because they are a standard, low cost SMD components.

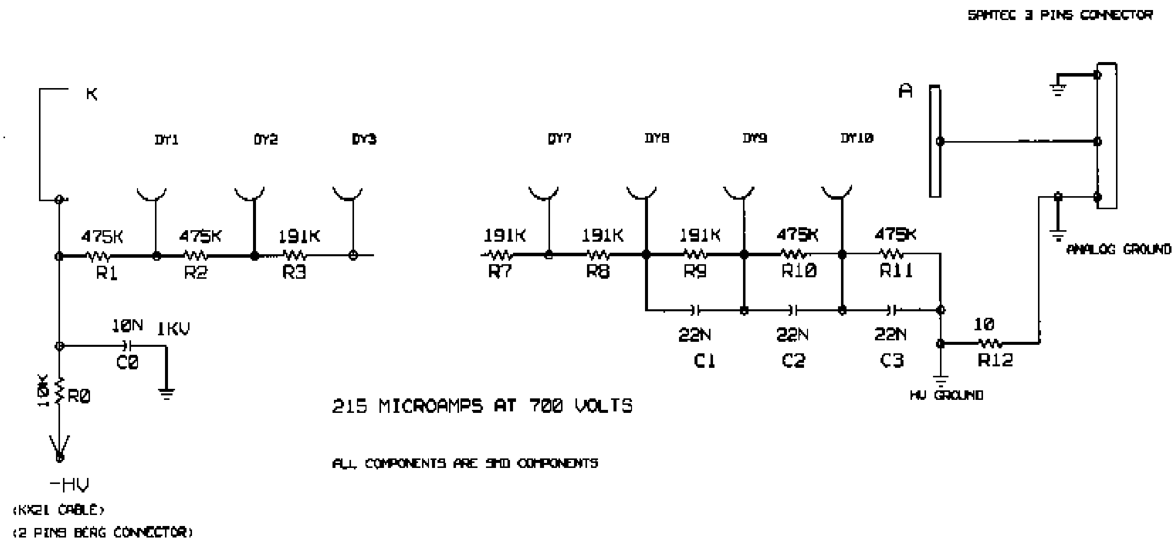

Figure 6-24 Design of the voltage divider for the R5900 PMT, operation with a (2.5:2.5:1...1:2.5:2.5) partition.

6.2.4.4 Divider Test Bench

The procurement, testing, and distribution of the dividers for the Tile Calorimeter will be performed by one institution within the collaboration. A dedicated test bench is designed to test individually each voltage divider. A value of the overall PMT high voltage is applied to the tested divider, and the voltage on each stage is read by an ADC through a multiplexer.The test bench will be fully automated, and the measured voltage repartition of each divider will be recorded in a database. Ten dividers are tested at the same time, in about 15 minutes.

6.2.5 3-in-1 boards

The 3-in-1 boards in the PMT block form the front-end of the electronics read-out chain. They provide 3 basic functions: pulse shaping and accommodation of the large dynamic range, charge injection calibration, and slow integration of the PMT signals for monitoring and calibration. The electrical characteristics of these circuits are described in Section 6.4 and Section 6.5.

The cards occupy a space of 7 cm by 4.7 cm inside the steel shield of the PMT and are directly connected to the PMT voltage divider through a 3-position, 90-degree header. Digital control signals and low voltage power is supplied by a flat 34-position ribbon cable. The fast analog output signal is brought out to the digitizing system, on a differential shielded twisted pair. For an analog LVL1 trigger summation, a second shielded twisted pair from the 3-in-1 card is connected to a 5-input analog adder located nearby in the drawer. A photograph of the prototype 3-in-1 card used for Module 0 is displayed in Figure 6-25.

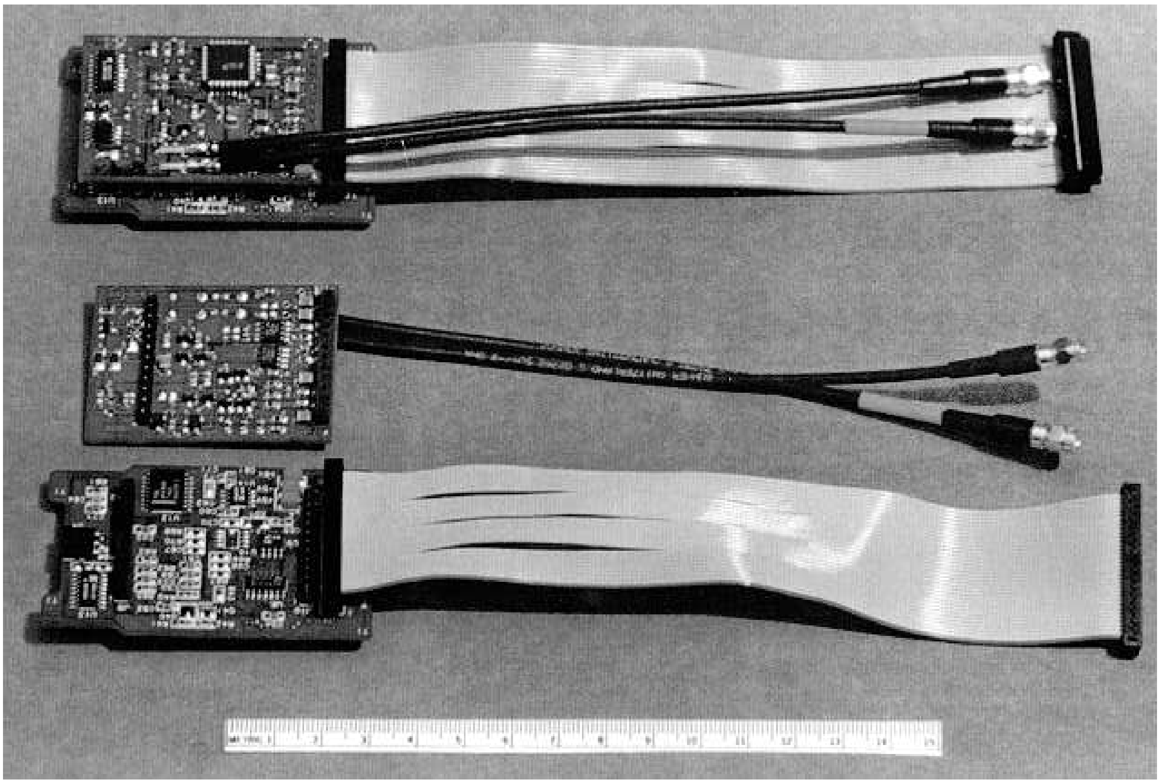

Figure 6-25 The 3-in-1 card. The elements are, from bottom to top, the digital control and integrator section, the shaper-compressor section with outputs, and the assembled card.

This location for the front-end electronics provides an excellent operating environment. It is shielded from electrical noise and magnetic fields. The ambient radiation levels are low and the thermal stability of the environment, inside the steel girder is excellent.

6.2.6 Assembly and test bench

As explained above, the PMT blocks are made with few pieces in order to simplify the assembly. The mounting is done outside the iron cylinder, using a plastic support as a master piece, so that the various steps may be verified before the complete assembly is inserted inside the shielding. A simple plastic tool is used to hold the support to prevent any contact between the front face of the light mixer and the workbench.

For the PMT blocks used in Module 0, it was possible to assemble 4 PMT blocks/hour/person.

The design of a test bench for the PMT blocks is in progress. It is very simple, since it will test the PMT blocks one by one. It consists of a black box in which the PMT block is placed. The block is connected to the internal part of a patch panel using its own HV, low voltage, and signal cables. A blue LED is positioned in front of the light mixer. The LED can work in a DC mode for testing the integrator electronics, and in a pulse mode for the pulse electronics. The calibration functions will also be tested. No temperature stabilization is required.

The entire automated operation, with a succession of tests, must be done within 15 minutes, including setup time, and must guarantee the correct operation of the assembled PMT block. The assembly and the test of the PMT blocks would easily follow the testing rate of the PMTs (30 PMTs per week).

6.3 Super-drawers

A drawer houses up to 24 PMT blocks, and supports electronics boards which are connected to each PMT block and provide the high voltage to the divider, the low voltages to the HV cards and the 3-in-1 card, and the control and calibration signals to the 3-in-1 card. They also contain electronics to process the signals coming from the shaper and the integrator. These electronics boards are arranged on the top and bottom sides of the drawers, with signal processing at the top and the HV distribution at the bottom. Figure 6-26 shows a cross section of a drawer inside the girder.

The links between the PMT blocks and the electronics boards are provided by long printed boards which are organized according to the super-drawer structure.

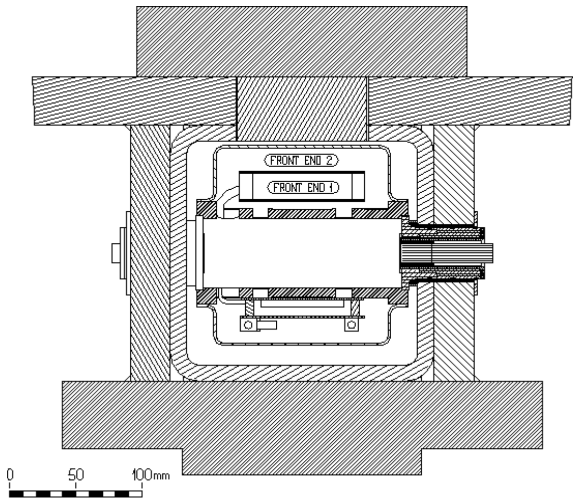

Figure 6-26 Cross-section view of a drawer inside the Tile Calorimeter girder.

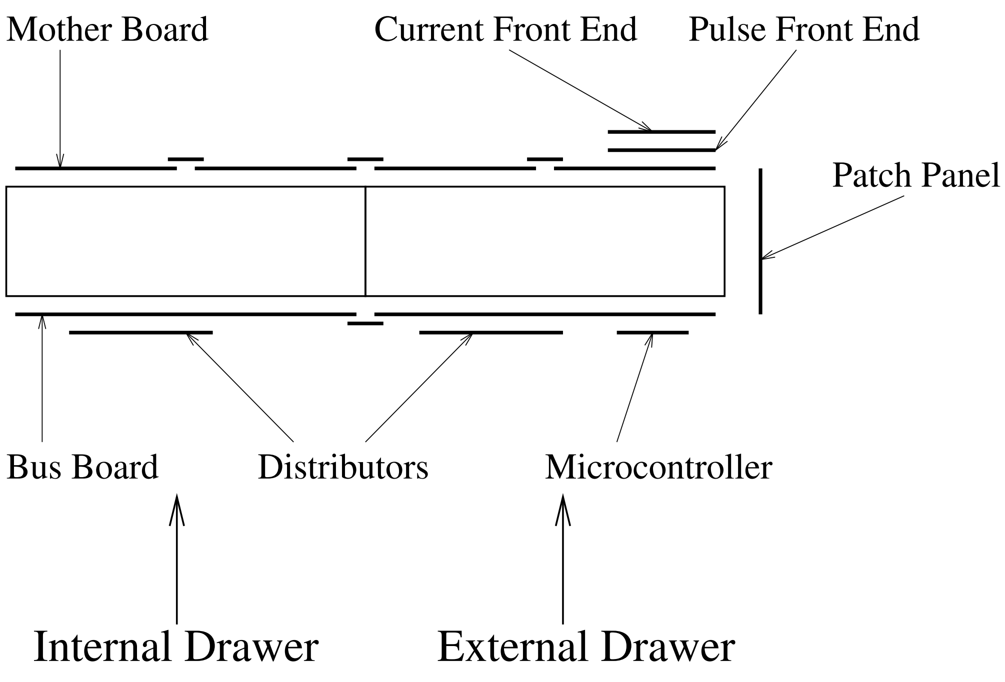

Figure 6-27 Organization of the super-drawer electronics.

6.3.1 General organization

The organization of the super-drawer electronics is shown in Figure 6-27. A super-drawer is a train of two drawers, which are coupled from the electronics point of view. It includes:

- an internal drawer on the opposite side of the access patch panel, and
- an external drawer, adjacent to the access patch panel.

The structure is the same for each half-barrel and each extended barrel module, with the major part of the "intelligent" electronics located in the outer drawers in order to minimize the cabling to the patch panel and to make possible an access without a full extraction of both drawers. These "intelligent" parts are the Pulse electronics, the Current integrator electronics, and the Microcontroller board for the HV distribution. The long printed boards include:

- Two mother boards per drawer (each about 70 cm long) for the 3-in-1 support, and
- One bus board per drawer (each about 140 cm long) for the HV distributors.

Flexible connections link these printed boards. Dedicated holes in the drawers are used for the routing of the PMT cables towards the long printed boards. Figure 6-28 shows the links between two drawers, and the holes for signal cables from the PMT blocks.

Longitudinal grooves along the two sides of the drawers contain the tubing system for the cooling, linked to the patch panel.

The total weight of a fully equipped super-drawer is about 100 kg. The number of super-drawers is 128 for the barrel and 64 for each extended barrel. Including the spares (which will not all be fully equipped), 270 super-drawers will be fabricated.

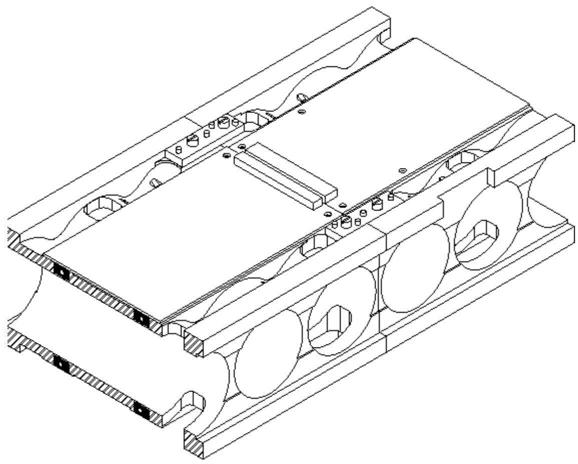

Figure 6-28 Connection between the drawers, and the holes in the PMT blocks for the cables.

In Figure 6-29 is a photograph of a super-drawer which has been partially extracted from Module 0. The HV part appears at the top side of the external drawer, and the microcontroller card and a portion of a distributor board are visible. Some PMT blocks are seen either from the light mixer side or from the end-cap side. The components of the super-drawers are described in the following sections.

6.3.2 Cooling

The electronics inside a PMT block are expected to consume 2.5 W. By setting some PMT blocks in an environment which reproduces a drawer and girder at room temperature, and using heating resistors to simulate this power consumption, it has been observed that after roughly 30 minutes the temperature reaches a plateau at $\sim 30°$ C. The conclusion is that no cooling is required inside a PMT block, due to the good thermal conductivity between the external iron cylinder of the PMT blocks and the aluminium material of the drawer.

The power consumption inside a super-drawer is roughly 120 W for the PMT blocks, 11 W for the HV distribution and 50 W for the digitizing electronics. Considering a super-drawer with 46

Figure 6-29 A drawer partially extracted from Module 0.

PMTs and an additional margin of about 20 W, the power consumption will never exceed 200 W inside a super-drawer.

During the Module 0 beam tests, two temperature probes (one in each drawer) showed that without any special cooling, the temperature stabilized around 35°C. The arrangement (with 46 PMT blocks, the HV distributors and the Cesium source integration) corresponds to roughly 70% of the total power consumption expected for the final system. Simulations have shown that by maintaining the temperature of the drawers at $18°$ C and relying on natural convection between the electronics boards, temperatures on the chips would be maintained at 40 to $50°\mathrm{C}$.

The iron mass near the drawers, in particular the girders, will be at the ambient temperature of the pit. The temperature of the drawers themselves will be maintained by the Leakless Cooling System [A.42], using water at 18°C. This cooling system is presently functioning in the L3 experiment at CERN, and is also under consideration for the electronics of the ATLAS Liquid Argon Calorimetry.

Figure 6-30 shows the arrangement of the cooling tubes inside the drawers. The main pieces are stiff tubes made with a material (duralumin) which is similar to the drawer material in order to prevent any chemical corrosion. The duralumin tubes are linked by plastic tubes to supply two crossed circuits, which are located at the top and bottom sides of the drawers for uniform cooling of the electronics.

The rigid tubes are designed with an internal diameter of 4 mm and a thickness of 0.5 mm. These tubes are glued inside dedicated grooves in the drawers, by using an aluminium loaded glue. The grooves do not require any machining after the drawer casting.

The flow rate and the temperature difference between the input and output of the system will be optimized during 1997 tests of Module 0 extended barrels.

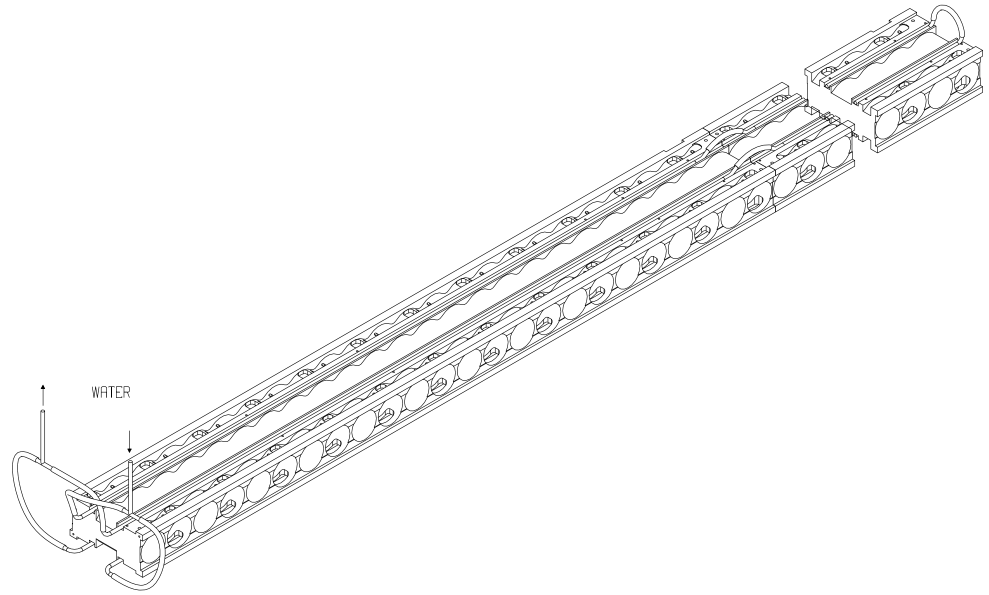

Figure 6-30 The Tile Calorimeter water cooling system.

6.3.3 Safety

The following sections describe different safety aspects which have been designed into the super-drawers, which house all of the on-detector electronics. The super-drawers are positioned inside the internal cavity of the girders. The girder-rings, which do not receive the fibre bundles, are closed by plastic pieces so that there is no communication at all between adjacent girders.

Cooling

The design of the Leakless Cooling System assures the water-tightness of the system under any circumstance. Depending upon the rate of water flow, the safety margin for cooling the electronics is at least a factor of 2 in the most pessimistic case.

Temperature probes

The microprocessor on the HV distribution boards also controls up to 6 temperature probes. Four probes are positioned near the microprocessor board, the current digitizing board, the pulse digitizing board, and the level-1 preparation board, and two others are located directly on each drawer. To prevent radiation damage, the silicon probes used in the Module 0 will be replaced by resistor probes.

Fire protection

One smoke detector is positioned on each internal drawer on the side of the HV distributors and near the link with the external drawer. The smoke detector uses an LED, and not a radioactive source. The power supply and read-out for this detector are fully independent from the other drawer electronics.

Power supplies

The HV source system is located in standard racks in the electronics room, and provides individual protection for each to the 256 channels. The HV distribution system inside the drawers, however, requires special care. In the case of a fault on an optocoupler, there are two possibilities: either the voltage is kept at the nominal HV value supplied by the corresponding HV source or this value is decreased by about 300 V (that is the working range of the optocoupler). In any cases the HV will be always lower than 900 V, with an individual control. Nevertheless an Interlock is foreseen at the patch panel level, which is a combination of a Fast Stop (red button) and microswitches cutting the power when the patch panel and/or the super-drawer are not well positioned. In the latter case the safety concerns also the darkness for the PMT workings. The interlocks are linked and fully independent from the electronics of the drawers. The individual protection of the LVs is given by fuses located at the level of the power supplies, and not near the super-drawers.

Cable insulation and connectors

The design of the super-drawers and PMT blocks minimizes the number and the length of the cables. The cables link mainly the PMT blocks to the super-drawer and the super-drawer to the patch panel. The characteristics and the insulation of the electric cables will comply to the ATLAS and the CERN safety specifications. Optical fibres will read-out the calorimeter into the counting room.

6.3.4 Connections and cabling

6.3.4.1 Patch panel

A conceptual design of the patch panel is shown in Figure 6-31. It is located on the end- plates at each end of the barrel modules, and on the external end-plates of the extended barrel modules. Heavy iron pieces are located at the ends of the barrel modules to guide return flux between the barrel extended barrels. These pieces are machined to leave space for the active portion of the patch panels.

The active portion of the patch panel is in the form of a box, the upper part of which contains the various connectors. In this scheme, the external cables are routed out of the detector radially. The passive portion of the patch panel is a plate which closes off the remaining space of the girder.

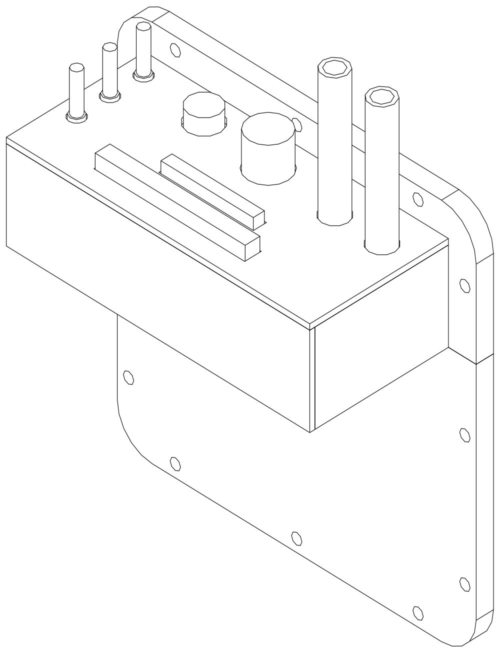

Figure 6-31 Conceptual drawing of the patch panel.

The cables attached to the super-drawer are connected to the inner part of this box. Optical interfaces for transmission of digitized data to the RODs or other elements are located inside the active portion of the patch panel, and connected by short cable links to the super-drawer electronics.

Connections on the patch panel include:

- Two tubes for the LCS water cooling,
- An SHV connector for the HV distribution,
- A low voltage power connector attached to the supplies of the HV distribution system,
- A low voltage power connector for the supplies of the 3-in-1 bases, the digitizing electronics, and the optical drivers,

- An optical link to the RODs,
- An electrical (or optical) link for the cesium calibration electronics,
- An electrical link for the field bus of the slow control for HV, 3-in-1 bases, digitizing electronics, etc.; probably twisted pair cables,
- An electrical (or optical) link for the Level-1 trigger,
- An optical link for the TTC distribution,
- An independent connector for the safety controls (smoke detector, interlocks).

Space for connectors is restricted; a first-pass optimization will be performed for the 1997 tests of Module 0.

6.3.4.2 General cabling

The cabling scheme between the patch panels and the electronics room depends upon the optimization of the patch panel, and decisions to use electrical or optical links for the different signals.

There is only one HV cable per super-drawer, so the HV cables can be easily routed in 4 bundles (corresponding to the two half-barrels and the two extended barrels). Each cable bundle is about 80 m long.

The LV cables which supply the HV distributors and the other electronics parts (3-in-1 bases, digitizing electronics, etc.) are separated. They are either 20 or 80 meters long, depending on the location of the LV power supplies, and are assembled in two sets of four bundles. All the other links (coaxial cables, twisted pair cables, optical fibres) are ~80 m long, but the final routing has yet to be decided. In any case, the total number of cables is small, and the radial routing scheme can be easily made to fit overall routing plans proposed by the ATLAS collaboration.

6.3.5 Super-drawer test bench

The various electronics components of the super-drawers are tested on dedicated test benches before the drawer assembly. The completed drawers are paired into super-drawers, and the super-drawer test bench performs a final certification of the entire drawer electronics system.

An initial design of a super-drawer test box has been built for Module 0: it consists of a support with rollers which enable insertion of the super-drawer in the box, a patch-panel which provides connections for the electrical connections and optical fibres for the HV distributor slow control, and optical fibres fed by blue LEDs for testing the PMT blocks. A second, portable system will be developed in 1997 which will be able to control, test, and record the data coming from a super-drawer.

The final super-drawer test bench is ~3.5 m long and accommodates two super-drawers. A closed-circuit LCS (now in construction) is connected to the two super-drawers in order to test the cooling of the drawers and to stabilize the temperature during the other tests. A sequential program carries out tests of all the components and the connecting hardware (bus boards, mother boards, cables and connectors, patch panel), as well as the slow control (including safety aspects such as the cooling, temperature probes, interlocks, and smoke detectors).

The PMT blocks are tested using:

- blue LEDs, working in a pulse or in a continuous mode, and
- the electronics calibration system.

Both of these tests also verify the operation of the shaper and integrator portions of the 3-in-1 base are tested, as well as the digitizing electronics.

Tests of the super-drawers are performed immediately after the assembly of the drawers. The full test sequence requires less than one day, and two super-drawers are tested per day.

The test bench will be designed and used by the institute responsible for the super-drawer assembly. The test bench will then be transported to CERN for use during the installation phase.

6.4 Fast Pulse Electronics

6.4.1 Introduction

The fast read-out electronics must process signals from 10,110 photomultipliers every 25 ns. As described above, these signals have a dynamic range of 16-bits and a precision of 10-bits. Signals corresponding to the energy in the 2000 calorimeter trigger towers must be formed and sent to the off-detector LVL1 trigger electronics on every beam crossing. During the 2.5 microsecond latency of the LVL1 trigger, the individual calorimeter signals are stored. Following the latency period, data from events accepted by the LVL1 trigger are passed to read-out driver modules (RODs) for further processing prior to transmission to the LVL2 trigger. Signals from beam crossings failing the LVL1 trigger are discarded.

Two approaches have been considered for signal storage during the LVL1 latency; either digital or analog storage. The digital approach offers straight forward use of digital memories but requires processing each signal with a fast ADC every 25 ns. Until recently there were no commercial ADCs with the necessary characteristics, but within the past year three have appeared on the market. Their power consumption is typically 0.5W and the cost is as low as 22 CHF. The alternative approach is to store analog signals on a capacitor for 2.5 microsecond and to digitize only the signals of events passing the LVL1 trigger. This permits the use of slower, multiplexed ADCs.

For the Tile Calorimeter, with its relatively modest number of channels and low channel density, the approach of digital storage has been developed, particularly for the Module 0 test activity. It is felt that this approach provides a straightforward solution to the Tile Calorimeter read-out requirements. As described below, a baseline design has been built, tested in two test beam periods, and costed in detail. This design uses a non-linear range compression scheme followed by a single ADC and a lookup table to restore linearity. As a backup, a second approach is being explored which uses a linear bi-gain pulse shaper and two commercial 12-bit ADC chips per channel. It is planned to evaluate the latter approach in future test beam studies. Both designs need further study before mass production begins in early 1999.

In September, 1996, the Liquid Argon Calorimeter community selects an analog pipeline solution for their Module 0 program. This solution will be available for evaluation at the end of 1997, and studies will be performed to evaluate its performance in the Tile Calorimeter framework.

6.4.2 Front-end electronics

The read-out electronics is divided into several parts. The front-end electronics is located on the 3-in-1 cards within the PMT Blocks described above. Here the current pulse from the PMT is shaped and converted to a voltage signal which is transmitted by short shielded cables to the fast digitizers located at one end of the Super Drawers. They receive services from the Mother Boards which run the length of the drawers.

In order to meet the physics goals of ATLAS, it must be possible to measure particles which deposit a wide range of energies in the Tile Calorimeter. A dynamic range of 16 bits is needed to measure both minimum ionizing energy deposits from muons and deposits of up to 2 TeV in a single cell from the highest energy jets. Since the intrinsic resolution of the calorimeter is less than 16 bits, it is desirable to compress the dynamic range and digitize the signals using ADCs with a resolution of 10 or 12 bits.

It is not practical to locate digitizers inside individual PMT Blocks because the space and access are limited, and the cost of distributing the additional services would be prohibitive. Noise considerations are also a concern.

6.4.2.1 Baseline Configuration

In this design the 16-bit dynamic range is accommodated with a non-linear compression circuit located on the 3-in-1 card. Thus the analog signal transmitted to the digitizer has only a 10-bit dynamic range. Following digitization, the compressed signal is re-linearized by a look-up table.

Shaper

The shaper is a linear circuit designed to process the current pulse from the photomultiplier tubes into a unipolar analog signal. Since the single shaper must cover the full dynamic range, a very low noise must be achieved. A 16-bit dynamic range and a maximum output swing of 4V (differential) requires an output noise level of less than 60 microvolts.

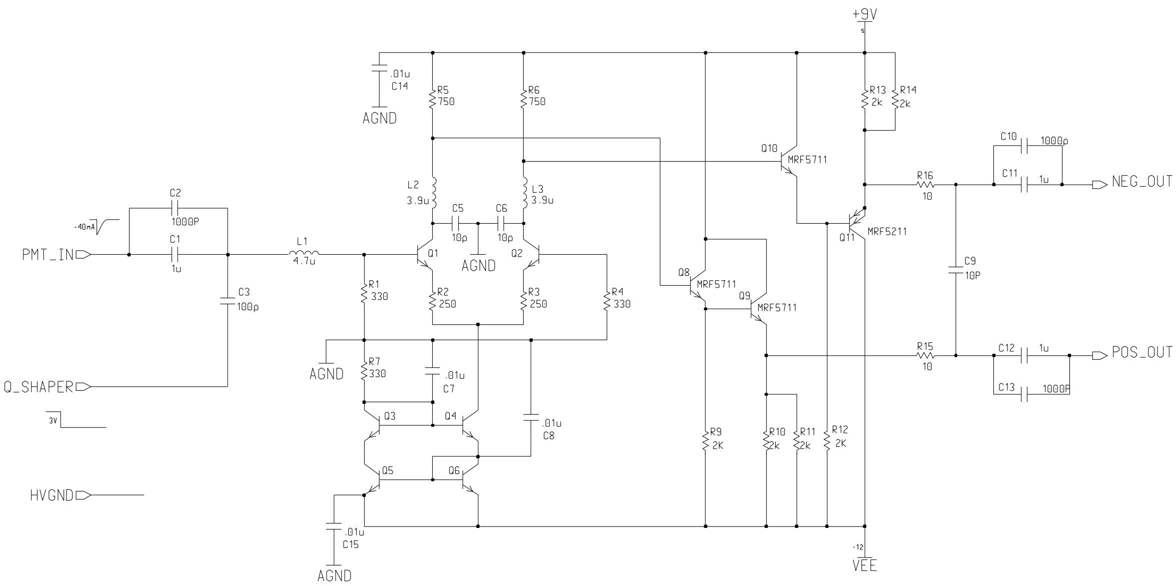

Figure 6-32 Schematic of the 3-in-1 shaper circuit.

The solution to this problem has been to utilize the current-source nature of the PMT output to minimize the number of active components, and to exploit the fact that capacitors and inductors are nearly noiseless devices. The PMT produces a fast current pulse with a FWHM of about 15 ns. The desired output from the shaper is a unipolar pulse of FWHM of about 50 ns.

The circuit design is based on a four-pole low pass Bessel filter and has been fully described in [A.37]. A schematic of the present version is shown in Figure 6-32. The computed noise of 35 microvolts arises from the low noise bipolar transistors required for impedance matching and from the few resistors used to set their gain, operating point, and impedance.

The shaper output is a unipolar pulse of 50 ns FWHM with amplitude proportional to the input charge. Studies of PMT pulse shapes from the calorimeter for both hadrons and muons using a high performance digital oscilloscope have been used as input to SPICE simulations of the shaper. It is found that the charge-to-amplitude relation is preserved for the range of shape variation seen in the tests. The output signal from the shaper is differential with a peak-to-peak amplitude of 4 V. The profile of the shaper output is shown in Figure 6-33.

In its original design, the shaper was not required to produce a signal for LVL1 trigger summation since a digital trigger signal was planned. In light of the recent technology decision, an additional output stage could be added.

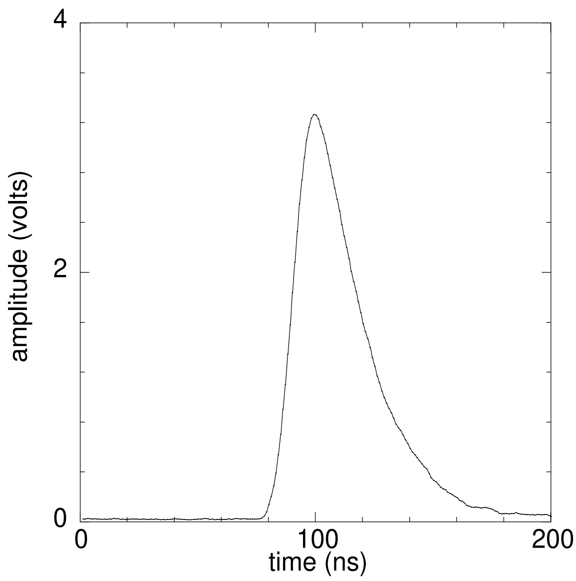

Figure 6-33 Shaper output for a typical pulse.

Compressor

The transfer function of the compressor circuit is designed to have a piece-wise linear form with four segments. Its schematic is shown in Figure 6-34. The output from the shaper is connected to four differential stages with different gains, and the output signals of these are added to form a compressed transfer function.

The compressor gain is 20 for small signals (35, in a version under development). The gain in the second stage is 1.2, and the attenuation of the largest part of the signal is typically a factor of 10. The piece-wise linear response of the compressor is demonstrated in Figure 6-44 (see Section 6.5.2.3). Figure 6-35 shows the response of the shaper and compressor to charge injector calibration pulses from the 1995 Tile Calorimeter test beam data. The effect of the compressor is evident as the pulse amplitudes increase.

For Module 0, the compressors are implemented in a semi-custom bipolar process (Genum Ga 911), and located on the 3-in-1 boards near the shaper stage. This implementation has a bipolar differential output with drivers which send the output signals via coaxial cables to receiver circuits at the front-end of the ADC boards. The specifications of the compressor are listed in Table 6-4.

The shaper is capacitively coupled to the compressor, which in turn is capacitively coupled to the digitizing circuit. This is not a problem in low rate test beams, but at high rates baseline shifts both before and after the non-linear element can lead to some unresolved errors. Further development work is needed to eliminate this problem.

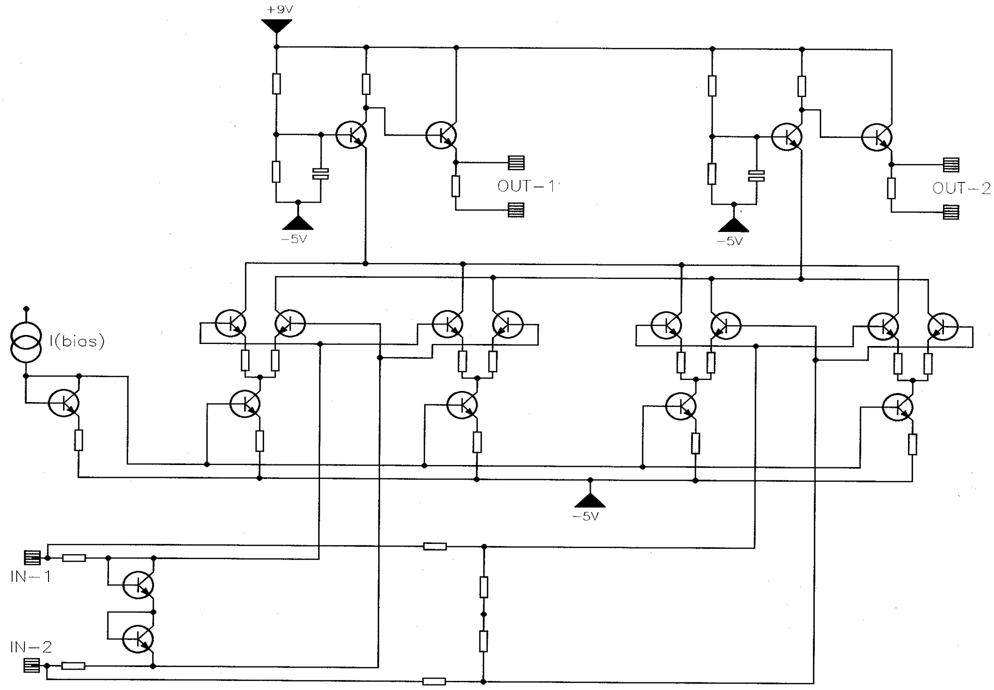

Figure 6-34 Schematic of the compressor circuit.

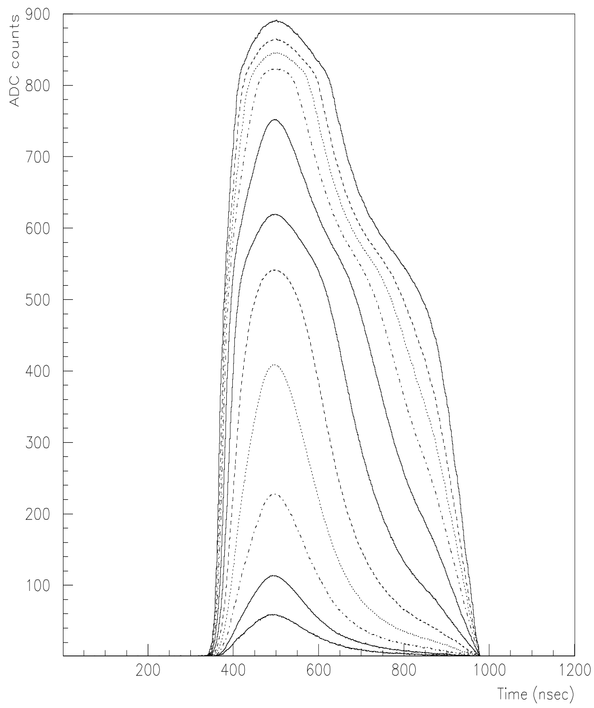

Figure 6-35 Response of the shaper and compressor for charge injector calibration pulses from the 1995 test beam data.

6.4.2.2 Options under study

One option being investigated instead of the non-linear compressor is the use of two linear outputs for each channel, differing in gain by a factor of 32. Each output covers a dynamic range of

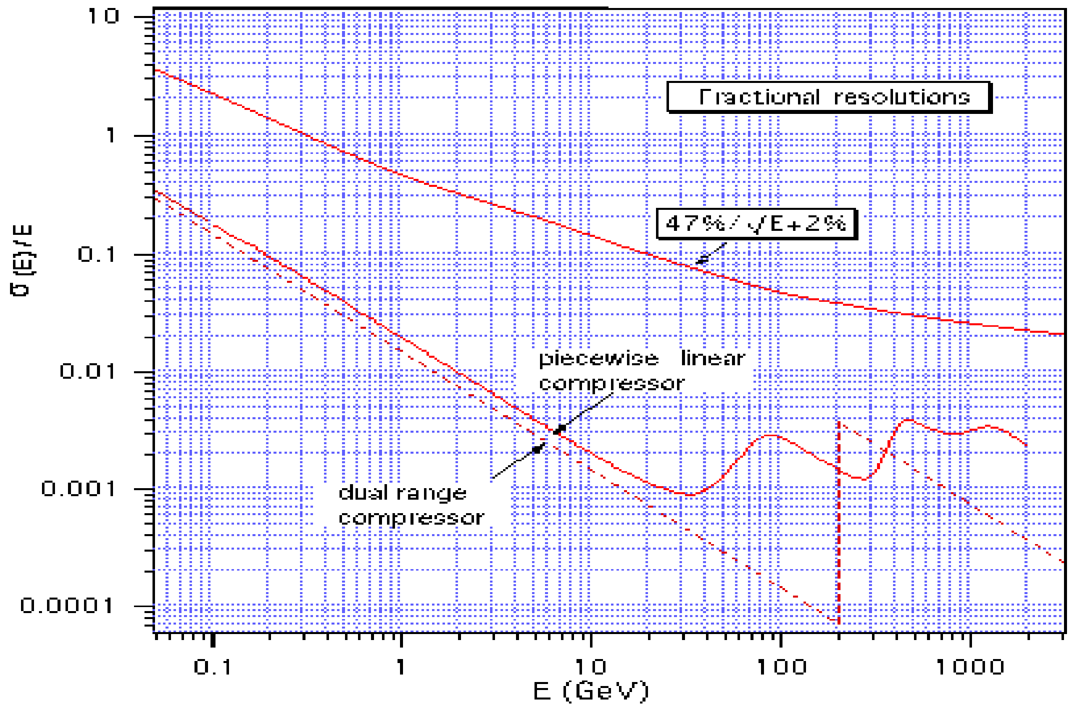

Figure 6-36 The intrinsic resolution of the Tile Calorimeter, with the resolutions of a four-stage piecewise-linear compressor and a dual-gain compression scheme for comparison.

Table 6-4 Compressor Characteristics.

Maximum input/output amplitude	±2V
Pedestal noise with shaper connected	1.5 mV (rms)
Small signal bandwidth	50 MHz
Power consumption +9V, ±5V (drivers not included)	60 mW

12 bits and is linear in the charge of the input signal. In addition, provision has been made for an output for analog trigger summation.

A circuit diagram for this shaper is shown in Figure 6-37. The shaper circuit uses a seven-pole Bessel low pass filter to give an even faster settling time than the previous four-pole design. The fabrication of the filter has been contracted to a commercial filter company to achieve a guaranteed time resolution and repeatability from unit to unit. The input impedance of this shaper is 250 ohms and the filter consists of three inductors and four capacitors chosen to take into account layout contributions from PC board traces and connecting elements. Two outputs would be provided; one through a gain of 32 amplifier, and the second through a unity gain amplifier. This will cover the dynamic signal range of 800 pC with the equivalent resolution of 17 bits and provide good overlap in the transition region between the two scales. The gain-of-32 amplifier is chosen to have excellent overload recovery characteristics. It recovers from a 32 times overload in about two nanoseconds.

An analog trigger will be developed from the unity gain buffer that exists between the amplifying components and the shaper proper.

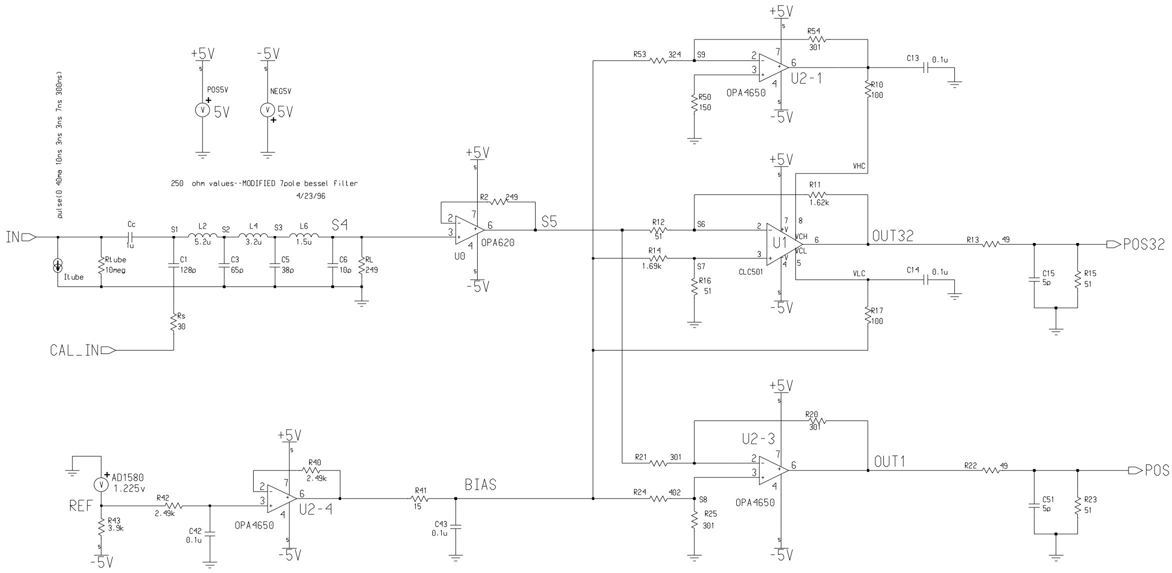

Figure 6-37 Shaper circuit diagram for a dual gain read-out.

Because of the multiple digital samples of each signal, this system can be AC coupled to the digitizer without introducing problems due to rate. The system is linear and hence the total baseline shift can be measured and subtracted. No special correction table is necessary.

6.4.3 Mother boards

Signals and services are transmitted along the electronics drawers with a 3-layer structure, as shown in Figure 6-38. The inner layer carries low voltage power and digital control signals to the PMT Blocks. The middle layer supports cables carrying the analog signals from the PMT Blocks to the digitizers, while the outer layer contains the LVL1 trigger summation circuits and their output cables.

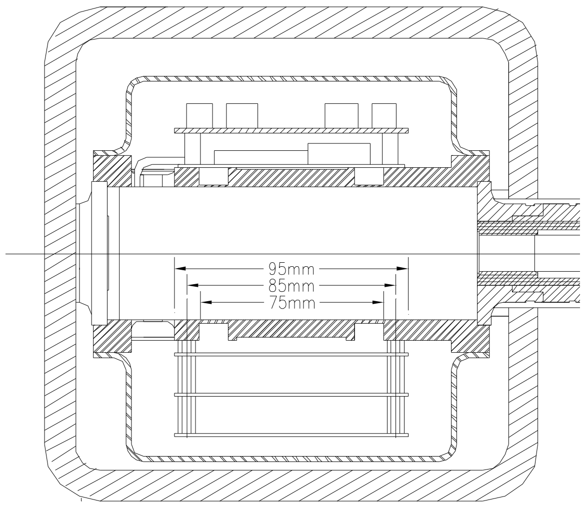

Figure 6-38 Motherboard cross sections.

6.4.3.1 Low voltage and control board

The innermost layer is formed by a printed circuit board carrying the low voltage power and digital control signals to the PMT Blocks. As discussed in Section 6.3, the mother board must be divisible into at least two sections to permit removal of the drawers in the space available. To facilitate maintenance, and to increase the number of potential suppliers, the mother board is formed from four 70-cm-long sections.

The mother board transports +5V, -5V, and +9V power. It also supplies a precise 4V reference voltage used for the charge injection calibration by each 3-in-1 card in the drawer. A differential analog bus for read-out of the integrators also runs the length of the mother board.

Digital control of the 3-in-1 cards is necessary for charge injection calibration, to control the gain of the slow integrator, and to control the switching of the slow integrator onto the analog output bus. To achieve these functions an RS-422 differential digital bus runs the length of the mother board. Since it is desirable for each of the 10,300 3-in-1 cards to be identical, they are addressed according to their location. Address decoding and selection is done on the mother board.

6.4.3.2 Analog signal board

The analog output signals from the PMT Blocks are connected to the digitizer board at the end of the drawer by shielded twisted pair cable. The cables are supported on a plate in the central position of the 3-layer structure. The cable lengths are chosen to equalize the timing of the signals at the input to the digitizer board to ± 2 ns. This allows a single phase of the digitizing clock for all signals in the drawer. The similar timing simplifies the calibration procedure and the subsequent processing of the digitized samples. The cables carrying the analog signals must contain a connector at the mid-point of the Super Drawer to allow the division of the drawer into two pieces.

A 40-cm-long printed circuit board containing the digitizer electronics is located in the outer section of the super-drawer at the same height as this analog signal board, and replaces the analog signal board in this region.

6.4.3.3 LVL1 trigger summation board

As discussed below in Section 6.4.6 the formation of analog sums for the LVL1 trigger towers is done on small printed circuit boards which form the third layer of the electronics drawer. Up to nine boards are needed in a Super Drawer. To reduce the amount of cabling, the boards are distributed over the length of the drawer close to the source of their five input signals. The output signal from each board is routed along this layer on a shielded twisted pair cable to the patch panel at the end of the drawer.

6.4.4 Digitization and pipeline

The current understanding of the Tile Calorimeter read-out is based on a fast digital sampling of a shaped waveform, and storage of the signal in a digital pipeline for later read-out upon a LVL1 trigger accept. The solution for the digitization which has been tested and implemented in the framework of the Module 0 activity is a 3 channel ADC board developed by CAEN, which uses 10-bit ADCs developed within the framework of RD-16, and stores the digitized samples in 256-bin FIFOs. The board has a height of 6U, and is controlled and read-out in VME.

Evaluation of this type of read-out is proceeding as part of the Module 0 test beam data analysis. To ensure that the final digitizing system is adapted to our needs and is cost effective we continue to explore the two alternatives described below. We expect to choose the final technology following beam tests in 1997 and to demonstrate the final system in beam tests in 1998, prior to the start of mass production the following year.

6.4.4.1 Options under study

FERMI MCM concept
One solution for the final Tile Calorimeter read-out in ATLAS is based on the RD-16 concept which is a Front End Read-out MIcrosystem developed for calorimetry applications within the

RD-16 group, and implemented as a multi-chip module (MCM). The basic version acquires data from 6 analog calorimeter channels which have been compressed by a non-linear amplifier. This permits pulses with a large dynamic range but of moderate resolution to be faithfully represented by a sequence of 12-bit samples. The compressed signals are sampled every 25 ns by a 12-bit ADC, then translated into a 18-bit representation by a lookup table which inverts the effect of a non-linear transformation.

The linearized values are fed to a pipeline memory where they wait for the trigger decision. Sample sequences which are not connected with events accepted by the level-1 trigger are eliminated, and the others are transferred to derandomizer memories and, when requested, filtered in a second digital filter processor prior to transmission to the second level trigger. In most cases only one value, i.e. the result of the filter operation is sent, but it is also possible to send a full time-sequence of samples for diagnostic purposes.This module is built on an MCM-D silicon substrate which provides a benevolent environment with respect to interference and signal strengths. The standard MCM design will contain one ADC and one "channel chip" per channel, an adder, a clock management chip, an output filter, and a read-out controller chip.

Based on the recent decision by the Liquid Argon community to use an analog solution for the LVL1 trigger tower summation and transmission, it is likely that both the hadronic and electromagnetic calorimeters will be required to supply an analog input to the LVL1 trigger. Once this approach is followed, some of the functionality of the proposed MCM design is no longer necessary; no digital summation and filtering is needed, and the function of the LUT can be performed in the ROD modules for events passing the LVL1 trigger. Therefore, some of the ASICs in the FERMI MCM could be eliminated.

A second alternative for a simplified MCM would be to use a switched gain ADC, together with the linear bi-gain shaper described above. This would preserve the 6 channel modularity of the MCM but again require fewer ASICS. This option, however, requires the development of a switched gain ADC which would be built around a commercial 40 MHz 12-bit chip.

Dual ADC Digitizer

The development of commercial 40 MHz 12-bit ADCs has greatly reduced the development effort needed for the digitizer system. There are currently three manufacturers of such devices and the cost per channel is as low as 22 CHF. The modest channel density of the Tile Calorimeter makes possible a system using two ADCs per channel, in association with a local FPGA controller. The system would process the output of the linear bi-gain shaper described above and store the digitized values in a 120-location memory. The system would be fully linear and be constructed from off-the-shelf components. It is planned to demonstrate the essential aspects of such a system in upcoming test beam studies.

6.4.5 Read-out drivers (RODs)

The read-out drivers (RODs) comprise the part of the front-end electronics farthest downstream from the analog front-end, and communicate directly with the read-out buffer. The task of the RODs is to collect digitized information from the front-end sources onto a single high-bandwidth link, to format the data, with some amount of preprocessing and inclusion of bunch crossing information, and to send the data to read-out buffers (ROBs) for processing by the Level-2 trigger.

According to the ATLAS trigger & DAQ architecture, the main ROD specifications are the following:

- Data gathering,

- Timing, trigger and control signals reception,
- Error detection and recovery,
- Data formatting,
- Output optical link,
- Test, calibration and monitoring ability.

The planning of the ROD described here assumes minimal data processing by the relatively inaccessible on-detector electronics. This is also the approach taken for the electromagnetic calorimeter. We assume that for all events passing the LVL1 trigger, a set of 7 samples of 2 bytes each are passed to the RODs from each PMT of the calorimeter. For the single fibre from each super-drawer this leads to a maximum data rate of 386 Mbits/s at the nominal maximum LVL1 trigger rate of 75 KHz. It is planned to process the data from eight super-drawers in a single ROD module, and this leads to a total of 32 modules. If each ROD processes data from two azimuthal sectors of the calorimeter over the full rapidity coverage then 308 PMT signals are processed per ROD.

Within the RODs, calibration corrections are applied to the samples from each PMT signal. Signals from the two PMTs viewing each cell are added and digital signal processing of the sum is done to extract an optimal estimate of the energy and time for each cell. After this processing the data is transmitted to the LVL2 trigger. The output data rate from each ROD, assuming two words of 2 bytes per cell together with header information, would be 50 Mbytes/s. Using current technology, a single optical fibre link of 1 Gbit/s from each ROD could handle this rate.

6.4.5.1 ROD prototype

A first functional ROD prototype has been implemented for detector tests. It consists of a commercial data processing board from LSI Corporation (DBV44) with three C40 DSPs. The input port has been implemented using an optical TAXI interface at 10 MB/s.

One DSP is in charge of receiving the data and passing them to the other two. The second DSP performs the header formatting, while the third performs the data processing, which at this point multiplies the data in each channel by a correction factor.

A daughter board has also been implemented which includes the hardware needed for the rest of the ROD functions, except for the TTC signal reception. It includes an optical output port at 1 Gb/sec using a commercial device by Finisar Corporation (FTR-1101). The daughter board block diagram for Prototype 1 is shown in Figure 6-39.

Initial tests have shown that the maximum number of channels which can be processed with this system is 30, if the data are 2 bytes long. This restriction is due to the C40 processing power and to the closed architecture of the DVB44. It is clear that further studies must be performed to increase the number of channels per ROD in accordance with the Tile Calorimeter requirements.

6.4.5.2 Test results

The processor for Prototype 1 was tested in a standalone system at CERN. A setup was used consisting of a NIM crate containing the trigger logic, and a VME crate containing a RAID VME Module running EP/LX operating system, a 3-channel FERMI module, an RCB Interrupter Module and the DBV44 board with a single C40 DSP processor.

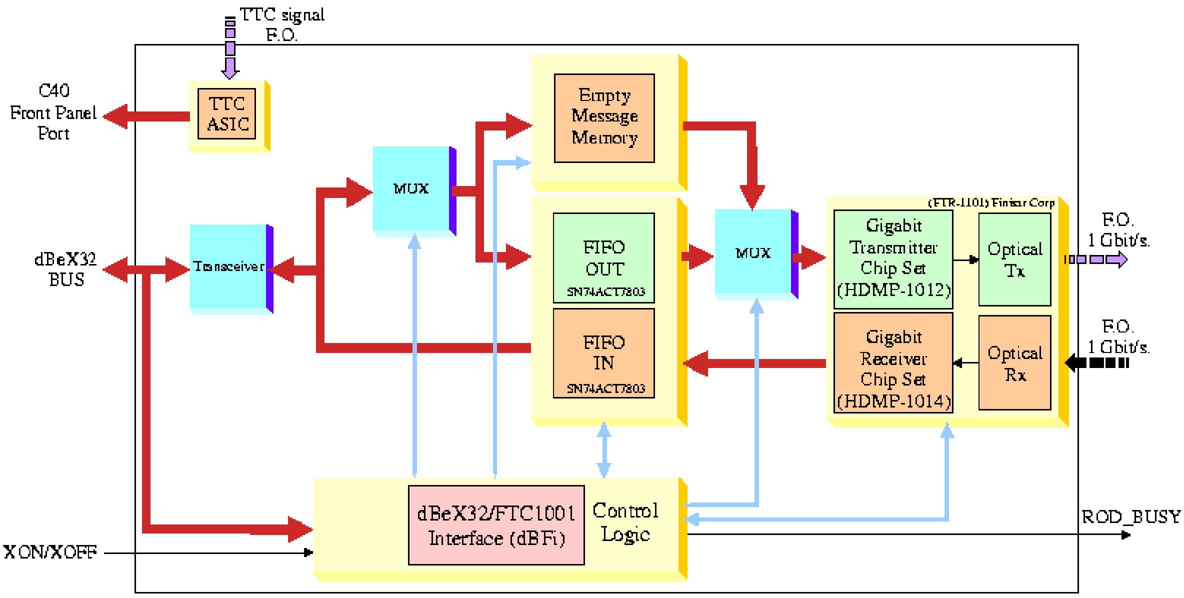

Figure 6-39 Tile-Cal ROD Prototype 1 daughter board block diagram.

Different tests were performed, and processing times were measured for two data processing algorithms. The first algorithm multiplied each channel by a constant factor (analogous to a calibration constant), and the second algorithm added the values of channels within a trigger tower.

In the tests, the RAID processor waited for a VME interrupt generated by the RCB module, and then wrote data to the DBV44, which processed and sent the data either back to the RAID or to the DBV44 external memory.

Results of these tests are presented in Table 6-5. The times presented include the period between sending the data from the RAID processor to the DBV44, the data processing, and the data transmission either back to the RAID or to the DBV44 external memory. In all cases, the amount of data processed corresponds to 60 FERMI channels with 40 samples each, treated as 16 bit words.

Table 6-5 Results of ROD Prototype 1 standalone tests.

DATA OUTPUT	OPERATION	TIME (ms)
VME	Calibration correction	6,3
	Trigger Tower gathering	4,1
DBV44 external memory	Calibration correction	2,4
	Trigger Tower gathering	1,93

6.4.5.3 R&D program

As stated in the last section, Prototype 1 is not suited as a final ROD design for the Tile Calorimeter. For that purpose, a 2-year R&D program has been proposed to design and build a final ROD module which will fulfil the requirements.

Between the end of 1996 and the beginning of 1997, standalone and beam tests of Prototype 1 will verify whether it fulfils the functionalities specified for it. From these tests, modifications of the prototype will be studied in view of the final ROD version.

In 1997, a final Tile Calorimeter ROD prototype will be designed. For this task, feedback from the front-end electronics chosen for the detector is needed. Also, aspects such as segmentation, data processing algorithms, and data multiplexing must be decided. At this level as well, input and output links and processor technology should be frozen in view of the construction of the final prototype.

With all of the experience gained, a final prototype will be constructed during 1998. This prototype should be ready, with the exception of minor changes, for operation of the Tile Calorimeter in ATLAS.

6.4.6 LVL1 trigger

The LVL1 trigger system requires trigger-tower signals from the calorimeter systems. The trigger towers are built by summing the sampling layers of the electromagnetic and hadronic sections, with a transverse size of 0.1 x 0.1 in η and φ (for rapidities up to 2.5).

For the tile calorimeter, this requirement in the barrel region translates into the summation of five signals from the three sampling layers: two from the first layer, two from the second layer and one from the last layer. For some towers in the overlap region between barrel and extended barrel, and in the extended barrel itself, fewer signal need to be summed. Nevertheless, for simplicity, the same 5-input circuit would be used for all towers.

An analog summation scheme has been suggested in the last few months and the detailed design is underway. Differential input signals are received from the shaper, and should be aligned in time to within about 2 ns. The adder is linear for output signals up to 250 GeV (2V), and noise levels should correspond to less than 0.25 GeV. The output will be on differential twisted pairs over a length of approximately 70 meters.

These LVL1 summing boards would make up the outer layer of the 3-layer structure in the drawer. The output signals would be routed along this layer to the patch panel at the end of the drawer.

6.4.7 Module 0 configuration and results

The Tile Calorimeter Module 0 is instrumented with 46 read-out channels following the baseline design described above. Signals from the shaper/compressor combination are routed along the electronics drawer to digitizers located near its end. In this case the digitizers are just outside the end of the drawer in VME modules. They contain custom 10-bit, 40 MHz ADCs followed by a FIFO memory and were developed as part of the FERMI RD-16 project. This configuration was used to record the Module 0 data collected in the September 1996 test beam run. A similar system was used in 1995, in parallel with a conventional CAMAC charge integrating ADC system. In this case it yielded better energy resolution than the conventional system. Because of the limited test beam energy, the use of a 10-bit ADC, and the importance of successfully studying the calorimeter characteristics, the shaper for these first studies of Module 0 was designed with a gain 4 times larger than it would have in the final ATLAS application.

Results of using this system are shown in other sections of this report. Figure 6-40 shows the calorimeter response to muons for the three sampling depths. The pedestal response for the same channels is superimposed on the plot. The muon signal is clearly resolved although more work is indicated to further reduce the pedestal noise.

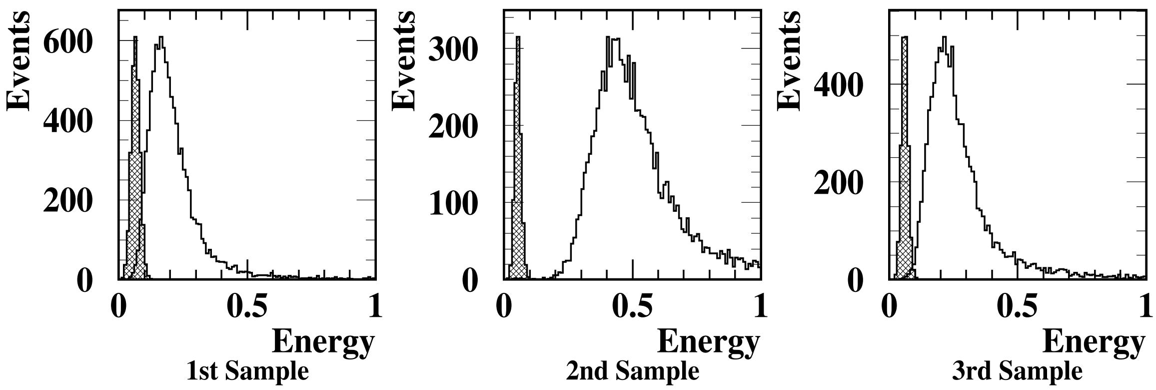

Figure 6-40 Tile calorimeter response to muons for the three sampling depths.

6.5 Calibration electronics

6.5.1 Charge integrator

The charge integrator is located on the 3-in-1 board, and is designed to measure the average current of each calorimeter cell due to the energy deposits from the radioactive source, or from Minimum Bias (MB) interactions. As described in Chapter 7, this procedure allows to the response of each cell to be calibrated and monitored. The currents from the PMTs must be averaged over a time scale which is long enough to suppress the ripple from individual pulses, as well as fluctuations in the amplitude and rate of energy deposits in each cell.

For calibrations using the movable source, the PMT signal consists mostly of single photoelectrons, with a rate of about 4 MHz. The average source currents observed with barrel Module 0 and a 9 mCi ^{137}Cs source are about 50 nA at the nominal PMT gain of 10^5. To measure such currents an integrator circuit based on a JFET-input operational amplifier with a suitable RC time constant is a simple and economical solution.

The MB signal spans a much broader range of frequencies and amplitudes, which depend on the LHC luminosity, pseudorapidity and the location of each cell in the calorimeter. MB currents are expected to span the range between 5 nA and 500 nA. The operational amplifier used for the source current read-out may also be used to measure MB currents, however a programmable transimpedance must be included as well.

Requirements on the coupling to the PMT anode (DC coupling, and large equivalent source impedance) are discussed further, together with the adopted solution for the anode-integrator-shaper input configuration.

The RC time constant of the integrator is the only remaining open parameter. It is found that a time constant between 0.7 to 10 ms range (depending on the selected transimpedance) is adequate to satisfy stability and speed requirements for both operation modes:

Calibration and monitoring with a movable source:
For the source calibration mode, the integrator would be run with an integration time constant between 2 and 5 ms, which:

- is (amply) sufficient to obtain a source current signal which is stable to better than 1%,
- is small enough not to limit the observed signal variation as the source moves between tiles at the design velocity of 30 cm/sec,
- does not limit the rate of data acquisition, which is instead limited by the source velocity.

Monitoring of minimum bias currents:
Due to the enormous range of cell signals (typically between 1 and 10^5 photoelectrons/crossing), one can only specify a probability to exceed a given signal. Based on the MB simulations described in Chapter 7, the ripple in the output of the integrator would be greater than 1% for cell signals of 8 to 10 times the rms value of the MB cell energy spectra. A more precise estimate of the probability of getting an anomalously large signal would require much greater statistics than are currently practical in simulating MB interactions.

Integrator digitization and read-out can be performed on the relaxed time scale set by the integration time constant. As explained below, the integrator outputs are multiplexed to one ADC/super-drawer. This is sufficient to keep up to the movable source signal variation, and to read-out the MB currents over the entire Tile Calorimeter within a few seconds.

The system as designed will allow MB current measurements for the whole Tile Calorimeter with a small time overhead with respect to other detector calibration measurements. This will allow occasional larger readings from the harder p-p interactions to be discarded.

6.5.1.1 Front-end circuit

The integrator uses a JFET input operational amplifier with a resistive and capacitive feedback which defines the integration time constant and the DC transimpedance of the circuit. A schematic of the integrator circuit is shown in Figure 6-41. Because the dynamic range of the minimum bias currents to be measured varies with the position of each cell relative to the interaction point and with the luminosity of the LHC, a programmable transimpedance is required to maintain an adequate resolution. The required resolution is fixed such that the smallest expected minimum bias current will be converted into 40 counts by a 12 bit ADC, thus allowing current measurements with a minimum resolution of 2.5%. During cesium source calibrations, a resolution better than 1% is achieved. The operational amplifier power supplies are +8 V and -5 V, providing an output signal range of 0 to 5 V. The feedback configuration is selected by four analog switches that are controlled remotely with the communication interface of the 3-in-1 card. The programmable gains are defined by six transimpedance values, namely 7.5 M, 20 M, 27.5 M, 54.3 M, 72.9 M and 100 M. The smallest transimpedance value is set by the largest calorimeter cell MB current at LHC design luminosity, with a margin of 1.5 for higher currents.

Because the largest resistance available in surface mounting technology is 20 M, a T feedback structure is required for the three highest gains. However, 100 M is fixed as a limit for this scheme to prevent the design from being too sensitive to the bias current and offset voltage of the operational amplifier. In this configuration the LSB of the 12 bit ADC is equivalent to 12.2 pA, making the smallest measurable MB signal of 500 pA equivalent to 40 ADC counts.

The photomultiplier tube is DC coupled to the integrator, since the average DC current is the quantity of physical interest. Additionally, the equivalent source impedance seen from the integrator input must be as large as possible to minimize the offset voltage at the integrator output. Since the PMT output is also connected to the shaper, which presents a relatively low input impedance, the shaper is AC coupled to the PMT. A cutoff is thereby introduced in the frequency response of the integrator, which is designed to be higher than the one needed for calibration

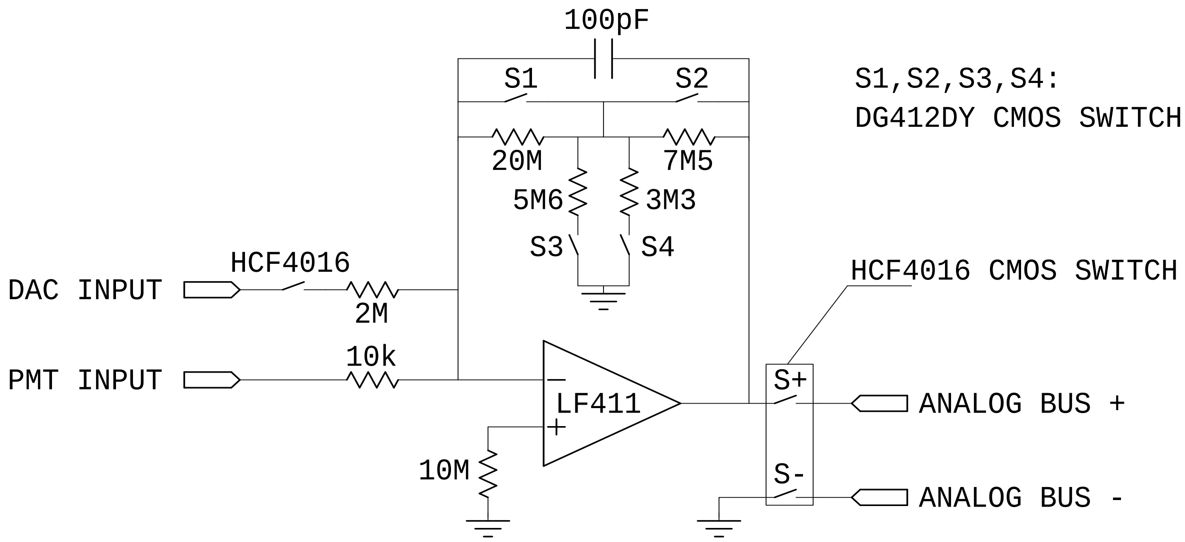

Figure 6-41 Schematic of the integrator circuit.

purposes. The capacitive feedback of the integrator fixes the time constant at 10 ms for the highest gain, giving a ripple of less than one LSB for cesium calibration operation.

The calibration of the six selectable transimpedances is done with a $2\text{M}\Omega$ precision resistor connected at the integrator input. Applying a known voltage to this resistance injects a reference current which is used to calibrate the transimpedance. The circuit is intrinsically linear, so only two calibration points are necessary to determine both the transimpedance and the pedestal.

The output of the integrator is connected via a CMOS switch to the output connector of the 3-in-1 card. When closed, the switch transfers the output via an analog bus to a single ADC per drawer.

Test results

The transimpedance measurements on integrator prototypes have showed deviations of less than 2% from the nominal value, with a non linearity of less than 0.3%. Due to the offset voltage of the operational amplifier, a negative zero-signal intercept of up to 150 mV is observed, the latter value corresponding to the highest gain. This intercept is cancelled by introducing a +200 mV pedestal in the ADC input stage. Pedestal drift over the time scale of the source calibrations was less than one LSB. Measurements of the 6 transimpedances and the pedestals were measured for each of the 46 integrators on the 3-in-1 cards in Module 0, giving a dispersion of gains less than 1.3%. In Table 6-6, the results of measurements of the 46 integrator channels of Module 0 are summarized.

Integrator test bench

The test bench for the integrator is the drawer's motherboard itself, using the 3-in-1 controller and ADC controller modules. This is in fact how the test results above were obtained. Tests may be made of the functionality of the CMOS switches and the integrity of the analog bus, and faults on the analog bus connection, crosstalk and current leakage through the output CMOS switches may be detected.

Table 6-6 Measured characteristics of integrator channels on Module 0.

Nominal Gain (MΩ)	Mean Gain (MΩ)	RMS Gain Variation (%)	Mean Pedestal (mV)	Pedestal Dispersion (mV)
7.5	7.6	0.5	-2	10
20.0	20.4	1.3	-4	25
27.5	28.0	1.0	-14	30
54.3	55.2	1.1	-29	50
72.9	74.4	1.2	-39	75
99.7	101.1	1.3	-44	80

6.5.1.2 Services and control

As described in Section 6.4.3.1, the services and control are supplied by a mother board running the length of the drawer. Some functions of the control are for the charge injection system described below in Section 6.5.2.

Digital control

The principle functions on the 3-in-1 card are encoded in a 12-bit word sent serially from a VME-based controller to the target card. Signal transmission is via RS-422 differential digital-data protocol. This provides good noise immunity, together with excellent speed and transmission distance capability.

The first 3 bits of the 12 bit control word contain a function code and the remaining bits comprise an action bit or data field. For single bit action commands, only 4 bits need be transmitted. The controller can interact with individual 3-in-1 cards or can execute functions in parallel (broadcast mode) on any subset of cards.

The functions are:

- enable/disable integrator output,
- set integrator input source (phototube/DAC),
- set integrator gain (6 values),
- enable/disable response to broadcast mode commands,
- enable/disable injection pulses,
- load calibration DACs.

In addition, the controller can read back a 12 bit status word from any 3-in-1 card to determine its current setting.

For the charge injection calibration, the controller precisely sets the timing of the injected signal with respect to the edge of the 40 Mhz digitization clock. This timing can be set with a precision of 0.2 ns.

Design

The controller is implemented as a custom VME board. The VME protocol, and basic functions are encoded in Altera EPLD chips. A base address is set in switches in the controller and functions are initiated through VME read and write operations to the appropriate addresses.

6.5.1.3 Integrator read-out

As mentioned above all integrators in a super-drawer are read-out sequentially by a single ADC. The ADC receives signals via an analog bus which runs along the entire length of the mother board, and each integrator is sequentially connected to the analog bus by closing a CMOS switch located on the 3-in-1 card. The analog bus consists of two lines (signal and ground) connected to an input differential amplifier on the ADC board in order to minimize common mode noise.

Design

Integrator digitization is performed on a separate board, which is mounted on the mother board. A diagram of the integrator read-out board is displayed in Figure 6-42. The individual integrator outputs, connected one at a time to the analog bus, are received and reconditioned by a differential amplifier which rejects common mode noise and adapts the signal to the ADC input range. A second inverting amplifier restores the polarity of the signal and adjusts, by mean of a potentiometer, the pedestal of the signal to 200mV to compensate for possible negative pedestals of the integrators. This stage can be configured as a low pass filter with a time constant of 10 ms by closing a CMOS bilateral switch which is serially connected with a feedback capacitor. The 12-bit ADC is a MAXIM MAX190BCNG; it uses the successive approximation technique, and is operated from a single 5V power supply. The result of the conversion is in serial stream format. The maximum conversion time is less than 12µs

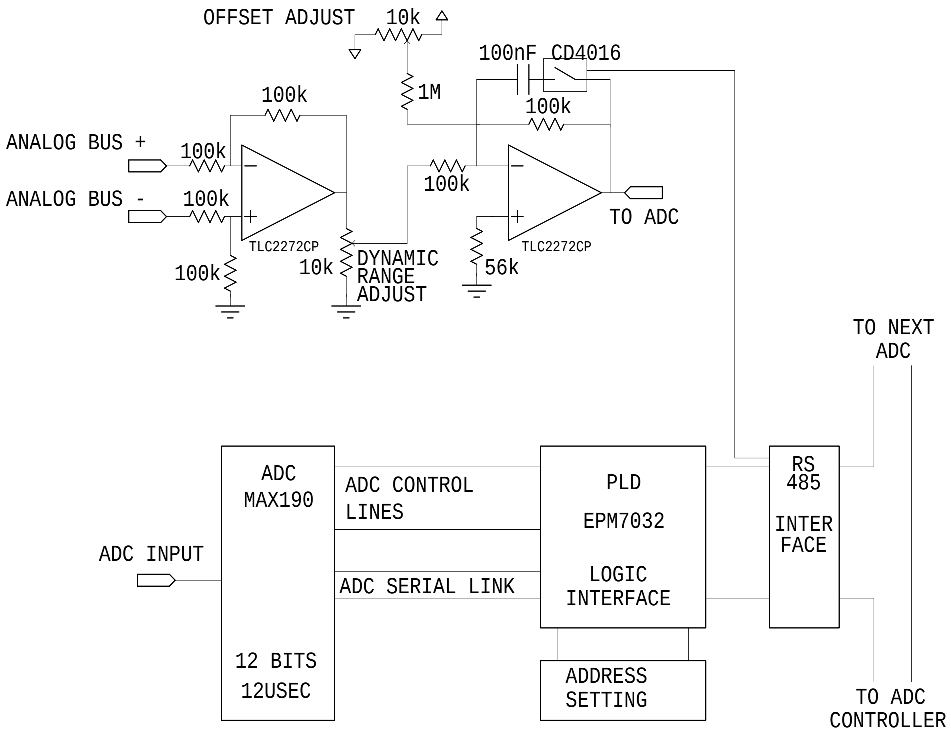

Figure 6-42 Block diagram of the integrator read-out.

The output of the differential amplifier is provided with an adjustable voltage divider to adjust the 5V dynamic range of the signal to the 4.096V ADC input dynamic range. A programmable logic device from Altera, the EPM7032, is used as logic interface between the ADC control lines and the ADC controller; it is located on the ADC board and decodes the ADC address sent by the ADC controller to route the start of conversion signal; this device adds an “end of conversion” flag to the serial stream and sends it to the ADC controller. The logic interface is supported with a RS485 link that allows each controller to access up to 32 drawers. The ADCs are addressed through these control lines with their internal address decoder.

Prototype performance

The Module 0 read-out speed was limited by the switching time of the integrators and the time required to stabilize the voltage on the bus. During Module 0 setup, a total transient time of $100\mu s$ was measured. The stabilization time depends on the parasitic capacities between the lines of the analog bus and the ground plane, as well as the number of 3-in-1 cards which share the bus. A read-out rate of 1 channel/msec was implemented in Module 0 calibrations. An improvement of the read-out rate by a factor of 4 to 10 is planned, with more advanced versions of the electronics and the associated software.

Test bench

It is important to estimate the leakage current of the integrators when they are switched off, as well as the levels of possible cross talk. The behaviour of the analog bus is tested by reading all the 3-in-1 cards sequentially; the same test must be done with the drawer fully equipped to check the available timing for the read-out system. The read-out sequence will be tuned to the tested timing. Such tests are planned for future setups.

6.5.1.4 Cesium source calibration

Outside of the drawer resides a VME standard ADC controller that acts as interface between the calibration machines, the data acquisition system and the drawer itself that contains all the integrators. A diagram of the system is presented in Figure 6-43. The channels are selected through the 3-in-1 controller (6.5.2.2) and the digitization of the output of the selected channel is done with the ADC placed on the mother board, controlled itself by the ADC controller located in a VME crate. This one sends the trigger commands to the drawer ADCs through a RS485 link that allows the access up to 32 ADCs at 10Mbps and 1200m length. It receives the result of the last conversion back through the same link, via a serial line. The controller stores temporarily this data into a buffer during the time required by the data acquisition system to process and store it.

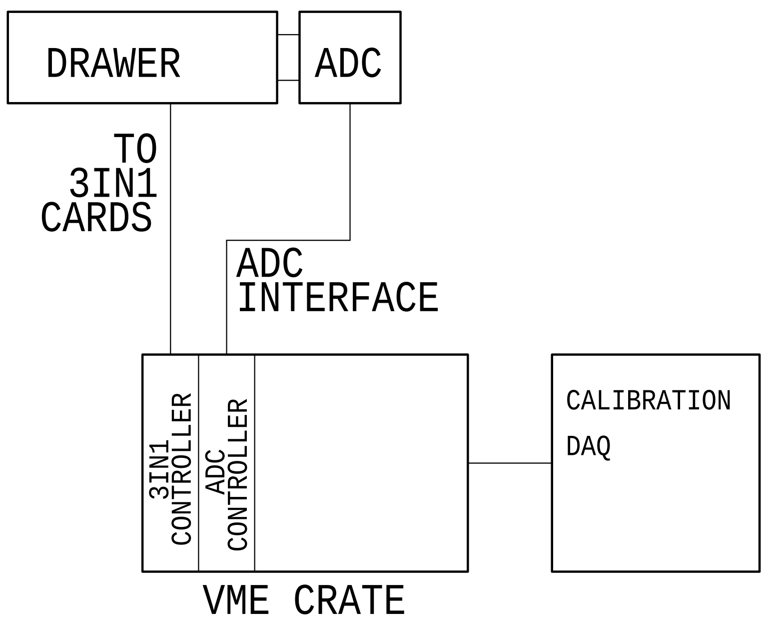

Figure 6-43 Diagram of the calibration control system.

6.5.1.5 Interconnections

The VME based controllers are located remotely from the detector. The controller output signals are transported on 60-conductor flat cables to a fan-out module from which equal length cables are routed to each Tile Calorimeter drawer. The cable lengths are important to maintain timing equalization of the charge injection pulses. This is useful for both calibrating channels in parallel and for providing patterns of energy deposition for trigger testing.

All drawer cards are identical and their location in the detector is indicated by address bits set in switches.

The address fields are:

- 3 bits: zone (barrel left, barrel right, extended barrel left,...),
- 6 bits: azimuthal detector sector (64),
- 6 bits: phototube number in drawer (46 in barrel, 36 in extended barrels).

The drawer cards decode the address and activate a select line for individual 3-in-1 cards. The selected card then responds to controller commands. If the controller raises its broadcast line, all enabled cards respond to commands regardless of the value of the address field.

6.5.2 Charge injection

It is important to test the behaviour of each read-out channel over its full dynamic range. This permits a prompt diagnosis of read-out faults, a test for cross-talk effects, and tests with realistic patterns of energy deposition over the full calorimeter. Each 3-in-1 card has circuitry to permit this and the system is controlled through the mother boards by external VME modules connected to the ATLAS detector control system (DCS).

6.5.2.1 Front-end circuit

To provide a 16-bit dynamic range with modest resolution and cost, each 3-in-1 card is equipped with a pair of 8-bit DACs connected in series. The DACs, supplied by a precise external reference voltage common to the entire drawer, charge a 1% precision capacitor at the input to the pulse shaper. On command from the control logic, one end of the capacitor is shorted to ground through a CMOS switch to discharge the capacitor through the shaper.

6.5.2.2 Services and control

The services and control are in common with the charge integrator and these have been described in Section 6.5.1.2.

6.5.2.3 Test results

Figure 6-44 shows the level of control of the charge injection phase relative to the digitizer clock. The amplitude of the peak channel is plotted as a function of the charge injection timing in steps of 0.2 ns. The 25 ns periodicity is clearly seen.

Figure 6-45 shows the overall transfer function of a read-out channel measured with this system. The various ranges of the compressor are evident.

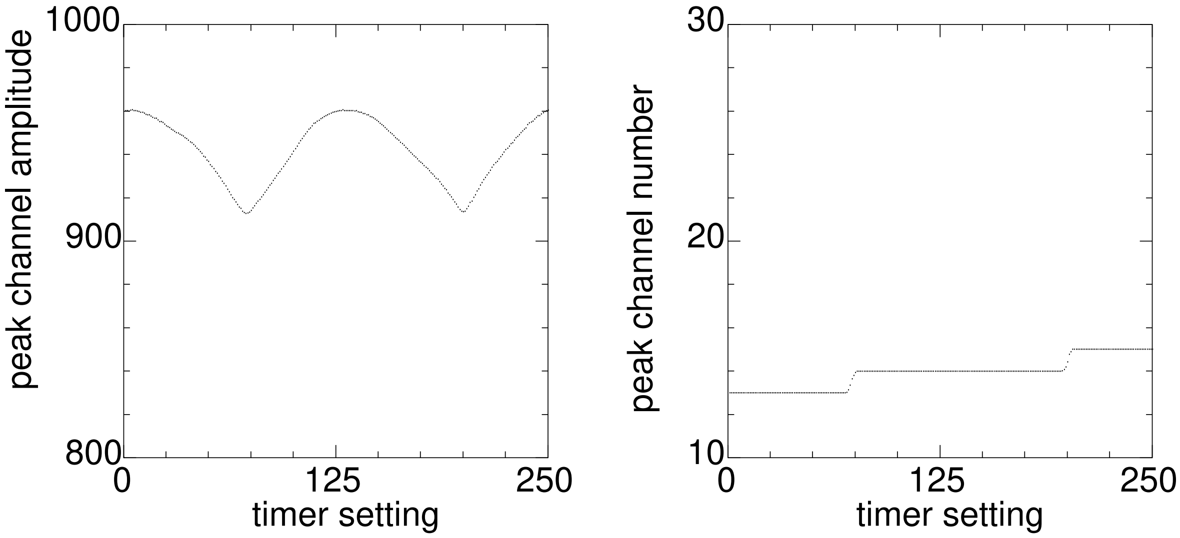

Figure 6-44 Charge injector tests of the 3-in-1 system, varying the timing of the pulse relative to the ADC clock in steps of 0.2 ns.

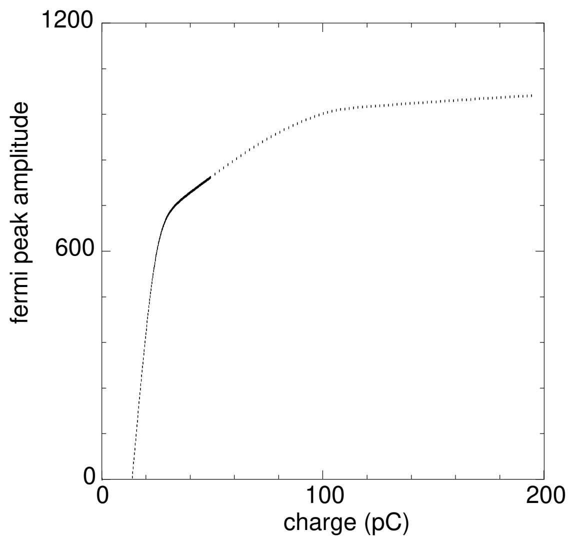

Figure 6-45 Charge injection test of the shaper-compressor stage.

In other tests, a LED has been used, together with a variable attenuation neutral density filter, to pulse a PMT driving the read-out chain. A second PMT and linear ADC were used to normalize each pulse. The measured transfer function is very similar to the one obtained with the charge injection system.

6.5.3 Laser electronics

This part is described in the Calibration chapter, Section 7.3.3.

6.6 Power supply and high voltage distribution

6.6.1 High voltage power supplies

The Tile Calorimeter PMTs are supplied by a high voltage (HV) power supply system. The system reflects the division of the Tile Calorimeter into 256 sub-modules, which are electronically equivalent and independent. Each HV channel leads into the sub-module drawer, where a special HV distributor (see Section 6.6.2) supplies up to 48 PMTs. The HV distributor inside each sub-module is able to set individual PMT voltages at up to 350 V below the supplied level. Only 3 HV power supply levels are needed to supply high voltages between 500V and 1100V, including wide overlap regions. The levels chosen are -1100V, -900V and -700V for each channel, with current of 20 mA/channel. The main requirements for the supplies are short and long term service stability, and very low noise (20 mV pp) over a wide frequency range. The source is remotely controlled, and provides safety protection against short circuits and HV cable disconnection.

6.6.1.1 High voltage source

The source consists of two racks, each containing 8 crates (Figure 6-46). Each crate has 8 cards with 2 HV channels per card, and a communication and control unit. Each HV channel provides three output voltage levels (-700V, -900V and -1100V). The schematic design is presented in Figure 6-47. The three input voltage levels are common for all 16 HV channels in a crate. Each output channel is individually set to the proper voltage level by means of the communication and control unit, and its status is indicated by LEDs. Each channel has overcurrent and undercurrent protection.

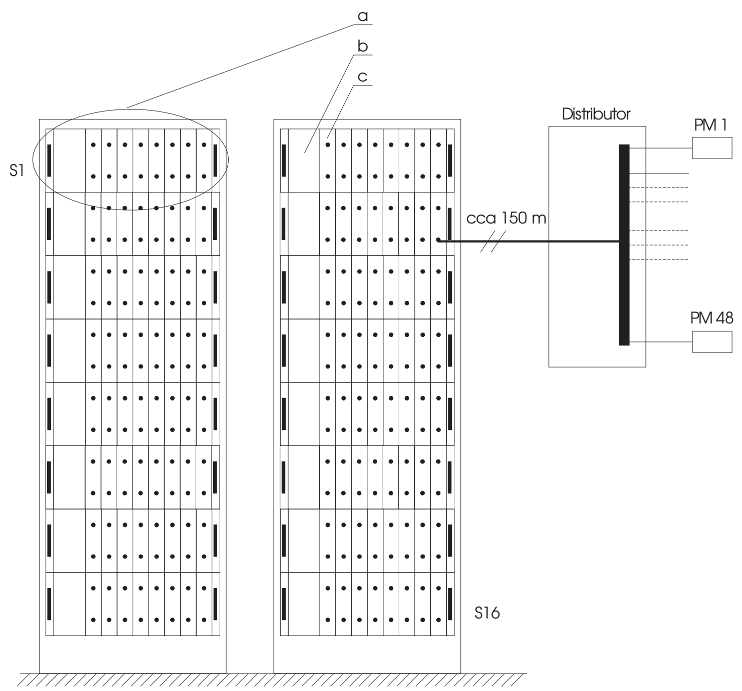

Figure 6-46 Main HV source layout. The source consists of 2 racks with 16 crates (a), each crate accommodates communication and control unit (b) and 8 cards with 2 HV channels (c) each. Each channel supplies a distributor with up to 48 photomultipliers.

The communication and control unit is based on a single-chip INTEL 8051 computer. The unit front panel has an LCD display and a small keyboard. All functions of the crate may be controlled either manually through the keyboard and display or automatically by means of remote control over serial line.

Modular design guarantees simple maintenance by simple exchange of a faulty part by one kept in stock.

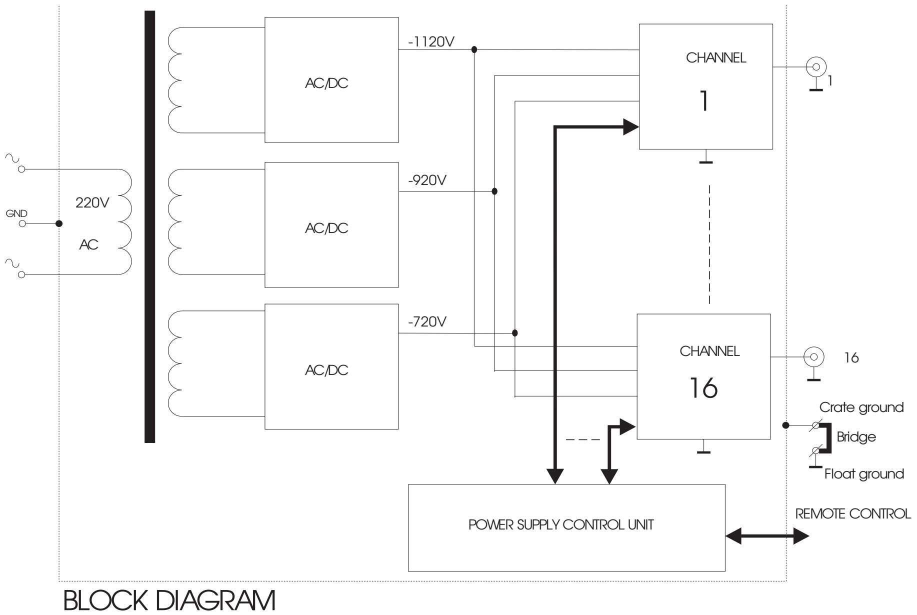

Figure 6-47 Principal scheme of 16 channel HV crate. The supplies deliver 3 levels of input voltage for each channel. Each channel is independently controlled by a control unit.

The HV source specifications are presented in Table 6-7.

The 16 output channel grounds in a crate are connected into single ground which is floating with respect to the ground of the crate. A removable bridge on the back panel of the crate connects the source single ground and the crate ground. The bridge is normally connected, but may be disconnected if ground loop problems occur. The maximum allowed voltage difference between the grounds is ±500 V.

A summary of the electronics specifications of the HV power supplies is presented in Table 6-7. Some specific notations have the following definitions:

- Output voltage accuracy: For a fixed output load, the tolerance in percent of the output voltage with respect to its nominal value, when other parameters are within allowed ranges.
- Line Regulation: The change in output voltage as the input voltage is varied between its specified limits, with constant load and temperature.
- Load Regulation: The change in output voltage from its nominal value when the load is varied between its specified limits.
- Long-term stability: The change in output voltage with time, due to component ageing.

Table 6-7 Electronics specifications of the HV power supplies, from the TESLA company design.

Input line voltage range	220 V ±10
Input line frequency	50 Hz
Output DC nominal voltage (switchable)	- 700 V - 900 V - 1100 V
Channel outputs with common floating ground: max. voltage between the floating ground and the frame of the device	±500 V
Output voltage accuracy	±0.5 %
Line regulation at input line voltage 200 V ±10 % (load current 12.5 mA)	±0.01 %
Load regulation of the channel voltage	±0.02 %
Long term stability	±0.1 %
Temperature coefficient	±0.005 % (50 ppm) / °C
Ripple and noise from switching and spurious voltage in the band up to 20 MHz, peak to peak	max 20 mV
Response time of current protection	max 50 ms
Protection initiating current	5 mA ±1 mA
Time of drop of output voltage to 5%	max 1 s
Disconnecting load: time of voltage drop to 5%	max 10 s
Load characteristics	cable of approx. 150 m length with distributed capacitance of 100-200 pf/m
Expected channel current	17 mA
Operating temperature range	5 to 40 °C
Remote control	RS485, 9600 baud, 8 bit data, 1 stop bit (3-wire null modem, without handshake)

The HV source is located in two 19-inch racks. Each rack contains 8 HV crates of 6U height. The HV output is distributed through HV BNC connectors, while the RS485 ports use Cannon 9-pin connectors. The components of the HV system are listed in Table 6-8. The power input of the system is less than 7kW.

Table 6-8 Components of the Tile Calorimeter HV source.

Part	Number of pieces
19-inch powered racks	2
19-inch, 6U crates with main power supply	16
6U cards with two HV channels each	128
6U communication and control units	16

6.6.1.2 HV source control

Each crate is controlled by an INTEL 8051 single-chip microcomputer. The computer monitors and controls all functions and parameters of the crate. Four LEDs indicate the output voltage level or the switch off state of each output channel. When switch-on of a voltage level is requested, the control unit checks whether:

- the load is connected,
- the load current is between 5 and 20 mA, and
- there is no overvoltage (e.g. from another source connected by chance)

If these conditions are not fulfilled, the protection algorithm is activated and the channel is automatically switched off. These conditions are continuously monitored by the communication and control unit. If they are violated, the channel is switched off, a red LED indicates the state, and a message is sent to the remote controller.

The main HV source can be controlled either manually or remotely over serial line.

Manual control allows one to switch each channel on to one of the three voltage levels and to switch the channel off. This is done by keypad on the communication and control card. A local address of the output channel is chosen and then desired voltage is set on or the voltage is set off.

The main HV source is remotely controlled by the serial interface line using RS 485 protocol. Transmission speed is 9600 Bd, 8 bit data, 1 stop bit without parity. The line may be connected to the simple text terminal (e.g. VT100), or other serial devices. Standard control may be performed by a PC, MVME 167, or a similar computer.

Each command sent to the source is analysed and executed by the source, and the source sends a reply. The command begins with two characters which indicate the crate number and the address of the output channel, and includes one character for the checksum. When the source is operated remotely, the manual control is disabled. Details on protocol descriptions can be found in N-79.

The power supply has an interlock with by-pass.

6.6.1.3 Performance

A functional sample of the HV power supply with 2 channels has been built at the TESLA company. It was tested at the CERN ECP division by the ESS group in Spring, 1996, and was used in the Tile Calorimeter Module 0 beam tests. All tested parameters fulfilled the specifications. After the final decision is made on the PMT type for the Tile Calorimeter, the number of output levels supplied by the HV sources will be reduced to 2 levels. The production of a prototype of the HV power supply crate with 16 output channels is planned for Spring 1998.

6.6.2 High voltage distributors

The photomultipliers in each super-drawer are supplied by one channel of the high voltage main power source (Section 6.6.1). To maintain all PMTs in the super-drawer at the same gain, each high voltage channel of the super-drawer must be individually controlled and regulated. This is done by the high voltage distributor in each super-drawer.

The main specifications for the high voltage distributor are the following:

- Each channel must be adjustable by up to 350 volts from the common voltage of the drawer.
- The precision of the voltage supplied to each channel must be less than 0.5V after corrections.
- The high voltage regulator must be located as close as possible to the PMT, and is therefore mounted on the girder behind each calorimeter sector.
- The general high voltage distributor control should be a component of the calorimeter control system, and located in the control room.
- The high voltage distributor must operate properly in the presence of residual magnetic fields.

The general organization of the high voltage distributor is shown in Figure 6-48. The system is organized in three hardware layers:

- The 256 super-drawer regulation units,
- A field bus,
- VME interface units which are included in the calorimeter control system VME crates.

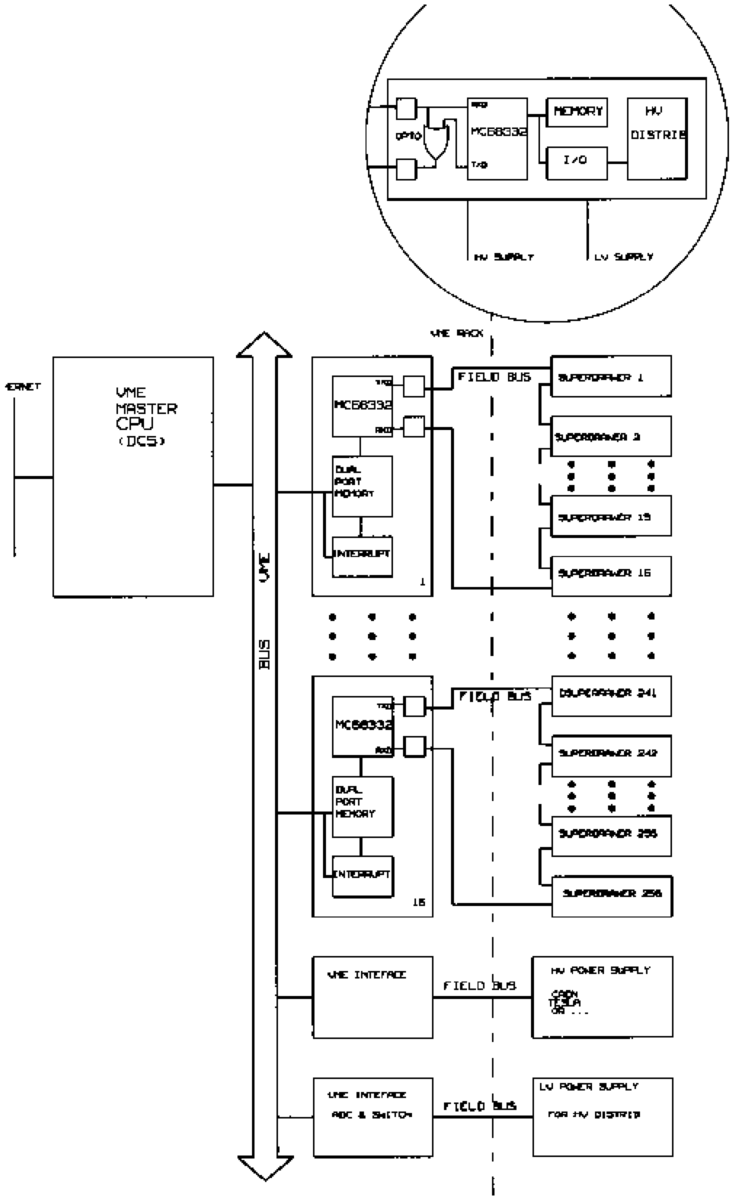

Figure 6-48 Organization of the HV distributor.

6.6.2.1 Super-drawer regulation units

The organization of the super-drawer resident regulation units is shown in Figure 6-49. Mechanically, each super-drawer consists of an "internal" and "external" drawer, with the external drawer located adjacent to the electronics patch panel. Two boards are assigned to each drawer:

- the distribution board, and
- the bus board.

Additionally, a CPU board is located in the external drawer. These components are described in the following sections.

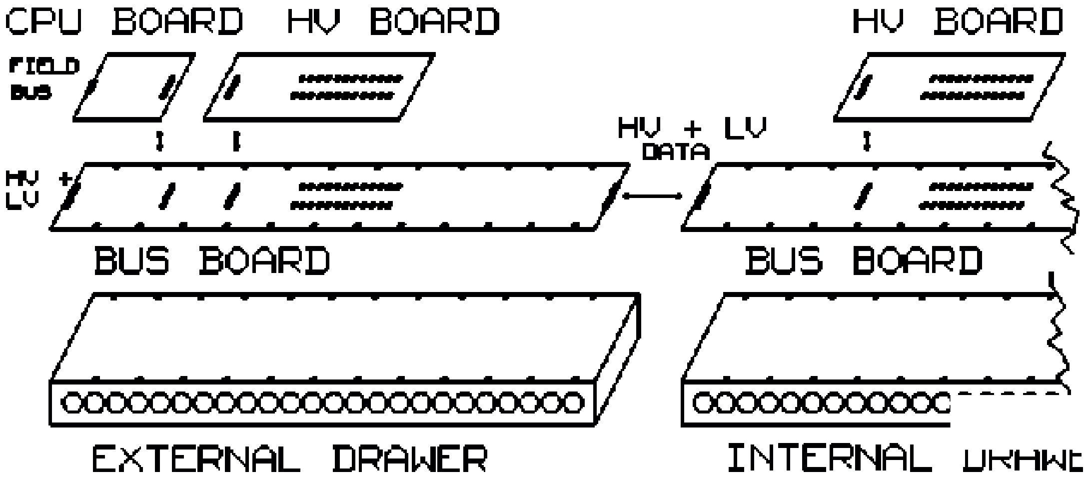

Figure 6-49 Organization of the super-drawer resident HV regulation units.

Distribution board

Figure 6-50 is a block diagram of the HV control systems. As the lower half of the diagram shows, one distribution board is able to supply and regulate 24 channels. The reference voltage is delivered by a DAC, and the applied voltage is read from an ADC. In the opto divider, the difference between the reference voltage and a portion of the applied one is applied as an input to an operational amplifier. The output of this amplifier is used to drive an optocoupler, thus operating as a short time regulation loop.

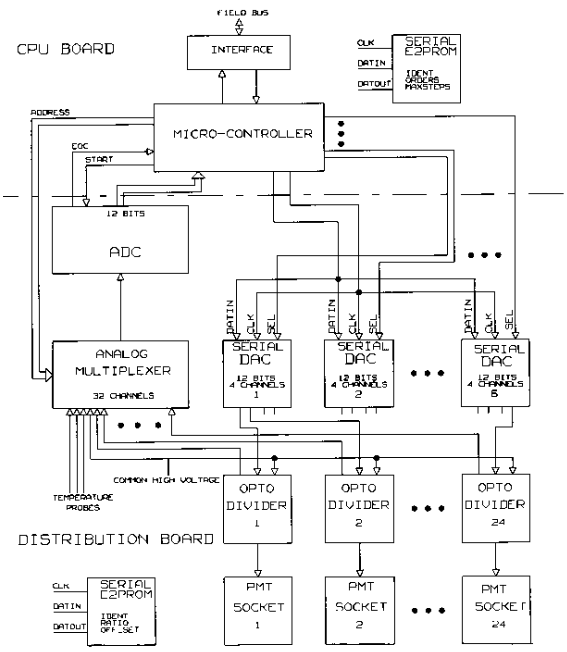

Figure 6-50 Block diagram of the HV control system.

The first prototype of the distribution boards used only one 12 bit DAC and 24 Sample-and-Hold chips. But glitches induced by commutation in Sample-and-Hold chips led to a decision not to use such a component. In the present design, a 12 bit, 4 channel serial DAC is used to adjust 4 channels. Applied HV values are read using only one ADC which receives its input from a 32 channel analog multiplexer. This ADC is also used to read temperature probe signals, as well as to measure the common main power voltage.

To allow identification of the distributor system components, identification data are stored in an EEPROM which is plugged into the distribution board. This EEPROM also saves calibration data for the ADC and the DACs, the date of last intervention or check of the distribution board, and the serial number of the board.

CPU board

The CPU board is used to:

- read the applied voltage on each channel using the ADC, and control the addresses of the analog multiplexer on each of the two associated distribution boards,
- read the reference voltage on each channel using one of the 12 DACs on the two distribution boards, and
- read the EEPROM on each distribution board.

This board is also in charge of receiving and executing commands from the master control VME located in the control room, and sending answer and status words to the master control VME.

The CPU board is based on a 32 bit microcontroller (MC68332). This chip has been chosen because it is a very standard commercial product with a low cost and long life. It also a very high transmission speed on its serial port, and is programmable using C language.

On the CPU board is also plugged an additional EEPROM, which stores reference voltages and maximum allowed variations for each channel. This chip also contains identification information for the CPU board, as well as the date of last intervention or check on that board.

It is also foreseen to be able to access the address of the corresponding super-drawer. This address could be fixed using DIP switches on the CPU board.

Bus board

The bus board has dimensions of 1400 x 90 mm, and is screwed on the bottom side of the drawer. The main purpose of this board is to carry the common high and low voltages to the two distribution boards, as well as commands from the CPU board to the distribution board connectors. The bus board is also used to deliver the high voltage to each PMT in the drawer. The two Bus boards are connected using flexible connectors. These connectors are also used at the entrance side of the external drawer.

6.6.2.2 Field bus

The configuration of the field bus is not fixed. In the first test beam run, dedicated optical fibres were used together with receiver/transmitters. As shown in Figure 6-50, the foreseen configuration is a number of daisy chains: 16 branches of 16 super-drawers each. This configuration is a compromise between the number of branches, which increase the number of interfaces on the control side, and the number of super-drawers in a branch, which increase the transit time for commands. This configuration is based on a token ring; a command is sent by the master control VME, follows the chain, and is received by a super-drawer unit. The super-drawer unit then repeats the command, which is sent back up to the master control VME. From preliminary studies, two candidates for the field bus have been selected: LonWorks and CANbus. Many interfaces using CANbus are currently available or being developed. But CANbus has the disadvantage of a limited transfer size of only 8 bytes (with 125 kbytes/s on a 500 m network). LonWorks is a full OSI configuration. The transfer size is limited to 228 bytes, together with 1.25 Mbytes/s on a 500 m network using specific transceivers. LonWorks also has now the advantage that it accepts every type of network media (twisted pairs or optical fibres), while CANbus is presently constrained to twisted pair media.

6.6.2.3 Control system

The control system is the interface between the calorimeter control system and the high voltage distributor. In the foreseen configuration, 2 or 4 control units are located on one VME board. Each active unit is based on a MC68332 microcontroller, and is in charge of transferring commands and data to and from the master control VME to the super-drawers. In this configuration, the entire system uses only one VME crate.

Different configurations are also in consideration:

- Passive interface units controlled by a dedicated CPU unit, together with the master control CPU unit.
- Passive interface units in different VME crates with only one CPU per crate.

The final configuration also depends on the choice of field bus, as well as the general ATLAS control system.

The main commands are:

- Reset of CPU of a super-drawer.
- Loading a program in super-drawer CPU flash memory for modification and update of the CPU board microcontroller.
- Write a new voltage reference for a channel (or a group of channels).
- Read a voltage reference of a channel (or a group of channels).
- Read a applied voltage of a channel (or a group of channels).
- Read the status words of super-drawers in order to check them.

The size of the data transfer is between 8 bytes and 136 bytes.

6.6.2.4 Tests and performance

Differences between the reference and applied voltages for each channel can arise from different sources:

- non linearity of the ADC's,
- poor calibration of the ADCs and DACs,
- time instability,
- temperature induced variations.

Figure 6-51 displays the difference between the actual measured voltage value for a typical channel, and the value read by the ADC. On the same figure is shown the effects of linear and second order corrections. Tests indicate that after the DAC calibration, the precision on the applied value is less than half a volt. Figure 6-52 displays the variation in time of the applied voltage for a typical channel. The time interval between two measurements is 5 seconds, and the measurement was run over a period of 6 hours. During that test, the drawer temperature was stabilized.

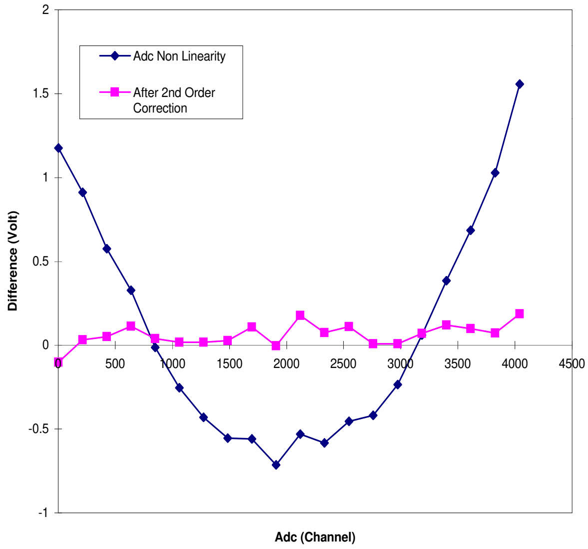

Figure 6-51 Difference between applied HV and reading from ADC channels.

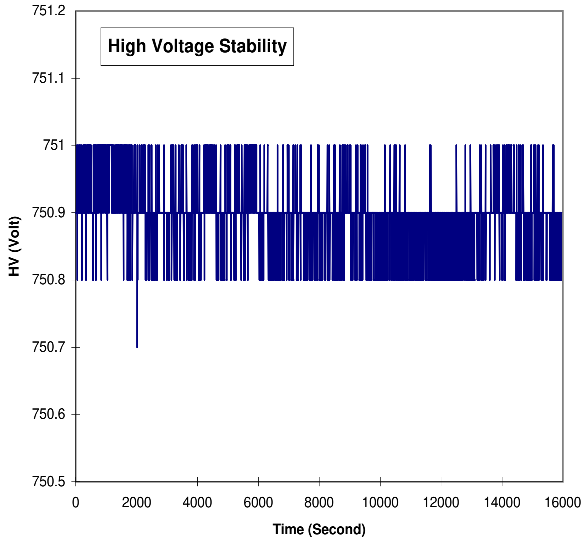

Figure 6-52 Time variation of applied high voltage.

6.6.2.5 Test benches

A test bench has been developed in order to check the distribution board. It consists of a test board, which is connected to a 16-bit VME ADC and to a command board which simulates the CPU board. The distribution board to be tested is first plugged to the test board. Using the command board, a reference value is applied to the distribution board DACs. The corresponding measured voltage is read, for each channel, by the 16-bit ADC, and compared to the value given by the distribution board ADC. These data are then used to calibrate the distribution board ADC and DAC. The resulting calibration parameters are saved in the EEPROM of the distribution board together with the calibration date. During the first test of the board, the identification data and fabrication date are also stored.

6.6.3 Low voltage power supplies

Two low voltage power supply systems are used by the Tile Calorimeter. One supplies power to the high voltage distributor electronics, and the second powers the read-out. Each system has different requirements, and the two are fully separated to suppress noise due to cross talk. This section describes each of the low voltage systems in turn.

6.6.3.1 Low voltage supplies for the HV distributors

From the projected power consumption of each super-drawer, it is proposed to design a low voltage power supply system for the HV distributors consisting of four power blocks. Each block provides power to 64 super-drawers, and services either one half-barrel, or an extended barrel. Each block has the following specifications:

- +5 V: 20 A (nominal current = 16 A),
- +15 V: 30 A (nominal current = 23 A),
- -15 V: 30 A (nominal current = 26 A).

Relays are used to distribute the low voltages to the 64 channels. A control card is driven by the DCS via a dedicated field bus.

6.6.3.2 Low voltage for the read-out electronics

The baseline configuration of the read-out electronics in the drawer requires three voltages for the front-end analog electronics. These are:

- +5V: 10A,
- -5V: 10A,
- +9V: 4A.

where the currents are given for each super-drawer. Since sensitive analog circuits are involved, the power should be series regulated rather than from switching supplies. Desirable specifications would be a power supply noise level less than 2 mv peak-to-peak, measured with a 20 Mhz bandwidth. The power supply lines to each drawer should be fused at the source.

In addition, the digitizing electronics in each drawer will require:

- +5V: 10A, and
- -5V: 4A.

For noise isolation it is desirable that the power for the digitizing electronics be separate from that for the front-end analog electronics. Here, switching supplies may be used. As for the front-end electronics, the supply lines should be fused at the source.

6.7 Production plan and schedule

The schedule for the specification, procurement, testing, and installation of the Tile Calorimeter electronics is presented in Figure 6-53.

Testing and evaluation of PMTs will continue for two years, and a production model will be chosen at the end of 1998. Six institutions will be responsible for the procurement and testing of the PMTs, and assembling the PMT blocks.

Six institutions will be responsible for developing and producing the various electronics components for the PMT blocks and the drawers. Each institution will have the responsibility for testing their respective components.

The full drawers will be assembled at one institution, which will also be responsible for their final testing and calibration before they are brought to CERN for final installation.

The major R&D decision still to be made is the final specification of the digitization and pipeline electronics. Testing and evaluation of prototypes will continue through 1997 and 1998, and procurement and testing of the production electronics will begin in the middle of 1999.

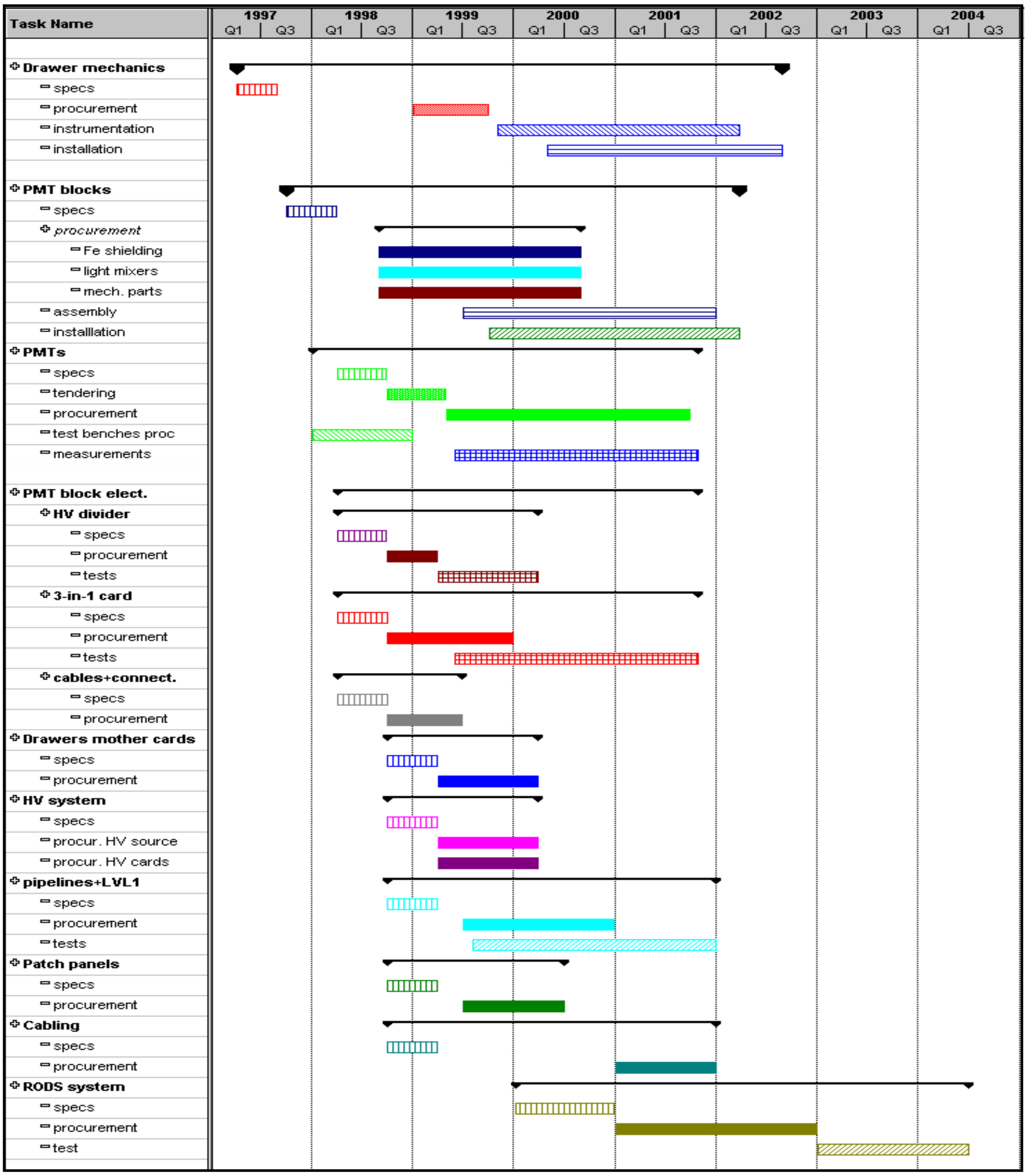

Figure 6-53 Schedule for the specification, procurement, testing, and installation of the Tile Calorimeter electronics.

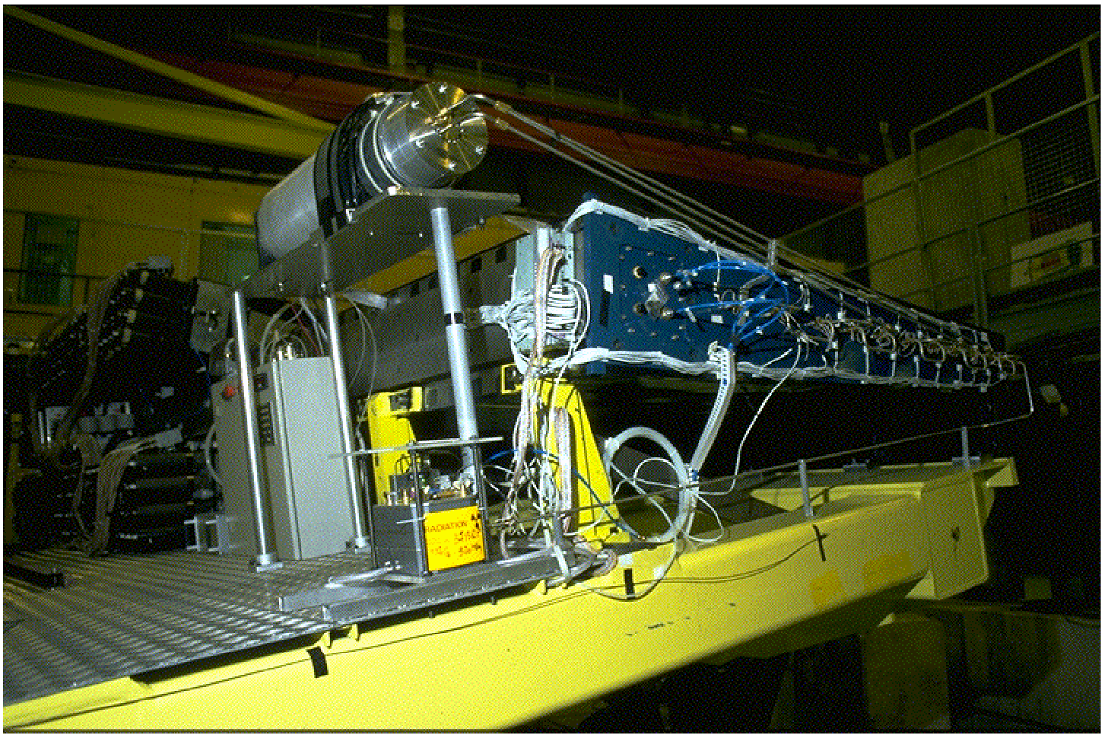

Figure 7-i The ^{137}Cs source calibration systems as installed on Module 0.

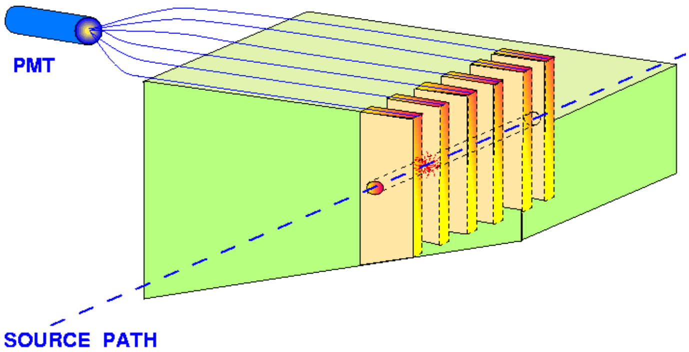

Figure 7-ii Conceptual view of a ^{137}Cs source scan.

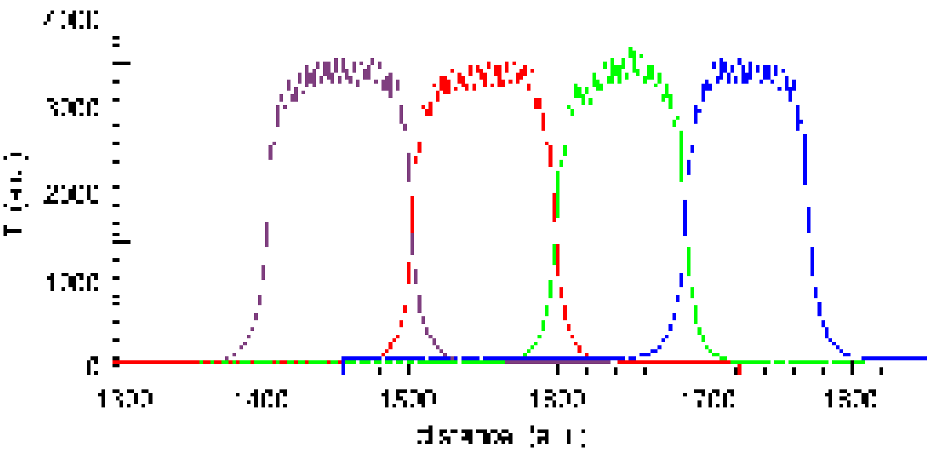

Figure 7-iii Online plot from a ^{137}Cs scan along four readout cells for each of the two different source drive systems: hydraulic (top), pneumatic(bottom).

7 Calibration and monitoring system

7.1 General considerations

In order to translate calorimeter signals to particle or jet energies over the duration of data-taking in ATLAS one needs:

- to determine the overall energy calibration scale, *i.e.* the factor that relates the energy released in the calorimeter to the digitized signal produced at the end of the read-out chain,
- to measure this calibration factor for each read-out channel, and/or to minimize its channel-to-channel variation,
- to monitor this set of calibration factors over the lifetime of the detector in order to correct for their variations in time.

Calibration, intercalibration and monitoring are of course closely interconnected. In this chapter, emphasis is first given to intercalibration and monitoring issues; the overall energy calibration scale is discussed last.

The instrumentation and the procedures to obtain these measurements are an essential component of the design of the Tile Calorimeter, and have been developed as an integral part of the prototype R&D program and of Module 0 construction and tests.

7.2 Strategy and tools

The signal path - from particle interactions in the calorimeter to the digitized output of the physics signal read-out chain - can be separated in three stages (see Figure 7-1):

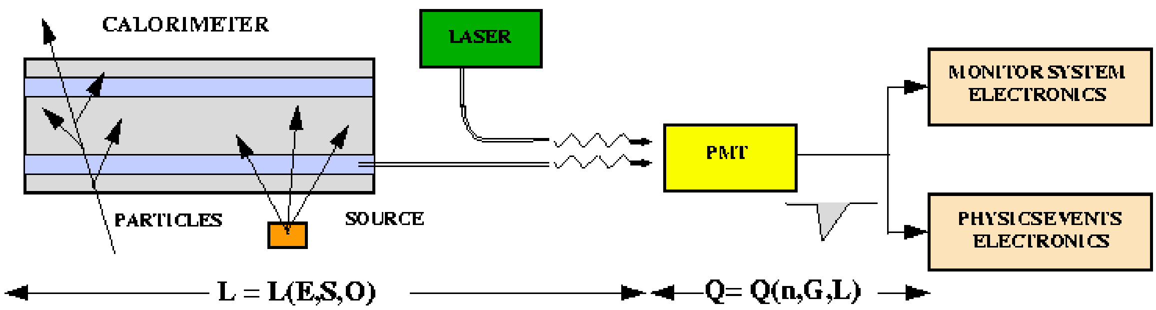

Figure 7-1 Conceptual diagram of signal path for the Tile Calorimeter and calibration entry points (see text for definitions of the functions L and Q).

1. interactions produce ionization in the scintillator, which eventually results in light at the PMT photocathode. This chain of processes can be characterized by a light response L=L(E;S,O) - where E is the energy released in the calorimeter, S is the sampling fraction and O summarizes the response of the optical components (scintillator and WLS fibres).
2. a light pulse L is converted into a charge at the PMT anode. This can be described by a charge response Q(η,G,L) - where η is the quantum efficiency and G is the gain of the photomultiplier.

3. the physics signal, contained in the charge Q, is read out and digitized.

The front-end electronics for the read-out of physics events and the monitoring electronics are discussed in Chapter 6; they are assumed here to be intercalibrated. The calorimeter read-out cells can be set to have the same response, for instance using a test beam. This effectively intercalibrates the product of the responses L and Q. However these two responses will change in time and will need to be monitored, because:

- The light yield may change due to ageing processes of the scintillators and fibres, or to radiation damage. These changes are typically slow, with time constants of hours to months. Other possible changes of the light yield, such as deterioration of optical contact, may be more abrupt.
- The photomultiplier response may change due to gain drifts (typically occurring over hours to days), deterioration of gain or quantum efficiency (much slower except for excessive signal loads), etc.

The intercalibration and monitoring strategy for the Tile Calorimeter is based on several tools:

1. movable radioactive sources which excite light in all scintillators by the same mechanisms as particles from LHC interactions,
2. a laser which produces on each PMT a light pulse which closely mimics calorimeter pulses,
3. during data-taking at the LHC, continuous monitoring of the signal produced in the calorimeter by minimum bias (MB) interactions.

The laser system allows to monitor the response of the PMTs over the full dynamic range of the light signal L. In particular, it monitors the conversion from light to charge Q, and its changes in time, due to gain drift. The laser pulses are read out through the same electronics used for physics events; therefore PMT response can be measured during data-taking with minimal interference. The linearity of the PMT response can be measured as often as desired and directly related to the energy scale of the calorimeter.

The response of the calorimeter to radioactive sources is measured by recording the average current produced in each PMT. Just as the charge Q from a hadronic shower in the calorimeter, the average current in each PMT is proportional to the $L \cdot Q$ product. Q is measured by the laser system, therefore the light response L can be obtained at every time the source response is measured, provided that there is a corresponding measurement of Q by the laser.

The first source measurements will be made module by module at assembly time, and will be repeated at regular intervals before and after installation into ATLAS. However during experimental runs it will only be practical to run sources when beams are off. It is obviously attractive to have a continuous monitoring system. This will be implemented by recording the MB current; as discussed below, this can be done using the same monitoring electronics used for the source signal. The front end electronics design allows to read out the MB signal during physics runs and with no interference with data taking. The minimum bias current is proportional to the instantaneous luminosity; factorising it out will give a full time record of the calorimeter overall response in time.

The requirements on the precision of the monitoring and of the intercalibration of the calorimeter read-out cells are different:

- For monitoring the calorimeter response (the product of the response functions L and Q) a precision of about 1% is useful for early detection of any degradation phenomena (for instance, from radiation damage). As will be shown in section 7.6, this precision has already been obtained with both the laser and the source system without exotic technology. This precision provides a good handle on the performance of the calorimeter system.

- Requirements on the intercalibration of the read-out cells must be set in terms of the overall resolution of the calorimeter, and will be discussed in section 7.7. These requirements turn out to be much weaker than 1%.

7.3 The laser system

The main purpose of the laser system is to monitor the response of the PMTs on any desired time scale, from the very shortest (minutes) to the duration of ATLAS. It is planned to obtain the PMT gain to a relative precision of 0.5% by measuring the laser light intensity pulse by pulse. This system will also be useful to check the pulse electronics following the PMTs.

7.3.1 Concept and general requirements

The core of this system is a frequency-doubled YLF solid-state laser in which the light pulses are externally triggered and intensity-modulated; the system is fully computer controlled. The laser pulses closely mimic the scintillating light produced by particles in the calorimeter, having a wavelength of 480 nm and a pulse width of about 15 ns.

The laser pulse intensity is precisely measured on a pulse-by-pulse basis by photodiodes. The linearity of the photodiode read-out electronics is checked with a charge injection system; the response of the photodiodes is monitored with an ^{241}Am alpha source, which provides a reference which is stable in time and insensitive to environmental changes.

Laser calibrations are performed generating a train of pulses of increasing amplitude, reaching the upper end of the PMT dynamic range. The light is transmitted to the PMTs through clear fibres. The effective dynamic range of the laser in this mode is only about 30, whereas the calorimeter dynamic range in ATLAS is about 60000. To obtain this range a set of remotely controlled filters will be installed on the laser light path. Amplitude monitoring and timing measurements are made upstream of these filters.

In the test beam, the laser system is used to continuously monitor the calorimeter PMTs. It plays several roles:

- fast on-line controls of the operation of the PMTs and the associated front-end electronics,
- measurements of the drift of the PMT relative gains,
- measurement of the linearity of each PMT,
- other test and diagnostic functions, such as cross-talk and measurements of calorimeter phototelectron statistics.

7.3.2 System implementation in the test beam

The fact than the Tile Calorimeter prototype was set on a movable table for the test beam runs has complicated the implementation in comparison with the ATLAS configuration. In particular, the laser system moves with the scanning table, where it suffers vibrations, halo particles, and temperature variations. Implementing the laser trigger away from the counting room also complicates the setup. Despite a situation less favourable than in the ATLAS configuration, the laser calibration has run and gave the results which were expected. The setup is shown in Figure 7-2.

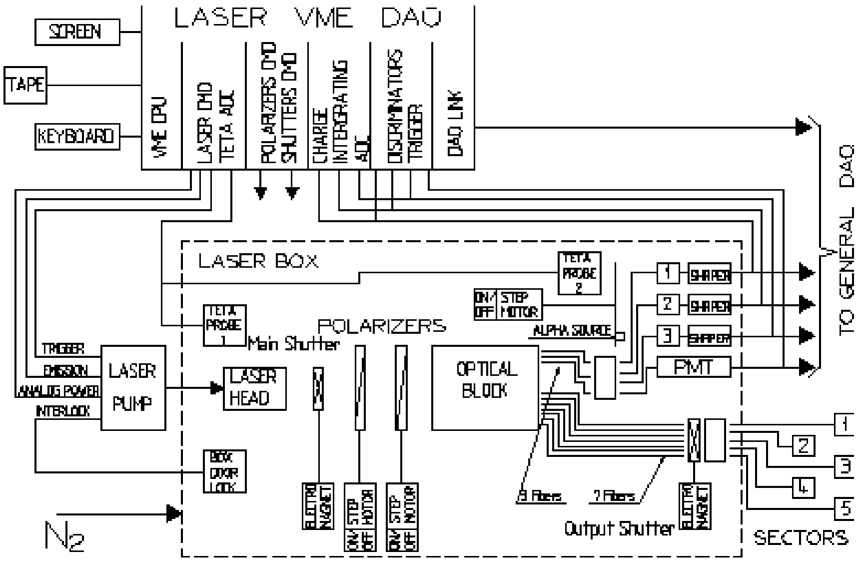

Figure 7-2 Basic implementation scheme of the laser system.

The VME system which drives the laser and collects system data is in the control room, while the “laser box” and the “laser pump” are on the scanning table. The following components are located in the laser box: the laser head and the frequency doubler, a first shutter designed to stop the laser light just after the head, two adjustable polarizers (controlling the light intensity in the calorimeter PMTs), optical blocks to divide and attenuate the light, a second shutter for stopping if necessary the laser beam before the calorimeter, two temperature probes (probe 1 near the laser head, probe 2 near the photodiodes), a thermoelectric cooler to regulate the temperature inside the box and pulse monitoring components. The latter include a fast PMT for timing, three photodiodes (PD) and their associated electronics to monitor the laser light, and an alpha source (mounted on a wheel) to monitor the three photodiodes. During test beam runs, the laser box was kept in a dry nitrogen flow to prevent condensation and the temperature was stabilized to $22 \pm 0.1\ ^0$C. As a safety measure, opening the box stops the laser, closes the output shutter and turns off the PMT and PD power supplies.

The timing is given by an R5600 Hamamatsu PMT having a “metal channel dynode” structure. Due to its very short rise time of about 0.6 ns, a classical threshold discriminator gives sufficiently accurate timing of the laser pulses. The timing is obtained directly from the light pulses, not from the train of pulses which modulate the laser.

The three photodiodes are excited from the laser (via optical fibres) and the Americium source. Three identical circuits made of a preamplifier and an output stage are behind the photodiodes. The large area PIN silicon photodiode (Hamamatsu S2662) has high quantum efficiency at the laser wavelength. The PD window would stop alpha particles and is therefore omitted. The preamplifier is an integrated circuit (EG&G HFD1060), set to obtain a pulse short enough to fit within the ADC gate used for the Tile Calorimeter PMTs. A calibrated charge is injected through a 2.7 pF capacitor in parallel to the PD. The output stage has three 50 Ohm outputs, driving the ADC of the test beam DAQ system, the ADC of the laser VME DAQ, and the Americium source trigger logic.

The VME-based laser acquisition system plays several roles: data acquisition, laser control and monitoring, Americium source control, and link with the test beam DAQ. The signals from the 3 photodiodes are read in a 12 bits charge-integrating ADC (CAEN V265), with a full scale of 800 pC. A custom-built card delivers 16 synchronized pulses, the amplitudes of which are programmable by a DAC to drive the laser light intensity. Within this card are also located the elements to measure the temperatures inside the laser box and to read out several characteristics of the laser pump (temperatures, current of the 2 laser diodes, total laser power). An other card drives the polarizers and the shutters. The Americium source step motor rotation is supervised by a dedicated microcontroller (MC68HC711) and a programmable ASIC (XILINX). This card manages also the cooling system of the laser box which uses Peltier elements. Written in C language, the software manages the human interface, the histogram presenter, the spy window and the acquisition itself. The VME DAQ is run using OS9 as an operating system.

The laser-associated logic interface to the test beam DAQ fulfils several functions:

- It supervises the acquisition of laser-triggered PMT pulses together with PD data and alpha peak positions.
- It assures that laser pulses are generated in well defined time windows with respect to particle bursts.
- It stops the system when the beam is off.

Furthermore, the user can set the rate of laser pulses and can choose the laser operation mode (calibration, or coordinated with the particle bursts) from the test beam DAQ process.

7.3.3 System design for ATLAS

The laser monitoring system for ATLAS is a relatively straightforward upgrade of the system implemented in test beam runs. The main difference is in the light pulse distribution system to the calorimeter, which naturally is much larger.

7.3.3.1 General specifications

The general specifications for the laser system can be seen in Table 7-1 for the laser itself and the associated services as well as for the distribution of the laser light to the Tile Calorimeter.

7.3.3.2 System layout

The system is divided in two parts, respectively located in the electronics cave and in the ATLAS cavern, as shown in Figure 7-3.

The active elements (laser pump, laser box, services, associated electronics, local DAQ, optical patch panel) are located in the electronics cave. This is where the electronic and optical adjustments are made, either to the laser box services (by VME control) or manually to the optical laser panel. The laser box is fully VME controlled (electronic control of the laser pulses, of the lasing diodes, control and adjustment of the temperature, of the polarizer and source wheels, of the shutters...) without opening the temperature-controlled box. The optical patch panel allows to tune the intensity of the light transmitted to each of 270 channels, using fine mechanical adjustments of the optical connectors.

Table 7-1 General specifications for the laser system

Elements	Quantity/Requirements
Laser head with a frequency doubler at 523 nm	1
Optical Shutters	2 (laser output, laser box output)
Polarizers	1
Optical blocks	3 (1 Main, 2 secondaries)
Timing PMTs	2
Photodiodes (without windows)	3 (2.5×7 mm^2)
Current preamplifiers and Splitter/Shapers	3
Moving Americium source (5.48 MeV alphas)	1
Moving set of neutral filters	4 filters (attenuations 1, 14, 14^2, 14^3)
Temperature probes	2 (near the laser head, near the photodiodes)
Temperature stabilization	(22.0 ± 0.1) °C
Thermocoolers (Peltier elements)	2 sets (one VME controlled, one VME independent)
Nitrogen injection	1 (20 litres per hour)
Thermo isolated Laser box	1
Services: control logic power supplies interlocks	 2 XILINX LVs and HVs 2 (laser, voltages)
Laser pump (outside the laser box)	2 diodes (power > 1 W each one)
VME electronics and Local DAQ (special electronics, charge injection, 3ADCs)	1 crate
NIM electronics for logics (and NIM logics)	1 crate
Laser light distribution in the Tile Calorimeter	
Laser box connector (in control room)	output 270 fibres
Laser box fibre bundle (in control room)	270 clear fibres, 2 m long
Optical patch panel with fine individual adjustments (in control room)	270 channels
TileCal coated clear fibre bundles (quartz or plastic)	4 (for LB, 2 for LE, 67 or 68 fibres each)
TileCal module connectors (input 1 fibre, output 50 fibres)	540 ($2 \times 2 \times 64$ for LB, $2 \times 2 \times 64$ for LE, 28 spares not mounted)
TileCal module clear plastic fibres	2 fibres/PMT block, length < 4 m each one
Plastic tubes for the fibre routing	2 tubes per half barrel module 2 tubes per external barrel module
Space occupied in the control room	3 racks(1 rack for the electronics, 1 rack for the laser system,1 rack for the patch panel)
Space occupied in the pit and the cavern	4 fibre bundles of 20 mm diameter.

Light is transmitted to the cavern through 80 m long clear fibres. Here two options are available: either to use plastic-clad quartz-core fibres, which are insensitive to radiation but are fragile and relatively expensive, or to use plastic fibres, which are less delicate and cheaper but less radiation-resistant. Each fibre terminates on a module through an optical connector which distributes the light to 50 plastic fibres per calorimeter module; each of the latter fibres terminates in one of the WLS fibre bundles coupled to the PMTs, and will be glued into the WLS fibre bundle. It is planned to run two fibres to each External barrel module (or to each end of barrel module) for the sake of redundancy, hence two clear laser fibres will be glued inside each WLS fibre bundle.

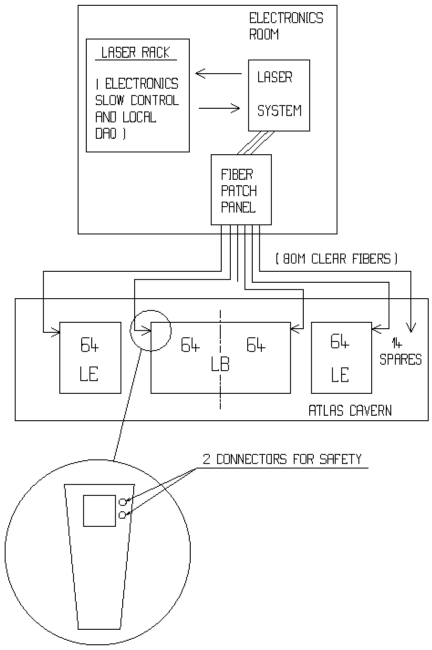

Figure 7-3 The laser system design for ATLAS.

7.3.3.3 Components

The components are essentially the same as used in the test beam setup. Only certain important details and the differences with respect to the system described in Section 7.3.2 will be highlighted.

Laser box

The laser box has about the same dimensions as the present prototype: 19” rack-standard width, a height of 40 cm and a length of 70 cm. The 3 mm thick Aluminium double walls sandwich a 20 mm polyurethane insulator.The electric motors are placed out of the box to prevent electronic noise. The thermo-coolers are in contact with the inner metal wall on one side and with the radiators and cooling fans on the other. As in the test beam, opening the laser box cover will automatically switch off the laser and all power supply voltages; however this feature can be overridden when it is desired to manually adjust the laser beam or the optical components within the box. The laser remote control system and the connector to the optical patch panel will be mounted in front for manual tests. In the back will be the patch panel for the electronics and the voltages, and for the optical fibre connected to the optical pump which transmits the power to the laser head.

Laser head and laser pump

Only the laser head and the frequency doubler are inside the laser box. The laser pump uses two infrared laser diodes and will be in a crate located under the laser box that also contains the laser control electronics.Regulation of the temperature inside the laser box is required for optimal operation of the frequency doubler, and to stabilize the photodiode electronics. The laser system is manufactured by Spectra Physics. Doubling the power of each laser diode (2W instead of 1 W) is a possible upgrade.

Timing and pulse amplitude monitoring

The same type of PMTs and photodiodes described above will be used. No significant changes are contemplated for the monitoring electronics.

Other elements

Optical components, shutters, motor drives, temperature control and monitoring elements will also be as described for the test beam setup.

7.3.3.4 Optical connections

Two kinds of optical fibre connectors were developed to be used with the laser calibration system. The first one, an adjustable fibre-to-fibre type, is used to control the light sent to each sector or module. The second distributes light from 1 to 50 fibres within each Tile Calorimeter module.

The adjustable connector
The adjustable fibre-to-fibre connector allows to control the amplitude of transmitted light changing the distance between fibre ends; a greater distance implies a greater light loss and a smaller amplitude of transmitted light. This is a very smooth and simple way to adjust light transmission. It is a precision mechanical device, robust and easy to operate. Each full turn of the connector screw changes the distance between the fibre tops by 0.75 mm; 8 turns are provided. The transmission as a function of the distance between the fibre ends is well described by an exponential with a decay constant of 2.75 mm; the light transmission when the fibres are in contact is about 90%. With this device the transmission range from input to output can be varied by a factor of 9.

The 1-to-50 fibre connector
In this connector the input fibre is axially placed on a cylindrical light mixer. Without additional elements there is much more light transmitted near the axis. To reduce this non uniformity a translucid plastic cone is glued at the output end of the cylinder; the cone absorbs more light near the axis, and in addition acts as a diffuser. The 50 output fibres are glued at the output; the whole assembly is enclosed in an Aluminium assembly.
The fibre-to-fibre variation of light output is good, with a measured maximum difference between any two fibres of 47% and an rms of 13%. With this connector, the measured fraction of incoming light transmitted to the output fibres is 30%.

7.3.3.5 Routing of the clear fibres within the modules

As shown in Figure 7-3, only 4 fibre bundles of about 70 fibres each are required to bring the light from the optical patch panel to the Tile Calorimeter in the ATLAS cavern. The routing of the 80 m long fibres, to be coordinated within ATLAS installation plans, will require considerable care if quartz fibres are found to be preferable. As mentioned above, two connectors per module will be installed, but only one will be used.

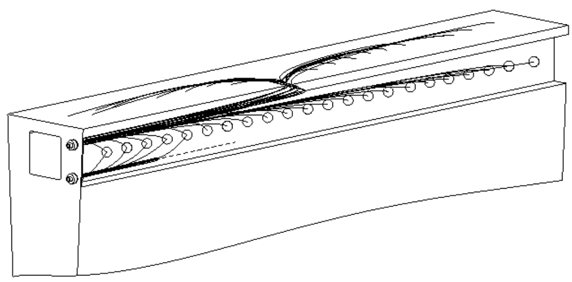

Figure 7-4 The clear fibres routing.

Figure 7-4 shows the routing of the fibres within a calorimeter module. The path is straightforward on one side, but passing the fibres to the other side of the girder will require to enclose the fibres into plastic tubes for protection and to avoid interference when inserting the electronics drawers into the girders.

7.3.4 Mode of operation in ATLAS

The laser system is a versatile tool that will certainly be used in ATLAS in modes which have not yet been developed in test beam runs. For instance, one can easily run single pulses rather than trains of pulses of increasing amplitude (as done at the test beam) for basic debugging purposes.

This section is partly speculative, because of the many possible modes and their dependence on details of general LHC and ATLAS operations.

Two main programs for the laser system can be anticipated:

Debugging and system development
From calorimeter installation to physics start-up, for instance:

- laser pulses can provide a variety of specific checks, of the HV system, the PMTs, the pulse electronics, even the current monitoring electronics.
- one could enable for read-out only a subset of the Tile Calorimeter channels, in which case laser pulses would simulate "virtual trigger towers" of programmable energies.

PMT gain and linearity monitoring
For the duration of ATLAS. This is of course the main purpose of the system. This program could be implemented by operating in several modes:

1. pulsing the laser during the LHC bunch-free periods. This mode would give continuous monitoring of the PMTs, but may interfere with general ATLAS operation and may not be necessary considering the gain stability observed during test beam runs.
2. brief (few minute) monitoring runs between beam fills (expected every about 7 hrs according to [A.39]). This would almost certainly be adequate to follow PMT gain drift. If minimum bias current monitoring (Section 7.5) is performed with this periodicity, one could also unfold the PMT response variation from the overall calorimeter response variation to obtain information about the calorimeter optical response. This latter step is probably more than is normally needed.
3. longer runs (10-15 minutes) to verify the linearity of the photomultipliers. This should go together with front-end electronics calibration runs; these laser runs could be taken maybe once every one-to-several weeks, when the beams are down.
4. special runs every time a source calibration is taken, during longer beam off periods. This is to extract the optical response of the calorimeter from the overall response measured with the source, by precisely measuring the PMT gains at that time.

7.3.5 Future work on the laser system

Improvements to the current laser system will be implemented beginning with the summer 97 test beam. This includes developing the laser control system as a standalone system and testing the filter system designed to match the PMT dynamic range in ATLAS.

Work on the longer term includes the construction and tests of the final laser system. The main issues to be addressed are:

- the choice of the new ATLAS-dedicated laser which will be a more recent version of the currently used instrument,
- the final design of the optical patch panel which will allow to individually adjust the light intensity of up to 270 channels,
- the choice between quartz fibres and plastic fibres (cheaper but radiation sensitive) for the 80 m long light connection from the control room to the detector, and
- the incorporation of the laser control system into the ATLAS control system.

Construction of the final laser system will be completed well in advance of Tile Calorimeter installation in order to gain plenty of experience with the full system including the 80 m long fibres and the optical patch panel.

7.4 Source intercalibration and monitoring system

In this section the concept of the Tile Calorimeter source intercalibration and monitoring system is described and the requirements for a system for the full ATLAS detector are specified.

Two system concepts for the full detector are given, based on a hydraulic and a pneumatic drive. These concepts were developed into prototypes; the performance obtained testing Module 0 is discussed, together with the performance of an older prototype system that serves as a reference. Based on the prototype results a design for ATLAS is given.

The plans for fabricating sources for this system, based on the already obtained results, are described.

A final appraisal of the status of this part of the project is given, including the issues that require further R&D.

The read-out electronics for the source signal is described in the Chapter 6.

7.4.1 General concept

The Tile Calorimeter is designed to allow a movable radioactive source to pass through every scintillator tile. Each scintillator tile has two holes along the symmetry axis; the source guide tube is inserted through one. The concept is schematically shown in Figure 7-5. Use of a movable γ source allows:

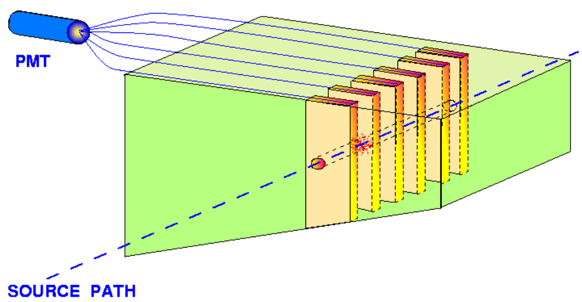

Figure 7-5 Mechanical concept of the source calibration system.

1. to check the quality of the optical response and its uniformity.
2. To equalize the response of all read-out cells, by adjusting the HV of the corresponding PMT to obtain the same average current from each cell.
3. to monitor in time the average current of each cell, by running again the source. As the average current for each cell is proportional to the overall signal/energy calibration of the calorimeter, monitoring it allows to maintain the overall energy calibration.

In Figure 7-6, from the first Tile Calorimeter publicationD-4, the current induced in five PMTs (reading out five consecutive calorimeter cells) is shown as a function of the source position. The multiple peak structure in the response of each PMT is due to the passage of a 5 mCi ^{137}Cs source through individual tiles; a case of faulty light collection from one tile is clearly seen. The capability to see individual tiles is due to the mean free path of the ^{137}Cs gammas, which is of the order of the 18 mm separation between tiles. This figure demonstrates the power of source scans of the calorimeter in testing its quality and uniformity. The source can "see" every scintillating tile, and therefore it can be used to obtain an "*x-ray picture*" of the response. Source scans could also be used to control the optical quality of modules in time to correct possible assembly faults.

The movable source system is the main tool to equalize the response of the calorimeter read-out cells within a module, and between different modules. This is done by adjusting the high voltage of each PMT to obtain the same average signal from each cell. The averages are obtained online from a computer controlled scan of each cell, giving response curves like those in Figure 7-6; the source-induced current is measured every about 3 mm, giving 6 points per tile (the tile-to-tile spacing is 18 mm). The average is simply obtained by summing the measurements over a cell, subtracting the baseline and dividing by the width of the cell (18 mm x the number of tiles). The average response values are measured again at later times, providing information about the stability of the overall calorimeter response and also the cross-calibration information for the analysis of test beam data.

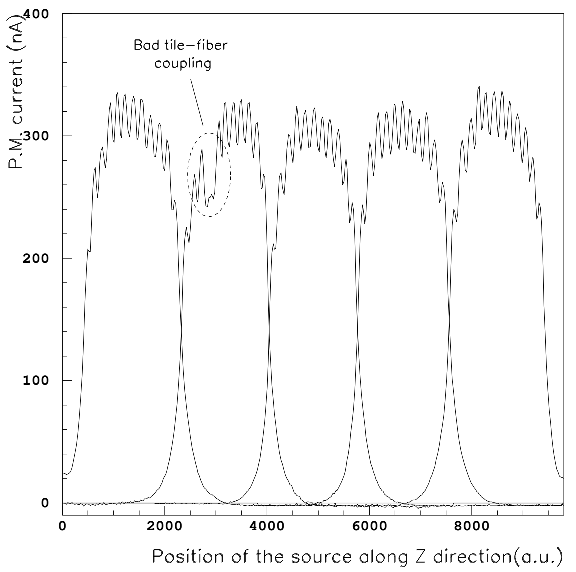

Figure 7-6 Current measured in the PMTs as a function of the source position along the rod (z axis).

A few of the basic parameters of source signal read-out are introduced here, to serve as reference in Section 7.5; the source read-out electronics is described in detail in Chapter 6.

Using an 8 mCi ^{137}Cs source in Module 0 tests, and operating at a nominal PMT gain of 10^5, anode currents of about 50 nA were observed. Considering that the ^{137}Cs gamma-rays typically give single photoelectron signals, this current is equivalent to about 4×10^6 photoelectrons/second. Using a JFET-input operational amplifier with an integrating time constant of a few msec this signal is converted to a voltage with negligible ripple. This type of read-out electronics has been used for all source monitoring work on Tile Calorimeter prototypes.

A movable source system allows to use just a few sources to calibrate the whole Tile Calorimeter. For long-term monitoring of the calorimeter response, the precisely known decay rate of the activity of sources is of course extremely useful.

7.4.2 System requirements

The R&D efforts described in this chapter have allowed to design a movable source system to do source scans of the entire Tile Calorimeter at any desired time after assembly of the full detector. Such a system must satisfy the following requirements:

- It must be remotely controlled from the electronics cave.
- The movable source system and its controls must operate over the duration of ATLAS with minimal access to the detector. A consequence of this requirement is that all system components that may need maintenance or replacement must be located outside the detector in areas that are accessible without opening ATLAS.
- Installation, operation and maintenance must not produce unacceptable radiation exposure to personnel and equipment.

- In case a source stops anywhere on its path, it must be possible to move it to a safe location without dangerous exposure to people or equipment and without significant loss of time to ATLAS.
- A full source scan of the Tile Calorimeter must be done during short beam down periods. This time should not exceed 8 hours; considering that a path scanning all tiles in the barrel is of approximately 4000 m - neglecting interconnections, this requirement translates into a capsule velocity of at least 15 cm/sec.
- The capability of partial scans is desirable.

The necessary performance in terms of repeatability and precision of the cell intercalibration and long term monitoring are discussed in Sections 7.6 and 7.7.

7.4.3 Two source drive concepts

7.4.3.1 Hydraulic drive

The concept is to fill the source tubes with a liquid and to set it in motion with a pump. A capsule containing the source is introduced in the liquid; for capsule diameters slightly smaller than the tube aperture there is negligible flow past the capsule and its velocity is practically the same as that of the liquid column.

Calculations and small-scale tests show that a liquid column of several hundred meters could flow at a velocity up to 50 cm/sec with a pressure drop of less than 1 atmosphere across the circuit provided that the viscosity of the liquid is low enough; these conditions are achieved using the most common liquids such as water.

This concept is attractive because it is simple, and the source velocity appears high enough. On the other hand, a practical and safe design must be shown to satisfy the following specific requirements:

- be safe against fluid leaks, particularly considering that the system would have more than 4000 interconnections,
- in order not to compromise the measurement of the average source-induced current the capsule velocity must be constant to within about 1%,
- the position of the capsule must be detected by an *ad hoc* system.

Regarding the first point, the concern about leaks can be alleviated by using a “safe” liquid. Interestingly, such a liquid exists: Perfluorohexane (C_6F_{14}) is non-flammable, chemically inert, non-corrosive, electrically insulating, non-toxic, and rapidly evaporates due to its high vapour pressure (about 0.2 atm at room temperature).

A conceptual design of the hydraulic system is given in Figure 7-7 for the case of the barrel. The drive liquid enters and exits the calorimeter through a number of parallel supply/return lines, connected to the source circuit every 2 modules (or every 4 modules for the extended barrel). When the source is in the circuit segment comprising Mods. 1 and 2 (see figure), the liquid flows into Module 1 and out Module 4; after the source reaches Module 3, the liquid flows into Module 3 and out of Module 6. The state of flow of the liquid is controlled by means of 3-way valves, located in the electronic cave.

With this mode of operation there is flow only through 4 modules (barrel) or 8 modules (extended barrel), which limits the pressure drop across any two points of the circuit. A source scan can be interrupted if desired and the source can be brought to rest in one of several radiation-shielded locations ("garages") along the source circuit and within the calorimeter.

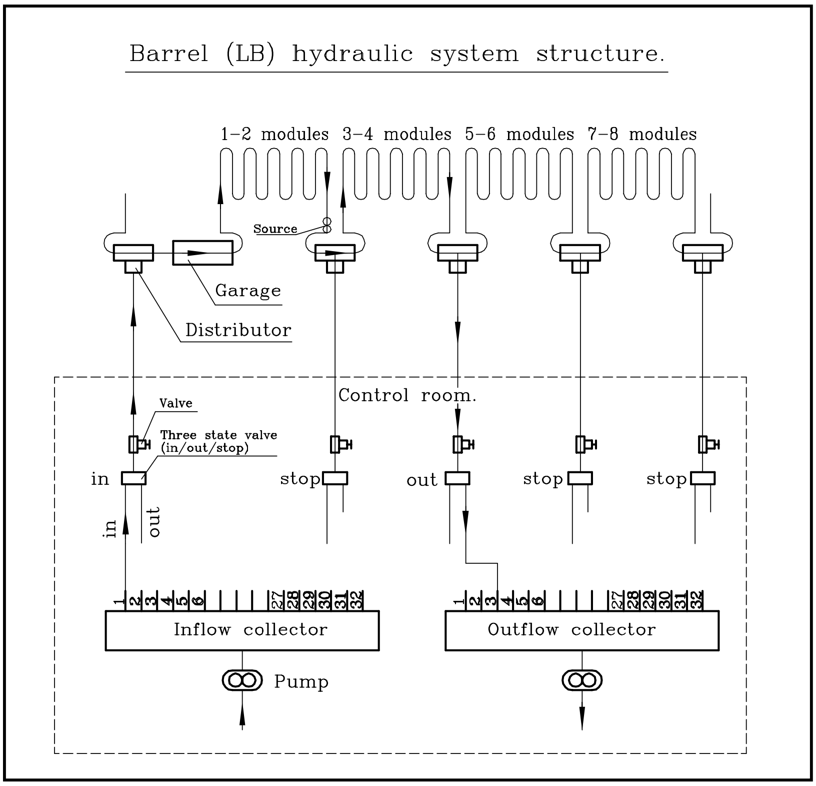

Figure 7-7 Schematic diagram of the hydraulic system for the barrel.

7.4.3.2 Pneumatic drive

The concept is to use compressed air to push the source capsule down the tubes.The capsule, restrained by a thin flexible line, is released at constant speed by an appropriate spooling mechanism. In this case the force is provided by the aerodynamic drag across the capsule, which is again slightly smaller that the tube aperture.Unlike the hydraulic drive concept, the pneumatic drive concept implies open paths: the capsule penetrates the calorimeter pushed by compressed air, and is extracted pulling on the line. The measurement of the source signal can be done in either mode.

The attractive features of this concept are that the velocity is intrinsically stable and repeatable, and that small leaks of the tube system are not a threat. Also, the position of the capsule is known by measuring the length of line spooled in or out as the capsule moves.

On the other hand, friction of the retaining line in the tubes (particularly in the bends) limits the maximum useful path due to the maximum total bend allowed by friction. Also, the possibility of breaking the line and thereby losing control of the source must be addressed seriously.

A design that addresses these concerns is schematically shown in Figure 7-8. The source is extracted from a radiation shield ("garage") and goes down one of several paths, selected by a rotating revolver mechanism, located outside the calorimeter.

A second stage of path selection, by means of similar mechanisms, take place on the calorimeter itself. The source then heads towards one of three paths for each module. In this scheme there are 192 paths for each of the 3 barrels; their lengths are chosen based on the friction losses observed in small-scale tests. The minimum velocity needed to scan the barrel in 8 hr is 30 cm/sec. Each of the source paths ends in a collector tube, which channels the compressed air out of the calorimeter and provides an exit path for the source in case the line breaks.

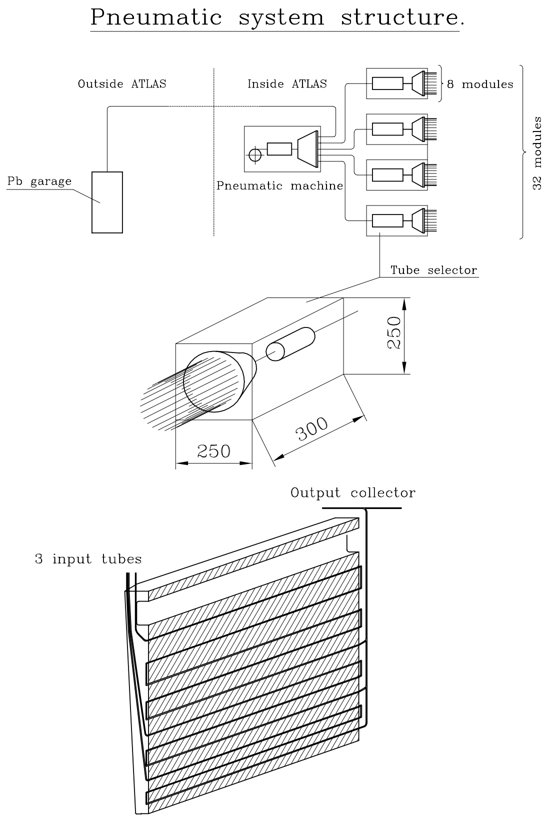

Figure 7-8 Scheme for the pneumatic drive system.

7.4.4 Experience with prototypes

Movable sources have been used since early 1993 to intercalibrate the first Tile Calorimeter prototypes. Experience was first gained using a system, developed by V. Barnes at Purdue University for CDF, which was generously lent to RD1 and later to RD34. In this system the source is contained within a thin steel capillary tube which is mechanically inserted in to the calorimeter. A new system, based on the same concept, was developed within RD34 and is still in use; it is described in the next section. The realization that this system would not be practical for the ATLAS detector led to the pneumatic and hydraulic concepts which are described above, and to prototypes which are also described here.

7.4.4.1 Mechanical drive prototype

This system is briefly described here because many of the results presented later in this chapter were obtained with it, and thus serve as a reference for the results obtained with the other systems N-44. Also, this system is particularly easy to set up and operate and therefore will be used for the first intercalibrations of several of the production modules.

A 5 mCi ^{137}Cs source, about 5 mm long, is embedded into a flexible stainless steel capillary tube, with an outer diameter of 0.7 mm. The early prototype calorimeter modules are traversed by tubes with an inner diameter of 2 mm (see Figure 7-5 for the concept) into which the flexible source tube is mechanically inserted; every raw of tiles is traversed by on or two such source guide tubes.

The source moving mechanism is schematically shown in Figure 7-9. The capillary tube is wound on a take-up reel (15 cm diameter) from which it is unwound by rotating the wheel by means of a step motor (M2). The source end of the capillary is normally kept in a lead “garage” for radiation protection reasons. Exiting the garage, the source first advances within a flexible plastic tube, which is connected to a motor-driven cursor which in turn aligns the source to one of 100 plastic tubes which lead it to the chosen source guide tube in the calorimeter. The system is driven from a PC which also controls the acquisition of the PMT current data.

This system was used for 3 years (1994-1996) to equalize the response of read-out cells across up to 5 prototype modules (in total, 200 PMTs) every time a module had undergone significant reworking (such as a different set of scintillators and/or WLS fibres) and then to monitor the variation of the response in time. Measurements are typically made by moving the source by 3 mm, stopping and then reading the current. The system was shown to be very reliable and easy to set up.

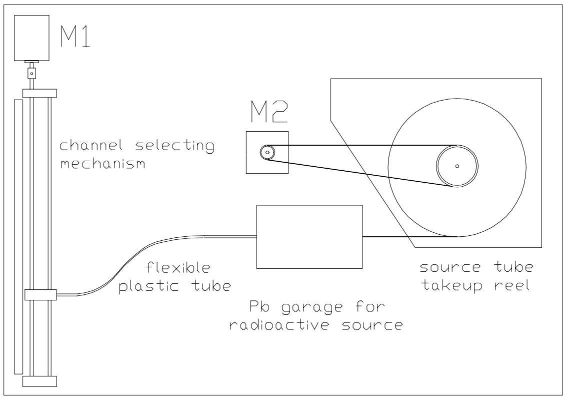

Figure 7-9 Small schematic diagram of the source moving system.

This source drive system is essentially limited by friction, which makes it difficult to negotiate turns of more than 360 degrees; fatigue of the capillary tube metal also makes it imperative to keep bending radii to more than 5 cm. The tight space requirements within the ATLAS calorimeter mandate smaller radii; also, the desirability of keeping the source drive mechanism outside the detector entails a minimal path of a few tens of meters, with a prohibitive number of bends. These considerations led to the development of different approaches for moving a radioactive source within ATLAS.

7.4.4.2 Pneumatic system prototype

The pneumatic drive concept was tested in the summer of 1996 by developing a prototype system for Module 0 of the Tile Calorimeter.

Preliminary R&D

Tests were carried out to measure the drag force produce by pressurized air on capsules of different designs, to choose the material of the restraining line and to measure the friction losses in a system of tubes reproducing the source path within a barrel Module 0. The drag force for different flows and capsule designs was measured by a dynamometer that gave the tension of the line at various points along the capsule path; this procedure also gave the friction coefficient.

The main results of these tests can be summarized as follows:

- The drag force grows approximately with the square of the flow, and is 70 g for a capsule of 5.6 mm diameter in a 6 mm ID tube at a flow of 5000 litre/h. The force rapidly grows as the capsule diameter approaches the tube ID; a 5.6 mm capsule diameter was specified to avoid excessive sensitivity to imperfections at tube joints.
- Attaching several capsules on the same thread allows to substantially increase the drag force for a given flow; the force per capsule is approximately additive if the capsules are separated by more than 10 mm.
- Axial rotation of the capsule (obtained by machining appropriate grooves on the capsule) stabilizes the capsule movement. In multicapsule trains, adjacent capsules are made to rotate in opposite directions to avoid twisting the restraining line.
- Restraining lines of polyamide (Nylon) monofilament, Kevlar and Carbon multifilaments, and Teflon-coated stainless steel were tested. Finally a Nylon monofilament with 0.4 mm diameter was chosen because it exhibited the least damage after a large number of capsule insertions despite the fact that its friction coefficient was not the lowest (obtained with Teflon-coated steel wire).

Design for the train of capsules

A train of 8 spherical capsules, axially mounted on a piano wire of 0.2 mm diameter, was used to provide the main drag force. The capsules are spaced by 15 mm long teflon tubes. At one end of the train, a bicapsule containing the radioactive source was attached, as shown in Figure 7-10. The source is contained in a 2 mm diameter steel tube, mounted in the bicapsule as described later.

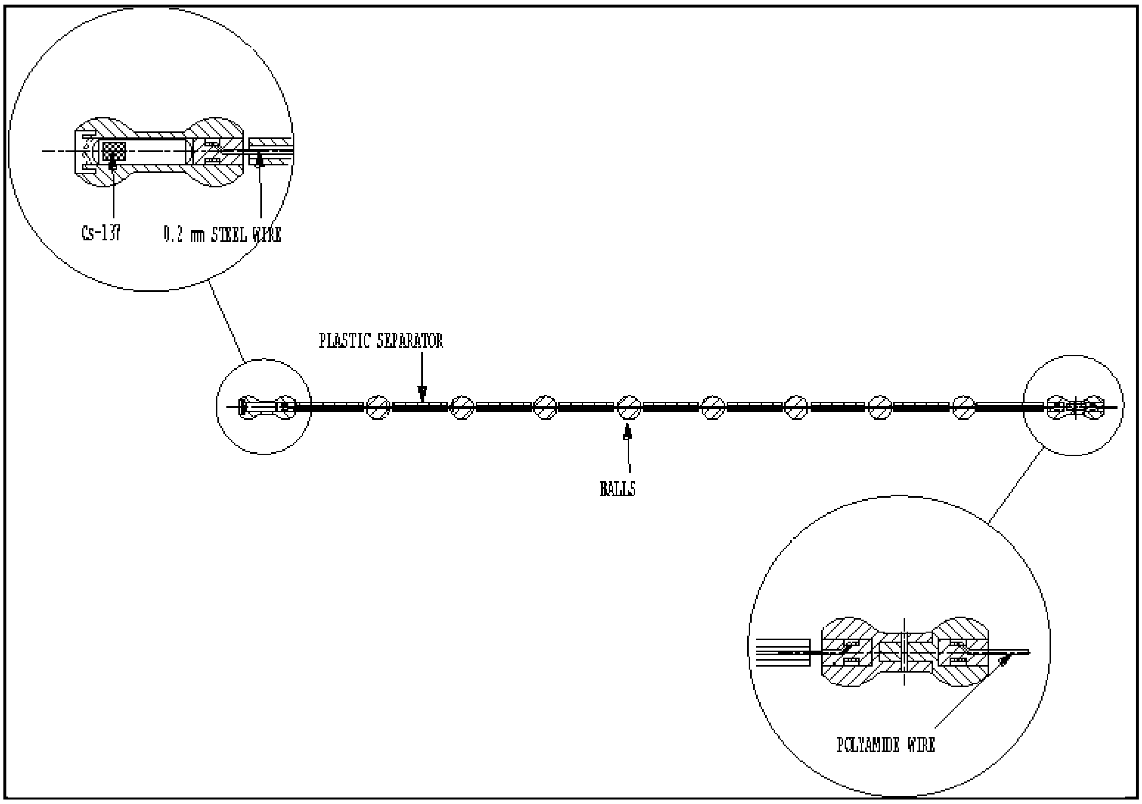

Figure 7-10 The train of capsules.

At the other end of the capsule train, an other dumbbell-shaped bicapsule is used to connect the capsule train to the nylon line. This bicapsule is made of two parts, which are screwed together when the source train is joined to the nylon line; a transverse pin prevents the assembly from coming loose.

The train assembly was found to carry a static load of more than 5 kg.

Capsule movement and control

The train of capsules is released and pulled back using the machine shown in Figure 7-11. The mechanism is housed within a pressurised chamber, connected to the air supply. When inserting the source into the calorimeter the nylon line unwinds from a storage reel, labelled (13) in the figure, onto the drive pulley (9) where it is wound twice. The line release velocity is set by the rotation rate of the pulley, which is driven by a DC motor with tachometric dynamo feedback. The tension on the line is measured by a load cell (7) attached to a second pulley (6) through which the line is fed. The capsule train is normally kept in the machine, with the radioactive source in the center of the Lead “garage” (21). A path selection mechanism is realized by a revolving cylinder containing a curved tube, which matches an axial hole on one side to one of 16 exit holes on the other side. The revolving mechanism is pneumatically actuated. The source train exits the machine pushed by the drag produced on the capsule train by air flow, and is pulled back at the end of its path by rewinding the nylon line onto the take-up reel.

The machine is located on the calorimeter scanning table, and is remotely or manually operated through a local microprocessor which controls the unwinding speed, measures the position of the capsule train by using the information from an encoder, and is programmed to respond appropriately to several capsule position sensors and to the line tension signal from the load cell. The source exit path is also selected through the microprocessor.

Pneumatic system layout

The Module 0 layout is shown in Figure 7-12. In order to keep the tension on the capsule restraining line to a conservative minimum value of 50 g, it was chosen to break the path of the source within Module 0, consisting of 11 tubes each 5.6 m long, into three paths of 3, 3 and 5 tubes. Each path terminates in a lead “source catcher”, which also provides a safety feature if the restraining line breaks.

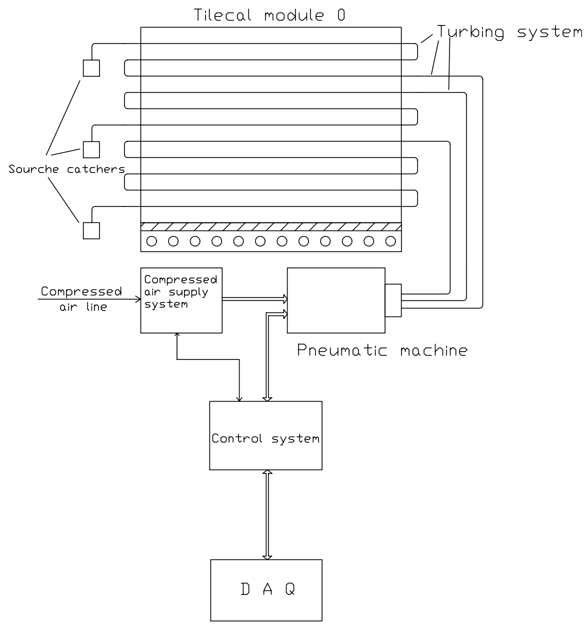

Figure 7-12 Layout of the pneumatic drive system for Module 0.

Operational experience

The pneumatic drive prototype was installed on the H8 test beam in summer 1996. Preliminary runs showed that it was possible to operate at capsule insertion velocities of up to 30 cm/sec and inserting the capsule through the full system of 11 tubes. However along this path the capsule velocity could not be maintained to this value, because of the loss of tension at the load call caused by friction in the bent sections connecting different tubes. Therefore it was chosen to operate at the conservatively low source velocity of 7.5 cm/sec, and to break the source path into three parts, as described above.

Measurements of the calorimeter response with this system were made with excellent control of the position of the source and its velocity. However the loss of tension on the restraining nylon line as the source goes through bent tube sections was seen to be much greater than previously seen in static tests. The unexpectedly large loss of tension prevents this system from being considered viable for ATLAS.

7.4.4.3 Hydraulic system prototype

The hydraulic drive concept was also tested in 1996 by developing a prototype system for Module 0 of the Tile Calorimeter.

System layout

A schematic diagram is given in Figure 7-13. The calorimeter tiles (11 rows) are traversed by 11 tubes, 5.64 m long, which are joined with bent tube sections to form a single circuit. The two ends of the circuit are connected by 45 m long flexible tubes to the liquid drive unit (“Hydraulic unit” in the figure), which is located in the control room and consists of a gear pump, pressure and temperature sensors, electromechanical valves and a reservoir. The system can be locally or

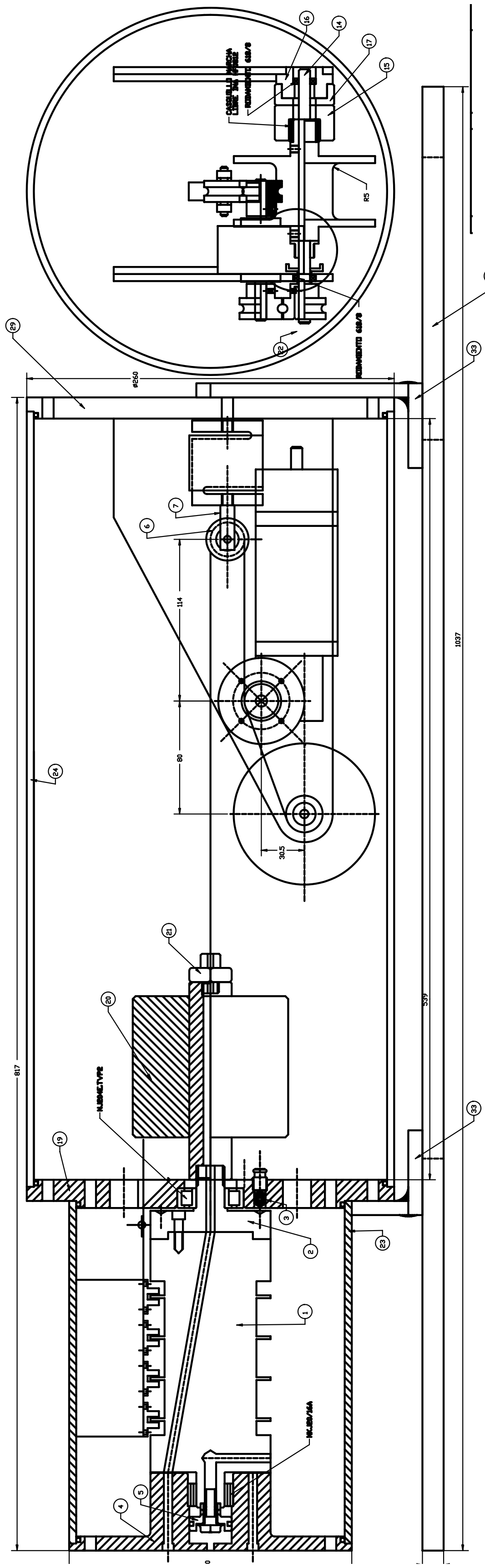

Figure 7-11 The pneumatic machine design.

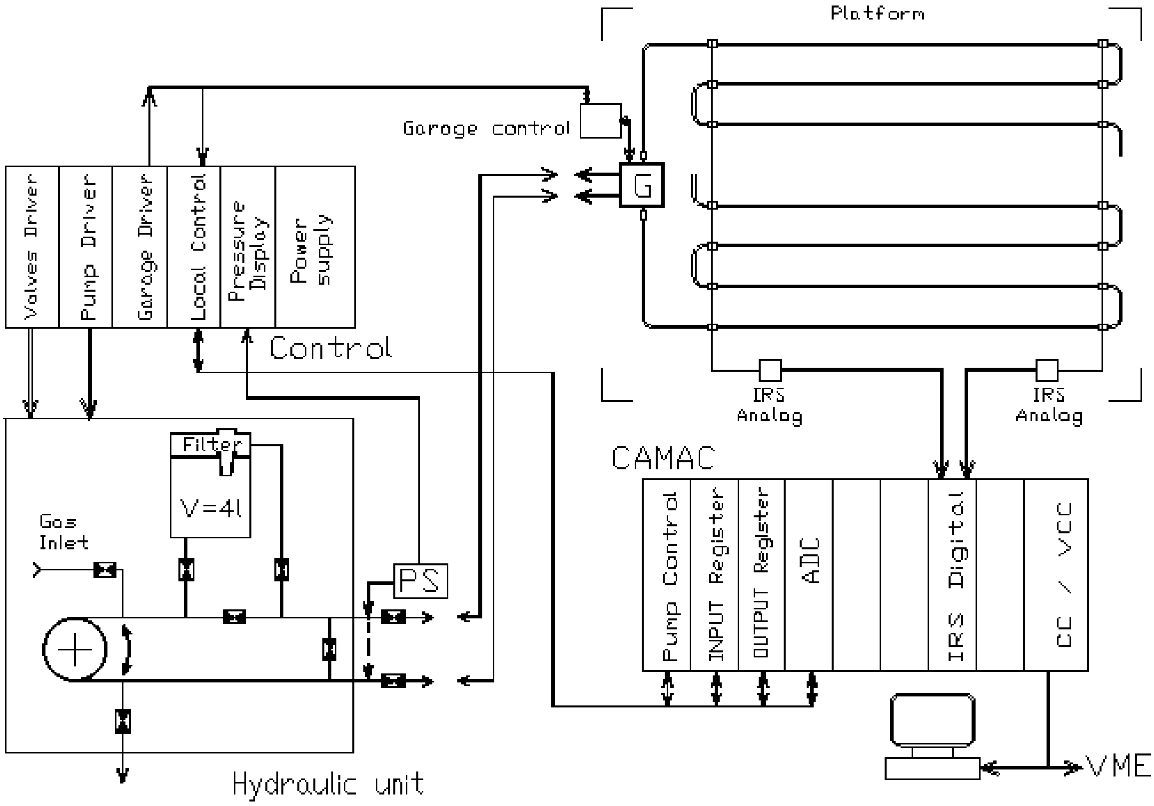

Figure 7-13 Diagram of the hydraulic system prototype used in the testbeam for the barrel Module 0.

remotely controlled. The liquid can be evacuated from the tubes into the reservoir when it is not in operation.

The source capsule geometry is shown in Section 7.4.5.3. The capsule is kept in a Lead garage, on the calorimeter scanning table. A remotely controlled mechanism inserts the source into the moving liquid column. At the end of its path through the calorimeter, the source comes to rest against a mechanical stop; the direction of the liquid flow is inverted, and the source returns to its starting position.

Capsule position monitoring
An optical system based on infrared LED and optical sensors was built in order to detect the passage of the capsule at selected points of the liquid circuit. An emitter-sensor pair is installed on the connectors at the joints of the straight tube sections; the interruption of a pulse train signals the passage of the capsule and allows to measure its velocity through all straight sections. Besides providing a useful check of where the source is this system permits to measure the velocity and its deviations from the mean.

Operational experience

The system was operated in the summer of 1996 with two liquids: distilled water, and perfluorohexane (C_6F_{14}). Capsule velocity, measured in the straight tube sections with the infrared sensor system, was found to be an almost linear function of the pump frequency as shown in Figure 7-14.

Operating with water, the velocity may vary by a few percent from run to run, depending on temperature conditions; however the variation of velocity values within the 11 straight sections is very small, having a typical rms dispersion well under 1% over a wide range of velocities, as also shown in the figure.

Operating with perfluorohexane, the rms dispersion of velocity during a run is 1% to 2% and the variation of the average from run to run is poorer than with water. This may be due to the much lower viscosity of the latter liquid, and needs more investigation.

For source calibrations, the system was operated at velocities of 24 to 30 cm/sec. The system appeared robust and easy to operate. There were no leaks and no system failures; a failure of the pump motor drive allowed to satisfactorily check the safety of the source extraction procedure, using compressed air. More than 50 scans of Module 0 were performed and produced data suitable for offline analysis.

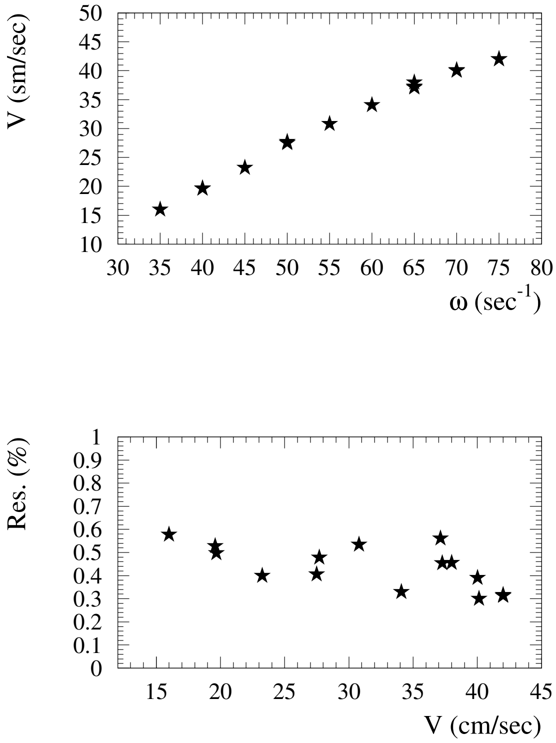

Figure 7-14 Measurements of the hydraulic drive performance with water.

7.4.4.4 Conclusions from prototype work

The only issue addressed here is the operational feasibility of a movable source system. It will be shown in section 7.6 that the performance of the movable source system is adequate for readout cell intercalibration and long term monitoring.

As indicated above, any of the three systems developed over the last three years can be used to check out and equalize the response of individual barrel or External barrel modules.

It appears that the requirements of a source system for all of the ATLAS Tile Calorimeter can be met by the hydraulic drive concept, provided that either the risk of a water leak is accepted or that perfluorohexane is confirmed to be acceptable as the source drive liquid. More experience with this material must be obtained before making this choice.

7.4.5 The radioactive sources

It is planned to manufacture the sources at the Joint Institute for Nuclear Research (Dubna, Russian Federation). This Institute has produced in 1996 several sources, for all three source drives described above. The sources for the pneumatic and hydraulic drive in particular have been made to ATLAS specifications, thereby proving that the necessary techniques are available.

7.4.5.1 Source specifications

The source specifications are based on the experience obtained in calibrating three generations of prototype modules (1993-1995) and the barrel Module 0 (1996). General requirements on the sources are:

- γ energy: must be high enough that attenuation through the 1 mm thick steel tubes is less than 10%, such that variation of the useful flux due to tube tolerances is less than 1%.
- Isotope lifetime: the lifetime of the source must be sufficiently long to permit at most one replacement over the lifetime of ATLAS, including the construction phase.
- Activity density: the activity in a volume not exceeding 5 mm^3 should be sufficient to produce average currents of more than 10 nA at the photomultiplier anodes.
- Purity: contamination by short-lived isotopes must not introduce an uncertainty of more than 1% in the gamma flux relative to the initial value.

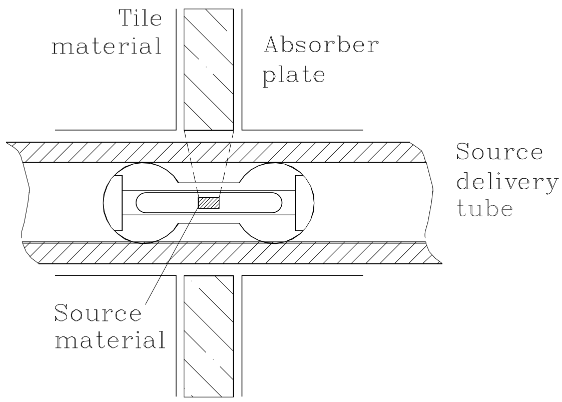

Figure 7-15 Source location with respect to irradiated tile; influence of the source length on the efficiency of the system.

^{137}Cs (E_γ= 0.662 MeV, $t_{1/2}$ = 30.2y) satisfies all these requirements. The activity density requirement arises because it is desirable for the source to extend less than 3 mm - the thickness of scintillating tiles -as illustrated in Figure 7-15. As described above, this requirement has been met by the sources manufactured at the Joint Institute for Nuclear Research. Finally, commercially available ^{137}Cs from nuclear fuel reprocessing contains a small enough contamination of the short-lived ^{134}Cs isotope (with $t_{1/2}$ = 2.9y) to meet the last requirement.

7.4.5.2 Source preparation

In the following the procedure developed at JINR is described. The purpose of the procedure is to concentrate about 10 mCi of ^{137}Cs into a volume of about 3 µl and then to seal it within a hermetic and durable shell.

Isotope concentration

Commercially available Cs from nuclear reprocessing is well-known to be heavily contaminated with inorganic impurities (Fe, Co, Ni, Cu, Cr, Mn, Ca, Ba, K, Na). The Cs salts constitute only about 10% of the total volume. The purification procedure is based on anion and cation exchange chromatography, and is outlined in Figure 7-16. At the end of the process the appropriate fraction of the cation exchange resin is separated, in grains of 0.7 to 1.2 mm diameter.

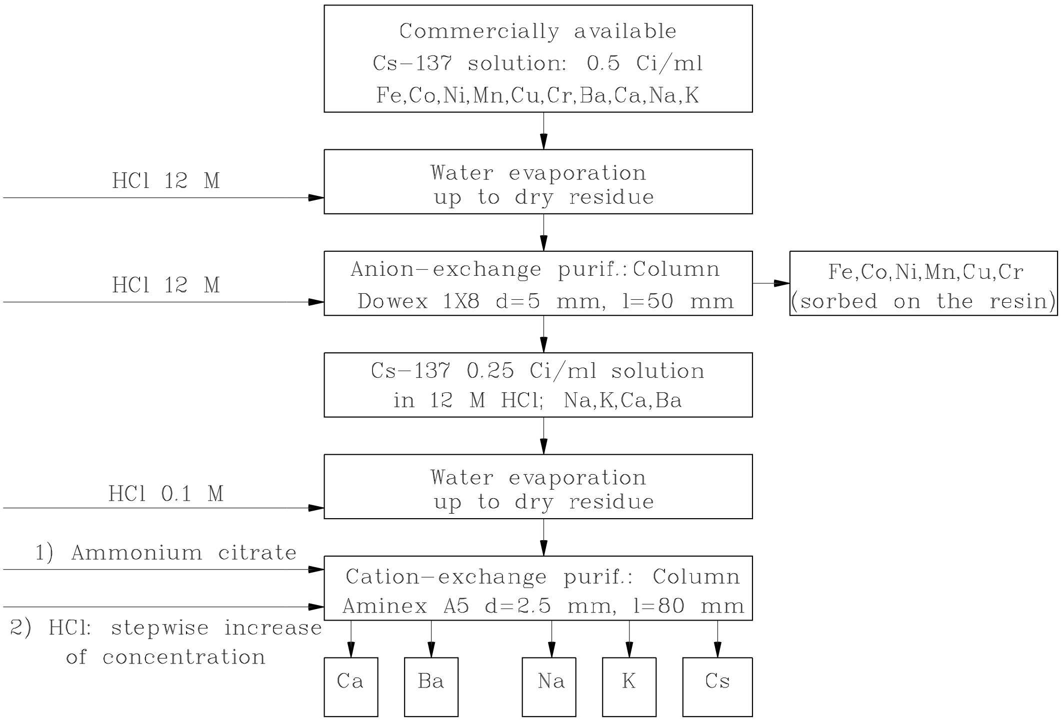

Figure 7-16 Scheme of ^{137}Cs purification procedure.

Implantation into a sealed container

The container is a stainless steel tube, with OD=2 mm, ID=1.6 mm, arc-welded at one end. After deposition of the isotope-loaded grains in the cell, the latter is sealed by arc-welding in Argon atmosphere. While welding the container is tightly pinched within copper jaws to provide a heat sink and thereby prevent cesium salt overheating and evaporation (Figure 7-17); all these operations are carried out in an air-tight ventilated box. Then etching with a hydrochloric acid solution is carried out to eliminate any surface contamination; this is followed by mechanical polishing of the welded point.

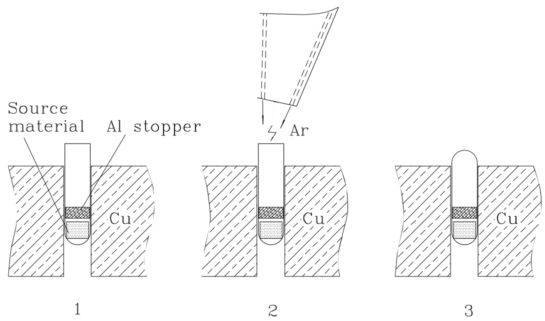

Figure 7-17 Scheme of the source container hermetization by electrical welding.

7.4.5.3 Source capsule design

The design of the capsule used in hydraulic drive source calibrations in 1996 is shown in Figure 7-18. The capsule material is aluminium, chosen to minimize the difference in density with the drive fluid.The dumb-bell shape was shown by extensive tests in a prototype hydraulic drive circuit to be optimal for reliable transport in bent sections in which the 8 mm OD, 6 mm ID tube was bent by 90^{o} with a curvature radius of to 20 mm. The 9 to 10 mm long sealed source shell is installed in the 2.1 mm diameter axial hole; then the reentrant rims of the hole are bent in with an appropriate tool. By this method the shell is fastened to the capsule without introducing any material which might suffer radiation damage over time.

Radiation effects on fluid and capsule surface

The formation rate of corrosive products due to radiolysis of the drive fluid was estimated; the subsequent effect on the capsule material was also examined. Two cases were considered:

- Production of H_2O_2 if the fluid is water.
- Production of free fluorine, if the fluid is C_6F_{14} (perfluorohexane).

The calculation uses published values of formation rate per unit absorbed dose of the chemicals [A.2] and integrates the effect of absorbed dose over the volume in which the source is stored (the "garage"). Assuming conservatively that the total exposure of the fluid to a 10 mCi source is 1 year out of 10 years of operation of the system, the formation of 2.5×10^{-6} moles of H_2O_2 is expected; for the case of perfluorohexane, the free fluorine produced would be enough to a 20 μ thick film on the capsule. These amounts of radiolysis products do not appear a threat to safety or system performance. Ordinary electrochemical corrosion effects on the Aluminium capsule would probably dominate, and make it advisable to add a corrosion-resistant metal coating to the design of the capsules.

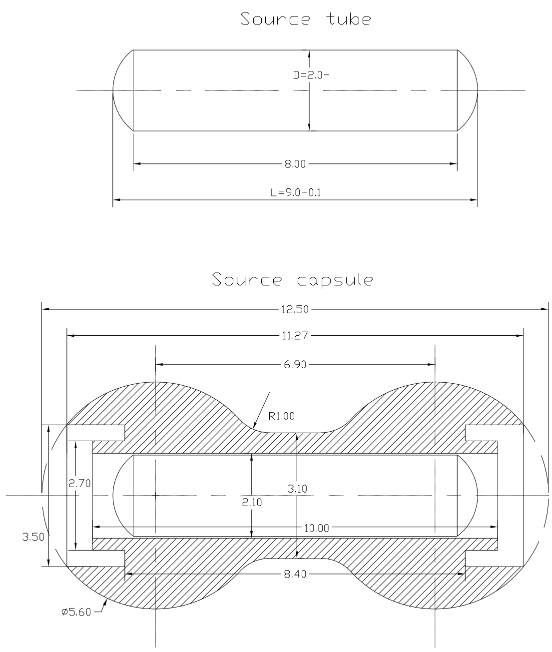

Figure 7-18 Tentative design of the source for the hydraulic option of the source drive system.

7.4.6 System design for ATLAS

Based on the encouraging results obtained with a prototype of the hydraulic drive concept, a movable source system for the ATLAS Tile Calorimeter has been designed using this approach. The system is composed of three independent parts, for the barrel and the two extended barrels respectively; these parts are identical in principle and design philosophy, differing only in the details of the layout. Each part is composed of a closed source circuit which passes through every tile of every module, and contains one source.

As outlined in Section 7.4.3.1, each circuit is accessed by the drive liquid through supply/return lines which divide the source circuit into a number of segments; the liquid enters or exits the calorimeter through only two of these lines at any time. The moving liquid column spans only a few modules at a time, which keeps the pressure drop across the moving fluid column to conservatively low values.

7.4.6.1 General specifications

For convenience the general system specifications, including part numbers and dimensions as well as operating characteristics are summarized in Table 7-2, to which reference is made in the following subsections.

Table 7-2 Source system specifications for the barrel and extended barrel regions.

ITEM	LB	LE
Number of sources	1	2
Source capsule length, diameter (mm)	L=11.5, D=5.6	
Straight tube length (m)	5.6	2.6
Number of straight tubes per module	11	12
Dimensions of tube section (mm)	OD=8, ID=6	
Total length of source circuit (m)	4270	2x2372
Modules per circuit segment (between supply/return lines)	2	4
Tee connections per circuit	32	2x16
Number of garages	3	2x2
Supply/return tube section (mm)	OD=10, ID=8	
Supply/return tube length	30	
Number of supply tubes	32	2x16
Total length of supply tubes (m)	960	2x80
Capsule velocity for calibration scans (cm/sec)	25	
Capsule maximum velocity (cm/sec)	50	
Pressure across circuit segments		
operating with water(atm)	0.8	1.2
operating with perfluorohexane(atm)	0.5	0.9
Calibration scan time (min)	285	160
Maximum time to reach a garage(min)	50	40

7.4.6.2 System layout

The pumps and their controls, the supply/return line collectors and the three-way valves that control the flow to these lines are located in the electronics cave. A total of 64 supply/return tubes connect the movable source system to the Tile Calorimeter. Within the Tile Calorimeter itself, the main hydraulic circuit components are:

1. The straight calibration tubes passing through the modules, as listed in Table 7-2.
2. About 2000 curved tube sections, joining the straight tubes to form the source circuits.
3. The tee joints, connecting the supply/return tubes to the source circuit.
4. Three source garages in the barrel and two garages in each external barrel. These garages are where the sources normally reside. More than one garage is provided along each circuit in order to be able to interrupt a scan and return a source to a situation that will not affect any part of the detector if it is desired to interrupt a scan for any reason. The garages include mechanisms to lock and release the sources. These are the only movable parts within the ATLAS detector.

5. Source passage sensors and local read-out electronics, described later in this subsection.

The general layout of the source circuit and the garages in the barrel is shown in Figure 7-19. The supply/return tube bundles are brought to a point at the outer radius of the Tile Calorime-

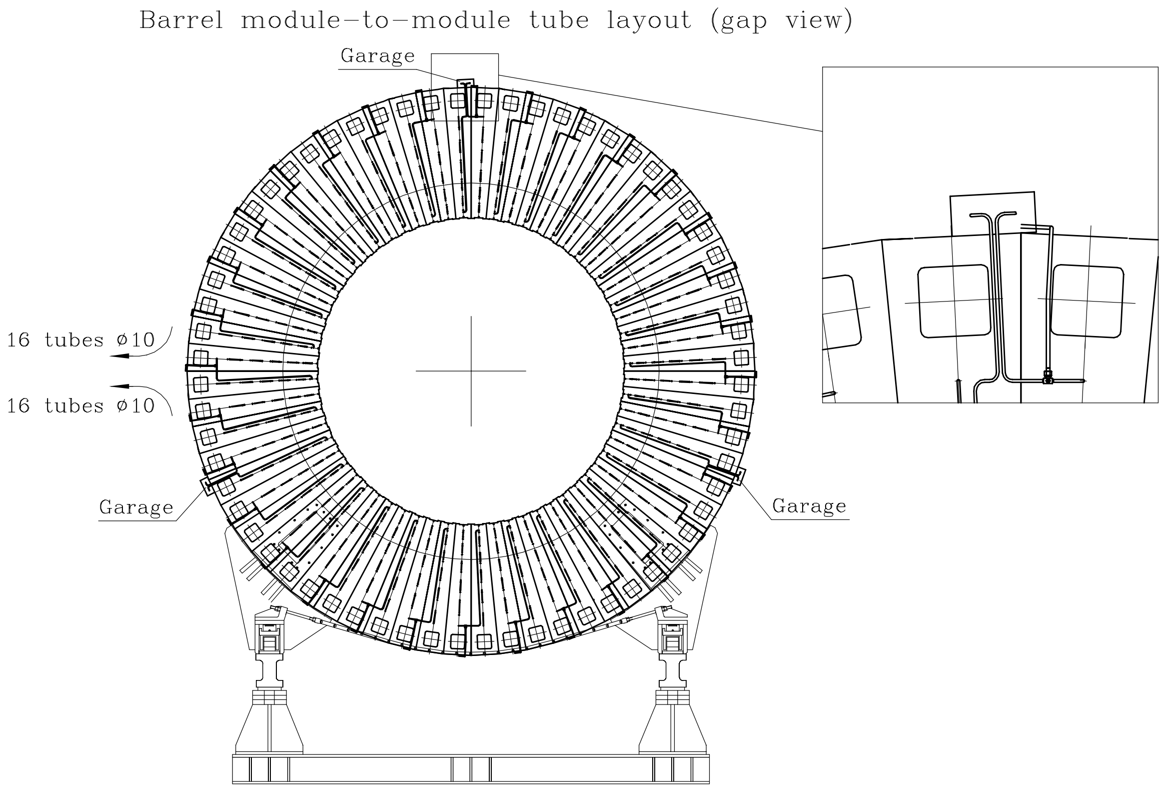

Figure 7-19 General source circuit layout for the barrel.

ter and reach the appropriate tee-joints around the external circumference of the barrel. The garages are symmetrically located around the barrel circumference to minimize the time to return the source to a garage (moving in either direction).

The tube routing within two adjacent barrel modules is shown in Figure 7-20. The straight radial sections are included in order to always scan the modules in the same direction and add less than 5% to the circuit length.The tubes always pass through the external hole of each tile.

The tube routing within an extended barrel module is shown in Figure 7-21. The tubes pass through the internal tile hole whenever necessary to avoid mechanical interference with Liquid Argon calorimeter electronic system hardware located in the LB-LE gap.

7.4.6.3 Hydraulic components

Pumps

The performance required is entirely conventional, namely the pumps must work at pressures of 1-2 atm with typical flows of 30 cm/sec.

A 25 W gear pump operated reliably in Module 0 tests, and gave sufficiently stable capsule velocities during source scans; it is anticipated that three 200 W pumps will be adequate for the

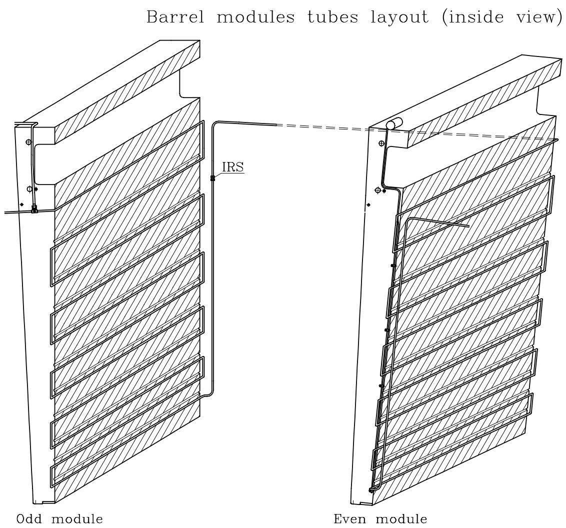

Figure 7-20 Tube routing within two adjacent barrel modules.

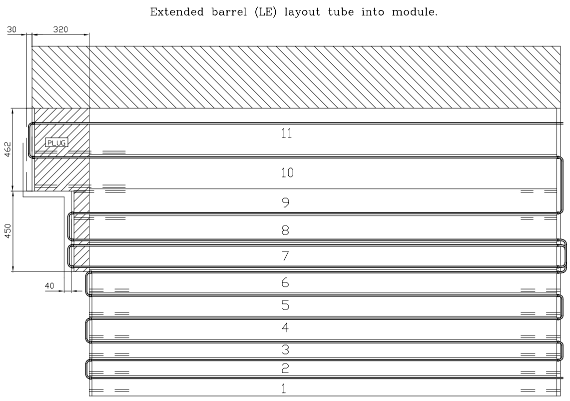

Figure 7-21 Tube routing within extended barrel modules.

full system. More work is needed to specify which type of pump is appropriate for operation with perfluorohexane.
A supplementary pump must be provided to fill the source circuits before a period of calibration scans and later drain them in no more than a few hours. Such a pump should be capable of flows about 10 times higher than the pumps to be used for source calibrations.

Source circuit tubes

The 8mm OD, 6mm ID stainless steel tubes must have a calibrated inner surface. Irregularities must be under 50 µm.

The same type of tube will be used to make about 2000 bent sections. Tubes with bending radii of 20 mm and a with a uniform cross section can be obtained with a variety of techniques, a few of which have been successfully used to obtain bent sections for Module 0 tests. This bend radius is adequate for the LB-LE gap.

The connections within a module must respect the very tight space requirements in the LB-LE gap; they have not been prototyped yet. It is envisaged to weld together assemblies of straight and bent tubes on one side of the module, fully insert the assembly, and then to use glue to realize the joints on the other side of the module, where space constraints and the presence of scintillating tiles preclude welding. The joints at the end of the barrel are shown in Figure 7-22.

Leak-tight connectors to join the tubes between modules at installation time present no problem; an example of a connector used in Module 0 tests is shown in Figure 7-23a. The central part of this connector can be used to house the infrared emitter/sensor pair, as shown in Figure 7-23b. Such connectors have been used in the tests of the hydraulic system built for Module 0.

7.4.6.4 Capsule position monitoring hardware

It is planned to further develop the infrared sensor system used for the prototype drive. The prototype system used the same LED as emitter and sensor; it planned to replace this system with commercial optocoupling components. It is expected that 1 or 2 sensors per module will be sufficient to check that a source scan is regularly proceeding; as experience is gained with the

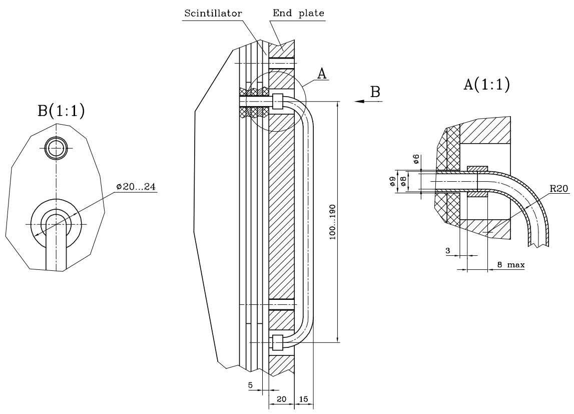

Figure 7-22 Tube joints at the barrel ends.

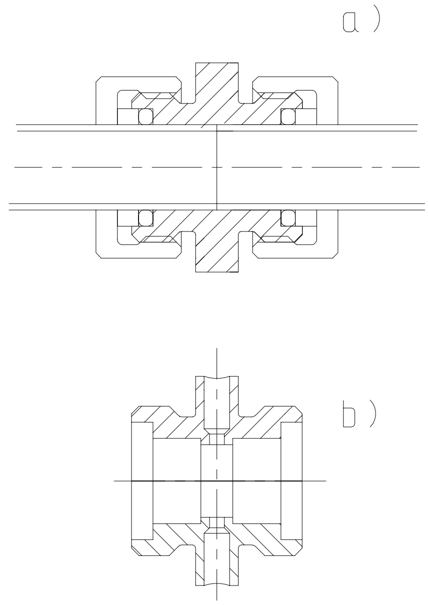

Figure 7-23 Connector schemes: (a)basic connector (b)incorporating optical sensor.

system, precise velocity measurements within the calorimeter will become unnecessary, because the signals from the scintillating tiles will provide the necessary information.

The system includes an analog electronics board, driving 16 sensors and recording the time of interruption of a pulse train of scalable frequency. This board must be within a few meters of the sensors; it communicates through digital signals with a control and memory module, which will be located in the electronics cave.

7.4.6.5 Further R & D and engineering issues

Experience with the prototype hydraulic system leads to the conclusion that an hydraulically driven source system for ATLAS can be designed with confidence that it will perform to specifications. However there are a few outstanding R & D issues that must be resolved before the design can be completed:

- the source-driving liquid must be chosen, and the associated hardware that depends on the physical properties of the liquid (pumps, optical sensors) must then be optimized,
- the techniques to join tubes within the tight space requirements must be fully tested,
- the concept of driving the source through a segmented circuit by switchable supply/return lines must be tested.

Other R & D and engineering issues that must be addressed but do not involve system design have been mentioned above and are repeated here. They include:

- Improving the surface hardness of the source capsule and testing it through a few hundred km of tube circuit.
- Defining a cost-effective technique to bend tubes to specification.
- Testing more optical sensors and choosing one, in order to then engineer the associated electronics.

Several of these issues will be addressed in 1997 while testing the Module 0 for the extended barrel.

7.4.7 Mode of operation in ATLAS

From installation of the Tile Calorimeter in the experimental pit to physics start-up the source system will be used to scan parts or all of the three barrels, first to tune up and verify its operation, and then to check the condition of the calorimeter after installation. The source system will give the first indications that the calorimeter is alive and well, without setting up special cosmic ray triggers.

It will also be necessary to verify that the scintillator light output depends on the magnetic field as predicted from the tests described elsewhere in this document.

Therefore it seems reasonable to expect that the source system will be operated rather often in this pre-start-up period - several times a year to several times a month just after installation. The relatively short time to scan each of the parts of the calorimeter (about 5 hours for the barrel, or 3 hours for the extended barrels) should make it possible to do so without interfering with ATLAS installation, by taking calibration scans at night or during weekends. The possibility to do partial scans (1/3 of the barrel or 1/2 of an external barrel) leaving the source in a garage may also be very useful.

As shown in Section 7.5 the current from minimum bias interactions will dominate the source signal, therefore source runs must be taken when the beam is off. When beams will begin circulating with a high duty cycle, the operation of the source system will become less frequent. However, as discussed in more detail in Sections 7.6 and 7.7, periodic source calibrations will be necessary to maintain the intercalibration of the modules and the absolute calorimeter energy scale; this will probably require source scans once or twice a year beginning from installation time for the lifetime of ATLAS.

7.5 Monitoring the minimum bias current

As is well known LHC detectors will have to cope with a background of inelastic proton-proton collisions at small momentum transfers, that will produce non-negligible occupancies in all detectors. These processes lead to the so-called Minimum Bias (MB) events; the associated noise in calorimeters is one of the limits on their performance. However these processes can be used to continuously monitor the response of the Tile Calorimeter.

7.5.1 Concept and mode of operation

The rate of energy deposition by MB processes has the following properties:

1. it is proportional to the LHC luminosity,
2. it is uniform in azimuthal angle,
3. it is moderately dependent on over the η range spanned by the Tile Calorimeter,
4. it produces a signal in the PMTs that is usually large enough to be recorded with inexpensive electronics,
5. the PMT anode current, averaged over a time scale of milliseconds, is almost constant.

The first property depends on clean running conditions, i.e. on the absence of appreciable contributions from beam losses due to beam-gas or beam-wall scattering. Under these conditions the average current in each read-out cell divided by the instantaneous luminosity gives a number proportional to the overall response of the calorimeter, that should be constant in time. Any variation of the MB current to luminosity ratio can be compared to information from the laser and movable source systems to understand the behaviour of the calorimeter in time and correct for it, once confidence in the method is gained.

The MB signal provides a manner to continuously monitor the response of the calorimeter because it can be read out during physics runs without interfering with normal data acquisition. This is because the quasi-DC component of the PMT anode signal is picked off without disturbing the fast pulse shaper, as shown in Chapter 6.

Even if running conditions at the LHC do not allow to quantitatively use the MB signal as just indicated, monitoring the MB current can still be used as an online diagnostic tool. Variations in the relative response of the two PMTs that read a Tile Calorimeter cell, of the distribution in ϕ and η of the MB signal, etc. can be taken as indications of phenomena that need to be investigated. This may be particularly valuable to check possible damage from sudden beam losses. As a diagnostic tool, monitoring MB currents is complementary to source scans, because it does not require the beams to be off.

Quantitative estimates of the MB signal and of its amplitude and frequency spectrum are necessary to design the monitoring electronics (and to justify some of these statements!). Detailed simulations were made for this purpose, and are summarized next.

7.5.2 Simulation of MB energy deposition rates

The mean energies deposited at each bunch crossing, at different depths and pseudorapities, in the Tile Calorimeter were estimated by using a full Montecarlo simulation of the ATLAS detector. The results given here are also documented in N-45.

A luminosity of 10^{34} cm^{-2}s^{-1} and an inelastic cross section of 70 mb were assumed, giving 17.5 MB events/crossing at the LHC bunch crossing frequency f=40 MHz. Three MB event tapes for a total of 1227 events were used; these events were generated by PYTHIA 5.7, with the standard ATLAS tuning. The interactions with the ATLAS detector were simulated with the DICE package. The mean energies per bunch crossing deposited in cells of $\Delta\eta \times \Delta\phi = 0.1 \times 0.1$, for the three radial segments, are shown in Figure 7-24, in which the barrel and extended barrel are separately shown. The mean energy depositions per crossing are 15-20 MeV in the barrel and up to 35 MeV in the first depth segment of the barrel and extended barrel respectively; at the edges of the barrels the

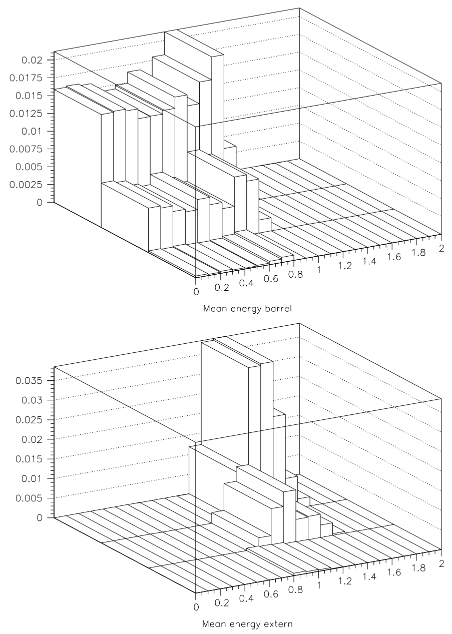

Figure 7-24 Mean energy deposition per crossing from MB interactions (GeV). The two horizontal axis represent the three radial(depth) segments of the Tile Calorimeter, and the segmentation in η.The two plots correspond to the barrel(top) and extended barrel(bottom).

mean energies are less because the average energy is shared between the two parts of the Tile Calorimeter or between the Endcap calorimeter and the extended barrel calorimeter. There is a factor of about 3 less energy in the second than in the first (innermost) depth segment, and a further reduction factor of 10 in the most external segment.

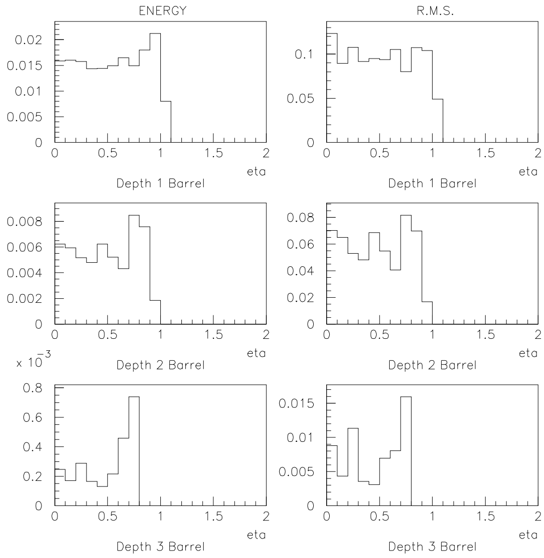

Figure 7-25 Mean energy/crossing and its rms value *vs* η for the three depth segments of the barrel The vertical scale is in GeV.

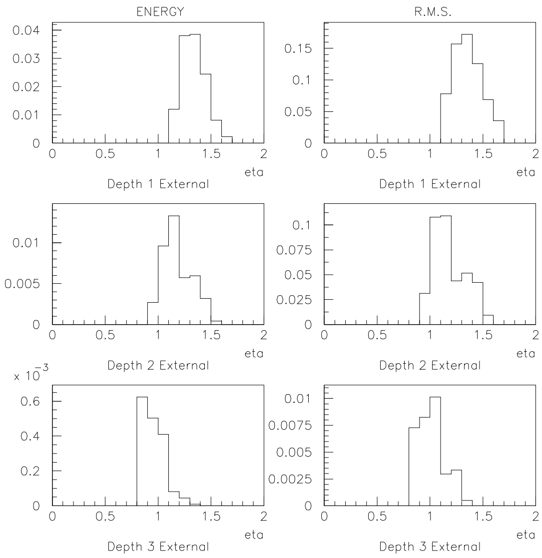

Figure 7-26 Mean energy/crossing and its rms value *vs* η for the three depth segments of the extended barrel The vertical scale is in GeV.

Fluctuations in energy depositions must also be simulated in order to properly specify the read-out electronics; for this purpose, the rms value of the MB energy/crossing was also calculated, taking into account the Poisson fluctuations of the number of MB interactions per crossing. The rms energy depositions per cell (as well as the means, in more readable form) are given in the plots of Figure 7-25 for the barrel and Figure 7-26 for the extended barrel. The rms values are typically a few times larger than the means, because even at these interaction rates the occupancy of calorimeter cells is much less than 1. The rms MB energy depositions are about 100-150 MeV in the first two depth segments of the barrel and extended barrel, decreasing to about 10-15 MeV in the external depth segment (in these figures the $\Delta\eta$= 0.2 segmentation of the external depth segment is not shown).

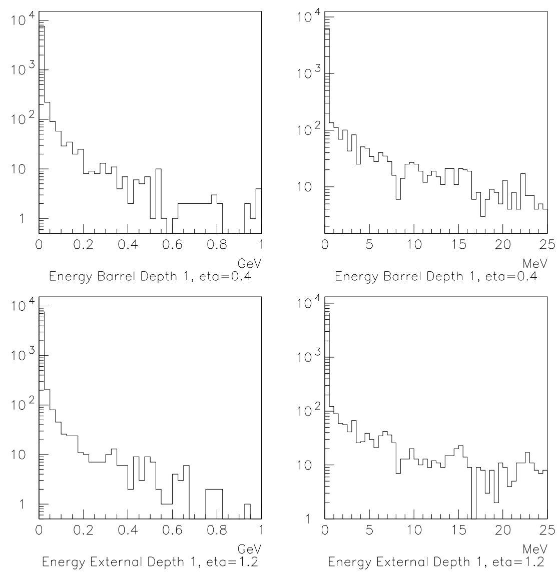

Figure 7-27 Distribution of MB energies/cell/crossing for η=0.4 (barrel) and η=1.2 (extended barrel), in the first depth segment. Left: bins of 25 MeV; Right: bins of 0.5 MeV.

Two MB energy spectra at mid-rapidity in the first depth segment of the barrel and extended barrel are shown in Figure 7-27. Two features are obvious: the distributions have no cut-off at high energy (because MB processes smoothly merge into high-momentum transfer interactions in the model used for the simulation, as is physically required); and there is a peak in the smallest bin which is due to the cells with no hits. This peak allows to estimate the occupancy, which in the cases shown in the figure is about 15% for signals of more than one photoelectron.

The MB energy estimates have an uncertainty of ±50%, associated to the extrapolation to the energy of the LHC. This uncertainty mandates a safety margin in designing the MB current read-out in order to avoid saturation at design luminosity.

7.5.3 Estimate of minimum bias currents

The conversion from the mean deposited energy E to the corresponding PMT current I is obtained by:

$$I = \frac{f \cdot n_{PE} \cdot G \cdot e}{2} \cdot E$$

where f is the LHC crossing frequency, n_{PE} is the number of photoelectrons/GeV detected in the Tile Calorimeter, G is the PMT gain and e is the electron charge. The factor of 2 in the denominator is introduced because each cell, receiving an energy E, is read out by two photomultipliers. Using n_{PE} = 50 p.e./GeV (about 20% lower than the best results obtained with module prototypes) and $G = 10^5$ as in chapter 6, the MB energy/current conversion factor is 16 nA/MeV; this value is used to obtain the following table.

Table 7-3 Maximum and minimum MB energy depositions in each depth segment and the corresponding currents.

Layer	E_{max} (MeV)	I_{max} (nA)	E_{min} (MeV)	I_{min} (nA)
1	36	576	8	128
2	11	196	2	32
3	1.2	19	0.4	6

Table 7-3 summarizes the maximum and minimum estimated energies and currents per cell in the three calorimeter layers. The numbers are extracted from Figure 7-25 and Figure 7-26, suppressing the obvious statistical fluctuations, and are used for the design of the MB current read-out electronics. In this table, the signals in the third depth segment are summed over cells of $\Delta\eta \times \Delta\phi = 0.2 \times 0.1$, and therefore correspond to the actual segmentation of the Tile Calorimeter.

7.5.4 Implications for operation in ATLAS

Using the simulation results and the estimated MB currents it can now be seen that the MB current can be monitored using the source current read-out electronics.

Qualitatively one can see that with an occupancy of 0.15 the MB current produces a random signal with a frequency of 0.15×40 MHz = 6 MHz, which is close to the frequency of source pulses. The observed source current of 50 nA lies in the range of the currents given in Table 7-3. Hence the MB monitoring electronics can use the same type of amplifier planned for source current read-out, but with larger or lower gains. In Chapter 6 the results from tests of a variable transmittances integrator designed to measure the MB currents estimated in Table 7-3 are shown; such amplifiers were built for Module 0 in 1996.

The lower limit of sensitivity to MB currents is reached when the MB current becomes comparable to the PMT dark current. As shown in Chapter 6, the PMTs tested in Mod. 0 have typical dark currents of 100 pA or less, well below the lowest MB currents in Table 7-3. However during initial LHC operation the luminosity may be small enough to make it un-practical to read out MB currents from the most external depth segment of the Tile Calorimeter, if PMTs are operated at nominal gain in this initial phase.

The question of the ripple of the MB signal due to large signals (in the limit, the physically interesting signals!) must also be addressed; as already remarked, the amplitude spectrum of the MB signal shown in Figure 7-27 has practically no upper limit. For an integrator as described in Chapter 6, with time constant RC, it is easy to prove that the fractional deviation $\Delta V/V$ from the average output voltage V due to an event depositing the energy ΔE in a cell with average MB energy E per crossing is:

$$\frac{\Delta V}{V} = \left(\frac{1}{f \cdot R \cdot C}\right) \cdot \left(\frac{\Delta E}{E}\right),$$

where f is the LHC bunch crossing frequency. Using RC = 0.75 msec, the worst-case integrator time constant given in Chapter 6 (corresponding to the innermost calorimeter segment), one obtains that a signal of 300 times the average MB energy/crossing will give a ripple of only 1%. This does not create a problem, considering also that MB current scans can be taken as often as desired, which makes it easy to discard this relatively rare occurrence.

7.6 Monitoring experience with the laser and source systems

As mentioned near the beginning of this chapter, the capability to monitor changes in response to particles at the level of 1% is a powerful handle on the overall performance of the calorimeter and its evolution in time. In this section the experience gained on prototype modules and an Module 0 with the laser and movable source systems is presented; the results show that this performance level has been achieved.

7.6.1 Performance achieved with the laser system

The limit on the monitoring accuracy of the laser system is set by the error on the reference signal given by the alpha source on the monitoring phototubes. The PD response to the alpha source has been monitored over the entire test beam periods.

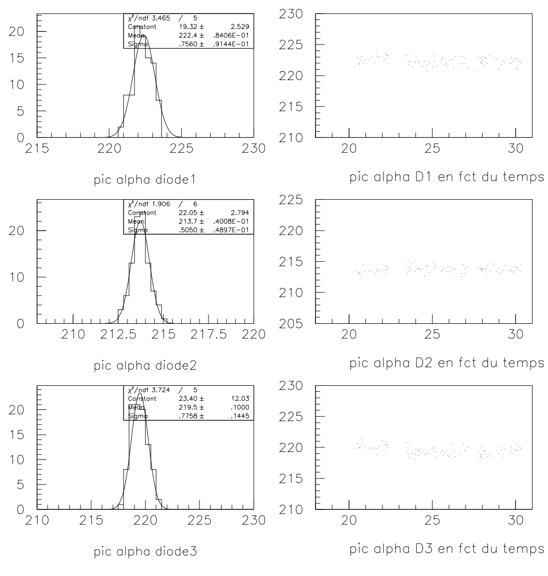

Figure 7-28 The alpha peak measurements over a period of 10 days.

Their dispersion is a convolution of the long term drift of the internal monitor and the intrinsic resolution of photodiodes in measuring the alpha particles.

Figure 7-28 shows the dispersion of the alpha peak measurements over a period of 10 days and indicates than the drift of the photodiode monitor over this period is very small. Temperature stabilization of the laser box is an important factor in obtaining this stability.

The rms spread of the three photodiode alpha signal distributions is about 0.3%. This accuracy can be improved by a factor of $\sqrt{3}$ combining the results of the three photodiodes.

Next, one may check whether a comparable level of accuracy is maintained in the relative PMT gain determination (we recall than the goal was set to an accuracy of 0.5%). There are two independent ways to evaluate the accuracy of the relative gain.

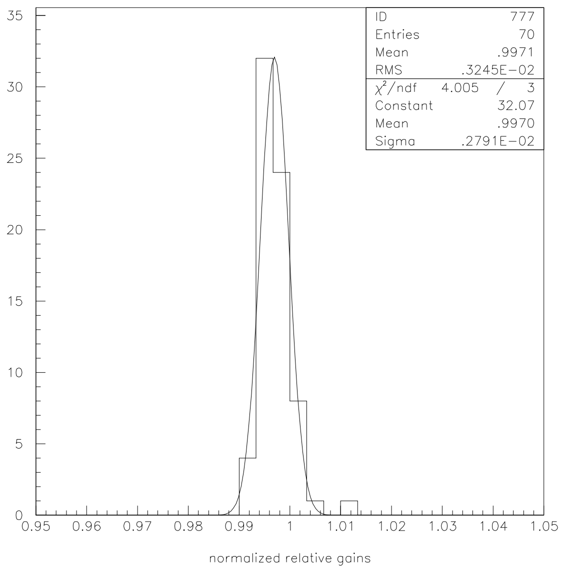

Figure 7-29 Normalised relative gains of 10 PMTs measured 8 times within one hour.

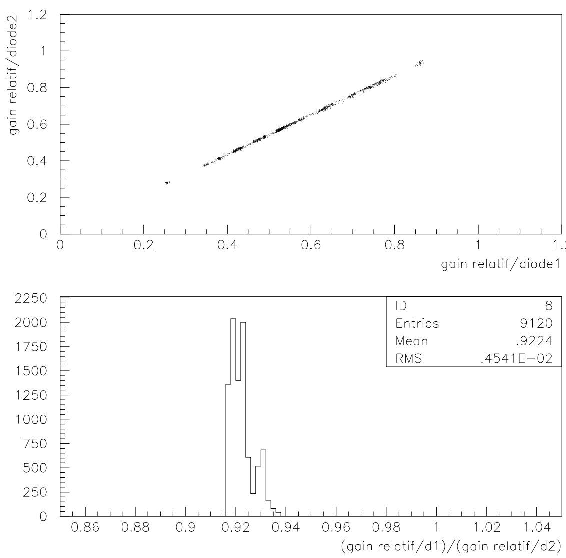

Figure 7-30 Correlation between relative gains obtained from two different photodiodes.

The first one consists in making several relative gain measurements of several PMTs in a short time (e.g. one hour). The spread of the results gives the accuracy, assuming there is no gain drift in such a short time.

Figure 7-29 shows the histogram of the normalized relative gains of ten PMTs measured 8 times within an hour. The dispersion indicates an accuracy of relative gain measurement of 0.32% in RMS and 0.28% in sigma.

The second way to calculate the precision on the relative gains to compare the values obtained calibrating the laser pulse with one photodiode with that obtained using an another photodiode (since there are 3 photodiodes, 3 comparisons can be made): Figure 7-30 shows the correlation between the relative gains obtained with PD1 and PD2. The comparison was made with the 40 PMTs of the central module over 228 runs. The slope of the correlation diagram is not 1, because the two photodiodes are see different fractions of the laser light pulses. The distribution of the ratios of the relative gains using PD1 and PD2 has an rms of 0.5%.

One may conclude than the goal of 0.5% accuracy in monitoring relative gains has been reached with the current system.

Stability of PMT gain

During each particle run, about 5% of the events are laser-generated. This allows to continuously monitor the PMTs, and to correct offline the PMT response to particles. Figure 7-31 shows the evolution during a test beam period of the relative gains (normalized by their mean value for each PMT) of the central module PMTs. In the upper diagram, the numbers of the PMTs are on the axis numbered 80 to 120, the dates (in days) are on the second horizontal axis and the relative gains are on the vertical axis. The distribution of the normalized relative gains (bottom plot in Figure 7-31) has an *rms* of 1.3%, which is a measure of the remarkable stability of the relative gain of the prototype calorimeter PMTs.

Because of the observed stability, offline correction of the PMT response for the measured gain drifts does not significantly improve the resolution of the calorimeter. Gain non-linearities have been measured observing the deviations from a straight line of the response of PMTs plotted against the PD response. At the upper end of the laser dynamic range, set for the prototype modules to correspond to 300 GeV particles depositing all their energy in one cell, deviations from linearity of about 1% are observed.

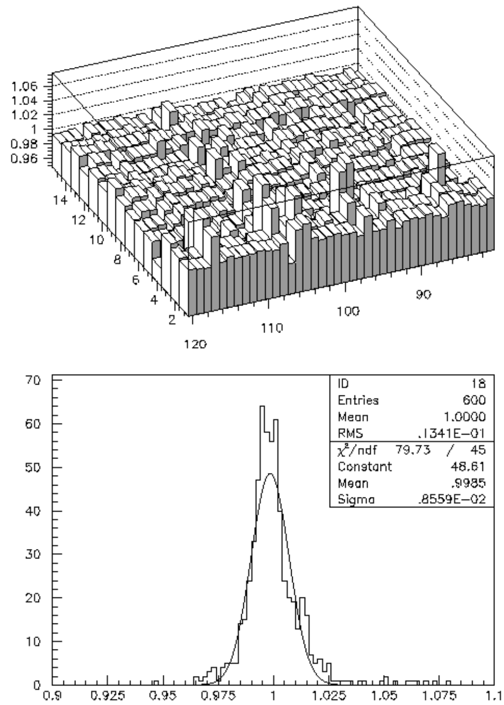

Figure 7-31 Evolution of the relative gains over a test-beam period.

Other results obtained in the test beam

The laser system is used in debugging each new setup (e.g. disconnected or miscabled channels). The laser system also allows to pinpoint crosstalk phenomena to the ADC modules.

A more fundamental application is the determination of the number of photoelectrons/GeV of the calorimeter. This is done by calculating the number of photoelectrons associated to laser pulses from the spread of the PMT signal. This gives a number of photoelectrons per pC measured in the ADCs, from which one obtains the photoelectrons/GeV dividing by the charge-to-energy conversion scale of the calorimeter (pC/GeV), measured with an electron beam. These calculations have provided useful confirmations of the measurements of photoelectron statistics done with muons (Chapter 3).

7.6.2 Performance achieved with the source system

First, a measurement of the intrinsic error affecting the measurement of the cell response of a cell is shown.

The response of each PMT to a ^{137}Cs source scan is summarized in one number, the average current A. For each PMT n numbers A_n are measured, corresponding to the n rows of tiles which constitute the calorimeter cell read out by that PMT. These numbers typically differ by a few percents because of the different light yields from different tile-fibre combinations, as discussed in chapter 5. However by taking two average responses for different tile rows read out by the same PMT, A_l and A_m, and two source scans taken at different times t_1 and t_2, one can form the double ratio:

$$R = \frac{A_1(t_1)/A_1(t_2)}{A_m(t_1)/A_m(t_2)}$$

in which the differences in source response, due to PMT gain drift from t_1 to t_2 and to tile-fibre yields, will cancel. The rms of the distribution of the double ratios will be $\sqrt{4}$ times the error of the individual measurement. Two such distributions are given in Figure 7-32; these results were obtained from scans made on Module 0 in September 1996. From these distributions the error on cell scans is found to be about 0.7%.

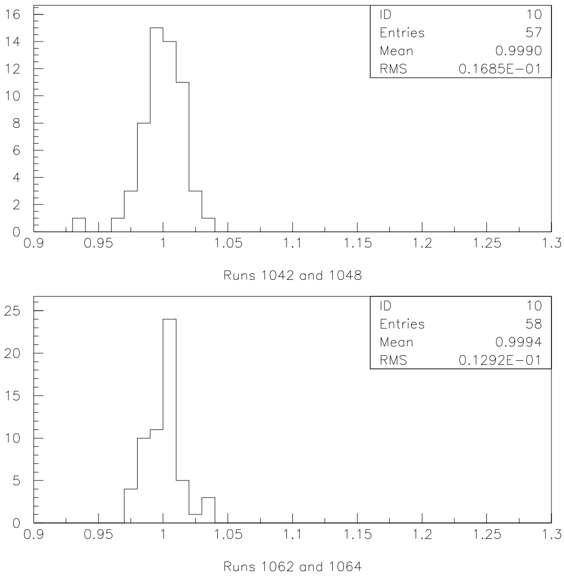

Figure 7-32 Two distributions of double ratios defined as in text from Module 0 source measurements.

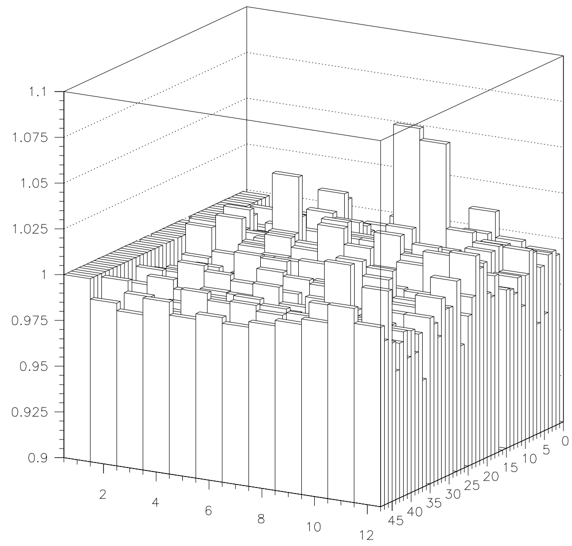

Figure 7-33 Source response of Module 0 PMTs over the Sept. 1996 test run to the first measurement for each PMT.Responses are normalized to the first measurement for each PMT.

During Module 0 test beam runs, source scans were taken at one or 2 day intervals; in Figure 7-33 the results of source scans of Module 0 (taken with the hydraulic system) over the September 1996 run are given. This gives a qualitative picture of the stability of the calorimeter response. To obtain a more quantitative assessment, the rms variation of the response for the Module 0 PMTs was calculated, normalizing the values of A_n for each of the n PMTs to the first measurement. The distribution is given in Figure 7-34. The typical variation of the response is 0.4% to 1.3%, which is about what is obtained for the intrinsic error of the measurement and shows that the response of the calorimeter - including drift of the PMTs - is stable to this level.

Information on the stability of the Module 0 response to the source over longer times is available from measurements made on the prototype modules (with the wire-driven system) in April and September 1996. Over this period of about 5 months the modules were taken out of the test beam, put into storage and then reinstalled on the test beam. The nominal HVs had been set to equalize the response to an rms spread of about 3% in 1995; then the response was measured in April 1996 and in September 1996.The plots of Figure 7-35 show the response at the earlier and later times for the 167 PMTs measured in September 1996. The ratio of the two measurements has an rms value of 4%. This may be taken as a worse case of response stability, considering that the movements of the modules may have affected the tile-fibre couplings, and that the precision of monitoring of the HV is not well known in this case.

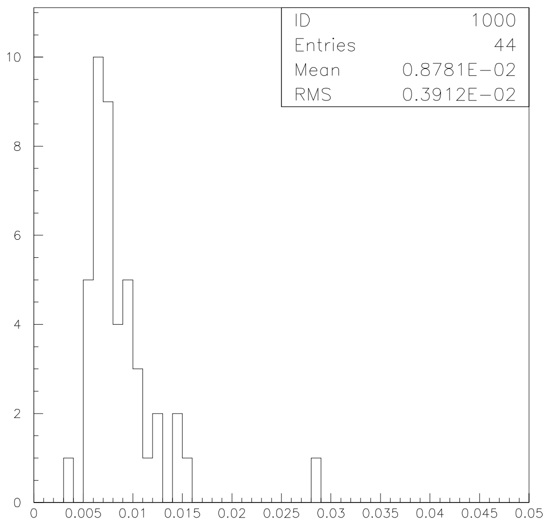

Figure 7-34 Variation of the response of the Module 0 PMTs during the Sept.1996 run: rms variation for all PMTs.

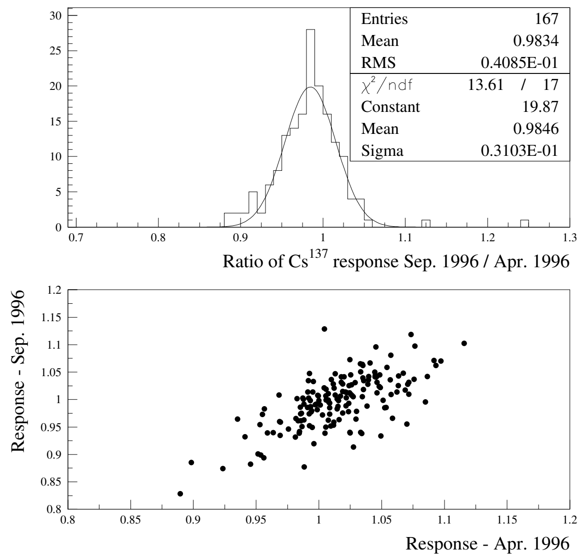

Figure 7-35 Response of 167 PMTs at the beginning and the end of the Sept. 96 test beam period.

7.6.3 Simultaneous monitoring with source and laser

For constant light response of the calorimeter the laser and source measurements must be strongly correlated. During normal test beam runs this correlation cannot be easily established because as shown above the PMT response and the calorimeter response are stable at the level of the precision of the two monitoring systems.

A special test of the correlation of the two was made by changing the HV on the PMTs in order to simultaneously change the signal seen by both systems. In Figure 7-36 the results of this test are shown. The 4 clusters of points are obtained measuring the response to the two systems of 10 PMTs, which were run at their nominal HVs and at 3 different sets of HV values (HV_{nom}-30V, HV_{nom}-15V, HV_{nom}, HV_{nom}+15V). The excellent correlation is obvious; the rms deviation from the linear regression is 0.6% and measures the combined error of the two systems.

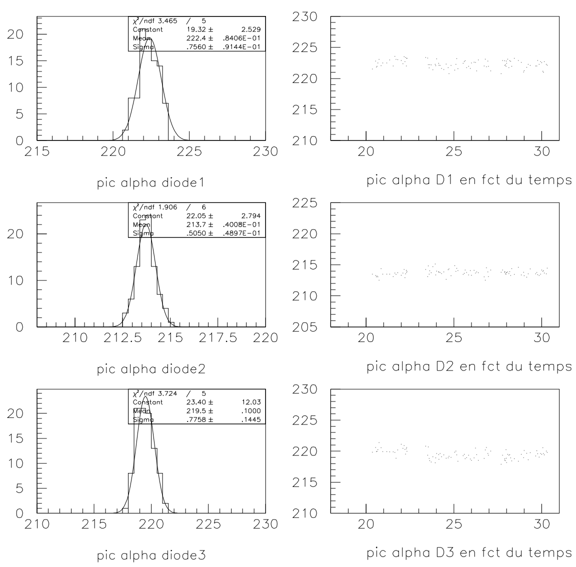

Figure 7-36 Correlation between source and laser measurements.

7.7 System intercalibration and the overall energy scale

7.7.1 Requirements on cell intercalibration

It is well known that cell intercalibration errors in calorimeters contribute to the constant term in the energy resolution. The effect of miscalibration errors for the Tile Calorimeter has been investigated by using either real data or simulated hadronic showers at different energies N-69, and smearing the signals of each of the cells according to a Gaussian distribution with σ_{mis} representing the rms miscalibration of the cells. In these simulations, a large number of "calorimeters" is simulated, each with one set of "miscalibration" parameters for the cells that compose it, which is the same for all energies but varies from one "calorimeter" to an other. The response of this set of calorimeters represents the Tile Calorimeter in ATLAS.

Smearing real data or Montecarlo-generated showers gives the same result:

- The resolution σ/E of each "calorimeter" is very robust, and begins deteriorating only for $\sigma_{mis} > 20\%$.
- However the mean value of the total energy measured in each miscalibrated "calorimeter" does vary. The rms value of this variation is about $\sigma_{mean}/E_{mean} = 0.3 \cdot \sigma_{mis}$ and independent on energy. This result is easy to derive from simple statistical arguments using as input the partition of energy of a hadronic shower between a few cells. It is a constant-term-type dependence (because it is independent of energy) and contributes in quadrates to the constant term of the calorimeter.

The conclusion of these studies is that a miscalibration σ_{mis} produces a contribution to the constant term of the resolution of $0.3\sigma_{mis}$ to the energy measured in the Tile Calorimeter. This is in turn roughly 1/2 of the energy of a jet.

In summary, a miscalibration with σ_{mis}= 5% would contribute 1.5% in quadrature to the constant term of the energy resolution for isolated hadrons that do not interact in the electromagnetic calorimeter and less than 1% for jets.

7.7.2 Expected precision of the overall cell intercalibration in ATLAS

As discussed above, the laser/source intercalibration systems allow to equalize and then monitor the response of each cell with an error of 1%. However summing over calorimeter cells to obtain jet energies will introduce an other error, namely the variation in light output from tiles of different geometries which are read out by the same PMT. The Tile Calorimeter does not provide the information of where the energy is deposited within a cell, therefore this variation is effectively an additional cell intercalibration error. Montecarlo studies of this effect show that the degradation of the energy resolution is almost imperceptible; this is in accord with the more general study discussed in the previous subsection.

One may include the effect of this additional error by giving an estimate of 2% for the effective intercalibration error of the Tile Calorimeter. As shown above, this will have a negligible effect on the overall resolution of energy measurements.

7.7.3 Strategy for setting and maintaining the overall energy scale

The conversion factor linking the calorimeter signal to single hadron energies must be found in a test beam, by measuring the response of barrel and extended barrel modules over the full η range. The measurements should be performed behind electromagnetic calorimeter modules, including all materials between the two calorimeters as they will be in ATLAS as realistically as it is possible.

Measuring and recording the source response cell by cell of all calorimeter modules of the barrel and extended barrel will give the information necessary to:

- correct in time the energy scale calibration of each calorimeter module that has been exposed to the test beam,
- "transport" to all modules the mean energy scale calibration of the modules exposed to the test beam.

Note that differences from module to module (or within modules) due to local or systematic changes in the sampling fraction, scintillator light yield, etc. will be taken out by means of the source calibration. More specifically, if two modules give different energy-to-charge conversion ratios, normalizing this ratio by the source response is expected to reduce the error on the one energy scale of the two modules to the level of the errors of the two measurements, because particles and source sample in virtually identical manners the calorimeter cells.

It would be very desirable (budget constraints allowing) to build a few extra Tile Calorimeter modules, identical to those installed in ATLAS, to periodically expose them to test beams and record their response to the laser/source monitoring system. This would allow to check the behaviour in time of the calorimeter outside the LHC radiation field and to gain experience in maintaining the energy scale calibration in a more accessible environment.

7.7.4 Use of the energy scale calibration in ATLAS

This chapter ends with a few obvious points about the problems with using a test-beam based energy calibration in ATLAS.

No calorimeter is uniform over the solid angle; the Tile Calorimeter is highly uniform in azimuth, but not in pseudorapidity. The gaps in coverage and the variation of non-detecting materials in η will produce much larger variations of the jet energy calibration scale than the instrumental calibration errors examined in this chapter. The conclusion -- as could have been anticipated -- is that well-understood physics processes must be used to obtain the physics energy calibration over the full η range.

Nonetheless an accurate "internal" knowledge of the Tile Calorimeter energy calibration scale will no doubt be useful as a starting point, and to extrapolate to the "crack" regions the measurements in the more uniform regions of the calorimeter.

7.8 Production plan and schedule

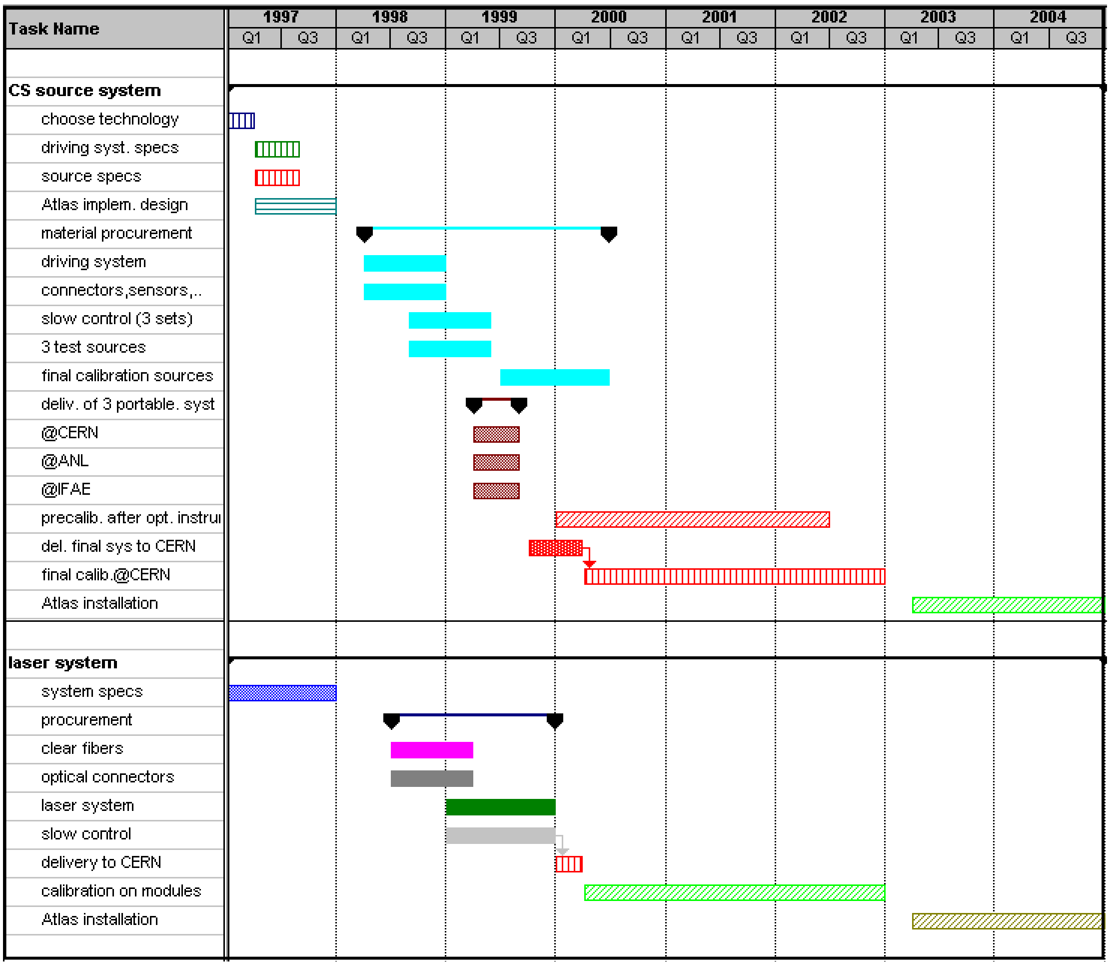

Figure 7-37 Schedule for the production and installation of the laser and the ^{137}Cs calibration system.

8 Installation, commissioning, running, access and repair

8.1 Installation

The installation of one complete barrel and two complete extended barrels in the ATLAS pit will be described in this section. The installation operation is scheduled to start at the beginning of calendar year 2003. The scenario for these operations is schematically illustrated in Figure 8-1.

The overall installation is envisioned as a sequential three-steps operation. In the first sequence of events, one extended barrel cylinder (C) will be installed on one side of the cavern (small shaft side). Following this completion on the opposite side of the cavern (main access shaft) the barrel cylinder will be assembled, followed by the installation of the second extended barrel cylinder (A).

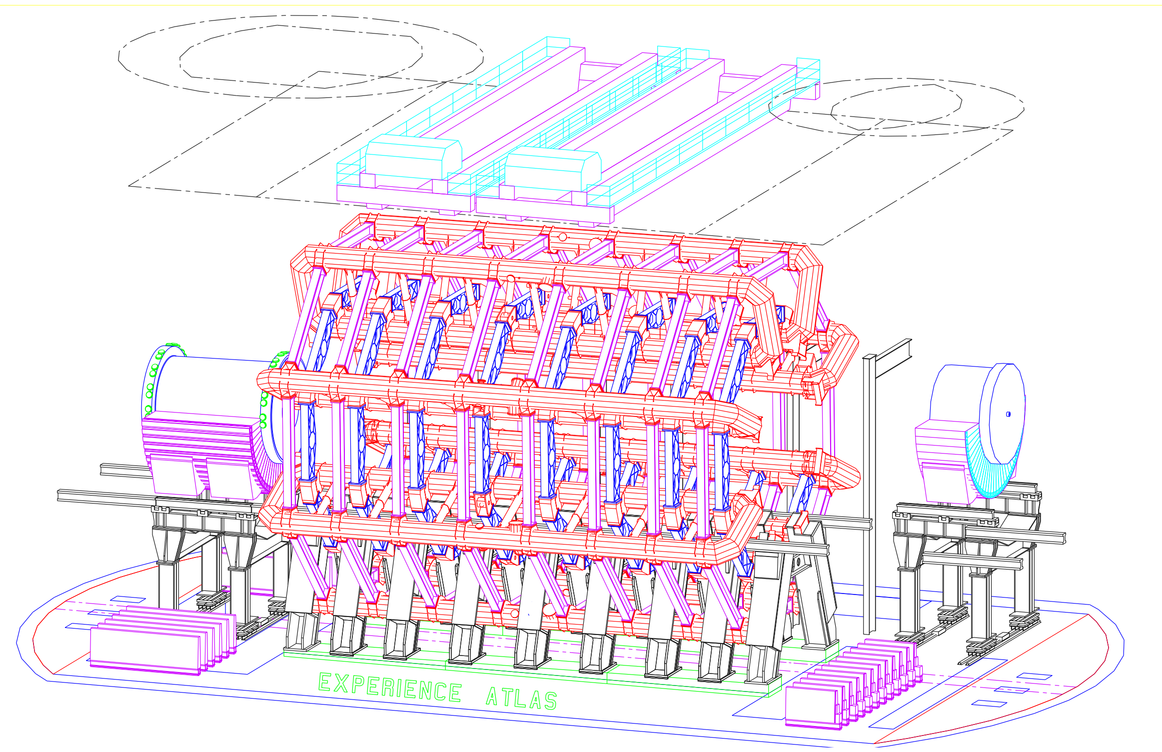

Figure 8-1 View of the ATLAS detector during assembly. Individual modules are store on the side ready to be mounted in place. One extended barrel is shown below the small shaft and the barrel below the large shaft.

The exact sequence for the fabrication of each cylinder is described in detail in the mechanical section (Figure 8-1). In general, the main idea is to first lower into the pit a preassembled lower part which includes the support saddle in one piece. The remaining modules will then be installed one by one on this lower support structure. This installation procedure introduces some requirements on the large surface crane and on the logistics of space and cranes in the cavern itself.

The heaviest object to be lowered down from the surface weights at the most 260 tons, including the support structure. The speed and precision of the crane should allow direct and final placement of each part of the detector. For final positioning, a speed approaching 10^{-3} of the normal speed (3-4 mm/minute) with a placement precision of the order of ±1 mm will be adequate.

For most of the operations where modules are individually installed, the small cranes inside the cavern are sufficient. Furthermore, a temporary storage space near the mounting area to hold about 12 modules should be allocated for the staging of modules ready to be assembled. The temporary storage area can hold modules in their six o'clock position. The most efficient way to load the staging area is to move the cylinder assembly to one side, and to keep the readied modules just inside the area directly accessible to the surface crane. Typically, two-three sub-modules at a time will be lowered down from the surface. This implies that at least for a one eight-hour period per week the surface crane will be needed for this operation. The speed and precision of the small crane should be the same as for the large one, but with an additional requirement on the lateral positioning precision of ±1 mm. It has been verified that the vertical clearance below the hook of the crane will be of the order of nine m in the worse case which is sufficient for our manipulations and installation. After completion of the assembly of the lower half of the calorimeter cylinder, the Liquid Argon Calorimeter cryostats will be lowered down and positioned. This operation is very complex and may add further requirements to achieve the positioning precision.

The assembly of the calorimeter systems will take typically four months for each of the end-caps, and five months for the barrel. The first extended barrel (C) should be fully connected in november 2003, the last extended barrel (A) by may 2004. Once fully connected each element will be tested and commissioned. The delivery dates (starting dates of installation in the ATLAS cavern) for the Tile Calorimeter have been fixed by the technical coordination of ATLAS as the following dates:

Table 8-1 Delivery milestones for the Tile Calorimeter.

1 / Jan / 2003	Extended Barrel C
1 / May/2003	Barrel
3 / Oct / 2003	Extended Barrel A

8.2 Final connections and commissioning

The read-out electronics of the Tile Calorimeter is fully integrated inside the girder structure. A minimal set of cables and services for each module is foreseen. For the barrel these cables and services will run on the outer girder surface up to the center of the barrel, and will then run radially out through the muon chamber system. The extended barrels' cables and services will provide a "loop" making possible axial movement of the endcaps of about 12 m.

The Tile Calorimeter services include the water cooling system and the calibration source driving system. The garage of the source system is placed on the ground floor inside the cavern. Particular care will be taken for this installation in order to avoid leaks in the system. Tests of the source driving mechanism will require a few shifts where the source will run out of the garage position and will circulate in and out of the calorimeters. For radiation safety reasons, access to the calorimeter region will be restricted.

After all connections are complete, the full movement of the extended barrels will be tested in order to make sure all connections - in particular the source lines - remain securely fastened. All cables and pipes should be pulled before the start of the calorimeter assembly.

Commissioning the detectors will mainly involve the source calibration of all the modules. The various electronics read-out systems for charge injection, laser calibration and physics data will have been already tested and certified at the surface for each module. One of eight modules will have been calibrated in the test beam and thus for each of the modules the source system will be used to cross calibrate. We foresee all functionalities of the read-out to be tested and operational shortly after the cables are connected and the electronics in the counting room operational. Cable connections will be continuously verified during the installation procedure. This can be done firing patterns of injected charges module by module with a temporary data acquisition system contained in a rack in the counting room. HV and direct tests of the entire line will be done once the entire calorimeter structure has been light tight. A complete and powerful check of the system is then possible pulsing the laser system and moving the radioactive source through the entire calorimeter.

8.3 Access and repairs

Four types of access are foreseen for the ATLAS calorimeters:

1. A short access to the USA hall to allow inspection and repairs to the racks and electronics installed in the cavern. In our case this access will be to the low voltage power supplies and to the source garage. This access mode should take only a few hours of detector interruption, depending on the magnetic field intervention.
2. To allow access to the extended barrel drawers' electronics. Here, first one of the end-cap toroids has to be retracted by a few meters and then the shielding disk just behind the calorimeters retracted. Two meters of displacement are sufficient to extract one drawer at a time to eventually exchange one entire PMT block assembly. The operation is not trivial with removal of the 200 kg shielding block mounted on the outer module face. In a next step the connector patch panel has to be removed which then will give access to the inside of the girder. All these operations require the intervention of at least two people and the availability of dedicated tools to access the drawer patch panel and to manipulate the drawer weight of about one hundred kg. Such access will require at least two weeks of shutdown.
3. To allow access to the barrel drawers' electronics, which is an access similar to the one of the extended barrels. In this case the extended barrel has to be retracted from the barrel by 4 meters. Access to the barrel region is possible via some small passage through the muon chamber. Here too some dedicated tooling is needed to manipulate the steel shielding and the drawer itself. All that tooling must be brought inside the gap region. Such access requires also at least two weeks of shutdown.
4. During the long ATLAS shutdown all three types of interventions are of course possible. End- cap toroids and extended barrels will be removed for full access to the inside of the detector. This scenario involves longer and detailed planned interventions over time scales of a few months.

Even if theoretically possible, a scenario of accessing the inside of the Tile detector is not foreseen. This is valid both for the inner side of the Tile Calorimeter and also for the outside surface of the cryostats. An operation of this kind would require the dismantling of half of the Tile modules. Such a major operation would require a very long shutdown. The ATLAS detector would be then totally non operational as all internal and part of the external elements (including muon chambers) would have to be dismantled. A more detailed scenario for that particular case can be found in the Liquid Argon Calorimeter TDR.

Besides the drawer electronics, the only part of the Tile detector which could be replaced is the layers of scintillators in the gap region and the optics of the ITC modules. In particular for the case of the scintillator layers, the level of radiation damage may require replacement after a few years of LHC operation. These layers can be replaced without removing anything but the scintillators. The read-out fibres will be reconnected using an optical connector external to the ITC module. A few weeks is sufficient for the entire operation.

The overall scenario of accessing the interior of the ATLAS detector with equipment, persons, the location of gangways and the respect of safety rules during the access will be treated in an other Volume of the ATLAS TDR's.

8.4 Preassembly and storage

The way this calorimeter is constructed will require large assembled and tested modules to be stored at CERN, ready for the final installation or preassembly. Space must be organized for 65 barrel modules and 130 extended barrels. Storage will be done in the 6 o'clock position, with enough space around to allow minimal inspection, checks and clearance to install the necessary manipulation tooling. This area requires a 30 tons crane, with an hook height of at least 6 m to allow loading on a truck.Temperature and humidity should be controlled. About 1200 m^2 of storage area is required starting in early 1999.

In order to certify the assembly procedure, at least the barrel and one extended barrel will be fully preassembled in a surface building. The lower part of this assembly will then be moved directly down into the ATLAS cavern. This operation of preassembly requires a large hall at CERN, capable of containing the barrel cylinder and equipped with a crane of at least 80 ton capacity. The height of the crane is also very critical: the upper cylinder assembly requires at least 15 m of crane hook height for the insertion of the last few modules. The crane speed and precision specifications are the same as for the one used in the ATLAS pit.

8.5 Installation schedule

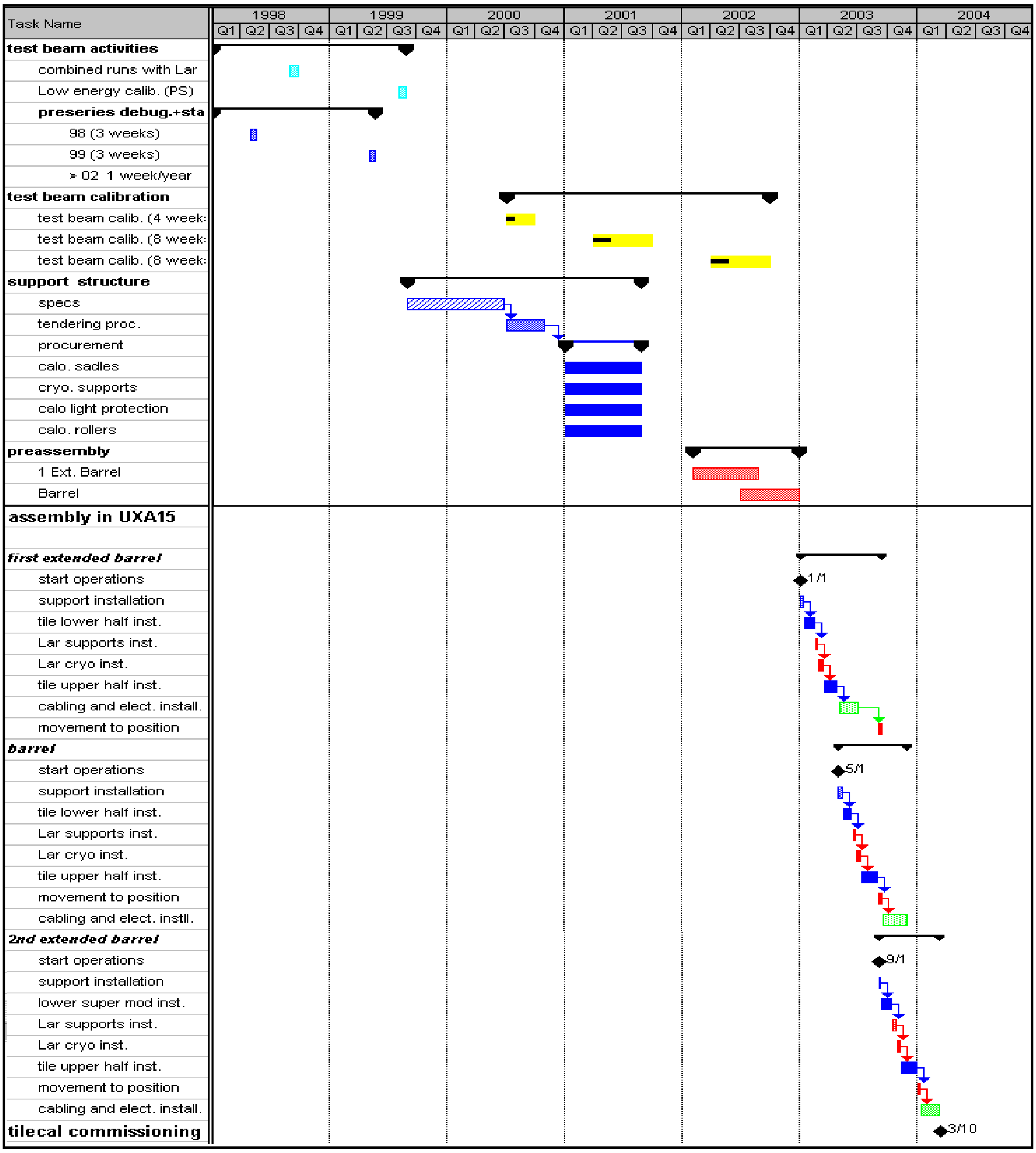

Figure 8-2 Installation, preassembly and test beam schedule for the Tile Calorimeter.

9 Safety

Most of the risks present in other sub-detectors, such as the leakage of cryogenic fluids or of toxic or flammable gases, do not exist in the Tile Calorimeter. The safety analysis is then essentially limited in our case to three subjects: the safety of the mechanical structures, electrical power and fire risks, and the calibration sources.

9.1 Mechanical safety

The Tile Calorimeter is composed of a large cylindrical structure divided into 64 azimuthal modules: each module is composed of the assembly of 19 sub-modules in the barrel, and 10 in the extended barrels glued together using epoxy. At their outer radius, the sub-modules are bolted to a large, sturdy girder which provides all the necessary mechanical rigidity to the whole module. At the inner radius, the sub-modules are welded to an inner steel plate.

The girder has a large cross section because it has to fulfil three separate functions:

- it provides the necessary rigidity to the module,
- the drawers for the electronics (see below) are housed inside it,
- it provides the return path for the solenoid magnetic fields and shields the electronics from the stray field of the toroid magnet.

The rigidity of the girder allows the module to be easily transported and assembled. The static forces acting on the modules have been investigated by considering the two typical periods in the lifetime of the detector: the normal operation and the assembly and dismantling period.

9.1.1 Static forces on the assembled detector

Once assembled, the Tile Calorimeter looks as a self-sustaining cylinder where the contacts (and the forces) between the modules are concentrated at the level of the girders and of the front part of the modules. Various situations have been simulated using different combinations of support structures and are detailed in Chapter 4. Resulting values of stresses are based on the 2D static analysis and on the 3D Finite Element method. It has to be emphasized that the equilibrium equations of the static analysis are rather simple and easy to check. Moreover, some mechanical tests for the sub-modules are in progress. In all considered cases, the finite element computations have confirmed that the resulting forces are compatible with the selected materials. In particular the stresses are always less than 130 MPa, which represents 60% of the allowable stress in steel structures. The detector is supported by equally spaced feet sitting on the rails and bolted to the girders. This last feature will also mitigate the effects of earthquakes with horizontal components.

During ATLAS operation the magnetic fields of the toroid and the solenoid will exert forcesin the radial and axial directions. Any misalignment can exacerbate gravitational and magnetic forces, thus the supports of the detector need to accommodate these forces. Magnetic field calculations were performed and reported in Section 4.9. A total radial force on the extended barrel of 6 tons, and an inward axial force of five tons are negligible compared to the support structure requirements of carrying loads up to 15% of the total detector weight.

9.1.2 Static forces during the assembly

The Tile Calorimeter will be assembled using preassembly supermodules which will be superposed starting from the bottom of the detector. After a pause to permit the installation of the Liquid Argon Calorimeter, the operation will continue until the last module will be positioned at the top of the cylinder. It is evident that at different stages during the assembly phase the distribution and the magnitude of the forces acting on the various modules will be different from that described in Section 4.6.3. The more critical situation where the forces are extreme is when all the modules are assembled, except for the last one on the top of the detector. This situation has been simulated using finite element calculations discussed in detail in Section 4.6 with the results such that the stresses are always less than 130 MPa, a value totally compatible with the used steels.

9.2 Power and electronics

All the Tile Calorimeter electronics are grouped inside the drawers which are housed in the module's girders. The thickness of the girder walls provides an excellent insulation between drawers belonging to different modules: this feature should prevent the propagation of fire. The drawers are assembled in blocks of two, called the super-drawer.

Two superdrawers are housed in the barrel girder, and one in each extended barrel girder. There will be bulkheads on either side of the 64 barrel modules, and bulkheads on one side of each of the 128 extended barrel modules. Each super-drawer is connected to the outside world using only ten cables: three power cables (Low and High Voltages) and six optical fibres. The high voltage will be brought into an SHV connector at about 700 V with up to 20 mA of available current. The high voltage will be locally regulated on each base within the drawers. The low voltage will most likely be brought in on multiconductor cables to a bayonet-type connector on the bulkhead. The voltages needed for the electronics inside the drawers will be ± 5 , and +9 Volts for the read-out part, ± 5 Volts for the digital part and +5, ± 15 Volts for the HV, with respective currents of about 10 A for the first and negligible for the others. Cables into the detector will be halogen free, and the use of halogen free materials inside the drawer will be maximised. In case of necessity, the drawers can be extracted from the girder using appropriate tools. In this way, maintenance and repairing operations can be carried out in more comfortable and safe conditions, outside the detector.

9.2.1 Electronics heating and fire risks

The electronics produce a certain quantity of heat (about 200 W per superdrawer) which must be removed in order to keep the temperature at about 25^{o} C. To accomplish this purpose, cooling pipes will be installed inside the drawers incorporating a cooling system which will be of the leakless type. The coolant's working pressure will be below atmospheric pressure thus in case of failure of a cooling pipe, air will be sucked into the coolant supply and return, preventing coolant leakage. Smoke detectors and temperature probes will continuously monitor the conditions inside the drawers: their outputs will produce interlocks and information will be sent to the slow control alarm system. Each superdrawer will have fuses at the level of the LV's to minimize excessive current draw in the event of component failure.

9.3 Calibration sources

Two external calibration systems are used in the Tile Calorimeter, both requiring safety actions.

9.3.1 Radioactive calibration source

Three sources each of 5 mCi ^{137}Cs (emitting γ's of 662 keV) will be used. Each source is housed in a miniature container, travelling axially through the detector inside appropriate pipes. When not in operation, the sources are housed outside the detector, in shielded areas.

Appropriate interlocks and alarms will guarantee that, when opening the detector, the sources are in their “garage” position. During source calibration runs, again appropriate alarms and warnings will exist to signal the presence of the ^{137}Cs source.

9.3.2 Laser calibration

A laser source of 2 W (classified in Cat 4 as powerful source) is housed in the electronics room: the light is guided into the detector by a bundle of optical fibres. The laser installation will comply with the CERN-TIS rules for the use of Lasers. In particular, reliable interlocks will be provided which will switch off the laser at the opening of the electronics drawers.

The integrity of the optical fibres bundle will be also continuously checked by a special fibre which brings back the emitted light after a complete loop. Finally, appropriate labels and emergency stops will be positioned in the critical points.

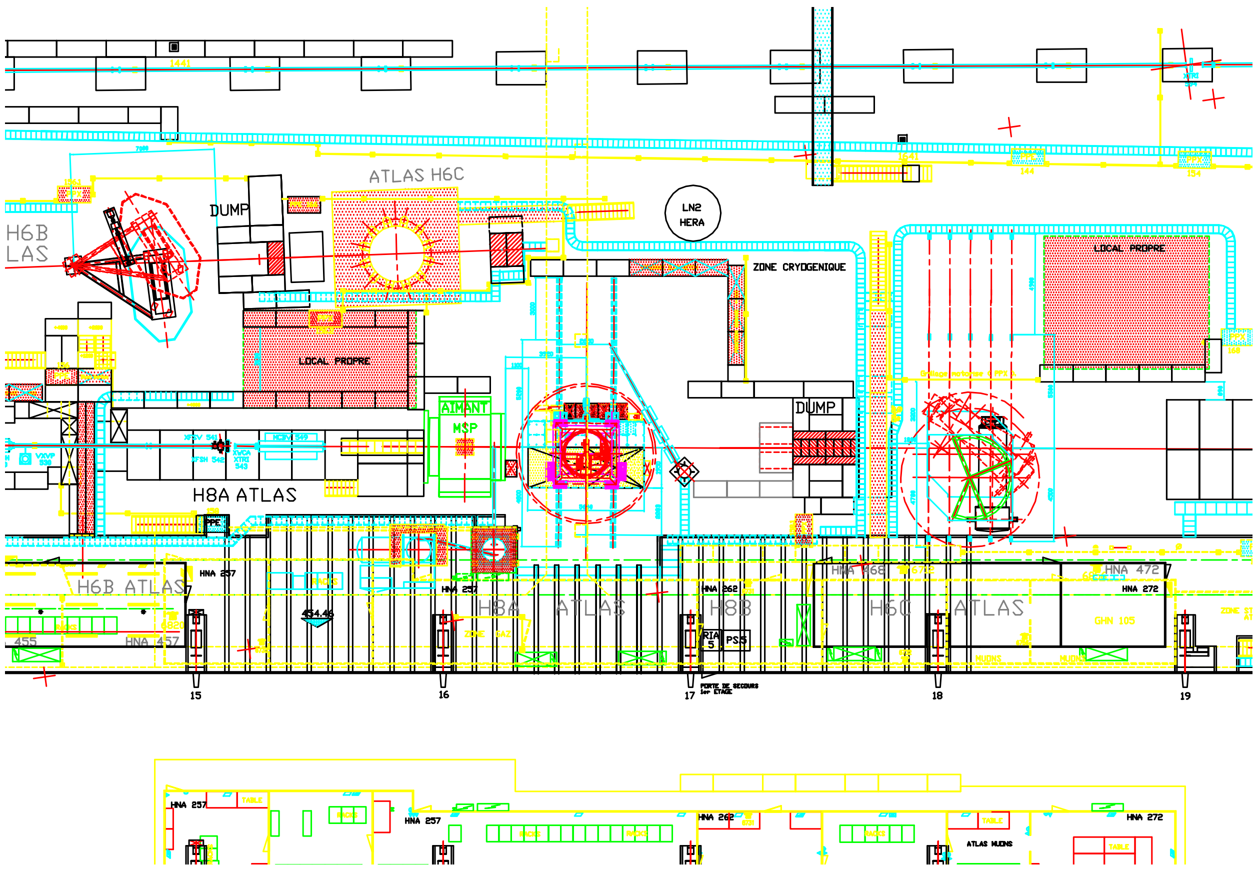

Figure 11-i A schematic view of the test beam installation in H8 area for the Tile Calorimeter standalone runs.

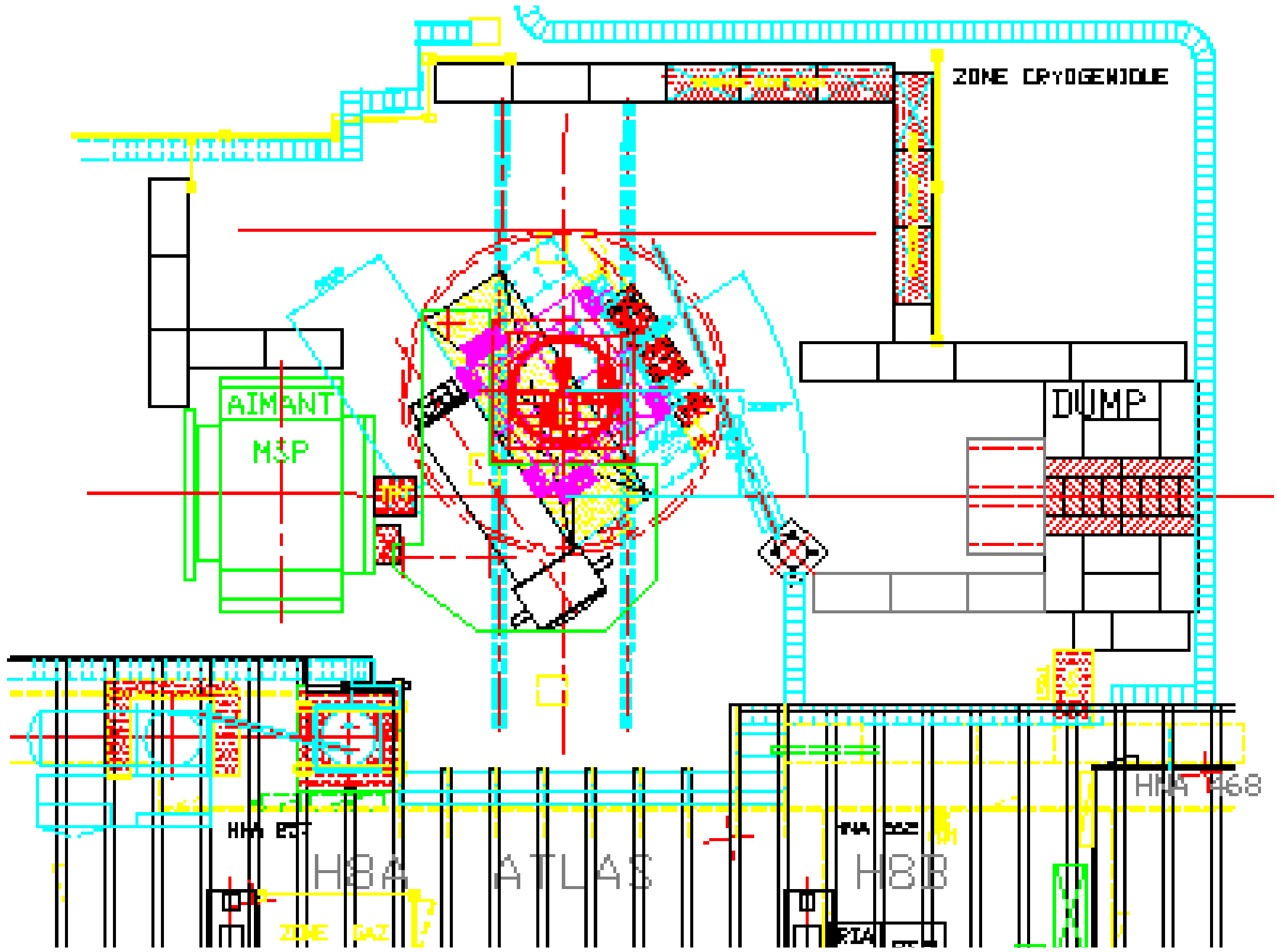

Figure 11-ii A schematic view of the test beam installation for the combined runs.

10 Tile Calorimeter test beam program

10.1 Objectives

The Tile Calorimeter community plans an exhaustive program of calibration and tests of both the production and the pre-series calorimeter modules in a beam line at CERN. The program is driven mainly by the need to ascertain the response of our modules over a variety of tests such as the exposure to the largest possible energy scale for single particles, the realisation of combined runs with the e.m. calorimeter in front etc., such that useful knowledge can be transported in the actual detector environment. Furthermore, a technology choice in front-end electronics, read-out and triggering will have a deep impact on the performance of ATLAS, and these devices need to be fully understood, including test of possible upgrades in the electronics. Included in our goals to understand the combined calorimeters, the response of the Tile Calorimeter to low energy pions is included.

Therefore we can summarize our objectives as follows:

- Calibration of a fraction of the production modules,
- Monitoring the stability of the optics and electronics, and
- Understanding linearity and low energy response of the combined calorimeter system.

10.1.1 Calibration

Based on the experiences of other groups such as CDF and ZEUS, we expect the inter calibration of the calorimeter modules will be determined by the ^{137}Cs source current. CDF[A.7] has found that setting of the high voltage with a source along the shower maximum layer allowed EMC module intercalibration to better than 5%. ZEUS [A.21], although using a source which was the intrinsic uranium noise, found that the intercalibration between modules was around 1% if all towers were set to the same uranium noise current. Indeed, in order to check these results a subset of the calorimeter modules were calibrated in a test beam; ZEUS calibrated 17% while CDF cross-calibrated 100% of their modules.

As seen in Chapter 3, we can expect the Tile Calorimeter to globally track the muon response to about 5-6%, while pion response has been shown to be about 2% when calibrating pairs of PMTs. Calculations from the SDC project [A.22] have shown that if the tower-to-tower calibration is good to within 5%, then the contribution to the constant term of the resolution to single hadrons due to the calibration uncertainty is about 2% for a hadron calorimeter (adding it in quadrature). Our work has shown that, for jets, the situation is better: a 10% cell-to-cell miscalibration results in a 2% contribution to the constant term. Miscalibration effects for the electromagnetic calorimeter are, however, far greater. N-69.

We have confidence that the calorimeters will perform as expected, but still need to verify the tracking of the source current to calorimeter performance with sufficient statistics to allow any uncertainties. Furthermore, a good quality assurance plan will require a complete test of some subset of the production run. We therefore propose to completely monitor the performance of about 12% of our production modules, both barrel and extended barrel. As will be shown later, this program will fit nicely into the schedule through the year 2002.

10.1.2 Stability

We expect that the Tile Calorimeter will exhibit only the standard ageing of about 1-3% per year as seen in other calorimeters such as UA2 or CDF. Critical optical components of the Tile Calorimeter which may perform in an unexpected way are the injection moulded scintillators and the optical fibres which couple to the tiles. Using an increased temperature test to simulate long term aging, the scintillators have shown a small degree of ageing. Tests on the bending of fibres also show that the stability is good when fibres are bent in a radius greater than some critical radius. We therefore expect that no serious problems will arise in the future. However, experience in the RD34 program and with Module 0 has limited statistics in measuring source currents under stable conditions, and it is difficult to say what if any changes have occurred during the periods. Therefoere, we will continue the monitoring of barrel Module 0 through the year 2002 to try to understand the long-term stability of the design. Besides source and laser scans, the response to pions and muons in a test beam will complete the measurements.

Electronics will evolve and Module 0 in the testbeam will be a natural environment for the evaluation of upgrades to the calorimeter system. Evaluation of noise in components such as shapers and pipelines can be determined in experimentally harsh environments and compared to bench measurements.

10.1.3 Combined Tile and Liquid Argon Calorimeter run

In view of the importance of understanding the performance of an ATLAS wedge, we propose to make a measurement of the response of ATLAS calorimetry, including tracking, in the SPS during 1998. A schematic view of the setup is shown in Figure 10-ii. This common run is meant mostly as a calibration with hadrons.

The two Liquid Argon and Tile barrel calorimeter modules will be mounted on the common platform. The platform is the current Tile Calorimeter scanning table, with an upstream section added to it to support the Liquid Argon detector and cryostat. The design of this support will start in 1997. The table will allow projective scans to be taken with both calorimeters unlike the prior combined runs, where the incident angle was fixed D-8. Thus the focus on the combined run will be to understand the detectors at all values of η. Furthermore, the prototype TRT and Si detectors will be installed in a solenoid magnet just upstream of the Liquid Argon calorimeter, providing additional tracking information.

Due to space limitations, the scan in η is limited at small values, starting at $\theta=5^o$ (η=0.09). The scans can continue through about $\theta=49^o$ (η=1.0), or up to the end of the Liquid Argon calorimeter. In ϕ, no scan will be possible because of mechanical problems. Due to this limitation, the η scans will be done at a fixed ϕ position, and only some small reange scan could be possible using the beam steering magnets.

Our plan with the combined test is a continuation of the work done in the previous combined test beam runs in 1994 and 1996, expanded to include data at all values of η, with both the Liquid Argon and Tile production modules in place. Furthermore, we are considering expanding the scanning table to support an ITC so that its response downstream of the Liquid Argon calorimeter and any dead material can be seen. It is possible that for this measurement, Module 0 may be replaced with two extended barrel Module 0s, with the ITC between them. From these measurements we can thus understand better properties of resolution enhancement and fibre routing.

10.1.4 Low energy response

A concern in reconstructing jet energies and directions involves the inclusion of low energy particles in the jet. We expect most of the jet is comprised of pions with momentum of the order of 1 GeV or so, and the response of the calorimeters to low energy particles is therefore important. It has been seen by UA2 that their calorimeter becomes very non-linear at energies below 1 GeV[A.6]. Also, the ZEUS calorimeter has a uniform response for electrons to very low energies, but the response to pions and protons also becomes non-linear at energies below 1 GeV [A.13].

At low energies, pions become indistinguishable from electrons as they interact in a calorimeter. Therefore for the Liquid Argon calorimeter the low energy measurement is a necessity. While more simulation is needed to understand the error in jet reconstruction if a simple linear calorimeter is assumed at very low energies, and in fact at these low energies what the real impact is from the hadron calorimeter, we reserve a period of time in the PS at CERN to measure the combined response. We expect that this measurement will be done with our 1m prototype calorimeter modules rather than going through the expense of moving the large barrel modules.

10.2 Requirements

Full use of the 85 ton capacity scanning table (see Figure 10-1) which was constructed and used in previous beam tests with Module 0 is foreseen. The design and modification of the table to accommodate the Liquid Argon detector is to be started in 1997. A study to realize the feasibility of extending the table structure to accommodate the Liquid Argon, ITC and Tile Calorimeters should be started in 1997. We require support from the ATLAS DAQ group for the Run Control and acquisition. We also require support from ATLAS for database management in order to track the parameters of the calorimeters. We expect that the elements in the database will consist of module components - scintillator, fibre and absorber - to PMT through high voltage and recorded response. We expect that the acquisition and Run Control will evolve as time goes on and we will require the assistance of CERN to maintain up to date software. The monitoring of the online data is expected to be done on workstations, with software maintained by our collaboration.

The test beam program will also includes tests of the Trigger/DAQ upgrades relevant to our system such as the implementation of the RODs being developed for the Tile Calorimeter. The RODs will replace a subset of the read-out that we will have in the early phases of the program. Furthermore, the trigger will eventually be upgraded to LVL1 and LVL2 prototypes. Thus we, and the DAQ and trigger groups, will gain valuable experience in a real-time environment with these systems.

10.2.1 SPS standalone program

We plan to use for the following years along with the other ATLAS detectors the H8 beam line in the North Area. The basic infrastructure for the needs of our detector exists already, nevertheless some modifications in the experimental area are foreseen needed for the large dimensions of our modules. Source calibrations, laser calibrations and electronics calibrations will naturally need to be performed in conjunction with all data taking. The desired beam line is the H8 one, where the detector infrastructure already exists. Currently our trigger rate is limited by CAMAC read-out speed since, with the 1m prototype modules, we are digitizing all their PMTs with CAMAC ADCs. With the final electronic in place for the modules, the trigger rate will be limited by the number of words read-out, also dependent on whether data compaction will be used. A conservative estimate can be made on our past experience that the trigger rate was of

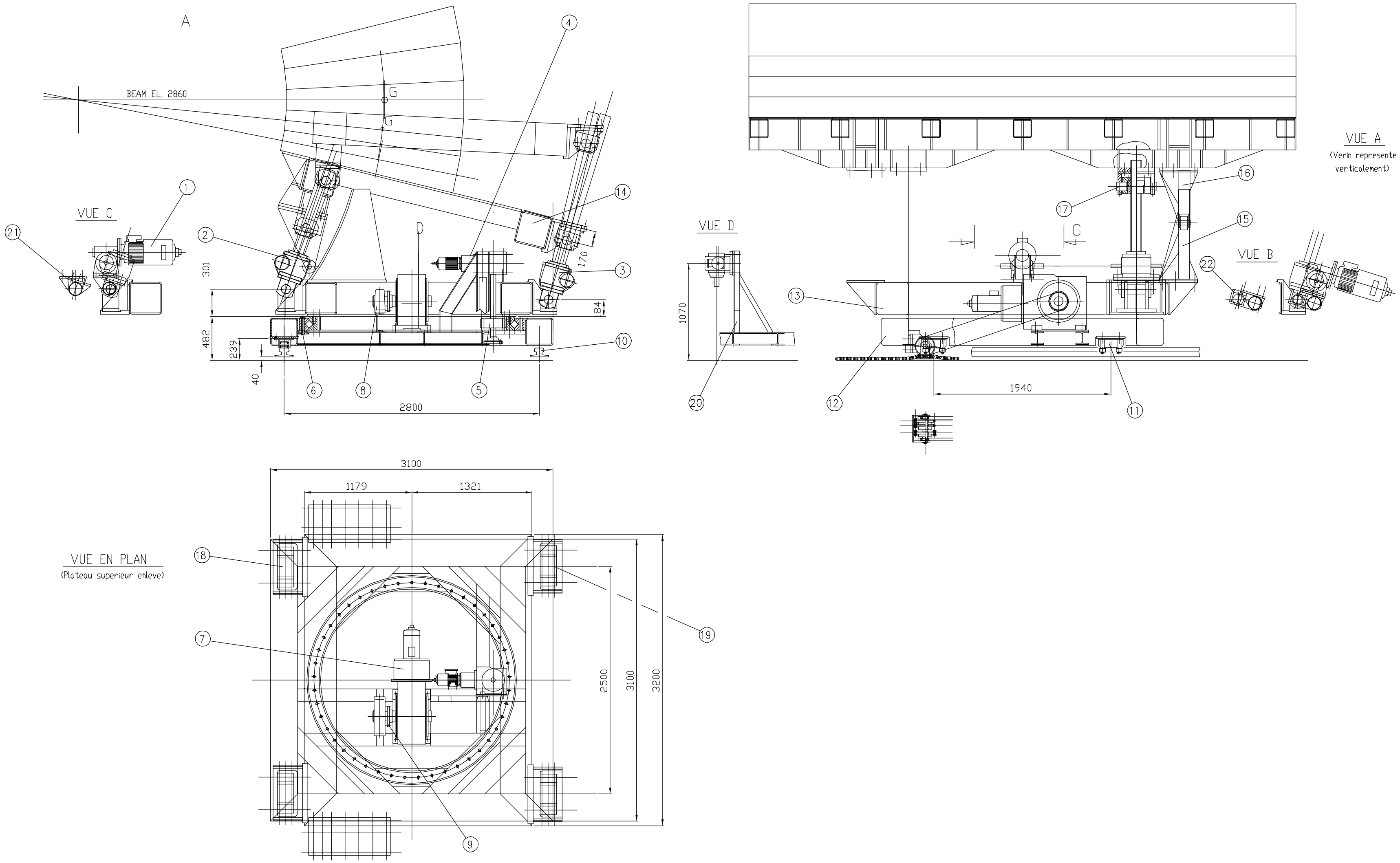

Figure 10-1 The Tile Calorimeter scanning table for the H8 test beam runs. The table is able to house three barrel modules and do 3D movements.

the order of 200/burst. Thus a beam intensity at our detector of a few kHz is sufficient. The resolution of our calorimeters at 300 GeV is about 4%, so that a momentum bite of 1% or less is acceptable.

At energies less than 20 GeV the separation of muons, electrons and pions is essential, and we will require a Cerenkov counter which has minimal noise and good efficiency for μ–π separation. Furthermore at low energies the beam momentum must be calibrated to obtain an absolute value. At 10 GeV and above the momentum is reliable, but at 5 GeV and below, the correlation between bending magnet current and momentum must be verified.

Production modules

We choose to implement our standard program of measuring the calorimeters' response to hadrons and muons. The particular program at the SPS will consist of the following measurements, all to be performed on (ideally, at least) 8 completed production barrel modules and 16 completed production extended barrel modules during the years 2000 through 2002:

- 100 GeV muons perpendicular to the tiles in order to determine light yield and uniformity,
- 100 GeV muon scans along η,
- Muon and pion scans along ϕ,
- Pion η scans at energies between 5 and 400 GeV,
- Pion scans along sub-module boundaries at two or three energies.

We estimate 14 days per module of beam time to complete these measurements. Installation and setup will be performed outside the beam enclosure in the Tile Calorimeter garage position. We estimate 10 days of setup time which will include rigging, cabling and module certification.

Pre-series modules

We wish to implement our standard program of measuring the pre-series Module 0's response to hadrons and muons following foreseen upgrades to the electronics and the optics. This particular program will consist of the measurements described in section "Production modules", all to be performed on one barrel Module 0 and two extended barrel Module 0s during the years 1998 and 1999.

We estimate 21 days of beam time to obtain a complete set of measurements. Installation and setup will be performed outside the beam enclosure in the Tile Calorimeter garage position. We estimate 10 days of setup time which will include rigging, cabling and module certification.

In addition we will continue the monitoring of the pre-series modules for at least 1 week per year well into ATLAS running so we can understand long term stability. Some subset of the run plan as described in "Production modules", will be undertaken to obtain this data. We expect 5 days of setup time to certify module read-out.

Combined Liquid Argon and Tile Calorimeter run

Again we choose to implement a fraction of our standard program of measuring the combined response to hadrons and muons. This particular program at the SPS will consist of the following measurements, all to be performed on the pre-series Tile and Liquid Argon modules in the year 1998:

- 100 GeV muon scans along η.

- Pion energy scans at energies between 5 and 400 GeV.
- Pion scans along sub-module boundaries at two or three energies.
- Measurements made with the tracking detectors inside the solenoid, about 3m upstream from the Liquid Argon cryostat.
- Measurements made with the tracking detectors near the Liquid Argon cryostat, but out of the magnetic field.

We estimate 21 days of beam time to complete these measurements. Installation and setup will be performed outside the beam enclosure in the Tile Calorimeter garage position. We estimate 7 days of setup time which will include rigging, cabling and module certification, and 7 days of cool down time in which we may take some beam.

10.2.2 PS program

The PS program needs the movement of the Liquid Argon calorimeter and a Tile Calorimeter from the SPS to a suitable PS beam line. Both calorimeters must be in a setup such as to simulate an ATLAS wedge, with the Tile Calorimeter downstream of the Liquid Argon detector.

Movement of our production modules or our pre-series Module 0 to the PS is not a reasonable proposal at this time. The transport of modules to the PS from the SPS, along with associated infrastructure is an enormous effort. Therefore we propose to use the stack of the five 1 m prototypes as hadron calorimeter, supported on an easily modified existing stand. These devices will be read-out with CAMAC as they are now. The calorimeter will be positioned just downstream of the Liquid Argon pre-series module. This situation will be analogous to our previous combined running periods.

Since jets are composed of a large component of electromagnetic energy, it is necessary to measure the response of the calorimeters to low energy photons rather than electrons, which interact differently. Thus we anticipate to use a Be target in the beam to create π^os.

We anticipate the following program, all data completed in about 21days:

- Muons at several energies to determine low energy response and monitor calibration,
- Pion energy scans at energies above about 500 MeV,
- Photons or π^os at several energies to understand the electromagnetic component of jets.

Since there is no motion of the Tile Calorimeter relative to the Liquid Argon, there is no need to take more extensive data. The electrons will be completely contained in the electromagnetic calorimeter, so the electron data for the Tile Calorimeter is not of outmost importance.

10.3 Schedule

Referring to the overall Tile calibration and installation schedule, we see a plan for testing the modules through the year 2002, with stability checks planned on Module 0 through the course of ATLAS.

In 1997 we will test the first two pre-series extended barrel Module 0's. In 1998 we will have the ATLAS wedge run, with the Tile Calorimeter in place behind the Liquid Argon Module 0. 1998 and 1999 will allow performance checks of the pre-series modules after undergoing optics and electronics upgrades. In 1999 we expect the PS run will occur. We expect each of these periods to have a 2 week setup and debugging time, with 3 weeks each of beam time.

In the years 2000 through 2002 we expect to calibrate in the SPS our production modules. According to production schedule, the first year will require 4 weeks of beam time, while each of the next two years will require 8 weeks each. Setup is expected to take of the order of 2 weeks, and this can be done outside the beam enclosure in the garage position.

Note that if the Liquid Argon community is not ready for the combined run in 1998 or the installation in the PS is delayed, then we anticipate these measurements will happen in their respective following years.

On a continuing basis, we expect to run beam through barrel Module0 throughout the course of other module calibration. This module will reside on the lower part of the scanning table, and will always be in position for monitoring. After production calibration, we propose to keep Module 0 in the H8 beam line for extended stability monitoring, with beam times of about 1 week per year.

Table 10-1 Summary of beam time requested until 2002 (units are allocated weeks per year with beam).

Beam line/Detector	1997	1998	1999	2000	2001	2002	>2002
SPS H8							
Pre-series Modules	3	3	3	1	1	1	1
ATLAS Common		3					
Production				4	8	8	
PS							
ATLAS Common			3				

11 Project organisation and management

The Tile Calorimeter is one of the ATLAS systems and is therefore organized according to the collaboration rules. Twenty-one institutions with about 200 scientists signing this technical design report constitute the core of this detector. The exact breakdown of this list is presented in Section 11.1. Most of these institutions were part of the R&D phase program RD34 at CERN, and have already cooperated together over the last three years on the construction and testing of various prototype calorimeter modules. In the list of institutions one can see a few large institutions and several medium-sized and small institutions, with an important geographical diversity. Size and geography have been an important factor in laying out the project, such as to optimize the potential of each group. Except for a few special cases, the Tile Calorimeter project represents the major commitment in the ATLAS construction for these groups.

11.1 Participating institutes

Below is a list of all the participating Institutes in the Tile Calorimeter system, listing all physicists and senior engineers committed to the project:

Argonne National Laboratory
E. Berger, R. Blair, J. Dawson, V. Guarino, N. Hill, E. May, L. Nodulman, L. Price, J. Proudfoot, R. Stanek, B. Wicklund
Contact person: L. Price

Institut de Fisica d'Altes Energies, Universitat Autonoma de Barcelona
G. Blanchot, M. Bosman, S. Bravo, M. Cavalli-Sforza, J.A. Crespo, M. Delfino, E. Grauges, Y. Ivanyushenkov, A. Juste, M. Martinez, Ll. Miralles, A. Pacheco, I.C. Park, J.A. Perlas, H. Ruiz, I. Vichou
Contact person: M. Cavalli-Sforza

Bratislava University and Kosice SAS Institute of Experimental Physics
S. Tokar, D. Brunckov
Contact Person: S. Tokar

University of Chicago
K. Anderson, E. Blucher, H. Evans, D. Glenzinski, F. Merritt, M. Oreglia, J. Pilcher, E. Pod, H. Sanders, M. Shochet, F. Tang, A. Turcot
Contact person: J. Pilcher

Institute for Atomic Physics, Bucharest
V. Boldea, S. Constantinescu, S. Dita, D. Pantea
Contact person: S. Dita

Clermont-Ferrand University
Ph. Brette, R. Chadelas, J.-C. Chevaleyre, M. Crouau, F. Daudon, Ph. Grenier, C. Hebrard, G. Montarou, D. Pallin, S. Poirot, G. Reinmuth, L.-P. Says, C. Santoni, F. Vazeille
Contact person: F. Vazeille

CERN
J. Blocki, M. Cobal, I. Efthymiopoulos, O. Gildemeister, A. Henriques, M. Nessi, A. Rios
Contact person: M. Nessi

Dubna JINR
A. Astvatsaturov, J. Budagov, I. Chirikov-Zorin, G. Chlachidze, V. Glagolev, V. Kalinichenko, V. Kolomoets, V. Kovtun, Yu. Kulchitsky, A. Lebedev, O. Lomakina, Yu. Lomakin, S. Malyukov, I. Minashvili, O. Pukhov, V. Romanov, V. Shigaev, N. Russakovich, V. Senchishin, A. Semenov, A. Sissakian, A. Shchelchkov, S. Studenov, N. Topilin, S. Vorozhtsov, V. Vinogradov, J. Sorokina
Contact person: J. Budagov

Institute of Physics, Belarus Academy of Science, Minsk
A. Alifanov, A. Bogush, V. Golubev, Y. Kulchitsky, M. Kuzmin, V. Rumyanstev, V. Shevtsov
Contact person: Y. Kulchitsky

Yerevan Physics Institute
H. Hakopian, V. Grabsky, E. Mnatsakanian, A. Vartapetian
Contact person: H. Hakopian

LIP-Lisbon/Coimbra (U. Lisbon, U. Coimbra, U.C. Fig Foz and U.N. Lisbon)
P. Amaral, A. Amorim, J. Carvalho, E. Casarejos, M. David, A. Gomes, J. Gomes, A. Maio, M. Maneira, J.P. Martins, A. Onofre, J. Pinhao, J. Santos, J. Silva, M.Varanda, H. Wolters
Contact person: A. Maio

Charles University and Czech Technical University, Prague
T. Davidek, J. Dolejsi, Z. Dolezal, R. Leitner, J. Palacky, J. Sodomka, K. Soustruznik, M. Suk, P. Tas, Z. Trka, S. Valkar, J. Walter, M. Zdrazil
Contact Person: R. Leitner

Academy of Sciences of the Czech Republic, Prague
I. Hanak, I. Hruska, M. Hudecek, M. Lokajicek, S. Nemecek, M. Soukup, V. Vrba, J. Weichert, K. Zitek
Contact person: M. Lokajicek

University of Pisa
D. Autiero, G. Bellettini, F. Bosi, V. Cavasinni, S. Cologna, D. Costanzo, A. DeSanto, T. Del Prete, B. Di Girolamo, V. Flaminio, S. Lami, G. Latino, E. Mazzoni, R. Paoletti, F. Raffaelli, G. Renzoni, D. Rizzi
Contact person: T. Del Prete

UFRJ Federal University of Rio de Janeiro
L. Caloba, F. Marroquin, A. Pereira, J.M. Seixas, Z. Thome
Contact person: Z. Thome

Institute for High Energy Physics (IHEP), Protvino
D. Amelin, A. Fenyuk, A. Karyukhin, Yu. Khokhlov, S. Kopikov, M. Kostrikov, V. Lapin, V. Matveev, N. Schalanda, A. Shalimov, S. Sidorov, V. Sidorov, M.Soldatov, A. Solodkov, E. Starchenko, A. Zaitsev
Contact person: A. Zaitsev

Stockholm University
S. Berglund, C. Bohm, E. Johansson, S. Hellman, S. Holmgren, K. JonAnd, B. Sellden, N. Yamdagni, S. Tardell, S. Silverstein
Contact person: S. Holmgren

IFIC, (Instituto de Fisica Corpuscular) Centro Mixto Univ. de Valencia-CSIC, Dept. of Informatics and Electronics (Univ. of Valencia)
J.M. Benlloch, R. Cases, M.V. Castillo, A. Ferrer, I. Gil, V. Gonzalez, E. Higon, J.M. Lopez, J.B. Romance, E. Sanchis, J. Zuniga
Contact person: A. Ferrer

University of Illinois
F. Cogswell, R. Downing, D. Errede, S. Errede, M. Haney, V. Simaitis, J. Thaler
Contact person: S. Errede

Michigan State University
C. Bromberg, J. Huston, R. Miller, R. Richards
Contact person: J. Huston

University of Texas at Arlington
K. De, J. Li, E. Gallas, L. Sawyer, M. Sosebee, R.W. Stephens, A. White
Contact person: K. De

Project Leader: M. Nessi, CERN

11.2 Organisation

The organization of this system unit relies strongly on the good experience of the group during the last three years, which demonstrated a remarkable ability to cooperate effectively. The high degree of cooperation allows the use of a simple management structure, with direct representation and responsibility lines. All operations are organized with direct assignments of responsibilities to the various institutions.

Two dedicated bodies control and organize the interaction of the groups and define all technological steps:

1. **The general meetings and the working groups** where all technical and technological issues are raised and where solutions to the various problems are proposed. Over the last few years we have created several topical working groups, convened by one or two experts in the field, with the mandate to distribute and organize the design and the prototype work necessary. Typically each of these groups meets regularly and reports to the general meeting their progress and proposals. These groups are dynamic structures whose existence is determined by the real needs of the moment. At present the following topical groups are active: mechanics engineering, electronics, test-beam organization, test-beam analysis, Monte Carlo simulations and detector slow control.

   To give an idea how these groups operate one can mention the mechanics group as an example. Typically, one or two engineers plus a few physicists per institution working on Tile Calorimeter mechanics are active in the working group. There the mechanical project evolves and individual assignments are given to each of the engineers for detailed further studies. Each participant reports regularly on his or her progress and discusses details with the working group. Cross-checks are made on any major proposal, and finally, for most of the issues, direct experimental work (prototypes or measurements) is proposed as a final proof. This work is documented in internal technical notes and the major issues are proposed for approval in the general Tile Calorimeter meeting. Typically this sub-group meets the week before the ATLAS meetings. For special issues special meetings are organized. All drawings are then collected by one librarian, certified and redistributed to the collaboration. The convener of this group represents the Tile Calorimeter in more general meetings at the ATLAS level (for example integration meetings) and specifies to ATLAS the needs and requests of our system.

For this initial phase of the project, this mode of operation has proven to be efficient. Several major technological choices have been made without compromising the motivation and the internal relations between groups. In the mass production phase, once all R&D work is finished, the role of these sub-groups will be reformulated and adapted to the new needs. The size of the Tile Calorimeter system is small enough to allow this flexibility.

The work of these groups is regularly presented in the ATLAS general meeting, at every ATLAS week.

2. **Institutes meeting**. The Tile Calorimeter system has decided to combine the functions of a steering group and of the meeting of institute representatives into a single body, as permitted by the ATLAS organization rules. Each institution defines a contact person, who automatically becomes a member of this executive body. At the Institutes meeting, issues raised in the general meetings are discussed and approved. The planning of the work and the sharing of resources and manpower are finalized here, too. This group meets regularly, typically during ATLAS weeks, and takes responsibility for the direction of all the construction work.

   This executive body has proven to be efficient and effective. The merging of the functions of the steering group and the Institutes meeting was motivated by the desirability of having direct visibility of all institutions independently of their size and strength in all executive decisions and operations. In general, all technical expertise is represented at the Institutes meeting, however expert colleagues will be invited to discuss specific points on the agenda. Decisions and organization have so far not needed majority votes, but rather have been made according to a general consensus.

   The present chairperson of this body is the overall **project leader**, whose functions are laid down in the general ATLAS organization rules. The project leader also organizes the general meeting. His or her function, on top of organizing the execution of the projects, deals also with the contact with the rest of ATLAS, in particular the **management of ATLAS** and its **Executive Board**, of which he or she is a member.

   Just before the Technical Proposal presentation and now in view of this Technical Design Report, special meetings have been organized where all responsibilities and commitments have been worked out and shared in detail between the 21 institutions involved.

11.3 Responsibilities and work organization

The construction of the Tile Calorimeter has been worked out with maximal sharing of effort between the various institutions. Our principle philosophy is to rely as much as possible on the expertise of the various participating institutions to execute work and assemble pieces. Some choices, like the one of the scintillators construction, heavily rely on this concept.

Some tasks are nevertheless too big for one single institution; clusters of activities are foreseen for major expenditures such as procurement of the absorber and of the photomultipliers.

Tables 11-1, 11-2 and 11-3 summarize the complex matrix of this sharing. Operations done in this fashion require a substantial amount of coordination and quality control. These responsibilities are primarily those of the project leader and his or her staff.

Table 11-1 Sharing matrix of the construction responsibilities (mechanics).

Activity	Institution
Mechanics:	
Barrel (LB) regional center (module assembly):	*JINR-Dubna*
• sub-module assembly (each 25%)	JINR-Dubna, IHEP-Protvino, Prague
• girder procurement	Bucharest, CERN
• absorber cutting and distribution	JINR-Dubna
• transport to CERN	JIINR-Dubna, CERN
Ext.Bar.(LE1)-regional center (module assembly):	*Argonne*
• sub-module assembly (each 30%)	Argonne, llinois, Chicago.
• ITC sub-module (for both ext. barrels)	U.T. Arlington
• girder procurement	Argonne
• absorber cutting and distribution	Argonne
• transport to CERN	Argonne
Ext.Bar.(LE2)-regional center (module assembly):	*Barcelona IFAE*
• sub-module assembly (each 50%)	Barcelona IFAE, Valencia
• girder procurement	Barcelona IFAE
• absorber cutting and distribution	Barcelona IFAE
• transport to CERN	Barcelona IFAE
Common small items	*CERN*
Calibration tubes for the source system	*IHEP-Protvino*
Calorimeter supports and assembly tooling	*CERN, JIINR-Dubna, Pisa, IHEP-Protvino*
Assembly work in the ATLAS pit	*CERN+ all institutions involved in mechanics*

This mode of operation has been already tested during the Module 0 prototype phase, which will be completed in summer of 1997. For the mechanics, all regional centres labelled in Table 11-1 and 90% of the sub-module assembly plants have participated in this initial phase thus proving their capabilities and, more importantly, putting in place all the needed infrastructure. The number of sub-module assembly plants is driven by the number of sub-modules to be constructed in each location during 3 years of operation (about 300 pieces). This number also optimizes resources and investments for tooling and manpower, and minimizes the risks involved should one of the committed institutions experience some problem. At the time of this writing, we are missing the commitment of one additional institution for the barrel sub-module construction. Negotiations are in progress with one possible candidate and its funding agency.

Table 11-2 Sharing matrix of the construction responsibilities (optics).

Activity	Institution
Optics:	
Scintillator material procurement, including moulds	CERN, IHEP-Protvino, Lisbon
Scintillator construction	IHEP-Protvino
Wrapping material and tooling	Michigan
Scintillator for the gap region	U.T. Arlington
Fibres procurement, preparation, aluminization	Lisbon/Coimbra, Pisa
Fibres profiles and insertion tooling	CERN, Lisbon/Coimbra
Girder rings and installation tooling	Clermont
Fibre bundle tools	Lisbon/Coimbra
Fibre bundle polishing tools	Yerevan
Instrumentation and testing of the barrel modules	CERN, Lisbon/Coimbra, Pisa, Prague, JINR, IHEP, Rio
Instrumentation and testing of ext. barrel A modules	Argonne, Illinois, Michigan, U.T. Arlington, Chicago
Instrumentation and testing of ext. barrel C modules	Barcelona IFAE

The same considerations are valid for the optics and electronics assignments as shown in Table 11-2 and Table 11-3. We have had a very successful outcome with the optical components from all institutions concerned for Module 0 with this endeavour. The scintillators production relies on one single institution, but to minimize the risks involved we successfully exported this technology to two other institutions in Portugal and in the USA. This will give us an effective back-up solution should it become necessary.

The electronics design and responsibilities have been distributed according to Table 11-3 already for the Module 0 construction phase. The electronics design is strongly coupled to other ATLAS systems. In particular, decisions made by the Liquid Argon system and the trigger and DAQ systems impact on the instrumentation the Tile Calorimeter needs of developments. More R&D has still to be done to prove the final technologies, in particular for the pipelines. Our matrix of responsibilities takes these situations into account.

11.4 Planning and milestones

The details of the time schedule for the mechanics, optics, electronics, calibration and installation work are summarized at the end of each chapter in this document. Figure 11-1 summarizes this working plan over the entire construction period. The schedule is constrained by several requirements and conditions. At the early side the end of the pre-series activities, which will be completed in summer 1997, will give the green light to the mechanics construction. At the late end the beginning of January 2003 when the installation in the ATLAS cavern will start, marks

Table 11-3 Sharing matrix of the construction responsibilities (electronics and calibration tools).

Activity	Institution
Electronics:	
PMT blocks:	
• PMT procurement	CERN, Clermont, Illinois, Lisbon/Coimbra, Pisa, Valencia
• PMT magnetic shielding	Yerevan, CERN
• HV dividers	Clermont
• 3-in-1 cards	Barcelona, Chicago, Stockholm
• light mixers	Lisbon/Coimbra, Prague
• mechanical parts of PMT blocks	Clermont, Lisbon/Coimbra
• PMT tests and PMT block assembly	Clermont, Illinois, JINR-Dubna, Pisa, Lisbon/Coimbra, Valencia
Drawers electronics and mechanics:	
• Drawer mechanics	Clermont
• Mother board buses	Chicago, Stockholm
• HV and LV for PMTs	Clermont, Prague
• Digitizing system + pipelines	Chicago, Stockholm, Barcelona
• LVL1 analog tower summation	Rio
• DC digitizing system	Barcelona
• Patch panels	Clermont, CERN
Outside drawer electronics:	
• ROD system and connections	Valencia
• LV power supplies	CERN,Rio
• Slow control hardware	Clermont
Calibration systems:	
• Laser system	Clermont, Lisbon/Coimbra
• Source mechanics, including sensors and sources	Barcelona, CERN, IHEP-Protvino, JINR-Dubna

the completion of the construction program. This leaves a time slot of 4 years for all the construction work, the instrumentation and the testing, plus one year needed for the preassembly of the entire structure on the surface and the final calibration. Starting in 2000, modules will arrive at CERN and will be tested and calibrated. A fraction of these will be exposed to the SPS beam for calibration. About 6000 tons of material will be travelling across Europe and the USA and the impact of shipping schedules on the general schedule is an important consideration.

Several component choices have not yet been finalized and will require further R&D time. This applies in particular to the final selection of the fibres and to the final technology for some of the electronics components. For these cases an early decision is not recommended, since state of the art is always improving and industrial R&D is still in progress. The fibres and the photomultipliers are an example where several industrial companies are actively working on different products and where more time is needed to optimize performance and costs.

While the mechanical work needs an early start, part of the optics and electronics production can still benefit from two years of development. These facts are embedded in our schedule and help us in distributing over time the expenditures and estimating the financing profile.

We summarise in the following table the list of milestones necessary to cope with the schedule presented in Figure 11-1.

Table 11-4 List of milestone for the Tile Calorimeter construction.

1996, September	Module 0 barrel ready for beam tests
1997, July	2 ext. bar. Module0s ready for beam tests
1997, September	start procurement of absorber material
1998, July	start the mechanical construction
1998, September	final choice of the fibre type
1999, March	final choice of the PMT device
1999, April	finish prototype work on the pipeline system
2000, July	first module calibration at the SPS
2002, April	start preassembly work on the surface area
2003, January	start installation inside the ATLAS UXA15
2004, April	start detector final commissioning

11.5 Cost and resources

The resource line for the Tile Calorimeter is divided into two components: material and industrial costs expressed in 1995 CHF, and assembly manpower expressed according to the ATLAS budgeting rules in man/years. These manpower needs account for all technical work done within the participating institutions.

For the Tile Calorimeter the manpower needs are very important and this is so since the beginning of the overall organization and costing of the project. Technical solutions have been adopted to maximize the work done in the institutes and to minimize industrial manpower and related work. The tooling needed to execute the project has been heavily coupled to the existing infrastructure in the involved institutions. This is particularly valid for the engineering expertise which is heavily used in this initial phase of the project.

In 1996, the material and industrial costs have been bounded across the various ATLAS systems in order to keep the overall project inside some realistic financial boundaries. For our particular sub-system, after some steps of optimization of performance and costs, this ceiling has been fixed at 14.750 MCHF. Recently the ATLAS collaboration has decided to upgrade this detector

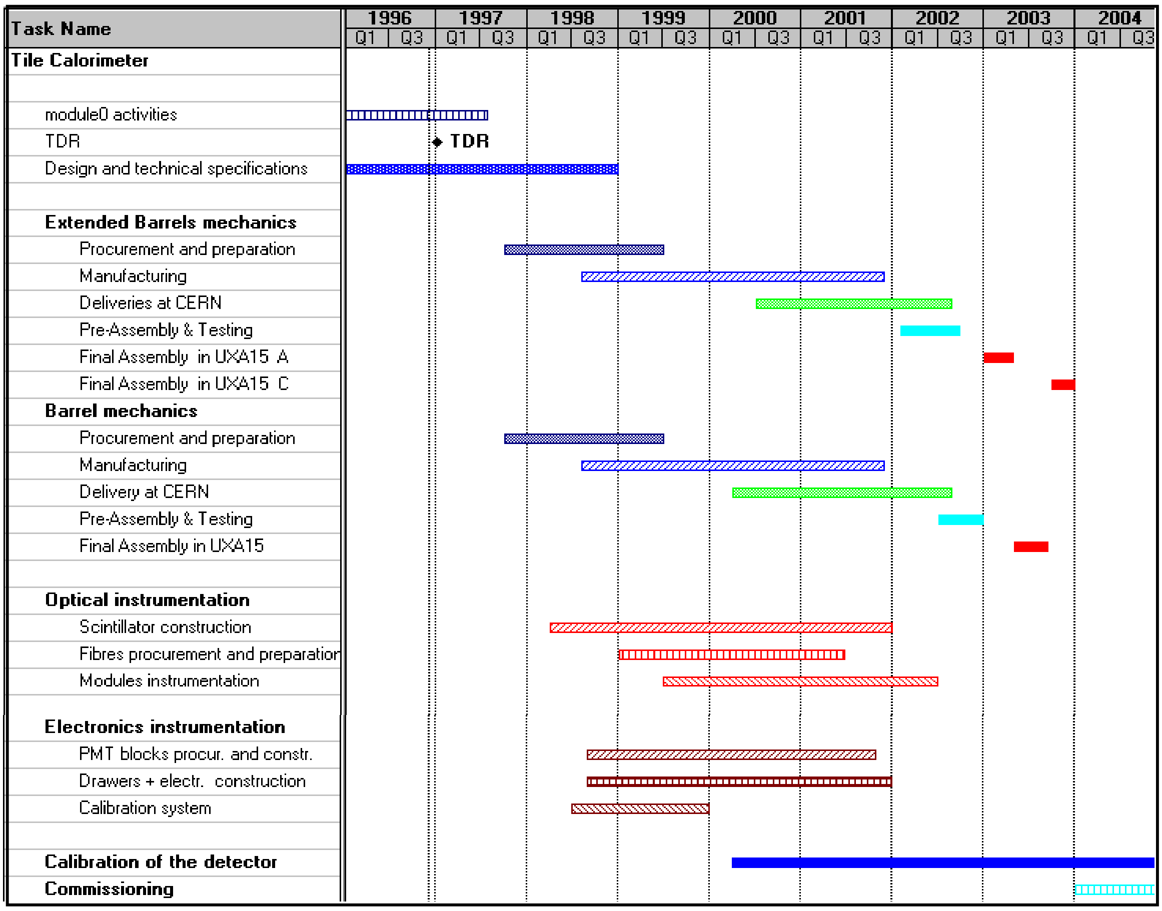

Figure 11-1 Overall schedule for the Tile Calorimeter construction.

with active calorimeter components in the so-called crack and gap region, where the general performance of the ATLAS detector is affected by the presence of dead material and/or space needed for the Liquid Argon Calorimeter read-out electronics and the routing of the inner detector cables and services. This cost should be reabsorbed inside the foreseen ATLAS ceiling.

To handle this situation we have decided to internally define a maximum cost for each of the 3 main activities, as they are indicated in Table 11-5. The details of the exact cost of the various components are presented in the CORE6 costing document. Most of this information has to be kept confidential until all final tendering procedures are completed.

Table 11-5 Cost table for the Tile Calorimeter, summary of the CORE6 document.

Activity	Material and Industrial costs (KCHF 1995)	Institutes manpower (in man/years)	Contingency (KCHF)
Mechanical construction	6665	139	333
Optics instrumentation	1225	60	123
Read-out and calibration system	6845	43	685
total	*14735*	*242*	*1141*

The figures quoted as contingency reflects the level of uncertainty with respect to some technological choices yet to be made. In the mechanics this has to do with the steel cutting procedure and the level of complexity of the final assemby which might require additional hardware. In the optics, the choice of the fibre producer has still to be made and at the end it might just not depend on economical factors. There the quoted value also contains the uncertainty in financing the level of manpower needed for the scintillator production. In the electronics the choices to be made are related to the digitizing and pipeline scheme for which a final experimental evaluation is still to be done.

A resource planning for the Tile Calorimeter has been presented in Annex 4.2 of the **Interim Memorandum of Understanding** (ATLAS RRB-D 96-9,19 March 1996), a document discussed by the **ATLAS Resource Review Board**. At this stage the 21 institutions participating to the construction have the support of their funding agencies to commit themselves to all the items and responsibilities discussed in this TDR. Based on this support the resources available within the community should cover the estimated costs, including the uncertainties expressed in the contingency figure.

A Appendices

A.1 Acronyms and abbreviations

A list of the acronyms and abbreviations used in this document follows in alphabetical order:

ADC	Analog to Digital Converter
ASIC	Aplication Specific Integrated Circuit
ATLAS	A Toroidal LHC ApparatuS
CPU	Central Processing Unit
DAC	Digital to Analog Converter
DCS	Detector Control System
DSP	Digital Signal Processing
EM	ElectroMagnetic calorimeter
FEA	Finite Element Analysis
FIFO	First In - First Out
FWHM	Full Width at Half Maximum
HV	High Voltage
ITC	Intermediate Tile Calorimeter
LB	Tile Calorimeter barrel
LCS	Local Control System
LE	Tile Calorimeter extended barrel
LED	Light Emmiting Diode
LHC	Large Hadron Collider
LSB	Least Significant Bit
LUT	Look-Up Table
LV	Low Voltage
LVL1	First level trigger
MB	Minimum Bias
MCM	Multi Chip Module
MIG	Metal-Inert-Gas
PC	Printed Circuit
PMT	Photomultiplier
ROB	Read-Out Buffer
ROD	Read-Out Driver
SHV	

SMD	Surface Mounted Devices
TDR	Technical Design Report
TIG	Tungsten-Inert-Gas
TileCal	Tile Calorimeter
TTC	Timing, Trigger and Control
UVA	UltraViolet Absorber
WLS	WaveLengthShifting fibres

A.2 Tile Calorimeter in Numbers

A table with the most significant numbers for the Tile Calorimeter detector follows below:

Inner radius	2280 mm
Outer radius	4320 mm total, 3980 active part
Number of modules in ϕ	64
Length in z for each module	barrel: 5640 mm, ext. barrel: 2910 mm
Rapidity coverage:	
barrel:	$-1.0 < \eta < 1.0$
ext. barrel:	$0.8 < \lvert\eta\rvert < 1.7$
ITC	calorimeter: $0.8 < \lvert\eta\rvert < 1.0$ gap scintill : $1.0 < \lvert\eta\rvert < 1.2$ crack scintil: $1.2 < \lvert\eta\rvert < 1.6$
No or readout samplings in radial direction	3 (1.4, 4.0, 1.8 λ accordingly)
Segmentation in $\eta \times \varphi$	0.1×0.1 (0.2×0.1 last samp.)
No. sub-modules/barrel module	19
No. sub-modules/ext. barrel module	10
Height of each standard sub-module	293.2 mm
Designed gap between sub-modules	1 mm
Weight:	
sub-module	~0.9 T
barrel module	~21 T
ext. barrel module	~14 T
Total Tile Calorimeter weight	2900 T
Width of a period (z direction)	18.325 mm
master	5.0 mm
spacer	4.05 mm
No. of periods per module	
barrel	305
ext. barrel	139
ITC	17

No. of tiles in radial direction	11
Scintillating tile thickness	3 mm
Size of tiles	
in the azimuthal direction	200 - 400 mm
in the radial direction	97 - 187 mm
No. of tiles per module	
barrel	3355
ext. barrel	1529
ITC	323
Total number of tiles	~463000
Tile responce uniformity (with masking)	3.3 - 4.5%
Tile attenuation length	38 - 49 cm
Average fibre length:	
barrel	155 cm
ext. barrel	170 cm
ITC	115 cm
Total length of fibres	1062+5% Km
Fibre attenuation length	~310 cm (long component)
No. read-out cells	
barrel module	92
ext. barrel module	28
ITC module	3
No. of fibres per PMT	min: 26, max: 92
Total no. of PMTs	
barrel	5980
ext. barrels	4030
No. of super-drawers	
barrel	128
1 ext. barrel	64
Required PMT quantum eff.	18% at 480 nm
PMT (R5900) char:	
Nominal PMT gain	10^5
Rise time	1.4 ns
HV at nominal gain	665 V
Useful photocathode area	324 mm^2
Length	20 mm
Dark current at nominal gain	< 100 pA

A.3 Tile Calorimeter Documentation

A.3.1 Internal Notes

N-1 *Preliminary results on a iron/scintillator TILES hadron calorimeter.* L. Poggioli, 13-12-1993

N-2 *Study of the effect of the radiation on the TILECAL Barrel Hadron calorimeter to be used in ATLAS.* A.Henriques, 13-12-1993

N-3 *Hadron Calorimeter of ATLAS: Conceptual integration project (preliminary).* A.Surkov, 13-12-1993

N-4 *Calibration of the Scintillator Tile Hadron Calorimeter Prototype for ATLAS*. J. Ivarsson, 21-12-1993

N-5 *Resposa i resolucio d'un prototipus del calorimetre hadronic per al detector ATLAS*. F. Teubert, 10-01-94

N-6 *Preliminary results of the TILECAL hadron calorimeter to be used in the ATLAS experiment.* RD34 Collaboration, 17-01-1994

N-7 *Preliminary results on the ATLAS solenoid magnetic field calculations in presence of hadronic tile calorimeter.* V.Klyuklin and B.Klochkov, 31-01-1994

N-8 *Hadron calorimeter of ATLAS*. A.Surhov, 10-02-1994

N-9 *RD-34 Status Report: Developments for a Scintillator Tile Sampling Hadron Calorimeter with "Longitudinal" Tile Configuration*. M.Nessi, 2-03-1994

N-10 *Response of ATLAS Injection Molded Scintillators*. D.Jankowski and R.Stanek, 18-04-1994

N-11 *Preliminary Technical Specifications for the supply of steel for the ATLAS tile hadron calorimeter.* M.Nessi, 6-05-1994

N-12 *Computer Models for the TILECAL Magnetic Field Distributions*. M.Nessi, 9-05-1994

N-13 *Engineering Design Evaluation of ATLAS Tile-Calorimeter.* N. Hill et al., 30-05-1994

N-14 *Report on Fabrication of ATLAS Hadron Calorimeter Prototype #5 in Dubna.* J. Budagov et al., 02-06-1994

N-15 *ATLAS Tile Hadronic Calorimeter. Mechanical Analysis of Barrel Part*. H. Gerwig, 15-06-1994

N-16 *Tilecal Module Assembly Proposal*. J.Blocki et al., 24-06-1994

N-17 *Hadron calorimeter of ATLAS.* A.Surkov, 24-06-1994

N-18 *Tilecal Magnetic Field Simulation.* M.Nessi, F.Bergsma, 24-06-1994

N-19 *Measurements of light output of TILECAL scintillators and fibres.* S.Nemecek, R.Leitner, 24-06-1994

N-20 *Argonne Mechanical Design proposal for the ATLAS Hadron Calorimeter.* N. Hill, 24-06-94

N-21 *TILE Calorimeter Module Assembly. JINR-DUBNA Group Proposal.* V.Romanov, N.Topilin, 07-07-1994

N-22 *General behaviour of the ATLAS solenoid magnetic field calculated with the modified CERN POISSON package.* V.Klioukhine, B.Klochkov, 15-08-1994

N-23 *B-meson tagging improvement using HCAL information,*.J.Budagov et al., 21-09-1994

N-24 *Measurements of TILECAL scintillators*,.A.Amorim et al., 22-09-1994

N-25 *Study of molded scintillator radiation hardness.* A.Karyukhin et al., 03-10-1994

N-26 *Estimation of the magnetic field in PM-cavities and tiles of the ATLAS tile-calorimeter.* F.Bergsma, 04-10-1994

N-27 *A Study of the Response Uniformity of the Injection Molded Scintillator Tiles for the TILECAL Calorimeter.* J.Proudfoot, 24-10-1994

N-28 *Mechanical Tolerances and their Effect on the Assembly of the ATLAS Tile-Cal Hadron Calorimeter.* N.F.Hill and E.Petereit, 25-10-1994

N-29 *Technical Specification for Plate Fabrication for the ATLAS Tile Hadron Calorimeter.* N.F.Hill, 25-10-1994

N-30 *Technical Specification for Steel for the ATLAS Tile Hadron Calorimeter.* N.F.Hill, 25-10-1994

N-31 *Stress State Estimations for the Premodule of Tilecal.* J.Blocki, 07-11-94

N-32 *Dimensions and Tolerances of the Premodule.* J.Blocki, 01-11-1994

N-33 *TILECAL Data Acquisition System for the ATLAS Test Beam Experiments.* R.Arsenescu, 16-11-1994

N-34 *Comparative Measurements of WLS Fibers.* M.David et al., 28-11-1994

N-35 *Support Girder Design for the ATLAS Hadron Calorimeter.* N.Hill et al., 16-11-1994

N-36 *ATLAS Tile Hadron Calorimeter Module Assembly Design.* J.Budagov et al., 02-12-1994

N-37 *ATLAS Tile Hadron Calorimeter Installation Procedure.* N.Krjakov et al., 12-12-1994

N-38 *Ponderomotive Force Calculations for the TileCal.* M.Nessi et al., 14-12-1994

N-39 *The Tilecal laser monitoring.* Z.Ajaltouni et al., 06-12-1994

N-40 *The measurements of magnetic field effects on scintillating tiles.* J.M.Chapuis et al., 15-12-1994

N-41 *The Tilecal 3-in-1 PMT Base concept and the PMT block assembly.* Z.Ajaltouni et al., 06-12-1994

N-42 T*he magnetic field studies of the Tilecal PMTs.* Z.Ajaltouni et al., 06-12-1994

N-43 *The drawer system concept for the ATLAS Tilecal readout.* Z.Ajaltouni et al., 31-12-1994

N-44 *Cell Intercalibration and Response Uniformity Studies Using a Movable Cs137 Source in the TILECAL 1994 Prototype.* G.Blanchot et al., 20-12-1994

N-45 *Long Term Monitoring of Tilecal Response in ATLAS: Design Considerations.* G.Blanchot et al., 20-12-1994

N-46 *Energy calibration of jets in the ATLAS Barrel Calorimeter.* A.Astvatsaturov et al., 12-12-1994

N-47 *Module Strap Tests and How they Effect the 25 cm Stack Construction.* N.F.Hill, 30-01-1995

N-48 *Measurements of WLS fibres.* B. Di Girolamo, 20-02-95

N-49 *Measurements of new Pol.Hi.Tech. WLS fibres.* B. Di Girolamo, 20-02-95

N-50 *Influence of the TileCal Parameter Modifications on the B-field.* M.Nessi, 03-05-1995

N-51 *Technical Specifications for the supply of steel for the ATLAS tile hadron calorimeter.* ATLAS Tilecal collab., 26-05-1995

N-52 *ATLAS Barrel Hadron Calorimeter: Module Assembly and Tooling Design Description.* J.Budagov et al., 26-05-1995

N-53 *The measurement of energy loss of 150 GeV positive muons in iron with the TILECAL prototype.* R.Leitner, 14-08-1995

N-54 *Calculation of the ATLAS magnetic field.* F.Bergsma, 16-08-1995

N-55 *CERN/LHCC 95-44 LRDB status report RD34, 16 August 1995.* RD-34 Collaboration, 16-08-1995

N-56 *Application of a real-time data processing VME module using a custom high speed I/O multiport board to "ATLAS Tile-Cal Read Out Driver".* V. Gonzalez, E. Sanchis, 29-08-1995

N-57 *Several aspects of the WLS fibre measurements. Measurements of spliced fibres.* B.Di Girolamo + E.Mazzoni, 08-09-1995

N-58 *Contribution to the ATLAS B-field 3D Model.* S.Vorozhtsov + I.Titkova, 11-09-1995

N-59 *Magnetic Property Measurements of Steel for TileCal.* V.Kalinichenko S.Fedorenk, 11-09-1995

N-60 I*mprovement in pi/mu separation at low pT in ATLAS hadron calorimeter using artificial neural networks technique.* (Updated 13 October 1995) A.Astvatsaturov et al., 11-09-1995

N-61 *Charge Collection Time from Scope Data Acquisition.* F.Marroquim and J.Seixas, 11-09-1995

N-62 *Low pT Muons in B-jets in ATLAS Tilecal.* J.Budagov et al., 11-09-1995

N-63 *Scintillator detector "Mu-wall" for measurement of charged particles leakage from the TILECAL prototype.* M.Lokajicek et al., 11-09-1995

N-64 *Measurement of pion showers longitudinal leakage in the TILECAL prototype.* M.Lokajicek et. al., 25-10-1995

N-65 *Measurements of scintillating tiles.* B.Di Girolamo and E.Mazzoni, 25-10-1995

N-66 *An Optical Model for the Prototype Module Performance from Bennch Measurements of Components and the Test Module Response to Muons.* J.Proudfoot and R.Stanek, 25-10-1995

N-67 *Analysis results of the first combined test of the LArgon and TILECAL barrel calorimeter prototypes.* M.Cobal et al., 22-11-1995

N-68 *The Muon energy losses in the Tile calorimeter.* A.Henriques et al., 23-11-1995

N-69 *Analysis of the hadronic performance of the TILECAL prototype calorimeter and comparison with Monte Carlo.* A.Juste, 29-11-1995

N-70 *First Study on the Angular Resolution of Hadronic Showers with the Combined LAr and Tile Calorimeters.* H.Plothow-Besch, 27-11-95

N-71 *Effect of the Tile Calorimeter thickness in the ATLAS Barrel Calorimeter Performance.* M.Bosman et al., 14-12-1995

N-72 *Electron Response and e/h Ratio of ATLAS Iron-Scintillator Hadron Prototype Calorimeter with longitudinal Tile Configuration.* J.A.Budagov et al., 02-02-1996

N-73 *Numerical Calculation of the Sampling Variation Intrinsic to the TileCal Sintillator Geometry.* C.Padilla & J.Proudfoot, 10-04-1996

N-74 *Absorber Plates Precision Laser Cutting for ATLAS Hadron Barrel Calorimeter 0-module.* B.Alikov et al., 10-04-1996

N-75 *H1-inspired analysis of the 1994 combined test of the Liquid Argon and Tilecal calorimeter prototypes.* M.P.Casado et al., 05-06-1996

N-76 *Experimental Study of the Effect of Hadron Shower Leakage on the Energy Response and Resolution of ATLAS Hadron Barrel Prototype Calorimeter.* J.A.Budagov et al., 05-06-1996

N-77 *Identification of b-jets with a low pT muon using ATLAS Tile Calorimeter simulation data and artificial neural networks technique.* A.Astvatsaturov et al., 31-07-1996

N-78 *Low Dose rate effects in scintillating and WLS fibers by ionizing radiation.* M. J. Moura David, 28-08-1996

N-79 *High Voltage Source For the TILECAL Hadron Calorimeter of the ATLAS Detector.* R.Chadelas et al., 13-09-1996

N-80 *Phi-scan with pions and muons - Analysis of TILECAL test beam data.* P.Amaral et al., 13-09-1996

N-81 *Measurements of Some Optical Properties of the Tiles for Module 0.* M.Cobal et al., 13-09-1996

N-82 *A Charge Injection System for the TileCal CAEN ADCs.* J.Dawson et al., 13-09-1996

N-83 *Results of test linearity of 10-stages and 8-stages R5900 PMTS.* G.Montarou et al., 13-09-1996

N-84 *Dose rate effects in WLS fibers.* M.David, A.Gomes, A.Maio, 13-09-1996

N-85 *An overview of the ATLAS TILECAL hadronic calorimeter.* B.Di Girolamo TILECAL Collab, 14-10-1996

N-86 *Injection modling scintillator for ATLAS Tile calorimeter.* A.Karyukhin et al., 14-10-1996

N-87 *Manipulation tool for TILECAL submodules.* J.Dolejsi,J.Palacky,P.Tas, 14-10-1996

N-88 *The First Three TILECAL Submodule Assembly in Prague.* I.Hruska et al., 14-10-1996

N-89 *Test of Module 0 fibres.* T.Del Prete et al., 14-10-1996

N-90 *Auxiliary Technology Equipment Calorimeter Module and Submodule Manipulations and the Quality Control of the Assembled Module.* J.Budagov et al., 14-10-1996

N-91 *Single vs. Double Clad Fibres (MonteCarlo Simulation).* D.Costanzo, T.Del Prete, 28-10-1996

N-92 *Comparison between the ATLAS/TileCal hadron barrel calorimeter prototype test beam data and Hadronic Simulation package.* I.Efthymiopoulos, 28-10-1996

N-93 *Optical fibre connectors for the laser calibration system.* K.Aitamar et al., 28-10-1996

N-94 *ATLAS Barrel Hadron Calorimeter 0-Module Assembly technology.* J.Budagov et al., 28-10-1996

N-95 *Systematics of WLS fibres with UV absorber.* M.David et al., 09-12-1996

N-96 *State of the art of (green) WLS fibres.* A. Maio et.al., 09-12-1996

N-97 *Characterization of the new R5900 Hamamatsu photomultiplier in Pisa..* P. Beschatnov et. al., 09-12-1996

N-98 *The procurement of the steel absorber for the TileCal barrel Module 0.* T. Davidek et. al, 09-12-1996

N-99 *Energy leakage measurement in TileCal using the scintillating detectors "Muon Walls".* T. Davidek et. al., 09-12-1996

N-100 *TileMon user manual* I. Efthymiopoulos et al., 10-12-1996

N-101 *AtMon user manual* S. Solodkov et al., 10-12-1996

N-102 *Monte Carlo for Module 0 simulation* M.Nessi et. al, 10-12-1996

N-103 *Muon Walls Setup in the TileCal Module 0 Beam Test* C.Bromberg et al., 16-12-1996

N-104 *Qualiry Control of WLS fibers for the TileCal/ATLAS detector* M. David et al, 17-12-1996

N-105 *Insertion of the fibres in the TileCal Module 0.* A. Gomes et al., 08-11-1996

N-106 *Barrel read-out cell geometry (Module 0 implementation).* A. Gomes et al, 20-11-1996

N-107 *Routing of the fibres in Module 0.* A. Gomes et al., 23-11-1996

N-108 *Characterization of the HamamatsuR5900 photomultipliers at Clermont for the Tile Calorimeter.* G. Montarou et al., 20-12-1996

A.3.2 ATLAS/Tile Calorimeter documents

D-1 ATLAS Collaboration, CERN/LHCC/94-93, *ATLAS Technical Proposal for a General-Purpose pp experiment at the Large Hadron Collider CERN*, CERN, Geneva, Switzerland.

D-2 *Interim Memorandum of Understanding*, ATLAS RRB-D 96-9, 19 March 1996

D-3 M. Bosman et. al. (RD34 Collaboration), *Developments for a scintillator tile sampling hadron calorimeter with "longitudinal" tile configuration.* CERN/DRDC/93-3 (1993)

D-4 F.Ariztizabal et al., (RD34 Collaboration) *Construction and perofrmance of an Iron-scintillator hadron calorimeter with longitudinal tile configuration.* Nucl. Instrum. Methods **A349** (1994) 384

D-5 E. Berger et al., (RD34 Collaboration), *Construction and Performance of an Iron-Scintillator Hadron Calorimeter with Longitudinal Tile Calorimeter Configuration*. CERN/LHCC 95-44, , CERN, Geneva, Switzerland.

D-6 Berger et al. (RD34 Collaboration), *A measurement of the energy loss spectrum of 100 GeV muons in iron.* CERN/PPE/96-115, 1996, CERN, Geneva, Switzerland. Accepted for publication in Z. Phys.

D-7 Z. Ajaltouni et al., ATLAS TileCal Collaboration, *Responce of the ATLAS Tile Calorimeter Prototype to Muons,* CERN/PPE 173-96, CERN Geneva Switzerland. Accepted for publication in NIM

D-8 Z. Ajaltouni et al., ATLAS Collaboration (Calorimetry and Data Acquisition), *Results from a combined test of an electromagnetic Liquid Argon calorimeter with a hadronic scintillating Tile Calorimeter.* CERN-PPE/96-178, CERN Geneva Switzerland. Accepted for publication in NIM.

A.4 References

[A.1] F. Sculli, Calorimeter Workshop, May 1975, Fermilab, USA.

[A.2] R.V. Jagatspagyan, M.T. Filippov. Radiation of Halogen-containing Organic Compounds. Moscow 1978.

[A.3] U. Amaldi, Phys. Scripta **23** (1981) 409.

[A.4] E.N.Ramsden, A-Level Chemistry, Stanley Thornes Ltd, 1985; T.L.Brown, H.E.Lemay jr, Chemistry the Central Science, Prentice Hall, 1981

[A.5] R.Delyatickaya et al., Optical and Scintillation Materials, Proc. of Kharkov Institute of Monocrystals, N.9, p. 109, Kharkov, 1982

[A.6] A. Beer et al., Nucl. Insr. and Meth. **A224** (1984) 360

[A.7] R. Wagner et al., CDF Note 374, 1986

[A.8] F.S. Merrit et al., Nucl. Instr. and Meth. **A245** (1986) 27

[A.9] A. Bernstein et al., Nucl. Instr. and Meth. **A262** (1987)

[A.10] R. Wigmans, Nucl. Instr. and Meth. **A259** (1987) 389.

[A.11] R. Wigmans, Nucl. Instr. and Meth. **A265** (1988) 273

[A.12] H1 Calorimeter group, W. Braunschweiget al., *Results from a test of a Pb Fe Liquid Argon Calorimeter*, DESY internal report, DESY 89-022 (1989)

H.P. Wellish et al., *Hadronic Calibration of the H1 Lar Calorimeter using Software Weighting Techniques*, MPI-PhE/94-03, H1-02/94-346 (1994)

H1 Calorimeter group, B.Andrieu et al., *Results from Pion Calibration Runs for the H1 Liquid Argon Calorimeter and Comparisons with Simulations*, DESY internal report, DESY 93-047 (1993)

[A.13] A. Andersen et al., Nucl. Instr. and Meth. **A290** (1990) 95 .

[A.14] E. Huges, Proceedings of the First Int. Conf. on Calorimetry in HEP, p. 525, 1990, FNAL, Batavia, USA.

[A.15] F. Barreiro et al., Nucl. Instr. and Meth. **A292** (1990) 259

[A.16] D. Green et al., *Depth requirements of SSC calorimeter*s, Solenoidal Detector Collaboration Note SDC-91-16, 1991, Dallas, USA.

[A.17] E.C.Dukes and J.White, FNAL report (1990)

[A.18] V.Semenov, Proc. of the IX Conf. on Scintillators, p.86, Kharkov, 1986; M.Kaykov et al., preprint JINR 13-90-16, Dubna, 1990

[A.19] D. Acosta et al., Nucl. Instr. and Meth. **A308** (1991) 481

[A.20] O.Gildemeister, F.Nessi-Tedaldi and M.Nessi, Proc. 2nd Int. Conf. on Calorimetry in HEP, Capri, 1991

[A.21] J. Kruger, Nucl. Instr. and Meth. **A315** (1992) 311, U. Behrens et al., Nucl. Instr. and Meth. **A339** (1994)498, I. Ambats et al., Nucl. Instr. and Meth. **A323** (1992) 611

[A.22] A. Beretvas and J. Freeman, Fermilab-SDC-100, (Feb. 1992)

SDC Technical Design Report, SSCL-SR-1215, (April, 1992)

[A.23] P. Aurenche et. al. Phys. Rev. **D45** (1992) 92

[A.24] D.E. Groom, Proc of the *II International Conference on Calorimetry in High Energy Physics,* (ed. A. Ereditato) World Scientific (1992) 376

[A.25] L.Hu et al., SDC note 91-119, 1991; A. Byon-Wagner, Radiat. Phys. Chem., Vol 41, 1993; SDC Technical Design Report, SDC-92-201, SSCL-SR-1215, 1992

[A.26] R. Brun and F. Carminati, *"GEANT Detector Description and Simulation Tool"* , CERN Program Library, Long Writeup W5013, September 1993.

[A.27] M. Aalste et al. (RD5 Collaboration), Z. Phys. **C60** 1 (1993)

[A.28] A. Fasso', A. Ferrari, J. Ranft and P.R. Sala, Proc. of the 2nd workshop on Simulating Accellerator Radiation Environment, SARE-2, CERN Geneva, October 9-11, 1995, Yellow Report CERN in press.

M. Aalste et al. (RD5 Collaboration), CERN-PPE/95-61

A. Bernstein et al., Nucl. Instr. and Meth. **A336** (1993) 23

[A.29] F.Coninckx et al., Nucl. Instr. and Meth. **B83** (1993) 181

[A.30] A.Benvenuti et al., Prototype design, construuction and test of a Pb/scintillator sampling calorimeter with wavelength shifter fibre optic readout, IEEE Transactions on Nuclear Science, 40 (1993) 537

[A.31] A.Amorim et al., Study of the effect of radiation on a TILECAL hadron calorimeter intended to be used in ATLAS Experiment on the Barrel region, Atlas Internal Note CAL-No-021, 1993

[A.32] F.W. Bopp et. al. Phys. Rev. **D49** (1994) 3236

[A.33] A. Fasso et. al. Proc. IV Int. Conf. on Calorimeters and their Applications, World Scientific, Singapore (1994) p. 493

[A.34] Tentative Data Sheet on R5900 PMT (Hamamatsu, October 1994)

[A.35] Ph.Brette and S.Poirot, “Light guide simulation”, Tilecal general meeting TILECAL-TR-005 (1994)

[A.36] A. Bodek and P. Auchincloss, Nucl. Instr. and Meth. **A357** (1995),292

[A.37] K. Anderson, et al.: *“A Low Noise, High Rate Shaper for the Tilecal Detector”,* delivered at the First Workshop on Electronics for LHC Experiments, Lisbon, September 1995.

[A.38] P.Amaral, graduation thesis, F.C.Univ. Lisbon, 1995

[A.39] The Large Hadron Collider Conceptual Design Report, CERN/AC/95-05(LHC)

[A.40] Ph. Brette, Clermont-Ferrand thesis (1996)

[A.41] S.Poirot, Clermont-Ferrand thesis (December 1996)

[A.42] M. Bosteels, Proceedings of the Weldec Conference, Lausanne (October 1996)

[A.43] Trigger & DAQ Interfaces with Front-End Systems: Requirement Document. Version 1.0. ATLAS Trigger-DAQ Steering Group. 22 January 96

[A.44] HDPM 1012/1014 Low Cost Gigabit Rate Transmit/Receive Chip Set Technical Data Sheet. Hewlett Packard

[A.45] The S-Link Interface Specification. Owen Boyle, Rober McLaren and Erik van der Bij. ECP Division. CERN. 29 May 1996

[A.46] GOST 20282-26, Moscow

[A.47] S.J.Alvsvaag et al., The performance of the DELPHI STIC detector at LEP, to be published in Proceedings of the VI International Conference on Calorimetry in HEP, Frascati, Italy, 1996.

[A.48] J.Silva, graduation thesis, F.C.Univ. Lisbon, 1996

List of Figures

List of Tables

This document has been prepared with Release 5 of the Adobe FrameMaker® Technical Publishing System using the Technical Design Report template prepared by Mario Ruggier of the Information and Programming Techniques Group, ECP Division, CERN, according to requirements from the ATLAS collaboration.

To facilitate multiple author editing and electronic distribution of documents, only widely available fonts have been used. The principal ones are:

Running text:	Palatino 10.5 point
Chapter headings:	Helvetica Bold 18 point
2nd, 3rd and 4th level headings:	Helvetica Bold 13, 11.5 and 10.5 point respectively
Figure and table captions:	Helvetica 9 point